The high energy properties of the Galactic X-ray binary population, as seen with the Fermi Large Area Telescope

HARVEY, MAX

The high energy properties of the Galactic X-ray binary population, as seen with the *Fermi* Large Area Telescope

Max Harvey

A thesis presented for the degree of

Doctor of Philosophy

Centre for Advanced Instrumentation

The University of Durham

United Kingdom

September 2022

The high energy properties of the Galactic X-ray binary population, as seen with the *Fermi* Large Area Telescope

Max Harvey

Abstract

The *Fermi* Large Area Telescope (*Fermi*-LAT) is a space instrument which has been in orbit since June 2008, and is sensitive to photons from 30 MeV to approximately 1 TeV. I use the *Fermi*-LAT data, alongside X-ray and optical data to perform an investigation of the high energy γ-ray properties of the X-ray binaries, stellar systems where either a neutron star or a black hole is in a close orbit with a main sequence star. The complex case of the low mass X-ray binary, V404 Cygni, is looked at; it is determined that there is no evidence for γ-ray emission from this system. The majority of the remaining Galactic X-ray binary population is then surveyed, and evidence for γ-ray emission is found from 5 systems: the high mass X-ray binaries SAX J1324,4-6200, GRO J1008-57, 1A 0535+262 and RX J2030.5+4751 and the low mass X-ray binary GS 1826-238. There are a number of additional systems where spatially coincident γ-ray excesses are identified, however evidence to associate these with their respective X-ray binaries is weak. I examine these systems alongside the X-ray binaries with known γ-ray emission and determine that γ-ray emission in high mass X-ray binaries is highly dependent on orbital phase, and X-ray accretion state so that many undetected systems may be weakly emitting transients. In the case of the low mass systems, I determine that these are nearby sources, and that almost all are known transitional millisecond pulsars. Future observatories such as CTA, SWGO and AMEGO are likely to discover more γ-ray emitting X-ray binaries, and these facilities are discussed.

Supervisors: Professor Paula Chadwick and Doctor Cameron Rulten

Acknowledgements

The list of people who have supported me with this thesis and my wider research, both directly and indirectly, is long; obtaining a PhD at any time is a journey, however obtaining one in the midst of a global pandemic has presented unique stresses and challenges. First and foremost, I need to thank my supervisors, Paula Chadwick and Cameron Rulten for their immeasurable help. Paula has always been there to listen and encourage my ideas (both good and ridiculous), and has always had confidence in me, even when I didn't have very much confidence in myself. Meanwhile, Cameron has always provided me with the three things a PhD student needs to succeed, coding advice, coffee and beer, all at the appropriate times. I genuinely couldn't have asked for better supervisors at all, so thank you.

It isn't hyperbolic to say that the Durham γ-ray astronomy group is arguably the best possible working environment imaginable, filled with some of the friendliest scientists one could hope to meet. I want to thank Anthony Brown and Jamie Graham for their ever useful advice. Patrick Stowell deserves a shout out because I now know far more about neutrons than I ever thought I would, and for being an all-round great bloke. I also want to thank Tim Roberts and Jamie Holder for their fantastic feedback on this thesis, and for making my viva voce a thoroughly enjoyable experience. Finally, I want to thank the gents with whom I have shared an office; Atreya, Alberto, Amrit, and Sheridan, I struggle to find the words to describe how much fun I've had with you all in the last 4 years and I still don't remember what happened after that conference dinner in Bologna.

I want to thank a list of other people who have been really helpful during the last 4 years: Chris Done, Alastair Edge, Ste O'Brien, John Quinn, Liz Hays, Julie McEnery, Alyson Joens, Michael Daniel, Greg Foote, Chiara Giuri, Gareth Hughes and Wystan Benbow. In addition, Vicky Fawcett, Jack Birkin, Jack Acton, Cameron Grove, Ellen Sirks, Jake Mitchell, Ed Elliott, Amy Etherington,

Joaquin Armijo-Torres, Jamie Davies, Lea Heckmann and Manika Sidhu, you have all made the last 4 years extremely entertaining, so thank you.

Maybe the real PhD is the friends we make along the way?

Outside of the academic sphere, a number of my family and friends deserve thanks too. My Mum (and Mark) for basically helping me with anything at all I've needed for the 8 years I've been at university, my Dad and second Mum, Nicola, for constant encouragement and my Auntie Carol and Uncle Kev for bringing me two large bottles of strong Belgian beer every time I publish something. I want to thank my friends as a whole, but particularly Matthew Capewell, who has helped and advised on every project I have done as part of my PhD. I guarantee he has the most experience of high energy γ-ray astronomy out of anyone in the UK tourism industry. I also want to thank Holly Telfer for her help in getting me a real job, and Tom Dutton for all the fwehs and gwehs.

Finally, and most of all, I need to thank my fiancée, Florence. We have come a very long way since I began this journey; we've bought a house, adopted three cats, endured lockdowns and social restrictions and both grown immeasurably during this time. Florence has guided, advised and supported me through professional and personal challenges whilst obtaining my PhD; she has defended me against others and has told me when I've been wrong. I've grown a lot in the last four years, and I think I've grown for the better because of Florence's love and support. There is truly nothing I can say to express how grateful I am to be with you.

I dedicate this thesis to my Grandmother, Betty Harvey, who can finally say that there is a doctor in the family. Her endless wit, sense of humour and energy is an inspiration to us all.

'Gentile or Jew
O you who turn the wheel and look to windward,
Consider Phlebas, who was once handsome and tall as you'
- The Wasteland, IV: Death By Water
- T.S. Eliot

Contents

Declaration

The work in this thesis is based on research carried out at the Centre for Advanced Instrumentation, Department of Physics, University of Durham, England. No part of this thesis has been submitted elsewhere for any other degree or qualification, and it is the sole work of the author unless referenced to the contrary in the text.

Some of the work presented in this thesis has been published in journals and conference proceedings - the relevant publications are listed below.

Publications

Harvey et al. (2020), *A search for γ-ray emission from a sample of local Universe low-frequency selected radio galaxies*, Monthly Notices of the Royal Astronomical Society, Volume 496, Issue 1, pp.903-912

Harvey et al. (2021), *The X-Ray Binary Population With Fermi-LAT*, Proceedings of the 37th International Cosmic Ray Conference, PoS(ICRC2021)395, DOI: https://doi.org/10.22323/1.395.0621

Harvey et al. (2021) *V404 Cygni with Fermi-LAT*, Monthly Notices of the Royal Astronomical Society, Volume 506, Issue 4, pp.6029–6038

Harvey et al. (2022) *The Galactic high mass X-ray binary population with Fermi-LAT*, Monthly Notices of the Royal Astronomical Society, Volume 512, Issue 1, pp.1141–1168

List of Figures

List of Tables

List of Terminology

3FGL The 3rd *Fermi*-LAT point source catalogue

4FGL The 4th *Fermi*-LAT point source catalogue

AAVSO American Association of Variable Star Observers

ACD Anti-Coincidence Detector

AGILE Astro-Rivelatore Gamma a Immagini Leggro (Lightweight Astro-Imaging Gamma Detector)

AGN Active Galactic Nucleus

AMEGO All-sky Medium Energy Gamma-ray Observatory

BAT Burst Alert Telescope (on *Swift*)

BATSE Burst and Transient Source Experiment (on CGRO)

BH Black Hole

BII Galactic Latitude

CCD Charge Coupled Device

CGRO *Compton* Gamma-ray Observatory

CMB Cosmic Microwave Background

CNO Carbon Oxygen Nitrogen (Cycle)

COMPTEL Imaging Compton Telescope (on CGRO)

CTA Cherenkov Telescope Array

CV Cataclysmic Variable (Star)

Dec Declination

DR Data Release

EDF Empirical Distribution Function

EGRET Energetic Gamma-ray Experiment (on CGRO)

EM Electromagnetic

ESA European Space Agency

eV Electronvolt

evclass Photon Event Class

evtype Photon Event Type

fits Flexible Image Transfer System (File Type)

FSRQ Flat Spectrum Radio Quasar

FWHM Full width at half maximum

GBM Gamma Burst Monitor (on *Fermi*)

GLAST Gamma-ray Large Area Space Telescope

GRID Gamma-ray Imaging Detector (on AGILE)

GTI Good Time Interval

HDU Header Display Unit

HAWC High Altitude Water Cherenkov Experiment

HEALPIX Hierarchical Equal Area Isolatitude Pixelisation

H.E.S.S. High Energy Stereoscopic System

HMXB High Mass X-ray Binary

IACT Imaging Atmospheric Cherenkov Telescope

IBIS Imager on-board INTEGRAL

IC Inverse Compton (Scattering)

IMF Initial Mass Function

IMXB Intermediate Mass X-ray Binary

INTEGRAL International Gamma-Ray Astrophysics Laboratory

IR Infrared

IRF Instrument Response Function

JEM-X Joint European X-ray Monitor (on INTEGRAL)

KS Kolmogorov-Smirnov (Test)

KSP Key Science Project (CTA)

LAT Large Area Telescope (on *Fermi*)

LHAASO Large High Altitude Air Shower Observatory

LIGO Laser Interferometer Gravitational-wave Observatory

LII Galactic Longitude

LMC Large Magellanic Cloud

LMXB Low Mass X-ray Binary

LST Large Sized Telescope (CTA)

MAGIC Major Atmospheric Gamma Imaging Cherenkov Telescope

MAXI Monitor of All-Sky X-ray Image

MET Mission Elapsed Time

MJD Modified Julian Days

MLE Maximum Likelihood Estimation

MSP Millisecond Pulsar

MST Medium Sized Telescope (CTA)

NASA National Aeronautics and Space Administration

NS Neutron Star

OMC Optical Monitoring Camera (on INTEGRAL)

OSO Orbiting Solar Observatory

OSSE Oriented Scintillation Spectrometer Experiment (on CGRO)

OVRO Owens Valley Radio Observatory

PMT Photomultiplier Tube

PSF Point Spread Function

PWN Pulsar Wind Nebula

RA Right Ascension

ROI Region of Interest

SAS Small Astronomy Satellite

SCT Schwarzschild-Couder Telescope (CTA)

SED Spectral Energy Distribution

SiPM Silicon Photomultiplier

SMC Small Magellanic Cloud

SPI Spectrometer on INTEGRAL

SSC Synchrotron Self Compton

SSD Silicon Strip Detector

SST Small Sized Telescope

SWGO Southern Wide-Field Gamma-ray Observatory

tMSP Transitional Millisecond Pulsar

TOV Tolman-Oppenheimer-Volkov (Limit)

TS Test Statistic (from the Likelihood ratio test)

UTC Universal Coordinated Time

UV Ultraviolet

UVOT Ultraviolet/Optical Telescope (on *Swift*)

WCD Water Cherenkov Detector

VERITAS Very High Energy Radiation Imaging Telescope System

VHE Very High Energy

XML Extensible Markup Language (File Type)

XRB X-ray Binary

XRT X-ray Telescope (on *Swift*)

YAML Yet Another Markup Language (File Type)

Chapter 1

High Energy Astronomy

1.1 Introduction

In this thesis I investigate the high energy γ-ray properties of the X-ray binary population, in an attempt to answer two questions.

1) Why is only a small fraction of the overall X-ray binary population seen to emit γ-rays?

2) Are there any other X-ray binaries with previously unidentified γ-ray emission?

To answer these questions, I perform an analysis using the full sky *Fermi* Large Area Telescope data at the position of every known X-ray binary system, and attempt to identify γ-ray emission from their position, before performing a multi-variable analysis of the whole population of γ-ray emitting X-ray binaries, to identify common features, and differences between the systems.

An introduction to γ-ray physics, and the science of γ-ray astronomy is given in Chapter 1, before giving an overview of the *Fermi* Large Area Telescope and the analysis of its data in Chapter 2. In Chapter 3 (and the supporting Appendix A) I provide an introduction to X-ray binaries and the other types of γ-ray emitting compact binaries.

In Chapter 4, I provide an in-depth investigation into claims of γ-ray emission

from the low mass X-ray binary microquasar V404 Cygni. Here I look at individual claims of γ-ray emission, and phenomena such as source confusion which may cause false positives to arise in *Fermi* analysis.

The methodology and results of the survey of the X-ray binary population are provided in Chapter 5. Chapters 6, 7 and 8 provide detailed results on individual high mass X-ray binaries, low mass X-ray binaries, and Galactic centre low mass X-ray binaries respectively. Additional survey information is contained in Appendices B - H.

In Chapter 9 I consider the population of known γ-ray emitting X-ray binaries, their properties, and statistical significances, alongside any new discoveries made in the previous chapters. I attempt to determine characteristics in the population which determine whether γ-ray emission is likely to be detectable from individual systems. Chapter 10 provides conclusions to the previous chapters, and looks at future work and the application of these results to future observatories and missions.

1.2 What is a γ-ray?

The waveband of the electromagnetic (EM) spectrum with the highest energy, shortest wavelength and highest frequency photons is the γ-ray waveband, and the range of energies that γ-rays take begins at 511 keV*, the rest mass energy of an electron, and carries on up to an observed maximum of over 1 PeV (Cao et al., 2021b), spanning over 10 decades of energy (significantly more than any other waveband). Unlike other wavebands, where photons can be produced thermally, no object in the universe is hot enough to produce γ-rays; instead they are produced exclusively by non-thermal interactions.

The most common means of producing γ-rays on Earth is as a by-product of the radioactive decay of unstable atomic nuclei. The γ-rays produced by such processes

*There is debate in the scientific community over the distinction between X-rays and γ-rays, with energies from 100 keV to 1 MeV being commonly used depending on the field and study in question.

typically have energies of a few MeV, and whilst radioactive γ-ray emission is seen from astrophysical sources such as supernova remnants, γ-rays are also detected from extra-terrestrial sources with much higher energies.

The more energetic γ-rays that are the subject of this thesis are by-products from the acceleration of charged particles with magnetic fields. Both leptons (primarily electrons) and hadrons (primarily protons*) can produce γ-rays as a by-product of their particle interactions.

1.2.1 γ-rays from Leptonic Interactions

1.2.1.1 Inverse Compton Scattering

In the case of leptons, the method of producing γ-rays is through a process called inverse Compton (IC) scattering. In classical Compton scattering, photons interact with electrons and change energy and direction (Compton 1923 & Christillin 1986). Equation 1.1 shows how the final wavelength of the photon and the scattering angle relative to the direction of travel of the initial photon (θ) can be used to reconstruct the original photon wavelength and thus its energy.

$$\lambda_{initial} = \frac{h}{m_o c}(1 - \cos\theta) + \lambda_{final} \tag{1.1}$$

Here, c is the speed of light, m_0 is the rest mass of the electron and h is Planck's constant. Like the photoelectric effect, each photon interacts with a single electron - scattering off single electrons is known as Thomson scattering, whereas coherent scattering off bound electrons is known as Rayleigh scattering. Both forms of scattering are elastic.

In inverse Compton scattering, the same process occurs. In the IC case however, the electron loses energy to the photon, and thus the scattered photon has a higher

*High energy extra-terrestrial protons and atomic nuclei are known as cosmic rays, and are the subject of study in the adjacent and overlapping field of multi-messenger astrophysics.

energy than the original photon. For IC scattering to occur, the electrons need to be of high energy (typically travelling at relativistic velocities) and interact with much lower energy photons (typically radio to optical wavebands) (Jones, 1965).

The interaction between a seed photon field (such as stellar or CMB photons) and a high energy lepton population produces a characteristic spectrum, which depends on factors such as the energies of the initial electron and photon populations, and the number of particles in each population (Jones 1968 & Khangulyan et al. 2014).

1.2.1.2 Synchrotron Emission

Populations of relativistic electrons also produce non-thermal emission called synchrotron radiation (also known as magnetobremsstrahlung radiation). When relativistic electrons travel through a magnetic field with curved field lines, the electrons will follow the field lines emitting a cone of photons in their direction of travel. Synchrotron radiation is polarised and beamed, which leads to it being extremely luminous. The energy range of synchrotron emission is wide, and extends from the low-frequency radio waveband (which is completely non-thermal, like γ-rays), and rises from the radio up in flux before peaking and sharply dropping off in flux. The peak of the synchrotron emission can vary in wavelength depending on the energetics and environment of the emitting particle population, but can be as high as the X-ray waveband in many cases.

Given that synchrotron emission is produced by the same populations of electrons which can produce γ-rays via inverse Compton scattering, the electrons which radiate synchrotron photons can be scattered into γ-rays by the electron population which produced the photons in a process called synchrotron self Compton (SSC) emission. Sources of SSC γ-rays have a very recognisable spectral energy distribution, with a double hump structure. The first hump is from the synchrotron emission, and can stretch from the radio up to the γ-rays where it sharply decays, before the smaller inverse Compton peak begins to rise and peaks in the γ-ray

waveband. The area between the two humps is known as the spectral dip (also known as the spectral valley).

As radio emission is non-thermal in nature and typically arises from synchrotron sources, strong radio emission often indicates the presence of γ-rays, as both may be produced by the same population.

Finally, in the case of an electron population travelling in a very strong magnetic field, the electrons will be confined to moving along the field lines. In this case, the radiation emitted by the particles is polarised in the plane of the field lines; as these field lines are curved (such as in the magnetosphere of a neutron star) this radiation is known as curvature radiation and curvature photons can extend up to γ-ray energies (Barsukov et al., 2006).

1.2.2 γ-rays from Hadronic Interactions

When a photon interacts with high energy relativistic protons, a neutral, or positive pion and a hadron are produced (Equation 1.2).

$$p + \gamma \longrightarrow p + \pi^0, \qquad p + \gamma \longrightarrow n + \pi^+ \tag{1.2}$$

All pions have an extremely short half life; 26 nanoseconds for charged pions and 85 attoseconds for neutral pions. Only neutral pions will decay into γ-rays, with each neutral pion decaying into two photons of at least 67.49 MeV, half the rest mass energy of the π^0 (134.98 MeV). Charged pions will decay into either muon-neutrino, or more rarely, electron-neutrino pairs (or their antimatter equivalents), with no photons emitted during these decays. Charge is always conserved in these decays, so that π^+ particles decay into antimuon/positron-neutrino pairs and π^- particles decay into muon/electron-neutrino pairs. The seed photons for photo-hadronic γ-ray production can come from a variety of sources, including cosmic microwave background photons or stellar photons (see e.g. Mücke et al. (1999)).

In addition to photo-hadronic interactions, high energy protons can also collide with nuclei, again producing pions. Similarly to the photo-hadronic interactions, the charged pions will decay into leptons and the neutral pions will decay into γ-rays. Finally, protons will also produce synchrotron emission as electrons do, and it is also possible for hadrons to upscatter particles through the IC mechanism.

1.3 Matter and photons

To understand how to detect γ-rays, it is necessary to understand their interactions with matter, and the way in which a photon interacts with matter depends on its energy. In this Section we discuss three mechanisms by which photons interact with matter, the photoelectric effect, Compton scattering and pair production; all three are illustrated in Figure 1.1.

For most photons up to baseline γ-ray energies (511 keV), photons impacting a metal will liberate electrons via the photoelectric effect, provided the photon energy is greater than the electron binding energy. Any excess energy that the photon has is converted into photoelectron kinetic energy. The photoelectric effect is the basis by which modern optical cameras work; incoming photons liberate electrons in charge-coupled devices. Each photon liberates a single photoelectron only, and thus photoelectron current scales directly with the intensity of the incoming photons. By combining CCDs (which record photon fluxes) with filters (which block out certain wavelengths of light), colour images of the sky can be built using the photoelectric effect as the principle of observation.

Between approximately 10 keV and 10 MeV, the dominant interaction between photons and matter becomes Compton scattering (Section 1.2.1.1). Unlike the photoelectric effect, where the initial photon is completely absorbed by the electron, the scattered photon in this interaction can go on to interact with electrons, by either scattering events or the photoelectric effect, depending on the scattered photon's energy.

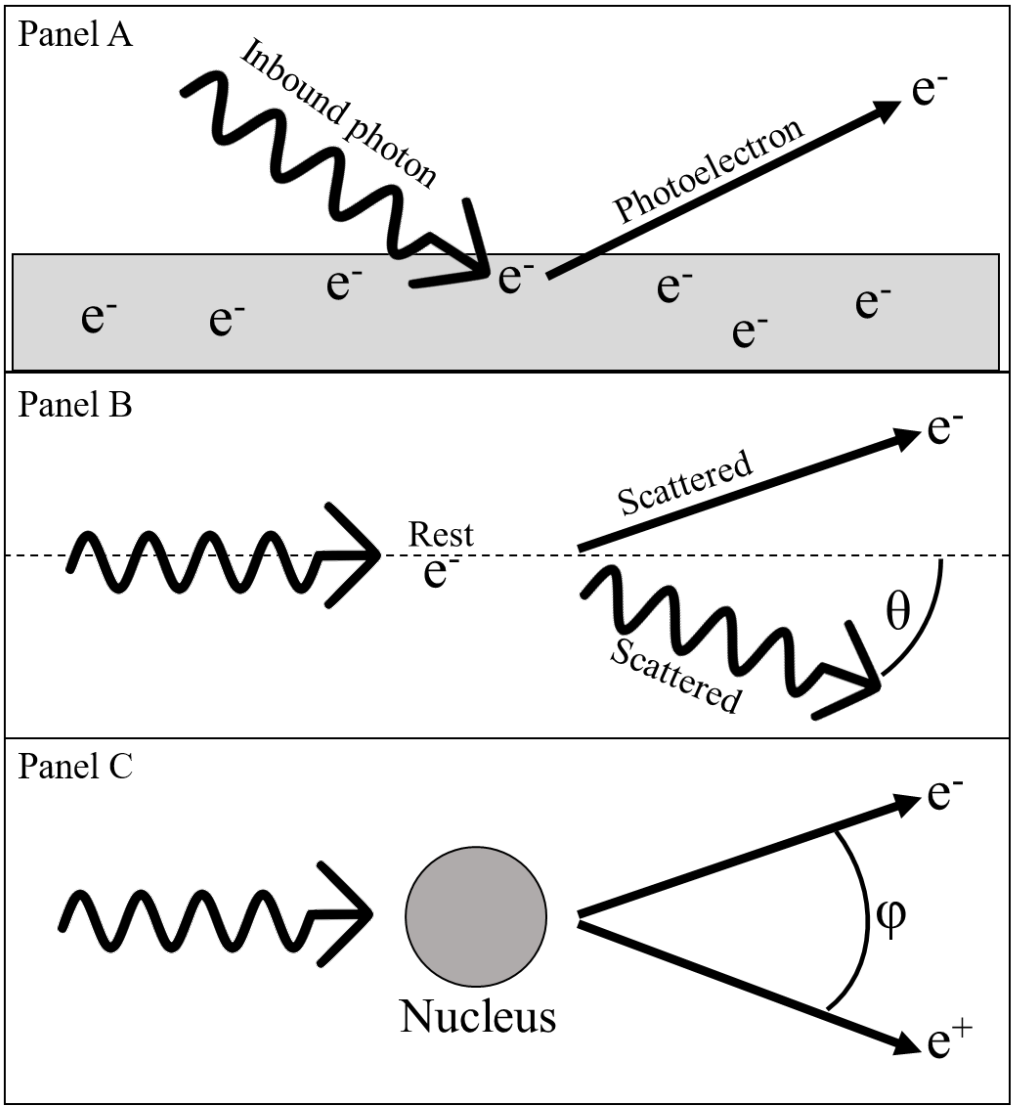

Figure 1.1: Interactions between photons and matter. Panel A depicts the photoelectric effect where a single photon liberates a single bound electron from a metal surface, where a population of bound electrons exist. Panel B depicts Compton scattering, where an inbound photon interacts with an electron at rest, scattering the electron and scattering the photon with a new energy, at a characteristic angle θ. Panel C depicts the pair production of an electron-positron pair, and their emission angle. Whilst the lepton pair will conserve the component of momentum of their progenitor photon, they will also move away from one another with an opening angle ϕ, depending on the initial photon energy.

At high energies, pair production becomes the dominant means of particle interaction. Pair production occurs when high energy* γ-rays interact with the nuclei of atoms (with the likelihood of interaction increasing with photon energy), and produce a charged lepton pair. This charged lepton pair has a velocity component which conserves the initial photon momentum, but each lepton also has a new velocity component as a new momentum component is introduced for each lepton, which sees them moving directly away from each other at the same rate (hence conserving momentum). The angle between the velocity components, φ, scales inversely with the initial energy of the progenitor photon (Olsen, 1963).

The lepton pair produced by the progenitor photon can, in principle, be any of the three charged lepton pairs: an electron-positron pair (e^-, e^+), muon-antimuon (μ^-, μ^+) and tau-antitau (τ^-, τ^+). As muons and τ-particles have higher rest mass energies than electrons (105.7 MeV for muons and 1.777 GeV for τ-particles) and therefore require progenitor photons of higher energies, at least twice the rest mass energy of the respective particle. In reality, the vast majority of lepton pairs produced are electron-positron pairs, with a minority being made up of muon-antimuon pairs, as seen by TeV observatories (Tyler, 2012). No τ particles have been detected outside of particle physics laboratory settings, due to their extremely short lifetimes.

As the electron-positron pair travels they will further interact with their environment. As they pass by nearby nuclei, they will interact and emit Bremsstrahlung radiation, as they change velocities, either cyclotron emission at non-relativistic velocities, or synchrotron emission at relativistic velocities. In extreme cases secondary lepton pairs are produced, and this is the mechanism by which γ-ray air showers occur.

In addition to pair production where γ-rays interact with matter, γ-rays can also pair produce by interacting with other γ-rays in a process called $\gamma\gamma$ absorption. Here, two photons collide and produce a lepton-antilepton pair (typically an elec-

*$E_{photon} \geq 2m_0$

tron and a positron), provided the energy of both photons combined exceeds the rest mass energy of the leptons being produced (1.022 MeV for an electron-positron pair). $\gamma\gamma$ absorption is a cause of opacity in intense γ-ray producing regions.

1.4 Astronomy with γ-rays

Observing γ-rays is less trivial than some other wavebands such as the optical or radio wavebands because the Earth's atmosphere is completely opaque to essentially all radiation with E > 10 MeV. Additionally, γ-rays must be generally detected via Compton scattering or pair production, as photoelectric effect-dependent CCDs are ineffective at γ-ray wavelengths, bringing additional challenges. Finally, γ-rays cannot be focused or reflected and they are rare in the universe compared to every other waveband.

Cosmic rays were detected at the onset of the 20th century (Hess, 1912)*, and their discovery led to predictions of astrophysical γ-rays before their first detection (Morrison, 1958). Such predictions were proved right when the Explorer 11 satellite launched in 1961, where 22 γ-rays were detected over 7 months, in addition to 22,000 cosmic rays ((Kraushaar and Clark, 1962) & (Kraushaar et al., 1965)). This marked the beginning of space based γ-ray astronomy.

1.4.1 Early Space Based Observations

Whilst Explorer 11 detected γ-rays, these were isotropic and no one source of origin could be detected; therefore it is probable that these photons originated from the γ-ray diffuse background, which itself has two components: the isotropic diffuse and the Galactic diffuse. The γ-ray background is well-established as consisting of unresolved point sources, emission from diffuse clouds of high energy particles, and possibly exotic components such as dark matter decay (Fornasa and Sanchez-Conde, 2015).

*Hess won the 1936 Nobel Prize in physics for the discovery of cosmic rays.

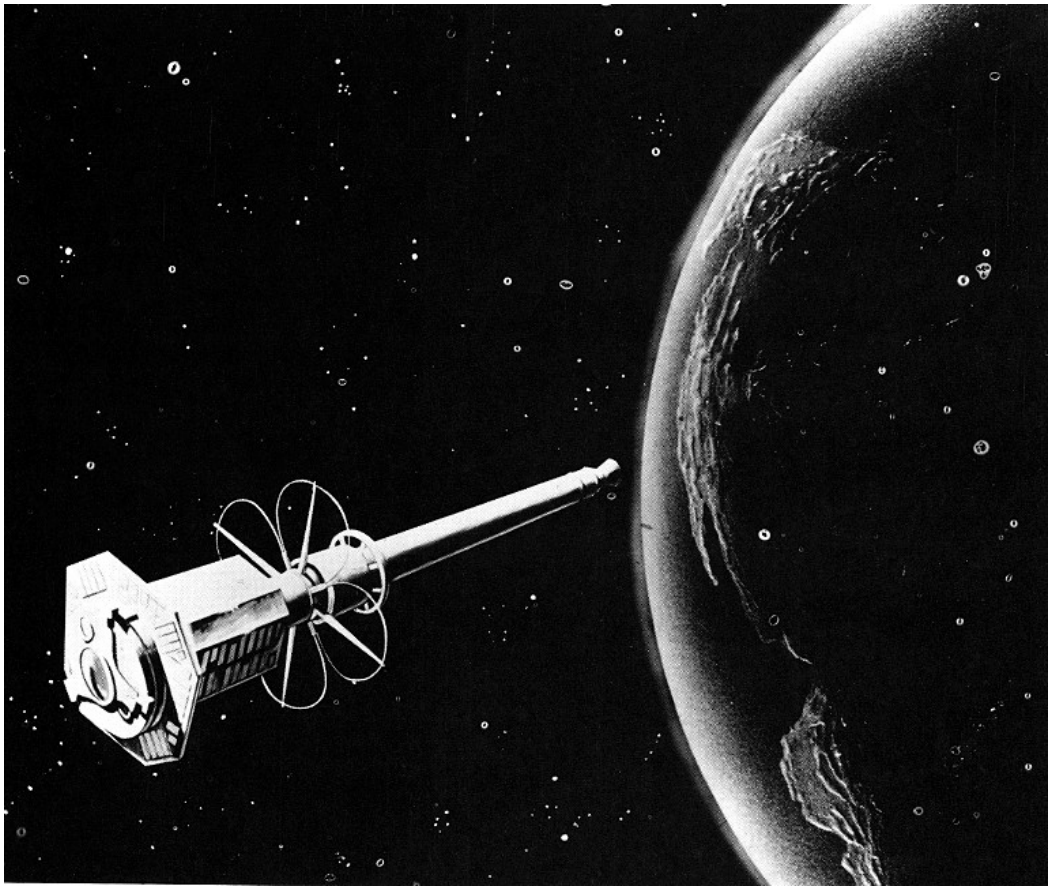

Figure 1.2: An artists impression of the Explorer 11 satellite, which carried a detector which made the first detection of astrophysical γ-rays. Image credit: NASA.

The scientific successor to the Explorer 11 mission launched in 1967 and was known as the Orbiting Solar Observatory 3 (OSO-3), which operated for almost 3 years, collecting both X-ray data and γ-ray data with a variety of instruments. Despite hardware failures, OSO-3 was a successful mission, capturing numerous solar flares, and also the first X-ray source*, Scorpius X-1 (Peterson and Jacobson, 1966). In addition to X-ray observations, OSO-3 carried a γ-ray detector capable of observing γ-rays at energies exceeding 50 MeV. Over the mission lifespan, OSO-3 detected 621 astrophysical γ-rays, a significant improvement over the results of Explorer 11. Several key results were derived from the OSO-3 mission; the principal result was that the γ-ray diffuse emission is highly anisotropic, and is much more luminous on

*Outside of the solar system.

the Galactic plane than at higher latitudes as a result of the Galactic component, and that softer* photons are seen at higher latitudes, as a result of the isotropic component. It was these data from OSO-3 which first described the two components of the γ-ray diffuse emission as it is known today. Whilst OSO-3 did not detect any discrete point sources of γ-rays, upper limits were calculated for several expected sources of γ-ray emission (Kraushaar et al., 1972).

Following the OSO-3 mission, both NASA and the European Space Agency (ESA) began production of new space-based γ-ray telescopes. The NASA mission, the Small Astronomy Satellite 2 (or SAS B), launched aboard the 48th Explorer class mission in 1972, operating for approximately 7 months before shutdown. The telescope was the first to employ the principle of pair-production to detect γ-rays, by using a spark chamber, and operated in the 20 MeV - 1 GeV range (Derdeyn et al., 1972). SAS B made a number of discoveries; in addition to confirming the OSO-3 results, and further constraining the γ-ray backrgound, SAS B made the first detection of a discrete γ-ray point source, the Crab Nebula, and also the Vela X supernova remnant (Fichtel et al., 1975).

The ESA γ-ray mission was known as Cos-B†. It launched in 1975, and operated for over 6 years before decommissioning in 1982. Like SAS B, Cos-B used a pair production spark chamber to detect γ-rays from 30 MeV to 5 GeV, and was responsible for the first catalogue of γ-ray sources, which included Cygnus X-3, the first X-ray binary to be detected at γ-ray energies (Bennett, 1990). Following Cos-B, numerous missions took place which improved on the results, including the NASA High Energy Astronomy Observatory program which ran throughout the 1970s and 1980s.

*In high energy astronomy, hard refers to higher energy photons, whereas soft refers to lower energy photons.

†Cos-B was the first mission to be launched by the newly formed European Space Agency.

1.4.2 The *Compton* Gamma-Ray Observatory

Arguably the next major leap forward in the field came in 1991, with the launch of the *Compton* Gamma-ray Observatory (CGRO); commissioned in 1977, CGRO was one of the four missions in NASA's Great Observatories program, and was the second to launch after the *Hubble* Space Telescope in 1990. CGRO covered a vast energy range, from the hard X-ray waveband to GeV γ-rays, and had 4 instruments aboard to facilitate such a wide observable energy range. A review of the CGRO instruments, and their science results can be found in Kurfess et al. (1997). An image of CGRO during deployment is shown in Figure 1.3.

Covering the lowest energies, the Burst and Transient Source Experiment (BATSE) monitored photons from the hard X-ray (at 20 keV) to low energy γ-rays (at 1 MeV), and consisted of 8 sodium iodide scintillators mounted around the body of CGRO, providing all sky coverage. The primary science goal of BATSE was the detection, and positional localisation, of γ-ray bursts and other transient sources. BATSE detected, on average, one γ-ray burst per day (detecting 2704 over the mission lifetime) and continuously monitored 110 sources of hard X-rays and low energy γ-rays (Kaneko et al., 2006).

The Oriented Scintillation Spectrometer Experiement (OSSE) provided coverage of the 50 keV to 10 MeV energy range, overlapping with the BATSE energy range. Like BATSE, OSSE used scintillator based detectors (in this case NaI(Tr) - CsI(Tr)), but was not an all sky instrument; 4 scintillators provided a 3.8° by 11.8° full width half maximum (FWHM) field of view and significantly better angular resolution than the BATSE afforded, providing synergies between the two instruments (Johnson et al., 1993b). OSSE observed a great number of sources; these included supernova remnants, active galaxies and the Galactic centre (Johnson et al., 1993a).

Covering the 750 keV - 30 MeV range was the Imaging Compton Telescope (COMPTEL), which used the principle of Compton scattering to force medium energy γ-rays into an interaction before detecting the scattered photon with scintillators behind the

Figure 1.3: A photograph of the *Compton* Gamma-Ray Observatory as it is deployed from the space shuttle *Atlantis* in 1991. The space shuttle robotic arm is shown in the bottom of this image. Image credit: NASA.

Compton detector instrument. COMPTEL was designed to survey the entire sky at MeV energies, as previously the MeV band had been poorly explored*, and thus had a very large field of view of 1 steradian (Schoenfelder et al., 1993). In addition to performing the first MeV sky survey, COMPTEL made a number of important observations. COMPTEL observed γ-ray emission from a variety of point sources such as pulsars, active galaxies and X-ray binaries, but also captured γ-ray bursts, thanks to its large field of view. In addition, COMPTEL measured radioactive

*As a lack of instrumentation has been designed to explore the MeV band since, it remains poorly explored since the end of COMPTEL operations. This lack of exploration has led to the MeV range being dubbed the 'MeV gap'.

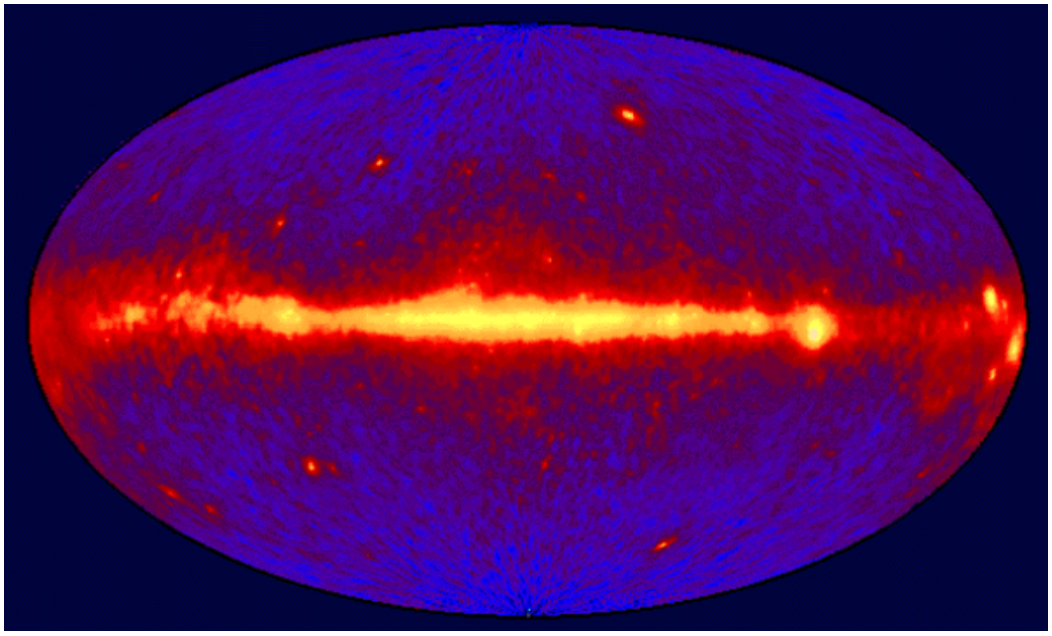

Figure 1.4: The image of the γ-ray sky at energies above 100 MeV taken by EGRET. The central horizontal band of emission shows the Galactic diffuse emission, which becomes more intense towards the Galactic centre. Several point sources of high intensity γ-rays are seen off the plane. Image credit: NASA

decay lines from several chemical elements in several parts of the galaxy, such as the Cygnus region (Schoenfelder et al., 1993).

The final instrument aboard CGRO was the Energetic Gamma-Ray Experiment Telescope (EGRET), which observed photons from 100 MeV to 30 GeV by the principle of pair conversion. The telescope itself consisted of tungsten foils, the nuclei of which caused γ-rays to convert into a lepton pair, which would then be detected in a spark chamber with an energy measuring calorimeter at the base (Nolan et al., 1992b). EGRET provided the first truly accurate look at the γ-ray sky at high (GeV) energies (Figure 1.4). EGRET made numerous important scientific discoveries over its lifespan, including that the photons emitted from γ-ray bursts extended to high energy ($>$ 30 MeV) γ-rays (Schneid et al., 1995) and that pulsed γ-ray emission is detected from pulsars, such as Geminga (Nolan et al., 1992a). EGRET was an extremely successful instrument which has seen two successors launched in the 2000s, *Fermi* and AGILE by NASA and the Italian Space Agency respectively, based on similar detection techniques.

Whilst CGRO was an extremely successful mission with regards to its science capabilities, it suffered a number of hardware malfunctions during its lifespan. In 1992, the onboard tape recorders failed, which limited the amount of data that could be stored aboard the satellite; to remedy this, a second data centre was built on the ground in order to download data more quickly from CGRO. Additionally, soon after launch, issues were detected with the fuel line of the satellite, which prevented the frequent orbital boosting which the spacecraft was designed for. As a result, only two reboosts took place over the lifespan of CGRO, although it was reboosted to an altitude which was sufficient to maintain orbit until the late 2000's. In 1999, one of the three gyroscopes failed. As the spacecraft had a mass of 17 metric tonnes (greater than a double decker bus), the decision was made to safely and intentionally deorbit the spacecraft, as if a second gyroscope failed there would be no option to perform a controlled deorbit. Thus CGRO was deorbited in June 2000, and was the first of NASA's Great Observatories to reach the end of its mission.

1.4.3 Contemporary Space Based Observations

With the wide energy range covered by CGRO and its previously unmatched sensitivity, numerous areas of γ-ray astronomy advanced very rapidly in the 1990s as new discoveries abounded. As a result of CGRO's rich science yield, four high energy satellites launched in the 2000s, all of which still operate today.

1.4.3.1 INTEGRAL

The International Gamma-Ray Astrophysics Laboratory (INTEGRAL) was designed and built by ESA (who had contributed to CGRO). INTEGRAL launched in 2002, and contains 4 instruments onboard. The Optical Monitoring Camera (OMC) is a refracting optical telescope with a CCD camera which covers the V-band range of 400-500 nm (Giménez et al., 1999). The two Joint European X-ray

Monitor (JEM-X) detectors cover the X-ray waveband between 3 and 35 keV, and is a coded mask telescope with a 4.8° field of view, and 3 arcmin FWHM angular resolution (Lund et al., 1999). Two γ-ray instruments are on board: the first is the Imager on Board INTEGRAL (IBIS) which images photons from 15 keV up to 8 MeV, using two layers of scintillating pixels to capture a high resolution image. Its 12 arcmin FWHM angular resolution was better than any other γ-ray instrument at its launch (Ubertini et al., 1999b). Complementing IBIS is the Spectrometer on Integral (SPI), which provides high energy resolution between 18 keV - 8 MeV, broadly the same energy range as IBIS. The combination of IBIS and SPI provides INTEGRAL with high spatial and energy resolution across the hard X-ray to medium energy γ-ray regime.

INTEGRAL is a notable mission because the combination of its 4 instruments provides coverage of the optical, X-ray and low-medium energy γ-ray wavebands, representing one of the first truly multi-wavelength space observatories. INTEGRAL has produced many scientific results over its lifespan, including examining the full sky at 511 keV to search for leptonic annihilation anisotropies across the sky, and detecting point sources such as active galaxies and supernova remnants. Whilst INTEGRAL data are not used in this thesis, INTEGRAL was one of the instruments used in 2015 to perform observations of the outburst of the low mass X-ray binary V404 Cygni, discussed extensively in Chapter 4. Additionally, INTEGRAL is responsible for the discovery of many X-ray binaries discussed in this thesis.

1.4.3.2 *Neil Gehrels Swift* Observatory

The *Neil Gehrels** *Swift* Observatory (formerly the *Swift* Gamma-ray Burst Explorer, henceforth *Swift*) is a satellite designed to observe γ-ray bursts and transient X-ray phenomena. *Swift* consists of three instruments. The first is the Burst Alert Telescope (BAT), which observes the 15 keV - 150 keV range, and is a coded aperture mask telescope with a wide field of view (1 steradian - 3 sterradians, depending on observing mode). The BAT is designed to observe transient events and rapidly provide localisation to within arcminute accuracy, and BAT alerts are used by other observatories for rapid follow up observations of γ-ray burst afterglows (Barthelmy et al., 2005). BAT data are available publicly, and are used in this thesis to produce multi-wavelength light-curves of X-ray binaries, which are themselves prone to transient outbursts.

The other instruments on *Swift* are designed to provide higher resolution follow-up observations of transient phenomena, following BAT triggers. The first is the X-ray Telescope (XRT), a Wolter grazing incidence telescope which focuses X-rays onto a CCD. The XRT is primarily used for improved positional localisation of γ-ray bursts, however is also used for the continuous observation of X-ray sources such as microquasars, supernovae and γ-ray burst afterglows (Burrows et al., 2005). The final instrument aboard *Swift* is the Ultraviolet/Optical Telescope (UVOT), which operates between 170nm - 600nm, and is designed to detect optical/UV counterparts to transient phenomena, primarily the optical afterglow of γ-ray bursts. *Swift*-XRT and UVOT data are not used directly in this thesis, although observations with these instruments are discussed, particularly in Chapter 4, in the context of the microquasar V404 Cygni.

*The late Neil Gehrels was the Project Scientist of the telescope, who died in 2017 at the age of 64, and for whom the telescope is now named. Gehrels played a leading role in γ-ray astronomy throughout his life as Chief of Astroparticle Physics at NASA's Goddard Space Flight Centre. In addition to his work with *Swift*, Gehrels was the deputy project scientist for the *Fermi* observatory, was project scientist for CGRO, was mission scientist for INTEGRAL, and was leading development of the Wide Field Infrared Space Telescope (WFIRST) before his death.

1.4.3.3 AGILE

The Astro-Rivelatore Gamma a Immagini Leggero* (AGILE) is a γ-ray space telescope which was launched by the Italian Space Agency in 2007, and acts as a successor to EGRET. AGILE consists of two instruments. The first is a hard X-ray imaging detector called Super-AGILE. Super-AGILE, like the X-ray instruments aboard INTEGRAL and *Swift*, is a coded mask telescope and is sensitive to photons in the energy range 18 keV - 60 keV. Super-AGILE uses silicon strip detectors, and has a wide field of view of approximately 1 steradian; it has an angular resolution of 6 arcmin (Feroci et al., 2007).

The second instrument aboard AGILE is known as the Gamma-Ray Imaging Detector (GRID), which detects γ-rays through the principle of pair-conversion as EGRET did. Whilst EGRET used a spark chamber to track the paths of the pair-produced leptons, AGILE uses silicon strip detector technology, which eliminates the performance deterioration that EGRET was prone to due to degradation of gas quality in the spark chamber over time†. GRID is sensitive to γ-rays between 30 MeV and 30 GeV, and largely covers the same range that EGRET did (Tavani et al., 2009a).

AGILE data have resulted in a number of important discoveries in the field, notably including evidence for variability from the Crab Nebula due to plasma outbursts in the inner regions of the system (Striani et al., 2013). AGILE data, unlike that of INTEGRAL and *Swift*, are not public, and are not used in this thesis; discussion of AGILE observations is made in Chapter 4 in the context of V404 Cygni.

1.4.3.4 The Fermi Gamma-ray Space Telescope

NASA's own direct successor to CGRO (particularly EGRET) is the *Fermi* γ-ray Space Telescope, which has two instruments aboard: the γ-ray Burst Monitor and

*Or, the Lightweight Astro-Imaging Gamma Detector in English.

†More information on the Si strip detectors is found in Chapter 2, where the same technology is discussed in the context of the *Fermi* mission.

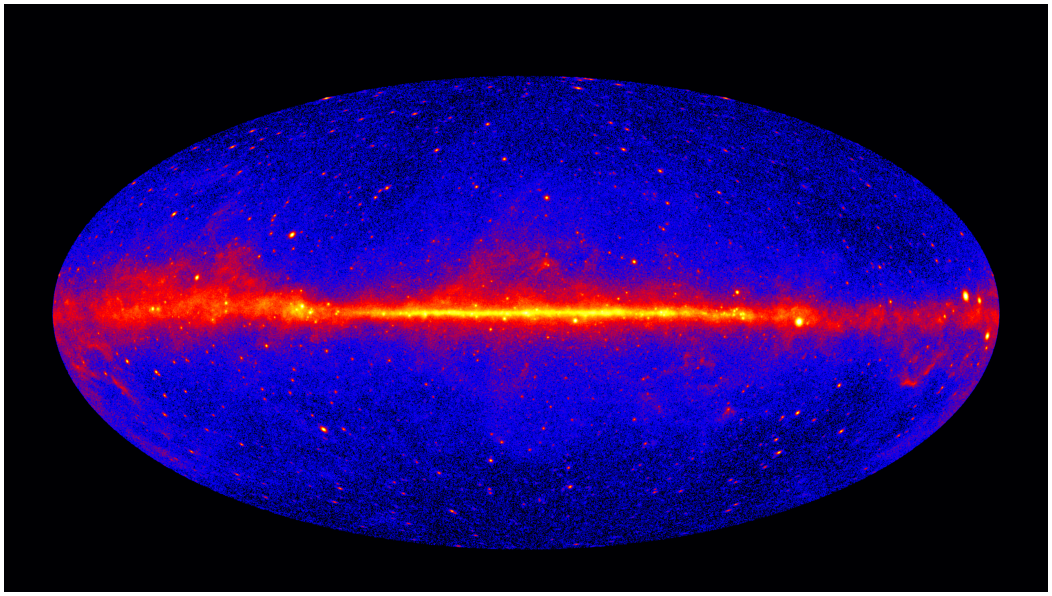

Figure 1.5: The image of the γ-ray sky at energies above 1 GeV taken by *Fermi*. The central horizontal band of emission shows the Galactic diffuse emission, which becomes more intense towards the Galactic centre. Several point sources of high intensity γ-rays are seen off-the-plane. Compared to the EGRET emission, the Galactic plane emission is narrower and better constrained, and more point sources are seen sue to the improved instrument sensitivity. Image credit: The *Fermi*-LAT Collaboration.

the Large Area Telescope. The latter is sensitive to photons between 30 MeV and 1 TeV, both encompassing and extending the energy range of EGRET. *Fermi* has significantly improved sensitivity and resolution compared to EGRET; whilst EGRET detected γ-ray sources in the hundreds, *Fermi* has identified them in the thousands; these include starburst galaxies, active galaxies, pulsars, pulsar wind nebulae, supernova remnants, binary systems and classical novae. Arguably one of the biggest discoveries made by this observatory has been the *Fermi* bubbles, lobes of high energy γ-rays extending orthogonally from the Galactic centre to kiloparsec scales (Su et al., 2010). The *Fermi* Large Area Telescope view of the whole sky is shown in Figure 1.5. The *Fermi* data are publicly available, and are what is primarily used in this thesis. Chapter 2 discusses the *Fermi* mission, data and software in depth.

1.4.4 Ground Based Observations

Whilst the Earth's atmosphere is opaque to cosmic γ-ray radiation, it is possible to observe the interactions between cosmic γ-rays and the upper atmosphere. As a result, ground based observatories can reconstruct the energy and direction of incidence of γ-rays, providing a means to perform γ-ray astronomy from the ground. The energy required to produce interactions visible from the ground is significant, meaning that only γ-rays with energies of at least 5 of GeV are detectable. As a result, ground based γ-ray astronomy complements space based astronomy (where instrument effective areas are much lower), by observing at higher energy bands and with better instantaneous sensitivity.

1.4.4.1 The Cherenkov Effect

As γ-rays hit the upper atmosphere, they will pair produce an electron-positron pair by interaction with atmospheric nuclei. At very high energies (very loosely between 100 GeV - 1 PeV), the progenitor γ-ray is so energetic that the electron-positron pair will travel close to the speed of light, and faster than the speed of light in the medium of the atmosphere. As a result of this, the lepton pair will emit a characteristic blue optical/UV light called Cherenkov radiation, which is akin to the sonic boom created due to super-sonic travel.

As the electron-positron pair travels towards the ground through the atmosphere, they lose energy in the form of secondary γ-rays emitted via Bremsstrahlung. These secondary γ-rays further interact with atmospheric nuclei, producing further electron-positron pairs, which emit further Cherenkov light. The resulting cascade of Cherenkov light-emitting leptons is known as an air shower. The Cherenkov light from air showers is luminous, but is extremely short lived as the entire air shower lasts only nanoseconds (Rao and Sreekantan, 1998).

In addition to γ-ray induced air showers, high energy cosmic rays produce air showers when they collide with the atmosphere, causing a noisy background for

γ-ray observers. However, as hadronic air showers have different signatures and cascade patterns to γ-rays, it is possible to filter the noisy background out with modern observing techniques (Hillas, 1996). Muons are also produced within the air showers themselves, which travel down towards the ground in the shower. These also produce Cherenkov light, however they are distinguishable from γ-rays as they form a distinctive ring/arc pattern on the ground.

1.4.4.2 Imaging Atmospheric Cherenkov Telescopes

Imaging Atmospheric Cherenkov Telescopes (IACTs) are optical telescopes designed to observe the Cherenkov light from air showers caused by γ-rays hitting the atmosphere. IACTs are large reflecting instruments, typically with mirror sizes exceeding 8m in diameter, and are designed to capture as much Cherenkov light as possible in order to reconstruct the incident γ-rays as accurately as possible. The cameras of IACTs do not use CCDs as most other telescope cameras do, but instead use photomultiplier tubes to enable the very fast light pulses of Cherenkov showers to be detected (Sinnis, 2009).

The first IACT was a single instrument known as the *Whipple* 10m Telescope, located on Mount Hopkins at the Fred Lawrence Whipple* Observatory in Southern Arizona. The *Whipple* telescope pioneered the imaging technique, and detected a wide range of sources including binary systems, active galaxies and nebulae (Kildea et al., 2007).

There are currently 3 major IACT observatories operating across the world. These are the High Energy Stereoscopic System (H.E.S.S.) in the southern hemisphere, the Very Energetic Radiation Imaging Telescope Array System (VERITAS, shown in Figure 1.6), and the Major Atmospheric Gamma Imaging Cherenkov Telescopes (MAGIC), both in the northern hemisphere. Each of these observatories consists

*Both the telescope and the observatory were named after Fred Lawrence Whipple, an American astronomer who established the facility and was the head of the Smithsonian Astrophysical Observatory.

Figure 1.6: One of the four IACTs that make up the VERITAS array. Note the segmented mirror design, which allows individual panels to be removed for cleaning, maintenance and saves money compared to a larger single mirror reflector. The scaffolding platform in the background of the shot allows for maintenance to be performed on the telescope camera.

of an array of multiple telescopes which generally observe the same objects simultaneously. The result is a much better instantaneous sensitivity and much better angular resolution than any space based instrument. However, IACTs must usually observe at small zenith angles, at night, with minimal moonlight, and in weather where interference from clouds is minimal. As a result, the duty cycle of an IACT observatory is approximately 10%, compared to the near 100% of space based observatories. Today, these three observatories carry out observations of a variety of sources across the sky, in coordination with one another and other instruments such as *Fermi* and *Swift*.

Whilst VHE data are not used in this thesis directly, results from all three major IACT arrays are drawn upon at various points, particularly in later chapters where the high mass X-ray binaries (a class of VHE source) are dealt with.

1.4.4.3 Water Cherenkov Detectors

In addition to IACTs, a second type of Cherenkov light detector is used for γ-ray astronomy, the water Cherenkov detector (WCD). These consist of a large (> 100,000 litre) tank of water, built to completely exclude any light. As electron-positron pairs from air showers pass through the water, they emit Cherenkov light which is detected by photomultipliers inside the tank. This allows for the angle of incidence and energy of the γ-ray to be reconstructed.

Currently, two major water tank detectors operate, both in the Northern Hemisphere. The High Altitude Water Cherenkov Experiment (HAWC) operates in Mexico (Smith, 2015), and the Large High Altitude Air Shower Observatory (LHAASO) operates in China (Cao et al., 2021b). WCD data are not used in this thesis, although results from HAWC are discussed.

Figure 1.7: The first labour of Heracles, the slaying of the Nemean Lion. By Peter Paul Reubens (Year Unknown).

Chapter 2

The *Fermi* Large Area Telescope

2.1 Mission Hardware

The Fermi Gamma-ray Space Telescope (henceforth *Fermi)* is a satellite in low Earth orbit with two instruments aboard designed for the detection of high energy γ-rays. Originally named the Gamma-ray Large Area Space Telescope (GLAST), development of *Fermi* began in the early 1990's, *Fermi* was designed as a successor to EGRET, and the wider Compton Observatory Satellite (e.g Atwood et al. 1992 & Gehrels et al. 1999). *Fermi* was launched on the 11th of June 2008 and the scientific payload aboard was switched on several weeks later on the 24th of June. *Fermi* orbits the Earth approximately once every 90 minutes, and the spacecraft has a rocking motion so that the instruments can capture a full image of the sky once every 2 orbits. The mission has been extended several times, and is operational to this day. On the 16th of March 2018, the rotation drive on one of the solar panels failed, causing downtime in observations. The observatory was moved to an orbital position where it could maximise solar exposure with only one rotating solar panel and full operations resumed soon after, largely due to the fact that the observatory generates a significant amount of extra energy than the instruments use.

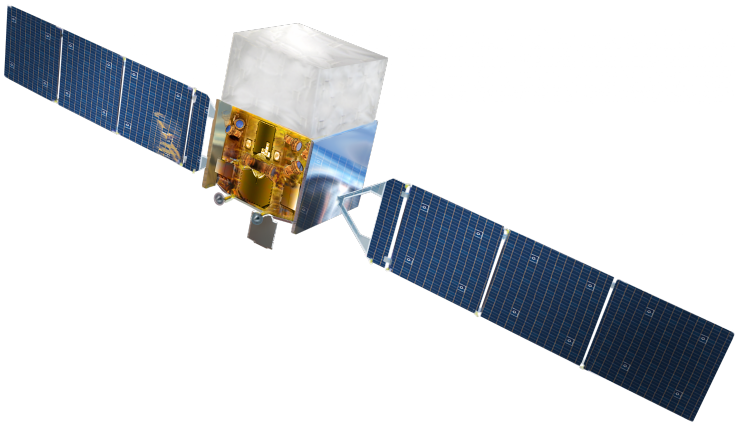

Figure 2.1: An artists impression of *Fermi* γ-Ray Space Telescope. The large silver cuboid at the top of the satellite's body is the Large Area Telescope. The Gamma-ray burst monitor scintillators are located on the body of the instrument below the large area telescope. The solar panels to the left and right are designed to rotate in orbit in order to maximise available power to the instrument at all times. (Image source: https://science.nasa.gov/toolkits/spacecraft-icons)

2.1.1 The Gamma-ray Burst Monitor

Fermi launched with two instruments onboard, the first of which is the Gamma Burst Monitor (GBM) which is designed to observe transient X-ray and γ-ray radiation between the energies of 8 keV and 40 MeV (Meegan et al., 2009). The GBM consists of 12 Sodium Iodide scintillators located at intervals around the body of the spacecraft to provide coverage of the lower energy photons, and 2 Bismuth Germinate scintillators located on opposite sides of the spacecraft to provide coverage of the higher energy photons. Whilst the GBM covers approximately two thirds of the sky at once, localisation of transient events is relatively poor (at approximately 5°), but temporal resolution is excellent at $5\mu s$, allowing for excellent time-resolved spectra of transient events. The GBM has detected a wide variety of events, including solar flares and high energy emission from thunderstorms called terrestrial γ-ray flashes; however, the primary aim of the GBM is the detection of γ-ray bursts, transient flashes of extragalactic high energy emission caused by exotic processes in stellar systems. (e.g. Schwartz et al. 2010, Berger 2014, Chronis et al. 2016 & Poolakkil et al. 2021). The GBM plays an important part in high

energy astronomy and has synergies with many other instruments. It complements several other detectors such as the Burst Alert Telescope on the *Neil Gehrels Swift* Satellite which together provide a near full view of the sky, and improved localisation over one instrument via triangulation (Barthelmy et al., 2005). Alerts from the GBM (in addition to instruments like *Swift*-BAT) also provide coordinates to ground based TeV observatories which then perform follow up observations on the afterglows of γ-ray bursts. This led to the first TeV detection of a γ-ray burst afterglow by H.E.S.S. in 2018 (Abdalla et al., 2019). Finally, the GBM works in tandem with the Large Area Telescope, the primary instrument on *Fermi*, and the Large Area Telescope has also identified γ-ray bursts in the MeV - GeV energy range (Ajello et al., 2019).

2.1.2 The Large Area Telescope

The primary instrument aboard *Fermi* is the Large Area Telescope (LAT), which is designed to build an image of the γ-ray sky by identifying point and extended sources of γ-rays amongst the γ-ray background, and their evolution over time. The LAT is sensitive to photons roughly between 30 MeV and 1 TeV, and as such high energy photons are targeted for detection, it is not possible to use the same techniques which optical telescopes use. The primary description of the LAT instrument is found in Atwood et al. (2009), however other references are given as appropriate.

The Large Area Telescope detects γ-rays based on the mechanism of pair-production (and is referred to as a pair-conversion telescope in the literature) as AGILE does, and EGRET did. In order to fully reconstruct a γ-ray, two pieces of information are needed: the directional vector of the initial γ-ray photon, and the energy of the photon.

The LAT consists of 16 detector 'towers' (called tracker modules), arranged 4x4 into a square when viewed from the top down and each tower consists of 18 'layers'.

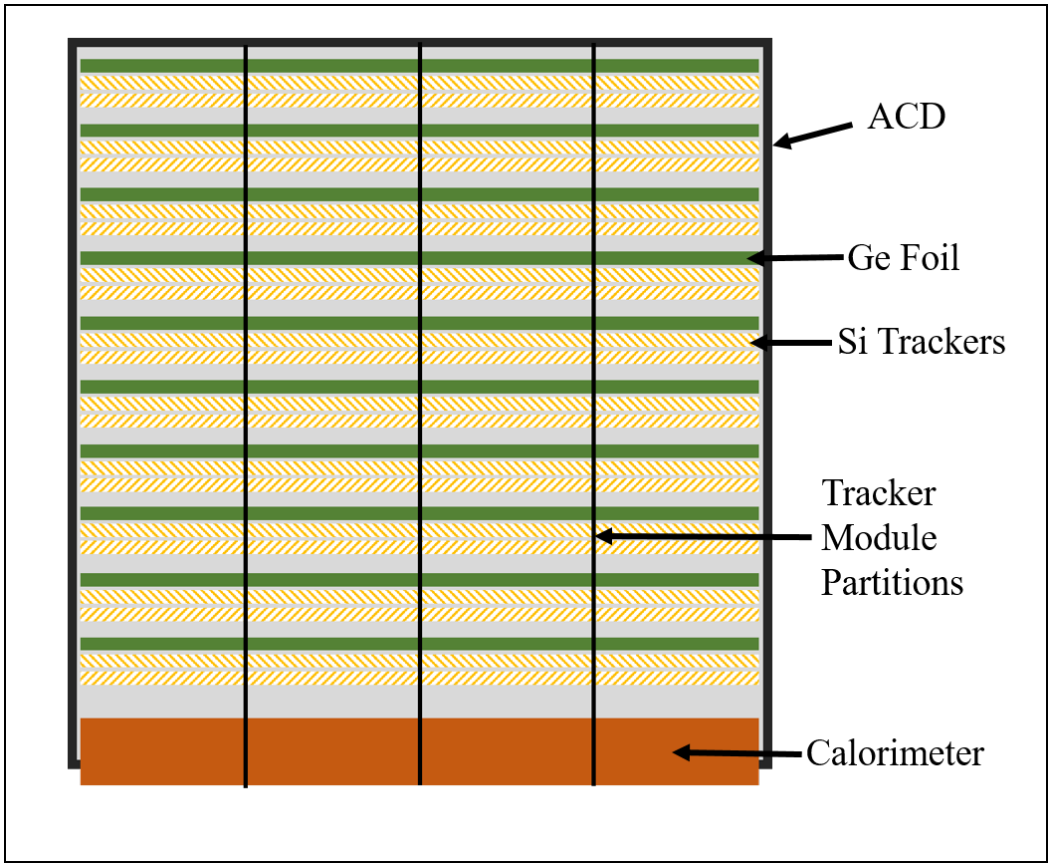

Figure 2.2: A side on view of the LAT detector, showing the 4 tracker modules from the 16 module structure. The Anti-Coincidence Detector (ACD) surrounds and shields the entire detector. Layers of Germanium foil and Silicon tracking strips make up the body of the LAT, maximising pair conversion probability and allowing for the accurate reconstruction of incident γ-ray direction. The calorimeter lies at the base of the detector, allowing for accurate measurement of the incident γ-ray's energy. The central tracker module partition also corresponds to the instrument axis, where 'on-axis' refers to any inbound photons which are perpendicular to this line.

Each layer first consists of a Germanium conversion foil, the point of which is to force incoming γ-rays to pair convert into an electron-positron pair through interaction with the Ge nuclei. Multiple layers of Ge foil are used to maximise the likelihood of pair-conversion, and thus a photon detection by the LAT. As Ge has a relatively high atomic number, γ-rays passing through the foil are likely to interact with this material, and most of the pair production in the LAT occurs in the Ge conversion foils.

Below each conversion foil layer are two layers of Silicon strip detectors (SSDs)

which measure the positions of the electron and positron as they pass through the tracker module. As the electron and positron are travelling at high velocities through the detector they are deflected by each layer of Ge foil, causing changes in their direction of travel, therefore they must have their positions measured after each layer of conversion foil in order to reconstruct the progenitor γ-ray's direction of origin. As a lepton moves through an SSD, it causes ionisation of the silicon atoms, and thus a small current at a point in the strip. Each strip is only able to track the position of a lepton in one spatial dimension, therefore each layer of a tracking module contains two SSD layers perpendicular to one another, which allows for the 2D localisation of a lepton within a layer in the X and Y planes. The LAT SSDs operate with over 99.9% efficiency, thus as layers of Ge conversion foil and SSD trackers are stacked on top of one another in each tracker module, the 2D measurement of lepton position at different points in the Z-dimension allows for a full 3-dimensional reconstruction of the path of the pair produced leptons as they move through the tracker module (Bregeon, 2011). This allows the onboard computer of the LAT to reconstruct the initial direction of a γ-ray which pair-converts within the LAT. A simplified view of the LAT detector is shown in Figure 2.2.

In order to measure the energy of the γ-ray, each tracking module tower contains a calorimeter at the base which contains a hodoscopic array of Caesium Iodide crystals (CsI(TI)) arranged into 8 layers perpendicular to one another. The calorimeter works by inducing an electromagnetic air shower from the leptons entering it, which occurs as the calorimeter has a total thickness of 8.6 radiation lengths (compared to the SSD/conversion foils 1.5 radiation lengths for all 18 layers). This air shower causes secondary γ-rays to be produced and thus further lepton pairs, which continue to move through the calorimeter crystals. As the air shower leptons move through the CsI(TI) crystals, they induce excited states in the crystal electrons, which causes scintillation light to be produced; this light is then measured by photodiodes attached to each CsI(TI) crystal, and the total intensity of scintillation

light produced by the air shower is used to calculate the energy of the progenitor γ-ray (Grove and Johnson, 2010). This is essentially the same mechanism used by ground based TeV observatories, where the intensity of Cherenkov light produced by γ-ray air showers is also used to calculate progenitor photon energy.

The LAT is highly effective at converting and detecting γ-ray events. Across the effective energy range of the LAT, 63% of on-axis photons are converted to a lepton pair, and of this 63% over 99% of conversions have a successful energy measurement from the instrument calorimeter. Photons are also detected off-axis, however as the off-axis angle increases, the conversion efficiency drops, as it is likely that the γ-ray will pass through less layers of conversion foil as it moves through the detector, thus reducing the pair-conversion likelihood. The entire process of pair-conversion, and measuring the direction and energy of an inbound photon and recording this information as a successful γ-ray event takes approximately 100 μs. This interval is referred to as the instrument deadtime.

The largest difficulty faced when recording γ-rays is the cosmic ray flux in low Earth orbit, primarily from high energy protons. Cosmic rays outnumber γ-rays by a factor of approximately 10^3, and like the lepton pairs produced via pair conversion, produce air showers in the LAT calorimeter. Cosmic rays threaten to overwhelm the LAT detector with false positives, so measures are put in place to filter out cosmic ray noise from genuine γ-ray signals. The first line of defence against cosmic rays is the anti-coincidence detector (ACD), a cover built of scintillating tiles which surrounds the tracker modules. As a cosmic ray passes through the ACD scintillation light is produced due to the cosmic ray's electric charge; as photons are electrically neutral, no scintillation light is produced when a γ-ray crosses the ACD. This allows the instrument to distinguish between γ-rays and cosmic rays. In addition to serving as a filter for cosmic rays, the ACD also shields as a micrometeorite defence shield, and is designed to have an extremely short radiation length to minimise γ-ray absorption.

Furthermore, as a cosmic ray passes through the instrument, it will leave a single

track through the SSD tracking layers, whereas a pair-converted γ-ray will leave two due to the lepton pair. Finally, the showers from cosmic rays in the calorimeter tend to extend out and past the calorimeter, whereas the γ-ray air showers tend to be contained. This provides a set of criteria which distinguishes γ-ray events from cosmic ray events in the LAT detector:

1) There is no scintillation light signal for an event in the ACD.

2) Two tracks are measured in the Silicon tracking layers, which both originate from the same point.

3) There is a well contained EM shower in the calorimeter, characteristic of a γ-ray.

Despite this criteria for onboard discrimination between γ-rays and cosmic rays, given that the rate of cosmic ray triggers is several orders of magnitude higher than that of γ-rays cosmic ray events are inevitably recorded in the data as γ-rays. To filter these out further, instrument response functions are applied during the data reduction and analysis stage which further reduces the impact of cosmic rays on the γ-ray images, improving the signal to noise ratio beyond the hardware level described here.

With the hardware described above, the *Fermi*-LAT represents a significant advance over EGRET, by offering greater instrument sensitivity, better cosmic ray rejection, improved positional, temporal and energy resolution, and reduced instrument deadtime. Given the robust design, the LAT has operated continuously for 14 years, significantly longer than EGRET did, and providing strong synergies with other long-term high energy astrophysics missions such as AGILE, INTEGRAL and *Swift*. Atwood et al. (2009) provides a summary of predicted LAT instrument parameters in Table 1, however over the 13 years of observation, certain parameters have been refined (such as energy range) as the instrument performance has become better understood. Therefore, the current instrument parameters based on the detector hardware are given in Table 2.1 (Ajello et al. 2021a & Abdollahi et al. 2020).

Total Energy Range	30 MeV - 1 TeV
Effective Energy Range	100 MeV - 500 GeV
Effective Area	$9500\,\mathrm{cm}^2$
Energy Resolution: 100 MeV - 1 GeV	9% - 15%
Energy Resolution: 1 GeV - 10 GeV	8% - 9%
Energy Resolution: 10 GeV - 300 GeV	8.5% - 18%
Angular Resolution: 100 MeV	3.5°
Angular Resolution: 1 GeV	0.6°
Angular Resolution: $>$ 10 GeV	$\leq 0.15°$
Field of View	2.4 sr
Temporal Resolution	$< 10\,\mu s$
Instrument Deadtime	$26.5\,\mu s$

Table 2.1: The instrument parameters of the *Fermi* Large Area Telescope, as understood in 2022. The total energy range refers to all energies where the LAT is capable of detecting photons; however the effective energy range refers to the energies where useful data are taken, and can be used for point source analysis. The effective area is given at normal incidence, this value changes with angle. All values of energy resolution are on-axis values. The angular resolution refers to the on-axis single photon 68% ($\approx 1\sigma$) containment radius, the 95% containment radius ($\approx 2\sigma$) is given as 3x the value of the 68% radius for a given energy. The off-axis resolution at 55° is given as 1.7x the on-axis value. The field of view refers to the solid angle of the sky which the LAT observes at once. The Temporal Resolution refers to the precision with which timestamps are applied to γ-ray events detected by the LAT, and is not to be confused with deadtime, which is the time taken after an event for the instrument to process that event and ready itself for another detection.

Several of the properties of the LAT detector, chiefly the energy and angular resolution, depend on the energy of the photon being detected, and these values vary significantly due to the extremely wide energy range which the LAT observes over. With regards to the angular resolution, the resolution improves from 3.5° at 100 MeV to a peak resolution of under 0.15° at energies greater than 10 GeV. Although the LAT is capable of detecting an abundance of photons below 100 MeV, these are generally excluded in most data analyses due to their extremely poor angular resolutions at such energies. The energy resolution improves from 100 MeV and is at its most precise between 1 GeV and 10 GeV, before worsening again at higher energies. Most analyses also typically exclude photons of energies above 500 GeV (historically 300 GeV), due to the scarcity of photons at such energies making flux calculations difficult. The temporal resolution is not energy-dependent in the LAT.

Full details about the observed energy dependencies for instrument properties are given in Atwood et al. (2009).

2.2 The LAT Data

The *Fermi*-LAT constantly records data, both γ-rays and noisy background events. These data form a list of discrete events, which is sent on a daily basis from the LAT itself to the *Fermi* Data Centre where the data undergo post-processing, and events are assigned information such as quality flags. The LAT data and analysis tools are non-proprietary and free to access, and an extensive suite of software is available to support LAT data analysis.

There are two types of data file required for analysis of LAT data, both of which are available from the LAT data server and are formatted as 'flexible image transfer system' (`.fits`) files. The first data file is known as the *photon* file, which contains a list of events, both γ-ray and otherwise, detected by the LAT. Each event is contained in a separate indexed sub-directory as part of the `data` directory in Header Display Unit (HDU) 1 of the photon file*.

Each event within the photon file contains a list of properties from this event. Some properties are universal to all events, such as the mission (labelled 'GLAST') and instrument (labelled 'LAT') and are not of much interest to us when we are analysing data. Some properties are technical and related to the file itself, such as the file checksum value and the file creation date. These properties may be useful for checking the integrity of the data files, or when creating new software tools to manipulate the data, but are not regularly looked at during data analysis. Finally, the remainder of the properties give the scientific properties of the event, which we *are* interested in, to perform data analysis.

The scientific information regarding each event observed by the LAT allows for the

*The `.fits` file HDUs start at 0, where HDU 0 typically contains the astronomical images in the data file. As our data file contains no images (only an events list) HDU 0 is left empty.

full reconstruction of the incident γ-ray which caused it, as well as the probability that it was, in fact, a γ-ray and not a noisy false positive caused by a cosmic ray. Each event in the photon file contains the Right Ascension (RA) and Declination (Dec) of the incident γ-ray event, reconstructed from the path of the pair-converted electron-positron pair through the silicon trackers. The incident direction of the event is also provided in Galactic coordinates in the file. The energy of the event as measured from the EM shower by the instrument calorimeter is given in MeV. The LAT data use a time system known as Mission Elapsed Time (MET), counted as the number of seconds since 00:00:00 on the 1st of January 2001 UTC, and this is the system I use throughout this thesis when performing analysis. As a result, the timestamp for the event is given in MET seconds, rather than the traditional Julian/Modified Julian scheme widely used in astronomy. Finally, the event inclination and azimuthal angles are given, along with the zenith angle of the event. These provide information on where the event entered the instrument, as instrument performance varies based on event geometry.

The above information in the photon file comes directly from the event reconstruction aboard *Fermi* and would allow us to build a basic image of the sky alone, using just this information. However, as previously mentioned, noisy background events also make their way into the events list and various factors (such as the way a photon enters the LAT) means that some γ-rays are reconstructed more accurately than others. As such, two additional event properties are calculated during post-processing and are included in the photon event data files. The first of these is the event type (often referred to as evtype). The event type is a numerical value, which allows one to discriminate between a number of properties for the event. The first is whether the event has entered the instrument at the front or the back, as front entry photons generally have better reconstruction than back entry ones due to different effective areas. The second property is the PSF quartile. All photons are defined by how well their point spread function (PSF) is constrained, so the event type allows one to distinguish between photons based on the quality of their

PSF, with all photons divided into 4 quartiles from worst PSF to the best PSF. The same is done with energy reconstruction, and the evtype of a photon allows one to distinguish between photons with accurate energy reconstructions based on their assigned quartile in the overall population of events. The most widely used event type value in analysis is 3, which allows for front and back entry photons, and no constraint on PSF or energy reconstruction.

In addition to the event type, the event class (evclass) provides a measure of how likely an event is to be a photon. The event classes form a nested hierarchy, with higher classes containing fewer photons and a lower efefctive area, with a better signal to noise ratio due to less cosmic ray contamination, and lower classes containing more photons and a higher effective area, but also a greater degree of cosmic ray contamination. The full hierarchy of event classes has been updated several times, as new datasets become available*, however the most recent set of event classes, and their uses are given below (Atwood et al. 2013 & Bruel et al. 2018).

`P8R3_TRANSIENT020` (evclass=16): This class includes all events so that the reference spectrum of this event class is twice that of the isotropic diffuse γ-ray background described in Abdo et al. (2010c). This class has the highest cosmic ray contamination in the standard event class hierarchy, and is typically used for observation of short term transient phenomena such as γ-ray bursts or solar flares.

`P8R3_TRANSIENT010` (evclass=64): This class includes all events so that the reference spectrum of this event class is equal to that of the isotropic diffuse γ-ray background described in Abdo et al. (2010c). This class is also used for transient phenomena, however has improved cosmic ray rejection rates compared to evclass=16, and consequently a lower photon count.

`P8R3_SOURCE` (evclass=128): This class has a lower background spectrum than the

*The most recent dataset is called 'Pass 8' and has seen 3 releases, hence we deal primarily with P8R2 or P8R3 data in this thesis. The changes between R2 and R3 are small, and do not affect the analysis in this thesis.

transient classes, and a much better cosmic ray rejection rate. It is the standard event class for point source analysis and extended source analysis and is used as the standard source class throughout this thesis.

`P8R3_CLEAN` (evclass=256): This class is identical to evclass=128 at energies below 3 GeV, however has a 1.3x - 2x lower background rate at energies above this, thus making this class ideal for hard spectrum sources at high Galactic latitudes.

`P8R3_ULTRACLEAN` (evclass=512) & `P8R3_ULTRACLEANVETO` (evclass=1024): These classes are extremely similar to one another in the P8R3 release. Below 10 GeV the background rate is 15% - 20% lower than evclass=128 and is 50% lower at 200 GeV. This class is used to examine the systematic effect of cosmic ray contamination on the LAT data and is not typically used for point source analysis due to the low effective area.

`P8R3_SOURCEVETO` (evclass=2048): This class is a hybrid of classes 128 and 1024 as it has the same background rate as 128 up to 10 GeV and then the 1024 background rate beyond that energy, with 15% more photon acceptance.

The transient event classes, and several additional non-hierarchical event classes, are not found in the typical photon files, but are instead found in the extended photon files, which contain additional information and many lower quality events.

In addition to the photon files, a second type of data file is needed for LAT analysis, the Spacecraft file. The Spacecraft file does not contain information about photon or cosmic ray events, but instead contains information about the spacecraft itself which is essential for the analysis of the photon file data. The *Fermi* spacecraft file contains information on the spacecraft at 30 second intervals, and contains both the beginning and end times of the interval in MET, and the livetime of the instrument during this interval (in seconds). The positional coordinates and pointing of the instrument are included from the start of each interval, as is the rocking angle of the instrument and the satellite velocity. Data flags are assigned to each interval, so that bad periods of data can be excluded from phenomena such as particle events

or solar flares where the instrument response functions do not accurately reflect the data in these times. Finally, magnetic field information is included, as certain points of the LAT's orbit can cause observational difficulties, such as the South Atlantic Anomaly. The spacecraft file is also presented as a `.fits` file, and both the photon and spacecraft files are available for any given time period from the *Fermi*-LAT data server*

2.3 Modelling LAT Data

In order to draw scientific inferences from the raw LAT data, the data must be analysed. The data analysis comes in 4 steps:

1) Data reduction: Unnecessary photons are removed from our list of photons, and the signal to noise ratio is improved via application of instrument response functions.

2) Data modelling: Through the use of background models and a source catalogue, a mathematical model is built which describes background, point and spatially extended sources of γ-rays, based on prior knowledge.

3) Model fitting: Maximum-likelihood estimation is used to fit the model to the data.

4) Advanced analysis: Investigation of the properties of individual γ-ray sources using the best fit model to the data.

There are a number of ways to analyse LAT data, and several pieces of software which allow for its analysis. In this thesis, I use the `Fermipy` analysis package which is written in `Python 2.7`, although a `Python 3.X` version has now been released†. `Fermipy` uses a set of tools written by the *Fermi*-LAT collaboration called the `Fermitools`‡, primarily for the data reduction steps of the analysis. The

*https://fermi.gsfc.nasa.gov/cgi-bin/ssc/LAT/LATDataQuery.cgi

†I have used the `Python 2.7` version as it was the more stable of the two releases.

‡Formerly the *Fermi* Science Tools

`Fermitools` are largely written in `Python 2.7`* and partially in shell script. In this Section, I will provide a breakdown of the relevant individual `Fermitools`, before discussing these in the context of a full analysis with `Fermipy`. All of the `Fermitools` begin with 'gt', this stands for GLAST Tools.

2.3.1 Photon Selection

`gtselect` is usually the first tool which is applied during any *Fermi* data analysis, and cuts down the list of events (which can be significant, particularly when using an all sky dataset) to a desired region of interest (ROI) in space, energy and time. This tool only operates on the photon events files, and takes either a single 'events.fits' file, or a list of such files provided in an 'events.txt' file. The output of this tool is a filtered 'events.fits' file, which has the format of the photon events file described previously, but only contains photons considered acceptable by the `gtselect` filters.

The following parameters describe how photons are cut using `gtselect`, and the different ways in which photons can be selected for analysis:

1) `tmin` and `tmax` define the start and end times of the range where photons are selected in MET.

2) `emin` and `emax` define the minimum and maximum values of the energy range of photons which are selected in MeV.

3) `evtype` and `evclass` allow photons to be selected by their event type and event class, allowing for cuts based on photon quality, point spread function, energy reconstruction and instrument effective area.

4) `RA` and `Dec` determine the central position of the ROI in equatorial coordinates (measured in °), within which we consider photons. The `rad` parameter determines the radius around this position which defines the ROI.

*Again, a `Python 3.X` is now released, but was less stable.

5) `zmax` determines the maximum allowed zenith angle of photons (°). This value is exclusively set to 90° in all analyses in this thesis, as is recommended in the *Fermi*-LAT cicerone.

6) `phasemin` and `phasemax` allow photons to be sorted by the orbital phase of a source. The photon files do not come with any phase information by default, and this must be calculated using an ephemeris for a source and applied to the photon files separately, before `gtselect` is used.

`gtmktime`, like `gtselect`, performs photon selection by applying information contained within the spacecraft file to the filtered events file created by `gtselect`. The tool does this by calculating a series of 'Good Time Intervals' where the instrument is active and collecting data which is not compromised by any external factors. The inputs for this tool are the spacecraft data file, the filtered events file and a filter string which is composed of three parts:

1) `DATA_QUAL` indicates whether the data during a given period of of good quality of not. A flag of 1 indicates okay data, 2 indicates that the data awaits review by the LAT team, 3 indicates the data is okay with bad parts and 0 indicates the data is compromised, and should not be used.

2) `LAT_CONFIG` indicates whether the LAT is operating normally during a given period. A flag of 1 indicates that the LAT is in its science configuration and is taking observations, whereas 0 indicates that the data are not recommended for analysis.

3) `ROCK_ANGLE` allows cuts to be made based on the rocking angle of the instrument. Whilst the LAT usually observes the sky in an 'all-sky' survey mode, pointed observations of specific targets are made. These can be eliminated from datasets by using this parameter.

By combining the above parts, we end up with a filter string which is used to calculate the Good Time Intervals. Currently the recommended filter is:

```
(DATA_QUAL>0)&&(LAT_CONFIG==1)
```

This is the filter I use throughout this thesis.

2.3.2 Instrument Livetime

The instrument response functions, which are used to map the detected LAT photon flux with the detected events list, depend on the inclination angle* of the instrument. Therefore, in order to calculate accurate photon fluxes for sources, each analysis uses a 'livetime cube', which contains a 3D model of the sky as a function of inclination angle and equatorial coordinates which contains the total amount of time the LAT spends looking at every point of the sky as a function of inclination angle, which facilitates the use of the instrument response functions in later steps.

`gtltcube` is the tool which produces livetime cubes, and requires the spacecraft file (which contains the instrument pointing history) the filtered photon events file (which contains the start and end times of the observations), and an inclination angle step value (as the inclination angle is approximated by a HEALPIX map, rather than as a continuous function). Typically the inclination angle is taken as 0.025°. `gtltcube` produces the livetime cube as a separate .fits file to the existing spacecraft and photon events files, and it does not alter these files in any way, unlike the previous steps. Generating a livetime cube is typically the most computationally expensive part of a single analysis, however given that each livetime cube encompasses the whole sky, livetime cube files can be used interchangeably between analyses, provided that the the time periods are the same. As is demonstrated in later Chapters, hundreds of analyses are performed over the same timescales, and in these cases the same livetime cube can be used for each, dramatically speeding up analysis time.

*A reminder, the inclination angle is the angle between the instrument z-axis (i.e. emerges out of the face of the instrument) and a γ-ray source.

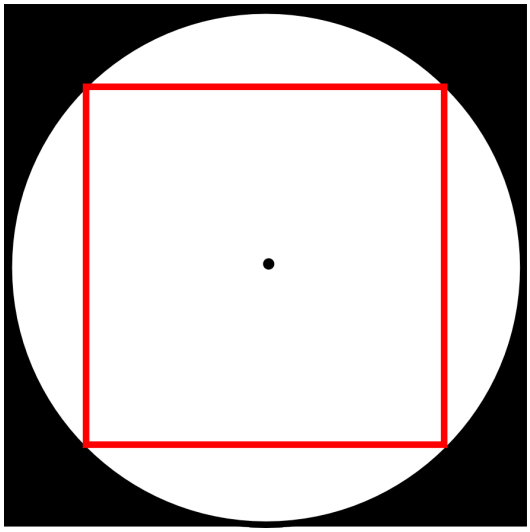

Figure 2.3: The shape of the photon acceptance region after `gtselect` is given by the white region within the circle, whereas the ROI after `gtbin` is shown by the area within the red square. Following `gtbin`, all photons within the circle but exclude from the square are removed from the model. The black dot indicates the centre of the ROI.

2.3.3 Model Binning Schemes

Photon events must be binned, as by varying model parameters to attempt to replicate the number of photon counts in each bin, we model our region. The tool used for binning photons is `gtbin`, and is a versatile tool which can bin photons into spatial bins across the ROI, energy bins (to create a spectrum of the ROI) and time bins (to create a light-curve of the ROI). We do not use this last function, as light-curves are created via a different method covered in Section 2.4.

In almost all of the analyses in this thesis, the photons are binned in both energy and space; this is referred to as a 'binned' analysis, and is generally used for almost all *Fermi* analyses. In cases where photons are binned in space but not energy, this is referred to as an 'unbinned' analysis. Unbinned analyses are only preferred when looking at an ROI where there are very few events; i.e. over a very short timescales, and unbinned analyses are not suitable where there are bright sources in the ROI, the ROI is on the Galactic plane, or over long time periods. In the case of a binned analysis, the output is a 3-dimensional binned events file (.fits format) called a

counts cube, and in the case of an unbinned analysis a 2-dimensional binned events file is produced called a counts map.

The input file required for `gtbin` to operate on is the filtered photon file which has been processed by `gtselect` and `gtmktime`; the livetime cube is not needed so `gtbin` may be run either before or after `gtltcube`. The output file must then be specified (counts cube, counts map or light-curve), and in the case of the counts cube and map, the central RA and Dec of the ROI must be provided along with the number of pixels (bins) to be used in the X and Y axes of the file, and the bin width in degrees. Additionally, the projection method must be specified, and any rotation angles which are to be used when producing the binned events file. In the case of the counts cube, where the file is also binned in energy, the lower and upper energy bounds must be specified for the photon binning (these should be the same as those given when cutting photons with `gtselect`), as well as the number of bins per decade of energy to be used for binning. Whilst `gtselect` cuts photons within a certain radius of the centre, resulting in a photon acceptance cone, `gtbin` cuts these further so that the resultant ROI is a square; this is illustrated in Figure 2.3.

2.3.4 Calculating Instrument Exposure

Whilst *Fermi*-LAT observes the entire sky, it does not observe it equally; the amount of time that the LAT spends looking at each point of the sky is referred to as the exposure time, and instrument exposure needs to be accounted for in LAT data models. Typically in astronomy, photons are more or less treated as continuous, and exposure is simply the integral of telescope effective area over time. For a telescope such as *Fermi*-LAT, where it is much more appropriate to treat each photon as a discrete event, the concept of telescope exposure is slightly different. Here, the exposure, ϵ, is calculated by integrating the total response of the instrument, R, over the full ROI, shown in Equation 2.1.

$$\epsilon(E,\,\mathbf{p}) = \int_{ROI} dE' d\mathbf{p}' dt R(E', \mathbf{p}', E, \mathbf{p}, t) \tag{2.1}$$

Here, primed quantities indicate the measured values of Energy, E, and directional vector $\mathbf{p}$.

Several tools have been released by the LAT Collaboration to calculate instrument exposure, however the most recent, and the one recommended for use, is `gtexpcube2`. `gtexpcube2` operates in a reasonably simple way. It takes the instrument livetime cube which was computed with `gtltcube`, which contains the instrument pointing history for the duration of observations, and the binned events file produced by `gtbin`, and produces an exposure map of the ROI for which we have our binned data file. `gtexpcube2` can be run without the binned events file from `gtbin`, however the parameters of this file (such as bin sizes and ROI pixel count) must be manually specified instead.

2.3.5 Assembling the Model

The next step in analysis is to produce the source model, an XML file with a list of the known γ-ray sources in the ROI, and information about these sources, such as their spectral parameters. There are a number of ways to produce this; in theory the user can write this file themselves using the information from the point source catalogues and the Galactic diffuse background model, however a `Python` script called `make4FGLxml.py` automates this process, and adds sources to the model from outside the field to account for the large point spread function of the LAT at lower photon energies.

In its initial form, the source model is not very useful as the parameters of each source are based on the catalogues and background models, i.e. prior information; as a result, the source model is very unlikely to represent the data in our events file very well. In order to improve how well the source model represents the events file, the parameters of each source are changed to better reflect their real observed

values. This is done through a technique called Maximum Likelihood Estimation (MLE), however in order to perform MLE using our model and events file, we must first produce a source map of our ROI.

The source map is essentially the product of the separate steps taken above, where the livetime cube, exposure map, binned events file, spacecraft data file and source model are convolved together with the instrument response function to produce a file (in .fits format). This is essentially a 'predictive' counts cube, where the predicted counts of each bin, N_{pred} comes from the expected source intensity, $S_i(E, \mathbf{p})$ and the exposure of the source, $\epsilon(E, \mathbf{p})$. The relationship between these quantities is given by the integral in Equation 2.2

$$N_{pred} = \int_{ROI} dE d\mathbf{p} S_i(E, \mathbf{p}) \epsilon(E, \mathbf{p}) \tag{2.2}$$

The tool used to produce the source map is called `gtsrcmaps`, and takes the aforementioned files and convolves them with the instrument response function. It is important that the appropriate instrument response function is chosen for the respective event class, and appropriate isotropic model, else significant additional uncertainties are introduced into the model, which are difficult to quantify.

2.3.6 Modelling with Fermipy

Following the production of a source map, one may use the `gtlike`* tool to perform MLE and improve the fit of the model to the data, before applying advanced analysis techniques to test scientific hypotheses with the model. Throughout this thesis I do not use `gtlike` itself but use it as part of a `Python` package called `Fermipy`, which automates the above steps, performs the likelihood fit, and provides a suite of additional tools for statistical modelling of the data and advanced source analysis (Wood et al., 2017). In addition to `Fermipy`, several other analysis packages exist which analyse *Fermi*-LAT data such as `Enrico` (Sanchez and Deil, 2013),

*https://fermi.gsfc.nasa.gov/ssc/data/p6v11/analysis/scitools/help/gtlike.txt

`easyFermi` (de Menezes, 2022) and `Gammapy`, which is primarily built for the analysis of IACT data (Deil et al., 2017).

`Fermipy` is built around the `Fermitools` themselves, which are also written primarily in the `Python` language; using `Fermipy` to complete the above steps is generally quicker and more efficient than executing the tools one-by-one, and allows more easily for analysis projects (such as surveys of populations of sources) to be completed.

The first step in creating a model using `Fermipy` is to produce a configuration file, which is written in the YAML format. The configuration file holds all of the information which is used to operate the `Fermitools` within `Fermipy`, rather than specifying parameters at the point of executing each tool. Such parameters include (but are not limited to) pointers to the data files, information regarding photon selection (such as the event class and type), and the information to produce a source model, such as the catalogue and background models to be used. An example configuration file is shown in Figure 2.4.

A detailed guide to analysing data using `Fermipy` is given in the software documentation, detailed in Appendix I.

Having produced a configuration file, two steps need to be taken. Having imported `Fermipy` into the `Python` environment, the first step is to define a `GTAnalysis`* object, by pointing to the configuration file. Any subsequent analysis done using this object will use the parameters specified in the configuration file.

Next, `gta.setup` is run. This command first creates a filtered events file by performing `gtselect` and `gtmktime` using the events file and spacecraft specified in the configuration file, before generating a livetime cube using `gtltcube`. Next exposure is calculated using `gtexpcube2`, before the data is binned with `gtbin` and a source map is created using `gtsrcmaps`, before `gtlike` is run. `Fermipy` provides the facility for binned analysis only, unbinned analysis is not currently supported.

*Abbreviated as `gta`.

```yaml
# NGC 1275 Configuration File

data:
  evfile : events.txt #our list of photon files
  scfile : data/L1910170847288E15477E17_SC00.fits #our spacecraft file

binning:
  roiwidth   : 15.0 # Let's keep a small roi
  binsz      : 0.1 # bin size in degrees
  binsperdec : 10 # Ebins per decade in energy - 10 is a good estimate

selection:
  emin : 100  #our minimum energy
  emax : 300000  #our maximum energy
  zmax : 90  #our zenith angle
  evclass : 128  #our event class
  evtype : 3  #our event type
  tmin : 283996802  #our minimum time
  tmax : 315532802  #our maximum time
  filter : DATA_QUAL>0 && LAT_CONFIG==1 #A standard filter for gtmktime
  target : 'NGC 1275' # As NGC 1275 is in our 4FGL catalogue, we can simply type its name in,
instead of the ra and dec of the source.

gtlike:
  edisp : True # Enable energy dispersion
  irfs : 'P8R2_SOURCE_V6'
  edisp_disable  : ['isodiff', 'galdiff'] # Never enable energy dispersion for the isodiff or
galdiff models

model:
  src_roiwidth : 25.0 #Includes sources outside of the ROI
  galdiff  : 'gll_iem_v07.fits' # The most recent and up to date model of the galactic diffuse
emission
  isodiff  : 'iso_P8R3_SOURCE_V2_v1.txt' # The most recent and up to date model for the
isotropic diffuse emission, and for our event class
  catalogs : ['4FGL'] # The 4FGL catalogue, 8 year Fermi-LAT point source catalogue.

```

Figure 2.4: An example of a `Fermipy` configuration file written in the YAML format. This configuration file describes the parameters for an analysis of the radio galaxy NGC 1275, located within the Perseus cluster. The nested structure of the YAML file shows that the parameters are grouped; these groups are the input data files; the binning parameters; the data selection criteria; the parameters for the likelihood fit, and the source model parameters. The turquoise text located after # signs indicate comments which are not read by the YAML interpreter.

2.3.7 Likelihood Fitting

Maximum Likelihood Estimation has been a method used to model γ-ray data for decades, and was used in the data analysis of the LAT's predecessor, EGRET, described in Mattox et al. (1996). MLE revolves around the Likelihood function $\mathcal{L}$, defined in Equation 2.3, which provides the link between the data (i.e. photon count) $X = x_i$, and the model ($\Theta = \theta_i$) (i.e. predicted photon count) in each bin (Fisher, 1922).

$$\mathcal{L}(\Theta|X) = P(X|\Theta) \tag{2.3}$$

Thus the likelihood represents the probability of the observed data being a function of a set of parameters of a given model. Through maximising the likelihood, we maximise this probability. In a practical setting, it is easier to work with the natural logarithm of the likelihood (the log-likelihood, ℓ), and to maximise this instead, as most common probability distributions are logarithmically concave. The log-likelihood is given by Equation 2.4.

$$\ell = \ln \mathcal{L}(\Theta|X) = \sum_i \ln P(x_i|\Theta) \tag{2.4}$$

In a practical sense, improving the fit of a *Fermi*-LAT model to the dataset is done by varying the parameters (such as spectral shape, normalisation, index) so that the log-likelihood value is maximised, indicating that the sources in the model accurately reflect those which are observed in the data. A large ROI can have 100 sources or more, each with many parameters, making the MLE calculations non-trivial, and numerous sources often contribute γ-rays to each bin. Several tools are available to fit source models to LAT data using MLE `Fermipy`; both of these are based on the `pyLikelihood` module.

Following the `gta.setup` command, the next step is usually to run `gta.optimize`. `gta.optimize` is an iterative tool which takes the 5 brightest sources in the ROI (although this number can vary), and simultaneously fits the parameters of these sources before moving on to the next 5 sources. This process sees the parameters of the sources within the model pushed close to their global log-likelihood maxima, and therefore usually significantly improves the fit of the model to the data.

Whilst `gta.optimize` improves the general accuracy of the model parameters greatly, they can often be improved further. A second tool called `gta.fit` performs a full likelihood fit, adjusting all freed parameters in the model and recalculating

the model log-likelihood until a maximum is found, and the fit is of sufficient quality. As the parameter space of the model grows very rapidly with additional sources being added, typically only select parameters (such as spectral normalisation), or select sources (such as bright or variable sources) have their parameters freed, else `gta.fit` may fail to converge. A number of computational optimization routines can be used within both `gta.optimize` and `gta.fit`; throughout this thesis, I use `MINUIT`*.

2.3.8 Likelihood Ratio Hypothesis Testing

Having used MLE methods within `Fermipy` to improve the model fit quality, it is possible to test scientific hypotheses using it. Given we use Likelihood modelling as our statistical framework, the simplest way to test scientific hypotheses with our model is by using the Likelihood ratio test. The Likelihood ratio test is one of a number of hypothesis tests, other examples being the score multiplier test and the Wald test, and as we generally have no unknown parameters in our model it is the most powerful of these tests according to the Neyman-Pearson lemma (Neyman and Pearson 1933, Silvey 1959 & Gregory and Veall 1985).

The Likelihood ratio test is mathematically the ratio of the likelihoods between two hypotheses, the alternative (Θ_1) and a null hypothesis (Θ_2), which results in the log-likelihood test statistic (TS), given in Equation 2.5.

$$\mathrm{TS} = 2 \ln \frac{L(\Theta_1)}{L(\Theta_2)} \tag{2.5}$$

Via Wilks' Theorem, the TS value is distributed as χ^2 with k degrees of freedom, where the degrees of freedom are equal to the difference in the number of parameters between the models used for the null and alternate hypotheses (Wilks, 1938). Therefore, as the TS value is distributed as χ^2, the TS value can be used to calculate a z-score for a hypothesis which reveals how many standard deviations away

*https://root.cern.ch/download/minuit.pdf

from the mean value of the null hypothesis distribution the alternate hypothesis is, therefore indicating the statistical significance of the alternate hypothesis. For $k = 1$ degrees of freedom between the two hypotheses, the z-score is distributed as $z = \sqrt{TS}$.

Log-likelihood ratio testing is the statistical backbone of *Fermi* analysis, and is used in numerous ways, including to test whether sources are temporally variable (TS_{var}), or spatially extended (TS_{ext}). The most common use however is to test the hypothesis that a point source of γ-rays exists at a particular position (simply the TS with no suffix), and therefore the TS value of a source is used as a statistical indicator of the significance of this source. Across most fields of science a z-score of 2σ (corresponding to $p = 0.05$ and TS $= 4$) is considered statistically significant, with only a 5% chance this result is a false positive. In γ-ray astronomy, the γ-ray background is poorly understood, hence a higher threshold of 5σ is used for a point source to be conventionally 'detected'. In this thesis we deal with many γ-ray point sources with $z < 5\sigma$ significances; these are referred to as γ-ray excesses to distinguish them from the conventionally detected sources.

2.4 Advanced Source Analysis

In addition to hypothesis testing, `Fermipy` provides functionality to examine numerous properties of γ-ray in *Fermi*-LAT models. These are all used at various points throughout this thesis, and therefore description of each advanced analysis technique is given below.

2.4.1 Identifying New Sources

When building a source model, a catalogue (usually the 4FGL) is used to populate the model with sources, however it is often the case that the catalogue will not include every point source in the dataset; hence any additional, uncatalogued

sources should be added in order to increase the model's accuracy. `Fermipy` has a tool designed for the identification of new sources known as `gta.find_sources`. The tool produces a TS map of the ROI, and iteratively fits point sources to the 4 highest TS peaks identified, before repeating this process 4 times so that 20 point sources are added under standard operating conditions, although the number of iterations and sources to be fit simultaneously can be changed. These sources all have a pre-determined spectral shape, the fit of which can be improved by freeing the spectral parameters of the added source and refitting using `gta.fit`. In addition to improving model accuracy, `gta.find_sources` can be used as a means to survey the sky for new sources; each added source has a positional error box surrounding it, and thus if this uncertainty region overlaps with an expected γ-ray emitter, then this source may represent emission from that object, although more evidence than simple spatial coincidence is needed to typically associate a γ-ray source/excess with a potential object seen at other wavelengths.

2.4.2 Spectral Energy Distributions

The spectral energy distribution (SED) of an astronomical object reveals how the flux of a source varies as the energy at which it is observed changes. SEDs can either be single band, such as those shown in this thesis which just cover the γ-ray energies, or broadband covering a larger swathe of the EM spectrum. The primary insight that plotting and modelling the spectra of γ-ray sources yields is information about the particle populations which emit the γ-rays, as different populations yield different observed spectral shapes (Section 1.2).

The tool which calculates source SEDs in `Fermipy` is `gta.sed`; this tool will calculate the flux of any source in the model in each of the model's energy bins (or a factor of the number of energy bins), and will also provide a diagnostic plot of the SED with flux plotted against energy.

In addition to plotting the SED itself `gta.sed` will also calculate the best fit shape

of the spectrum. A wide range of spectral shapes are used in *Fermi* modelling*, however two are primarily used throughout this thesis: the power-law and the log-parabola.

The power-law model is essentially a straight line (as SEDs are plotted in logarithmic space) given by Equation 2.6, where N_0 is the source normalisation, Γ is the spectral index, and E_0 is the scale energy. The spectral index can be positive (a hard power law) or negative (a soft power law), depending on the source; most power-law sources are soft.

$$\frac{dN}{dE} = N_0 \left(\frac{E}{E_0}\right)^{\Gamma} \tag{2.6}$$

The second commonly used spectral model is the log-parabola, which as its name suggests, is a parabola in logarithmic space. Equation 2.7 shows the equation for the log-parabola. Here N_0 is the normalisation, E_b is a scale parameter and α and β are shape parameters.

$$\frac{dN}{dE} = N_0 \left(\frac{E}{E_b}\right)^{-(\alpha+\beta \ln(\frac{E}{E_b}))} \tag{2.7}$$

2.4.3 Light-curves

Just as spectral energy distributions plot how the flux of a source varies with observed energy, a light-curve shows how the flux of a source varies over time. Light-curves do not tend to be broadband, as many objects vary differently at different energies, hence multiple light-curves of a single source at different wavelengths are commonly used, as opposed to a single light-curve. In this thesis I use primarily γ-ray light-curves computed with `Fermipy`, however also use precomputed X-ray light-curves from *Swift*-BAT and MAXI, and optical light-curves from AAVSO.

*A full list of spectral models used for *Fermi*-LAT analysis can be found here: https://fermi.gsfc.nasa.gov/ssc/data/analysis/scitools/source_models.html

Light-curves are powerful tools in the analysis of LAT sources; not only can multi-wavelength correlated variability associate γ-ray sources with their counterparts at other wavelengths, but variability (such as rapid flux increases) can indicate physical changes in a system, such as outbursts from an X-ray binary system, which are examined in Chapter 4.

`Fermipy` has a tool for producing light-curves of sources called `gta.lightcurve`; this tool produces a light-curve by doing a full likelihood analysis in each specified time bin and calculating the flux of the source during each. Unlike `gta.sed` `Fermipy` does not fit variability models to light-curves.

In addition to observing flux changes over time, separate SEDs can be calculated to examine whether the parameters of the spectral shape vary over time. Sources with variable spectral parameters are referred to as being spectrally variable.

In both light-curves and SEDs, photons are binned by time/energy which reduces the number of source photons available for the flux calculation in each bin, increasing the uncertainty on the flux, and decreasing the TS values of the bins compared to the overall energy/time range. Therefore it is common for bins to have very large uncertainties on their flux measurements. Therefore throughout this thesis when the TS value of a particular bin in either an SED or light-curve is below 4 (2σ), a 95% upper confidence limit on flux is used instead, rather than an imprecise value of flux (Helene, 1983).

Many sources vary in a cyclical way, with their observed flux being a function of some other physical parameter such as rotation phase (commonly seen in pulsars) or their orbital phase (commonly seen in compact binaries). Therefore light-curves can also be produced where instead of examining an object by time, flux is calculated by orbital phase; the resultant product is a phase-folded light-curve, and `Fermipy` can produce these by selecting photons by phase, provided that the events file have already been altered to include the ephemeris of the source to be observed, with a

tool such as `gtophase` *.

2.4.4 Spatial Extension

All *Fermi*-LAT source models are made up of three types of sources: the diffuse γ-ray background components, the point sources, and the spatially extended sources. Extended sources are rare, and the vast majority are Galactic sources such as supernova remnants or pulsar wind nebulae. Being able to determine whether a source is spatially extended or not provides information about its nature, as many sources (such as stellar scale systems) are not extended, allowing for easier identification of *Fermi*-LAT sources.

`Fermipy` has a tool for extension testing called `gta.extension`, which performs a likelihood ratio test between an extended source alternate hypothesis and a point source null hypothesis, resulting in a TS value (the TS_{ext}) which can be converted into a significance value. Two extended models can be fitted, a radial Gaussian model, and a radial disc model, and it is generally advisable to test both models against the point source hypothesis when testing for source extension.

2.4.5 Source Localisation

The final advanced analysis technique is source localisation, which is a smaller scale likelihood fit centered on one single source with the aim of adjusting the source's position in the model to it's most likely position. This is done with a tool called `gta.localize`, which operates in two steps. The first sees a TS map produced around the source in question where a 99% uncertainty region on the position of the source is then calculated. The second step sees a likelihood scan of this region alone performed, and the sees the source adjusted to the new best fit position and new uncertainties on that position calculated (which are typically smaller than the uncertainties on the original position). The primary use of source localisation

*https://fermi.gsfc.nasa.gov/ssc/data/p7rep/analysis/scitools/help/gtophase.txt

is that the improved positional fit and correspondingly smaller uncertainties on this position means that it is easier to determine whether a γ-ray source is truly spatially coincident with an object thought to be producing the emission. Therefore localisation is especially useful to constrain the positions of uncatalogued sources, such as those identified by `gta.find_sources`.

Figure 2.5: The second labour of Heracles, the slaying of the Lernaean Hydra with Iolaus. By Hans Sebald Beham (Year Unknown).

Chapter 3

Compact Binaries

In this chapter, I detail the basic features of stellar remnants and the mechanics of binary star systems, before discussing the populations of binary star systems which produce γ-ray emission detectable with *Fermi*-LAT. Special emphasis is placed on the X-ray binaries, their sub-classes and different morphologies, as these objects are the focus of the subsequent chapters of this thesis. In addition to in-text references to the scientific literature in this Chapter, I have also referenced undergraduate level equations and material covered in Tipler and Mosca (2007), Ostlie and Carroll (2007) and Ryden and Peterson (2020). Additional background information regarding the basic principles of stellar evolution can be found in Appendix A.

3.1 Stellar Remnants

What remains of a star after a supernova, or a planetary nebula phase, depends on the original mass of the star. For stars with $m < 8M_{\odot}$, electron degeneracy pressure will halt the core collapse and prevent any further collapse resulting in a white dwarf. Most white dwarfs have carbon cores, however as progenitor stars approach the $m = 8M_{\odot}$ limit layers of heavier elements begin to build up inside the star in the 'Russian Doll' structure. It is not until this limit is reached that an iron core is formed which prevents any further fusion, and causes a core collapse supernova. For stars in the mass range $8M_{\odot} < m < 20M_{\odot}$ a core collapse

supernova will occur and the core collapse will be halted by neutron degeneracy pressure. The subsequent stellar remnant is known as a neutron star, and they are much smaller and denser than white dwarfs are. Neither white dwarfs nor neutron stars produce any elements within them via nuclear fusion. For stars which exceed the $m > 20M_{\odot}$* limit, the gravitational force of the collapsing core overcomes neutron degeneracy pressure, and hydrostatic equilibrium is unable to be reestablished. The stellar core collapses into a gravitational singularity, and the resulting object is known as a black hole.

All three types of stellar remnant (also known as compact objects) are important objects in astrophysics, due to their interactions with other objects. Black holes in particular are known to evolve to astonishing sizes, and influence processes such as star formation on galactic scales. Furthermore, it is possible for neutron stars to collapse into black holes when these systems gain mass either through stellar mergers, or through accreting matter from their local environment. All three types are seen in some form of γ-ray emitting star system, and as a result it is necessary to explore the basic properties of each class.

3.1.1 White Dwarfs

White dwarfs represent the endpoint of the majority of stellar systems, and are approximately the mass of the sun. They were the first stellar remnants to be detected in observations where 40 Eridani B was identified to have a spectral type of A (corresponding to a hot white star in the Hertzsprung-Russell diagram) despite being less luminous than a typical main sequence A-type star (Adams, 1914). More observations of white dwarfs followed, and now they are recognised to be an observationally distinct class of stars with the typical colour and temperature of massive main sequence stars but much lower luminosities and therefore occupy a unique region of the Hertzsprung-Russell diagram (Figure A.1), below the main se-

*Whilst I use a $20M_{\odot}$ value for the mass boundary between neutron star and black hole progenitors this figure is an estimate, and the true mass boundary is still a subject of debate.

quence. Such systems are relatively common compared to neutron stars and black holes, with over 100 white dwarfs identified within 20 parsecs of Earth (Sion et al., 2009).

These systems are composed of carbon, and smaller amounts of other heavier elements (mainly oxygen), up to but excluding iron depending on the mass of the progenitor star. These systems are extremely dense at $10^9\,\mathrm{kg\ m^3}$ and hot, at temperatures up to $2 \times 10^5\,\mathrm{K}$, however do not produce any meaningful amount of energy themselves. White dwarfs instead remain hot from the pressure and heat of the nuclear fusion which occurred during the main sequence and red giant phases, and as the white dwarf ages it cools down (Althaus et al., 2010). The hypothetical endpoint of a white dwarf is a cold, dark, dense star called a 'black dwarf' which is in thermal equilibrium with its surroundings; however, the expected cooling timescales of white dwarfs mean that the time taken to produce a black dwarf is much longer than the age of the universe (Salaris et al., 2013).

When taken in isolation, white dwarfs are not considered to be a source of γ-ray emission, as they lack magnetic fields powerful enough to accelerate particles to the required energies to emit γ-rays. A subclass of white dwarf system known as Cataclysmic Variables (CVs) which can emit γ-rays is discussed in Section 3.2.2.

3.1.2 Neutron Stars

When the iron core of a star exceeds $1.44 M_\odot$, the Chandrasekhar limit, electron degeneracy pressure is no longer sufficient to prevent core collapse (Chandrasekhar, 1931). What remains of the star is the extremely dense core which is now held in hydrostatic equilibrium by neutron degeneracy pressure, which allows for a much denser star than electron degeneracy pressure does. These remnants are known as neutron stars, they have densities comparable to atomic nuclei, temperatures exceeding $6 \times 10^5\,\mathrm{K}$ and stellar radii of approximately 10 km (Zdunik et al., 2016).

When the stellar core collapses the rotational rate of the core increases dramatically

in order to conserve rotational angular momentum, hence newly collapsed neutron stars have initial spins of approximately 1 ms. As the stellar core collapses, the magnetic field of the core is conserved, and hence the field lines are forced much closer together in the neutron star, leading to neutron stars having extremely high magnetic field strengths. The magnetic field strength of a neutron star after collapse is given by Equation 3.1, and is of order 10^9 times stronger than the progenitor star (Peng and Tong, 2007).

$$B_{NS} = \left(\frac{R_{Core}}{R_{NS}}\right)^2 B_{Progenitor} \tag{3.1}$$

If the rotational and magnetic poles do not align (as is the case with Earth), this leads to the beamed emission sweeping across the sky, and hence many neutron stars appear to have 'pulsed' emission when observed. Such stars are known as pulsars*, and it was the identification of pulsed radio emission which led to the first detection of a neutron star (Hewish et al., 1968)†. Whilst pulsed emission is typically seen at radio wavelengths, it is also seen at optical and γ-ray wavelengths (Grenier and Harding 2015 & Ambrosino et al. 2017). They are detected with *Fermi*-LAT which has software developed to resolve neutron stars by their rotational phase.

Observationally, neutron stars are far rarer than White Dwarfs, which is to be expected given that they require more massive progenitors which are rarer. Whilst over 100 white dwarfs are observed within 20 parsecs of Earth, the nearest neutron star (1RXS J141256.0+792204) is approximately 200 parsecs away. Known neutron stars order in the thousands (e.g. Manchester et al. (2005)), and γ-ray emitting neutron stars number just over 100 in the latest *Fermi*-LAT catalogue (Abdollahi et al., 2020). It is now generally accepted that γ-rays are produced by pulsars near their magnetic poles through inverse Compton emission of cyclotron X-rays

*According to Jocelyn Bell-Burnell, the name 'pulsar' comes from a Daily Telegraph reporter who shortened 'pulsating radio source' in their article.

†The discovery of the first pulsar was by Jocelyn Bell-Burnell, not her supervisor Antony Hewish as the naming convention of this paper suggests. Whilst Hewish (and and the first Nigerian radio astronomer Samuel Okoye) discovered radio emission from the Crab nebula, Hewish was solely (and wrongly) awarded the 1974 Nobel Prize for Physics for the discovery of the pulsar, without Bell-Burnell who played a key role.

produced by particles accelerated in the powerful magnetic fields of the pulsar, and given that γ-ray pulsations are seen to be synchronised with radio pulsations, the γ-rays are produced in the same region as the radio emission (Lyutikov, 2013).

As neutron stars age, they radiate both energy (in the form of broadband EM radiation) and matter in the form of a pulsar wind. This wind can form a gaseous cloud around the star, known as a pulsar wind nebula (PWN), within the supernova remnant of the progenitor star. As the particles within the wind are relativistic, they form a shock front against the interstellar medium where particles are accelerated, and inverse Compton scatter photons up to γ-ray energies (Keshet et al. 2003 & Fiori et al. 2022). PWN are therefore also a class of *Fermi*-LAT γ-ray source independent of the pulsar population, and are associated with young, rapidly rotating, pulsars. As pulsars radiate matter and light, their rotation rate slows down as they lose rotational energy. Consequentially, older neutron stars have slower spin rates (on the order of 10s of seconds) compared to the millisecond rotations of younger pulsars. The lengthening of the rotational period does not mean a decrease in magnetic field strength; a subclass of neutron star called magnetars are characterised by exceptionally powerful magnetic fields, and long rotation times (Kaspi and Beloborodov, 2017). These sources are associated with repeating soft γ-ray bursts.

It is possible for older pulsars to increase their rotation rates through interactions with other stars. These older spun-up pulsars are called millisecond pulsars (Lorimer, 2008), and are seen to be γ-ray emitters with *Fermi*-LAT (Espinoza et al., 2013). They are concentrated within the inner reaches of the Galaxy, and in globular clusters where older stellar populations exist. Millisecond pulsars are associated with spider binaries, discussed in Section 3.2.3.

It is possible for neutron stars to gain mass through either the accretion of matter, or through mergers with other stars. Like white dwarfs with the Chandrasekhar limit, there is a maximum mass a neutron star can attain before the force of gravity overcomes the neutron degeneracy pressure and the neutron star collapses further into a black hole. This limit is currently understood to be $2.3\,M_{\odot}$ from recent

analysis of gravitational wave events, and is known as the Tolman-Oppenheimer-Volkov (TOV) limit (Shibata et al., 2019).

3.1.3 Black Holes

In cases with very massive stars ($m > 20M_{\odot}$) or where a neutron star grows to exceed the TOV limit, not even the pressure from neutron degeneracy is capable of preventing collapse, so instead of a neutron star, a gravitational singularity is formed where the core mass of the star is collapsed into an infinitely small space, causing a breakdown in relativistic spacetime called a singularity. Singularities cannot be observed directly, as the spacetime around them bends so that the gravitational escape velocity in a region around the singularity exceeds the speed of light. This leads to a horizon from which light cannot escape surrounding the singularity called the event horizon, which takes the shape of a sphere in 3 dimensions. The size of the event horizon is determined by the mass of the singularity, and the radius of the sphere is given by Equation 3.2

$$r_s = \frac{2GM}{c^2} \tag{3.2}$$

As the singularity is surrounded by a spherical event horizon, this type of stellar remnant is known as a black hole.

Black holes are predicted as a consequence of the Einstein field equations, where four different solutions describe four different 'types' of black hole. In reality, astronomical black holes are expected to be Kerr black holes, rotating systems (as like neutron stars, angular momentum is conserved upon core collapse) with an an approximately zero charge (as in most real situations the positive and negative charges would cancel within the singularity itself) (Kerr, 1963). Black holes themselves do not emit radiation, apart from the theoretical Hawking radiation which arises from quantum fluctuations at the surface of the event horizon and is expected

to be negligible on the macroscopic scales of astronomical black holes (Hawking, 1974).

Two types of black hole are seen to exist*: the stellar mass black holes with masses between the TOV limit and approximately $100M_{\odot}$ (Farr et al., 2011), and the supermassive black holes with masses in the range of $10^6 M_{\odot}$ and $10^9 M_{\odot}$ found in the centres of almost all galaxies, including the Milky Way (Cattaneo et al., 1999). Both types of black hole are seen to exist by their interaction with infalling matter (accretion); the process of accretion onto a black hole releases an extraordinary amount of energy per unit mass, more so than nuclear fusion, due to the extremely high gravitational potential energy around a black hole. As a result the radiation from stellar mass black holes seen from systems such as Cygnus X-1 comes from accretion, rather than the black hole itself. The same can be said for the supermassive black holes at the centre of most galaxies, infalling matter from the galactic core causes a significant amount of radiation to be emitted from the matter itself, which when it reaches a certain level can cause the galactic nucleus to become disproportionately brighter than the rest of the galaxy. Such a galaxy is known as an active galaxy, and active galaxies are a major area of study across astrophysics, and within γ-ray astronomy (Frank et al., 2002).

3.2 Binary Star Systems

Many star systems contain more than one star, with this phenomenon known as *stellar multiplicity* (Duchene and Kraus, 2013). Multiple star systems are found throughout the universe, with a common form being the binary star system, where two stars orbit a common gravitational barycentre. The idea of a binary star system was first described in 1802 by William Herschel, based on his earlier observations of optical double stars (Herschel and Watson, 1782). Herschel discovered

*A third type, the intermediate mass black hole, is now also established to exist within globular clusters and dwarf galaxies, with masses between stellar and supermassive black holes (e.g. Kiziltan et al. 2017 & Patruno et al. 2006).

changes in the positions of certain optical double star systems which could not be explained simply by the motion of the Earth alone, and therefore concluded that this unexplained motion was due to the mutual gravitational attraction between the two stars in the binary system (Herschel 1802).

The properties of a binary star system depend on the initial mass of each star and the orbital mechanics of the system. Both stars in a binary are typically born in the same stellar nursery as one another at approximately the same time, but may evolve at different rates, as it is commonplace for binary stars to be of different masses to one another. Therefore we see systems where a main sequence star is in a binary with a stellar remnant such as a black hole, which burned through its hydrogen more quickly and experienced core collapse before the main sequence star even moves onto the red giant branch. Binaries contain both Population I and II stars; however, binaries with massive stars tend to be concentrated amongst the Population I stars (Hurley et al., 2002).

The orbital periods of binary systems vary greatly. In the case of the binary Cygnus X-3, there is an extremely short orbital period between the massive main sequence star and compact object (probably a black hole) of 4.8 hours (Bhargava et al., 2017). Longer than this system is the pulsar binary PSR J2032+412 which has a 50 year orbital period (Ho et al., 2017). Longer again is the Proxima Centauri system which orbits around the Alpha Centauri system with a period of 547,000 years (Kervella et al., 2017). Cygnus X-3 exhibits signs of constant interaction between the star and the black hole, whereas the further away PSR J2032+412 and its companion exhibit signs of interaction only at periastron. Proxima Centauri exhibits no signs of interaction at all with Alpha Centauri beyond being gravitationally bound.

The frequency of particular orbital periods is represented by a log-normal distribution, with its peak located at approximately an orbital period of 100 years (Raghavan et al. 2010 & Korntreff et al. 2012). Therefore many binaries see interactions between their stars at periastron, such as shocking between stellar winds or exotic interactions such as accretion onto a compact object. Some binary systems

are close enough that the two stars play a significant role in each other's evolution through phenomena such as accretion of stellar matter, supernova kicks and stellar wind interactions. Such systems where at least one component is a compact object (a white dwarf, a neutron star, or a stellar mass black hole) are known as compact binaries (e.g. Postnov and Yungelson 2014 Ivanova et al. 2006 & White 1989).

Compact binaries make up the vast majority of γ-ray emitting binary systems, spread across multiple system morphologies. They are multi-wavelength sources, emitting EM radiation from the radio up to the γ-ray wavebands, and multi-messenger sources, with gravitational waves having been detected from the coalescence of objects in compact binary systems, together with the coincident detection of a γ-ray burst in at least one case. Compact binaries are seen both within the Milky Way and in other galaxies, and represent the most energetic stellar-scale astronomical objects.

3.2.1 Double Compact Object Binaries

Double compact object binaries consist of two compact objects in an orbit around one another, some combination of two black holes, white dwarfs or neutron stars. Such systems are rare; very few double neutron star or neutron star-white dwarf systems are observed within the Galaxy, and there are no known Galactic black hole binaries (Hulse and Taylor 1975*, Lyne et al. 1988 & Burgay et al. 2003).

Whilst no double stellar mass black hole binaries have been observed in our Galaxy, there is evidence in a number of galaxies for supermassive black hole multiplicity at the galactic centre (e.g. Valtonen et al. 2008 & Rodriguez et al. 2006). These systems are thought to have originated as a consequence of galactic mergers, and the black holes are expected to eventually in-spiral† and coalesce (Salcido et al., 2016).

*This paper, the first discovery of a double neutron star system, won the 1993 Nobel Prize in Physics.

†The exact mechanisms for the black hole in-spiralling is still under debate; i.e. the 'final parsec problem'.

Double compact object binaries are notable objects as mergers in these systems have caused the first detections of gravitational wave signals, hence confirming one of the predictions of General Relativity. Detections of double black hole (Abbott et al., 2016), double neutron star (Abbott et al., 2017) and black hole-neutron star (Abbott et al., 2021) mergers have been made with the Laser Interferometer Gravitational-Wave Observatory (LIGO), and electromagnetic counterparts (i.e. kilonovae) have been observed (Troja et al., 2018). Whilst white dwarf mergers have not been previously detected, the merger between two white dwarfs would likely cause the resulting star to exceed the Chandrasekhar limit, triggering a Type Ia supernova. In this scenario the resulting explosion would unbind the freshly merged white dwarf and no stellar remnants would remain.

3.2.2 Cataclysmic Variable Stars

Cataclysmic variable (CV) stars are binary systems where a white dwarf is in a binary orbit with a main sequence or red giant companion. Traditionally referred to as classical novae, due to their extreme variability, the white dwarf accretes matter (primarily hydrogen) from the outer layers of its companion star. This hydrogen then forms a layer on the surface of the white dwarf, which grows until the hydrogen is hot enough to begin nuclear fusion via the pp chain or CNO cycle, causing the white dwarf to brighten significantly (Smith, 2006). Novae from CV stars are a relatively rare source of γ-rays, with only a small percentage being γ-ray emitters. Given the lack of any obvious common features between the γ-ray emitting novae, it is likely that those observed are simply those which are nearby (Morris et al., 2017).

As the mass of a white dwarf increases via accretion it approaches the Chandrasekhar limit ($1.44M_{\odot}$), at which the mass of the white dwarf is sufficient to ignite carbon fusion in the stellar core. The rapid increase in temperature that such fusion brings causes a Type Ia supernova, where the white dwarf completely explodes leaving no

stellar remnant (in contrast to a Type II supernova where a neutron star or black hole remains) (Maoz et al., 2014).

3.2.3 Spider Binaries

Spider binaries are a subclass of binary system where a pulsar orbits a stellar companion, and the pulsar wind causes ablation of the atmosphere of the companion star. The pulsars within spider binaries are non-accreting sources, and typically have very short orbital periods of less than 24 hours (Roberts 2012).

The archetypal spider binary is PSR B1957+20; discovered in 1988 (Fruchter et al., 1988), PSR B1957+20 consists of a pulsar in orbit with either a super-Jupiter exoplanet, or a brown dwarf, with an orbital period of 9.2 hours. PSR B1957+20 is an eclipsing binary (i.e. $\theta_i = 90°$), with an eclipse duration of approximately 20 minutes. The very compact nature of this binary, together with the very low mass system, means that the small companion is gradually being destroyed by the pulsar wind (e.g. Huang et al. 2012 & van Kerkwijk et al. 2011). The destructive relationship between PSR B1957+20 and it's companion has led to the system being nicknamed the 'Black Widow' pulsar, due to the apparent similarity between the pulsar ablating its companion with the cannibalism observed in a very few species of black widow spiders.

Many spider binaries are now known, and are divided into two subclasses: the black widow binaries with very small companions ($M < 0.1 M_\odot$) and the redback binaries* with slightly larger companion stars ($0.2 M_\odot < M < 0.4 M_\odot$). Many spider binaries are γ-ray emitters as seen by *Fermi* (Hui and Li, 2019), including both black widow and redback binaries. In both cases, the collision between the pulsar wind and the matter of the companion star is expected to produce synchroton emission, while self Compton interactions subsequently produce γ-ray emission as exemplified by PSR B1957+20 (Wu et al., 2012).

*The Redback is a large highly venomous black widow spider, native to Australia.

Finally, black widow binaries are linked to a class of γ-ray emitting neutron stars called Millisecond Pulsars (MSPs). Pulsars typically form during supernovae due to the conservation of angular momentum of the in-falling matter during core collapse; the resulting neutron star has a very rapid spin which allows us to see the characteristic pulsed emission typical of these sources. This pulsar then emits a wind, and angular momentum is carried away over time, thus the pulsar's period lengthens and the spin becomes less rapid as the neutron star ages. MSPs are aged neutron stars which have an unusually rapid spin for their age, and are thought to be the aftermath of a spider binary. As the companion orbits the pulsar, the effect of the companion star's gravity increases the rotation rate of the pulsar, causing a 'spin-up' to occur (di Salvo et al., 2008). The pulsar subsequently ablates and destroys the companion, and what remains is an aged pulsar with an accelerated spin, but no companion star, resulting in an isolated MSP (Kong et al., 2012). MSPs, like core collapse pulsars, are γ-ray emitting systems seen with *Fermi*-LAT, and are found in number in globular clusters, which typically contain old stars (King et al., 2003).

3.2.4 Colliding Wind Binaries

Colliding-wind binaries are rare systems, where two (or more) massive stars orbit close to one another. Due to the massive nature of both stars they both lose matter in the form of stellar winds - a typical process for massive stars. Such winds collide with one another, and due to their proximity, a shock front forms (e.g. Pittard and Stevens 1997, Moffat 1998 & Walder 1998). The particles within this shock front undergo Fermi acceleration, gain energy and subsequently radiate in the form of synchrotron emission; consequently colliding wind binaries are seen from the radio waveband (Dougherty et al., 2003) through to X-rays (Corcoran, 1996). The presence of powerful winds causes the expansion of the stellar material beyond the locality of the binary itself, and thus nebulae commonly surround colliding wind binaries, such as the Homonculus Nebula around η-Carinae, where the structure of

the stellar winds from each star can clearly be seen.

Two colliding wind binaries are known to be γ-ray emitters: the aforementioned η-Carinae and γ-Velorum (Abdo et al. 2010a & Pshirkov 2016). In these systems the accelerated particles in the shock fronts produce γ-ray emission not through inverse Compton mechanisms, but by hadronic means; protons are accelerated in the shock fronts between stellar winds leading to the collision of nucleons and subsequent π^0 particle decay, producing γ-rays (Grimaldo et al., 2019). In both of these systems the γ-ray emission is modulated by the orbit, although it peaks at periastron in η-Carinae and at apastron in γ-Velorum (Martí-Devesa et al. 2020). Furthermore, VHE emission is seen from η-Carinae but not from γ-Velorum, and no synchrotron emission is seen from η-Carinae, at odds with the bulk of the colliding wind binary population. These observed behaviours suggest some fundamental differences between the two systems (Abdalla et al., 2020).

3.3 X-ray Binaries

X-ray binaries (XRBs) are binary star systems where a main sequence star (i.e. one that is undergoing nuclear fusion through one of the processes discussed in Section 3.1) is in a close enough orbit with a compact object (either a neutron star or a black hole, but not a white dwarf*) that the compact object accretes matter from the companion star. The terms 'primary' and 'secondary' are used throughout the literature to refer to the more and less massive members of the binary, however I will avoid these terms in favour of 'companion' and 'accretor' as in high mass systems the primary tends to be the more massive donor star and the secondary is the compact object, whereas in low mass systems the converse tends to be true.

The accretion of matter from the companion onto the black hole causes the matter to heat up, and thermal energy is released in the form of X-ray radiation, hence

*These are the aforementioned CV stars, and although they do share many characteristics with the X-ray binaries, and are often referred to as symbiotic X-ray binaries, they are not 'true' X-ray binaries due to the nature of their accretor.

the name 'X-ray binary' (Verbunt 1993 & Casares et al. 2016). X-ray binaries are an extremely diverse group of systems and can be categorised based on their morphologies and phenomenological properties. The most common subdivisions are based on the mass of the companion star; high mass systems typically have late A, O or B type stars, whereas low mass X-ray binaries typically have M dwarf to early A type stars. Additionally, microquasars and γ-ray binaries are two subclasses of X-ray binary which span the high and low mass regimes; both produce γ-ray emission but from different mechanisms (Dubus, 2013).

3.3.1 High Mass X-ray Binaries

High mass X-ray binaries (HMXBs) are X-ray binary systems where a massive star is in orbit around a compact object. As massive stars are extremely hot and luminous, matter within the outer layers of their atmospheres is accelerated to velocities greater than the local escape velocity, and subsequently escapes the surface of the star. This accelerated material is called a stellar wind. The most massive stars can lose matter at a rate of $10^{-3}\,\mathrm{M_{\odot}yr^{-1}}$; in the most extreme cases stars can lose up to 50% of their initial mass over their lifetimes through winds (Crowther 2001 & Pauldrach et al. 2012). In HMXBs, a fraction of this stellar wind is captured by the gravitational pull of the compact object, which then falls into an accretion disc around the object due to the angular momentum of the system. The matter then in-spirals around the disc, liberating the gravitational potential energy in the form of X-ray radiation before falling onto the compact object. This is shown in Figure 3.1.

The vast majority of known HMXBs are Galactic sources, and are hence predominately distributed along the Galactic plane. However as they are young stars, they are relatively local (within a few kpc) and are not found concentrated in globular clusters, nor in the Galactic bulge or Galactic centre. Over 100 Galactic high mass X-ray binaries are known (Liu et al., 2006), and extragalactic HMXBs are also known in local galaxies, particularly the Large Magellanic Cloud (LMC) and the

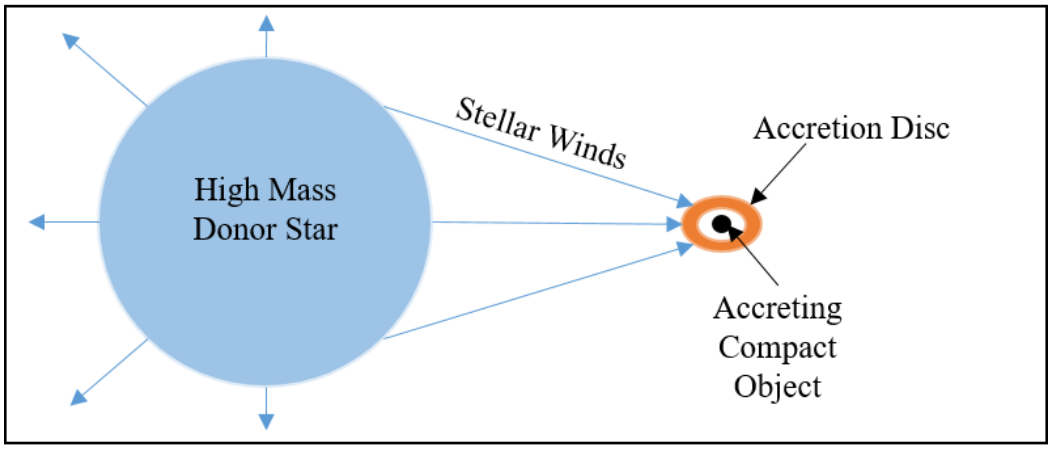

Figure 3.1: A typical high mass X-ray binary system showing stellar winds moving away from the stellar surface in all directions, and a portion of those winds being captured by the gravitational pull of the accreting compact object, and forming an accretion disc before falling onto the compact object.

Small Magellanic Cloud (SMC), and face-on systems. All of the detected γ-ray emitting HMXBs are found in our Galaxy with the exception of LMC P3 which is found in the LMC.

HMXBs are variable sources across the EM spectrum, with much of their X-ray, radio and γ-ray variability linked to the accretion rate (Section 3.3.3), and additional γ-ray variability linked to the orbital interactions between neutron star accretors and the companion stars (Section 3.3.4).

HMXBs typically have a short lifespan, as it is limited by the rapid burning of nuclear fuel in the companion star, and as a result a number of evolutionary changes may happen to a HMXB as it ages. If a neutron star HMXB gains sufficient mass to exceed the TOV limit, core collapse will occur in the neutron star and the system will evolve into a black hole HMXB. Regardless of the nature of the accretor, if the companion star depletes its reserves of nuclear fuel, a second Type II supernova will occur in the system (the first having produced the accretor) and the companion star will collapse into a second compact object, resulting in a double compact object system (Section 3.2.1) such as the double neutron star systems that have been observed in our Galaxy (Hulse and Taylor, 1975).

Finally, as objects in a binary orbit one another, the orbit very slowly decays over time, emitting gravitational waves as it does so. In rare cases, it may be possible for a super-giant star to merge with a neutron star, resulting in a giant star with a neutron core (Thorne and Zytkow, 1977). Such an object is known as a Thorne-Żytkow object, and whilst there are no confirmed objects of this nature, a few candidates have been identified in the SMC (Levesque et al. 2014 & Beasor et al. 2018). It is eventually expected that Thorne-Żytkow objects will breakdown, and the envelope around the neutron star will collapse into a giant accretion disc around the neutron star, which will eventually be accreted onto the star itself. The accretion of such a disc may push the mass of the neutron star over the TOV limit, causing collapse into a black hole (Brandt et al., 1995). It is likewise possible for black holes to spiral in towards their companions, although in such cases the black hole will not fall into the star and form a (relatively) stable core, unlike a neutron star. The intense gravitational field of a stellar mass black hole will cause tidal disruption to the star, as different parts of the star are subjected to the black hole's acceleration due to gravity at different rates. The result of this is a tidal disruption event, where the star is subjected to spaghettification, and may end in the destruction of the star and the formation of a giant accretion disc around the black hole. Such tidal disruption events are observed around supermassive black holes in the centres of galaxies, however they are thought to be rarer and more complex on a stellar scale (Kremer et al., 2021).

3.3.2 Low Mass X-ray Binaries

Low mass X-ray binaries (LMXBs) are X-ray binaries in which a few solar mass star is in orbit around a compact object. Due to their comparatively lower energy output, low mass companion stars have a far lower mass loss rate in the form of stellar wind, and therefore whilst wind material does fall onto the accretor as in HMXBs, it is only a fraction of the overall accreted material. It is not the dominant method of mass exchange between the companion and accretor, instead it is Roche

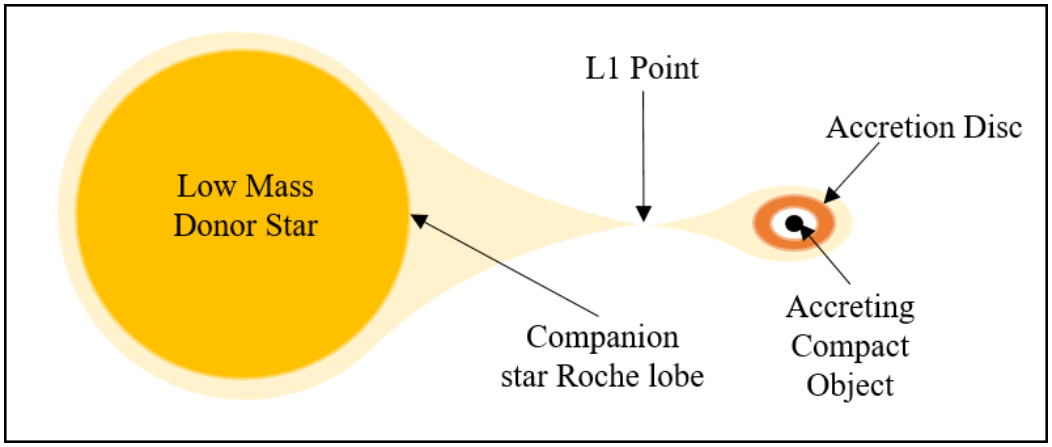

Figure 3.2: A typical low mass X-ray binary showing the overflow of matter from the companion star through the L1 point and into the gravitational field of the accreting compact object, forming an accretion disc due to the angular momentum of the rotating accretor.

lobe overflow (Van Paradijs and Van der Klis, 2001). In binary systems, the Roche lobe (Paczyński, 1971) is defined as the gravitational region around a star to which matter is orbitally bound and the radius of the Roche lobe is given in Equation 3.3 as a function of q, the mass ratio of the two stars in a binary where the semi major axis of orbit is set to unity (Eggleton, 1983).

$$r_{lobe} = \frac{0.49q^{\frac{2}{3}}}{0.6q^{\frac{2}{3}} + \ln\left(1 + q^{\frac{1}{3}}\right)}, \quad 0 < q < \infty \tag{3.3}$$

Both the companion and accretor in the binary have their own Roche lobes defined by this equation, and the point where they meet in the binary is the L1 Lagrangian point, where the net gravitational force between the stars is zero. In LMXBs, the masses of the companion and accretor are more comparable to one another than HMXBs where the companion is significantly more massive, so in these systems the matter of the companion star exceeds its own Roche lobe. This excess matter is therefore siphoned from the surface of the star through the L1 point, and onto the Roche lobe of the accretor, where the matter forms an accretion disc around the accretor. This is depicted in Figure 3.2

There is no sharp distinction between the HMXBs and the LMXBs, and a class

of 'in between' objects known as the Intermediate Mass X-ray binaries (IMXBs) exists, typically main sequence A-type (or early B-type) stars. In these systems, it is common for both Roche lobe overflow and stellar winds to play a part in accretion (Podsiadlowski et al., 2002). For the purposes of this work however, I follow the simple distinction of high and low mass and treat systems by their designation in the Liu et al. (2006) and Liu et al. (2007) catalogues of HMXBs and LMXBs respectively.

Compared to HMXBs, LMXBs contain older stars. They are also found on the Galactic plane, however are concentrated towards the Galactic bulge and Galactic centre, correlating with the lower metallicity Population II stars. LMXBs are also found concentrated in globular clusters, which are themselves dense gravitational clusters of old Population II stars, in which a recycled millisecond pulsar population is found and expected to contribute to the globular clusters' γ-ray emission (Ivanova 2013 & Lloyd et al. 2018). As would be expected from the Initial Mass Function, LMXBs are more common than HMXBs, with more than 200 having been discovered (Liu et al., 2007). However, given that many of the LMXB companion stars are both less luminous and further away, far fewer have clearly identified companion stars in the optical or infrared wavebands and many are only known through the X-ray emission of their accretion discs, where they are brightest. Currently, eight LMXBs are identified as γ-ray emitters by *Fermi*-LAT, and these are all Galactic sources (Abdollahi et al., 2020). Unlike the HMXBs where some of these systems are detected at very high energies by TeV detectors, no LMXBs are identified with such instruments.

Like the HMXBs, the LMXBs are variable in the X-ray, optical and radio wavebands (as well as theoretically the γ-ray waveband) due to changes in their accretion state (Section 3.3.3). Neutron star LMXBs also display a unique kind of variability known as Type I X-ray bursts, generally unseen in HMXBs. In neutron star LMXBs, matter from the companion star builds up on the surface of the neutron star and increases in density until sufficient temperature and density is realised to

ignite nuclear fusion of the matter. The resulting fusion causes a thermonuclear explosion on the surface of the neutron star resulting in a rapid brightening in the X-ray waveband in a similar manner to the cataclysmic variable systems (Lewin et al., 1993). Unlike the CV binaries where γ-rays have been seen from such thermonuclear processes, no γ-rays have been discovered from Type-I X-ray bursts in LMXBs.

LMXBs are much longer lived systems than HMXBs, and their evolutionary pathways are less exotic than those of the HMXB population. If the accretion rate in a system is low, it is likely that the companion star will continue to evolve until it runs out of nuclear fuel, at which point a planetary nebula will form and the resulting system will become a double compact binary, with a white dwarf remnant from the companion star and a neutron star/black hole accretor. If the accretion rate is high it is, in principle, possible for a star to be completely disrupted and accreted onto the compact object, however physical limits on the accretion rate make this unlikely in the majority of cases. In-spiralling on the compact object and companion star would result in a tidal disruption event regardless of whether the compact object was a black hole or a neutron star, as the weaker gravitational field of the less massive companion would prohibit the formation of a Thorne-Żytkow object.

3.3.3 Microquasars and the Accretion Cycle

X-ray binaries do not accrete matter at a constant rate as seen by variations in the X-ray flux of these systems. As a consequence of accretion, X-ray binaries (regardless of the nature of the accretor) may emit collimated astrophysical jets of matter and radiation extended from the rotational poles of the compact object, caused by the rotation of the magnetic field of an accretor. Whilst neutron stars have their own magnetic fields, black holes in the physical universe are expected to be electrically neutral, but matter falling onto a black hole is largely ionised causing a magnetic field of its own. Several proposed mechanisms have been established for the formation of jets, including the Blandford-Znajek process which is linked

to the warping of magnetic fields (Blandford and Znajek, 1977), and the Penrose process which is linked to relativistic frame dragging (Penrose and Floyd, 1971). It is thought that the Blandford-Znajek process is responsible for most astrophysical jets seen in the universe, and jets are seen from a variety of accreting sources including protostars and active galaxies (Añez-López et al. 2020 & Blandford et al. 2019).

The link between the accretion disc and the astrophysical jet of an XRB is known as disc-jet coupling, and both the jet and the disc behave in a broadly cyclic way although the timescales and exact behaviours vary from system to system. Observationally, changes in both the X-ray hardness (i.e. the spectral index) and intensity are seen, leading to this observed behaviour being dubbed the 'Hardness-Intensity Cycle' (Figure 3.3) (Fender et al., 2004), described below.

1) The XRB is in a low intensity/hard state, also known as 'quiescence'. Transient XRBs* are not observed during this time. At this point, matter is draining onto the compact object, and a compact jet exists, the luminosity of which is the square root of the overall X-ray luminosity. The majority of the X-ray emission at this time comes from a hot corona of matter surrounding the compact object, and the accretion disc is optically thin. At this point the Lorentz factor of the jet is very low, and the jet is not relativistic.

2) As the jet builds in size, the intensity rises and the spectrum begins to soften slightly. This state is known as the very high intensity/intermediate hardness state. At this point, the jet still has a Lorentz factor of $\Gamma < 2$, and X-ray corona emission still contributes significantly as the accretion disc is still optically thin.

3) The spectrum of the source softens and the intensity drops slightly, referred to as the high intensity/soft state. The jet becomes decoupled from the disc, and the accretion disc is no longer contributing matter to the jet. The jet becomes relativistic, with $\Gamma > 2$, and internal shocks propagate through the jet. With the

*Transient XRBs are those which are only seen in the X-ray waveband during periods of X-ray brightening, and are typically LMXBs. Also referred to as 'X-ray Transients' in the literature.

cessation of disc contribution to the jet, an optically thick accretion disc builds, and X-ray emission from the disc begins to contribute significantly to the overall emission from the system.

4) Some sources, such as the LMXB GRS 1915+105, will oscillate between states 2 and 3. In this case jet production restarts and multiple episodes of relativistic jets/jet termination are seen.

5) The source drops in luminosity, however the spectrum remains soft thus the object enters the low intensity/soft spectrum state. At this point a jet is no longer being produced at all, and the emission from the jet produced in stage 3 has become optically thin and fades over time. The accretion disc builds to become optically thick, and X-ray emission from the accretion disc dominates over X-ray emission from the corona.

6) The source hardens, and dips again in intensity, reentering the low intensity/hard state and quiescence. The accretion disc which has built up around the compact object in the low intensity/soft spectrum state begins to drain onto the compact object, and the production of a low-luminosity, compact jet resumes.

When an X-ray binary moves between the very high intensity/intermediate hardness state and the high intensity soft state, and a relativistic jet is produced, the X-ray binary is known as a microquasar, due to the observed similarities between these systems and the quasar population of active galaxies. Of the hundreds of X-ray binaries, only tens of these are known to be microquasars. Whilst the X-ray emission from the X-ray corona and the accretion disc is thermal, due to energy liberated from the accretion process itself, the emission in a jet originates from charged particles accelerated by a magnetic field, making this non-thermal emission (Bosch-Ramon, 2012). Microquasars (Mirabel and Rodriguez, 1994) are extremely luminous sources from the radio up to the γ-ray wavebands and are detected both in our Galaxy and others (Middleton et al., 2014). They can be both high and low mass sources, and are established as the stellar mass analogues to the active

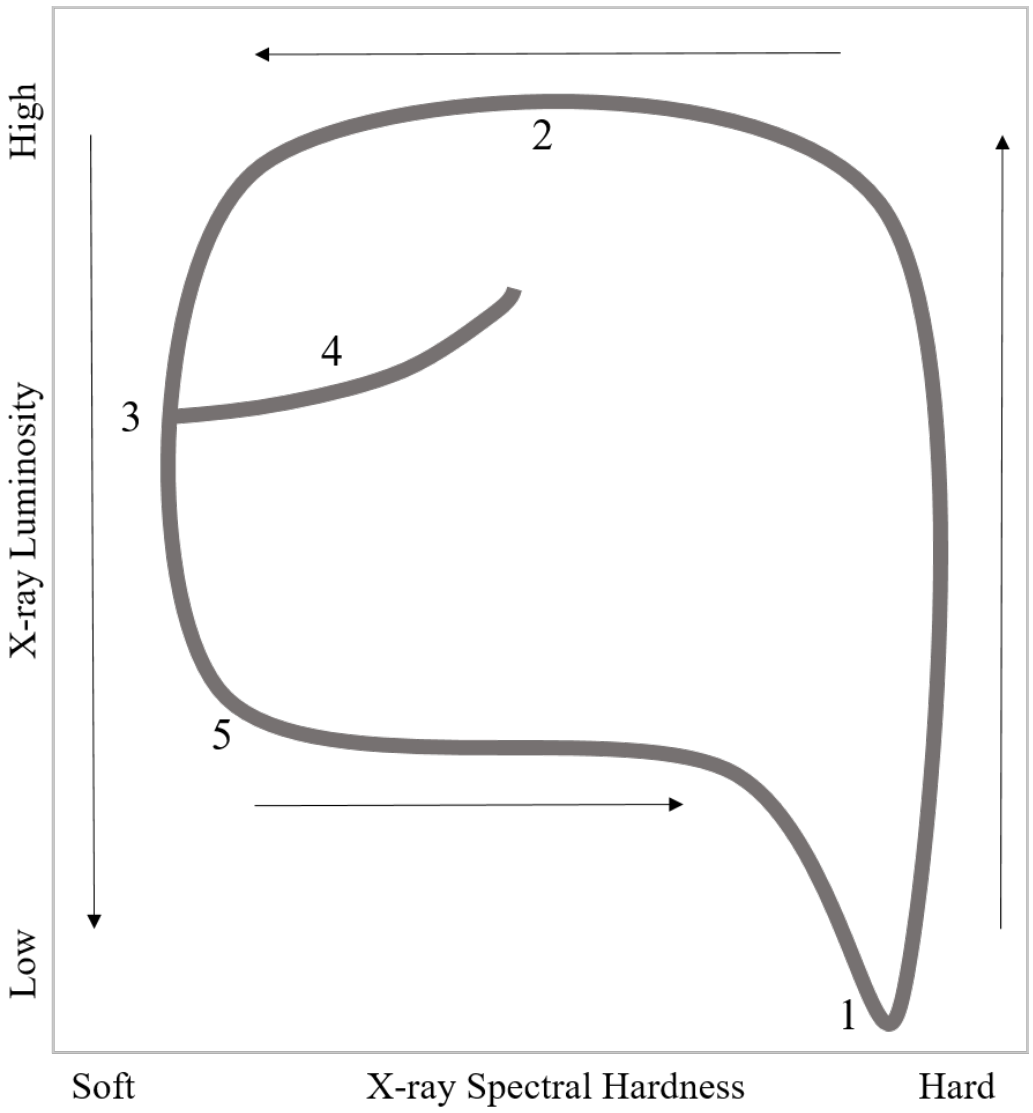

Figure 3.3: A diagram which graphically shows the hardness-intensity microquasar cycle. The horizontal axis shows spectral hardness and the vertical axis shows X-ray luminosity, both with arbitrary units. the numbers represent the different stages of the diagram described in the text. The cycle occurs in an anticlockwise manner, with the curved branch (4) showing the oscillation between states 2 and 3.

galactic nuclei (AGN), a form of which (the blazars) makes up the most numerous identified source class in the LAT catalogue (Abdollahi et al., 2020). Due to the relativistic properties of their jets, and the geometry of the systems, these sources often appear superluminal from the Earth's frame of reference.

As electrons are accelerated along the jet at relativistic velocities, they emit synchrotron radiation. This synchrotron radiation is broadband, but is particularly powerful in the radio waveband thus astrophysical jets are spatially well-mapped by radio instruments. This synchrotron radiation then re-interacts with the relatavistic electron population via inverse Compton scattering, where the electrons transfer energy to the synchrotron photons, and the photons are upscattered to become γ-rays. Additionally, for inverse Compton scattering close to the compact object, corona/disc photons may be upscattered as well as photons from the companion star. The acceleration of protons to relativistic velocities in the jet is also hypothesised to cause the hadronic emission of γ-rays. In this scenario, high energy protons interact with photons to produce a proton-π^0 pair. The pion has a short lifespan, and will decay causing γ-ray emission. Of the two mechanisms, the inverse Compton scenario is thought to be the dominant means of γ-ray production in microquasars, however hadronic contributions may be non-negligible (Bosch-Ramon et al. 2006 & Orellana et al. 2007). Three microquasars (all HMXBs) are confirmed γ-ray emitters, Cygnus X-1, Cygnus X-3 and SS 433 which are all discussed in depth in Chapter 9. Reports of γ-ray emission from the LMXB microquasar V404 Cygni are discussed in depth in Chapter 4.

As previously mentioned, there is a constraining factor to the accretion rate of X-ray binaries, known as the Eddington limit. As gravitational potential energy is liberated in the form of thermal photons during accretion, these thermal photons then subject the accreting matter to a radiation pressure, carrying away some of the accreting material slowing the accretion rate down. The Eddington limit is the maximum luminosity which can be achieved by an accreting source before the radiation pressure is sufficient to completely halt accretion onto the compact object

(Frank et al., 2002). The calculation of the Eddington luminosity of an accretion disc is non-trivial due to the geometry of the system, however almost all X-ray binaries are sub-Eddington sources (Heinzeller and Duschl, 2007).

The first microquasar discovered, and one of the best studied, is SS433, a HMXB system with resolvable jets (Fabian and Rees, 1979). SS433 is thought to be a unique object, with persistent jets due to a persistently super-Eddington accretion disc (Fabrika, 2004). Several studies have identified evidence for γ-ray emission from the jets of SS433 (e.g. Bordas et al. 2015, Rasul et al. 2019, Li et al. 2020), including notably at TeV (Abeysekara et al., 2018b). However, neither the binary nor any components of the jets are catalogued γ-ray sources in the 4FGL due to the fact that this emission does not reach the typical $z = 5\sigma$ level required for a conventional claim of detection at the catalogue position of SS 433 over the energy range used in the production of the 4FGL.

In addition, a class of extragalactic X-ray sources called the ultraluminous X-ray sources are known to emit at super-Eddington luminosities (Kaaret et al., 2017). These sources can be either persistent or transient. No persistent ULXs are seen in our galaxy (although transient Galactic ULXs are seen (Wilson-Hodge et al., 2018)), however a hypothesis for their existence is that these are super-Eddington X-ray sources like SS 433, although one system, HLX-1 is established to be the central black hole of an accreted dwarf galaxy (Farrell et al. 2009 & Atapin 2018). ULXs are not known to be sources of observable γ-rays; if they are microquasar-like systems the γ-rays should, in theory, be produced in the relativistic jet in the high intensity/soft state, although whether this emission could be resolved from the background emission of the host galaxy is highly questionable.

3.3.4 The γ-ray Binaries

Whilst γ-rays are established to be produced in the jets of microquasars, the majority of γ-ray emitting XRBs do not produce their γ-rays through this mechanism.

As previously established, neutron stars emit winds (Section 3.1.2), which in the case of an isolated neutron star will go on to form a pulsar wind nebula. In the case of a binary system the circumstellar matter, particularly from massive stars, is a much more dense environment and hence these winds will shock against the stellar material, in a similar manner to the massive stars in the colliding wind binaries (Section 3.2.4) (Mirabel 2007 & Dubus 2013). All of the currently detected γ-ray binaries are HMXB systems. Whilst the label γ-ray binary originally referred to any X-ray binary which had the majority of its energy released in the form of γ-rays i.e. a purely phenomenological label, it is now used to refer to any X-ray binary where γ-rays are produced through wind-wind interactions, and this is the definition I use throughout this thesis.

In the γ-ray binaries, the shock front between the pulsar wind and stellar wind causes the acceleration of electrons, resulting in synchrotron photons, which are then upscattered via the inverse Compton mechanism. Unlike the colliding wind binaries, there is little evidence to suggest hadronic processes play a major role in the γ-ray emission in the γ-ray binaries. Unlike the microquasars, γ-ray binaries are also known to be TeV γ-ray emitters, where the γ-ray emission is constrained to the apex of the bow shock of the pulsar wind. The high energy GeV emission is expected to originate throughout the bow shock, whereas the lower energy γ-rays and X-rays from the shock are expected to be synchrotron photons emitted by Fermi accelerated particles across the whole system (Dubus et al., 2015), although alternative proposed origins for different components of the high energy emission exist, such as GeV emission occurring due to the Fermi acceleration of particles in pulsar magnetospheres (Chernyakova and Malyshev, 2020).

A key feature of the γ-ray emission in these systems is orbital modulation. As the binary approaches periastron, the shocking between the two wind fronts increases in magnitude, and γ-ray emission peaks just after periastron, before decaying away again. This is seen in every γ-ray binary, with *Fermi*-LAT and with TeV detectors, and indeed some of these systems have detectable γ-ray emission only at periastron

(Dubus, 2015).

In addition to peaking at periastron, some systems discussed in this thesis, notably including LSI +61 303, also see a γ-ray peak at apastron. LSI +61 303 displays apparently unique* interactions between the neutron star accretor and companion, where pressure on the neutron star magnetosphere at periastron causes the pulsar wind to shut off and the neutron star to subsequently enter an ejector regime at apastron, where the pressure is lowest causing the observed γ-ray peak (Ahnen et al., 2016). Such a unique system in combination with a small overall population of γ-ray binaries suggests that the overall picture of their behavior is complicated, and whilst there general picture seems to be understood, there are many unknown factors to the behavior of these systems.

In total, there are 9 γ-ray binaries detected with *Fermi*-LAT, one of which is an extragalactic source which is located in the LMC. An additional system is also detected only at periastron with TeV instruments, however is not detectable with *Fermi*-LAT (Abeysekara et al., 2018a). The properties of the known γ-ray binary population are discussed along with the microquasars in Chapter 9.

*The orbital solution of thi system is under debate.

Figure 3.4: The third labour of Heracles, the capture of the Ceryneian Hind. By Lucas Cranach the Elder (After 1537).

Chapter 4

The Curious Case of V404 Cygni

In this chapter I consider the possibility of the X-ray binary microquasar V404 Cygni being a γ-ray emitting source. V404 Cygni has a history of massive outbursts, with the most recent being in 2015, and was observed across the EM spectrum. Here, I look at the *Fermi*-LAT data before, during, and since this outburst and explore the concepts of the look-elsewhere effect and source confusion, both of which cause false positive results (Type I errors) in *Fermi*-LAT data analysis.

4.1 V404 Cygni, a Microquasar

V404 Cygni (GS 2023+338) is a low mass X-ray binary system consisting of a K-type star with a mass just below $1 M_\odot$ (Wagner et al., 1992) and a black hole with a mass of approximately $9 M_\odot$ (Khargharia et al., 2010). V404 Cygni is located on the Galactic plane with at LII = 73.11°, BII = −2.09°, away from the Galactic centre. V404 Cygni is visible across the EM spectrum but peaks in the X-rays, which are produced from accretion of the donor star's atmosphere onto the black hole via Roche lobe overflow.

V404 Cygni is a microquasar, which means that rather than observing γ-ray emission from wind interactions one would expect to see γ-ray emission associated with particle acceleration from internal shocks within the jet, like other γ-ray emitting

microquasars such as Cygnus X-1 (Bodaghee et al. 2013, Zanin et al. 2016 & Zdziarski et al. 2017) and Cygnus X-3 (Tavani et al., 2009b), where orbital modulation is seen in the γ-ray flux due to the very short binary orbital period of 0.2 days (Abdo et al., 2009d). In the cases of Cyg X-1 and X-3, we see γ-ray emission at the transition between the hard and soft states of the hardness-intensity cycle (Fender et al., 2004) which corresponds to the formation of a relativistic jet and the classic X-ray outbursts which microquasars are seen to produce, and in Cyg X-1, γ-ray emission is also seen during the hard state before this transition (Zdziarski et al., 2017). A third γ-ray microquasar has been detected, SS 433 ; this is not a catalogued *Fermi*-LAT source but numerous studies have identified γ-ray emission from this system (Rasul et al. 2019 & Li et al. 2020). SS 433 is discussed in Chapter 9 and it is a unique object which appears to be in a constant super-Eddington accretion regime which constantly supports the production of relativistic jets (Fabrika, 2004), unlike the rest of the microquasar population.

Throughout the 20th century, there have been at least 3 historic outbursts of V404 Cygni thought to correspond to the hard to soft state transition. The first occurred in 1938 and was detected only in the optical waveband, and was designated Nova Cygni 1938. There was a possible outburst in 1979, identified through archival imaging plates, and the very well studied outburst of 1989 (Richter 1989, Makino 1989 & Han and Hjellming 1992). During the 1989 outburst the *Ginga* X-ray Astronomy Satellite captured X-ray emission from V404 Cygni, leading to the designation GS 2023+338 (Kitamoto et al., 1989). The X-ray emission was accompanied by optical variability (Wagner et al., 1989).

In June 2015 the *Swift*-BAT team reported that V404 Cygni had begun an outburst, the first since 1989, with enhanced fluxes from the radio up to the X-ray wavebands. *Fermi*-GBM also triggered on this outburst, approximately 30 minutes after *Swift*-BAT. This outburst was the direct consequence of higher accretion rates leading to the formation of a relativistic jet, causing V404 Cygni to begin its transition from the hard state to the soft state of the hardness intensity cycle. A coordinated multi-

wavelength campaign was undertaken to observe V404 Cygni during this time, with INTEGRAL, *Swift*, AGILE, MAGIC, VERITAS all taking observations at high energies, and the all-sky coverage of *Fermi*-LAT also capturing the position of V404 Cygni during this time. While it returned to its pre-outburst luminosity in August 2015, there was also a small outburst in December 2015. Such sequel outbursts are not uncommon, as it is possible for the relativistic jet of a microquasar to restart after it has been quenched.

Swift-XRT detected a variable X-ray flux which, at times, exceeded 40 times the luminosity of the Crab (Barthelmy et al. 2015 & Motta et al. 2017), in addition to enhanced and variable optical and UV emission reported from *Swift*-UVOT (Oates et al., 2019). INTEGRAL showed enhanced fluxes from the V-band optical up to the soft γ-ray regime (40 - 100 keV) (Rodriguez et al. 2015 & Roques et al. 2015). AGILE reported a 4.3σ γ-ray excess in the 50 - 400 MeV energy range which was contemporaneous with a giant X-ray and radio flare occurring between MJD 57197.25 and MJD 57199.25, though no significant emission above 400 MeV was reported. A similar excess is reported with *Fermi*-LAT in Loh et al. (2016), although the more recent study, Xing and Wang (2020) is in conflict with this result. The VHE observatories MAGIC (Ahnen et al., 2017) and VERITAS (Archer et al., 2016) both took observations (10 hours and 2.5 hours respectively) of V404 Cygni during the outburst, however report only upper limits, suggesting that the high energy emission cuts off below the GeV energy range, consistent with the report of a 400 MeV cutoff.

No studies detected any γ-ray emission during the December 2015 outburst, however Xing and Wang (2020) report a significant ($\approx 7\sigma$) γ-ray excess in August 2016, and a marginal γ-ray excess of ($\approx 3.9\sigma$) during August 2015 towards the end of the initial outburst period, both using *Fermi*-LAT data.

4.2 V404 Cygni as seen with *Fermi*-LAT

V404 Cygni is not a listed source in any of the *Fermi*-LAT catalogues. This is unsurprising as one would only expect to see γ-ray emission from an X-ray binary when there is a jet to accelerate particles, which occurs at the transition between the hard and soft states. Over the years-long observation times used to generate the *Fermi*-LAT point source catalogues, any emission over the period of a month is rendered insignificant.

As V404 Cygni is located on the Galactic plane, there are challenges to identifying transient γ-ray emission from this X-ray binary, particularly if the γ-ray emission is reasonably faint, or occurs over short timescales, which appears to be the case for the excesses described in the literature. The Galactic plane is itself a luminous source of γ-ray emission, and in the case of V404 Cygni there is a luminous nearby source of γ-rays: 4FGL J2025.3+3341. This is the γ-ray source associated with the BL lac type blazar B2023+336 (Kara et al., 2012), which is a significant (16σ) source of variable emission, with a variability index of 116 in the 4FGL-DR2. As B2023+336 is located only 0.3° away from V404 Cygni on the sky, this is problematic as the resolution of the LAT varies from between an optimal 0.15° at energies > 10 GeV, down to a substantially poorer resolution of 3.5° at 100 MeV* This is a particular issue for any analysis of V404 Cygni, as B2023+336 may also flare in a way that appears superficially similar to V404 Cygni, and this only becomes a non-issue if photons are observed the highest detectable energies, where the resolution of the LAT is such that the two sources can be distinguished.

In this chapter I present a thorough analysis of the region surrounding V404 Cygni, discussing the results and analysis techniques of previous works, and some of the key issues with attempting to detect γ-ray emission from X-ray binaries.

*see Figure 17 in Atwood et al. (2009) for a full breakdown of the energy dependent resolution of the LAT.

4.2.1 Loh et al. 2016

Loh et al. (2016) (referred to as *Loh 16* throughout this chapter) explore the *Fermi*-LAT data together with multi-wavelength data from the position of V404 Cygni during the 2015 outburst.

Loh 16 perform a variability analysis of the position of V404 Cygni by first carrying out a binned analysis from 4th August 2008 to 17th July 2015, considering photons in a 15° radius around V404 Cygni. They use γ-rays across *Fermi*-LAT's entire effective energy range at the time, 100 MeV - 100 GeV, however discard the quartile of photons with the worst PSF label. Whilst this improves the positional accuracy of an analysis, when attempting to examine emission that is both faint and transient, the optimal approach is usually to maximise the available photons in order to maximise the significance of any observed emission. Therefore, by removing 25% of the available γ-ray photons, *Loh 16* may have understated the statistical significance of their analysis. The `SOURCE` photon class was used, together with the `P8R2_SOURCE_V6` instrument response function, and the `iso_P8R2_SOURCE_V6_v06.txt` isotropic diffuse model. The 4 year point source catalogue, the 3FGL, and the associated Galactic diffuse model `gll_iem_v06.fits` were used. *Loh 16* use a standard zenith angle cut of 90° in their analysis. This choice of catalogue and background models reflect the most up-to-date choices available at the time, and their analysis was performed using an earlier version of the `Fermitools`, the `Fermi Science Tools (v10r1p1)`, predating the publication of `Fermipy`.

To model the ROI around *V404 Cygni*, *Loh 16* perform a binned maximum likelihood analysis using the `optimization` routine included in `gtlike` to fit sources from the 3FGL within a 25° radius of V404 Cygni together with the background components using the `NewMinuit` optimiser. They leave all sources within 5° of V404 Cygni's position, or which are variable*, with free normalisations during this

**Loh 16* define 'variable' as having a 3FGL variability index > 72.44.

optimisation, with the normalisations of the background components also being free. Loh 16 find that the parameters of their ROI are consistent with those given in the 3FGL, and that B2023+336 does not appear to be flaring during the time of V404 Cygni's outburst.

Loh 16 construct light-curves of the ROI using two binning schemes, 12 hour bins overlapping each other by 6 hours, and 6 hour bins overlapping each other by 1 hour. Both light-curves cover the time range MJD 57140 - 57225 (28/04/2015 - 22/07/2015). Each bin represents a separate unbinned likelihood analysis executed over the 12/6 hour period. To model V404 Cygni, *Loh 16* add a point source with free spectral index and normalisation, with all other parameters left fixed to the values computed in the 7 year binned analysis.

Loh 16 report a peak TS of 15.3 in the 6 hour bin on MJD 57199.2 ± 0.1, and measure a photon flux of $(2.3 \pm 0.8) \times 10^{-6}$ photons $\mathrm{cm}^{-2}\mathrm{s}^{-1}$. *Loh 16* describe this excess as having an approximately 2% chance of occurring randomly based on 320 trials. This excess is also coincident with a peak in the *Swift*-BAT hard X-ray light-curve, which corresponded to a transition to a softer X-ray state, and also follows a massive radio flare recorded by OVRO. *Loh 16* claim that the probability of this excess occurring at this time by chance is 4×10^{-4}. In order to test for source confusion, *Loh 16* also generate a light-curve of B2023+336 using a 12 hour binning scheme. They make no detection of the blazar over a 30 day period, and note that, given the intensive multi-wavelength study of the field around V404 Cygni, there is no reported activity at any other wavelength either. *Loh 16* do note that a TS of 8.1 is recorded in the time bin coincident with the γ-ray excess they associate with V404 Cygni, however state that this is likely due to V404 Cygni's photons being misassigned to the blazar. We will henceforth refer to the excess discussed here as the June 2015 excess, in order to distinguish it from other, later γ-ray excesses observed at the position of V404 Cygni.

4.2.2 Piano et al. 2017

A second paper discussing the June excess, Piano et al. (2017) (referred to as *Piano 17* throughout this chapter) described an analysis using data from the AGILE γ-ray Imaging Detector (GRID) (Barbiellini et al. 2002 & Prest et al. 2003) and also an analysis of the *Fermi*-LAT data independent of that of *Loh 16*. AGILE operates at a lower energy range than *Fermi*-LAT (30 MeV - 30 GeV), with a comparatively poorer PSF at 100 MeV of 4.2° (Sabatini et al., 2015) compared to *Fermi*-LAT's 3.5° (both PSFs are the 68% containment radius). Like the *Fermi*-LAT team, the AGILE collaboration uses the maximum likelihood method of Mattox et al. (1996) to model their data and perform hypothesis testing by calculating a TS. Unlike *Fermi*-LAT, AGILE data are not public and thus studies with AGILE are not independently reproducible.

Piano 17 analyse the AGILE data in two energy bands, 50 MeV - 400 MeV and >400 MeV. In both energy bands, a light-curve is generated covering 6am on 20th June 2015 to 6am on 30th June 2015, a 10 day period which overlaps the γ-ray excess noted by *Loh 16* and the giant X-ray flare observed by *Swift*-BAT. The light-curve is binned in 48 hour intervals, and is unstated whether a binned or unbinned analysis is performed. In the modelling of the region around V404 Cygni, three nearby and luminous pulsars are accounted for, however B2023+336 is not mentioned despite the fact it is the nearest source to V404 Cygni and is also listed in the Second AGILE catalogue (2AGL) (Bulgarelli et al., 2019).

Piano 17 report no excess γ-ray flux in the >400 MeV energy band, however in the time range from 6am on 24th June 2015 to 6am on 26th June 2015 (MJD 57197.25 - 57199.25). They report a γ-ray excess with TS = 18.1 (4.3σ for $k = 1$) and a peak flux of $(4.6 \pm 1.5) \times 10^{-6}\,\mathrm{photons\,cm^{-2}s^{-1}}$. The time range and position of this γ-ray excess are consistent with that of *Loh 16*.

In their *Fermi*-LAT analysis, *Piano 17* use the `Fermi Science Tools (v10r0p5)` together with the `Enrico` analysis pipeline. They produce a light-curve of a 25°

ROI centered on V404 Cygni using daily bins from 6pm on 17th June 2015 to 6pm on 2nd July 2015 (MJD 57190.75 - 571205.75), which encompasses the excess observed by both AGILE, and *Fermi*-LAT in *Loh 16*. *Piano 17* use a different set of photon cuts to *Loh 16*; they analyse all 4 PSF quartiles, but with the `P8R2_TRANSIENT_v16` photon class, together with the `gll_iem_v06.fits` Galactic background model, the `iso_P8R2_SOURCE_V6_v06.txt` isotropic background model and the 3FGL catalogue. A zenith angle of $< 90^{\circ}$ is used.

To fit their model, *Piano 17* free all sources within 6° of V404 Cygni, and execute a likelihood fit using the `Minuit` optimiser. They then fix all sources, and the background components, except for a source added at the position of V404 Cygni (with a power law spectral shape) before running a second likelihood fit with only the V404 Cygni source freed. It is unstated whether a binned or unbinned analysis is used. *Loh 16* again produce their light-curves in two different energy bands: 60 - 400 MeV and > 400 MeV.

Piano 17 report no excess γ-ray flux in the > 400 MeV energy band; however, in the time range from 6pm on 25th June 2015 to 6pm on 26th June 2015 (MJD 57198.75 – 59199.75) a γ-ray excess is reported with TS = 13.3 (3.7σ for $k = 1$) and a γ-ray flux of $(1.4 \pm 0.4) \times 10^{-6}$ photons cm^{-2}s^{-1}, a result consistent with that of *Loh 16*. The *Fermi*-LAT analysis of the V404 Cygni field in *Piano 17* is sub-optimal, particularly when compared to that of *Loh 16* and the analysis I will present in this chapter. This is primarily due to the choice of photon class and the associated files which should accompany it. Each *Fermi*-LAT photon class has a corresponding isotropic model and instrument response function, and it is good practice for these to be used together when carrying out LAT analysis. *Piano 17* use the `P8R2_TRANSIENT_v16` photon class together with the `iso_P8R2_SOURCE_V6_v06.txt` isotropic diffuse model and an unspecified IRF. The use of a mismatched isotropic background and photon class will cause the misidentification of cosmic rays, and therefore introduce further systematic uncertainty into their analysis which is difficult to quantify given that they do not state which IRF they use. Consequently, throughout this chapter

I deal with the more reliable results of *Loh 16* as these do not have this additional uncertainty, their LAT analysis is described in greater detail, and they observe a more significant excess coincident with V404 Cygni (although still consistent with that of *Piano 17*).

4.2.3 Xing and Wang 2020

The most recent work on V404 Cygni, Xing and Wang (2020) (henceforth referred to as *Xing 20*) carried out an analysis of the *Fermi*-LAT data which is independent to those of *Loh 16* and *Piano 17*. *Xing 20* is admittedly confused, with incorrect statements regarding V404 Cygni and previous studies of the 2015 outburst* throughout the text. *Xing 20* perform a wider study of the V404 Cygni system: in addition to searching for a γ-ray signal from the 2015 outburst as *Loh 16* and *Piano 17* do, they also search for γ-ray emission from the entire *Fermi*-LAT mission.

Xing 20 use the 10 year 4FGL-DR2 catalogue together with the 8 year `gll_iem_v07.fits` Galactic diffuse model and the `iso_P8R3_SOURCE_V2_v1.txt` isotropic diffuse model and an unstated instrument response and photon class to model a 20° ROI centered on V404 Cygni over the energy range 100 MeV - 500 GeV and time range 4th August 2008 to 5th March 2020. *Xing 20* populate their ROI with sources within 20° and free sources within 5° of V404 Cygni, the normalisations of the two background components. The routines used to fit their model to their data are not described, and the software used by *Xing 20* is unstated. It is not clear whether a binned or an unbinned analysis is performed when producing their light-curves.

Xing 20 first attempt to reproduce the June 2015 excess by following the method of *Loh 16*, but with the more up-to-date catalogue and background models. They perform a binned likelihood analysis using the same 11.5 years time range, but with an energy range of 100 MeV - 100 GeV: consistent with the energy range of *Loh 16*.

*For example, the abstract refers to GeV emission whereas *Loh 16* and *Piano 17* clearly establish the emission is very soft and that there appears to be a cutoff at approximately 400 MeV. In addition, they refer to a 4.5σ excess reported in *Loh 16*, this is not the case. I would urge the reader to carefully review *Loh 16* and *Piano 17* before *Xing 20*.

Sources within 5° of V404 Cygni are freed during this fit, then fixed afterwards, but it is unclear whether the background components are freed. In a similar manner to *Loh 16*, *Xing 20* generate an unbinned light-curve with 12-hour bins, overlapping one another by 6-hours each.

Xing 20 identify a source coincident with the June 2015 excess with a significance $2\sigma < z < 3\sigma$ (for $k = 1$) (no TS value is given). Additionally, they re-run their analysis without the quartile of photons with the poorest PSF and find that the TS in this bin increases to approximately 10 (3.2σ for $k = 1$). *Xing 20* also repeat the analysis of *Piano 17* with the `TRANSIENT` photon class, obtaining TS=5, however it is unclear whether they replicate the mistakes of *Piano 17* in choosing an isotropic background model and IRF.

Xing 20 argue that given that Cygnus X-1 and Cygnus X-3 both show detectable variability on timescales of days (Corbel et al. 2012, Bodaghee et al. 2013 & Zanin et al. 2016) V404 Cygni may also display detectable variability on such timescales. *Xing 20* generate at least 3 different light-curves across the 11.5 year dataset, using 1 day, 3 day and 6.5 day binning, and determine that the 3 day binning shows the most promising results. There are many bins in these light-curves leading to statistical issues from the Look-Elsewhere effect, which are not discussed. *Xing 20* determine that the only source nearby which shows any variability is B2023+336; they generate light-curves with 3 day, 15 day and 60 day binning schemes and determine that no source confusion occurs, except for when B2023+336 flares, close to MJD 55000.

Xing 20 identifies two events as evidence for γ-ray emission from V404 Cygni, independent of the June 2015 excess. The first occurs close to the end of the 2015 X-ray outburst in August 2015, where a 12 hour bin is identified with TS = 15 and a flux of $(0.7 \pm 0.7) \times 10^{-7}\,\mathrm{photons\,cm^{-2}s^{-1}}$ in the energy range 300 MeV - 500 GeV. They do not consider data at energies below 300 MeV. I refer to this excess as the August 2015 excess.

The second of the two excesses reported occurs during August 2016, when V404 Cygni appears to be in quiescence, specifically between MJD 577623 - 57625. The peak TS of this excess is observed to be 45 (6.7σ for $k = 1$) and a γ-ray flux of $(2.6 \pm 0.6) \times 10^{-7}$ photons cm^{-2}s^{-1}, again in the 300 MeV - 500 GeV energy range. This excess is reported as the August 2016 excess.

Overall, a lack of information regarding the analysis setup used in *Xing 20* make it impossible to reproduce their results. Furthermore, the curious choice to exclude photons in the 100 MeV - 300 MeV energy range will impact the significances of the reported excesses.

4.3 LAT Observations of V404 Cygni

The goal of my analysis is to detect evidence for γ-ray emission from V404 Cygni, during both the 2015 outburst and during August 2016 where *Xing 20* report their flare. I use 11.5 years of *Fermi*-LAT data across a 100 MeV - 300 GeV energy range, which at the time of analysis was the full effective energy range of the instrument* to focus on an ROI centered on V404 Cygni. The dataset used is Pass 8, which has improved analysis methods and event reconstruction when compared to previous versions. I use `Fermitools (v1.2.23)` together with `Fermipy v0.19.0` for advanced analysis techniques.

Given that V404 Cygni is located both on the Galactic plane and near a bright point source of γ-rays (B2023+336), I use a binned likelihood analysis as recommended by the *Fermi* Cicerone. I use spatial bins of 0.1° width (approximately the LAT's optimal resolution at high energies) together with 8 energy bins per decade. Having reduced the data following the cuts described in Table 5.1, I then follow the method of Mattox et al. (1996) to populate the model with point sources from the 4FGL and

*It should be noted that *Xing 20* use a different energy range and more recent catalogue than I do in my analysis. This is because my analysis predates the release of *Xing 20* on arxiv.org, and the release of the 4FGL-DR2. My study was adapted to include *Xing 20* during the latter stages of research.

Observation Period (Dates)	04/08/2008 - 10/01/2020
Observation Period (MET)	239557417 - 600307205
Observation Period (MJD)	54682 - 58423
Energy Range (GeV)	0.1 - 300
evtype	3 (FRONT + BACK)
evclass	128 (`P8R3_SOURCE`)
Data ROI width	25°
Model ROI Width	30°
Zenith Angle	$< 90°$
Instrument Response	`P8R3_SOURCE_V2`
Isotropic Background Model	`iso_P8R3_SOURCE_V2_v1`
Galactic Background Model	`gll_iem_v07`
Point Source Catalogue	4FGL

Table 4.1: The parameters used in the likelihood analysis of the region of interest around V404 Cygni.

the Galactic and isotropic diffuse background components, resulting in a prediction of photon counts for each bin. Following this, I then improve the fit of the model to the data by running `gta.optimize` which iteratively pushes the model parameters close to their maxima with the `Minuit` optimiser. The normalisation of all sources within 5° are freed, as are all parameters of the background components and a full likelihood fit is executed with respect to the freed parameters. To further improve the fit, I run `gta.find_sources` to calculate a TS for each bin in the model, and then fit a point source if the TS exceeds 9 (for the 20 highest TS peaks in the model). This populates the model with point sources which are not catalogued in the 4FGL, and further increases the accuracy of the model.

Given the proximity of V404 Cygni to B2023+336 I test for spatial extension. Spatial extension is not expected from B2023+336 given it is a blazar, all of which are point sources. The TS of extension when a radial Gaussian spatial fit is tested against a point source null hypothesis is -0.01, which strongly favours the point source model as one would expect.

4.3.1 Spectral Analysis of the V404 Cygni Field

4.3.1.1 Spectral analysis of B2023+336

B2023+336 is a notable γ-ray blazar, as it is one of the few that is seen through the Galactic plane, itself a luminous γ-ray emitter. Although some contamination of photons from B2023+336 with those from the Galactic plane (which has a soft spectrum) is expected, use of the 8 year Galactic background model should minimise this. In this section, I detail the spectral analysis of B2023+336, and compare it with the spectral analyses of the three γ-ray excesses. If the spectrum of any excess is significantly different from that of the blazar, this is evidence that the excess is not a product of source confusion between B2023+336 and any emission from V404 Cygni. If the spectra are similar, this may imply source confusion, but this could be circumstantial. Further evidence, such as correlated variability between B2023+336 and V404 Cygni, would be needed to draw a firm conclusion.

In order to generate the SED of B2023+336, I use `gta.sed` and, as B2023+336 is a luminous source, the full 8 energy bins per decade of the analysis are used when producing the SED.

The spectral energy distribution of the blazar B2023+336 is given in Figure 4.1, where 95% confidence upper limits are fixed to bins with a z-score of less than 2. The best fit to the bins is a log-parabola spectral shape, with a z-score of 4.4σ against a power law model*. For the photon index of the SED, I use the log-parabola index, $\Gamma_{\mathrm{LP}} = 2.74 \pm 0.08$, which is in reasonable agreement with the photon index if a power law was fitted instead ($\Gamma_{\mathrm{PL}} = 2.65 \pm 0.05$). For the power law with exponential cutoff there is a slightly lower photon index ($\Gamma_{\mathrm{PLEC}} = 2.20 \pm 0.05$) with an exponent index of 0.66 ± 0.19. All models describe the spectral shape in a similar way: flux generally anti-correlated with energy, i.e. a soft γ-ray spectrum. There is a peak flux of $9.22 \times 10^{-6}\,\mathrm{MeV\,cm^{-2}\,s^{-1}}$ in the energy range 133 MeV

*A power law with an exponential cutoff (PLEC) model fits to a 4.0σ significance, so the difference in the goodness of fit between the log-parabola and PLEC is marginal.

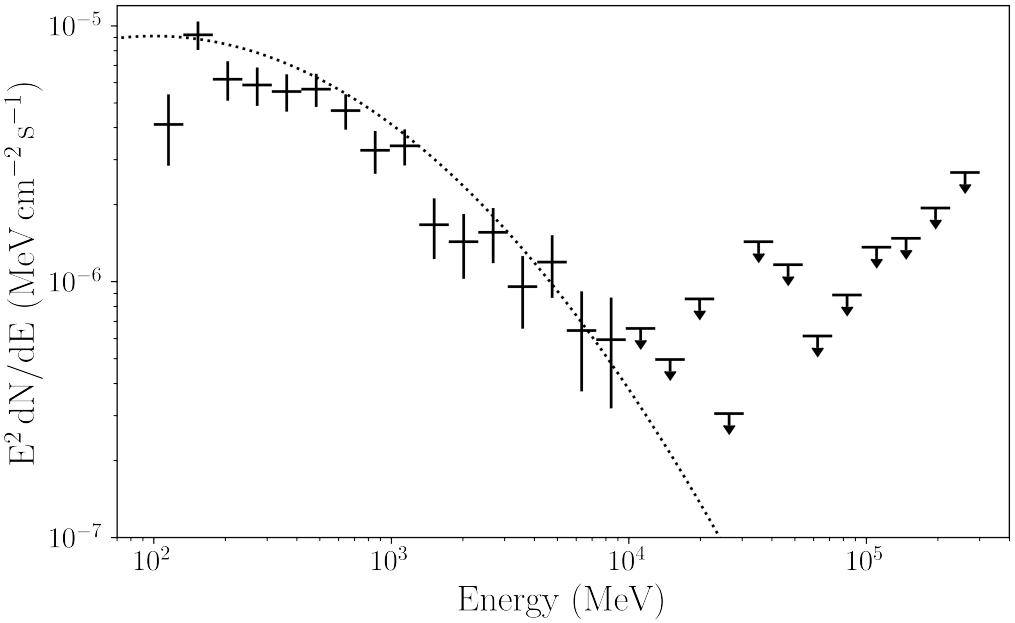

Figure 4.1: The Spectral Energy Distribution of the blazar, B2023+336, with $E^2 \frac{dN}{dE}$ energy flux plotted against bin energy. The best fit to the bins is a log-parabola spectral shape, with a z-score of 4.4σ against a power law model. The dotted line shows the log-parabola best fit, using the parameters described in Section 4.3.1.1, with a good fit to the data. This is unsurprising as a log-parabola spectral shape is common amongst the LAT detected blazar population. We calculate an upper limit on energy flux for any bin which does not have a TS of at least 4.

to 177 MeV, with a cut-off at energies above 9.7 GeV. This fit is compatible with that described in the 4FGL-DR2 (Abdollahi et al., 2020), where the log-parabola index is given as $\Gamma_{\rm LP} = 2.73 \pm 0.07$. I find no evidence for variability of the spectral shape of B2023+336, suggesting that the best fit spectral parameters are an accurate description at all times.

4.3.1.2 Spectral Analysis of the V404 Cygni Excesses

The most significant of the three excesses reported in *Loh 16* and *Xing 20* is the August 2016 excess. The authors fit a power law spectral model to this excess, although there are only 4 energy bins significant enough to be plotted. Their spectral fit has a power-law photon index of $\Gamma_{\rm PL} = 2.9 \pm 0.3$, indicating soft γ-ray emission.

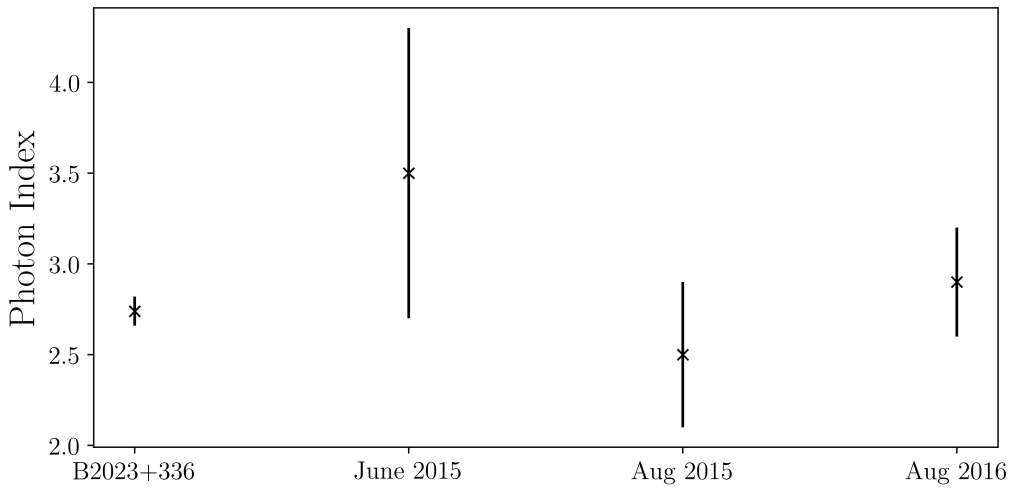

Figure 4.2: A comparative plot of the spectral indices for the Log-Parabola fit of B2023+336, compared to the power law indices of the June and August 2015 and August 2016 γ-ray excesses observed to be coincident with V404 Cygni.

The other two excesses from June and August 2015, observed during the microquasar outburst of the binary system, also have published spectral analyses available. The June 2015 excess described by *Loh 16* had a maximum flux of $1.4 \pm 0.5 \times 10^{-6}$ photons cm^{-2} s^{-1}, and a soft power law spectrum ($\Gamma_{PL} = 3.5 \pm 0.8$). These spectral parameters were derived from the highest TS bin in their light-curve. *Piano 17* do not report the spectral parameters associated with their *Fermi*-LAT analysis, and assume a power law spectrum of $\Gamma_{PL} = 2.1$ for their AGILE analysis, which is the default for an AGILE source with low photon-statistics or an unknown spectrum (Pittori et al., 2009). *Piano 17* show that the AGILE spectral parameters are consistent with the *Fermi*-LAT spectral parameters from *Loh 16*.

The August 2015 excess described by *Xing 20, Figure 4* has an SED calculated in the same way as the August 2016 excess. A soft power law is fitted ($\Gamma_{PL} = 2.5 \pm 0.4$), although only two bins are used.

4.3.1.3 Comparison of the Spectral Analyses

Figure 4.2 shows the a comparison between the spectral index of B2023+336, and the three γ-ray excesses; these have large uncertainties compared to that of the

blazar, which was detected over a much longer period, with much greater significance. There is overlap between the uncertainties of the photon indices of the putative excesses and the blazar index; this similarity between the excesses and the blazar spectra means there is insufficient evidence to determine whether the origin of these excesses is B2023+336 or V404 Cygni. The similarity does suggest the possibility of source confusion, particularly in the case of the *Xing 20* August 2015 and 2016 excesses, where the photon indices lie closer to that of the blazar with smaller uncertainties than those determined during the June 2015 excess.

4.3.2 Variability Analysis of V404 Cygni

As is generally true for blazars detected with *Fermi*-LAT (Meyer et al., 2019), B2023+336 is variable, with a variability index of 116 (Ballet et al., 2020). A variability index greater than 72.44 indicates variability on the timescale of months. This long-term variability is illustrated in Figure 4.3, which shows a rise in flux from the start of the LAT data, with a peak flux of approximately $8 \times 10^{-5}\,\mathrm{MeV\,cm^{-2}\,s^{-1}}$ in early 2010, followed by a sharp drop-off, with flux levels between 1 and $3 \times 10^{-5}\,\mathrm{MeV\,cm^{-2}\,s^{-1}}$ for succeeding bins. From June to December 2015, the flux of B2023+336 plateaus at between 1 and $2 \times 10^{-5}\,\mathrm{MeV\,cm^{-2}\,s^{-1}}$ with all points within the 95% confidence limit of one another, indicating a broadly steady γ-ray flux during the two apparent outbursts of V404 Cygni.

The three γ-ray excesses reported from V404 Cygni are reported on timescales of less than 12 hours rather than months. In general only the brightest sources seen with *Fermi*-LAT have variability that is detectable on short timescales, one example being Cygnus X-3 (Abdo et al. 2009d, Corbel et al. 2012). For V404 Cygni to be regarded as a γ-ray emitter, its emission must reach the 5σ level which is conventional for a discovery over this timescale. For reference, the blazar B2023+336 reaches a 5σ significance over 12 hours in August 2016, with a flux of approximately $5 \times 10^{-4}\mathrm{MeV\,cm^{-2}\,s^{-1}}$.

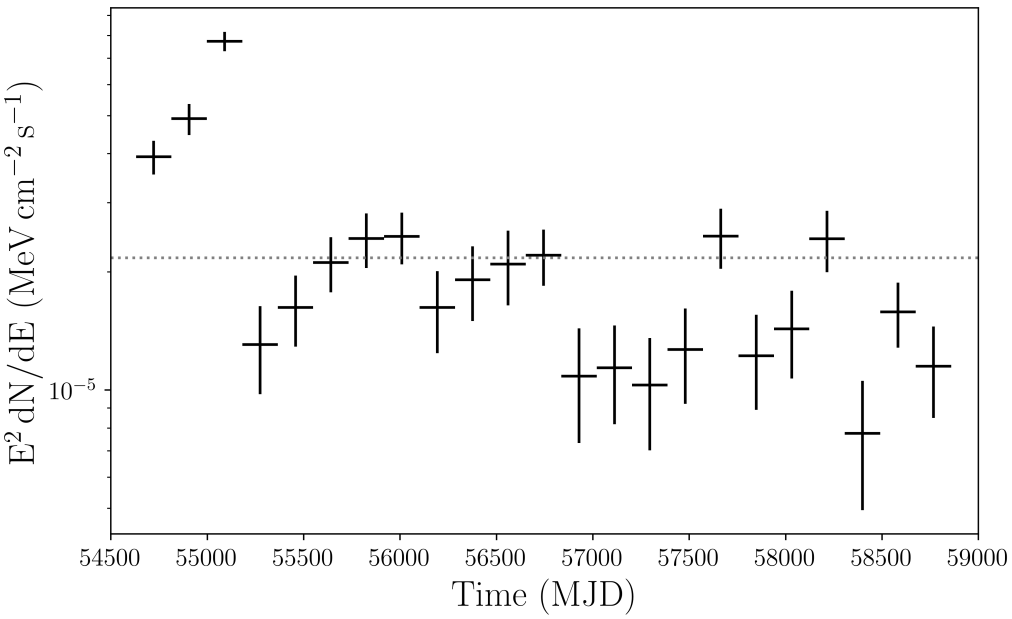

Figure 4.3: The light-curve of the blazar B2023+336, with approximately 6 month time bins spread out across the observation period given in Table 5.1. The grey dotted line indicates a constant-flux model, which results in a poor fit to the observed data. This is expected given the blazar's 4FGL catalogue variability index of 116.

The June and August 2015 excesses reported by *Loh 16* and *Xing 20* respectively do not reach the 5σ level. Furthermore, the fact that the June 2015 excess was identified using a now outdated model and an older catalogue necessitates a repeat analysis of this period with the most recent models. Such an analysis, performed by *Xing 20* failed to detect the 2015 events significantly, although as I have noted, differences in the analyses may explain this discrepancy.

Using the `gta.lightcurve` routine, I perform a binned light-curve analysis of the *Fermi*-LAT data between June 2015 and September 2015, a time period which covers the outburst of V404 Cygni. For this analysis, both background components are freed in the model, along with the normalization of all sources within 5° of V404 Cygni's position (including B2023+336). I use a 12 hour independent binning scheme, and place a 95% confidence upper limit on flux in any bin where the bin TS is less than 4 (corresponding to 2σ, or $p = 0.05$).

It is established that any potential excess may have a soft spectral energy distribution. The angular resolution of the *Fermi*-LAT is energy dependent, such that the point spread function (PSF) is worse at low energies. This is several degrees in the MeV range, where one would expect both the flux of the blazar and that of the binary to peak. As a measure to test for source confusion between the binary and the blazar, I produce an identical light-curve, but at the position of the blazar 0.3° away from V404 Cygni.

4.3.2.1 June 2015 Excess

Figure 4.4 shows a comparison between the V404 Cygni light-curve (black) and B2023+336 (red) γ-ray flux and the TS value of each bin during the June 2015 outburst period, as well as the *Swift*-BAT light-curve of V404 Cygni for this time. There is no γ-ray excess from the position of V404 Cygni during June 2015, when *Loh 16* report a 4σ excess at the peak of the *Swift*-BAT light-curve highlighted by the TS map in Figure 4.5. This is not entirely surprising, as both *Loh 16* and *Piano 17* used older background models and an older catalogue for their analysis. A key difference between the 3FGL used by *Loh 16* and the 4FGL used in this analysis (and *Xing 20*) is the addition of weighting in the maximum likelihood method employed in LAT analysis. The weighted maximum likelihood method better reflects the systematic uncertainties of the instrument, and results in larger parameter uncertainties and correspondingly smaller TS values. This could explain why an apparently significant time bin in the *Fermi*-LAT results of *Loh 16* and *Piano 17* is no longer seen when using the 4FGL, although this does not explain the AGILE result described in *Piano 17*. This result is in agreement with *Xing 20*, who similarly find no 4σ γ-ray excess in June, although there is a lack of information regarding the analysis parameters of *Xing 20.*

A further difference between this analysis and that of *Loh 16* is that *Loh 16* use an unbinned analysis. A binned analysis is preferred for sources on the Galactic plane;

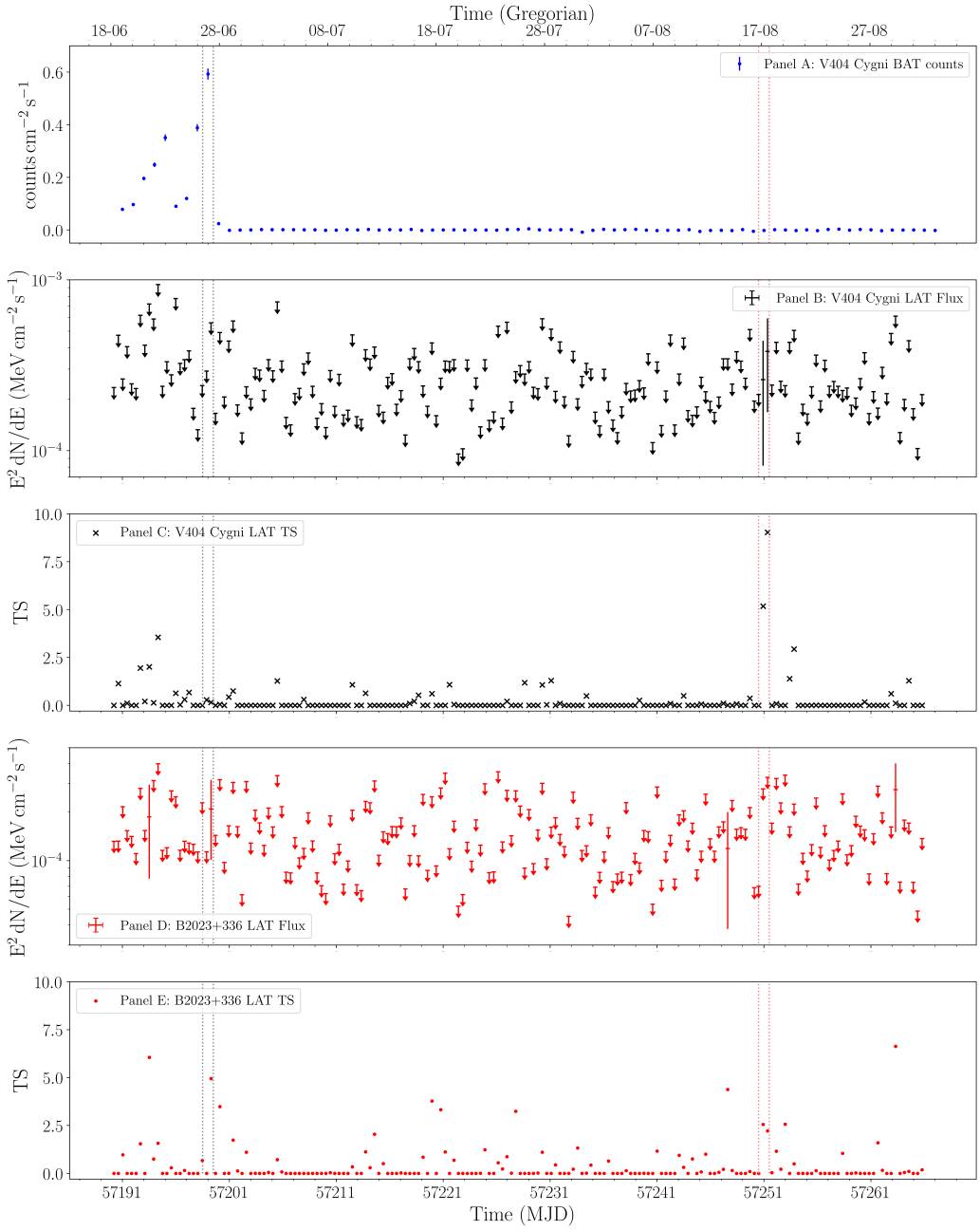

Figure 4.4: The light-curves of V404 Cygni and B2023+336 during the 2015 outburst. Panel A shows the *Swift*-BAT light-curve for V404 Cygni with daily independent binning. Panels B and C show the *Fermi*-LAT light-curve and TS values respectively for this period for V404 Cygni with 12 hour independent binning. Panels D and C show the *Fermi*-LAT light-curve and TS values respectively for B2023+336 with 12 hour independent binning. Units of time are Gregorian, and Modified Julian dates. The vertical grey dotted lines indicate the beginning and end period of the June 2015 excess, whereas the vertical pink dotted lines indicate the beginning and end period of the August 2015 excess.

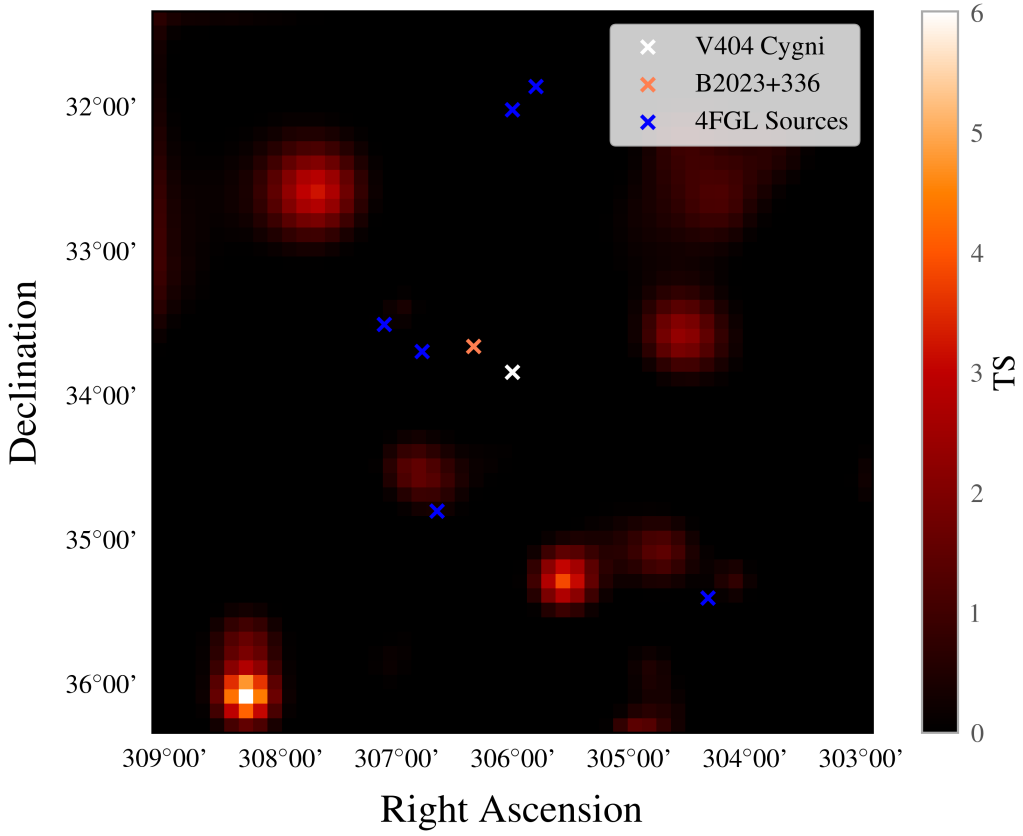

Figure 4.5: A TS map of the position of V404 Cygni over the 12 hour period (MJD 57199.25-57199.75) where *Loh 16* describe their γ-ray excess (coincident with the peak in X-ray brightness). We observe no excess of γ-rays from the position of V404 Cygni during this time that cannot be accounted for by any of the neighbouring 4FGL sources, or the background models. This TS map is taken over the full effective *Fermi*-LAT energy range of 100 MeV to 300 GeV with 0.1° spatial bins.

however, I also performed an unbinned analysis over the 12 hour period shown in Figure 4.5, and find that this analysis agrees with the binned result.

4.3.2.2 August 2015 Excess

Xing 20 report a separate 4σ γ-ray excess in August 2015 through use of independent binning. Two bins in my V404 Cygni light-curve have significances above the upper limit threshold in August 2015, ($\sim$ MJD 57521), which is the same time period as that reported by *Xing 20* in their analysis. Whilst *Xing 20* reports this excess at the 4σ level, I find that one bin reaches the 2σ level, and the second,

consecutive, bin reaches 3σ, with no corresponding rise in the count rate of the *Swift*-BAT light-curve. There is no corresponding flux increase in the light-curve of the blazar. Given that I use the same LAT catalogue and background models as *Xing 20*, it is likely that this discrepancy in results is down to the photon selection (I use energies greater than 100 MeV, and *Xing 20* use energies greater than 300 MeV), and potentially other differences between our analysis and that of *Xing 20*.

It is necessary to consider the likelihood of an apparently significant result arising simply by chance. The binomial distribution provides a suitable representation of our 184 bins, and I calculate that the chance of finding exactly one 3σ bin out of 184 is 30.3%, with a probability of finding at least one 3σ result rising to 39.2%. We therefore do not believe this August 2015 excess to be significant, as despite the fact these bins are adjacent to one another, the low TS of these indicates that they are likely to reflect a Galactic plane background fluctuation rather than genuine γ-ray emission from a point source.

4.3.2.3 August 2016 Excess

Xing 20 also claims a more significant 7σ γ-ray excess from V404 Cygni during August 2016, a year after the X-ray outburst finishes. This is by far the most significant excess in their light-curve. Figure 4.6 shows the light-curves of V404 Cygni and B2023+336 during August 2016. Using independent 12 hour binning, I do not find such high TS values as *Xing 20* (although, as for the analysis of the August 2015 event, the photon selection and analysis parameters differ to those of *Xing 20*). Nevertheless, there are three bins at the 3σ to 4σ level over a short period, with measurable fluxes. However, when one looks at the light-curve of B2023+336, similar fluxes are detected in these bins and others around this time, suggesting confusion as to whether the flare originates from V404 Cygni or B2023+336.

There are no available multi-wavelength observations of B2023+336 during the time of this apparent detection of V404 Cygni. However, neither the optical AAVSO or

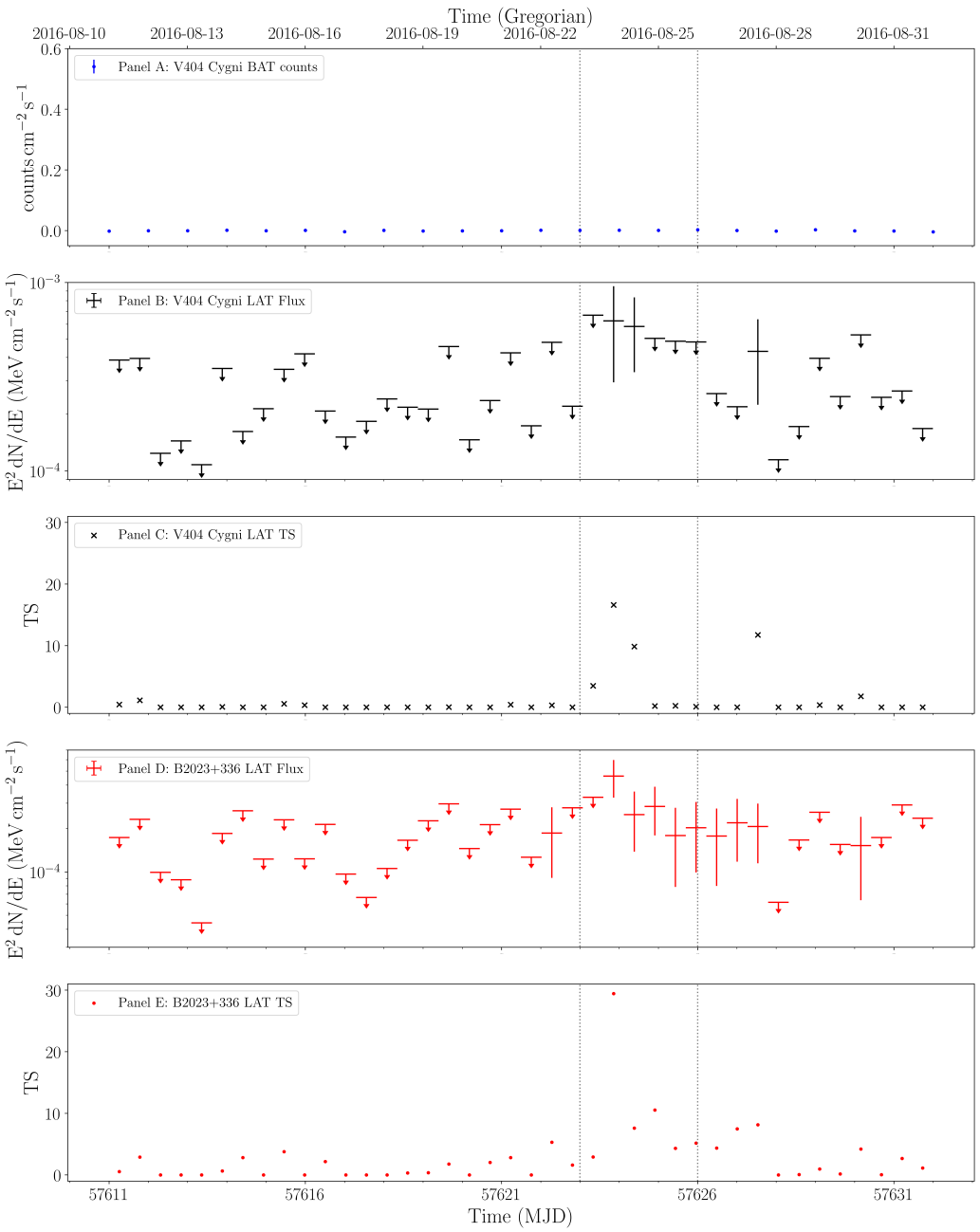

Figure 4.6: The light-curves of V404 Cygni and B2023+336 during August 2016, when *Xing 20* claim their detection of V404 Cygni. Panel A shows the *Swift*-BAT light-curve for V404 Cygni with daily independent binning. Panels B and C show the *Fermi*-LAT light-curve and TS values respectively for this period for V404 Cygni with 12 hour independent binning. Panels D and E show the *Fermi*-LAT light-curve and TS values respectively for B2023+336 with 12 hour independent binning. Units of time are Gregorian, and Modified Julian Dates. The vertical grey dotted lines indicate the beginning and end of the 3-day time bin *Xing 20* used to identify the August 2016 excess. We also observe γ-ray emission outside this time period at comparable TS values.

X-ray *Swift*-BAT light-curves of V404 Cygni (Figure 4.6) show any enhancement during August 2016, nor is there any significant enhancement since the December 2015 flare. For V404 Cygni to form a jet which emitted γ-rays, an enhancement in the X-ray flux similar to that seen in June 2015 would be expected (Figure 4.4). As this is not seen, this suggests that there was no outburst from V404 Cygni at this time, supporting the hypothesis that the flare is from the blazar, not the binary.

4.4 Statistical Analysis

4.4.1 Statistical Tests of Similarity

In order to look for similarity between the γ-ray emission of V404 Cygni and the blazar, B2023+336, I perform a 2-sample Kolmogorov-Smirnov (KS) test (Kolmogorov 1933 & Smirnov 1948) in order to explore the hypothesis of source confusion. This tests whether two numerical distributions are drawn from some common overall distribution by calculating a KS statistic using Equation 4.1.

$$D_{a,\,b} = \sup |F_{1,\,a(x)} - F_{2,\,b(x)}| \tag{4.1}$$

Here, $D_{a,\,b}$ is the KS statistic for two samples $a(x)$ and $b(x)$, where the KS statistic is equal to the supremum of the absolute difference between the empirical distribution functions (EDFs) of the two samples. The EDFs for all of our samples are shown in Figure 4.7*.

For the 2015 outburst period, I calculate $D = 0.11$ indicating a p-value of $p = 0.23$ for the hypothesis that the samples are drawn from separate distributions. This is unsurprising, as Figure 4.7 shows that the EDFs for the blazar and binary at this time are not substantially different and, although B2023+336 is a luminous

*Alternative tests of similarity exist, such as the Mann-Whitney test (Mann and Whitney, 1947), or the well known Student's t-test. However, I use the KS test as it is more powerful in detecting changes in the shape of the distribution, which is essential when analysing time series data.

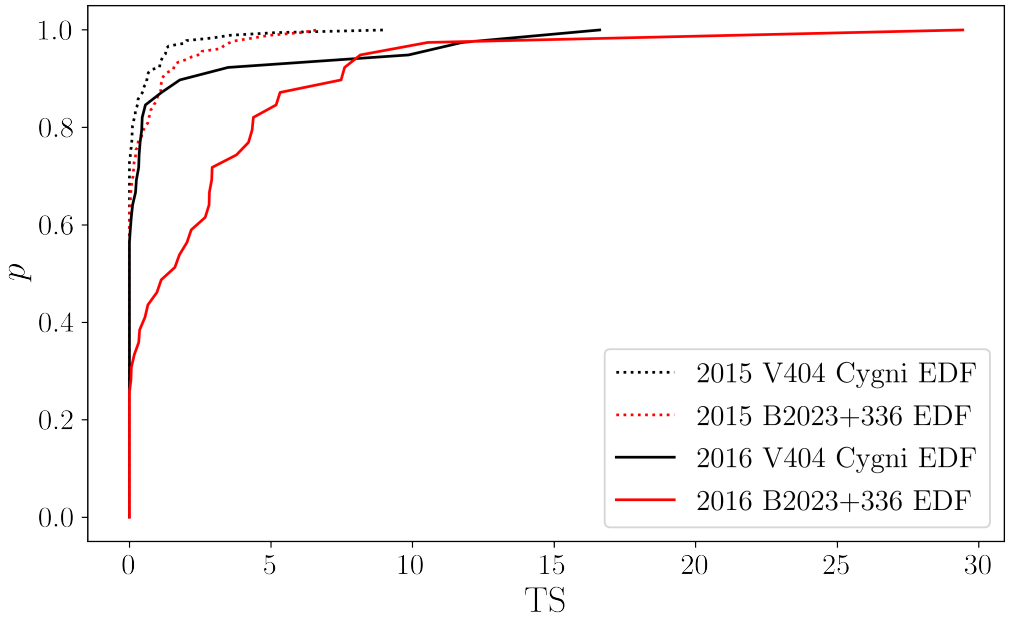

Figure 4.7: The empirical distribution functions of V404 Cygni and B2023+336 during the 2015 outburst and the 2016 flare for the TS of each time bin. The B2023+336 and V404 Cygni distributions in 2015 are very similar, and are dominated by the noisy background. During 2016, the V404 Cygni distribution reaches a higher peak TS, with a higher probability of increased TS values over 2015. The most significant emission comes from B2023+336 during 2016, where there is a TS peak higher than the V404 Cygni distribution.

γ-ray source, it is not known to be regularly detected on timescales as short as 12 hours. Both sources are likely dominated by the same noisy γ-ray background on the Galactic plane during the outburst, which provides the most likely source of the common distribution of TS values during the 2015 outburst.

For the 2016 excess period, I calculate $D = 0.425$ corresponding to $p = 0.001$ for the same hypothesis, indicating a significant difference in the TS distributions of both the blazar and binary system. In Figure 4.7 there is an increased probability of higher TS values for both systems when compared to the 2015 outburst period where both systems are noise dominated, indicating increased γ-ray emission from both B2023+336 and the position of V404 Cygni. The plots of TS against time shown in Figure 4.6 for August 2016 also show that the increased TS (and therefore flux) occurs for both systems at the same time, with the peak of both light-curves

occurring in the same bin indicating that this emission could have the same origin. Given that the EDF of B2023+336 shows an increased probability of higher TS values, and therefore more significant γ-ray emission than from V404 Cygni, this serves as statistical evidence at the 3σ level that the origin of the August 2016 flare is B2023+336 rather than V404 Cygni.

In conjunction with the lack of X-ray emission observed by *Swift*-BAT from V404 Cygni during August 2016, there is sufficient evidence to state that the August 2016 γ-ray flare originates from B2023+336 and not V404 Cygni. Any γ-ray emission observed from the position of V404 Cygni is a product of source confusion with B2023+336, due to the properties of the LAT itself (resolution, point spread function etc), which are less precise at the lower energies where this flare occurs, as established in Section 4.3.1. Given that the LMXB system was in quiescence at this time, a blazar origin for this emission is much more likely.

4.4.2 Degrees of Freedom with Overlapping Bins

Loh 16 (and *Xing 20* in replicating their study) use light-curve bins which overlap one another, rather than an independent binning scheme. Whilst the majority of light-curves produced in γ-ray astronomy (including all the light-curves in this thesis) are independent, dependent light-curve binning has a key advantage, and two key drawbacks.

Dependent light-curve binning allows for greater resolution in measuring changes in the flux levels of a source by increasing the number of measurements taken, whilst not incurring the penalties associated with shortening the light-curve bins, which would be the usual way to increase the number of measurements taken in an independent binning scheme. A downside of this is increased computational cost associated with the analysis of more time bins. Whilst the computational cost is of no consequence here, the second drawback to dependent binning is.

In independent binning, each singular photon belongs exclusively to one bin, and

no others. This is true in both spectral and temporal analysis for the *Fermi*-LAT data as each photon has a discrete energy and arrival time associated with it in the *Fermi*-LAT data files. This is no longer the case for dependent binning as each photon can be binned multiple times, as its energy or arrival time meets the criteria for multiple bins. Dependent binning in astronomy in general is rarely used, and there is little literature discussing the statistical impact of counting photons in γ-ray analyses multiple times, however a study by Orford (1990) reveals that the simplest way to account for the impact of double counting photons is through the treatment of statistical degrees of freedom when applying Wilks' theorem to the calculated TS values of each bin*.

Assuming that each photon is counted the same number of times, the number of degrees of freedom scales as the number of times a photon is counted. This is because increasing the number of bins increases the amount of sampling done without increasing the sample size, thus increasing the chances of an apparently significant false positive result arising and increasing the degrees of freedom.

Neither *Loh 16* nor *Xing 20* account for the higher number of degrees of freedom present in their dependent light-curves, and both (mistakenly) take the degrees of freedom to be $k = 1$, which corresponds to an independent binning scheme. In the cases of the 12 hour, shifted by 6 hour, light-curves of both *Loh 16* and *Xing 20* this means a relatively minor correction to both significances as both need to be recalculated with $k = 2$, rather than $k = 1$. In the case of the 6 hour, shifted by 1 hour, binning scheme of *Loh 16* this is a more significant change as each photon is counted 5 times, so that $k = 5$.

As a result, both *Xing 20* and *Loh 16* overstate the significance of their results by improperly dealing with the degrees of freedom which arise from their binning schemes. This likely explains, in part, why the light-curves shown in this chapter

*Whilst (Orford, 1990) makes reference to statistical searches for periodicity in VHE pulsar data, the techniques discussed are broadly comparable to the *Fermi* data given the use of hypothesis testing. Furthermore, (Orford, 1990) use the term 'oversampling'; this simply refers to dependent binning.

fail to reproduce such high TS values: fewer trials were used in order to obtain them.

4.4.3 The Temporal Look-Elsewhere Effect

Xing 20 find the August 2015 and August 2016 excesses by running a light-curve over 11.5 years with 3-day independent binning, having also created but discarded light-curves using 1-day and 6.5-day binning. This light-curve is shown in *Xing 20 Figure 3*. Given the very large number of bins used in this light-curve, one must consider the Look-Elsewhere effect, where significant time bins may appear as a result of the number of bins searched.

In addition to the June 2016, August 2016 and August 2017 γ-ray excesses, which are attributed to the large number of bins searched and source confusion with a B2023+336 flare, *Xing 20* find 10 other 3-day bins with TS values at the 3σ level or above. The first four of these excesses (in time), labelled Period 1 in *Xing 20 Figure 3*, occur during the first 18 months of the *Fermi*-LAT mission. From our mission-long light-curve of B2023+336, one can see that for the first 18 months of the *Fermi*-LAT mission, the flux is in an enhanced state with respect to all later bins. Both *Loh 16* and the *Fermi* All-Sky Variability Analysis team (Ackermann et al., 2013) report on the enhanced state of the blazar. Considering the previously established evidence with regards to source confusion, particularly during flares, it is likely that the γ-ray flux enhancement during Period 1 is from the blazar.

Having accounted for the flux excesses in Period 1 and the August 2015 and 2016 excesses, 6 other γ-ray excesses are described in *Xing 20 Figure 3*. As this light-curve covers 11.5 years, with 3 day binning, there are approximately 1400 bins in this time. Using the binomial distribution to predict how many γ-ray excesses are likely to occur at the 3σ level, I find that there is an 9.25% chance of finding these 6 γ-ray excesses by chance, indicating a strong possibility that there is no γ-ray emission from V404 Cygni that cannot be accounted for either by source confusion

with B2023+336 or by considering the effect of apparently significant bins arising by chance. Given how poorly the Galactic γ-ray background is understood, that it is non-uniform and often sees small local fluctuations in time, it is also possible that these bins are caused by background fluctuations.

4.5 V404 Cygni, Discussion and Future Prospects

The definitive identification of novel γ-ray emission from an X-ray binary would be a scientifically important result, particularly from V404 Cygni: an LMXB and a microquasar. Hence, given that the multi-wavelength campaign to observe V404 Cygni's 2015 outburst is one of the largest in history, intense interest in the γ-ray properties of the system has abounded. Three γ-ray excesses have been linked with V404 Cygni across multiple papers; my reanalysis has not been able to convincingly associate V404 Cygni with any of these excesses.

The first of these excesses is described by *Loh 16* and *Piano 17*, and occurred in June 2015 coincident with the hard X-ray peak of the outburst, during the peak of the AAVSO optical light-curve, and shortly following the peak radio emission. The background models, catalogue and instrument response functions used in this analysis are now superseded by more accurate models, and when I carry out binned (and unbinned) analyses, I find no significant γ-ray emission. This γ-ray excess is likely to be a product of the older models available at the time for *Fermi*-LAT data analysis supported by the fact that the peak significance reaches only 4σ. The *Loh 16 analysis* also contains a miscalculation with the degrees of freedom of the light-curve, causing an over-estimation in significance. The excess observed within the AGILE data discussed in *Piano 17*, remains the strongest independent evidence for γ-ray production in V404 Cygni in June 2021.

The next of these excesses is a separate 4σ at the end of the outburst in August 2015, claimed by *Xing 20*. Unlike the first, there is no corresponding X-ray enhancement, but we do also see this excess in my own analysis. However, a wider issue with

apparently significant bins arising by chance both in my own light-curve (Figure 4.4) and the work of *Xing 20* leads us to believe that this is probably a chance occurrence.

The final, and most significant, claim of γ-ray emission occurring from V404 Cygni was the 7σ August 2016 excess reported by *Xing 20*, after the X-ray outburst had finished. I find that this is more than likely a product of source confusion with B2023+336, which also appeared to be active at this time. Given that the γ-ray emission from B2023+336 is present longer, more consistently, and more significantly than that reported from the position of V404 Cygni, and the spectral similarity between this excess and the spectrum of B2023+336, this γ-ray excess is likely a product of source confusion between the blazar and V404 Cygni. This is supported by the fact that V404 Cygni was in quiescence at this time, and is not likely to become an active microquasar again for another decade or two, based on its history of outbursts.

Whilst the lack of detection of γ-ray emission from V404 Cygni could be considered a negative result, it is still an interesting one. Three microquasars are seen with *Fermi*-LAT (Cyg X-1, Cyg X-3 and SS 433), and only SS 433 has evidence for emission at VHE (Abeysekara et al., 2018b). These objects enter outburst much more frequently than V404 Cyg does, with SS 433 being persistently supercritical, suggesting fundamental differences in the makeup of these systems.

Since the V404 Cygni outburst other microquasars have also undergone outbursts. One such outburst, that of MAXI J1820+070* in 2018, was comprehensively studied at γ-ray wavelengths with combined observations from VERITAS, MAGIC and H.E.S.S. supplemented by *Fermi*-LAT all-sky data presented in Abe et al. (2022). Like V404 Cygni, these observations covered the state transitions in the outburst, where no significant detection of γ-ray emission was made. This study suggests that the emission from this particular microquasar during outburst was approximately 20 times lower than the threshold for detection with current instruments,

*Like V404 Cygni, MAXI J1820+070 is an LMXB with a black hole accretor.

and that prospects remain positive for future detections with upcoming instruments such as CTA. Given the similarities between the outburst of V404 Cygni and MAXI J1820+070, it is possible that many microquasars are simply not luminous enough to be detected in γ-rays with current instruments.

An interesting prospect for the future detection of V404 Cygni is AMEGO (McEnery et al., 2019), proposed to launch in 2030. AMEGO will operate in the MeV range, where one would expect V404 Cygni to emit γ-rays, and will operate with greater sensitivity and resolution than *Fermi*-LAT. It is very possible that, if V404 Cygni becomes active again, AMEGO will make a significant detection. The 2030 target launch date, and the 1 to 2 decade microquasar cycle of V404 Cygni, means the next time this system becomes active the scientific community will hopefully have a clearer picture as to the high energy physics involved in such a system. AMEGO, alongside other observatories in development, is discussed further in Chapter 10.

Figure 4.8: The fourth labour of Heracles, the capture of the Erymanthian boar. By Lucas Cranach the Elder (After 1537).

Chapter 5

Surveying the X-ray Binaries I: Methodology and Results

In Chapter 4, a detailed analysis of V404 Cygni was presented, including individual investigations into each claim of γ-ray emission/excesses given in different studies. V404 Cygni is just one of hundreds of X-ray binaries, and it is impractical to conduct such an in-depth investigation into all of these systems. Therefore, this Chapter details a survey of the X-ray binary population, which investigates each X-ray binary in a more efficient and systematic way. Coordinates, orbital periods and other information on each system is taken from Liu et al. (2006) and Liu et al. (2007), which were published in the mid 2000's, when a large number of new X-ray binaries had been discovered by INTEGRAL. As a result, whilst these catalogues do not encompass the entire known X-ray binary population, they do encompass almost all of it. The proceeding Chapters (6 - 8) provide an in depth look at the systems where the survey indicates that there is a reasonable probability of γ-ray emission from an X-ray binary.

5.1 Methodology

5.1.1 Data Reduction and Modelling

To perform the survey of the XRB population, `Fermipy 0.19.0` and `Fermitools 1.2.23` are used to analyse the *Fermi*-LAT data. Like V404 Cygni which was discussed in Chapter 4 the vast majority of the XRB population lies on the Galactic plane. The Galactic plane itself is a luminous, non-uniform, source of diffuse γ-ray emission and is additionally overlaid with a dense field of point, and extended, γ-ray sources. As shown in Chapter 4, if one searches for 'novel' γ-ray emission close to a known source of γ-rays, especially at low energies (as *Fermi*-LAT has an energy dependent point spread function), it can be difficult to resolve one source from another and source confusion occurs. In the case of V404 Cygni source confusion is identified as being responsible for the apparently significant August 2016 excess through simultaneous variability and spectral analysis of the blazar and the position for the binary, and in order to survey the X-ray binary population, the techniques explored in Chapter 4 are vital in correctly identifying whether any potential γ-ray emission from XRBs is a product of source confusion.

Compared to the analysis of Chapter 4, where the 8-year 4FGL catalogue is used, for the XRB survey presented in Chapters 5, to 8 a more recent catalogue is used, the 4FGL-DR2 (Data Release 2) (Ballet et al., 2020), which encompasses 10 years of data providing a more accurate reflection of the nature of the γ-ray sources seen by *Fermi*-LAT. A third version of the 4FGL, the DR3 (with 12 years of data) has since been released, however given that the entire XRB survey detailed here took approximately a year to perform the analysis for, it would be impractical to repeat the analysis with a newer catalogue. In addition to the 4FGL-DR2, the 8-year extended model templates are used to provide the most up-to-date parameters for extended sources, which are particularly common on the Galactic plane, and the 8-year Galactic and isotropic diffuse background models are also used to provide the

most accurate and up-to-date parameters for the γ-ray background (Acero et al., 2016).

To survey the XRB population, I use the Mattox et al. (1996) maximum-likelihood estimation method to construct a binned model of the ROI around each XRB independently, with each model centered on one particular XRB. Whilst there is a substantial amount of overlap between XRB ROIs, by analysing each independently I am able to build a smaller, more accurate model for each XRB, as opposed to trying to fit multiple new sources to one large model which is likely to be less accurately modelled (due to the larger number of parameters that will need to be estimated).

The parameters for the analysis of each ROI are the same, and are given in Table 5.1, with the only difference between each being the coordinates that each ROI is centered on; these coordinates are those of each XRB given in the Liu et al. (2006) and Liu et al. (2007) XRB catalogues. These coordinates, and the waveband from which they are derived are given in Appendix B for the HMXB sample, and Appendix D for the LMXB sample. Additionally, as the analysis of the LMXB sample was performed several months after the analysis of the HMXB sample, several more months of data was available for analysis, hence the observation period for the LMXB sample is several months longer than the HMXB sample. This is reflected in Table 5.1, where dates for both the HMXB and LMXB samples are provided.

Following the `gta.setup` command, I initially perform photon selection using `gtselect` to cut down the photon sample to only the required energy range, and ROI followed by computing good time intervals using the mission long spacecraft file with `gtmktime`. Having pre-computed an instrument livetime cube for both the HMXB and LMXB time periods, I skip the `gtltcube` step of `gta.setup`, as this step is the most computationally expensive of the algorithm and the livetime cube for each ROI is identical, provided that the analysis time period is the same (which it is). I subsequently bin the data using `gtbin` and generate a source map

LMXB Observation Period (Dates)	04/08/2008 - 26/07/2021
LMXB Observation Period (MET)	239557417 - 648950405
LMXB Observation Period (MJD)	54682 - 59421
Energy Range (GeV)	0.1 - 500
Data ROI width	10°
Model ROI Width	15°
Zenith Angle	$< 90°$
GTI Filter	`DATA_QUAL>0 && LAT_CONFIG==1`
Instrument Response	`P8R3_SOURCE_V2`
Isotropic Diffuse Model	`iso_P8R3_SOURCE_V2_v1`
Galactic Diffuse Model	`gll_iem_v07`
Point Source Catalogue	4FGL-DR2
Extended Source Templates	8 Year Templates

Table 5.1: The parameters used in the likelihood analysis of the regions of interest around the X-ray binary systems in the Liu et al. catalogue.

for each source in the model using `gtsrcmaps`.

Following the completion of `gta.setup` on a ROI centered on each of the approximately 300 XRBs in the sample, there is an unoptimised model for each of the XRBs. In order to improve the fit of the model to the data I initially use `gta.optimize`, a fitting routine which iteratively pushes the parameters of the model close to their global maxima. This significantly improves the accuracy of the model in describing every point, and extended source as well as the background components. In order to populate the model with any point sources that are not included in the 4FGL-DR2*, I use `gta.find_sources` to iteratively fit point sources to test statistic peaks in the model where TS > 9, with the caveat that the algorithm will not fit a point source to a peak where a more significant source is in the model within 0.5° angular offset. Finally, to improve the fit of the model in the immediate vicinity of the XRB position (i.e. at the centre of the ROI), I free the normalisation of all sources within 1° of the centre of the ROI, including the isotropic and Galactic background components, and execute a full likelihood fit, using the `MINUIT` optimiser, until an optimal fit quality of 3 is obtained. This ensures that any sources close to the XRB position, and that are likely to cause source confusion at the XRB position

*I use 12.5 - 13 years of data compared to the 10 years of the DR2 so there will be sources in the data not included in the catalogue, which will need to be added to the model.

are modelled as accurately as possible. Having modelled the data for each XRB's ROI, I generate a TS map of each ROI in order to highlight any significance peaks which have not been modelled, and residual maps as a quality check to test for systematic under/over-modelling.

5.1.2 Testing for persistent γ-ray emission

To assess whether γ-ray emission is detected from the position of an X-ray binary, I use the likelihood ratio test to perform a hypothesis test with the null hypothesis (Θ_2) being that no γ-ray point source is present at the position of the XRB, and the alternate hypothesis (Θ_1) being that there is a significant γ-ray point source present at the position of the XRB.

As with previous uses of the test statistic, the TS value can be translated into a z-score as the TS is distributed as a χ^2 statistic for k statistical degrees of freedom between the two hypotheses (Wilks, 1938). As the alternate hypothesis has 1 additional degree of freedom than the null hypothesis (the XRB source), the z-score for this hypothesis test, and therefore the significance of the γ-ray source at the position of the X-ray binary is given by Equation 5.1

$$z = \sqrt{\mathrm{TS}} = \sqrt{2 \ln \frac{L(\Theta_1)}{L(\Theta_2)}} \tag{5.1}$$

In order to perform this hypothesis test, a 'test' source must be added to the position of the XRB for which a TS value can be calculated with a likelihood fit, using `gta.fit`. There are two ways in which I can add and fit such a test source.

The first way to fit a test source has already been described in the previous section, and occurs with the use of the `gta.find_sources` algorithm which is ran during the fitting of the model to the data. This algorithm will fit point sources to the 4 highest TS peaks, and then repeat either 5 times, or until there are no more peaks above a user-defined minimum TS value, which I set to TS = 9, being equivalent to

$z = 3\sigma$. As a measure to avoid source confusion, I define a minimum separation for the algorithm, whereby a source cannot be fitted within 0.5° of a higher TS peak. Each source added to the model with `gta.find_sources` algorithm has a positional uncertainty, which reflects the systematic uncertainty of the LAT instrument itself. I define a γ-ray source as being spatially coincident with the position of a XRB if the angular offset from the position of the XRB is less than the 95% angular positional uncertainty* of the point source, i.e. the XRB lies within the positional uncertainty of the γ-ray source.

The `gta.find_sources` algorithm has limitations in how it fits sources to excesses of γ-rays. For instance, In each ROI I am limited to fitting point sources of the 20 most significant TS peaks, which excludes any sources that are not necessarily one of these 20, but still have a TS > 9 and would otherwise be considered γ-ray point sources within the survey. Additionally, with a minimum separation of 0.5°, it is entirely possible for a HMXB to be emitting detectable and distinguishable γ-ray emission, but to be within this minimum angular separation. This is a particular issue on the Galactic plane, where catalogued point sources are packed closely together, and would exclude many of the HMXBs from the discovery of γ-ray emission.

Therefore, in ROIs where no test source is fitted by `gta.find_sources`, I add a point source manually with `gta.add_source`. This added source has an initial soft power law spectrum with spectral index $\Gamma = 2.0$, which is the same as the sources added by `gta.find_sources`. I then free all parameters of this added source and the normalisation of the sources within 1° of it, and both components of the γ-ray background. I then execute a maximum likelihood fit which calculates a TS for this added source.

Adding a source to the position of the central XRB in each ROI either with `gta.find_sources` or with `gta.add_source` results in the same hypothesis test

*The PSF of *Fermi*-LAT is large and energy-dependent and therefore the 'position' of a source is simply the point where the origin of the γ-rays is most likely to be, given the PSF. The angular positional uncertainty is the statistical uncertainty on this likely position.

either way; the only difference being that there is usually a small (approximately 0.1°) angular offset between the sources fitted by `gta.find_sources` and the position of the XRB, whereas the test sources added with `gta.add_source` will be fitted exactly to the XRB coordinates from Liu et al. (2006) or Liu et al. (2007). Regardless of which way the hypothesis test is done, the difference between the two due to the offset is usually negligible.

As is conventional in γ-ray astronomy, I use a TS threshold of 25 ($z = 5\sigma$) to claim full detection of a γ-ray source coincident with the position of an XRB. I also report γ-ray fluxes for γ-ray excesses in the $9 \leq \mathrm{TS} < 25$ ($3\sigma \leq z < 5\sigma$) range as, while these do not meet the conventional significance for detection and often lack the photon statistics for further analysis, they may be worthy of further study. For those sources (either detected using the `gta.find_sources` algorithm, or added later) which exceed the 3σ threshold, I carry out further investigation detailed in Chapters 6, 7 and 8 in order to explore whether this γ-ray emission is likely to originate from the X-ray binary in question.

5.1.3 Testing for transient/variable γ-ray emission

As XRBs (both low and high mass) are generally variable sources across a variety of wavebands, therefore in addition to testing for persistent γ-ray emission, it is also necessary to test for variability within this persistent γ-ray emission, and also test for transient γ-ray emission from these systems. To do this, I construct a light-curve at the XRB positions using either the coincident source found by the `gta.find_sources` algorithm or the source added afterwards. I use approximately 6 month time bins (25 bins over the observation period) in all cases*. To produce the light-curves I use the `gta.lightcurve` algorithm which carries out a full likelihood fit of the ROI in each time bin to calculate an integrated flux and TS value for the

*As the HMXB and LMXB observation periods differ, the LMXB bins are marginally longer than the HMXB ones.

source on a bin-by-bin basis. For each bin I report an energy flux value if TS ≥ 4, or a 95% confidence limit otherwise.

In order to see whether a light-curve shows evidence for γ-ray emission in any bin(s), I use a mathematical 'light-curve condition' which, when satisfied, indicates that there are bins in a light-curve with significant γ-ray flux. If the condition is satisfied, I can then examine these bins to see whether γ-ray emission is constant (non-variable), the flux values vary (variable), or a γ-ray flux appears only during a certain time interval (transient). The likelihood fitting used in `gta.lightcurve` results in a TS value for each bin giving us a measure of how significant the γ-ray flux is in this bin. Using Wilks' Theorem, I then calculate a p-value for each bin, which gives the probability that each bin arises by chance. I then take all of the p-values for each bin with TS > 4, and use Equation 5.2 below to calculate a p-value for all the significant ($> 2\sigma$) bins:

$$p_{lc} = 1 \times \prod_{i=1}^{n} p_i, \tag{5.2}$$

Here, n is the number of bins with TS > 4, and p_i is the p-value of each bin. Bins with TS < 4 are excluded, because these have insufficient photon statistics to provide a reliable flux value and are therefore generally less useful for trying to understand the properties of a source. This is particularly true on the Galactic plane (where most of the XRB population lies) where the luminous diffuse γ-ray emission and crowded field mean that bins with TS < 4 are likely to be noise-dominated.

I consider a source to have satisfied the light-curve condition and to have evidence for significant emission in its light curve if $p_{lc} < 5 \times 10^{-7}$, the p-value for $z = 5\sigma$. This is consistent with the threshold for testing for persistent γ-ray emission. It is important to note that the light-curve condition does not provide information on the nature of any transient emission or variability, but only that significant γ-ray emission is present in the light-curve itself.

5.1.4 The Look-Elsewhere Effect

In Chapter 4, the look-elsewhere effect was discussed in depth with regards to spurious claims of γ-ray emission from V404 Cygni. In searching for emission from hundreds of XRBs in one survey, this invites the likelihood of seemingly significant γ-ray detection arising through chance. Furthermore, searching for transient excesses from the position of each of these XRB increases this likelihood further.

Given that the surveyed XRBs are distributed across the sky, some on-the-plane and some off the plane, the probability of a false positive varies from XRB to XRB, as the likelihood of source confusion or background fluctuations depends on the region of the sky the XRB is located within. It is therefore impractical to perform a 'catch all' calculation to quantify the look-elsewhere effect across the entire survey, as the required knowledge of the ROI around each XRB makes such a calculation extremely complex with a very large number of parameters involved.

To mitigate the impact of the look-elsewhere effect, a conservative approach to modelling and observation is taken. A detection of γ-ray emission is not claimed unless a 5σ persistent excess can be localised to the position of the XRB, some evidence for multi-wavelength variability is observed between an excess and the XRB, periodicity in an excess is seen matching the XRB, or ideally several of these. If any of these are true, then it is very unlikely that the observed excess is a false positive. Observations of sources near to XRB coincident excesses are also performed to identify cases of false positives.

These steps reduce the impact of the look-elsewhere effect, and increase confidence in the survey methodology so that genuine detections of γ-ray emission an be distinguished from false positives.

5.2 Survey Results

Here I present the results for the survey analysis, indicating whether γ-ray emission (either persistent or transient) has been found at the position of each XRB. Where spatial coincidence between a γ-ray excess and an XRB is identified, further analysis of the excess, and surrounding ROI, is required in order to verify that the excess is indeed produced by the XRB, and is not an artefact of the γ-ray background nor caused by source confusion. Such further analysis generally falls into two categories: temporal and spatial analysis.

In temporal analysis I analyse the light-curve of the excess and attempt to correlate features with those of other nearby γ-ray sources in order to identify source confusion, or I produce a multi-wavelength light-curve using data from the American Association of Variable Star Astronomers (AAVSO; optical V-band data), the Monitor of All-Sky X-ray Image (MAXI; 2-20 keV X-ray data) and the *Swift* Burst Alert Telescope (*Swift*-BAT, 15-50 keV X-ray data), the latter of which is used in a similar fashion to the analysis in Chapter 4. Given that previously detected γ-ray binaries have displayed orbitally modulated γ-ray emission with a peak at periastron and a minimum at apastron, I am also able to perform a phased analysis of select binary systems with coincident γ-ray emission, as the detection of phased emission would be powerful evidence to associate an excess with a binary. For phased analysis to be performed however, a precise orbital period must be known, with a precise ephemeris for peri/apastron in order to match any γ-ray peaks with features in the orbit. Additionally, the orbit itself must be reasonably long (10's to 100's of days), otherwise the systematic error in measuring the orbital period will be propagated through the analysis when the phase folding is performed, rendering the analysis too noisy to be useful. These conditions therefore generally restrict the systems upon which such analysis can be performed to select HMXBs, as LMXBs generally have far too short a period for such an analysis.

Spatial analysis is a simpler process than temporal analysis but still an extremely

powerful way of determining whether a γ-ray excess can be associated with an XRB. I use `gta.localize` to generate a TS map of the ROI around a source, and then performing a full likelihood fit, with all parameters free, of the region immediately around, and centered on, the source providing a refined positional fit. This method also provides uncertainty contours for position, and I once again consider 95% to be the threshold for spatial coincidence. In order for source localisation to work, there must be sufficient photon statistics to identify a significant peak during the likelihood scans. Therefore I usually only consider significant excesses where $z \geq 5$ for spatial analysis.

I consider any ROI from the modelling which has a source coincident with the position of the binary and TS ≥ 25 to show significant evidence for γ-ray emission from the binary's position. These excesses are significant enough (and have enough photon statistics) for further spatial and spectral analysis. For ROIs where a γ-ray excess coincident with the position of the binary lies in the $9 \leq$ TS < 25 range it is often impossible to carry out meaningful spectral analysis or localisation. Additionally, these sources lie below the threshold for a conventional detection, and therefore ascertaining the presence of γ-ray emission from such systems is challenging. Nonetheless, temporal qualities such as flares or phased emission can still be used to associate a sub-threshold γ-ray excess with an X-ray binary. For ROIs from which no significant γ-ray flux (TS < 9) is detected, I report a 95% confidence upper limit on flux in the Appendices.

I present the high mass X-ray binaries as discussed in Liu et al. (2006) in Section 5.2.1 and the low mass X-ray binaries as discussed in Liu et al. (2007) in Section 5.2.2. Further discussion and analysis of each case where an excess is coincident with an XRB is provided in Chapter 6 for the HMXBs, 7 for the LMXBs outside the Galactic centre and 8 for the LMXBs within the Galactic centre. These chapters contain the details of the temporal and spatial analysis of each excess as described above.

5.2.1 High Mass X-ray Binary Results

In total, I find 20 HMXBs with evidence for a spatially coincident persistent γ-ray excess, or where the light-curve condition is fulfilled, or both. 14 HMXBs have both a persistent excess and the light-curve condition fulfilled, 2 HMXBs have no persistent spatially coincident excess, but the light-curve condition is fulfilled anyway, and 4 HMXBs have a persistent excess but the light-curve condition is not fulfilled. Of these HMXBs with a persistent γ-ray excess, 5 of these excesses are significant with $z \geq 5$, and 11 are weaker, with significances in the $3\sigma \leq z < 5\sigma$ range. The remaining 2 excesses are very weak ($z < 3\sigma$), and are only included as the light-curve condition is fulfilled at the position of the source. Table 5.2 gives the names of all HMXBs with a coincident excess, along with their significance statistics, the energy flux of their respective excesses, and other relevant information. Upper limits on energy flux are calculated for each HMXB without a spatially coincident excess, and these upper limits are given in Appendix B.

Several X-ray binaries with known γ-ray emission are also included in the Liu et al. (2006) HMXB catalogue. These are the microquasars Cyg X-1, Cyg X-3 and SS433, and the γ-ray binaries LS 5039 and LS I +61 303. With the exception of SS433, I detect all of these sources with a z-score within a factor of 3 of their 4FGL-DR2 values. These values are shown in Table 5.3. That I do not detect SS433 in my analysis in contrast to previous studies is unsurprising as Li et al. (2020), the most recent study of the system, used a phased analysis in order to resolve the extended emission of SS 433 from the highly luminous, nearby pulsar PSR J1907+0602, which I do not use here. Previous studies, including Rasul et al. (2019) use different background models, and a different catalogue without the inclusion of maximum likelihood weighting, which makes a direct comparison difficult. Finally, the position of the γ-ray emission from SS 433 appears to correspond to the jet termination lobe, itself offset from the central position of the binary which I analyse (Rasul et al., 2019). I discuss these XRBs further in Chapter 9.

Binary name	TS	z-Score	Energy Flux ($\mathrm{MeV\,cm^{-2}\,s^{-}1}$)	LC Condition	Section	Radio
SAX J1324.4-6200	12.8	3.6σ	2.98×10^{-6}	Yes	6.1	No
1H 0749-600	14.4	3.8σ	7.23×10^{-7}	No	6.2	No
1H 1238-599	10.6	3.3σ	1.70×10^{-6}	Yes	6.3	No
GRO J1008-57	24.3	4.9σ	3.24×10^{-6}	Yes	6.4	Yes
IGR J16320-4751	31.1	5.6σ	8.31×10^{-6}	Yes	C.1	No
IGR J16358-4726	9.5	3.1σ	4.86×10^{-6}	Yes	C.2	No
IGR J16465-4507	50.8	7.1σ	9.71×10^{-6}	Yes	C.3	No
1WGA J0648.0-4419	18.5	4.3σ	8.64×10^{-7}	No	C.4	No
AX J1740.1-2847	7.2	2.7σ	N.A.	Yes	C.5	No
IGR J17544-2619	19.7	4.4σ	4.33×10^{-6}	No	6.5	No
H 1833-076	29.2	5.4σ	6.74×10^{-6}	Yes	C.6	No
GS 1839-04	17.8	4.2σ	4.76×10^{-6}	Yes	C.7	No
IGR J19140+0951	N.A.	N.A	N.A.	Yes	6.6	No
1A 0535+262	12.4	3.5σ	1.45×10^{-6}	Yes	6.7	Yes
GRO J2058+42	16.4	4.0σ	2.44×10^{-6}	No	6.8	No
W63 X-1	13.1	3.6σ	1.51×10^{-6}	Yes	6.9	No
SAX J2103.5+4545	N.A.	N.A.	N.A.	Yes	C.8	No
RX J2030.5+4751	30.8	5.5σ	2.10×10^{-6}	Yes	6.10	No
4U 2206+543	30.5	5.5σ	1.71×10^{-6}	Yes	6.11	No
IGR J00370+6122	7.3	2.7σ	N.A.	Yes	6.12	No

Table 5.2: All high mass X-ray binaries with a spatially coincident γ-ray source/excess (of TS $\geq$ 9), along with the calculated TS and the energy flux value (units of $\mathrm{MeV\,cm^{-2}\,s^{-}1}$) integrated across the analysis energy range (100 MeV - 500 GeV), and whether each source has detectable transient γ-ray emission in its light-curve. Some sources have evidence for only intermittent γ-ray emission, and cannot be fitted with the model over the full observation period. I do not calculate the TS and energy flux for these objects and they are not included in this table.

Binary name	TS	z-Score	4FGL z-Score	Energy Flux ($\mathrm{MeV\,cm^{-2}\,s^{-1}}$)
LS 5039	18000	130σ	62σ	2.14×10^{-4}
Cyg X-1	88	9.4σ	8.6σ	3.49×10^{-6}
Cyg X-3	860	29σ	11σ	2.42×10^{-5}
LS I +61 303	170000	410σ	250σ	4.67×10^{-4}

Table 5.3: The four 4FGL sources included in the HMXB catalogue, together with the TS value and corresponding z-score from the analysis over the full 12.5 years of LAT data. For comparison, I include the detection z-score for each source provided in the 4FGL-DR2. It should be noted when comparing the z-score values that the photon selection for the computation of the 4FGL parameters is different (100 MeV - 1 TeV compared with 100 MeV - 500 GeV for my analysis), and the observation time is lower (10 years vs. 12.5). The analysis methodology is also different.

5.2.2 Low Mass X-ray Binary Results

In total, I find 44 LMXBs with evidence for a spatially coincident persistent γ-ray excess, or where the light-curve condition is fulfilled, or both. Thirty-two LMXBs have both a persistent spatially coincident excess, and the light-curve condition is fulfilled. Five LMXBs have a persistent γ-ray excess but the light-curve condition is not fulfilled, and seven have the no persistent excess but the light-curve condition is fulfilled. Of these LMXBs with a persistent γ-ray excess 10 are significant with $z \geq 5\sigma$, and 17 are weaker, with significances in the $3\sigma \leq z < 5\sigma$ range. The remaining 9 excesses are very weak ($z < 3\sigma$), and are only included as the light-curve condition is fulfilled at the position of the XRB. Tables 5.4 and 5.5 give the names of all LMXBs with a coincident excess, along with their significance statistics, the energy flux of their respective excesses, and other relevant information. Upper limits are calculated for each LMXB without a spatially coincident excess, and these upper limits are given in Appendix D.

Whilst the detailed analyses of the HMXBs are split across one Chapter and a respective Appendix, the LMXBs (being a larger population) are split across 2 Chapters, and two Appendices. Chapter 7 gives LMXB analyses for those binaries not within the Galactic centre, and Chapter 8 gives an analysis of the Galactic centre region. Appendix E gives analyses of those LMXBs within globular clusters,

and Appendix F gives analysis of those LMXBs with a confirmed false positive.

Unlike the HMXBs where several 4FGL sources are included in the survey, none are included in the LMXB survey.

Binary Name	TS	z-Score	Flux (MeV cm^{-2} s^{-}1)	LC Condition	Section
SAX J1603.9-7753	4.0	2.0σ	N.A.	Yes	7.1
4U 1323-62	18.9	4.3σ	3.37×10^{-6}	Yes	7.2
3A 1516-569	16.9	4.1σ	2.48×10^{-6}	Yes	7.3
1E 161348-5055.1	56.0	7.5σ	1.13×10^{-5}	Yes	F.1
4U 1642-45	4.3	2.1σ	N.A.	Yes	F.2
4U 1708-40	14.6	3.8σ	2.88×10^{-6}	Yes	7.4
4U 0513-40	51.1	7.1σ	1.18×10^{-6}	Yes	E.1
GRO J1655-40	10.9	3.3σ	1.51×10^{-6}	No	7.5
2A 1822-371	12.6	3.5σ	1.10×10^{-6}	Yes	F.3
2S 1711-339	9.3	3.0σ	1.59×10^{-6}	No	7.6
XTE J1814-338	20.5	4.5σ	1.43×10^{-6}	Yes	7.7
MXB 1730-335	25.0	5.0σ	5.61×10^{-6}	Yes	E
SLX 1746-331	19.3	4.4σ	2.45×10^{-6}	Yes	F.4
XB 1832-330	10.0	3.2σ	9.75×10^{-6}	No	E
1E 1746.7-3224	8.4	2.9σ	N.A.	Yes	7.8
SLX 1744-300	15.7	4.0σ	5.99×10^{-6}	Yes	F.4
1E 1740.7-2942	2.0	1.4σ	N.A.	Yes	8.2.1
1A 1742-294	12.3	3.5σ	2.84×10^{-6}	Yes	8.2.2
GC X-2	2.9	1.7σ	N.A.	Yes	8.2.3

Table 5.4: All low mass X-ray binaries with a spatially coincident γ-ray source/excess (of TS ≥ 9), along with the calculated TS and the energy flux value (units of MeV cm^{-2} s^{-}1) integrated across the analysis energy range (100 MeV - 500 GeV), and whether each source has detectable transient γ-ray emission in its light-curve. Some sources have evidence for only intermittent γ-ray emission, and cannot be fitted with the model over the full observation period. I do not calculate the TS and energy flux for these objects and they are not included in this table.

Binary Name	TS	z-Score	Flux (MeV cm^{-2} s^{-}1)	LC Condition	Section
GC X-4	3.6	1.9σ	N.A.	Yes	8.2.4
SAX J1750.8-2900	6.3	2.5σ	N.A.	Yes	8.3.2
AX J1745.6-2901	52.5	7.2σ	1.90×10^{-5}	Yes	8.1.2
1A 1742-289	N.A.	N.A.	N.A.	Yes	8.1.2
GRS 1741.2-2859	53.6	7.3σ	1.36×10^{-6}	Yes	8.2.5
CXOGC J174540.0-290031	12.0	3.5σ	6.70×10^{-6}	Yes	8.1.2
2E 1742.5-2858	12.0	3.5σ	6.63×10^{-6}	Yes	8.1.2
1E 1742.2-2857	55.1	7.4σ	1.87×10^{-5}	Yes	8.1.2
GRS 1741.9-2853	60.6	7.8σ	1.64×10^{-5}	Yes	8.2.5
1E 1743.1-2852	N.A.	N.A.	N.A.	Yes	8.1.3
1E 1742.9-2852	N.A.	N.A.	N.A.	Yes	8.1.3
4U 1735-28	N.A.	N.A.	N.A.	Yes	8.3.3
XTE J1748-288	11.9	3.4σ	2.79×10^{-6}	Yes	8.2.6
IGR J17497-2821	2.0	1.4σ	N.A.	Yes	8.3.4
GRO J1719-24	9.1	3.0σ	1.36×10^{-6}	No	7.9
EXO 1745-248	N.A.	N.A.	N.A.	Yes	E
GS 1826-238	4.0	2.0σ	N.A	Yes	7.10
XMMU J181227.8-181234	23.3	4.8σ	6.72×10^{-6}	Yes	7.11
4U 1811-17	N.A.	N.A	N.A.	Yes	F.5
4U 1812-12	N.A.	N.A	N.A.	Yes	F.6
GRS 1915+105	18.1	4.3σ	4.04×10^{-6}	Yes	7.12
CXO J212958.1+121002	93.3	9.7σ	2.56×10^{-6}	Yes	E
4U 2129+12	94.2	9.7σ	2.58×10^{-6}	Yes	E
4U 1918+15	38.6	6.2σ	6.67×10^{-6}	Yes	F.7
2A 1655+353	16.3	4.0σ	7.03×10^{-7}	No	7.13

Table 5.5: Continued from Table 5.4

Figure 5.1: The fifth labour of Heracles, the cleaning of the Augean stables. From 'The House of Heracles' mosaic.

Chapter 6

Surveying the X-ray Binaries II: High Mass X-ray Binaries

In this chapter I detail the advanced analysis of each HMXB included in the survey where there is either a spatially coincident γ-ray excess or the light-curve condition is fulfilled, as detailed in Chapter 5. Twelve such HMXBs are discussed in this chapter, with a further 8 systems discussed in Section 6.13 and Appendix C; these eight additional systems are those where a false positive is confirmed, rather than a genuine signature of γ-ray emission from an HMXB.

6.1 SAX J1324.4-6200

SAX J1324-6200 (henceforth SAX13) is an X-ray pulsar, thought to be an accreting high-mass neutron star in orbit with a Be star (Angelini et al. 1998, Mereghetti et al. 2008, Kaur et al. 2009). No orbital period is known for this system. I report a persistent TS of 12.8 over the full 12.5 year dataset; however, there is some evidence for sustained γ-ray emission from the position of SAX13 over an 18 month period throughout 2018 and 2019 (MJD 57972 - 58520), at the 2σ to 3σ level, suggesting this emission is likely transient. The γ-ray light-curve for this source is shown in Figure 6.1. There is no *Swift*-BAT or MAXI light-curve for SAX13, nor are there

any optical photometric measurements in the AAVSO database for the time period in question.

There are several catalogued sources near SAX13. The closest of these are 4FGL J1328.4-6231 (TS = 69.7 at an angular offset from SAX13 of 0.690°), 4FGL J1321.1-6239 (TS = 116, offset: 0.749°), 4FGL J1320.5-6256c (TS = 22.4, offset: 1.033°) and 4FGL J1329.9-6108 (TS = 545, offset: 1.093°). Additionally, I add a new source to the model with the `gta.find_sources` algorithm, PS J1317.8-6157 (TS = 20.0, offset: 0.779°). None of these have a 4FGL variability index high enough to indicate variability on monthly timescales. I generate light-curves for each of these sources (with the exception of the faint 4FGL J1320.5-6256c and PS J1317.8-6157 because these sources are sufficiently faint and have a large enough angular distance from SAX13 that I can be confident that they are not causing source confusion at the position of SAX13) using identical binning to the SAX13 light-curve, and do not see any significant enhancement in these light-curves at the time of the 18 month apparent SAX13 γ-ray excess, meaning that it is likely that this excess is independent of these sources.

Considering only the photons detected within the 18 month excess I carry out an independent analysis of the same ROI over this 18 month period (using the same parameters, other than observation time, as in Table 5.1). I generate a TS map (Figure 6.2) of the centre of the ROI, and find that the peak of this excess is approximately spatially coincident with the position of SAX13. Fitting a power-law point source to the position of SAX13, I free this source and those within 1° of the central position of SAX13 and execute a likelihood fit. I then run the `gta.localize` algorithm on the added SAX13 source, and find that the optimal position of the added source is LII = 306.8362° ± 0.0699°, BII = 0.5534° ± 0.0826°, offset from SAX13 by 0.0707°. Considering that this offset is less than the 95% and 68% containment radii of the added source (0.1859° and 0.1152° respectively) this excess can be regarded as spatially coincident with the location of SAX13. With the point source at its optimal position, I calculate a TS of 28.7 over this 18 month

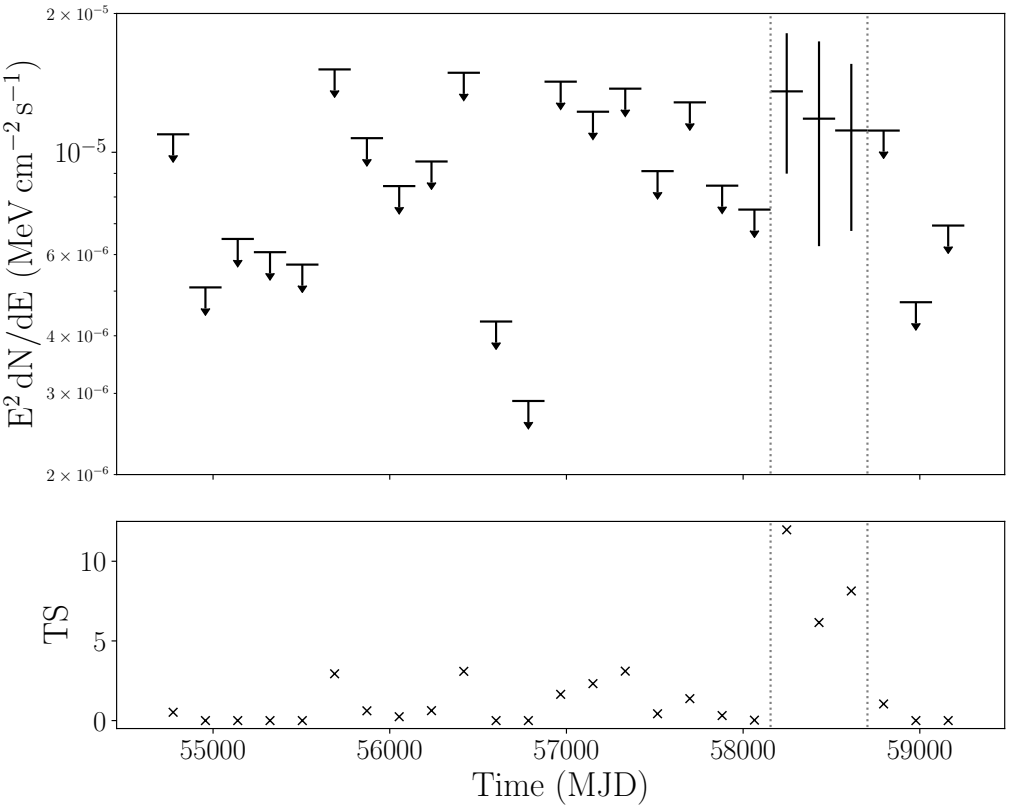

Figure 6.1: The *Fermi*-LAT 6-monthly binned light-curve of SAX J1324.4-6200, showing the energy flux in the top panel, and the corresponding TS of each bin in the bottom panel. For bins with TS < 4 I calculate a 95% confidence upper limit on flux. The vertical dotted lines indicate the beginning and the end of the γ-ray excess.

period. Over the same period, there is no significant detection of 4FGL J1256.1-5919 or 4FGL J1320.5-6256c. 4FGL J1321.1-6239 is detected with a TS of 24.9 and 4FGL J1329.9-6108 with a TS of 49.4, making the SAX13 source comparable to these objects in terms of statistical significance during this time.

Given that the TS of the SAX13 source exceeds 25, there are sufficient photon statistics to carry out a spectral fit, shown in Figure 6.3. I find the best fit spectrum is a power-law with normalisation $N_0 = 1.95 \times 10^{-12} \pm 5 \times 10^{-14}$, spectral index $\Gamma = -2.43 \pm 0.10$ and scale energy $E_0 = 1000\,\mathrm{MeV}$.

The power law spectral fit and calculated spectral index are consistent with those known HMXB systems in the 4FGL with lower detection significances (the more

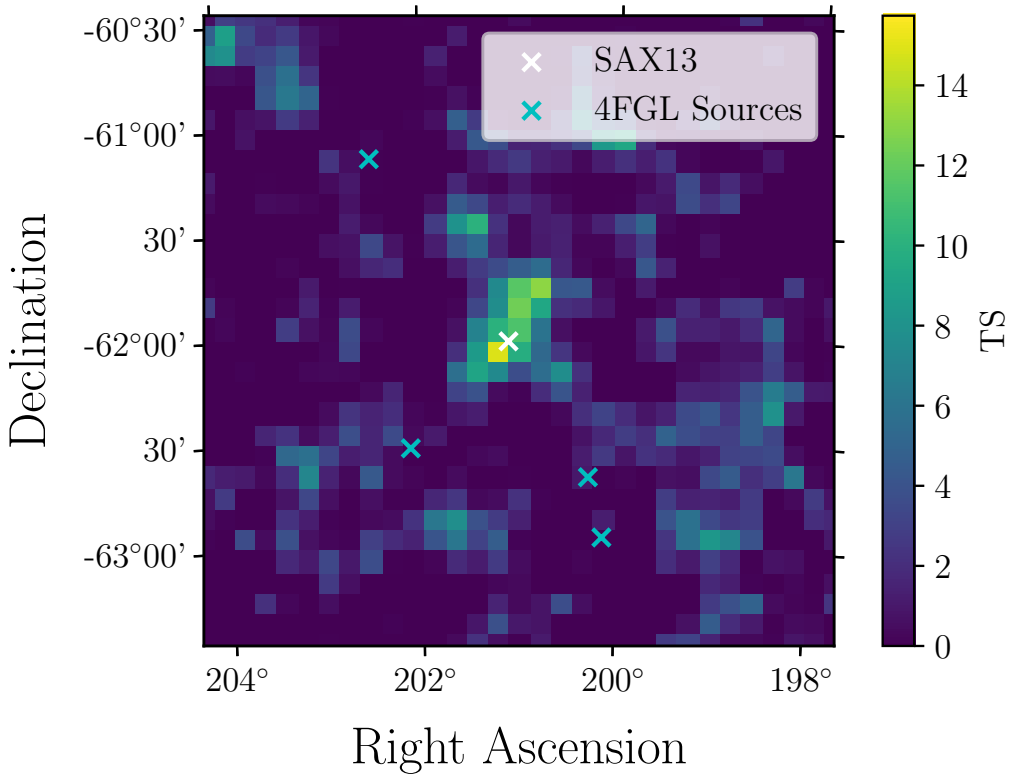

Figure 6.2: The TS map of the central 3° of the SAX J1324.4-6200 ROI during the 18 month period during which the γ-ray excess is observed. Here, the positions of the closest 4FGL sources are indicated by blue crosses, whilst the position of SAX J1324.4-6200 is indicated by a white cross. This TS map is generated after the ROI optimization and fit, but before a point source for SAX J1324.4-6200 is fitted to the model to highlight the spatial coincidence between the excess and the position of SAX J1324.4-6200. Bin widths are 0.1°.

significantly-detected systems are best fit by a log parabola spectral model). These are Cyg X-1 with $\Gamma = -2.13$ and $z = 8.55\sigma$, HESS J0632+057 with $\Gamma = -2.17$ and $z = 4.62\sigma$ and PSR B1259-63 with $\Gamma = -2.75$ and $z = 5.64\sigma$, compared to SAX13 with $\Gamma = -2.43$ and $z = 5.36\sigma$. Considering that the accretor in this system is known to be a pulsar, and SAX13 is not a known microquasar, if this γ-ray emission does indeed come from SAX13 then it is likely to be from a pulsar wind interaction. However, without any corroborating multi-wavelength data, it is difficult to be certain that this is indeed from SAX13 and not another undetected source nearby. Additionally, if this γ-ray emission is indeed from a pulsar wind interaction, the fact that there is only one emission episode during the lifetime of

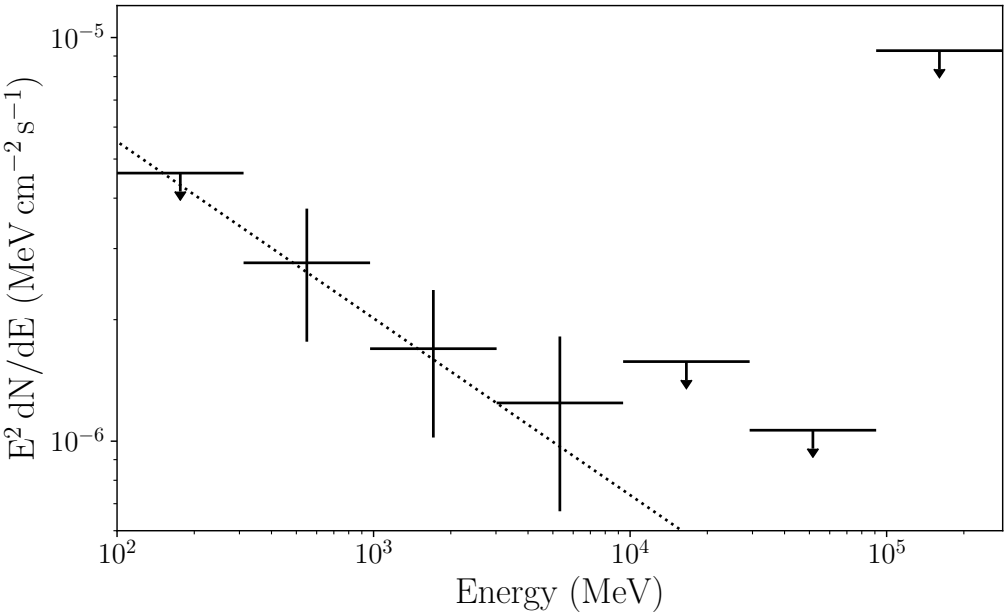

Figure 6.3: The Spectral Energy Distribution of the SAX J1324.4-6200 coincident source during the 18 month excess, with the power law fit indicated by the black dotted line. I place upper limits on any bin with TS < 4. Whilst the baseline analysis uses 8 energy bins per decade, here I use 2 energy bins per decade to ensure sufficient photons for an accurate flux measurement in each bin.

Fermi-LAT suggests that the period of the system may be so long that it would be difficult to obtain the frequency of these interactions.

6.2 1H 0749-600

1H 0749-600 (henceforth 1H07) is a HMXB with an unknown accretor and a Be companion star (Apparao, 1994). Over the 12.5 year observation period I find a spatially-coincident excess with a TS of 14.4, which is assigned the name PS J0750.5-6116, with a slight angular offset from the position of 1H07 of 0.170°. The nearest 4FGL sources are 4FGL J0807.0-6102, which is the blazar PMN J0806-6101 (TS = 69.7 at an angular offset from 1H07 of 2.028°) and 4FGL J0756.3-6431, which is the BL Lac blazar SUMSS J075625-643031 (TS = 52.53, offset 3.489°). As neither of these blazars is particularly luminous, it is unlikely that source confusion is the cause of the persistent γ-ray excess PS J0750.5-6116.

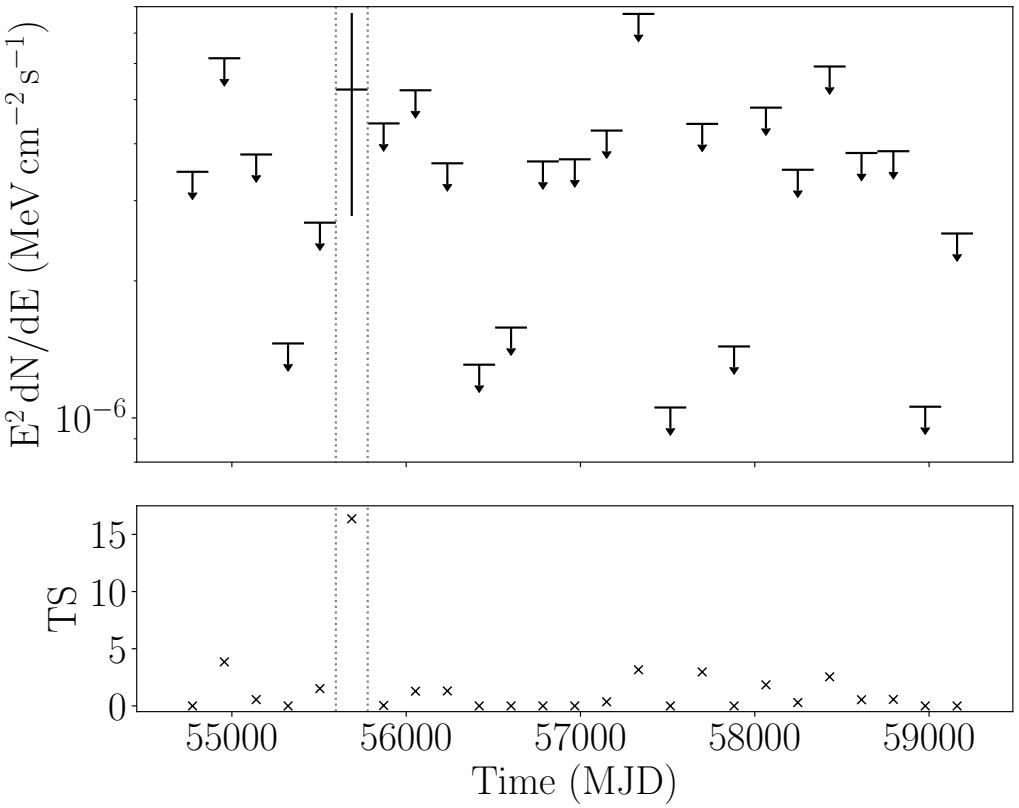

Figure 6.4: The *Fermi*-LAT light-curve of the γ-ray excess coincident with 1H 0749-600 shown in 6-month time bins. Upper limits are placed on any time bin where the TS of that bin is less than 4. The vertical dotted lines indicate the beginning and end of the apparent γ-ray excess.

The light-curve of PS J0750.5-6116, is shown in Figure 6.4; a γ-ray excess is observed in one bin with TS = 16.4 (4.05σ) (MJD 55597 - 55779), and upper limits in the other 24 bins. Light-curves of the two nearest 4FGL sources, both blazars, show no enhancement in the same bin as the PS J0750.5-6116 excess, suggesting the 4σ time bin is independent of the γ-ray emission of the blazars. It is likely that this single 6-month period is responsible for the majority of the γ-ray emission observed from the position of PS J0750.5-6116. A re-analysis of this 6-month period results in a slightly increased TS of 17.2, having used the `gta.localize` algorithm to obtain a best fit position of LII = 273.8571° ± 0.0816°, BII = −16.8787° ± 0.0688°. This gives an angular offset of 0.1581° from the (IR) position of 1H07, compared to the 95% positional uncertainty of PS J0750.5-6116 of 0.1814°.

This low-significance excess cannot be firmly associated with 1H07. Furthermore, as the nature of the accretor in this system is unknown, and no microquasar-like behaviour or pulsations have been observed, the physical mechanisms behind any γ-ray emission from this system are unclear. No orbital period is known for this system, so examining the γ-ray emission by orbital phase is not possible. I conclude that whilst PS J0750.5-6116 likely represents faint γ-ray emission from 1H07, a lack of information makes a firm detection claim impossible.

6.3 1H 1238-599

1H 1238-599 (henceforth 1H12) is an X-ray pulsar HMXB system (Huckle et al., 1977). Over the full 12.5 year dataset, the TS is 10.6, with the light-curve (Figure 6.5) showing borderline significance (approximately 2σ) γ-ray excesses across 6 of the 25 bins (MJD 54865 - 55231, MJD 55962 - 56145, MJD 57241 - 57425, and MJD 57607 - 57973). The nearest catalogued sources are 4FGL J1256.1-5919 (TS = 174 and an angular offset from 1H12 of 1.983°), which is the blazar PMN J1256-5919, 4FGL J1244.3-6233 (TS = 428, offset: 2.370°) and 4FGL J1253.3-5816 (TS = 48.1, offset: 2.404°), which is the pulsar PSR J1253-5820. None of these sources has a catalogue variability index which would indicate variability on monthly timescales. As these sources are at some distance from the position of 1H12, it is unlikely that any γ-ray signal from the position of 1H12 is due to source confusion with a 4FGL source. Similarly, no uncatalogued sources of γ-rays are detected close to 1H12 by `gta.find_sources`, the closest being approximately 3° away.

Given that the bins in which I measure an apparent flux are all at the 2σ level, it is difficult to perform any detailed tests of emission (for example, localisation) at the position of 1H12. As multi-wavelength data for this HMXB are not available, cross correlation of the γ-ray light-curve with other wavelengths is not possible. Finally, an orbital period for this binary has not been measured, so correlation of the light-curve with the system period is also impossible. As a result, while there

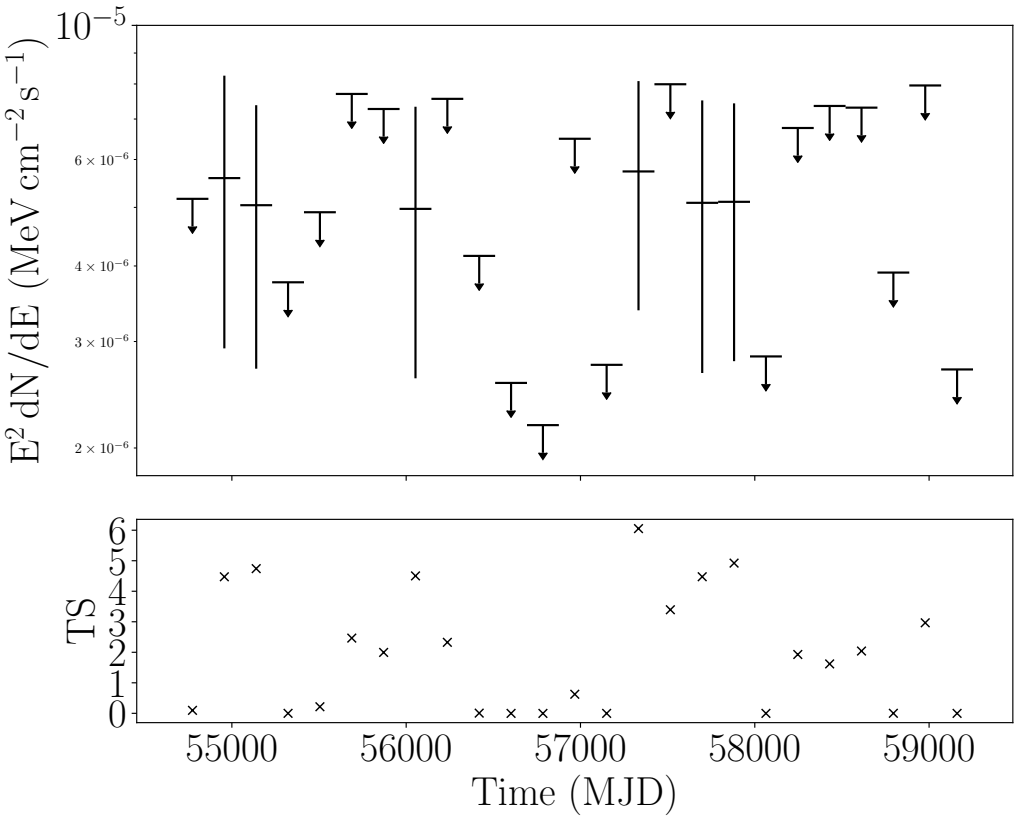

Figure 6.5: The *Fermi*-LAT light-curve of the γ-ray excess coincident with 1H 1238-599 with time bins of 6 month width. Upper limits are placed on any time bin where the TS of that bin is less than 4.

could be a very faint signal that could be from 1H12, this excess could equally be caused by fluctuations in the Galactic diffuse background.

6.4 GRO J1008-57

GRO J1008-57 (henceforth GRO10) is an X-ray pulsar/Be star HMXB system, with an orbital period of 135.0 days (Petre and Gehrels, 1993). Over the 12.5 year observation time, I find a source, PS J1014.5-5834, that is spatially coincident with GRO10 with `gta.find_sources`. The angular offset between GRO10 and PS J1014.5-5834 is less than the 95% positional uncertainty of the source. However, PS J1014.5-5834 has an unusually large positional uncertainty of approximately 0.7°. Running the `gta.localize` algorithm, I find that, while the position

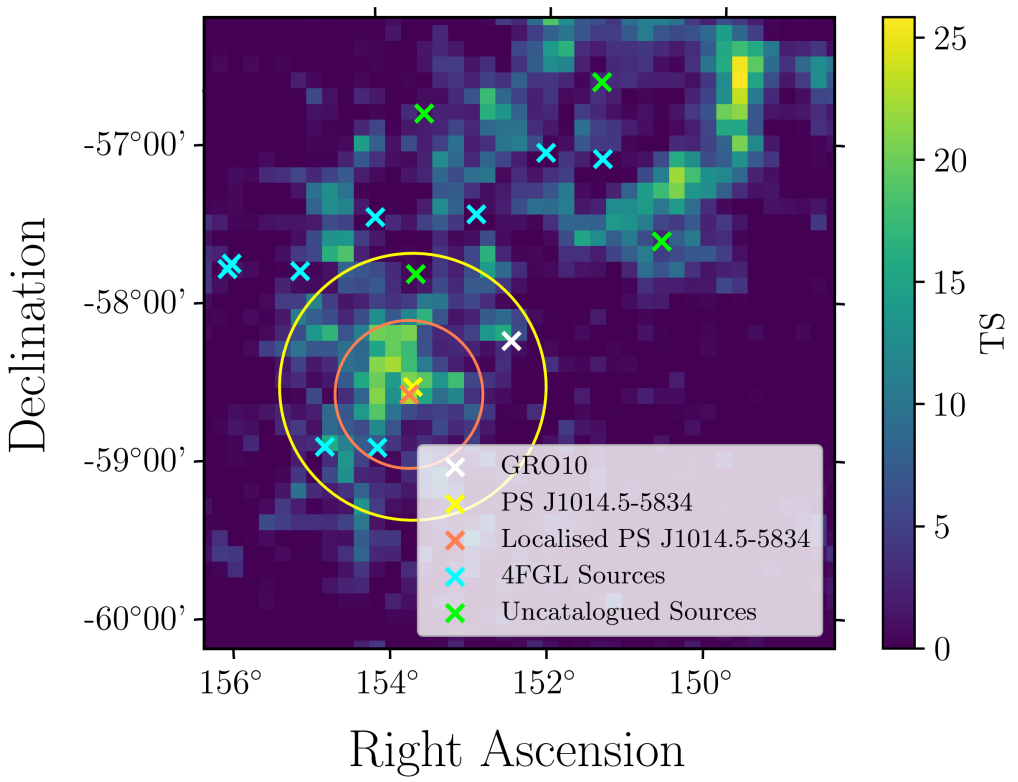

Figure 6.6: The TS map of the central 4° of the GRO J1008-57 ROI, after the likelihood fit and the `gta.find_sources` algorithm, but with the coincident source, PS J1014.5-5834, removed from the model to reveal the TS of the coincident γ-ray emission. Here, the yellow and orange crosses refer to the positions of PS J1014.5-5834 both before and after the `gta.localize` algorithm, which the corresponding circles referring to the 95% positional uncertainty of the source before and after localisation. The white cross indicates the catalogued location of GRO J1008-57, the blue crosses indicate the positions of other 4FGL sources, and the green crosses indicate the positions of the other uncatalogued sources added to the model by `gta.find_sources`.

of the source does not change significantly, the positional uncertainty decreases to the extent that this source is no longer coincident with the position of GRO10. Figure 6.6 shows the position of GRO10 together with the positional uncertainty of PS J1014.5-5834 both before and after localisation, and shows a somewhat extended γ-ray structure around PS J1014.5-5834.This is likely the cause of the large positional uncertainty, as `gta.find_sources` does not account for spatially-extended γ-ray structures.

GRO10 is a well-studied system, particularly in the X-ray waveband, with semi-

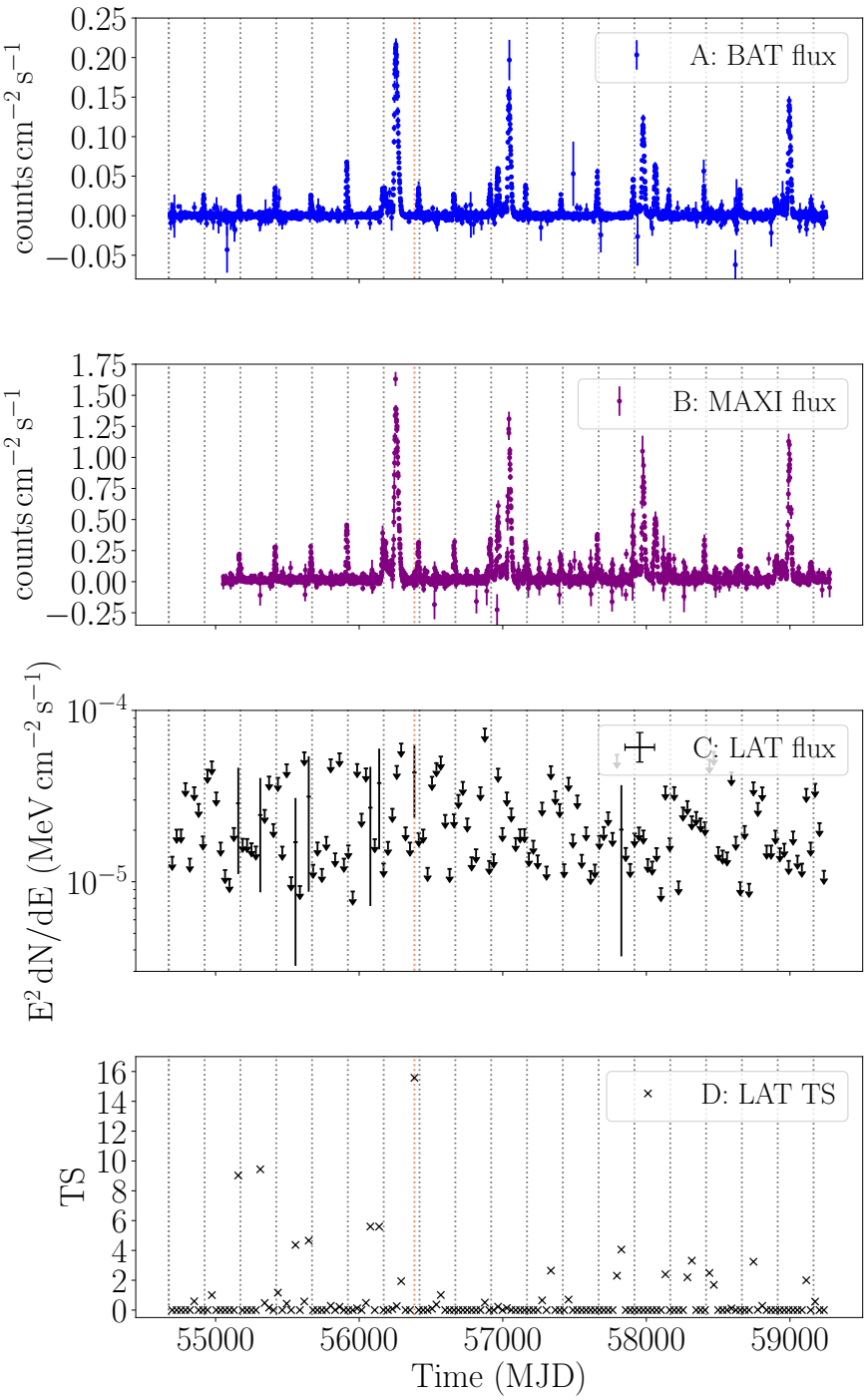

Figure 6.7: The daily binned light-curve of GRO J1008-57 from *Swift*-BAT (Panel A) and MAXI (Panel B). The calculated monthly binned *Fermi*-LAT light-curve for a source fitted to the position of GRO J1008-57 is shown below in Panel C, and the corresponding TS values of these bins shown in Panel D. I place 95% confidence limits on any *Fermi*-LAT energy flux bins with TS < 4. The vertical orange line reflects the centre of the bin with peak γ-ray emission, and the vertical grey lines mark each periastron passage of GRO J1008-57 over the observation time.

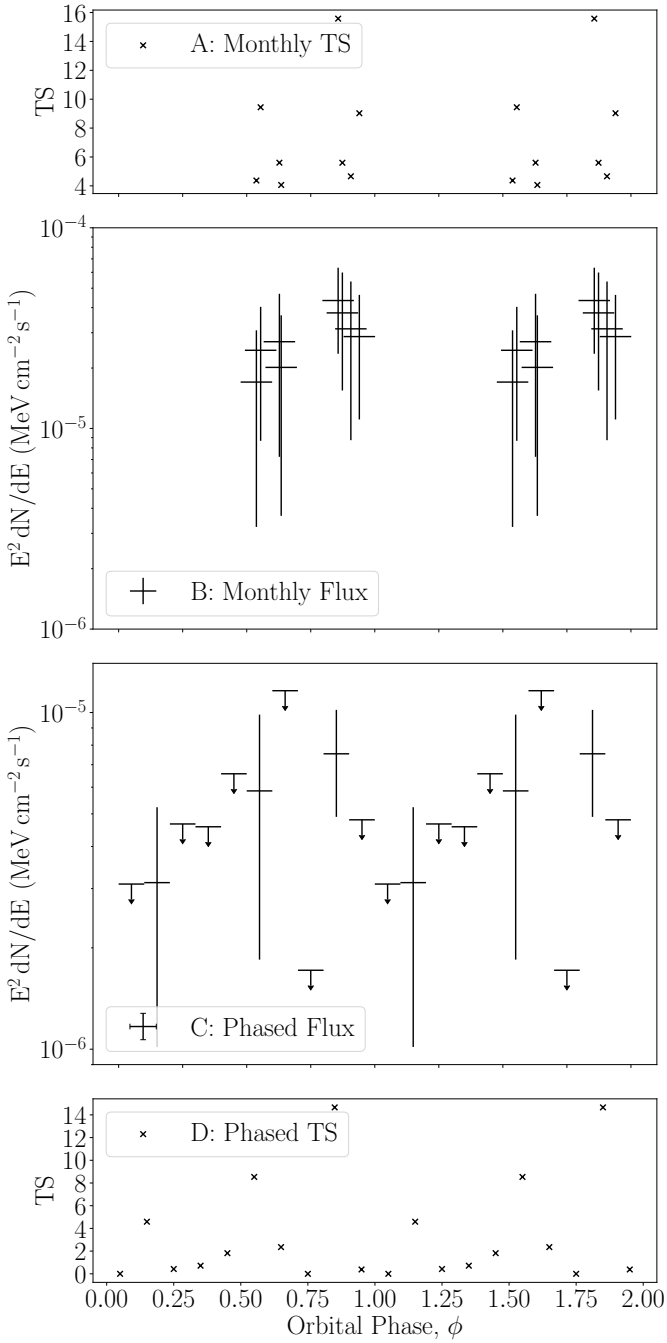

Figure 6.8: This figure displays the variability of GRO J1008-57 based on orbital phase, showing two full orbits. Panels A and B respectively show the TS and γ-ray flux of each monthly bin from Figure 6.7, plotted by orbital phase. I do not include bins from the monthly light-curve where upper limits on flux were calculated. Panels C and D respectively show the γ-ray flux and TS of the phase folded light-curve of GRO J1008-57, with the orbit divided into 10 equal intervals. Here I fix upper limits on flux for any phase period where the TS < 4. On the left vertical axis of the flux plots (B and C) I plot energy flux ($E^2 \frac{dN}{dE}$). On the horizontal phase axis, phase is defined so that 0, 1, 2 refer to periastron.

predictable X-ray flares occurring at periastron (Kühnel et al., 2013), the most recent of which was observed in 2020 (Nakajima et al. 2020a and Nakajima et al. 2020b). Xing and Wang (2019) (henceforth *Xing 19*) studied the possibility of γ-ray emission using approximately 9 years of *Fermi*-LAT observations but employing the 4 year LAT catalogue and correspondingly older background models. *Xing 19* observed a γ-ray excess at the position of GRO10 to a TS of 7 ($z = 2.65\sigma$) by adding a point source to the model, and carrying out a likelihood fit. They then carried out a stacked temporal analysis binned by orbital phase, dividing each orbit into 10 equal time bins and summing the bins from each orbit. Through this method, *Xing 19* identified 3 excesses, two around the middle of GRO10's orbit with TS $\approx$ 5 ($z \approx 2\sigma$), and one in the penultimate orbital phase bin preceding periastron with TS $\approx$ 20 ($z \approx 4.8\sigma$) Additionally, *Xing 19* identified 3 excesses by deriving a light-curve for their entire observation time and found TS $\approx$ 9 excesses in the bins centered on MJD 55135 and MJD 55559 and a $TS \approx 17.5$ excess in the bin centered on MJD 56383. Given the significance of these excesses, and the lack of other emission, it is likely these dominate their stacked orbital analysis and are primarily responsible for the TS values seen in the phased light-curve.

As I reject the hypothesis that PS J1014.5-5834 represents γ-ray emission from GRO10, I manually add a point source to the model and fit to it (after I have localised PS J1014.5-5834). I find a total TS of 7.9 over the 12.5 year observation time of this source, consistent with the TS of 7 found by *Xing 19* given the increased observation time used in this work. I take a slightly different approach to *Xing 19* by using monthly time bins (rather than dividing each orbit into 10 phases), so that there are approximately 8 time bins per orbit, and 149 bins in total, one per month. Figure 6.7 shows the *Fermi*-LAT light-curve together with the *Swift*-BAT and MAXI light-curves of this source, where four significant outbursts are seen mid-orbit, along with periodic brightening events which correspond to the periastron of GRO10's orbit. With respect to the 3 excesses observed by *Xing 19*, I identify the MJD 55135 (TS = 9.7) excess to TS = 9.0, the MJD 55559 (TS =

9.1) excess to TS = 4.4, and the MJD 56383 (TS = 17.5) excess to TS = 15.6, although my bins are approximately 20% longer than those of *Xing 19*, and are not perfectly contemporaneous. In total, I observe one bin with approximately 4σ γ-ray emission, two with approximately 3σ emission and five with approximately 2σ emission, although it must be stressed that the 2σ bins are very marginal, with an approximately 5% chance that these individually arise by coincidence (given the 25 bins present in the light-curve, one would expect 1.25 2σ bins to appear by chance).

Using the `Fermitools` algorithm `gtophase`, a phase is assigned to each photon in my analysis. Whilst `gtophase` is typically used for assigning phases to pulsars, Rasul et al. (2019) demonstrate its suitability for dealing with the orbital phases of binary systems, and presumably this is the method that *Xing 19* employed, although this is not clear in the paper. The orbital ephemeris and period from Bissinger et al. (2013) is used and it is assumed that the first and second derivatives of period are zero. Given that the period of the orbit is 135.0 days, the period is not expected to change significantly over the *Fermi*-LAT mission time. Having assigned phases to each photon, a likelihood analysis in 10 evenly-spaced phase bins is used to produce a phase-folded light-curve.

Figure 6.8 shows the phase-folded light-curve of GRO10, alongside the flux points from the monthly-binned light-curve (Figure 6.7) with a phase calculated for each bin. I see that of the 10 bins across the orbit, a γ-ray flux is apparent in 3 of these, the 2nd (TS = 4.6), 6th (TS = 8.5), and 9th bins (TS = 14.7). The latter two bins are consistent with the results of *Xing 19*. However, where they measured a γ-ray flux in the 7th bin, I find only an upper limit. The monthly bins appear to cluster into two groups, with the first being coincident in phase with the 6th phase-folded bin (2.9σ), and the second being coincident with the 9th bin (3.8σ). There are no monthly flux points coincident with the third phase-folded flux measurement, but given the result in this bin is marginal in significance, this is unsurprising.

Considering the flux measurements in each bin are all below 5σ, it is not possible

to claim detection of any γ-rays from this system. While *Xing 19* establish that the most significant flux point (in the ninth phase bin) precedes periastron by a bin, the lack of detectable emission in either the first or 10th bin (immediately following and preceding periastron) casts some doubt on these being due to emission from GRO10. That said, the fact that every detectable monthly bin in the light-curve clusters around one of the two points indicates that there is likely some pattern to the apparent γ-ray excesses in this system, as it is unlikely* that these flux points would cluster by chance in phase space, were they random background fluctuations.

6.5 IGR J17544-2619

IGR J17544-2619 (henceforth IGR17) is a HMXB system and the prototypical super-fast X-ray transient consisting of a likely pulsar in an unusually short 4.926 ± 0.001 day orbit with a massive (likely O-type) donor star (Bozzo et al., 2016). Over the 12.5 year *Fermi*-LAT observation period, I detect a γ-ray excess coincident with the position of IGR17 with TS = 19.7 (4.4σ), at a slight angular offset from the position of IGR17 of 0.151°. Using the `gta.localize` algorithm, the best fit position for this excess is LII = $3.3742° \pm 0.0402°$, BII = $-0.2747° \pm 0.0441°$. At this best fit position, the new angular offset from the position of IGR17 is 0.0372° and the TS of the excess increases slightly to 23.7.

The nearest 4FGL sources in the sky are a source of unknown type, 4FGL J1754.4-2649 (angular offset from IGR17 of 0.499°, TS = 93.8), 4FGL J1755.4-2552 (SNR G003.7-00.2, offset: 0.506°, TS = 157), and the luminous unassociated γ-ray source 4FGL J1753.8-2538 (TS = 1500, offset: 0.703°). There is no detectable variability in the 6-monthly binned light-curve (Figure 6.9) of the excess, with 3 bins having a TS in the $2\sigma \leq z < 3\sigma$ range. These 3 bins do not correlate with any significant enhancements in the 6 monthly binned light-curves of the 3 closest γ-ray neighbours

*I find a 4.13×10^{-9} chance of these two clusters occurring by chance.

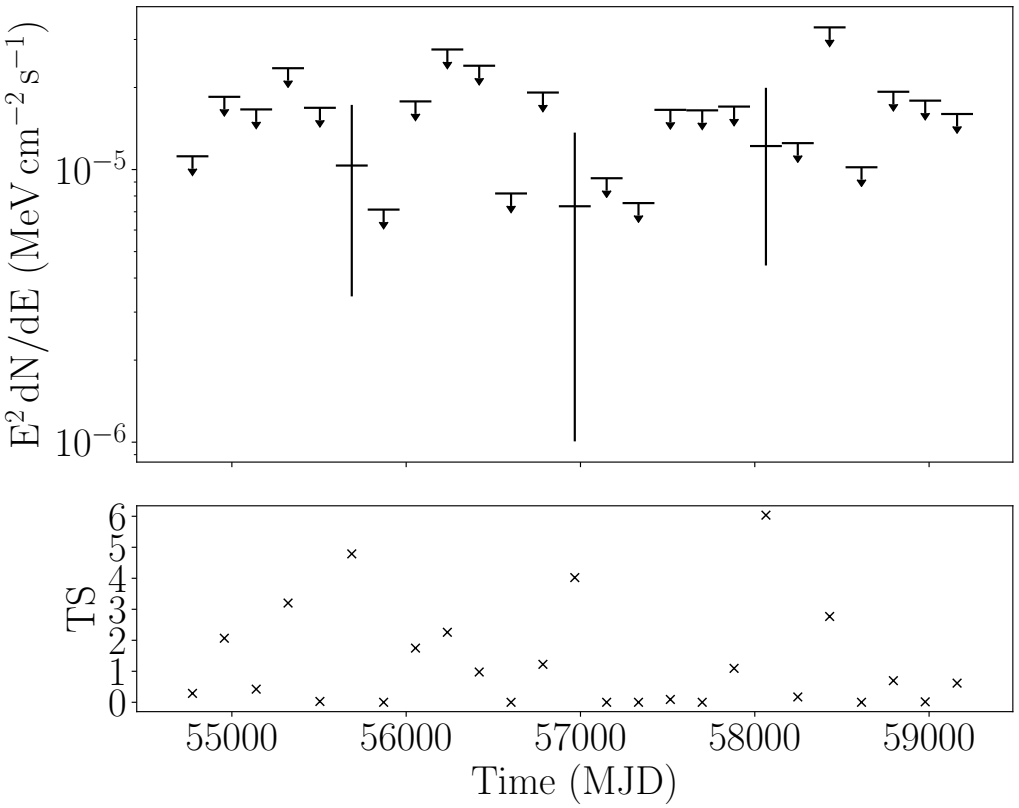

Figure 6.9: The *Fermi*-LAT light-curve of the γ-ray excess coincident with IGR 17544-2619 with 6-month time bins. Upper limits are placed on any time bin in which the TS is less than 4.

in the sky. This suggests that the γ-ray emission is unlikely to be due to confusion with a flare from a nearby object.

A model cannot be fitted reliably to the SED of the IGR17 coincident excess due to limited photon statistics, so the spectrum of the excess cannot be compared with those of nearby sources. This excess cannot be conclusively ascribed to source confusion with the brightest nearby catalogued 4FGL source, 4FGL J1753.8-2538, although as 4FGL J1753.8-2538 is very luminous (TS = 1500), one cannot rule this out either.

6.6 IGR J19140+0951

IGR J19140+0951 (henceforth referred to as IGR19) is a HMXB with a likely neutron star accretor (Hannikainen et al., 2004) and a supergiant B star donor (Hannikainen et al. 2007 and in't Zand et al. 2006). Unlike most cases discussed, no persistent γ-ray excess is identified coincident with the position of IGR19. However, there are 3 bins with a TS $>$ 4 in the 6 monthly binned light-curve; none of these 3 bins corresponds to any significant enhancement in the X-ray waveband indicated by the *Swift*-BAT daily light-curve (Figure 6.10).

Three catalogued sources lie within a 0.5° angular separation from the position of IGR19. These are 4FGL J1912.7+0957 (TS = 188 and an angular offset of 0.335°), 4FGL J1914.7+1012c (TS = 110, offset: 0.369°) and 4FGL J1913.3+1019 (TS = 137, offset: 0.476°), confirmed to be the pulsar PSR J1913+1011. The three apparent excesses in the light-curve do not correlate with any enhancements in the light-curve of any of the three closest sources, so it is unlikely that source confusion is responsible for these γ-ray excesses. As there is no known orbital information for IGR19 it is not possible to perform a phased analysis for this system, and the lack of a persistent γ-ray excess means that neither spectral analysis nor source localisation are possible. Although the small excesses at the position of IGR19 are independent of nearby sources, they are not significant enough to claim a detection, nor is there evidence to associate them with IGR19.

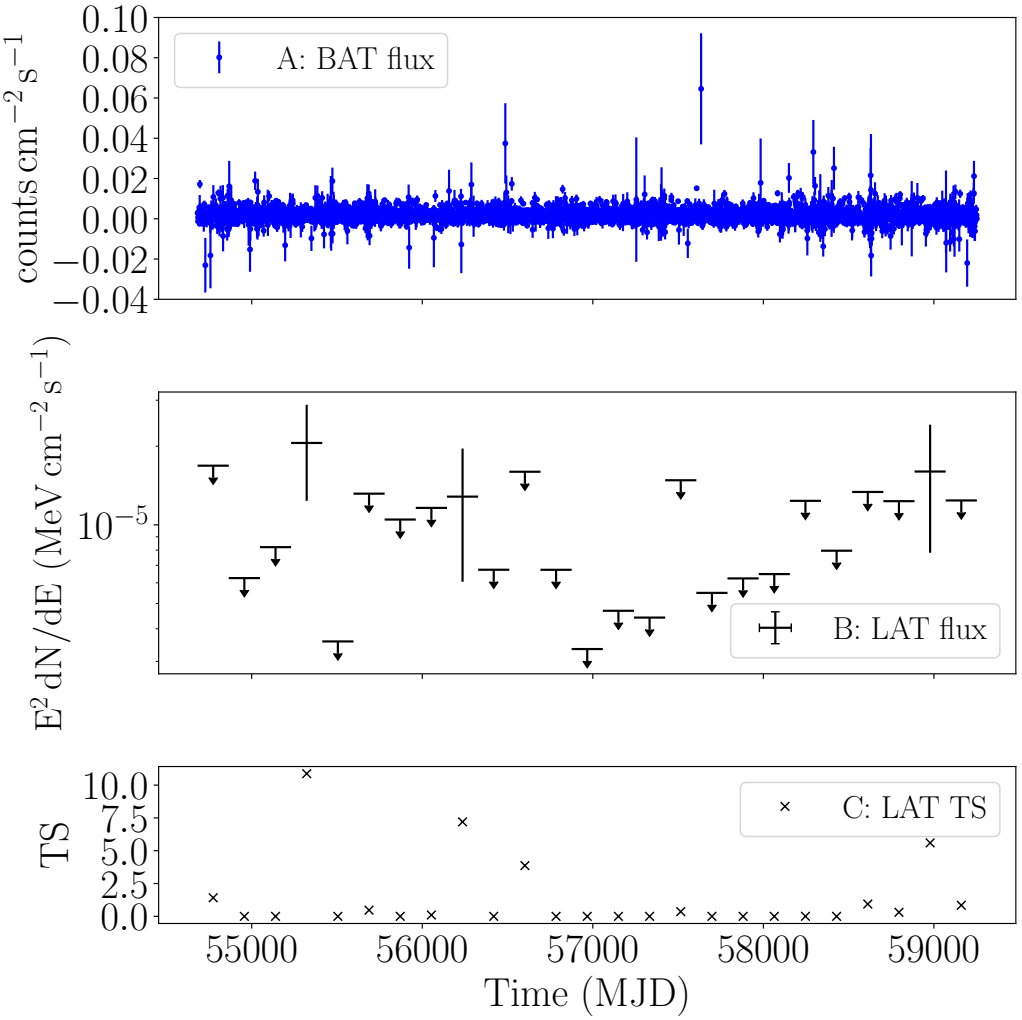

Figure 6.10: The daily binned light-curve of IGR J19140+0951 taken with *Swift*-BAT shown in Panel A, with the 6-monthly binned *Fermi*-LAT light-curve for a source fitted to the position of IGR J19140+0951 shown below in Panel B, and the corresponding TS values of these bins shown in Panel C. I place 95% confidence limits on any *Fermi*-LAT energy flux bins with TS < 4.

6.7 1A 0535+262

1A 0535+262 (henceforth 1A05) is a well-studied pulsar-Be star binary system with an orbital period of 110.3 days (Finger et al., 1996). 1A05 has been the target of previous searches for γ-ray emission (Acciari et al. 2011 & Lundy 2021). It is well known for its giant X-ray outbursts, the most recent of which was in November 2020 (Bernardini et al. 2020 & Jaisawal et al. 2020), and is a known source of non-thermal radio emission (van den Eijnden et al., 2020). I find a γ-ray excess at the position of 1A05 with TS = 12.4, with the binary system itself being located roughly at the edge of the extended γ-ray source 4FGL J0540.3+2756e: the supernova remnant S 147, which has an extension radius of 1.5° (Abdollahi et al., 2020). The centroid of S 147 is offset from 1A05 by 1.625°, and S 147 has a TS of 1080. The closest nearby 4FGL sources lie within S 147, the most significant of which is the unattributed point source 4FGL J0533.9+2838 (TS = 146, angular offset from 1A05 of 2.572°). Given the large (several degree) separation of the nearest γ-ray point sources and the position of 1A05, if source confusion is responsible for the 1A05 coincident γ-ray excess, the confusion is likely with S 147, which is a steady source*.

1A05's giant Type II X-ray outbursts peak at several times the brightness of the Crab Nebula. Figure 6.11 shows the multi-wavelength light-curve of 1A05, with three very bright X-ray outbursts and numerous smaller outbursts seen with *Swift*-BAT. There is no obvious correlation between these outbursts and the AAVSO optical measurements, although these observations don't cover the entire *Fermi*-LAT mission.

The two brightest outbursts occurring during the *Fermi*-LAT observations analysed in this work occur during December 2009, with a peak X-ray flux of 1.2 counts $\mathrm{cm}^{-2}\,\mathrm{s}^{-1}$, and during November 2020, with a peak X-ray flux of 2.4 counts $\mathrm{cm}^{-2}\,\mathrm{s}^{-1}$. A γ-ray flux in the $2\sigma \leq z < 3\sigma$ significance range is detected in the 6 month bin contempor-

*Supernova remnants are a non-variable class of γ-ray emitter, and S 147 has a variability index of 6.7 in the 4FGL-DR2 which supports the hypothesis that no variability is observed on monthly timescales.

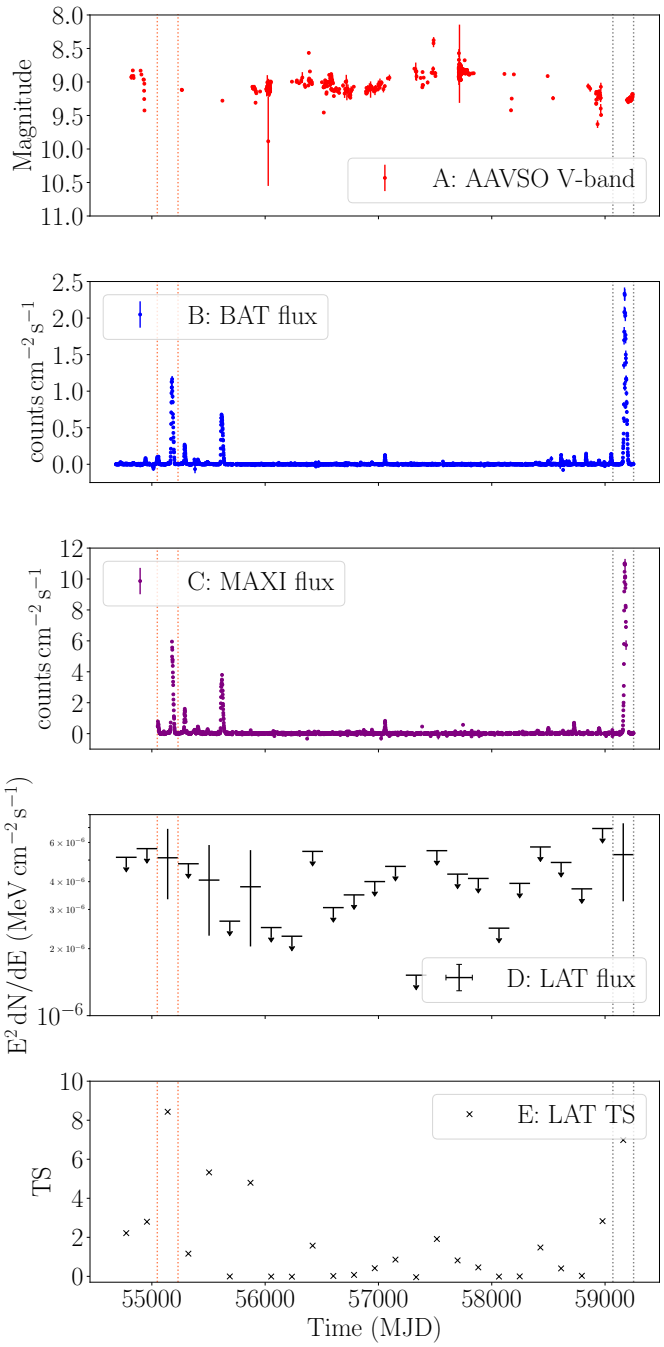

Figure 6.11: Light curves for 1A 0535+262 - Panel A: AAVSO V-band optical light-curve; Panel B: *Swift*-BAT daily light-curve; Panel C: MAXI daily X-ray light-curve. Panel D shows the γ-ray energy flux measurements of the excess coincident with the position of 1A 0535+262 with approximately 6 month bins, and Panel E shows the respective TS values of these bins. Upper limits on energy flux are calculated for any bin where TS < 4. The vertical dotted orange lines indicate the start and end times of the γ-ray flux bin which is temporally coincident with the December 2009 Type II X-ray outburst, and the vertical grey dotted lines indicate the time interval of the γ-ray flux bin which is coincident with the November 2020 Type II X-ray outburst.

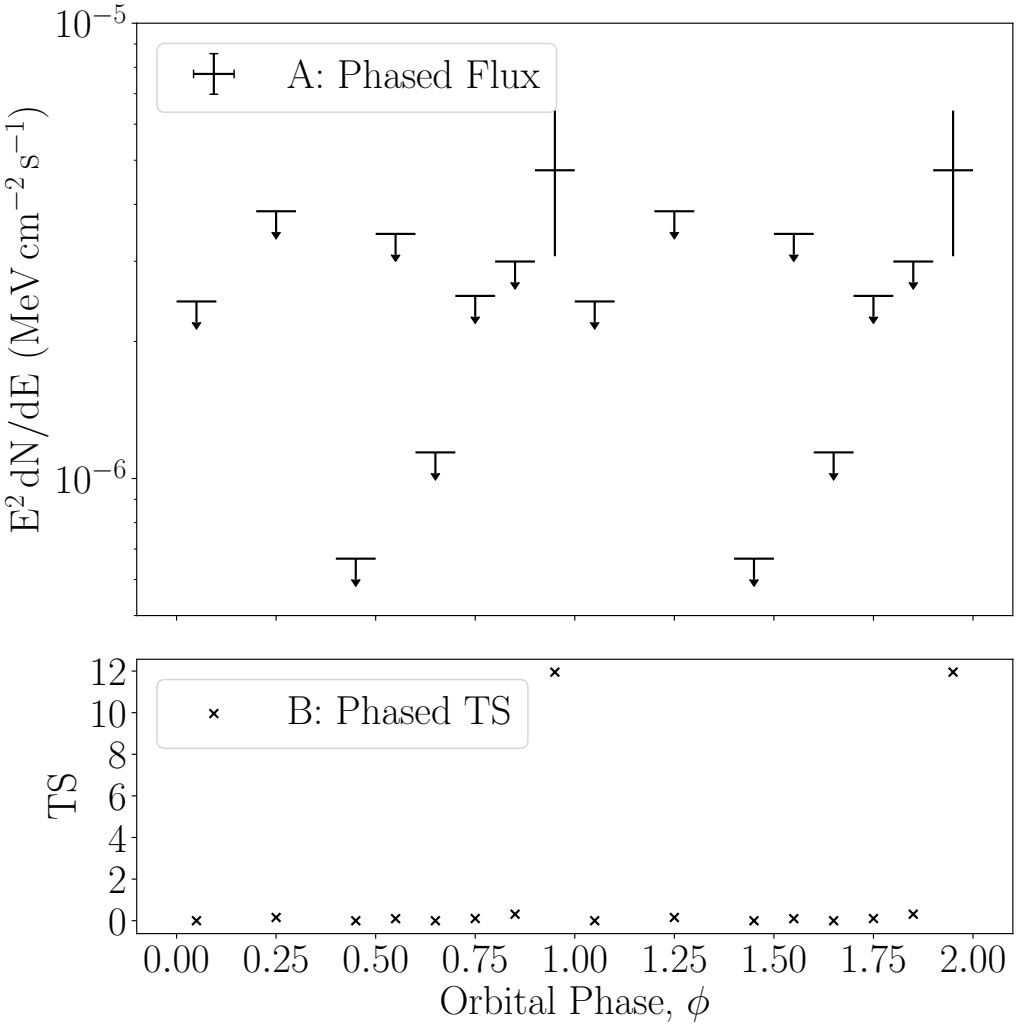

Figure 6.12: The orbital phase-folded light-curve of the γ-ray excess coincident with 1A 0535+262 over the phase range $0 \leq \phi < 2$, with 10 phase bins per orbit. Panel A shows the phase folded energy flux of 1A 0535+262, and Panel B shows the respective TS values of these phase bins, where upper limits are placed on any bins where TS < 4. I note that my likelihood fit fails to identify a point source in the second and fourth orbital phase bins, thus no upper limit or TS is calculated for these bins. I define $\phi = 0, 1, 2$ as periastron and $\phi = 0.5, 1.5$ as apastron; the entire γ-ray excess is distributed in the phase bin immediately preceding orbital periastron.

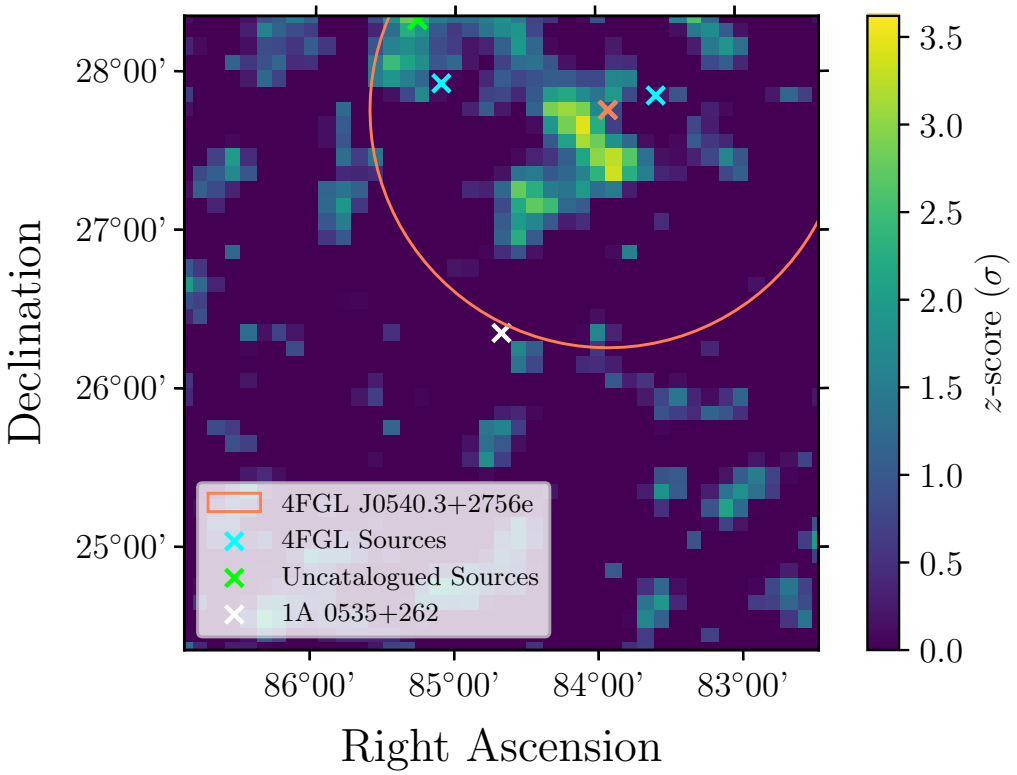

Figure 6.13: The significance map of the central 5° of the 1A 0535+262 ROI, after my likelihood fit and the `gta.find_sources` algorithm, in the phase range $0.9 \leq \phi < 1.0$. The blue crosses refer to the positions of 4FGL sources and the green crosses refer to the positions of uncatalogued sources. The orange circle and cross refer to the extent and centroid of the supernova remnant S 147. The white cross indicates the catalogued location of 1A 0535+262. The γ-ray excess appears to be slightly offset from the position of 1A 0535+262, however such offsets are common with low significance excesses. Furthermore, the combination of several lower significance bins causes the 3.5σ excess I observe from 1A 0535+262.

aneous with both of these outbursts, with these two bins being the most significant in the entire light-curve. In addition to these two bins, two additional γ-ray flux measurements are made with slightly lower significance, one of which immediately precedes the third largest observed outburst in the *Swift*-BAT light-curve. I observe that for the majority of my *Fermi*-LAT observation time (the majority of the 2010s) 1A05 appears to be in relative quiescence, and that the γ-ray flux points are broadly concentrated around the active periods near the December 2009 and November 2020 outbursts. Although the bins are all of low significance (and thus have limited photon statistics), and longer than the X-ray outbursts themselves,

there does appear to be some correlation between the evidence for γ-ray emission and X-ray activity.

1A05 has a known orbital period of 110.3 days, which enables us to phase-fold the γ-ray data using `gtophase`. Figure 6.12 shows the phase-folded light-curve of the excess coincident with 1A05. This shows that the only measurable γ-ray emission occurs in the range $0.9 \leq \phi < 1.0$, immediately preceding periastron. This flux bin has a TS of approximately 12 ($z = 3.5\sigma$), which is comparable to the significance of the excess over the total *Fermi*-LAT observation time; a significance map for this flux bin is shown in Figure 6.13. All other bins have a TS of approximately 0, and in two bins it was not possible to fit a point source at the position of 1A05 at all. This indicates that essentially all of the γ-ray flux from the excess coincident with 1A05 is concentrated in the one phase bin preceding periastron. Whilst it is possible for a phase folded light-curve to be dominated by a short, single, significant event, Figure 6.11 shows that the flux is spread across several bins, each with comparable significance, so this is not the case here.

Given the 1A05 γ-ray excess has only a 3.5σ significance, I lack the photon statistics to generate an SED of the source. A combination of this with the fact that 1A05 lies on the edge of the diffuse emission of S 147 also makes positional localisation impossible. Nevertheless, the evidence (if only at the 3.5σ level) suggests that 1A05 could be a very faint γ-ray binary fueled by wind-wind interactions, or neutron star accretion. This is further supported by the fact that there are no other variable γ-ray sources near 1A05. Finally, the γ-ray flux from the mission-long light-curve of the 1A05 excess shows a weak correlation between γ-ray flux and X-ray activity, with measurable γ-ray fluxes generally corresponding to periods when 1A05 was in outburst, suggesting that neutron star accretion outbursts could be responsible for the γ-ray emission.

In order to reach the 5σ threshold required for a typical claim of discovery, another 12.5 years of all-sky observations would be needed with *Fermi*-LAT, assuming the object's emission characteristics do not change. It is unlikely that *Fermi*-LAT will

continue to operate for this long, but future observatories (see Chapter 10) which will operate in the MeV gap where the peak γ-ray emission of many XRBs may be located could detect the emission from 1A05 more significantly.

6.8 GRO J2058+42

GRO J2058+42 (henceforth GRO20) is a pulsar-Be star HMXB (Wilson et al., 2005) with a 55 day orbital period (Wilson et al., 2000), discovered with the Compton observatory during a Type II outburst in 1995 (Wilson et al. 1995 & Grove 1995). The most recent outburst of GRO20 was in March 2019, with triggers from both *Swift*-BAT (Barthelmy et al., 2019) and *Fermi*-GBM, and additional follow up observations from *AstroSat* (Mukerjee et al., 2020).

There is a small γ-ray excess coincident with the position of GRO20 with a TS of 16.3 ($z = 4.0\sigma$), with a single flux measurement (MJD 55414 - 55596) in the 6-month binned light-curve (Figure 6.14) and upper limits otherwise. This measurement is not coincident with the March 2019 X-ray enhancement, which is the only known outburst during the mission time of *Fermi*-LAT*. Additionally, given that the most significant bin in the light-curve of the excess reaches only TS = 8.61, evidence for long-term variability is very weak.

Figure 6.15 shows the TS map of the region around GRO20, with the HMXB located within a wider γ-ray excess. There are no catalogued γ-ray sources within the immediate vicinity of GRO20, the closest sources being 4FGL J2050.0+4114c (TS = 34.0 and an angular offset of 1.729°) and 4FGL J2056.4+4351c (TS = 297, offset 2.122°) associated with the X-ray source 1RXS J205549.4+435216. Neither of these sources displays any variability according to their variability indices in the 4FGL-DR2.

Given the low ($z < 5\sigma$) significance of the observed excess, no spectral analysis or

*The outburst in May 2008 (Krimm et al., 2008) occurred several months before the beginning of *Fermi*-LAT observations.

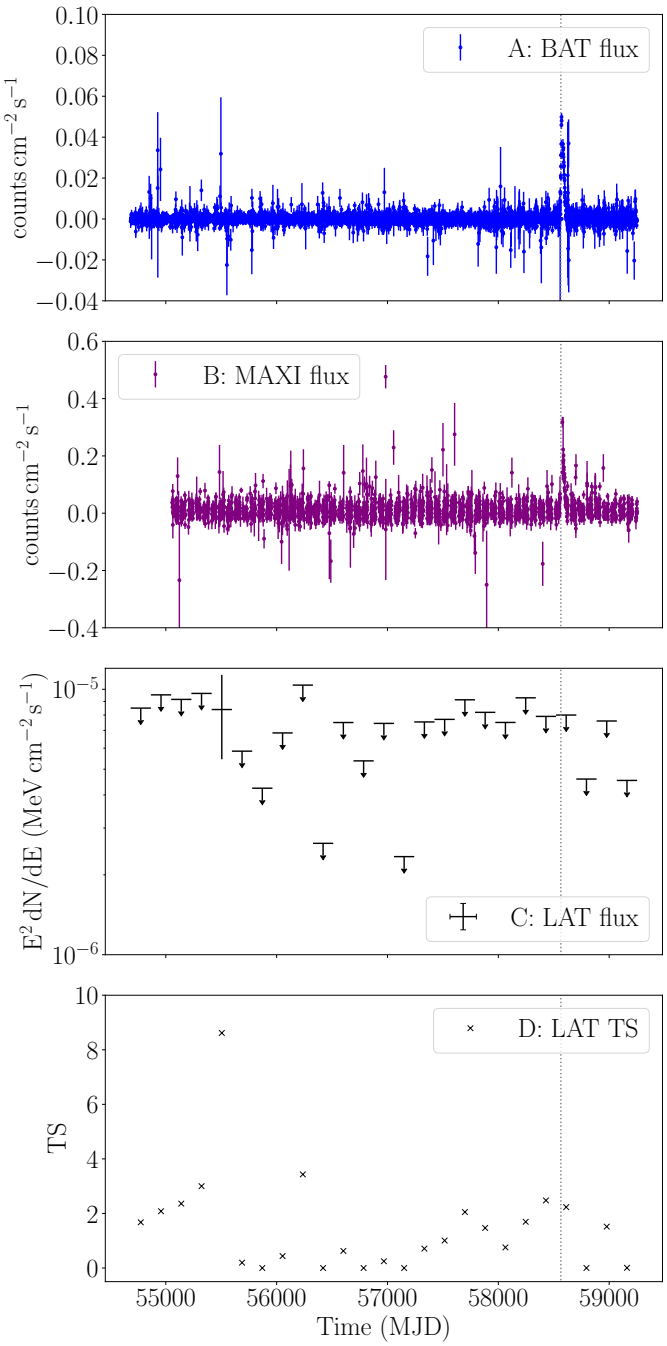

Figure 6.14: The *Swift*-BAT and MAXI daily binned light-curves of GRO J2058+42 are shown in Panels A and B respectively, with the 6-month energy flux measurements and respective TS values of the coincident γ-ray excess shown in Panels C and D respectively. I place 95% confidence limits on any *Fermi*-LAT energy flux bins with TS < 4. There is only one flux measurement from the light-curve of GRO J2058+42; this is not coincident with the March 2019 X-ray enhancement, the beginning of which is indicated by the vertical grey dotted line.

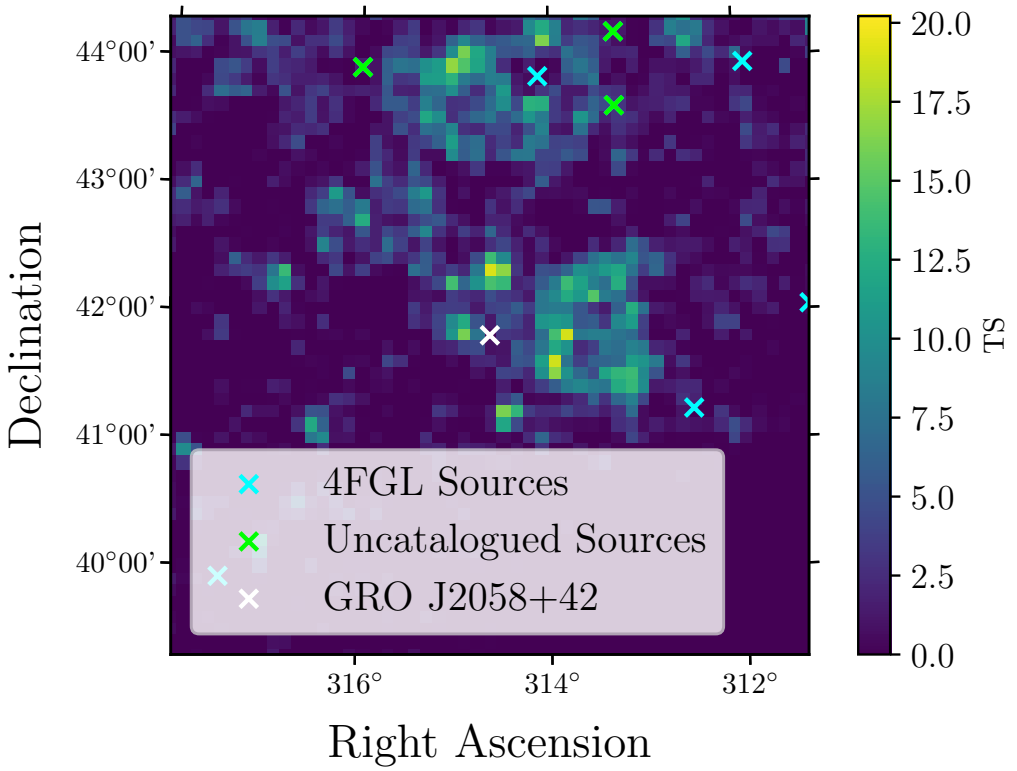

Figure 6.15: The TS map of the central 3° of the GRO J2058+42 ROI, after the likelihood fit and the `gta.find_sources` algorithm. The blue crosses refer to the positions of 4FGL sources and the green crosses refer to the positions of uncatalogued sources. The white cross indicates the catalogued location of GRO J2058+42. The spatial bins have an angular width of 0.1°.

localisation is possible. However, there is an orbital period and ephemeris for this system (Wilson et al., 2000) so I am able to produce a phase-folded light-curve with phase steps of 0.1. Given that GRO20 is a pulsar system with a Be companion star, one might expect γ-ray emission to peak around periastron ($\phi = 0, 1, 2$), where the shocks between the pulsar wind and stellar wind are most intense, although if the neutron star is accreting during outburst it is likely that γ-ray emission could be fuelled by the accretion processes rather than a wind-wind interaction at periastron. The phase folded light-curve of the GRO20 excess is shown in Figure 6.16.There are weak ($z \approx 2\sigma$) indications of γ-ray emission in the phase ranges $0.2 \leq \phi < 0.3$ and $0.8 \leq \phi < 0.9$. I conclude that there is likely no orbital modulation in the weak γ-ray excess I observe from the position of GRO20.

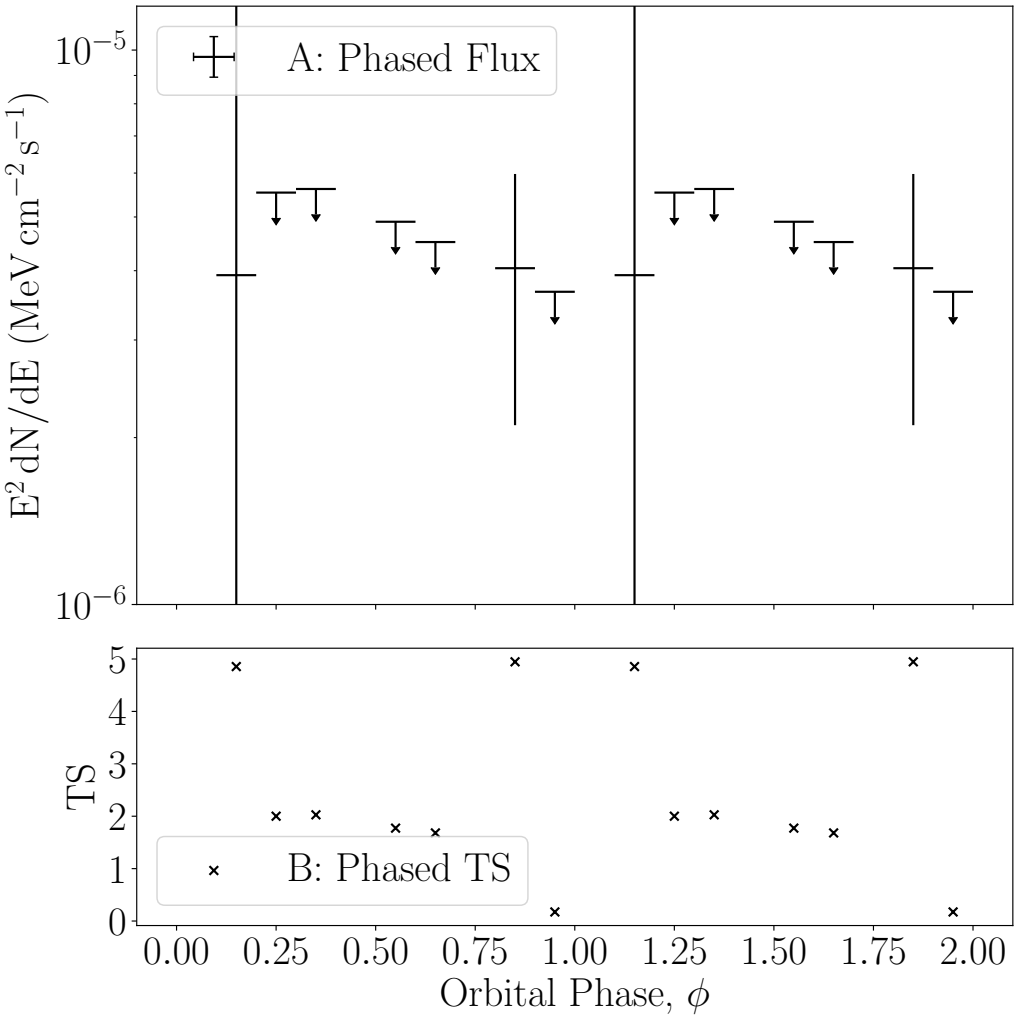

Figure 6.16: The orbital phase-folded light-curve of the γ-ray excess coincident with GRO J2058+42 over the phase range $0 \leq \phi < 2$, with 10 phase bins per orbit. Panel A shows the phase folded energy flux of GRO J2058+42, and Panel B shows the respective TS values of these phase bins, where upper limits are placed on any bins where TS < 4. I note that my likelihood fit fails to identify a point source in the first, fifth and eighth orbital phase bins, thus no upper limit or TS is calculated for these bins. I define $\phi = 1$ as periastron and $\phi = 0.5$ as apastron. I note that there is a very large uncertainty ($\pm\, 4.18 \times 10^{-5}\,\mathrm{MeV\,cm^{-2}s^{-1}}$) associated with the flux measurement in the second and twelfth bins due to the very limited photon statistics.

There is no evidence for any significant variability over the mission time of *Fermi*-LAT, nor is there evidence for any significant orbital modulation of the putative γ-ray flux. I conclude that there is no evidence for γ-ray emission from GRO20. As the immediate area around GRO20 appears to contain diffuse γ-ray emission, it is possible that a weak, unknown, extended source could be causing source confusion at the position of GRO20. There could also be one, or multiple, unresolved γ-ray point sources.

6.9 W63 X-1

W63 X-1 is a pulsar X-ray binary system, likely with a Be or OB star companion (Rho et al., 2004) and located within the W63 supernova remnant, itself located within the Cygnus X star forming region (Sabbadin, 1976). I observe a persistent γ-ray excess coincident with the position of W63 X-1 with TS = 13.2 ($z = 3.6\sigma$). W63 X-1 is a poorly-studied X-ray binary system; no orbital period is known and there is no recorded flux variability in any waveband.

The closest γ-ray neighbour to the W63 X-1 excess is the highly variable BL Lac type blazar 4FGL J2012.0+4629 also known as 7C 2010+4619, which is detected with a significance of TS = 4710, and an angular offset from the position of W63 X-1 of 1.435°. Although it is unlikely, given the separation between the W63 X-1 excess and the blazar, the highly variable and luminous nature of this source means I must test for source confusion, so comparative light-curves of the blazar and binary are generated using the same binning scheme.

Figure 6.17 shows the light-curves of both the W63 X-1 coincident excess, and 4FGL J2012.0+4629. There is weak evidence ($2\sigma \leq z < 3\sigma$) for emission from the position of W63 X-1 in 4 time bins, all spread across the first half of the *Fermi*-LAT mission. At this time, 4FGL J2012.0+4629 appears to be in a lower flux state before a year-long flux enhancement, the beginning of which corresponds with the last γ-ray bin in the light-curve of the apparent W63 X-1 excess. Confusion with the blazar is therefore unlikely to be the source of the γ-ray excess.

Given the marginal nature of all of the γ-ray flux measurements in the light-curve, the lack of measurable variability of the excess and a lack of multi-wavelength data, it is impossible to identify any correlations between wavebands. Poor photon statistics preclude spectral analysis or localisation. The γ-ray excess cannot be associated conclusively with W63 X-1. Given that both the excess and W63 X-1 lie within the larger supernova remnant W63 itself, it is possible that the small γ-ray

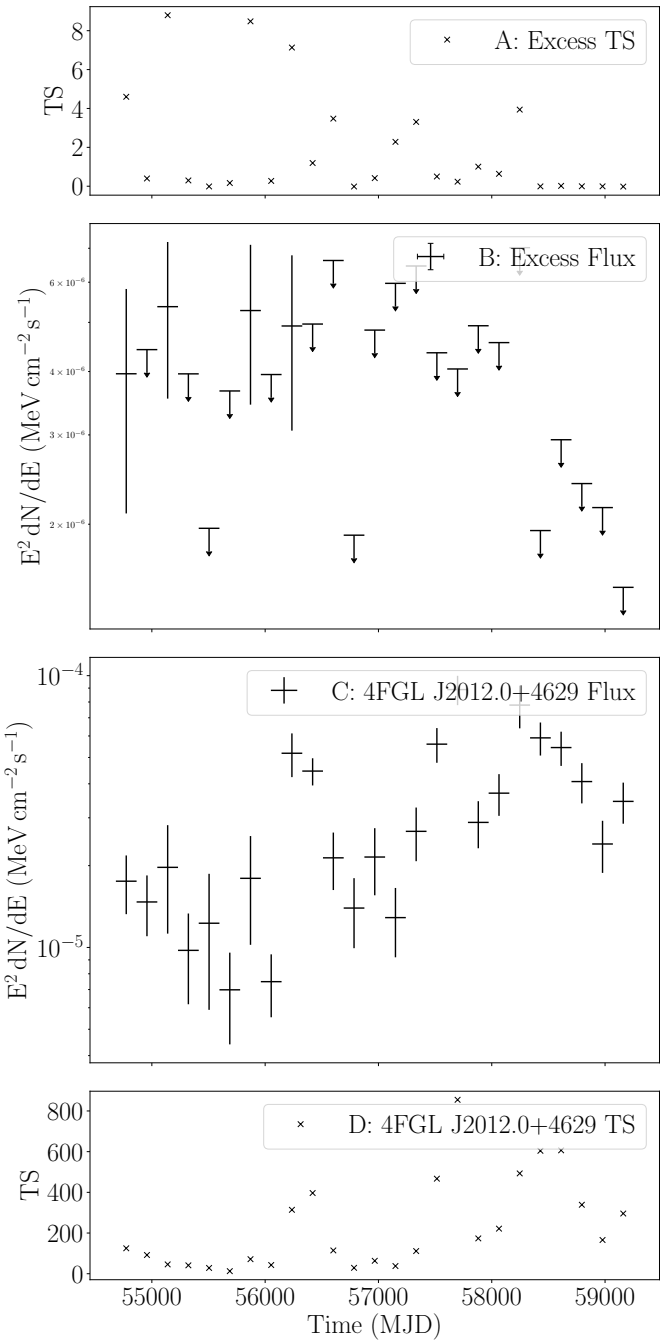

Figure 6.17: Panels B and A show the γ-ray fluxes and associated TS values for the excess coincident with the optical position of W63 X-1. Panels C and D show the γ-ray fluxes and associated TS values for the nearby Bl Lac 4FGL J2012.0+4629, without the excess in the model. I use approximately 6 month bins in each of these light-curves, and 95% confidence upper limits on flux are used for any bin where the corresponding TS value is less than 4.

excess represents very faint γ-ray emission from the supernova remnant rather than the binary system.

6.10 RX J2030.5+4751

RX J2030.5+4751 (henceforth referred to as RX20) is a HMXB system consisting of a neutron star or black hole and a Be star (Belczynski and Ziolkowski, 2009). The orbital period of this system is unknown, but the 100 year optical light-curve indicates long-term variability on the timescale of decades (Servillat et al., 2013). There is a γ-ray excess spatially coincident with the position of RX20 with a TS of 30.81. The 6-monthly binned light-curve of the source indicates that this excess seems to be largely dominated by one bin from MJD 56145-56328 (which reaches approximately 5σ). A measurable flux is observed in 7 other time bins, although at a lower level and with larger uncertainties, so I place upper limits on those bins. There is no enhancement contemporaneous with this γ-ray enhancement in the V-band optical. There are no X-ray light-curves for this source available from either *Swift*-BAT or MAXI.

The nearest γ-ray sources to RX20 are 4FGL J2026.0+4718 (TS = 25.4 and an angular offset of 0.942°), 4FGL J2035.9+4901, associated with the blazar 2MASS J20355146+4901490 (TS = 25.4, offset: 0.942°) and 4FGL J2029.5+4925, associated with the BL Lac type blazar MG4 J202932+4925 (TS = 454, offset: 1.567°). In addition to these catalogued sources, I also identify a second γ-ray excess which I name PS J2027.4+4728 (TS = 25.4, offset: 0.942°).

Whilst the observed excess exceeds 5σ in significance, the photons almost entirely lie at just above 100 MeV, meaning any SED of the excess would not provide any meaningful information. This is also the case during the time bin of the flare. The very soft nature of the γ-ray excess coincident with RX20 is somewhat problematic, as *Fermi*-LAT's angular resolution in the MeV range is several degrees. There is also a relatively low photon count (a few thousand), meaning the `gta.localize`

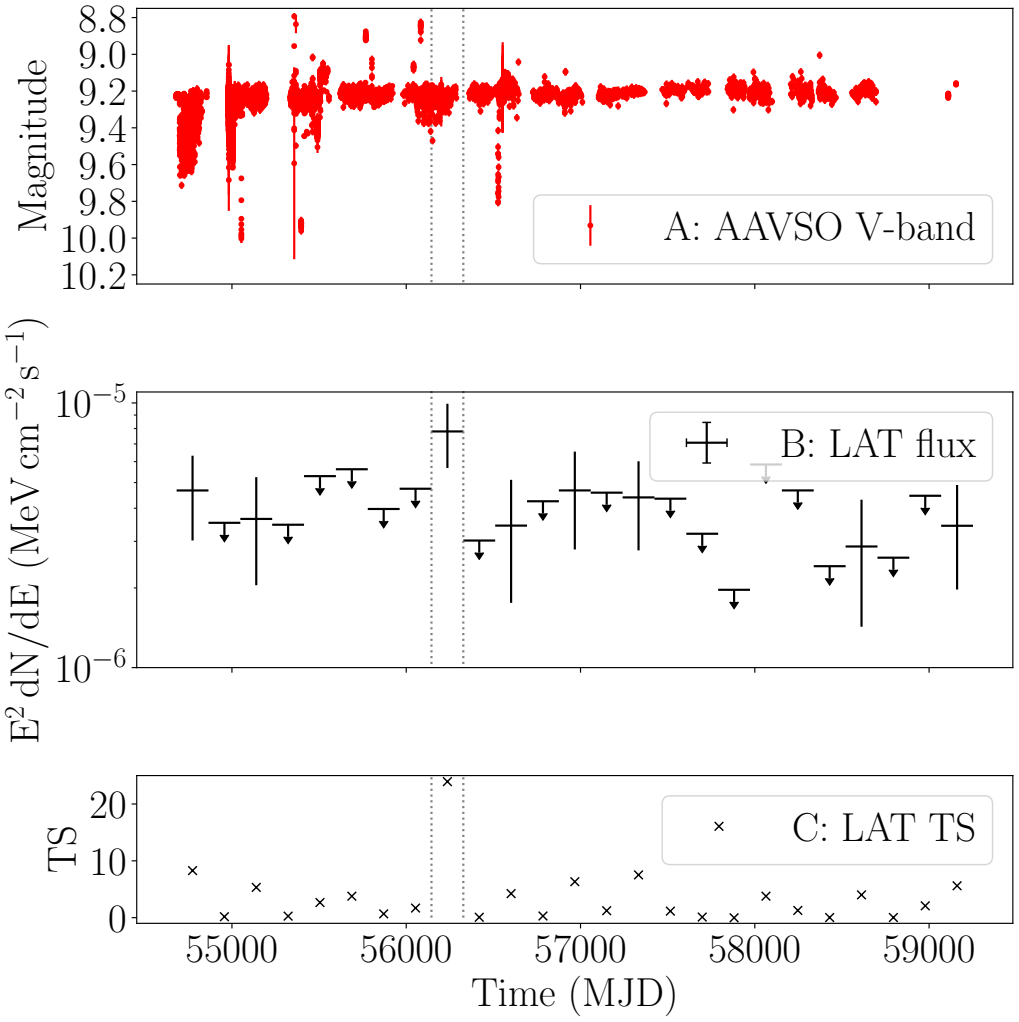

Figure 6.18: The AAVSO V-band optical light-curve of RX J2030.5+4751 is shown in Panel A, with the 6-monthly binned *Fermi*-LAT light-curve for a source fitted to the position of RX J2030.5+4751 shown below in Panel B, and the corresponding TS values shown in Panel C. I place 95% confidence limits on any *Fermi*-LAT energy flux bins with TS < 4. The vertical dashed lines indicate the beginning and end of the 6-month period in which there is a significant enhancement of the excess.

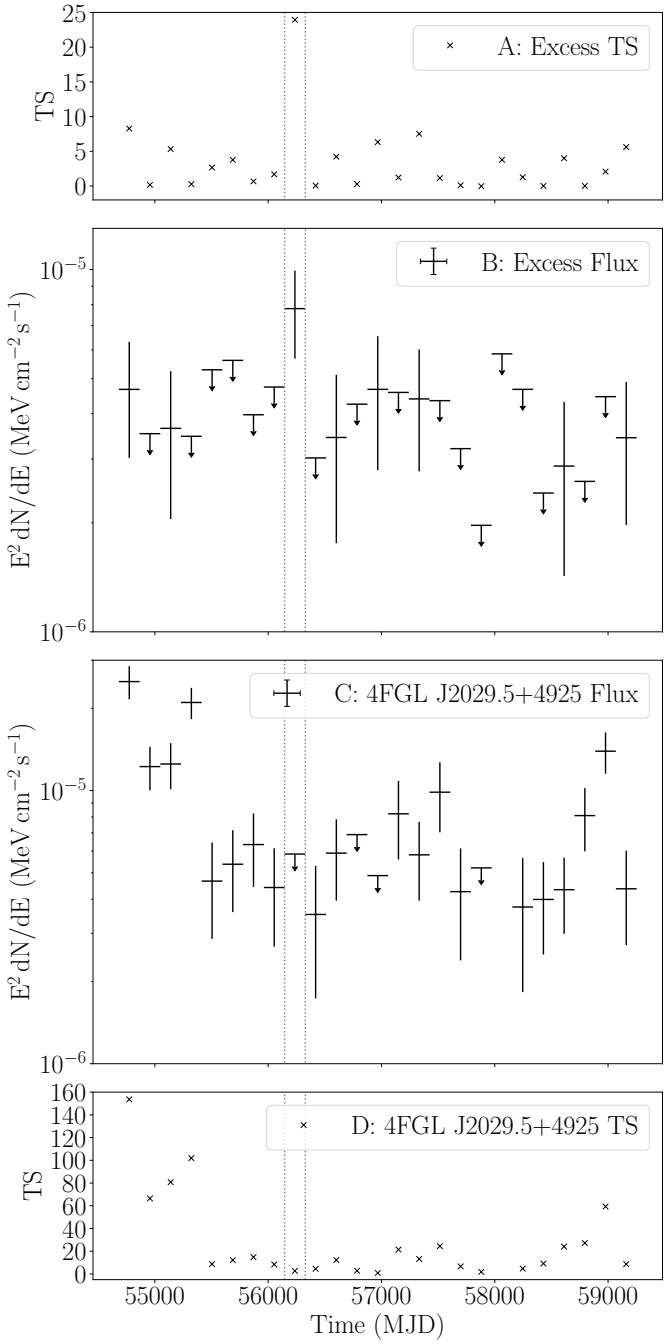

Figure 6.19: Panels B and A show the γ-ray fluxes and associated TS values for the excess coincident with the optical position of RX J2030.5+4751. Panels C and D show the γ-ray flux and associated TS values for the nearby γ-ray source 4FGL J2029.5+4925, without the excess in the model. I use 6-month bins in each of these light-curves, and 95% confidence upper limits on flux are used for any bin where the corresponding TS value is less than 4. The dotted lines indicate the duration of the observed soft γ-ray flare.

algorithm is unable to properly converge in this case and I cannot unambiguously associate the excess with RX20. As two of the three nearest 4FGL sources to RX20 are blazars, which are usually variable, and the third source is of unknown nature and may also be variable, I generate light-curves of each source in order to examine whether a flare from one of these sources is causing source confusion. Whilst 4FGL J2026.0+4718 and 4FGL J2035.9+4901 are not significantly variable, the BL Lac object, 4FGL J2029.5+4925, is. Figure 6.19 shows the light-curve of 4FGL J2029.5+4925, and clearly shows that for approximately the first two years of the *Fermi*-LAT mission the blazar is in an enhanced flux state relative to the rest of the mission. However, during the time where I observe the flare coincident with RX20, there are only flux upper limits from 4FGL J2029.5+4925. Hence I am confident that the γ-ray excess observed at the position of RX20 is independent of nearby 4FGL γ-ray sources.

The orbital period and the nature of the accretor in RX20 are unknown, and the system is not a known microquasar which makes γ-ray emission from a jet unlikely. Given that most Be star HMXBs have a neutron star accretor (Belczynski and Ziolkowski, 2009), it is likely that this is also the case for RX20, and it is possible that the soft γ-ray flare I observe coincident with RX20 is representative of either a wind driven interaction at the periastron of the system, as observed in the known γ-ray binary population, or a neutron star accretion outburst. However, without X-ray data one cannot be certain.

6.11 4U 2206+543

4U 2206+543 (henceforth 4U22) is a HMXB system with a Be star companion, a pulsar accretor (Negueruela and Schurch 2007, Finger et al. 2009 & Wang 2013) and a 9.57 day orbital period. I find a γ-ray excess coincident with the position of 4U22 with a TS of 30.53. With a Galactic latitude of BII $= -1.11°$, 4U22 is on the Galactic plane; however, it is relatively isolated from other γ-ray point

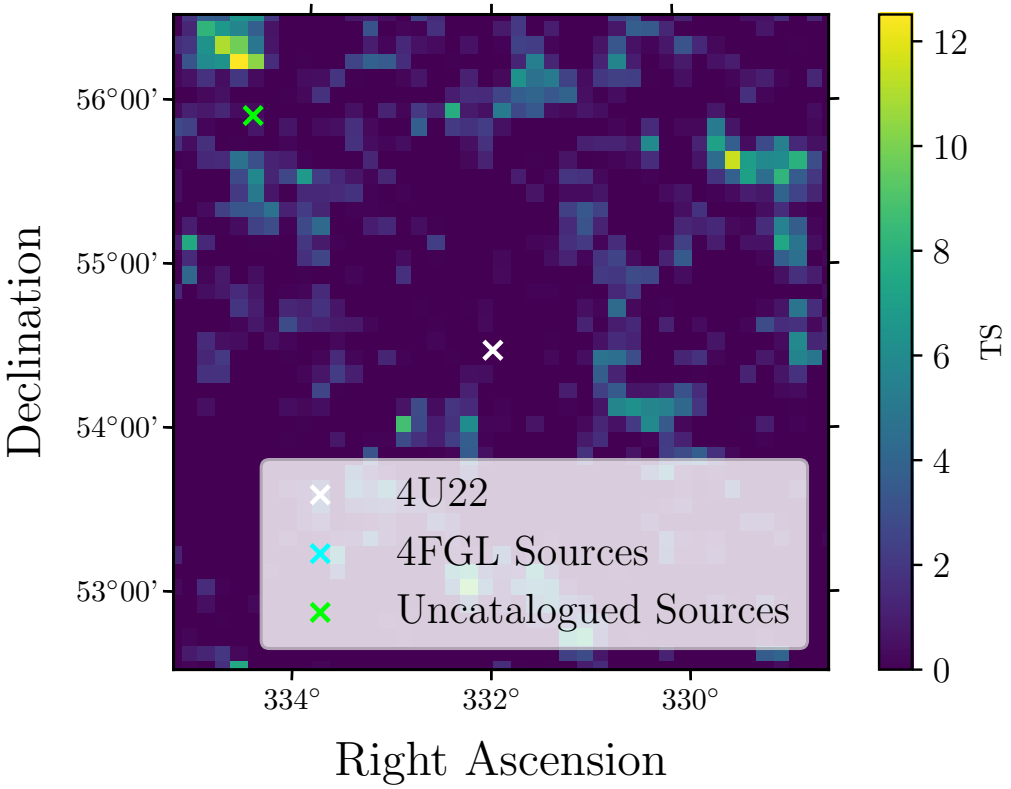

Figure 6.20: The TS map of the central 3° of the 4U 2206+543 ROI across the full 12.5 year observation time. The positions of the closest 4FGL sources are indicated by blue crosses, whilst the positions of sources identified with the `gta.find_sources` algorithm are indicated by green crosses. This TS map is generated after the ROI optimization and fit, but before a point source for 4U 2206+543 is fitted to the model, to highlight the spatial coincidence between the excess and the position of 4U 2206+543. Bins are 0.1° across. I note that given the soft nature of this excess, it is possible that this is a product of very soft photons from the Galactic plane itself, rather than a genuine signature of γ-ray emission from a HMXB. This would explain why no excess is observed at the position of the white cross, as this apparent 'source' is a product of background photons.

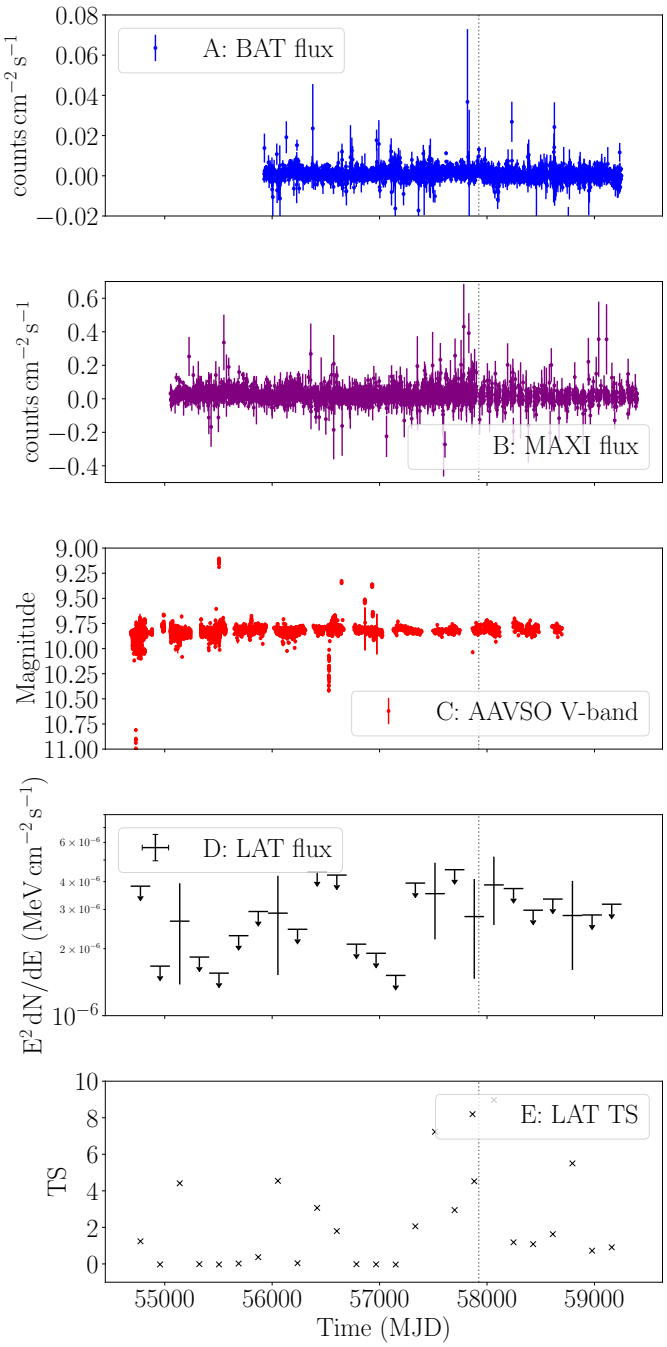

Figure 6.21: The multi-wavelength light-curve of 4U 2206+543, and the coincident γ-ray excess. Panel A shows the *Swift*-BAT X-ray data, which does not cover the entirety of the LAT observations, and Panel B shows the MAXI daily X-ray light-curve. The bin sizes for each X-ray light-curve are the same, with 1-day bin widths. Panel C shows the available AAVSO V-band optical photometry observations of 4U 2206+543 for the duration of the LAT mission. Panel's D and E show the energy flux and respective TS of 4U 2206+543 from the *Fermi*-LAT light-curve, where upper limits are fixed to any flux bin where TS < 4. The vertical grey dotted line indicates the beginning of the INTEGRAL period where an enhancement in X-ray data is observed.

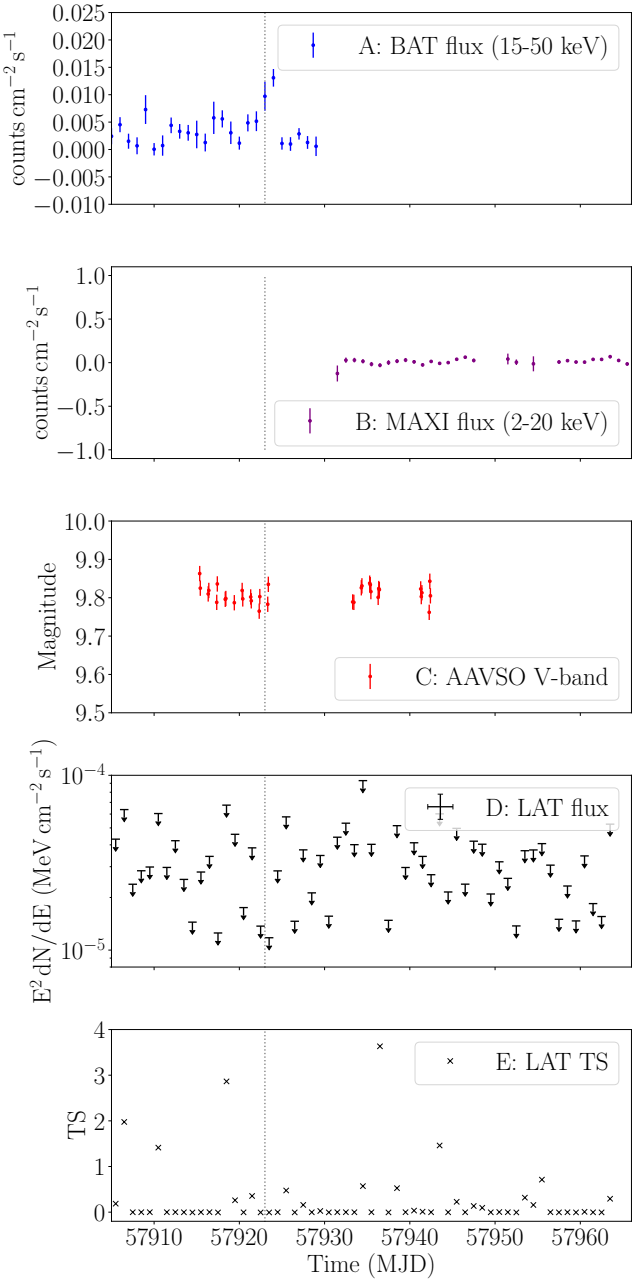

Figure 6.22: The multi-wavelength light-curve of 4U 2206+543, and the coincident γ-ray excess during June and July 2017, when the INTEGRAL enhancement was detected (the start of which is denoted by the grey dotted line). Panel A shows the *Swift*-BAT X-ray data, which covers the time of the enhancement and Panel B shows the MAXI X-ray data, available only for the time period after the enhancement measured with *Swift*-BAT. The bin sizes for each X-ray light-curve are the same, with 1 day bin widths. Panel C shows the available AAVSO V-band photometric observations of 4U 2206+543; no significant optical enhancement is seen. Panels D and E show the energy flux and respective TS of 4U 2206+543 from the *Fermi*-LAT daily light-curve, where upper limits are fixed to all flux bins, as no bin has a TS greater than 4.

sources. The nearest catalogued source is the pulsar 4FGL J2215.6+5135 (PSR J2215+5135), with a TS of 1940 and an angular offset from the position of 4U22 of 3.149°. This is a highly significant source, but given the separation between the pulsar and the position of 4U22, it is unlikely that source confusion explains the excess at 4U22's position. I also identify 4 uncatalogued, sub-threshold γ-ray excesses between 2° and 3° angular offset from 4U22; these are also unlikely to cause source confusion with 4U22 given that they are all less significant than the excess coincident with 4U22, and are $> 2°$ from it.

Similar to RX20, 4U22's spectrum is extremely soft with all the γ-ray flux being concentrated at just above 100 MeV, making any meaningful spectral analysis impossible. Given the very soft nature of this apparent excess, the localisation fit fails and as shown in the TS map (Figure 6.20) there is no visually obvious excess centered on the position of 4U22.

Figure 6.21 shows the multi-wavelength light-curve of 4U22, with daily X-ray data from both MAXI and *Swift*-BAT, AAVSO V-band photometry and the 6-month binned *Fermi*-LAT energy flux and associated TS of the spatially coincident excess. The γ-ray flux of the excess is generally consistent with each other for the bins where a measurement is made, and the upper limits consistent otherwise. The statistical significance of all bins is relatively low, with a maximum measured TS of approximately 9 (3σ). Due to the short orbital period of 4U22, regular Type I X-ray outbursts cannot be identified, nor it is possible to identify orbital periodicity from the *Fermi*-LAT data.

An enhancement of emission between 20 and 100 keV was observed from 4U22 in June 2017 with INTEGRAL (Di Gesu et al., 2017), together with a small enhancement in the *Swift*-BAT data. No MAXI data are available during the INTEGRAL observation period. There is a measurable γ-ray flux in the 6-month bin coincident with the 2017 enhancement (denoted by the grey vertical line in Figure 6.21), but such a flux is not unique to this time. As the hard X-ray/soft γ-ray enhancement lasted only days, I also generate a daily γ-ray light-curve to establish whether any

γ-ray emission exists on the timescale of this enhancement (Figure 6.22). No significant γ-ray emission is detected on daily timescales during June and July 2017. I conclude that the enhancement reported by Di Gesu et al. (2017) produced no measurable, contemporaneous, high-energy γ-ray flux.

A lack of variability from the excess coincident with the position of 4U22 and a lack of information regarding the true position of this very soft excess (which has a PSF of 3.5°) makes it impossible to associate this excess with 4U22. It is possible that this apparent source is a product of excess very soft photons from the Galactic plane itself, which is very difficult to model, rather than a genuine signature of γ-ray emission from a HMXB. This hypothesis is further supported by the apparent lack of any point source excess shown in the TS map (Figure 6.20), coincident with the position of 4U22, despite a 5.5σ point source being fitted to this position.

6.12 IGR J00370+6122

IGR J00370+6122 (den Hartog et al., 2004) (henceforth IGR00) is an X-ray binary system with a pulsar accretor (in't Zand et al., 2007) and a B1Ib class companion star (Negueruela and Reig, 2004) with an orbital period of 15.7 days (Grunhut et al., 2014). There is a very marginal persistent γ-ray excess coincident with the position of IGR00, with a TS = 7.30 ($z = 2.7\sigma$), however in the six monthly binned light-curve I see evidence for emission at TS = 21.9 ($z = 4.7\sigma$) in one of the bins (MJD 56328-56511), and see weak (2σ) evidence for emission in two other bins (MJD 56693 - 56876 and MJD 58155 - 58338). This suggests that there may be transient γ-ray emission at IGR00's position. The γ-ray light-curve of the excess and the IGR00 X-ray light-curve are shown in Figure 6.23. There is no apparent correlation between the X-ray light-curve of IGR00 and the γ-ray light-curve of the excess.

There is a variable blazar 4FGL J0035.8+6131 (also known as LQAC 008+061, TS = 71.3 at an angular offset of 0.225°) close to the position of IGR00. Given the

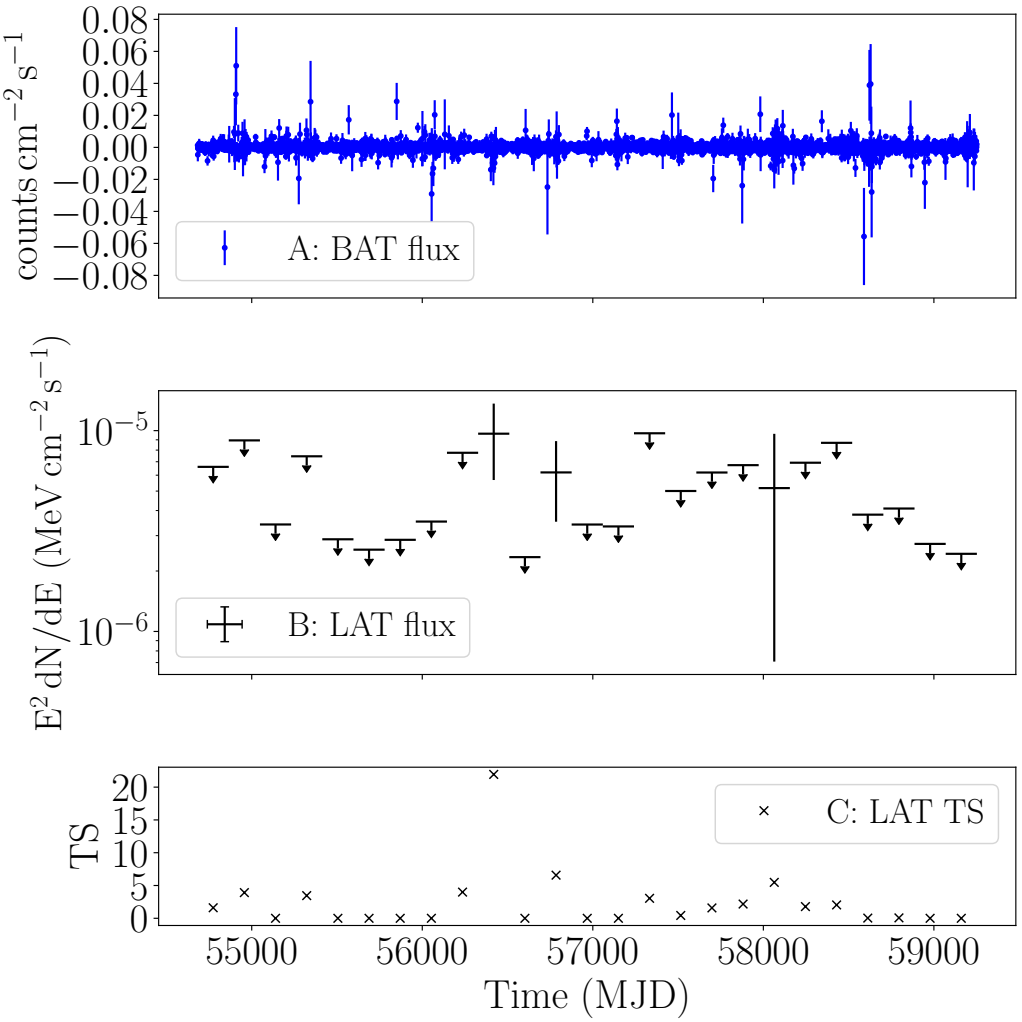

Figure 6.23: The *Swift*-BAT daily binned light-curve of IGR J00370+6122 is shown in Panel A, with the 6 month energy flux measurements and respective TS values of the coincident γ-ray excess shown in Panels B and C respectively. As is consistent with the other light-curves I produce, I place 95% confidence limits on any *Fermi*-LAT energy flux bins with TS < 4.

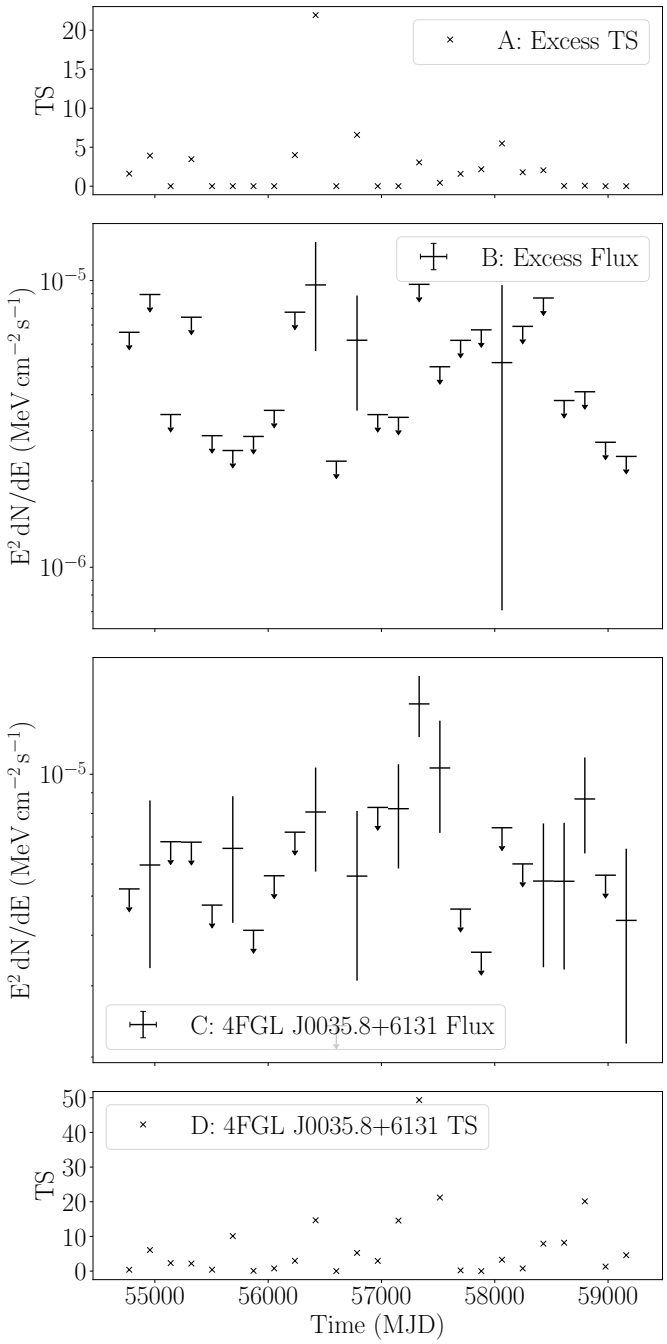

Figure 6.24: Panels B and A show the γ-ray flux and associated TS values of these flux points for the excess coincident with the position of IGR J00370+6122. Panels C and D show the γ-ray flux and associated TS values of these flux values for the nearby γ-ray blazar 4FGL J0035.8+6131, without the excess in the model. I use approximately 6 month bins in each of these light-curves, and 95% confidence upper limits on flux are used for any bin where the corresponding TS value is less than 4.

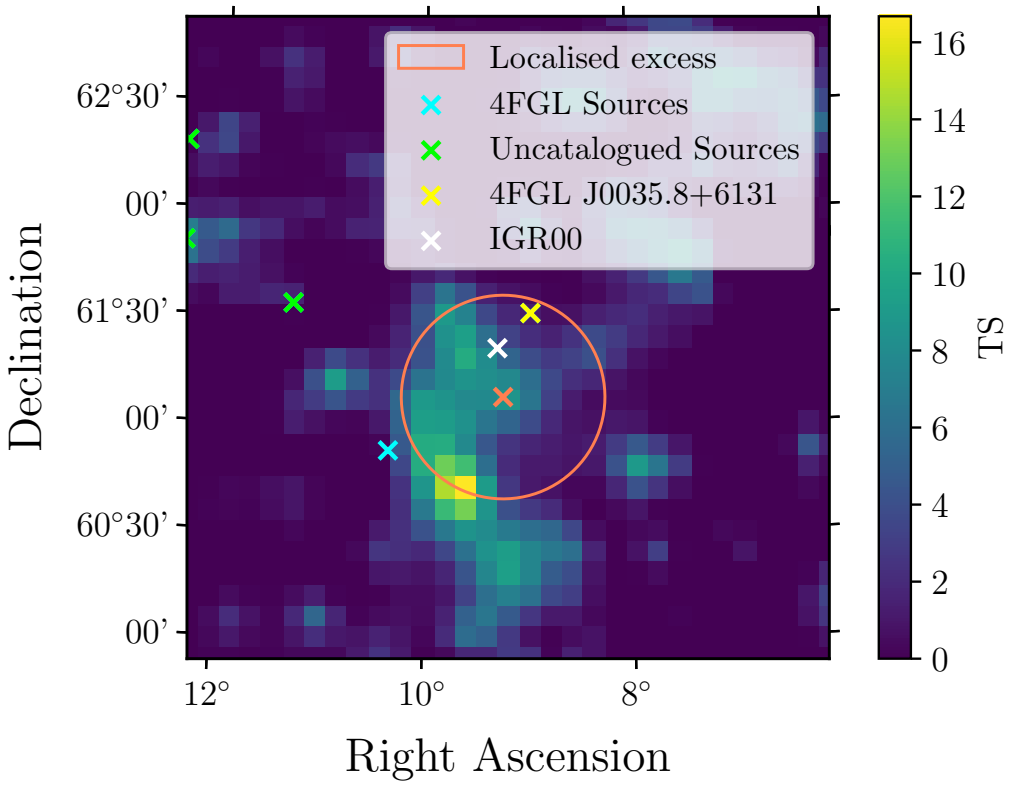

Figure 6.25: The TS map of the central 3° of the IGR J00370+6122 ROI across the MJD 56328 - MJD 56510 period. Here, the positions of the closest 4FGL sources are indicated by blue crosses, whilst the positions of sources identified with the `gta.find_sources` algorithm are indicated by green crosses. The position of IGR J00370+6122 is indicated by a white cross, the position of the blazar is indicated by a yellow cross and the localized excess is indicated by an orange cross, with the 95% positional uncertainty on the excess indicated by the orange circle. As both the blazar and the binary lie within the positional uncertainty of the excess, I conclude it is not possible to determine which object is the cause of the excess. Bin widths are 0.1°.

small angular offset between the blazar and position of IGR00, it is likely that source confusion is responsible for the excess, rather than it being a genuine signature of γ-ray emission from a HMXB. I generate a light-curve of 4FGL J0035.8+6131 using the same 6-month binning scheme used for the light-curve of the excess (Figure 6.23). As shown in Figure 6.24, Where I see apparent emission in the excess light-curve, a similar flux is observed in the light-curve of the blazar. Furthermore, the two proceeding bins (an upper limit and a flux measurement) are also similar in value to those of the blazar. A third, lower significance, flux measurement is

observed later in the light-curve of the IGR00 excess where only an upper limit is observed from the blazar. This is likely a chance fluctuation.

The light-curve alone suggests that source confusion is likely the cause of the excess at the position of IGR00. Nonetheless, I reanalyse the ROI using the same parameters as described in Table 5.1 over the time range of the most significant γ-ray bin in Figure 6.23 (MJD 56328 - MJD 56510). I then add a point source to the position of IGR00, and perform a localisation fit to optimise the positional fit of the excess.

Figure 6.25 shows the position of the blazar, 4FGL J0035.8+6131, together with the position of IGR00 and the positional uncertainty of the localised excess. As both the position of the blazar and the binary lie within the 95% uncertainty bound, it is impossible to determine which of these is the cause of the excess, or indeed if there is an unresolved source causing it. Therefore I conclude that this γ-ray excess is unlikely to represent γ-ray emission from IGR00.

6.13 Confirmed False Positives

Of the 20 binaries where I detect either a persistent or transient γ-ray excess, I determine that 8 (IGR J16320-4751, IGR J16358-4726, IGR J16465-4507, 1WGA J0648.0-4419, AX J1740.1-2847, H 1833-076, GS 1839-04 and SAX J2103.5+4545) of these are likely a false positive result. Discussions of each of these are included in Appendix C.

These false positives can be broken down into two categories; the first is where I see a significant excess which appears to be coincident with the position of the HMXB in question. Given the significant photon statistics available, I perform a localisation of this excess, and upon examining the new positional fit find that the excess is no longer spatially coincident with the position of the binary. The second group of false positive excesses are those which are definitely due to source

confusion with another source. In this case, this excess cannot be proven to be independent, and therefore cannot be associated with the HMXB in question.

6.14 Summary of the HMXB Survey

There are 20 HMXBs where there is either some transient or persistent γ-ray excess suggestive of γ-ray emission from the HMXB. Of these 20, 8 of these are confirmed false positives and are discussed in Section 6.13 and Appendix C. Of the remaining 12 HMXBs, 4 of these have some convincing evidence to associate the γ-ray excess with the HMXB itself.

These HMXBs are:

- SAX J1324.4-6200, where an 18 month transient excess exceeds 5σ in significance and can be localised to the position of the HMXB. This excess has a soft power law spectrum, consistent with other known γ-ray emitting HMXBs.
- GRO J1008-57, where phased variability is seen peaking in 3.8σ significance preceding periastron, and 2.9σ following apastron.
- 1A 0535+262, where a phased excess is seen immediately preceding periastron with 3.5σ, and a weak correlation is seen between γ-ray excesses and X-ray outbursts.
- RX J2030.5+4751, where a 5.6σ persistent excess is seen and localised to the position of the HMXB, and there is apparent variability from the excess which cannot be attributed to source confusion.

In these four systems, the accretor is expected to be a neutron star and given that no contemporaneous microquasar activity is seen alongside the γ-ray emission, they are all expected to be γ-ray binaries.

The remaining eight HMXBs (1H 0749-600, 1H 1238-599, IGR J17544-2619, IGR J19140+095, GRO J2058+42, W63 X-1, 4U 2206+543 and IGR J00370+6122) are marginal cases

where there is no evidence to suggest there is a false positive, but also not enough evidence to be confident that the excess is associated with the HMXB itself.

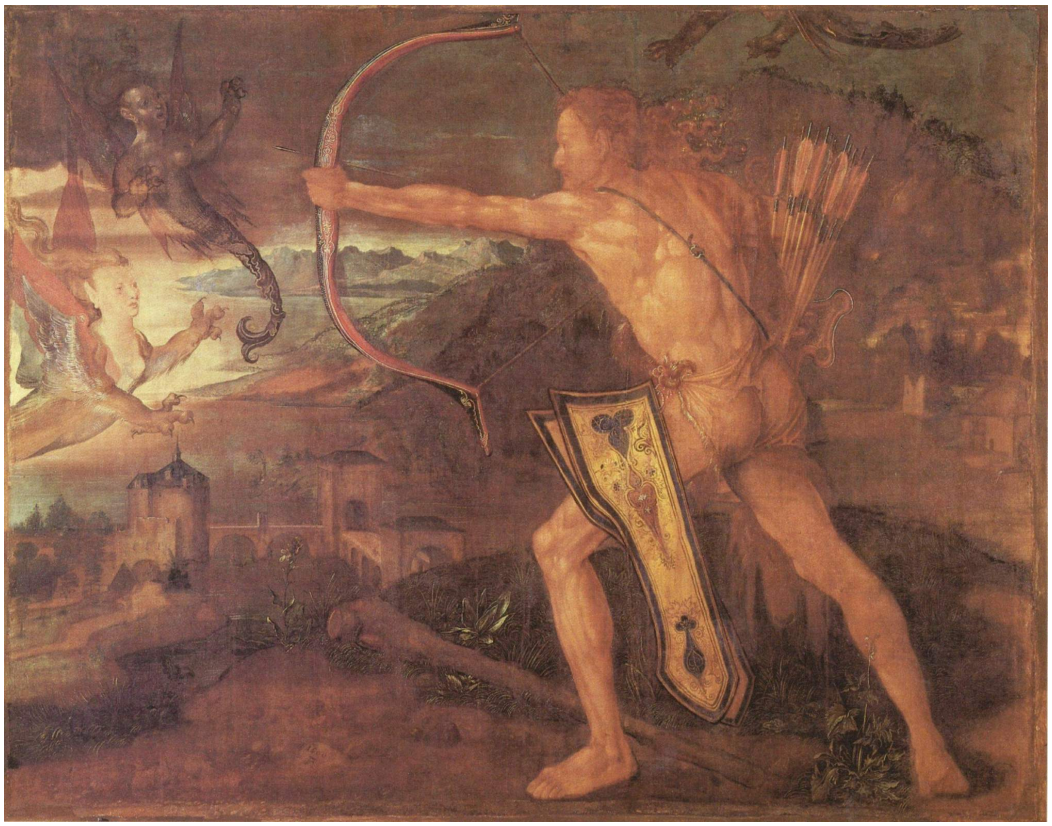

Figure 6.26: The sixth labour of Heracles, driving away the Stymphalian birds. Albrecht Durer (1500).

Chapter 7

Surveying the X-ray Binaries III: The Galactic Disc Low Mass X-ray Binaries

7.1 SAX J1603.9-7753

SAX J1603.9-7753 (Muller et al., 1998) (henceforth SAX16) is a low mass X-ray binary system, where the nature of the accretor and the spectral type of the star are unknown, there are no apparent multi-wavelength counterparts, no known orbital period, and no neutron star pulsations. A very weak γ-ray excess is observed to be spatially coincident with the position of SAX16 with a TS of 4.05 ($z = 2.0\sigma$), however in the light-curve of this excess, two bins with 3σ significance are observed and a third bin with 2σ significance (Panels A and B of Figure 7.1).

The nearest catalogued γ-ray source to the position of SAX16 is the FSRQ 4FGL J1617.9-7718 (a.k.a. PKS 1610-77) which has an angular offset from the position of SAX16 of 0.951° and a TS of 1910. The light-curve of 4FGL J1617.9-7718 is shown in Panels C and D of Figure 7.1; there is giant γ-ray flare observed in the bin MJD 57526 - 57715 (TS = 1310). One of the two 3σ bins in the light-curve of the SAX16 excess appears to be temporally coincident with this flare, which suggests

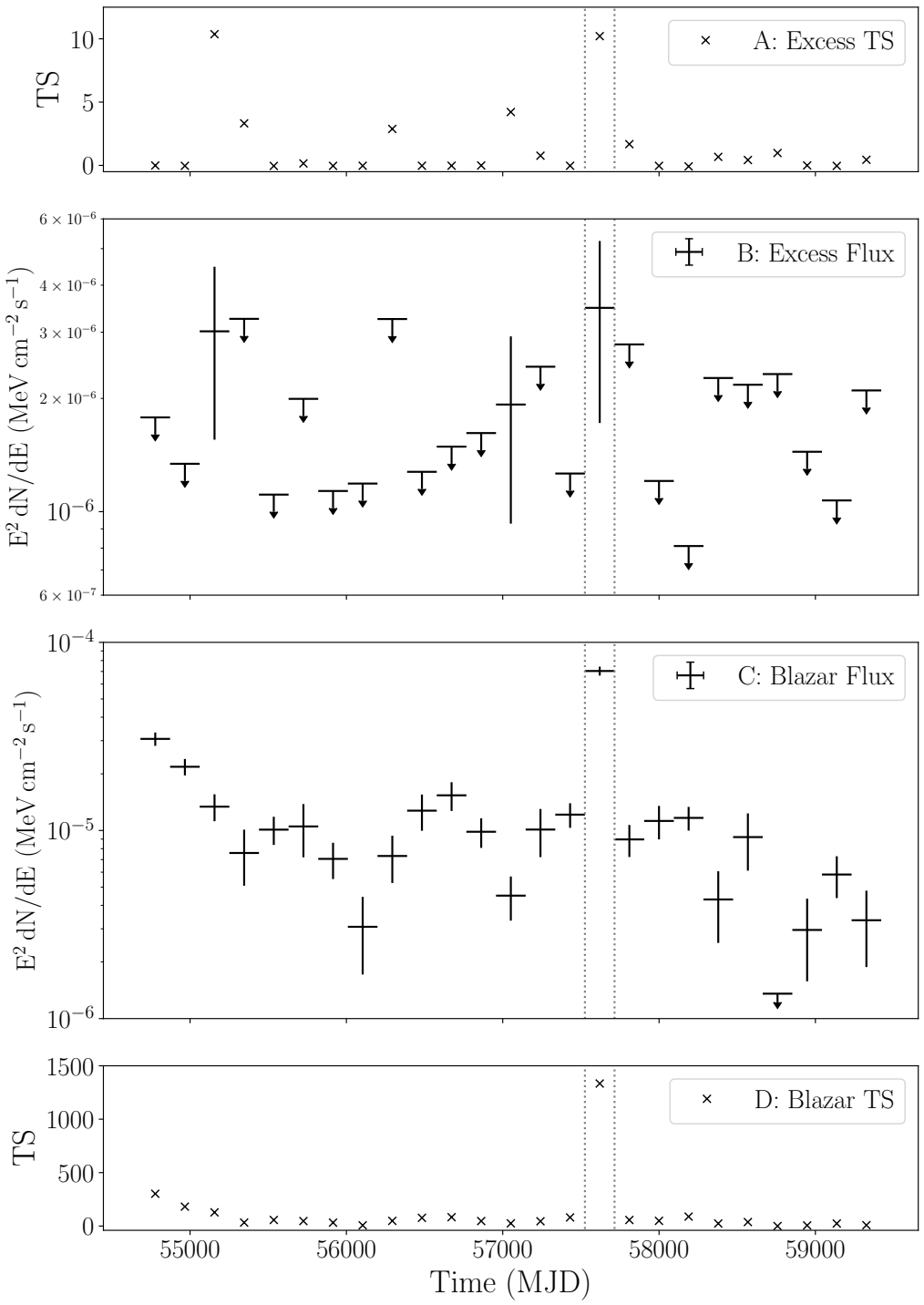

Figure 7.1: Panels A and B respectively show the TS and flux of each bin in the 13 year light-curve of the SAX J1603.9-7753 coincident γ-ray excess, and Panels C and D respectively show the flux and TS of 4FGL J1617.9-7718 over the same period. The vertical grey dotted lines highlight the bin where a significant flare is seen from the blazar. For bins where TS < 4 a 95% confidence limit on flux is calculated.

that source confusion *may* be responsible for this bin. However, there is no flaring in the light-curve of the blazar coincident with the other two flux points, so it is unlikely that source confusion is responsible for these. Therefore this γ-ray excess is most likely independent of the 4FGL J1617.9-7718, at least outside of the time range MJD 57526 - 57715.

Given that the significance of the excess is so low, it is not possible to perform a positional localisation of the excess or any spectral analysis due to limited photon statistics. Furthermore, at only 2σ over the mission lifetime of *Fermi*-LAT, a lack of evidence prevents us from associating this excess with SAX16.

7.2 4U 1323-62

4U 1323-62 (Seward et al. 1976 & Forman et al. 1976) (henceforth 4U13) is an LMXB system with a neutron star accretor and an M-type companion star (Gambino et al., 2016). The orbital period of the system has been identified as 2.9 hours from the X-ray light-curve (Parmar et al., 1989); this periodicity is not seen from the counterpart star. A γ-ray excess is observed to be spatially coincident with the position of 4U13, with a TS of 18.94 ($z = 4.35\sigma$) (Figure 7.2. There are several nearby catalogued γ-ray sources, with 4FGL J1328.4-6231 (TS = 58.1, angular offset from 4U13 of 0.441°) and 4FGL J1321.1-6239 (TS = 117, angular offset: 0.821°) both lying within 1° of 4U13. Neither of these sources is identified at any other wavelength. Light-curves of these sources show some evidence for flaring in both sources but there is no evidence to suggest that the γ-ray excess at the position of 4U13 is caused by source confusion with either of these. It is not possible to carry out spectral analysis or localisation of this excess due to limited photon statistics.

Figure 7.3 shows the *Swift*-BAT X-ray light-curve of 4U13 with daily time bins. No variability is seen on daily timescales; given that $P_{orb} < 1\,\mathrm{day}$, neither would any orbital modulation be expected in this light-curve. No Type II outbursts are observed from 4U13 during the 13 year observation period. There appears to be

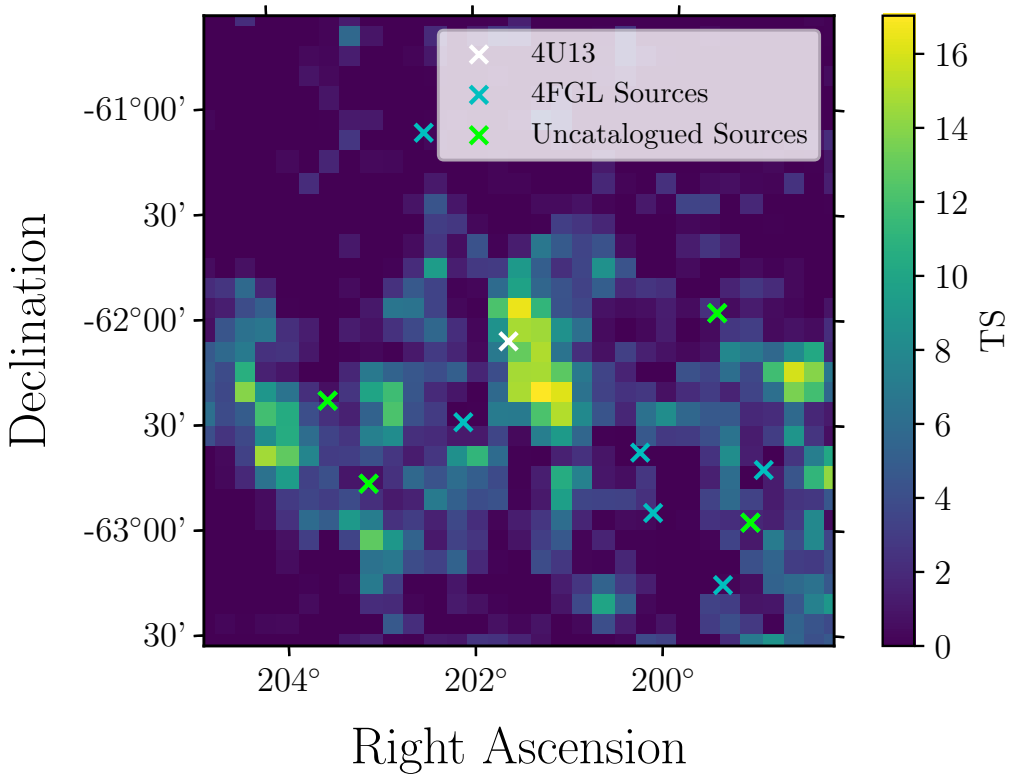

Figure 7.2: The TS map of the central 3° of the 4U 1323-62 ROI over the full mission time. Here, the positions of the closest 4FGL sources are indicated in blue, whilst the position of 4U 1323-62 is indicated in white. The positions of uncatalogued sources are indicated in green. Bin widths are 0.1°. Whilst localisation isn't possible in this case, 4U 1323-62 appears coincident with the excess, although slightly off centre, and the excess itself appears to be spatially resolved from 4FGL sources.

no significant variability from the γ-ray excess, 4 weakly detected flux points are seen in the light-curve at the $2\sigma < z < 3\sigma$ level. The 4 flux measurements have large uncertainties (caused by low photon statistics in each bin), but appear to be consistent with the 95% upper limits on the other bins, supporting the hypothesis that there is no detectable variability on the timescales are examined here.

Gambino et al. (2016), a recent study of 4U13, has reaffirmed the period of the system to be 2.9419 hrs. Even with a very accurate estimate of the orbital period, and the associated first order derivative, it is not possible to phase fold the γ-ray data over such short periods, particularly without an accurate ephemeris for the periastron of the system. Nonetheless, that 4U13 may harbour a neutron star

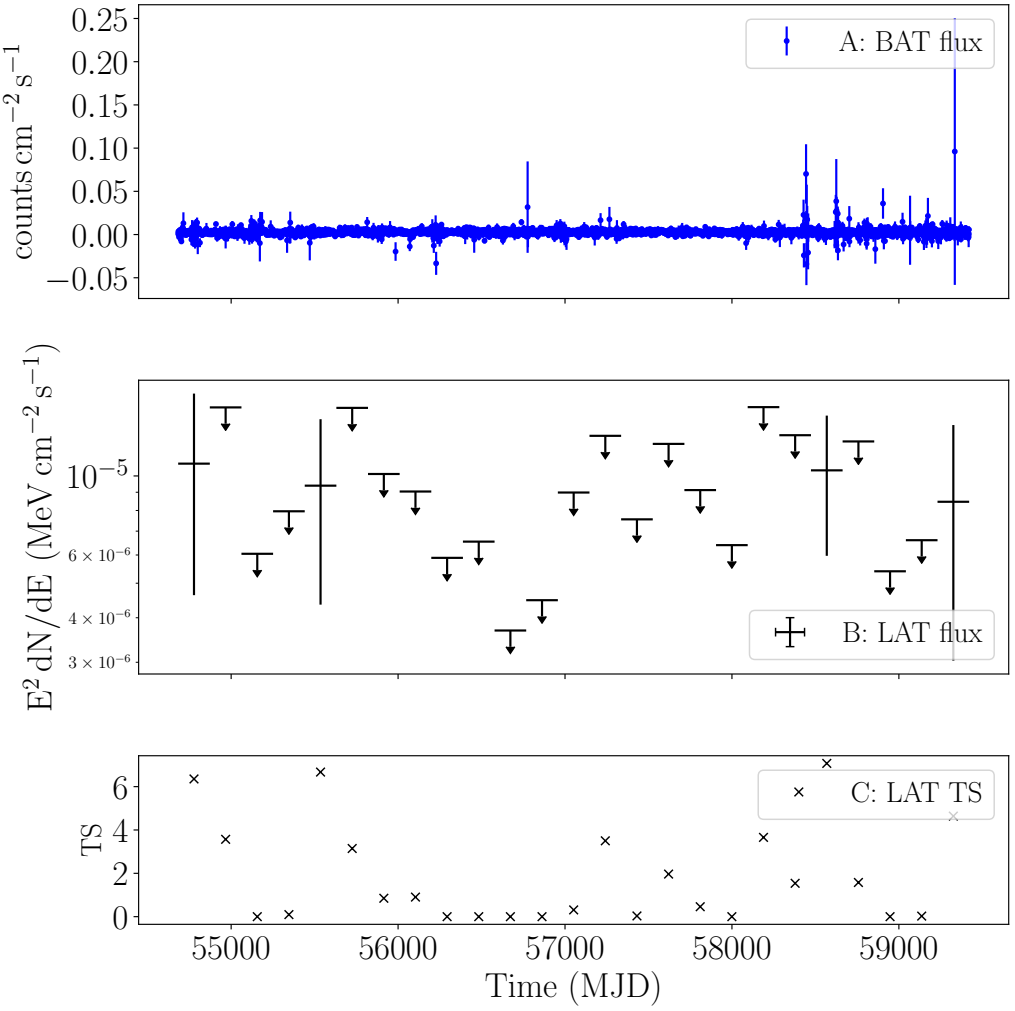

Figure 7.3: Panel A shows the daily binned light-curve of 4U 1323-62 with *Swift*-BAT in the 15 - 40 keV hard X-ray waveband. Panels B and C respectively show the energy flux and TS of the 4U 1323-62 coincident γ-ray excess, and 95% upper confidence limits on energy flux are calculated for any bin where TS < 4.

indicates that this system may be responsible for observed γ-ray excess, whether the γ-ray emission comes from binary processes, or the neutron star alone, although it is possible that the excess is a fluctuation in the background, given it's low significance.

7.3 Cir X-1 (3A 1516-569)

3A 1516-569 (Margon et al., 1971b), most commonly known as Cir X-1 is a unique X-ray binary, which has been identified at various points as a high mass system (Jonker et al. 2007 & Li 2020) and as a low mass system (Liu et al. 2007 & Johnston et al. 2016) with debate still ongoing as to the nature of the companion star in this system. Given the presence of Type I X-ray outbursts from Cir X-1 (Tennant et al., 1986), the accretor is expected to be a neutron star, and Cir X-1 shows evidence for a 16.6 day orbital period from modulations in the X-ray (and radio) light-curves (Kaluzienski et al., 1976). The system is a known microquasar with radio jet activity observed (Stewart et al. 1993, Fender et al. 1998, Heinz et al. 2007 & Coriat et al. 2019), providing an environment for the acceleration of cosmic particles required for γ-ray emission. Additionally, Cir X-1 is the youngest known X-ray binary system at approximately 3000 years old* (Clarkson et al. 2004 & Li 2020), and is associated with the supernova remnant G322.1+0.0 (Heinz et al., 2013). This SNR is not a known γ-ray source. Cir X-1 has been the previous target of searches for γ-ray emission, though these searches only identified upper limits (Abdalla et al., 2018).

A persistent γ-ray excess is identified coincident with the radio position of Cir X-1 with TS = 16.9 (4.11σ). There is only one source within 1° of Cir X-1's position, the luminous and non variable pulsar 4FGL J1521.9-5735 (a.k.a. PSR J1522-5735), with an angular offset of 0.457° and TS = 3920. Additionally a variable blazar, 4FGL J1512.9-5639 (a.k.a. PMN J1512-5640), is seen (angular offset: 1.167°, TS

*Or rather, 3000 years since the supernova which caused the formation of the neutron star accretor.

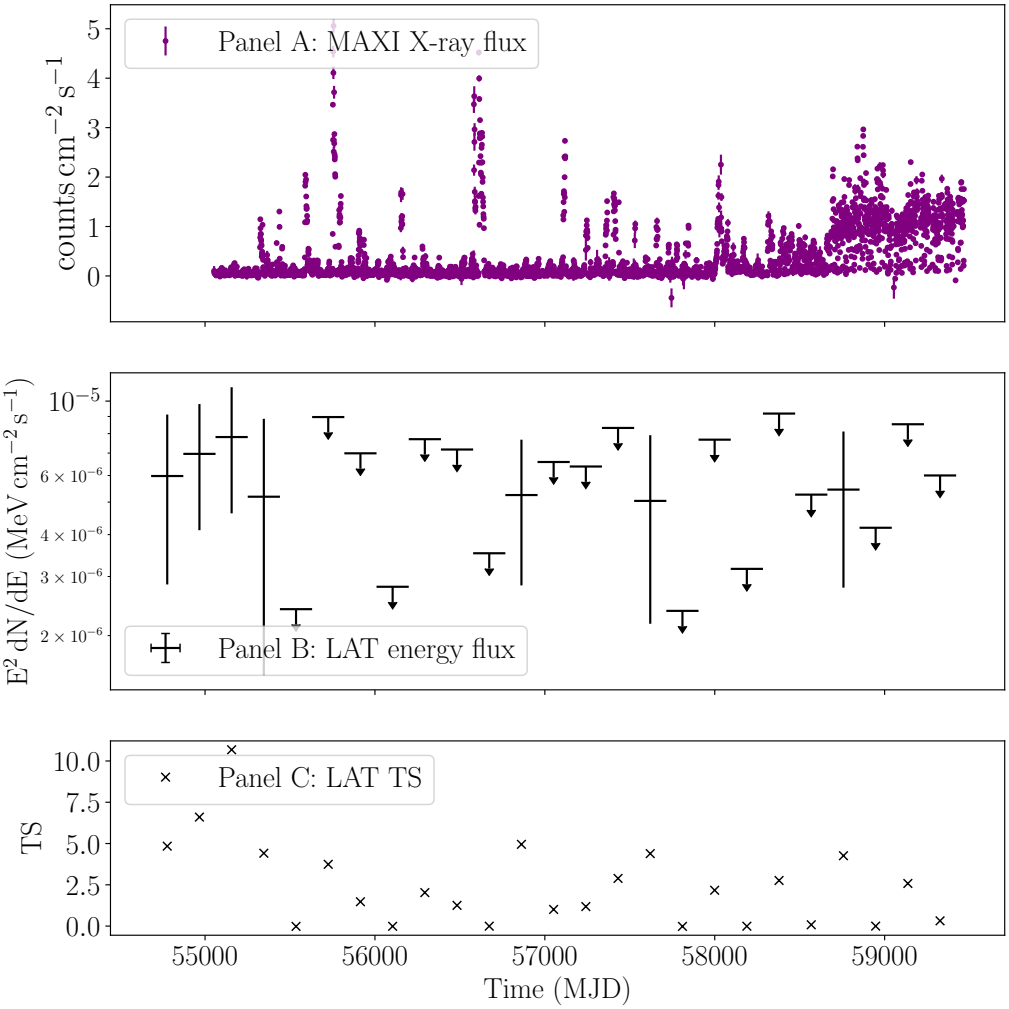

Figure 7.4: Panel A shows the daily binned light-curve of Cir X-1 with MAXI in the 2 - 20 keV soft X-ray waveband. Panels B and C respectively show the energy flux and TS of the Cir X-1 coincident γ-ray excess, and 95% upper confidence limits on energy flux are calculated for any bin where TS < 4.

= 496). Given that the pulsar is twice as close, and a much more significant γ-ray emitter than the blazar, if source confusion is responsible for the γ-ray excess at the position of Cir X-1 then it is likely caused by photon contamination from the pulsar.

As a microquasar, Cir X-1 is extremely variable in the X-ray waveband. whilst *Swift*-BAT data is unavailable for the vast majority of the *Fermi*-LAT observation period, MAXI data is available from the instrument's first light in 2009. Figure 7.4 shows the MAXI light-curve in Panel A with numerous clear and significant outbursts, and a persistent, noisy, luminous state for the last two years. The Fermi-LAT data (Panels B and C) show that the γ-ray excess coincident with Cir X-1 appears largely non-variable over 6 monthly timescales, and there appears to be no obvious correlation between the measured flux points and X-ray outbursts. A two year period at the beginning of the light-curve shows a sustained, low level of γ-ray emission, however given that this two year period, in part, lies outside of the MAXI observation range it is difficult to determine whether this two year period of γ-ray emission is due to any particular physical process in Cir X-1.

Given the apparent non-variability of the γ-ray excess (based on Figure 7.4) and the close proximity to the γ-ray pulsar 4FGL J1521.9-5735, there may be source confusion with the pulsar, although this conclusion is not concrete as their is no direct evidence to associate the excess with either the pulsar, or Cir X-1. For an excess such as this, spectral analysis, and source localisation would be ideal tools in determining the true origin of the excess, however neither are possible due to limited photon statistics. Nonetheless, as a unique member of the X-ray binary population, and a microquasar, Cir X-1 is a target of interest for future γ-ray (and more generally multi-wavelength) observatories.

7.4 4U 1708-40

4U 1708-40 (Forman et al., 1976) (henceforth 4U17) is a low mass X-ray binary with a neutron star accretor (as it displays Type I X-ray outbursts) and an unclassified companion star (Migliari et al., 2003). My analysis shows an unusually hard γ-ray excess coincident with the position of 4U17 with TS = 14.6 ($z = 3.8\sigma$). Given that the vast majority of the excesses detected across this survey are soft (in the case of several, extremely soft) this presents something of an anomaly. All of the significant γ-ray emission is detected in the 9.4 - 29.2 GeV energy bin, as shown in Figure 7.5. This energy bin has TS = 14.8, leading to the conclusion that the emission from the overall excess is concentrated in this energy bin. All other energy bins have upper limits in place given their low significances, therefore fitting a spectrum is not possible, nor is it possible to localise the excess.

No orbital period is known for 4U17 so a phased analysis of the γ-ray data is not possible. Figure 7.6 shows the daily X-ray light-curve of 4U17 with both MAXI and *Swift*-BAT, together with the γ-ray light-curve of the excess. Two flares are seen in the MAXI light-curve reaching over 8 counts $\mathrm{cm}^{-2}\,\mathrm{s}^{-1}$ (approximately 2 Crab), and in the case of the most recent flare, a small enhancement in the *Swift*-BAT light-curve is also seen. These flares last for one day, much less than the γ-ray bin width. In the light-curve of the γ-ray excess, 4 bins have flux measurements with upper limits otherwise. All of these bins have marginal significances ($2\sigma < z < 3\sigma$), and whilst the most significant of these appears to correspond to the first significant X-ray flare, poor statistics prevent analysis of this time period in greater resolution. Overall there is no significant evidence to associate the excess with 4U17 based on the light-curves.

The γ-ray excess is close to several catalogued γ-ray sources, including the luminous supernova remnant 4FGL J1713.5-3945e (the well known VHE source RX J1713.7-3946), a spatially extended source of radius 0.5° (Tang and Liu, 2021) and TS = 1000 ($z = 31.6\sigma$). Three other sources lie between the excess and RX J1713.7-3946

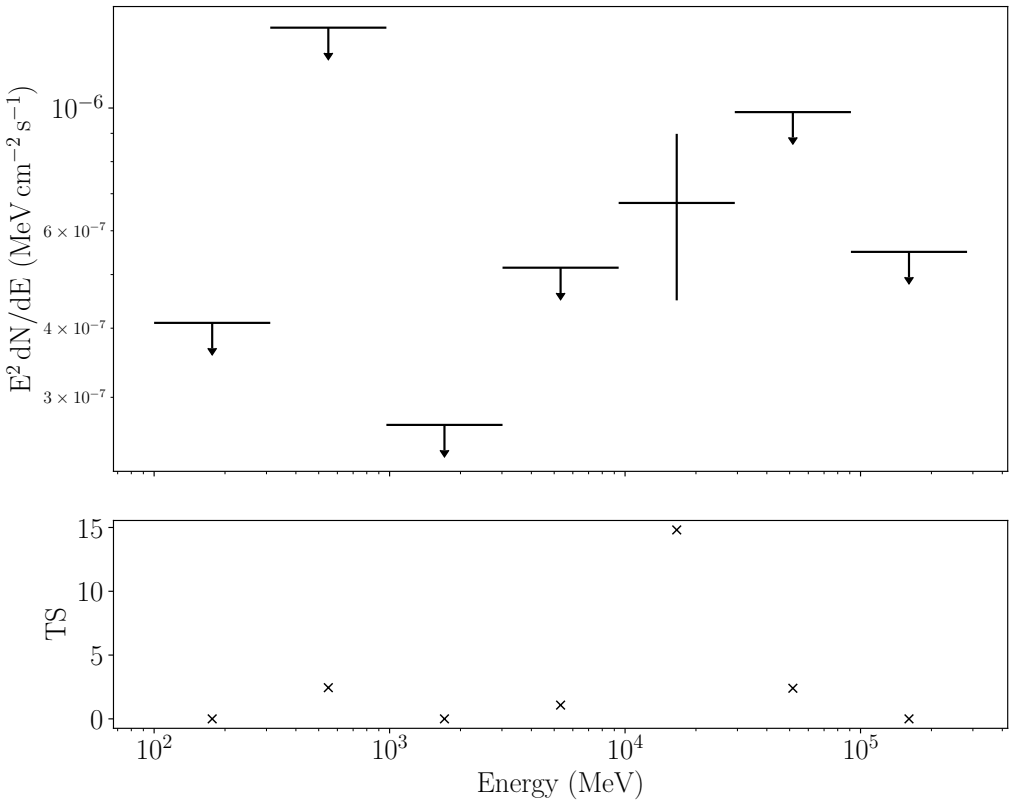

Figure 7.5: The spectral energy distribution of 4U 1708-40 with two energy flux bins per decade and the respective TS values of these bins. 95% confidence upper limits are placed on flux for any bin where TS < 4. No spectral fit is done for this SED, as all but one bin have upper limits.

in terms of angular offset from 4U17, and all are much less significant than the supernova remnant: the unidentified source 4FGL J1712.9-4105 (TS = 24.9 and an angular offset of 0.273°), the blazar 4FGL J1715.4-4025 (TS = 72.7, angular offset: 0.716°) and the unidentified source 4FGL J1717.5-4022 (TS = 29.4, angular offset: 1.087°) (Figure 7.7). Given that this γ-ray excess is only measurable at $E > 10\,\mathrm{GeV}$ the PSF of *Fermi*-LAT will be at its optimal 0.15°, confusion with any of these nearby known sources is unlikely.

Many XRBs have log-parabola spectral shapes, and hence this excess could represent the peak of a log-parabola in the SED of 4U17, and therefore further observation time would be needed for a detection of this LMXB.

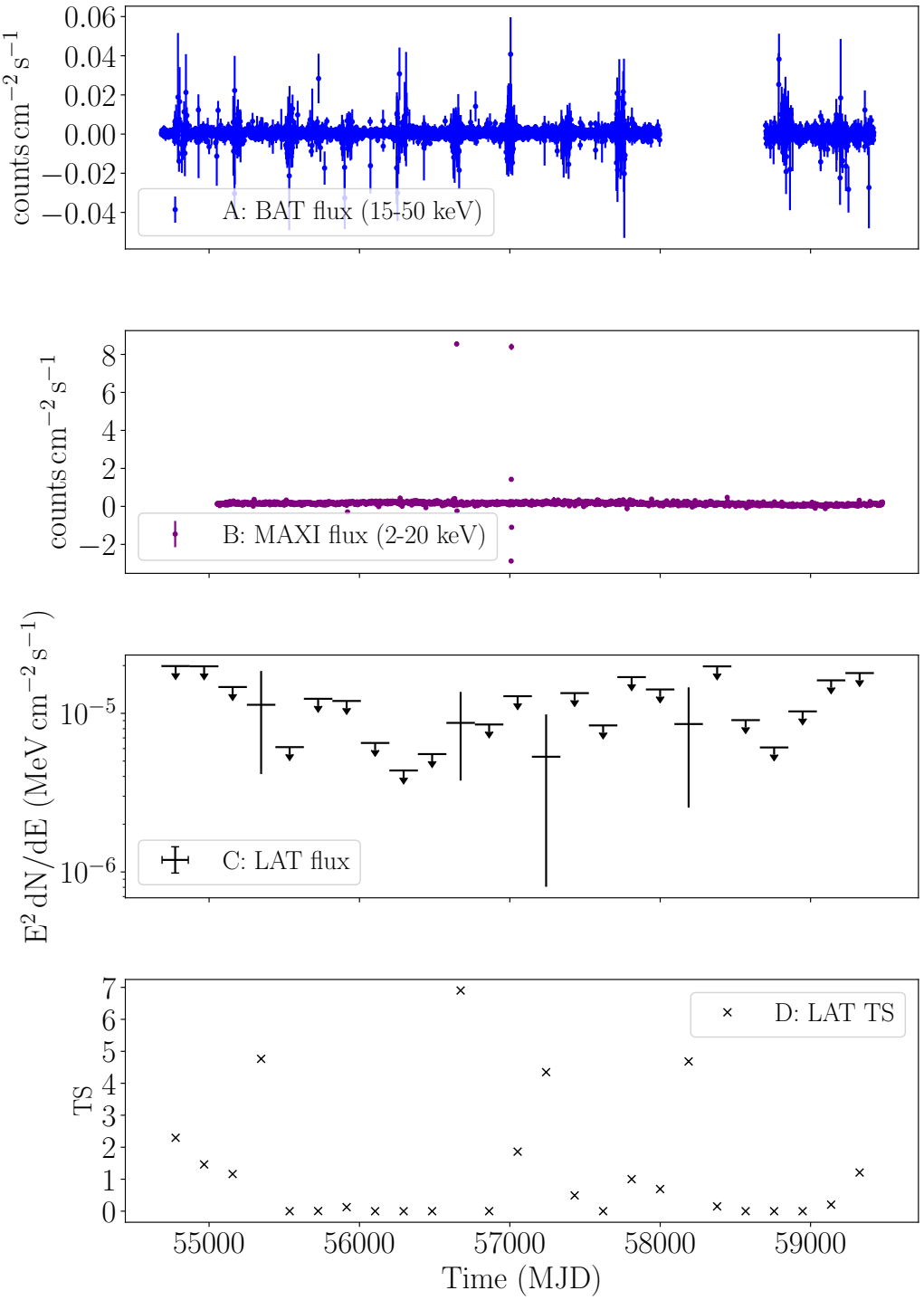

Figure 7.6: Panels A and B show the daily hard and soft X-ray fluxes from *Swift*-BAT and MAXI respectively for 4U 1708-40. Panels C and D show the energy flux and respective TS of the coincident γ-ray excess where 95% confidence upper limits are placed on any bin where TS < 4. A gap in *Swift*-BAT observations where the source is not detected is present.

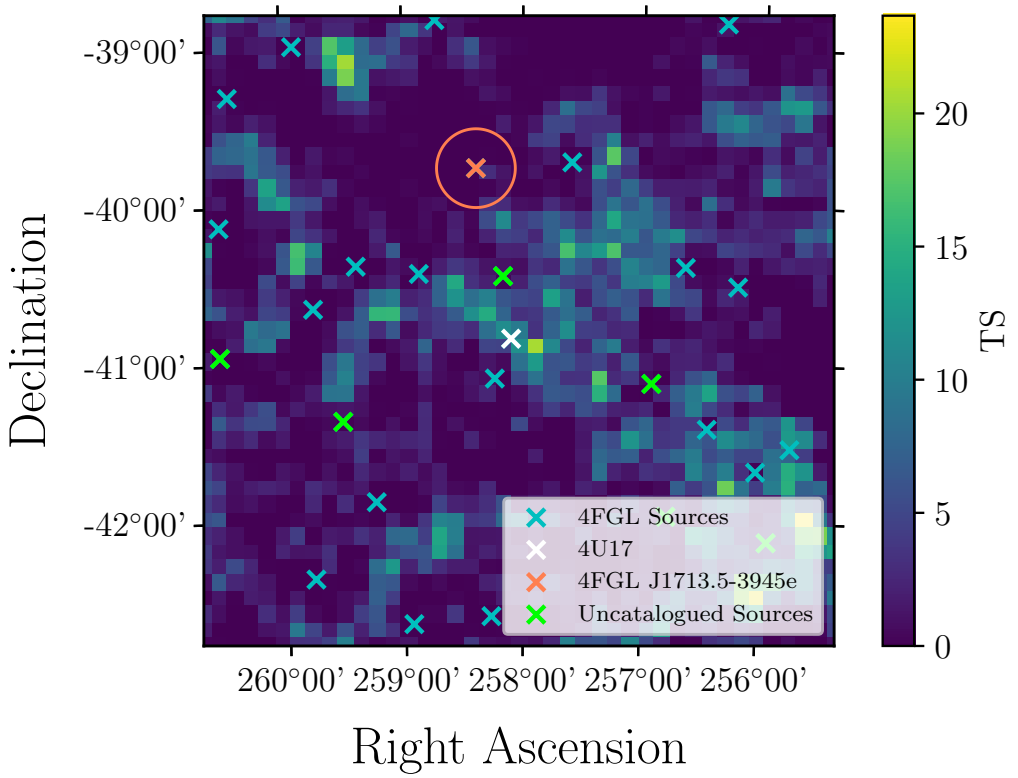

Figure 7.7: The TS map of the central 4° of the 4U 1708-40 ROI over the full mission time. Here, the positions of the closest 4FGL sources are indicated in blue, whilst the position of 4U 1708-40 is indicated in white. The positions of uncatalogued sources are indicated in green. Bin widths are 0.1°. The orange circle denotes the spatial extent of the extended supernova remnant RX J1713.7-3946.

7.5 GRO J1655-40

GRO J1655-40 (Zhang et al. 1994 and following publications*) (aka V1033 Sco, henceforth referred to as GRO16) is a microquasar LMXB consisting of a black hole and an F-type companion star (e.g. Tingay et al. 1995, Hjellming and Rupen 1995, Bailyn et al. 1995 & Buxton and Vennes 2001). GRO16 has been the target of several searches for high energy γ-ray emission, both during, and outside of, its outburst periods; these searches have so far yielded only upper limits (Levinson and Mattox 1996 & Reimer and Iyudin 2003).

*There are 14 different IAU Circulars from August to November 1994 all entitled 'X-Ray Nova in Scorpius', all by different authors with different instruments. I believe Zhang et al. (1994) is the first one, so that is the one I reference for the discovery of the system.

I observe a weak γ-ray excess from the position of GRO16 with TS = 10.9 ($z = 3.3\sigma$), and find that over the 6 month binned light-curve of this excess, the light-curve p-value indicates that the combined light-curve bins do not reach the 5σ level, unlike the majority of the excesses observed in the survey. Whilst there is a known orbital period of 2.62 days for this system, this period is too short to perform a phased analysis, as error will dominate over such short timescales rendering such an analysis essentially meaningless. The low significance of this excess also prohibits localisation or spectral analysis.

There are two sources within a 1° radius of the excess, neither of which have a known multi-wavelength counterpart or morphology: 4FGL J1712.9-4105 (TS = 66.7 and an angular offset of 0.407°), and 4FGL J1657.4-3917c (TS =50.0, angular offset: 0.859°). Given that these sources are reasonably faint, it is unlikely that source confusion is causing this excess. Therefore it is likely that the excess is independent of any known sources, but due to limited photon statistics cannot be associated with GRO16.

7.6 2S 1711-339

2S 1711-339 (henceforth referred to as 2S17) (Carpenter et al., 1977) is an LMXB burster, with a neutron star accretor and unknown companion star orbiting with an unknown period (Cornelisse et al., 2002). I observe a weak, very marginal excess coincident with the position of 2S17 with TS = 9.31, and in this case the light-curve condition is unfulfilled indicating a lack of any significant γ-ray emission in the light-curve of this source.

Figure 7.8 shows the TS map of 2S17 and the surrounding region, where a weak excess at the position of 2S17 is seen (although this excess is part of a larger, diffuse excess). Several known γ-ray sources are in the vicinity of 2S17; the blazar 4FGL J1716.3-3421 (TS = 91.2, offset: 0.513°), the unknown sources 4FGL J1711.6-3407 (TS = 22.78, offset: 0.556°) and 4FGL J1714.9-3324 (TS = 210, offset: 0.646°) and

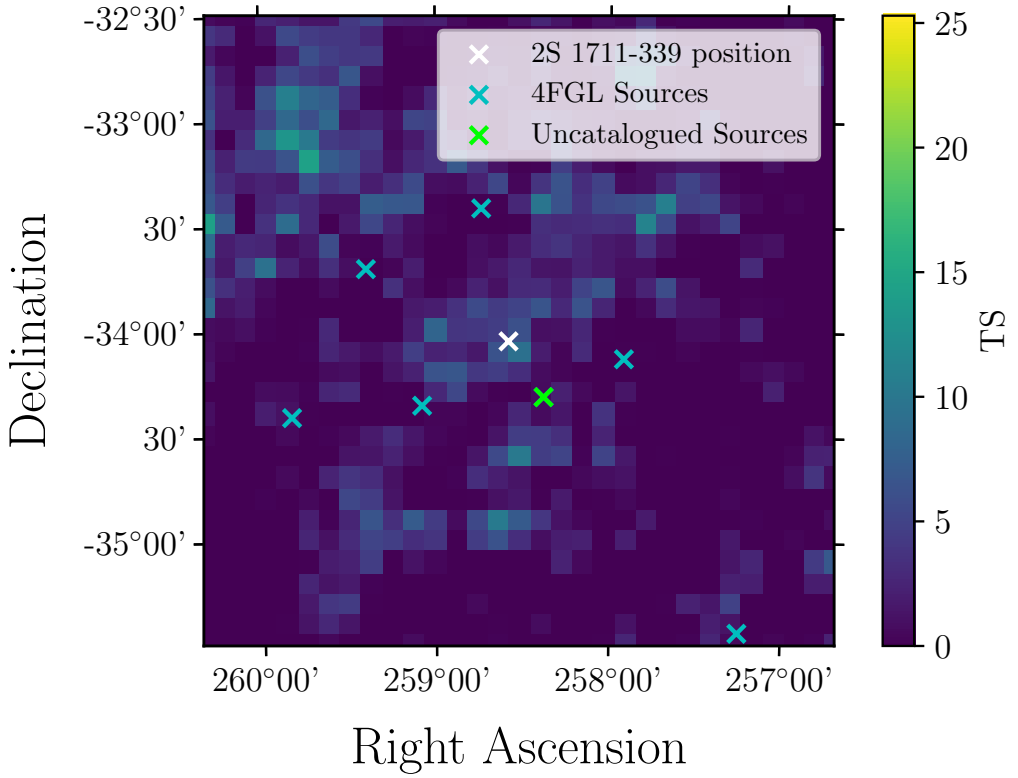

Figure 7.8: The TS map of the central 3° of the 2S 1711-339 ROI over the full observation time. Here, the positions of the closest 4FGL sources are indicated by blue crosses, whilst the position of 2S 1711-339 is indicated with a white cross. The positions of uncatalogued sources are indicated by green crosses. Bin widths are 0.1°.

the Bl Lac type blazar 4FGL J1717.5-3342 (TS = 603, offset: 0.646°) all lie within 1° of 2S17. Additionally, I observe an uncatalogued source which is designated PS J1713.5-3418 (TS = 16.7, offset: 0.314°).

Given the lack of significant emission in the 2S17 light-curve, and the lack of an orbital period, temporal analysis for this source is not possible. Additionally, given the marginal significance of the excess, positional and spectral analysis are also not possible for this excess. Therefore whilst it is possible that this excess represents weak γ-ray emission from 2S17, the evidence is weak other than positional coincidence. Furthermore, as there are a number of nearby γ-ray sources, and the excess is on the galactic plane, source confusion could be responsible for this excess, although again, it is impossible to prove this.

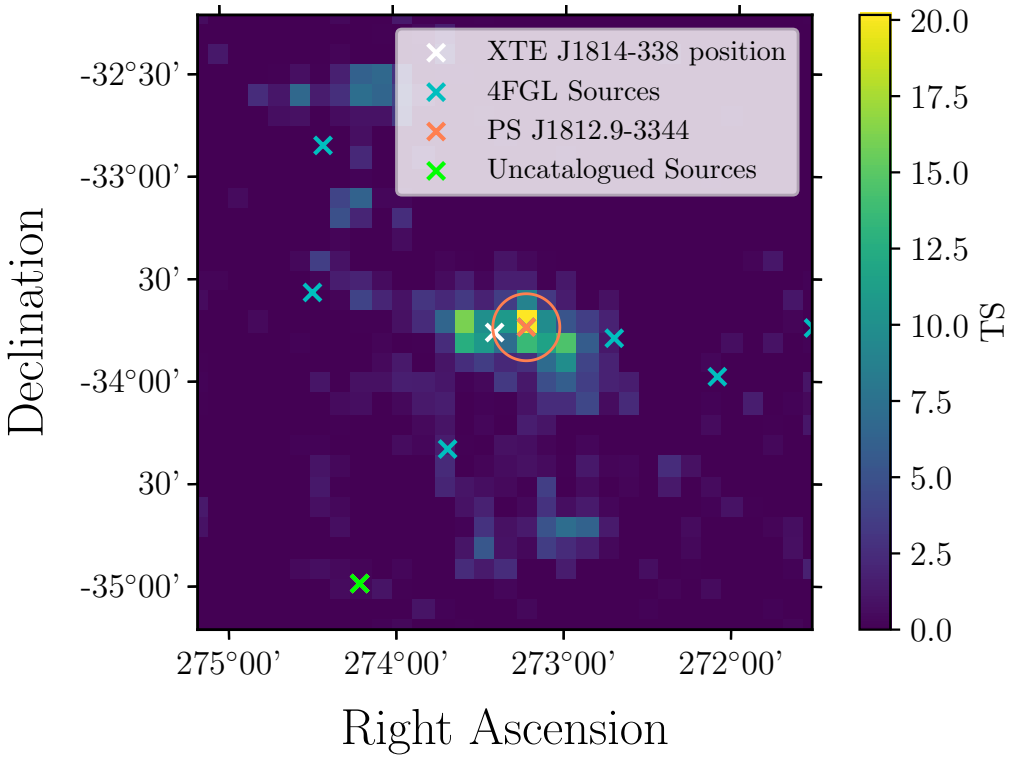

Figure 7.9: The TS map of the central 3° of the XTE J1814-338 ROI over the full observation time. Here, the positions of the closest 4FGL sources are indicated by blue crosses, whilst the position of XTE J1814-338 is indicated with a white cross. The position of PS J1812.9-3344 is indicated by the orange cross, with the 95% positional uncertainty of PS J1812.9-3344 being shown by the orange circle. The positions of uncatalogued sources are indicated by green crosses. Bin widths are 0.1°.

7.7 XTE J1814-338

XTE 1814-338 (henceforth referred to as XTE18) (Steeghs 2003, Krauss et al. 2003, Markwardt and Swank 2003), is an LMXB system consisting of an accreting millisecond X-ray pulsar and an unclassified companion star, orbiting one another with a period of 0.178 days (Markwardt et al., 2003). Additionally, the system is a known thermonuclear X-ray burster (Strohmayer et al., 2003). I find a persistent γ-ray excess with TS = 20.5 to be spatially coincident with the position of XTE18, with an angular offset of 0.157° and a 95% uncertainty of 0.164°. This excess is designated PS J1812.9-3344. In addition, the light-curve condition for this LMXB

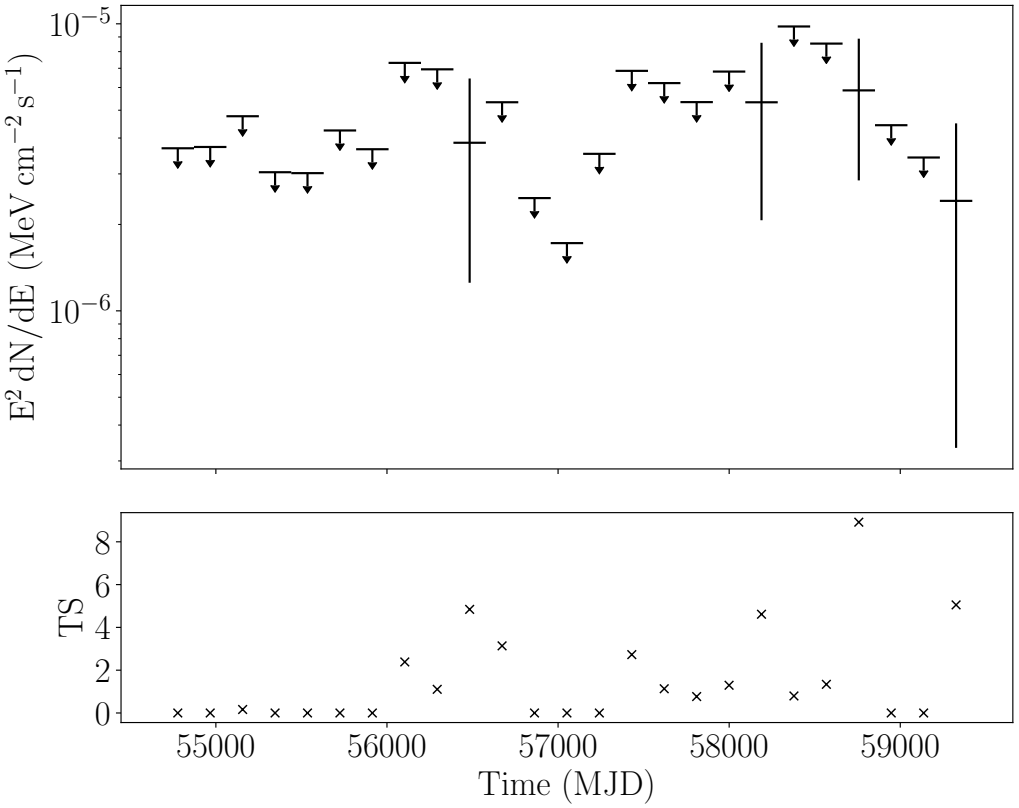

Figure 7.10: A light-curve showing the energy flux and respective TS values of PS J1812.9-3344 (the source coincident with XTE 1814-338) over the full LMXB analysis time. 95% upper confidence limits are placed on any energy flux bins where the corresponding TS < 4.

is fulfilled, indicating that there is γ-ray emission in at least some of the bins in the light-curve.

Figure 7.9 shows the ROI around XTE18, with PS J1812.9-3344 clearly corresponding to the peak of the γ-ray excess, slightly offset from the position of XTE18. As $z < 5\sigma$ for PS J1812.9-3344, there are insufficient photon statistics to perform a positional localisation for PS J1812.9-3344, making it difficult to associate with XTE18, as the binary lies almost at the 95% uncertainty boundary, meaning that the spatial coincidence between the excess and binary is marginal. Furthermore, I observe a weak γ-ray source slightly to the East of PS J1812.9-3344. This source is the unassociated 4FGL J1810.8-3347 (TS = 36.1, offset from XTE18: 0.584°), and given it's relatively low significance, I find it is unlikely to be causing source

confusion with PS J1812.9-3344.

Figure 7.10 shows the γ-ray light-curve of PS J1812.9-3344; where I observe 4 energy flux bins in the significance range, TS $>$ 4 and TS $<$ 9 and TS $<$ 4 otherwise. Given that the flux values of the light-curve are all roughly consistent with one another, and also consistent with the upper limits, PS J1812.9-3344 does not appear to be a variable source of γ-rays when observed with *Fermi*-LAT.

Given the significance of PS J1812.9-3344, it is unlikely that this source is a fluctuation in the γ-ray background, particularly as XTE18 is located at BII = 7.588°, where the Galactic diffuse emission is less luminous than on-the-plane itself. However, given poor photon statistics and a lack of multi-wavelength data it is not possible to associate PS J1812.9-3344 with XTE18.

7.8 1E 1746.7-3224

1E 1746.7-3224 (Hertz and Grindlay, 1984) (henceforth 1E1746) is low mass X-ray binary with an unclassified accretor and companion star, and an unknown orbital period. I observe no persistent excess with the position of 1E1746, although the light-curve condition is fulfilled in this case.

Figure 7.11 shows the light-curve at the position of 1E1746, where 3 bins are seen roughly in the $2\sigma \leq z < 4\sigma$ significance range, and upper limits are seen otherwise. None of these bins are significant enough to justify an independent analysis of the time periods where the fluxes are detected, as demonstrated in Section 6.1, and and the flux values appear to generally be consistent with one another indicating a lack of detectable variability. X-ray light-curves are not available for 1E1746, hence a multi-wavelength light-curve is not possible. Similarly, as no persistent excess is observed, spectral and positional analysis are also impossible.

The three closest sources to the position of 1E1746 are the unassociated 4FGL J1747.9-3224 (TS = 38.5, angular offset: 0.449°) and 4FGL J1750.9-3301 (TS =

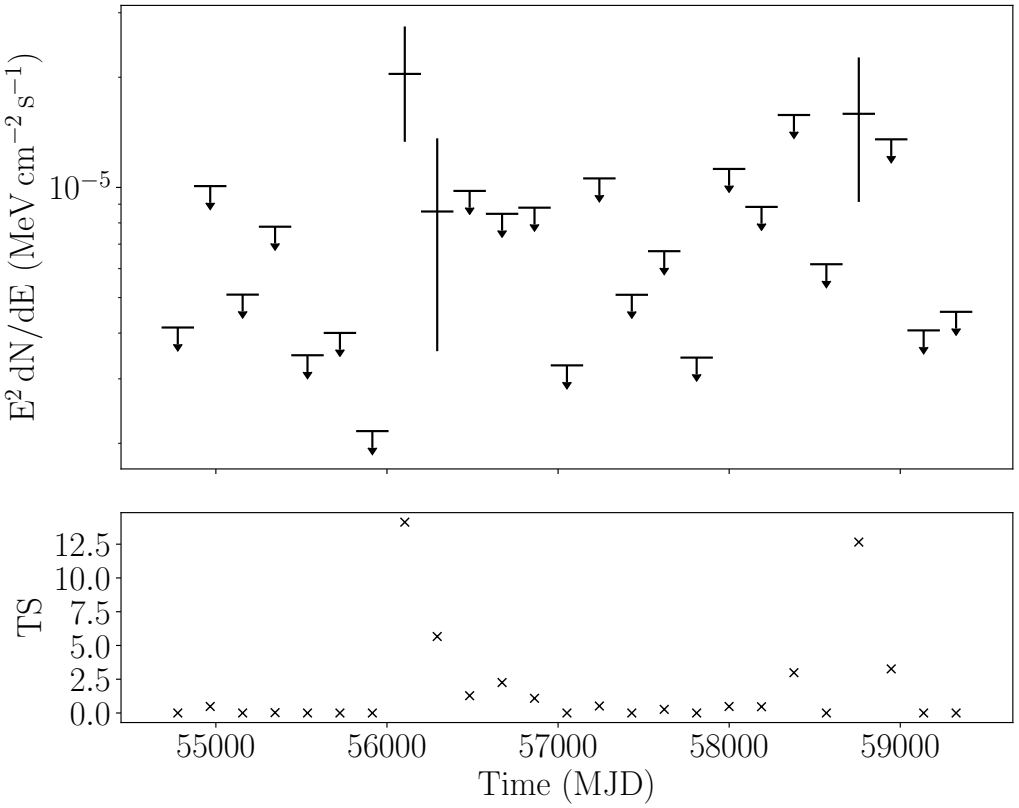

Figure 7.11: A light-curve showing the energy flux and respective TS at the position of 1E 1746.7-3224, where 95% confidence upper limits are placed on any bin where TS < 4.

29.8, angular offset: 0.616°). Source confusion between these and 1E1746's position is unlikely, give their low significances and photon counts. The more significant pulsar 4FGL J1746.8-3239/PSR J1746-3239 (TS = 2790, angular offset: 0.710°) is the most significant source within 2° of 1E1746. Given that this is a much more significant source, it is possible that the excesses observed in the light-curve are due to source confusion with this pulsar. Additionally, as 1E1746 is on the Galactic plane, (BII $= -2.62334°$), these excesses could also be due to background fluctuations in the Galactic diffuse. Regardless, there is no evidence to associate the excesses in Figure 7.11 with 1E1746 itself; hence source confusion is a possible cause of the excesses.

7.9 GRO J1719-24

GRO J1719-24* (Ballet et al. 1993 & Harmon et al. 1993) (henceforth GRO17) is a hard X-ray transient and black hole candidate system with a companion star of unknown spectral class (e.g. Cúneo et al. 2020, Bassi et al. 2020 & Jiang et al. 2020). The system was discovered during a 1993 outburst, and underwent a second detected outburst in 2016 (Negoro et al., 2016). I observe a weak persistent γ-ray excess coincident with the position of GRO17 with TS = 9.1. The light-curve condition is not fulfilled for this excess, meaning that there is a lack of significant γ-ray emission in the light-curve. An orbital period of 0.61 days is known for this system, too short to produce a phase folded light-curve as uncertainties in the orbital period measurement would propagate through each orbit over the 13 years of data used.

Figure 7.12 shows the immediate region around GRO17, with both 4FGL-DR2 sources displayed alongside uncatalogued sources identified by `gta.find_sources`. The γ-ray excess at the position of GRO17 is very weak, with several bins appearing to show very low significance γ-ray emission, probably due to the background diffuse emission. More significant TS peaks are seen within approximately 0.5° of GRO17, and no TS peak appears at the position of GRO17 itself, suggesting that the excess at the position of GRO17 may be due to one of these offset excesses. Given the absence of any sources close to the position of GRO17, it is unlikely that confusion with a known source is responsible for this γ-ray excess.

Although this excess does not satisfy the light-curve condition, given that the X-ray flux is known to be variable in the lifetime of *Fermi*-LAT I nonetheless plot the γ-ray light-curve in Figure 7.13, alongside the X-ray light-curve from *Swift*-BAT and MAXI. The 2016 outburst is clearly seen in the X-ray data by the sharp rise in flux followed by a decay over a period of 6-12 months. There is a 3σ bin in the γ-ray light-curve at the start of the observation time which does not correspond to

*also known as GRS 1716-249

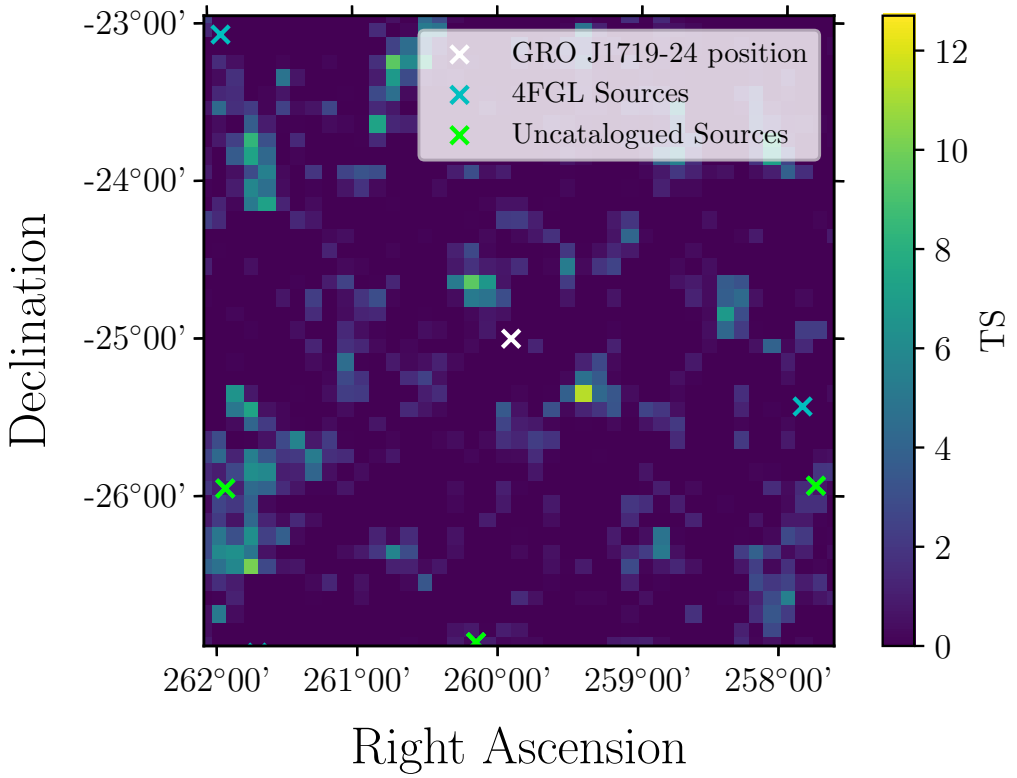

Figure 7.12: The TS map of the central 4° of the GRO J1719-24 ROI over the full observation time. Here, the positions of the closest 4FGL sources are indicated in blue, whilst the position of GRO J1719-24 is indicated in white. The positions of uncatalogued sources are indicated in green. Bin widths are 0.1°.

any enhancement in X-ray flux and precedes the 2016 outburst by approximately 7 years. A second, very marginal 2σ enhancement is seen following the outburst, indicated by the vertical grey dotted lines overlaid on Figure 7.13. The evidence for association of either of these transient excesses or the persistent one is non-existent beyond spatial coincidence, as the emission is too insignificant for further analysis.

7.10 GS 1826-238

GS 1826-238 (Makino, 1988) (henceforth GS1826) is a neutron star LMXB burster (e.g. Bazzano et al. 1997a, Ubertini et al. 1999a, & Zamfir et al. 2012) with a 2 hour orbital period (Homer et al., 1998). There is no persistent γ-ray excess coincident with the position of GS1826, although the light-curve condition is fulfilled which

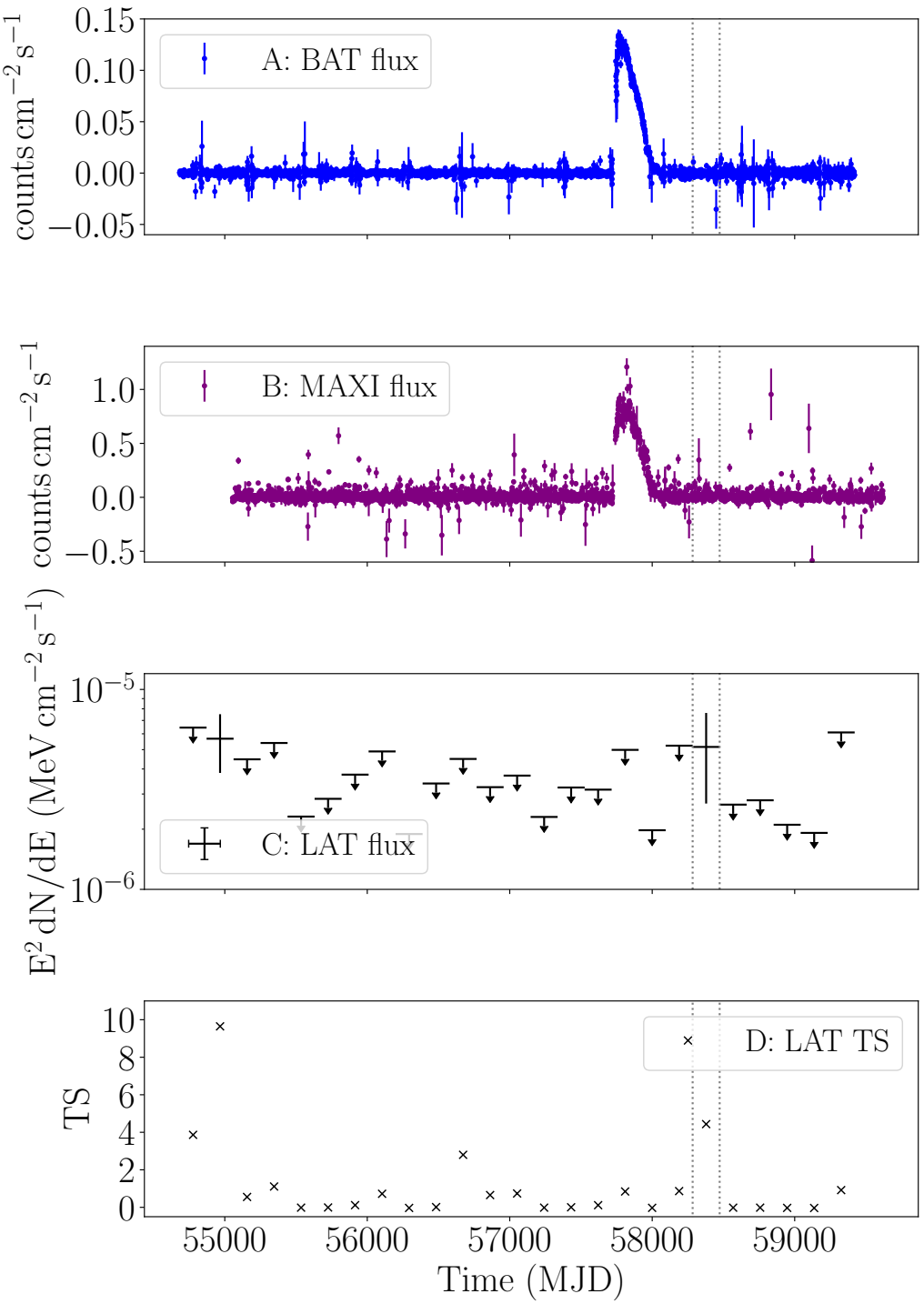

Figure 7.13: Panels A and B show the daily X-ray flux from *Swift*-BAT and MAXI respectively for GRO J1719-24. Panels C and D show the energy flux and respective TS of the excess coincident with GRO J1719-24 where 95% confidence upper limits are placed on flux for any bin where TS < 4. The grey dotted lines indicate the start and end of the 6 γ-ray bin where a TS > 4 flux measurement is made following the 2016 X-ray outburst.

indicates that there is some significant γ-ray excess in the light-curve of the LMXB.

Figure 7.14 shows the X-ray and γ-ray light-curves of GS1826. Over the mission time of both MAXI and *Fermi* the X-ray flux of GS1826 steadily increases, and there appears to be a γ-ray excess earlier in the light-curve when the LMXB is in a lower flux state. This γ-ray excess is bounded on the light-curve plot by the vertical grey dotted lines, and appears from MJD 55062 - 56009, a period of approximately 31 months (or 5 bins). During this period, I measure a flux value in every bin except the midpoint bin of the excess, where an upper limit is recorded. Using the broad methodology followed for the HMXB SAX J1324.4-6200, The ROI during only MJD 55062 - 56009 is considered, once again performing data optimisation and fitting a new model. I find that the TS of the excess during this 30 month period increases from the TS < 9 calculated over the full observation time to 27.6, or 5.3σ during the 31 month excess.

Figure 7.15 clearly displays this γ-ray excess centered on the position of GS1826; source localisation shifts it by only very slightly by 0.0567°, well within the most stringent 68% positional uncertainty radius of 0.0824°. The coordinates of the localised source are LII $= 9.350^\circ \pm 0.524^\circ$, BII $= -6.0412^\circ \pm 0.564^\circ$, positionally coincident with GS1826. The closest source to the position of GS1826 is the variable BL Lac blazar 4FGL J1829.0-2417/1RXS J182853.8-241746 which is 0.504° away from GS1826 and has a TS of 46.95 over the 30 month excess period. I perform a light-curve analysis of this source over the full observation period in order to rule out the possibility of source confusion between 4FGL J1829.0-2417 and the GS1826 excess. I find no obvious correlation between the two light-curves, such as simultaneous variability (Figure 7.16). Given the dissimilarity between the two light-curves, and the fact that the blazar is excluded from the localised excess positional uncertainty region, this excess is very likely to be independent of the blazar 4FGL J1829.0-2417.

As the excess significance exceeds 5σ, I am able to calculate the spectral energy distribution of the excess shown in Figure 7.17. It is best modelled by a soft power

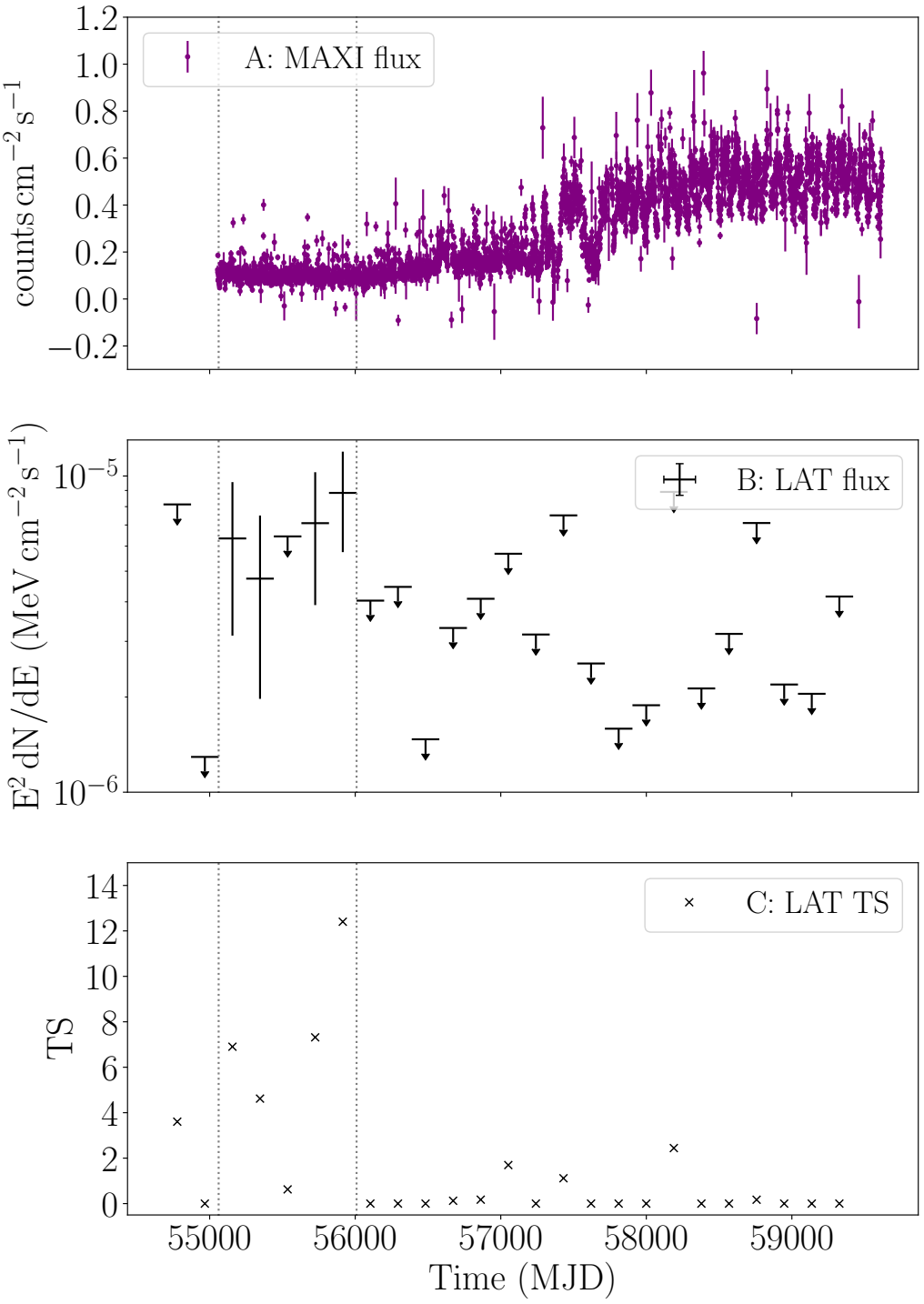

Figure 7.14: Panel A shows the daily X-ray flux of GS 1826-238 measured by MAXI. Panels B and C show the energy flux and respective TS of the excess coincident with GS 1826-238 where 95% confidence upper limits are placed on flux for any bin where TS < 4. The grey dotted lines indicate the start and end of the 30 month γ-ray excess.

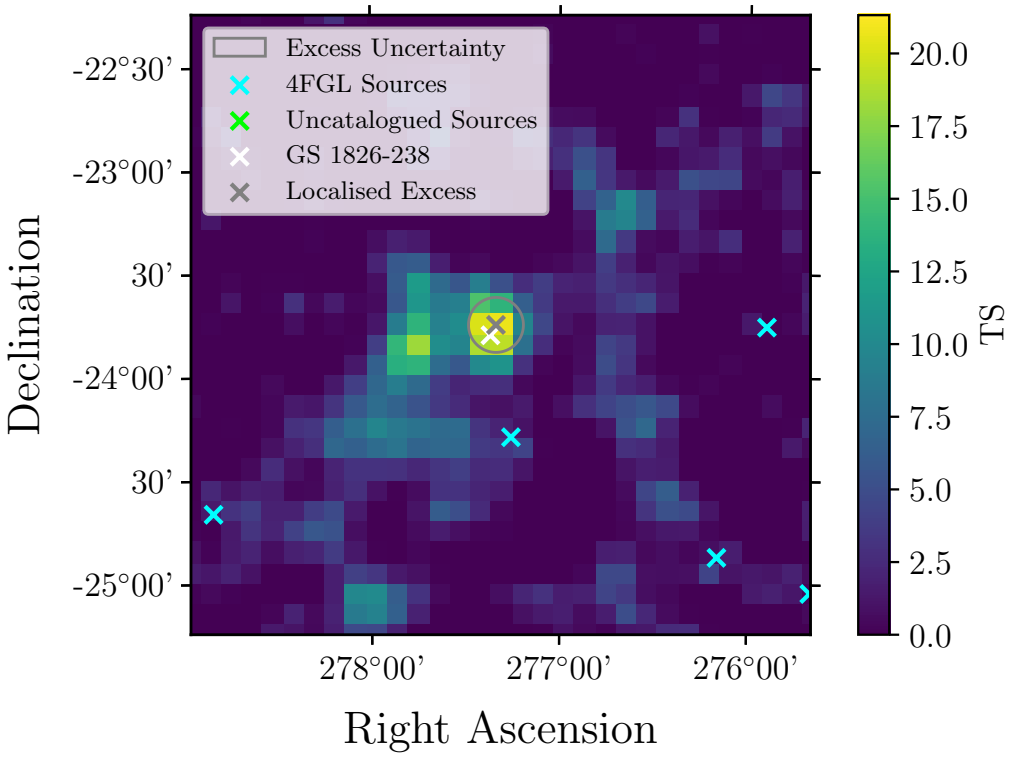

Figure 7.15: The TS map of the central 3° of the GS 1826-238 ROI over the 31 month γ-ray excess period. Here, the positions of the closest 4FGL sources are indicated by the blue crosses, whilst the position of GS1826-238 is indicated by the white cross. The localised position of the γ-ray excess is indicated by the grey cross, with the 95% uncertainty region indicated by the grey circle. Bin widths are 0.1°.

law with a spectral index, $\Gamma = -2.33$, normalisation, $N_0 = 8.93 \times 10^{-13}$ and a scale energy of 1000 MeV. Most LMXBs in the 4FGL have log-parabolic spectra with the exception of 1SXPS J042749.2-670434 which also has a soft power-law spectrum with $\Gamma = -2.38$. The limited photon statistics for the excess make it unlikely that a log-parabola spectrum could be distinguished from a power-law, but the SED of the excess is *broadly* comparable to that of the wider LMXB population.

Whilst the lack of multi-wavelength contemporaneous variability means that it is impossible to associate this transient 30 month γ-ray excess with GS1826 for certain, it is positionally coincident with the LMXB. Furthermore, within the limited statistics, the soft spectral index resembles other LMXB systems. Finally, confusion with the only nearby source is ruled out as the cause of this excess, meaning

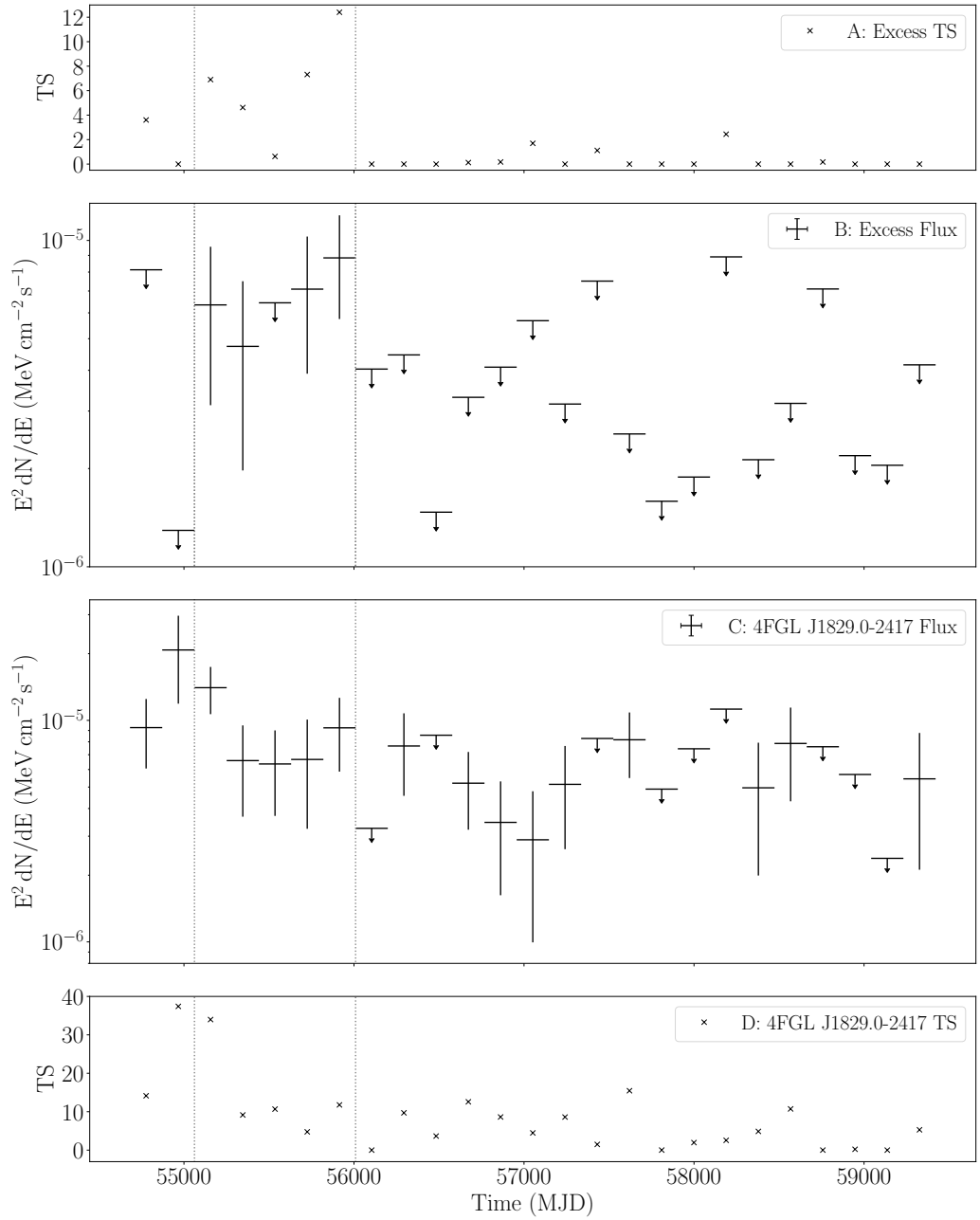

Figure 7.16: Panels A and B show the TS and γ-ray energy flux respectively of GS 1826-238. Panels C and D show the γ-ray energy flux and TS respectively of the blazar 4FGL J1829.0-2417. 95% confidence upper limits are placed on flux for any bin where TS < 4. The grey dotted lines indicate the start and end of the 30 month γ-ray excess.

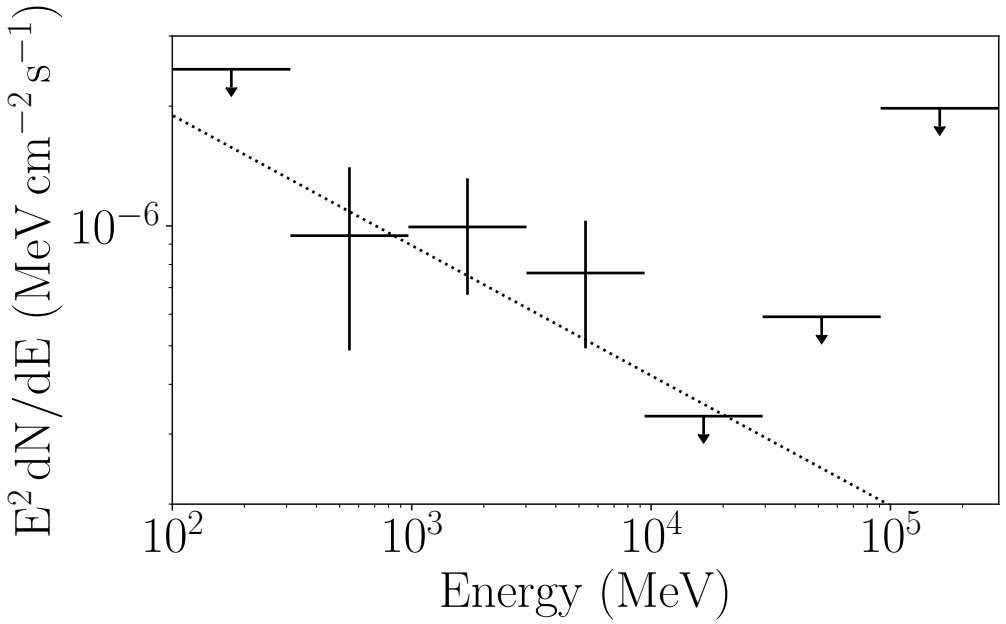

Figure 7.17: The SED of the GS 1826-238 excess, during the 31 month excess period, fitted with a power law spectral model. Upper limits are placed on any bin where TS < 4.

that the only alternative cause of this transient excess is an unresolved background source, such as a blazar.

If this excess does represent γ-ray emission from GS1826 it may be the result of one, or more, physical processes occurring in the system. Given that the accretor in this system is a neutron star, it is possible that this excess is produced by the shocking of the neutron star wind against the dense stellar environment which would cause particle acceleration, and thus γ-ray emission. Whilst orbital modulation is often seen in wind driven systems like these (for example in PSR B1259-63 and LSI +61 303), the orbital period of this system is a short 2 hours. It is impossible to perform an accurate phase-folded analysis over this time, and it is extremely unlikely that the system would be detected over such short timescales unless a stacked phase-folded analysis was used. If the system is wind-driven it is unclear why the excess appears for 31 months, which is far greater than the orbital period of the system.

Alternatively, Figure 7.14 shows that during the time of the γ-ray excess, the X-

ray flux appears to be in a low luminosity state, before beginning to rise as the γ-ray excess ends. It is possible, that the particle acceleration could be linked to the hardness intensity cycle of the system, and that a compact jet (e.g. as in Cyg X-1 (Zanin et al., 2016)) could be causing γ-ray emission at this time, if this time corresponds to the low-hard state. However, the X-ray luminosity increase seen after the end of the excess typically corresponds to an increase in the Lorentz factor of the jet, so one would expect to see an increase, rather than decrease in the flux of the γ-ray excess during the rise in the X-ray flux. Additionally, given that the Lorentz factor in the compact jet during the low-hard state is usually less than 2, this may not be sufficient to produce a noticeable γ-ray excess.

Finally, as this system is an X-ray burster it *may* be possible that these γ-rays are emitted as a consequence of the thermonuclear X-ray bursts from the neutron star. Whilst γ-rays in the MeV-GeV energy range have not previously been observed to originate from X-ray bursters in general, they have been observed to originate from out-bursting cataclysmic variable systems, where similar accretion driven thermonuclear bursts take place on the surface of white dwarf stars. However, this system was not undergoing an X-ray burst at the time of the γ-ray excess, so this seems unlikely.

The wind-driven emission regime is most the likely cause of the γ-ray excess observed to be coincident with GS1826. Wind interactions are responsible for γ-ray emission in most of the observed X-ray binaries with γ-ray emission. Given that a rise in X-ray flux began at the conclusion of this γ-ray emission episode, it is possible that such emission could be observed again when the system is next at a lower X-ray flux level.

7.11 XMMU J181227.8-181234

XMMU J181227.8-181234 (Cackett et al., 2006) (henceforth XMMU18) is a transient LMXB burster consisting of a neutron star accretor in orbit with an unclassified

companion star (in't Zand et al. 2017a & in't Zand et al. 2017b). Since its discovery as a transient X-ray source in 2006, it has been detected by several instruments at various times, most recently in 2020 (Torres et al. 2008, Markwardt et al. 2008 & Chenevez et al. 2020). This source has recently been identified as an ultra-compact binary candidate; no orbital period is known (Goodwin et al., 2019).

I identify a persistent γ-ray excess at the X-ray position of XMMU18 with a TS value of 23.3 (4.8σ). The nearest source to this excess is an uncatalogued source, which I designate PS J1814.0-1750 with TS = 136 and a 0.535° angular offset from the position of XMMU18. Additionally, two 4FGL sources are seen within 1° of the position of XMMU18, these are 4FGL J1811.5-1844 (TS = 303, offset: 0.577°), associated with SNR G012.0-00.1, and the extended source 4FGL J1813.1-1737e (TS = 2130, offset: 0.612°), associated with HESS J1813-178, a pulsar wind nebula. Given the nature of these sources, neither is expected to be variable.

Figure 7.18 shows the TS map of the region around XMMU18 over the full observation time of *Fermi*-LAT. One can clearly see that XMMU is coincident with a somewhat diffuse γ-ray excess, and that PS J1814.0-1750 is surrounded by apparently diffuse, but significant, γ-ray emission. It is unclear whether the excesses coincident with PS J1814.0-1750 and XMMU18 are part of the same structure; this is complicated further by the fact that PS J1814.0-1750 lies on the boundary of the luminous 4FGL J1813.1-1737e. It is therefore possible that some of this diffuse emission is caused by 4FGL J1813.1-1737e. Unfortunately, it is not possible to localise the emission from the position of XMMU18 with `gta.localize` due to a lack of photon statistics, which also prevents meaningful spectral analysis.

Figure 7.19 shows the light-curve of the XMMU18 coincident γ-ray excess, where six bins show some evidence for emission ranging in significance from 2σ to 4σ. Although it is very difficult to say for certain without improved photon statistics, the XMMU18 excess appears to be non-variable, and there appears to be no correlation between the γ-ray and X-ray wavebands.

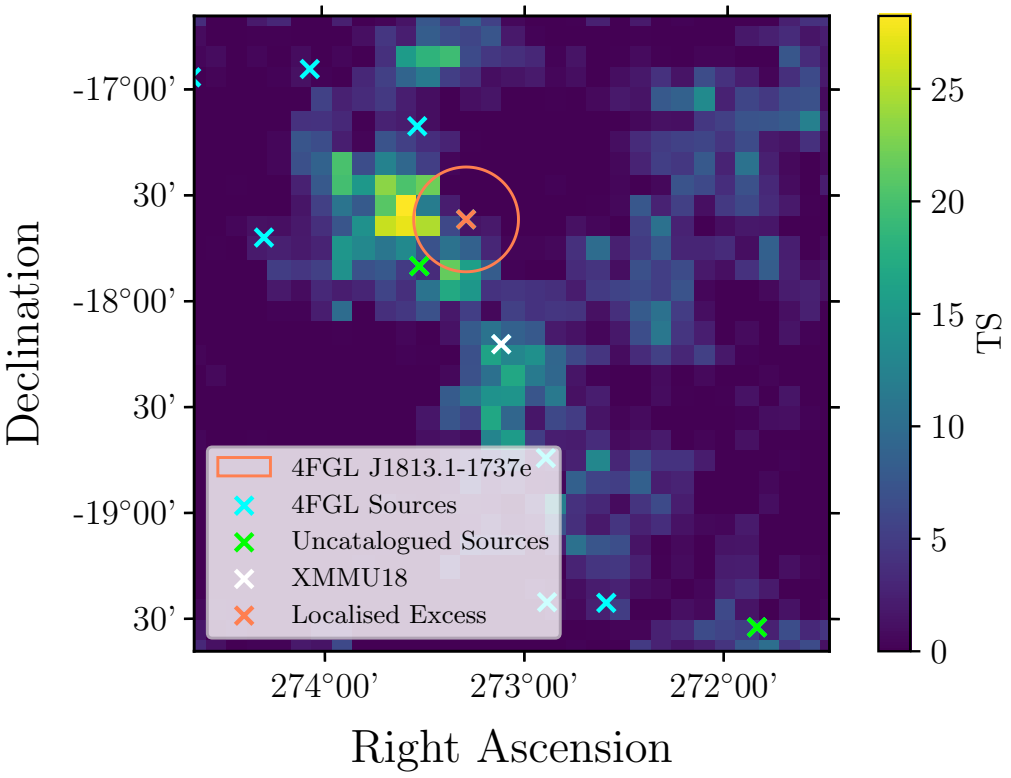

Figure 7.18: The TS map of the central 3° of the XMMU J181227.8-181234 ROI over the full *Fermi* 13 year observation time. Here, the positions of the closest 4FGL sources are indicated by the blue crosses, whilst the position of XMMU J181227.8-181234 is indicated by the white cross. The positions of uncatalogued sources (including PS J1814.0-1750) are indicated by green crosses. The orange circle indicates the extent of the spatially extended pulsar wind nebula: 4FGL J1813.1-1737e, with the orange cross indicating the centroid of this source. Bin widths are 0.1°.

While the excess coincident with XMMU18 could be caused by the binary itself, as the excess appears to belong to a larger γ-ray diffuse structure (seen in Figure 7.18) it is unlikely that this γ-ray emission originates from the binary. This is supported by the lack of apparent variability in the light-curve of the excess (Figure 7.19).

7.12 GRS 1915+105

GRS 1915+105 (Castro-Tirado et al., 1992) is a low-mass X-ray binary, and one of the earliest microquasars discovered after SS 433 was identified as such in 1979 (e.g. Clark and Murdin 1978, Fabian and Rees 1979, Mirabel and Rodriguez 1994,

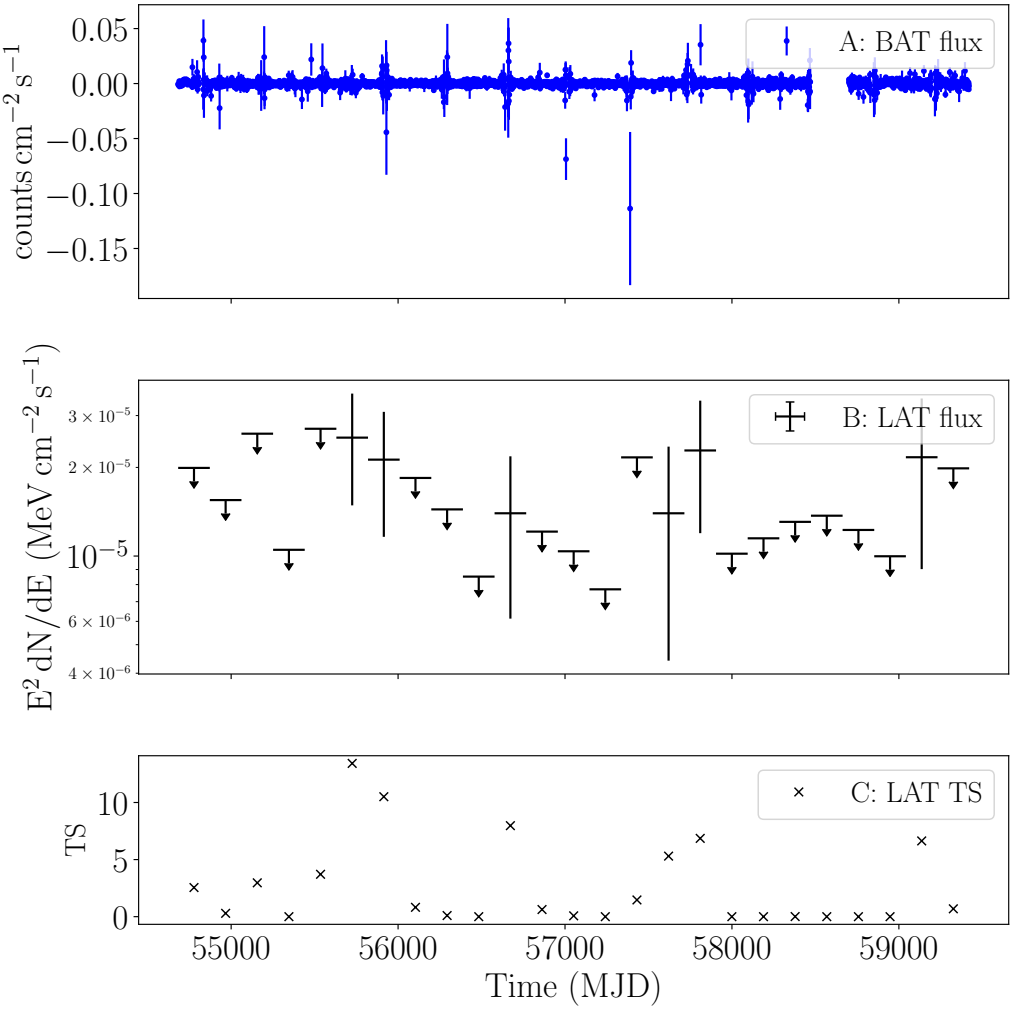

Figure 7.19: Panel A shows the daily X-ray flux of XMMU J181227.8-181234 measured by *Swift*-BAT. Panels B and C show the energy flux and respective TS of the excess coincident with XMMU J181227.8-181234 where 95% confidence upper limits are placed on flux for any bin where TS < 4.

Foster et al. 1996, Belloni et al. 1997). It is one of the best studied X-ray binary systems, with outbursts and flares frequently occurring in the system, most recently in 2020 (Trushkin et al. 2020 & Takagi et al. 2020). Though there were several unsuccessful studies which attempted to discover the nature of the companion star in this binary (Wenzel et al. 1993 & Boeer et al. 1996), its spectral type is now established to be K-M III (Greiner et al., 2001). The accretor is a large stellar mass black hole, of mass $12.4^{+2.0}_{-1.8}\mathrm{M}_{\odot}$ (Reid et al., 2014), with an extremely rapid spin (Middleton et al. 2006 & McClintock et al. 2006). The orbital period of the system is 33.85 days, the longest of any of the LMXBs (Steeghs et al., 2013).

I identify a persistent γ-ray excess coincident with the position of GRS 1915+105 with TS = 18.1 (4.2σ), and also find that the light-curve condition is fulfilled indicating that there is at least one significant ($> 2\sigma$) γ-ray excess in the light-curve generated at the position of GRS 1915+105. Figure 7.20 shows the X-ray light-curve of GRS 1915+105 as seen by both MAXI and *Swift*, together with the γ-ray light-curve as seen by *Fermi*-LAT. I observe that 21 of the 25 bins in the LAT light-curve are upper limits, where the significance of the bin fails to exceed 2σ, and four bins do exceed this threshold, and therefore have energy flux measurements in place of upper limits. The X-ray data show oscillations between a high and low state, associated with recurrent jet activity, before a drop off in X-ray activity from approximately MJD 58300, probably associated with the system entering the low-hard state. The four γ-ray flux points occur during the oscillating 'active' phase, prior to entering the low-hard state. *If* the microquasar is responsible for the production of this γ-ray flux, then this observation matches the theoretical prediction of when γ-ray emission would occur (Fender et al., 2004).

The most recent orbital ephemeris gives an orbital period of 33.85 ± 0.16 days, with the periastron zero-point measured at JD 2455458.68 ± 0.06 Steeghs et al. (2013).This information can be used to produce a phase-folded light-curve for the excess coincident with GRS 1915+105, shown in Figure 7.21. All but two of the phase bins show flux upper limits, with the average TS level lying just below 4,

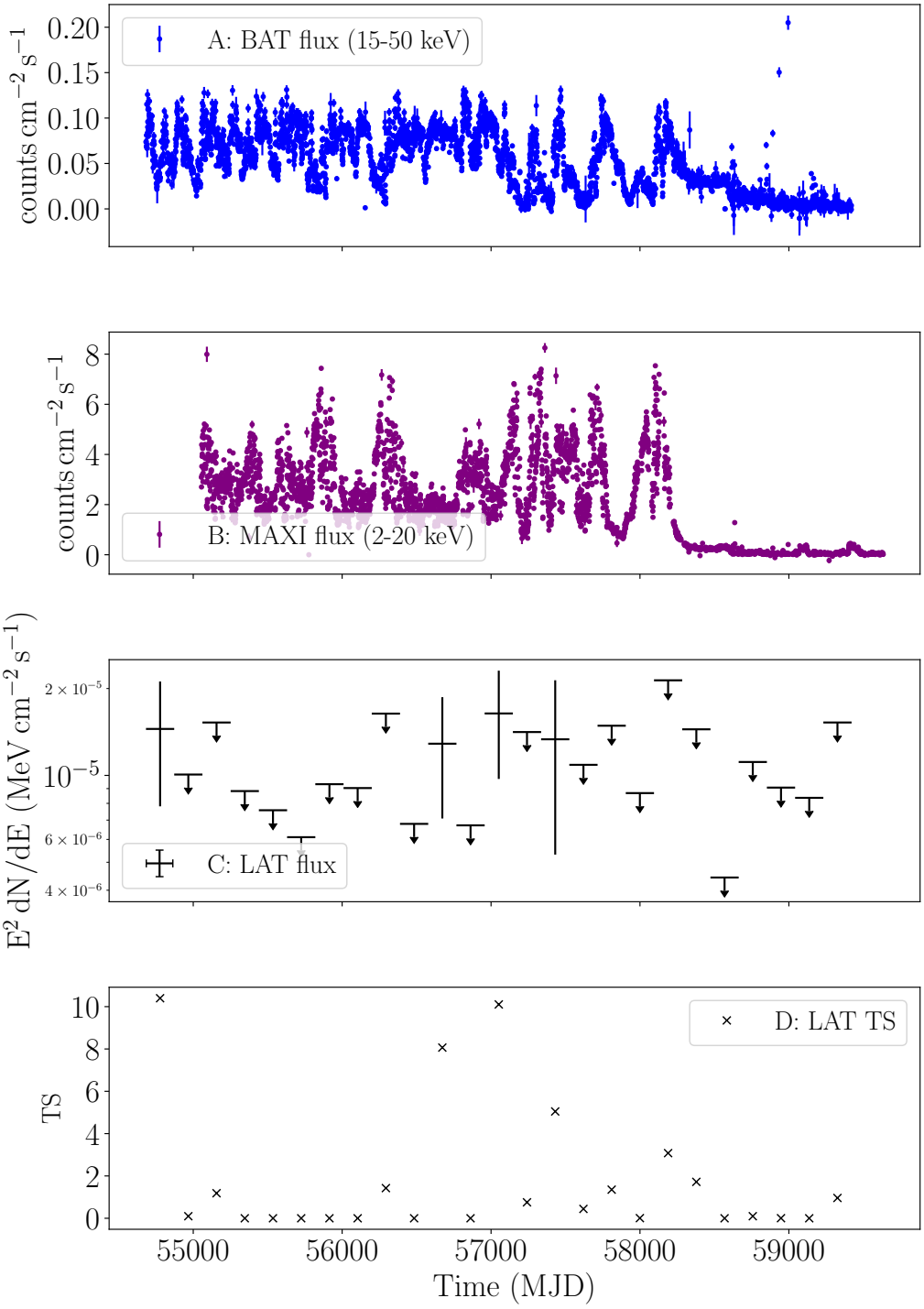

Figure 7.20: Panel A shows the daily X-ray flux of GRS 1915+105 measured by MAXI; Panel B shows the daily X-ray flux of GRS 1915+105 measured by *Swift*-BAT. Panels C and D show the energy flux and respective TS of the position of GRS 1915+105 where 95% confidence upper limits are placed on flux for any bin where TS < 4.

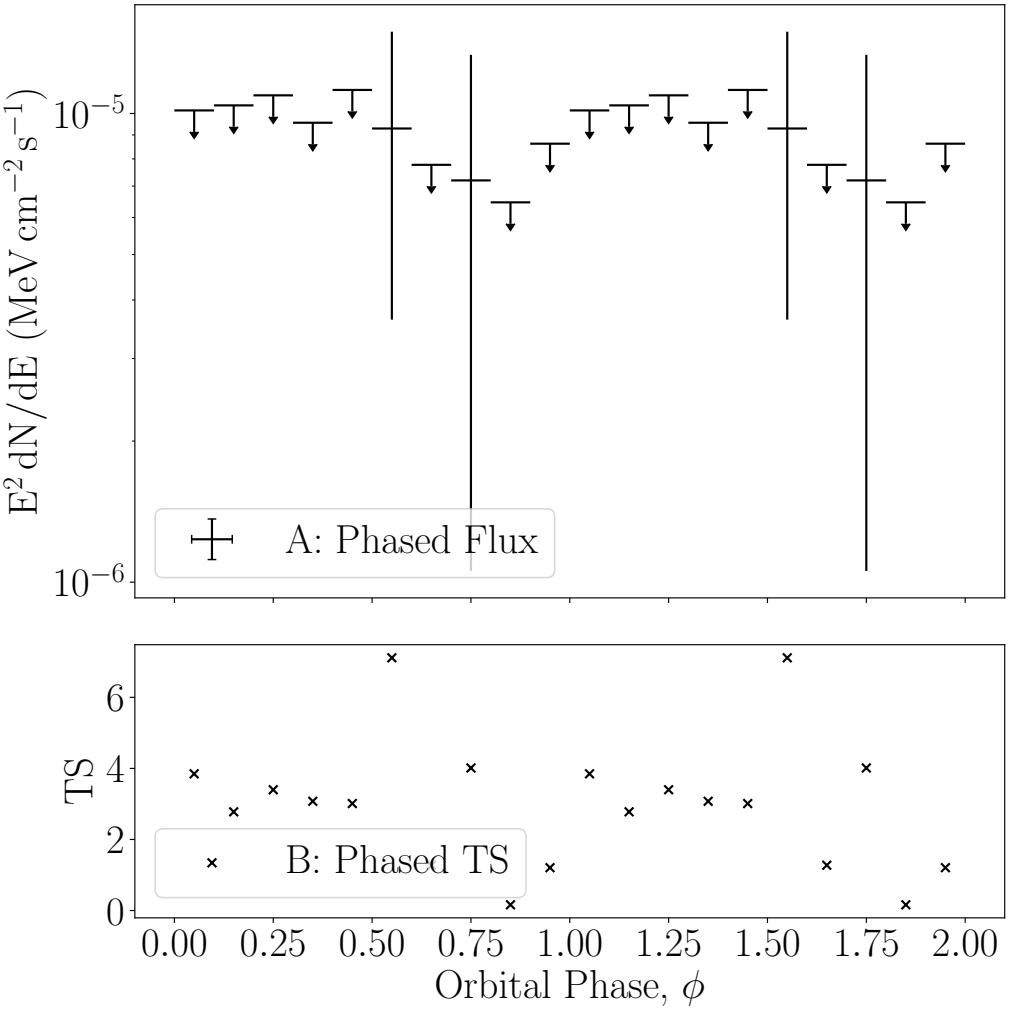

Figure 7.21: The phase-folded light-curve of GRS 1915+105. Panel A shows energy flux against phase, whereas Panel B shows TS against phase. Phase bins are $\phi = 0.1$ in width, and periastron is defined at $\phi = 0$, 1, 2. Two full orbits are shown. 95% confidence upper limits are placed on flux for any bin where TS < 4.

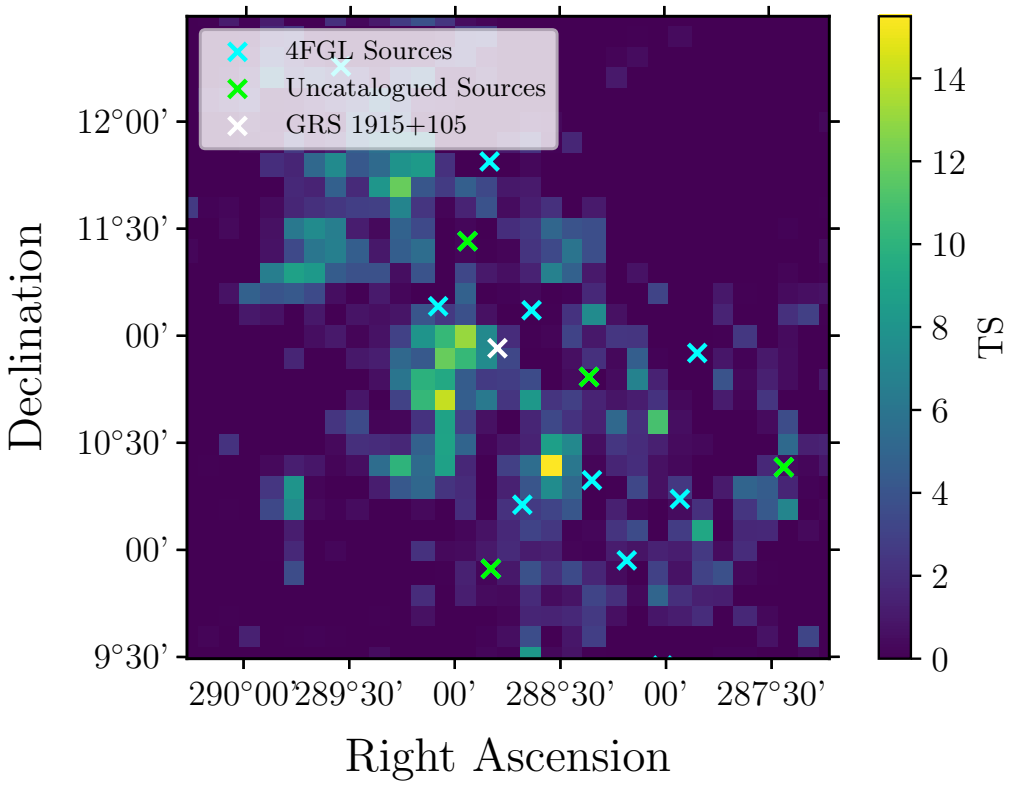

Figure 7.22: The TS map of the central 3° around GRS 1915+105. The position of GRS 1915+105 is indicated by the white cross, with the positions of 4FGL sources indicated by blue crosses. Uncatalogued sources are indicated by green crosses. Bin widths are 0.1° across.

indicating that there is no significant evidence for orbital modulation of the γ-ray emission from this system. This is unsurprising, as GRS 1915+105 contains a black hole, rather than a neutron star, and wind-driven neutron star systems are typically responsible for orbitally modulated γ-ray emission.

Figure 7.22 shows the TS map of the ROI around GRS 1915+105 over the full *Fermi*-LAT observation time. One can clearly see that GRS 1915+105 is coincident with a γ-ray excess, and that this excess appears to be somewhat spatially extended; no X-ray binaries are spatially extended sources in *Fermi*-LAT. Additionally, GRS 1915+10 does not appear to be at the peak of this excess, casting further doubt upon whether this emission can be associated with the binary. The photon statistics are insufficient for a positional localisation to establish whether

the excess is truly positionally coincident with GRS 1915+105.

Close to the position of GRS 1915+105 there are two catalogued 4FGL sources: the unidentified source 4FGL J1914.5+1107c (TS = 61.5, angular offset: 0.238°) and the supernova remnant 4FGL J1916.3+1108/SNR G045.7-00.4 (TS = 326, offset: 0.339°); neither of these sources is variable. Figure 7.20 shows that the γ-ray flux points are reasonably similar values to one another, suggesting that the excess is likely non-variable (although one cannot say for certain with so many upper limits). Given that there is no clear variability in GRS 1915+105 and none in either of the close neighbours, it is difficult to resolve the excess from the two 4FGL sources.

While the bins in the light-curve match the X-ray period in which one would expect activity, evidence for associating this excess with GRS 1915+105 is otherwise weak. The excess may be part of a larger extended source, which is highly unlikely to be produced be an X-ray binary, and source confusion may be responsible for this excess. It is unlikely (though not impossible) that this excess is caused by GRS 1915+105.

7.13 Her X-1 (2A 1655+353)

Her X-1/2A 1655+353 (Tananbaum et al., 1972) is an intermediate mass X-ray binary, consisting of a pulsar and a class B3 star with an orbital period of 1.7 days (e.g. Bahcall and Bahcall 1972, Giacconi et al. 1973 & Middleditch and Nelson 1976). An extremely well studied source, Her X-1 is highly variable in both the X-ray and optical wavebands. Previous evidence for γ-ray emission exists for Her X-1, and my analysis shows a persistent γ-ray excess coincident with the position of this binary with TS = 16.3. The light-curve condition is not fulfilled for this LMXB, indicating a lack of significant γ-ray emission in the light-curve of this source.

Given that the significance of this excess is below 5σ it is not possible to perform a spectral analysis, or positional localisation. The lack of any significant emission in the light-curve renders it impossible to look for variability or any multi-wavelength

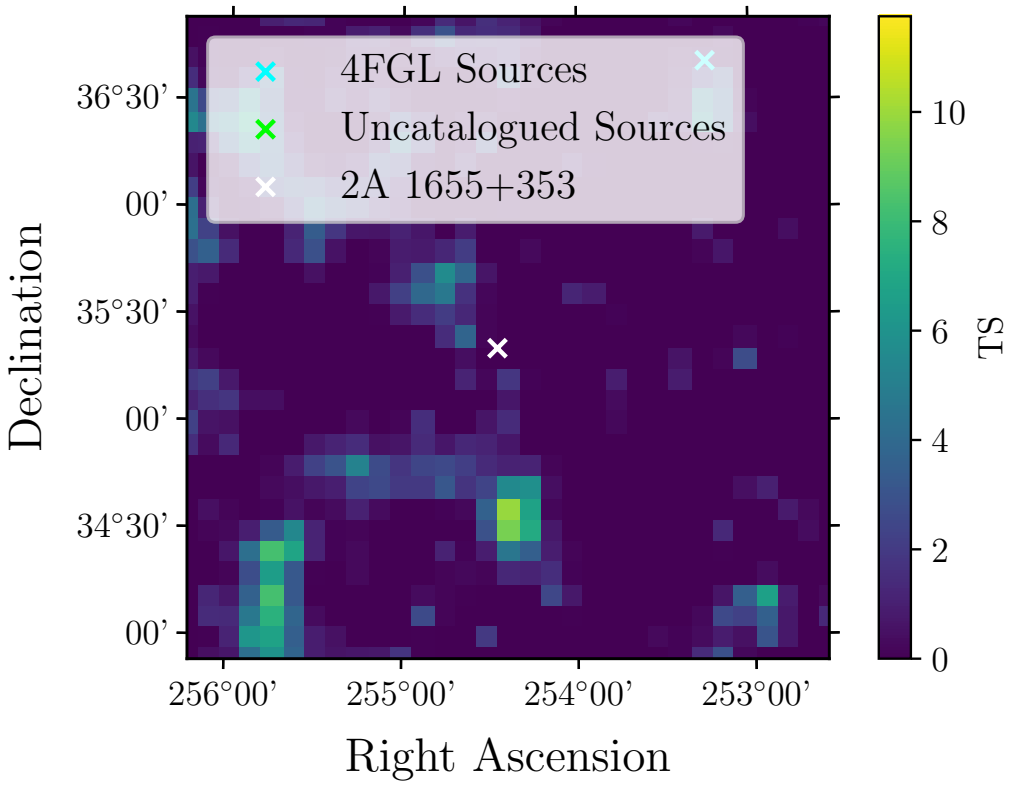

Figure 7.23: The TS map of the central 3° around Hercules X-1/2A 1655+353. The position of Her X-1/2A 1655+353 is indicated by the white cross, with the positions of 4FGL sources indicated by blue crosses. Uncatalogued sources are indicated by green crosses. Bin widths are 0.1° across.

correlations. Given the short orbital period of the system, a phase-folded light-curve analysis is impossible.

Figure 7.24 shows the TS map of the region around Her X-1, which is a sparsely populated region of the sky as seen with *Fermi*. The nearest source to Her X-1 is the (relatively) weak, unidentified 4FGL J1653.0+3640 (TS = 39.7 and offset: 1.657°), and there are no other sources within 3.5° of *Fermi*-LAT. It is therefore extremely likely that the excess observed at Her X-1's position is independent of any other known source, but any association with the binary itself would be based on spatial coincidence alone.

7.14 Confirmed False Positives

Of the 20 LMXBs away from the Galactic centre where I detect either a persistent or transient γ-ray excess, I determine that 7 (1E 161348-5055.1, GX 340+0 (4U 1642-45), 2A 1822-371, SLX 1746-331, 4U 1811-17 (GX 13+1), 4U 1812-12, 4U 1918+15) of these are likely a false positive result. Discussions of each of these are included in Appendix F.

The false positives can be broken down into two categories; the first is where a significant excess appears to be coincident with the position of the LMXB in question. Given the significant photon statistics available, I perform a localisation of this excess, and upon examining the new positional fit, find that the excess is no longer spatially coincident with the position of the binary. The second group of false positive excesses are those which are definitely due to source confusion with another source. In this case, this excess cannot be proven to be independent, and therefore cannot be associated with the LMXB in question.

7.15 Summary of the LMXB Survey

There are 20 LMXBs located outside of the Galactic centre where there is some transient or persistent γ-ray excess suggestive of γ-ray emission from the LMXB. Of these 20, 7 are confirmed false positives and are discussed in Section 7.14 and Appendix F. Of the remaining 13 LMXBs, one has some convincing evidence to associate the γ-ray excess with the LMXB itself: GS 1826-238.

In the case of GS 1826-238, a 31 month excess is observed corresponding to a low luminosity X-ray state. The excess is significant with a z-score of 5.3σ, and is well localised to the position of the binary. The spectrum of the excess is modelled as a soft power law, consistent with the spectra of other LMXB systems. It is unknown whether this emission could be caused by wind interactions, a compact

jet, or thermonuclear X-ray bursts from the surface of the neutron star, making it a particularly interesting candidate in this survey.

The remaining 12 LMXBs are marginal cases where there is no evidence to suggest there is a false positive, but also insufficient evidence to be confident the excess is associated with the LMXB itself.

Figure 7.24: The seventh labour of Heracles, the capture of the Cretan Bull. By B. Picart (1731).

Chapter 8

Surveying the X-ray Binaries IV: The Galactic Centre Low Mass X-ray Binaries

The distribution of LMXBS across the sky is not isotropic and a significant proportion of the Galactic LMXB population can be found in the Galactic centre, due to the presence of a large stellar population in the Galactic bulge (e.g. Revnivtsev et al. 2008, Haggard et al. 2017 & Generozov et al. 2018). Surveying a considerable number of LMXBs in a relatively small and complex region of the γ-ray sky requires a careful and conservative approach, due to the greatly increased chances of source confusion with respect to the rest of the Galactic plane.

The Galactic centre is the position LII = 0°, BII = 0°, and in this section I consider all the LMXBs within 3° angular offset of the Galactic centre which show some evidence for either a persistent or transient γ-ray excess coincident with their position. Eighteen such LMXBs are found in my analysis. Fourteen of which lie within a 1° radius of the Galactic centre: 1E 1740.7-2942, 1A 1742-294, GC X-2, GC X-4, AX J1745.6-2901, 1A 1742-289, GRS 1741.2-2859, CXOGC J174540.0-290031, 2E 1742.5-2858, 1E 1742.2-2857, GRS 1741.9-2853, 1E 1743.1-2852, 1E 1742.9-2849 and XTE J1748-288. The other four LMXBs lie within $1° < r < 2°$ of the

Galactic centre: SLX 1744-300, SAX J1750.8-2900, 4U 1735-28, and IGR J17497-2821. There are no LMXBs with a coincident γ-ray excess in a $2^\circ < r < 3^\circ$ range.

Figure 8.1 shows the Galactic centre region, with all 18 LMXBs plotted along with the 4FGL-DR2 catalogue sources. There is a very strong clustering of LMXBs in the immediate vicinity of Sgr A*, with fewer LMXBs lying further away from the position of Sgr A*. Throughout these following sections I describe the aforementioned 18 binaries as the Galactic centre LMXBs, and investigate the causes of their coincident γ-ray excesses.

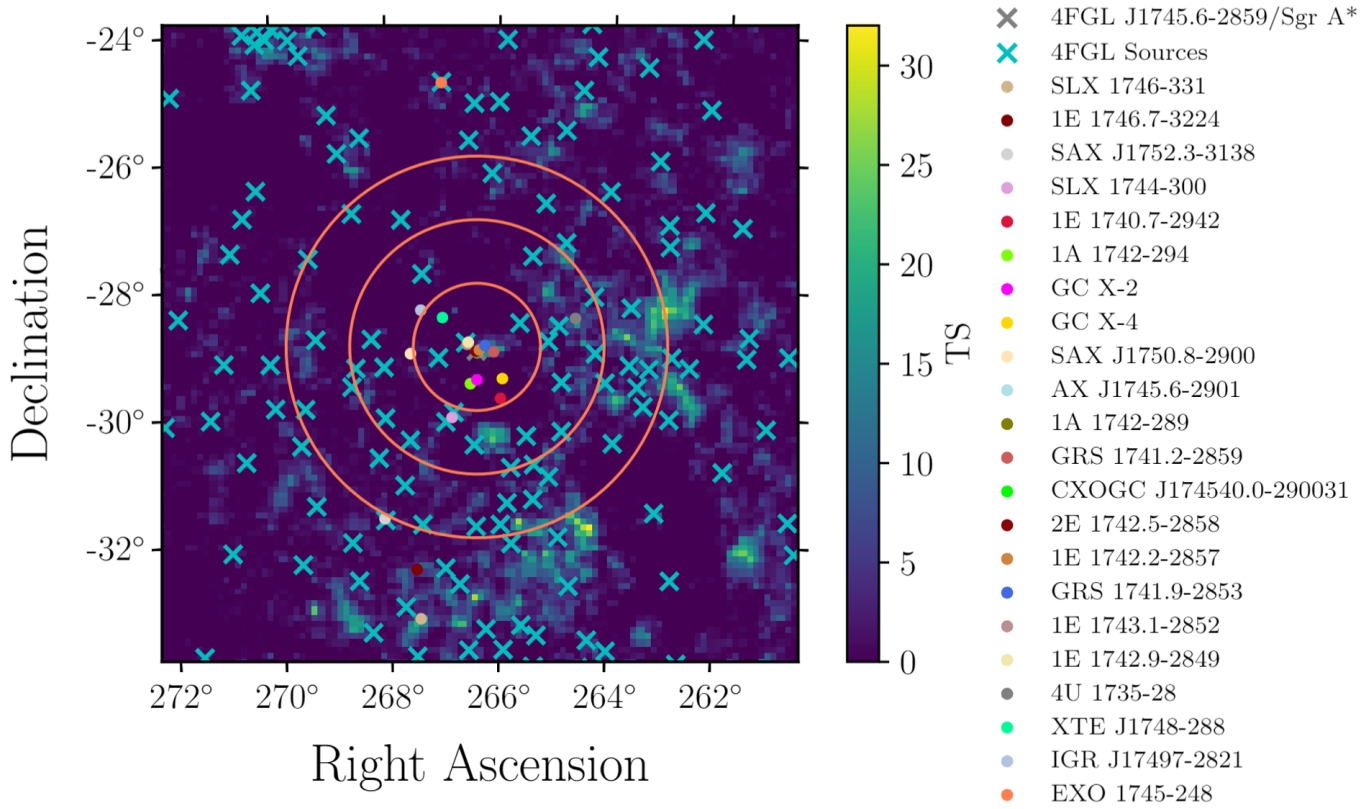

Figure 8.1: A TS map of the Galactic Centre, with 10° width and 0.1° spatial bin widths. This map is centered on LII = 0°, BII = 0°, and is an independent analysis than that of the analyses centered on each LMXB position. Here the crosses indicate γ-ray sources whilst the coloured dots indicate the positions of different LMXB systems. Each LMXB system shown in this plot has a persistent and/or transient γ-ray excess which is spatially coincident with it. Figure 8.1 shows the full legend for this plot. The orange concentric rings have radii of 1°, 2° and 3° centered on the Galactic centre. Note that there is significant overlap between some of the points on this plot, particularly around Sgr A*. Note that SLX 1746-331, 1E 1746.7-3224, SAX J1752.3-3138 and EXO 1745-248 do not lie within a 3° radius of the Galactic centre, and are thus discussed in their own respective sections of this Chapter, they are simply shown on this plot for the purpose of completeness. Note that γ-ray sources are indicated with crosses, and LMXBs with coincident γ-ray excesses are shown by the different coloured dots.

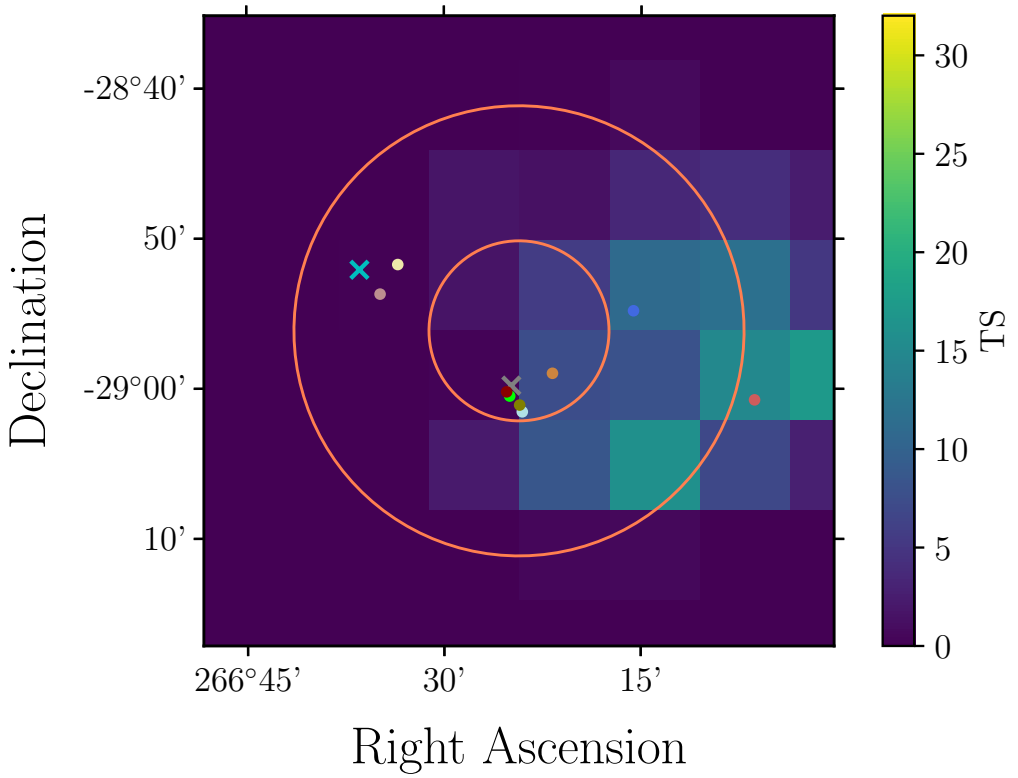

Figure 8.2: A TS map of the inner Galactic Centre, with 0.8° width and 0.1° spatial bin widths. This map is centered on LII = 0°, BII = 0°, and shows the same analysis as Figure 8.1. Here the crosses indicate γ-ray sources whilst the coloured dots indicate the positions of different LMXB systems. Each LMXB system shown in this plot has a persistent and/or transient γ-ray excess which is spatially coincident with it. Figure 8.1 shows the full legend for this plot. The orange concentric rings have radii of 0.1° and 0.25° centered on the Galactic centre.

8.1 Within 0.25° of the Galactic centre

In addition to the analysis of the position of each Galactic centre LMXB, I produce an analysis centered on LII = 0°, BII = 0° using the same analysis parameters and method as the analysis of the LMXB population to investigate the γ-ray sources in the Galactic centre. The TS maps shown in Figure 8.1 and 8.2 are all produced from this analysis, which I will refer to as the 'Galactic centre analysis', to differentiate it from any of the analyses of LMXB ROIs. This independent analysis of the Galactic centre has no sources added to the positions of LMXBs, and can therefore act as a control model with only sources catalogued in the 4FGL-DR2 included; this allows

the independent investigation of the γ-ray properties of the Galactic centre without the effects of adding additional sources to the model*.

8.1.1 Analysing the Galactic centre: 4FGL J1745.6-2859

Offset by 0.061° from the position LII = 0°, BII = 0°, the γ-ray source 4FGL J1745.6-2859 is the closest 4FGL-DR2 source to the Galactic Centre, and the most significant γ-ray source within the 3° radius within which I consider the Galactic Centre LMXBs. My analysis shows that 4FGL J1745.6-2859 has a TS of 19000 (138σ) over 13 years of observations, twice that of the 4FGL-DR2 detection significance of 68σ. 4FGL J1745.6-2859 is catalogued as a point source rather than being spatially extended, as having a log-parabola spectral shape, and a variability index of 2.6, strongly indicating that this source is not variable. 4FGL J1745.6-2859 has been the subject of a number of studies throughout the lifetime of *Fermi*-LAT, as it is associated with the Galactic centre in the 4FGL-DR2, and the Galactic centre is connected to many of the observed high energy features of our Galaxy such as the GeV Galactic Centre excess (Hooper and Goodenough, 2011) and the *Fermi* Bubbles (Su et al., 2010). It is connected with a TeV component, as observed by the H.E.S.S. Collaboration (Parsons et al., 2015); there is a poorly understood spectral break between 20 and 200 GeV. The majority of the emission at the GeV level is thought to originate from the central supermassive black hole of the Milky Way, Sagittarius A* (Malyshev et al. 2015 & Cafardo and Nemmen 2021, and also Balick and Brown 1974, Genzel et al. 1997, Ghez et al. 1998, Ghez et al. 2008, Genzel et al. 2010 & Abuter et al. 2018).

My Galactic centre analysis shows that 4FGL J1745.6-2859 has a strong log-parabola spectral shape, in agreement with previous studies of the source (Figure 8.3). The fit is accurate until approximately 100 GeV, where the spectrum hardens, con-

*For example, adding an additional source at the position of a γ-ray source will split the γ-ray count between the two and decrease the TS of the original source.

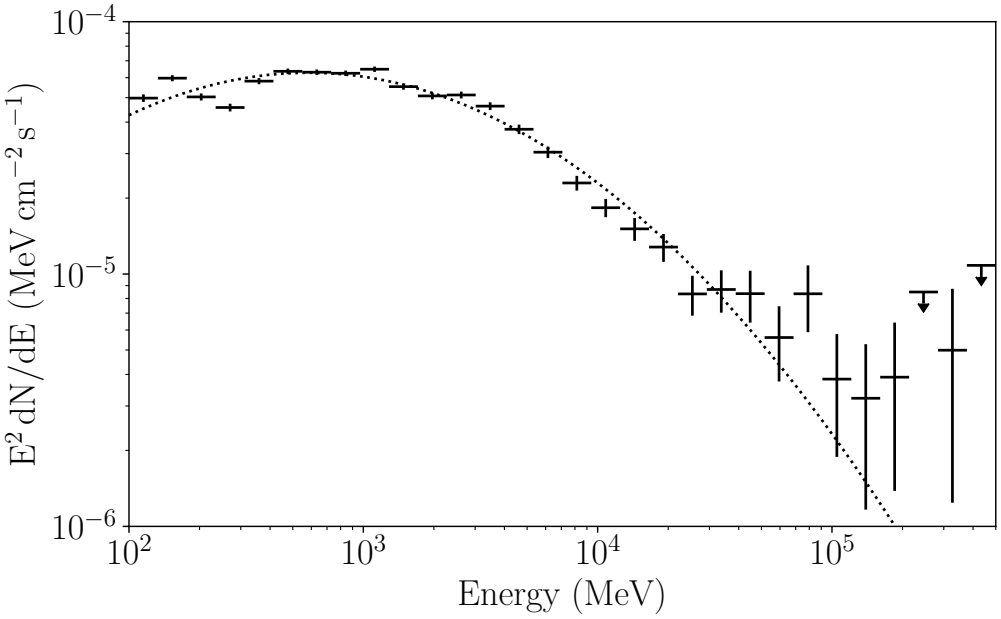

Figure 8.3: The spectral energy distribution of 4FGL J1745.6-2859, the γ-ray source associated with the Galactic Centre and Sgr A*, with 8 energy bins per decade and upper limits placed on bins where TS < 4. A log-parabola spectral shape is fitted to this SED with the best-fit parameters of $\alpha = 2.478 \pm 0.018$, $\beta = 0.1245 \pm 0.0052$, $N_0 = (2.511 \pm 0.005) \times 10^{-12}$ and $E_B = 3.98$ GeV.

sistent with the observed spectral break between the MeV/GeV spectrum and the GeV/TeV spectrum observed with H.E.S.S..

A spatial analysis (localisation and extension fitting) of 4FGL J1745.6-2859 using `gta.localize` finds that the best fit position of 4FGL J1745.6-2859 is LII = 359.9292 ± 0.0132, BII = 0.0082 ± 0.0175. I next test for spatial extension from the source using `gta.extension` and two spatial models: the radial Gaussian and radial disc models. Both models are preferred over a point source model, with the radial Gaussian being marginally more significant with $TS_{ext} = 69.2$ ($z = 8.3$), and the disc model having a significance of $TS_{ext} = 67.1$ ($z = 8.2\sigma$).

During the extended model fitting, I free all point sources within 1° of 4FGL J1745.6-2859, in addition to both components of the diffuse background. Figure 8.4 shows the curve of $\Delta \log(\mathcal{L})$ plotted against the angular widths of the extended models, and a peak is found at an angular width of $0.0684° \pm 0.0050°$, indicating that this is

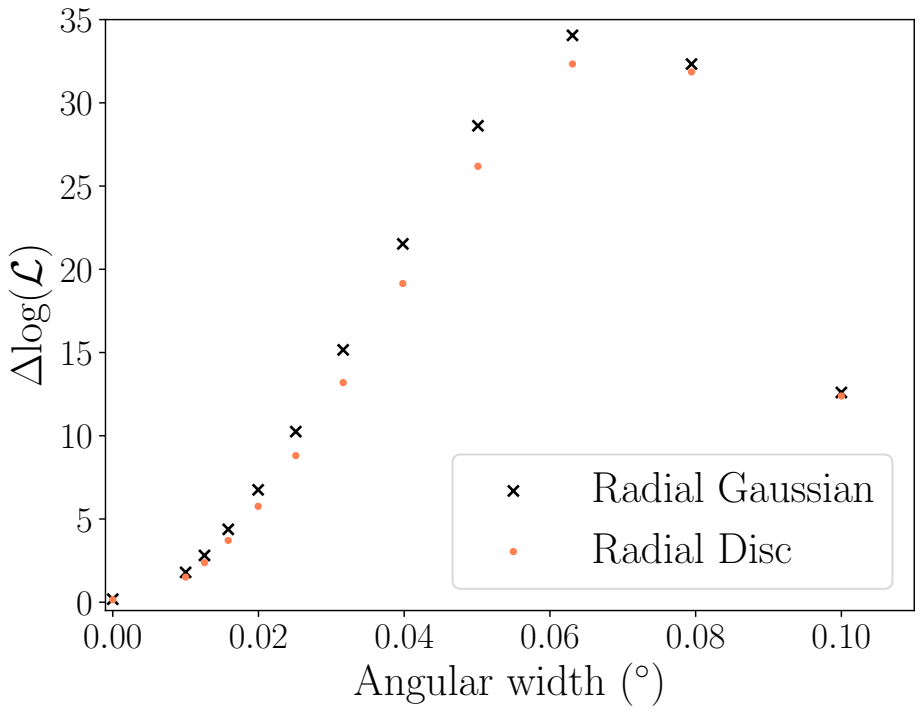

Figure 8.4: The values of $\Delta\log(\mathcal{L})$ from the log-likelihood ratio tests of the (alternate) extended shape hypotheses versus the (null) point source hypothesis at each angular width tested for the extended shapes. The black crosses show values of $\Delta\log(\mathcal{L})$ for the radial Gaussian shape, and the orange dots show the values of $\Delta\log(\mathcal{L})$ for the radial disc shape. The x-axis is constrained from values of angular width ($2r$) from 0° to 0.1°, however widths of up to 1° were tested. Values of $\Delta\log(\mathcal{L})$ in the $0.1° < 2r \leq 1.0°$ range were excluded as these are negative (strongly favouring a point source hypothesis at these widths), and much greater in magnitude than those in the range shown, and would cause the plotting of the positive values to become disproportionately affected by the axis scaling.

the most likely angular width of the radial Gaussian shape for 4FGL J1745.6-2859.

Although the extended model is preferred statistically, given that the extension width itself (0.0684°) is less than the spatial bin width (0.1°), in practical terms this essentially represents a point source. Therefore for the purpose of simplicity, 4FGL J1745.6-2859 will be treated as a point source.

8.1.2 The Innermost Galactic Centre LMXBs

As Figure 8.2 shows, a number of LMXBs are extremely close to the position of 4FGL J1745.6-2859. These are: AX J1745.6-2901, 1A 1742-289, CXOGC J174540.0-290031, 2E 1742.5-2859 and 1E 1742.2-2857. Given the significance and luminosity of 4FGL J1745.6-2859, particularly at lower energies where one would expect the log-parabola/power law spectrum of a γ-ray emitting LMXB to peak all of the LMXBs within the innermost grey circle of Figure 8.2 are broadly spatially coincident with 4FGL J1745.6-2859. Therefore it will not be possible to to resolve any γ-ray emission from these LMXBs from that of 4FGL J1745.6-2859; all of the γ-ray excesses coincident with these LMXBs are likely caused by source confusion with 4FGL J1745.6-2859.

Given the complex combination of sources at the centre of the Galaxy, it is entirely possible that one, or more of these LMXBs are γ-ray emitters and that they are contributing to the γ-ray emission of 4FGL J1745.6-2859, particularly given the similar spectral shape of this source and the LMXB population. However, it is impossible to resolve sources so close together, even at high energies where the resolution of *Fermi*-LAT is optimal.

8.1.3 4FGL J1746.4-2852 and Nearby LMXBs

4FGL J1746.4-2852 is the second closest γ-ray source to the Galactic centre included in the 4FGL-DR2 and is thought to be the pulsar wind nebula PWN G0.13-0.11, which is similarly detected at TeV energies under the name HESS J1746-285 (Abdollahi et al., 2020). Unlike many pulsar wind nebulae, 4FGL J1746.4-2852 is not extended and the association with PWN G0.13-0.11 is tentative as it does not reach the probability threshold of 0.8 for declaring associations using either the likelihood or Bayesian methods in the 4FGL-DR2.

Figure 8.5 shows the spectral energy distribution of 4FGL J1746.4-2852, a log-parabola peaking in the 1-10 GeV range. An extension fit with `gta.extension`

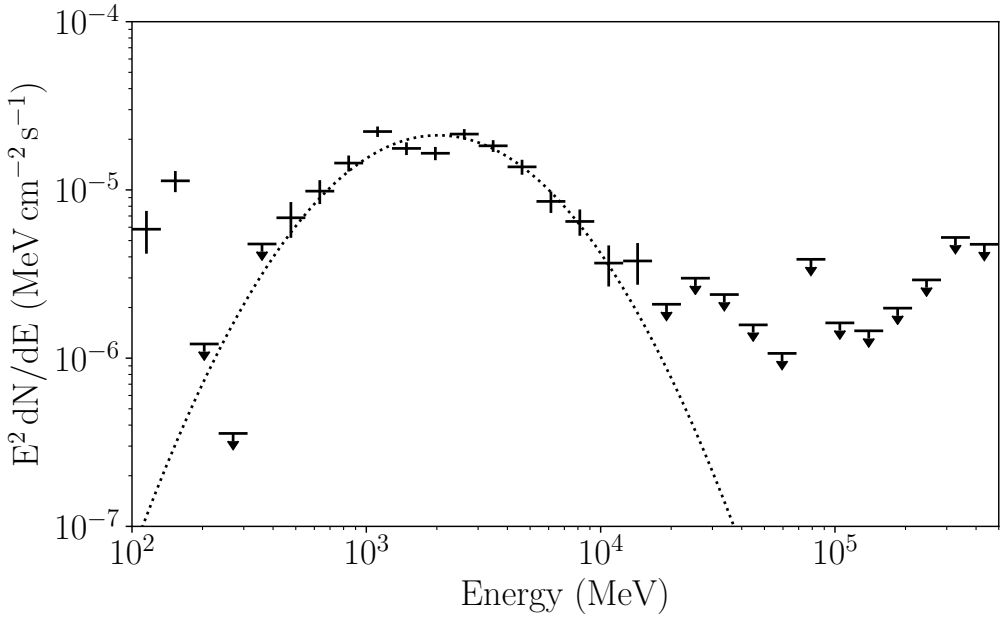

Figure 8.5: The spectral energy distribution of 4FGL J1746.4-2852, the γ-ray source tentatively associated with PWN G0.13-0.11, with 8 energy bins per decade and upper limits placed on bins where TS < 4. A log-parabola spectral shape is fitted to this SED with the best-fit parameters of $\alpha = 2.806 \pm 0.073$, $\beta = 0.6340 \pm 0.0531$, $N_0 = (1.116 \pm 0.045) \times 10^{-12}$ and $E_B = 3.83$ GeV. The two lowest energy bins do not appear to fit the log-parabola curve, this is likely because they are dominated by background emission.

finds that the radial Gaussian model is preferred to the point source model with $\mathrm{TS_{ext}} = 22.3$ (4.7σ); however with an extension width of only 0.1081°, this still represents a point source in the model as it is comparable to the spatial width of a bin (see 8.1.1 for a more detailed example). A localisation of 4FGL J1746.4-2852 fails, indicating it is already in its best fit position.

Two LMXBs with spatially coincident γ-ray excesses are close (less than a 0.1° angular separation) to the position of 4FGL J1746.4-2852; these are 1E 1743.1-2852 and 1E 1742.9-2849. Neither of these LMXBs have persistent γ-ray excesses associated with them, but both have 4 excess bins appearing with $z < 3\sigma$ in their 6 monthly binned light-curve (Figure 8.6 & 8.7). Both light-curves are best described by a constant flux model, and that any excess at the position of either binary is not variable over the observation times available.

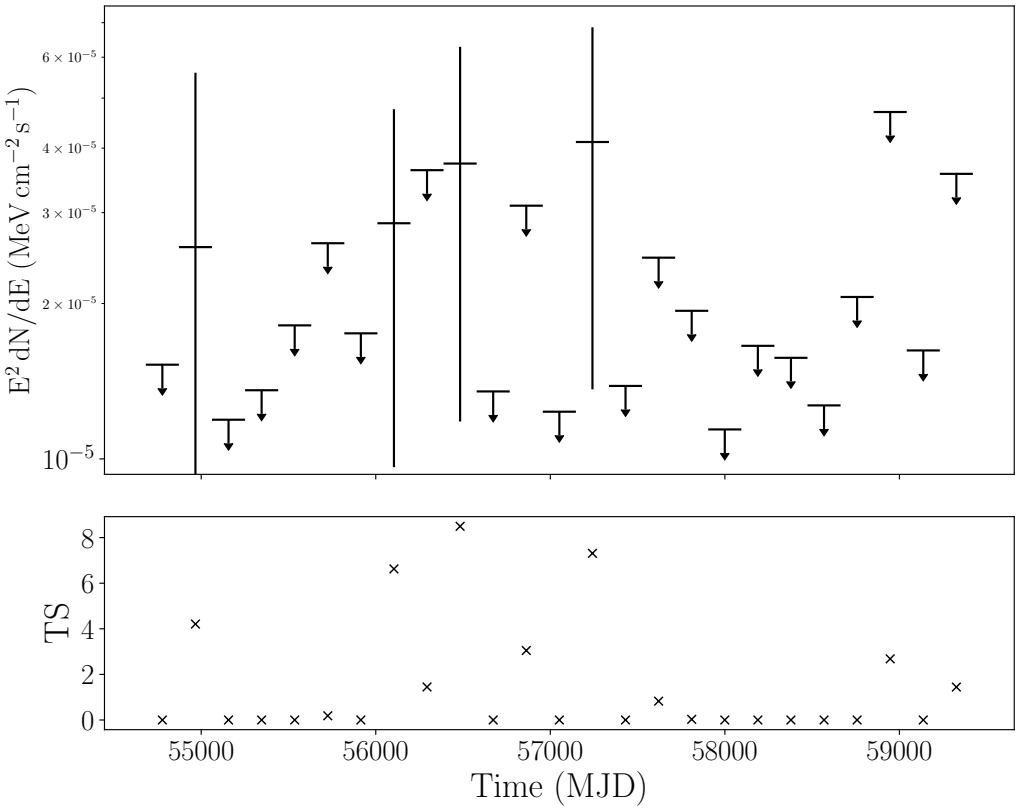

Figure 8.6: The light-curve of the position of 1E 1742.9-2849, with approximately 6 monthly bins. The top panel shows energy flux against time, and the bottom panel shows the TS of each bin. Upper limits are placed on any bins where the TS < 4.

4FGL J1746.4-2852 is also a non-variable source, so these excesses cannot be distinguished from it. Furthermore, as the expected γ-ray spectra of the two binaries would also be log-parabolic in shape it is not possible to distinguish these excesses based on spectral analysis. It is possible that the two binaries are contributing to the γ-ray emission seen from 4FGL J1746.4-2852, however it is unlikely that the emission from this source is dominated by either of the binaries, given that it is distinctly non-variable in nature. The most likely cause of the 4FGL J1746.4-2852 emission is PWN G0.13-0.11.

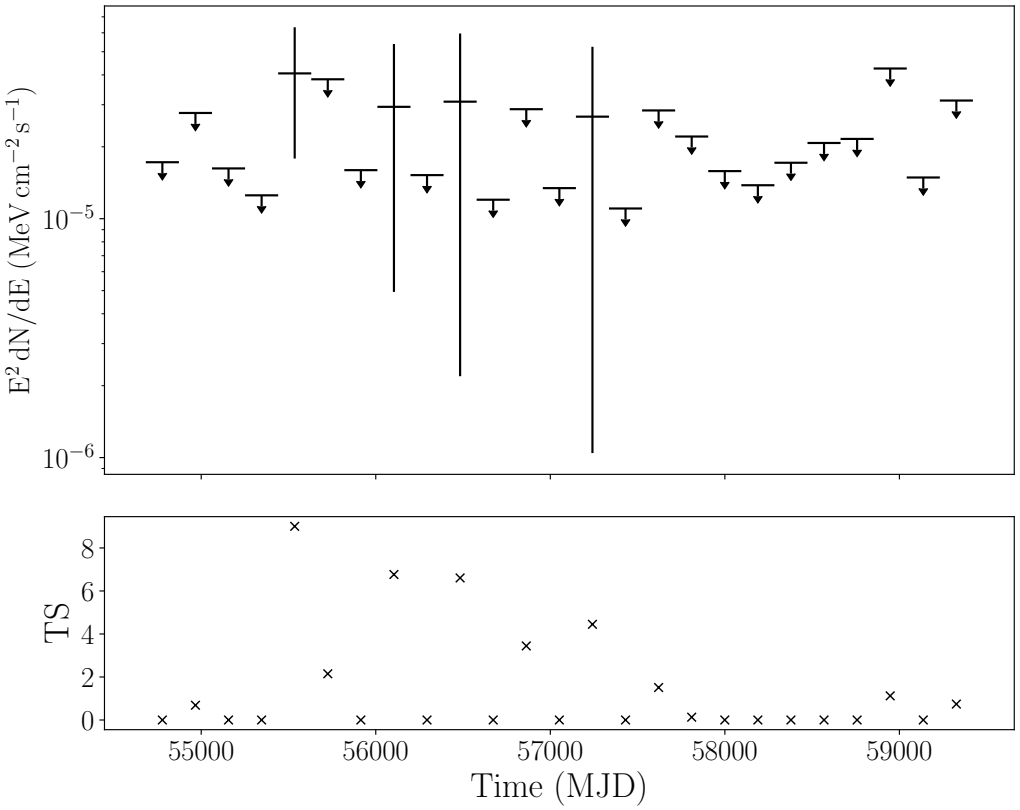

Figure 8.7: The light-curve of the position of 1E 1743.1-2852, with approximately 6 monthly bins. The top panel shows energy flux against time, and the bottom panel shows the TS of each bin. Upper limits are placed on any bins where the TS < 4.

8.1.4 GRS 1741.9-2853

The only other LMXB with a coincident γ-ray excess within 0.25° of the Galactic centre is GRS 1741.9-2853 (Pavlinsky et al., 1994). GRS 1741.9-2853 is close to the position of the Sgr A* associated 4FGL J1745.6-2859, but appears to have an excess independent of this source when one examines a TS map of the region. This γ-ray excess is persistent with TS = 60.6 ($z = 7.8\sigma$), and appears to be variable, with an enhancement in the first time bin with respect to the other time bins in this light-curve (Figure 8.8). This variability distinguishes it from 4FGL J1745.6-2859.

The significance ($z > 5\sigma$) of this excess enables further analysis to determine whether it is associated with GRS 1741.9-2853. We run a positional localisation of

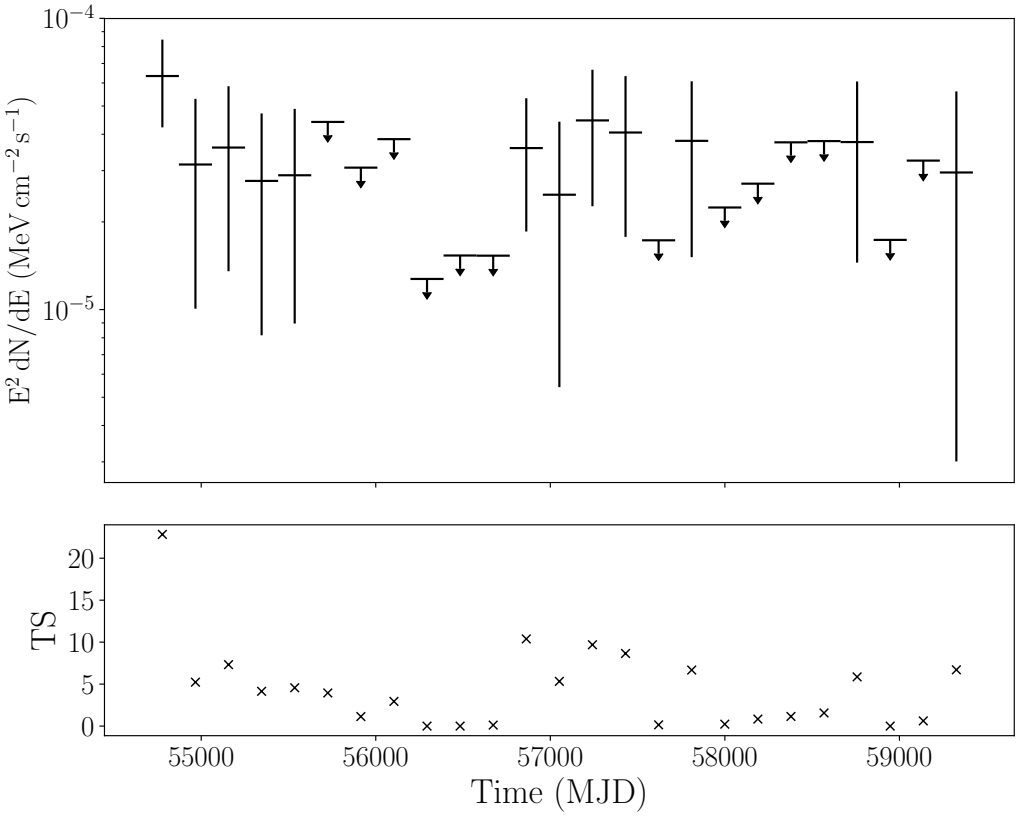

Figure 8.8: The light-curve of the excess coincident with of GRS 1741.9-2853, with approximately 6 monthly bins. The top panel shows energy flux against time, and the bottom panel shows the TS of each bin. Upper limits are placed on any bins where the TS < 4.

the excess at the position of GRS 1741.9-2853 with `gta.localize` and find that the best fit position of the excess shifts to the position LII $= 359.8514° \pm 0.0213°$, BII $= 0.0719° \pm 0.0253°$, with a 95% positional uncertainty of 0.0093°. Given these new coordinates, it is very unlikely that this γ-ray excess originates from GRS 1741.9-2853 and it is likely caused by one of the other, numerous possible sources in the Galactic centre.

8.2 The 0.25° to 1° LMXBs

There are an additional six LMXBs with a coincident γ-ray excess between 0.25° and 1° of the Galactic centre. These six LMXBs are: 1E 1740.7-2942, 1A 1742-294,

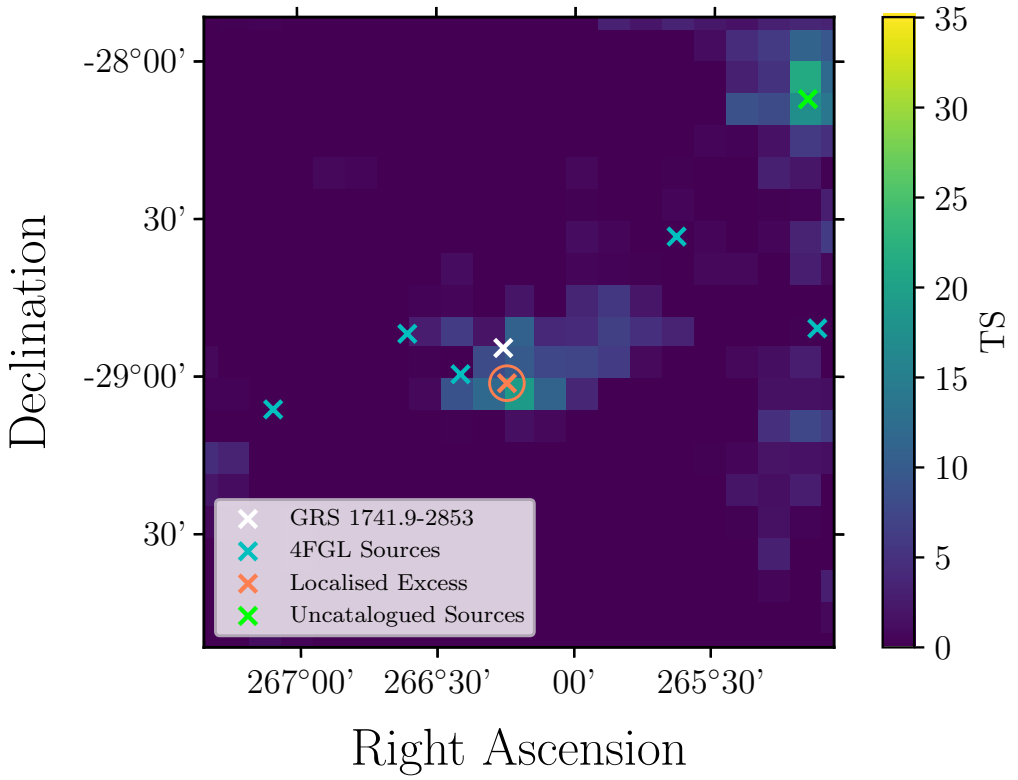

Figure 8.9: The TS map of the region around GRS 1741.9-2853 with a width of 2°. Here the X-ray position of GRS 1741.2-2859 is indicated by the white cross, and the localised position of the γ-ray excess is indicated by the orange cross. The orange circle indicates the 95% positional uncertainty of the localised excess, and the blue crosses indicate 4FGL γ-ray sources.

GC X-2, GC X-4, GRS 1741.2-2859 and XTE J1748-288. Figure 8.10 shows this region, and their positions. In addition to 4FGL J1746.4-2852 and 4FGL J1745.6-2859 within the inner 0.25° region, a further two 4FGL-DR2 sources are present in this 1° region; these are the unattributed sources 4FGL J1748.3-2906 (TS = 308) and 4FGL J1742.5-2833 (TS = 144). Neither of these sources particularly close (i.e. within 0.5°) to any of the observed γ-ray excesses. Given the relative separation of these excesses from the neighbouring 4FGL-DR2 sources, and from each other it is possible to consider these 6 sources on a case by case basis, consistent with the rest of the survey.

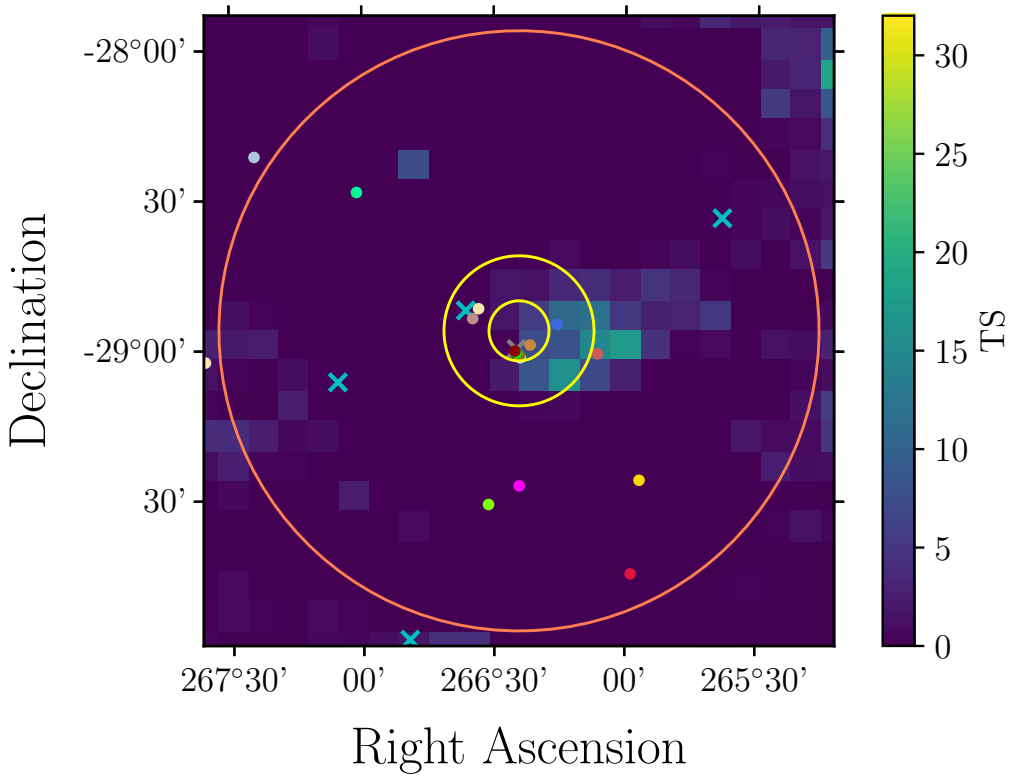

Figure 8.10: A TS map of the Galactic centre calculated from the independent Galactic centre analysis. This TS map has 2° width and a spatial binning size of 0.1°. The icons on this map correspond to the legend in Figure 8.1. The outer orange circle has a 1° radius whereas the inner yellow circles have radii of 0.25° and 0.1° and correspond to those displayed in Figure 8.2. All circles, and the map itself is centered on the geographic centre of the Galaxy (LII = 0°, BII = 0°). In this section, I consider the six LMXBs enclosed by the orange circle, however excluded by the yellow rings.

8.2.1 1E 1740.7-2942

1E 1740.7-2942 (Hertz and Grindlay 1984 & Skinner et al. 1987) (henceforth 1E1740) is a low mass X-ray binary and microquasar, with the sobriquet the 'Great Annihilator'* due to the strong electron-positron annihilation line at 511 keV associated with the source (Bouchet et al. 1991 & Sunyaev et al. 1991). 1E1740 is a black hole LMXB with an unknown class of companion star so any high energy γ-ray emission is expected to originate from the jet activity of the system (Skinner et al., 1987).

*Also the name of the ninth studio album by the experimental rock band, Swans.

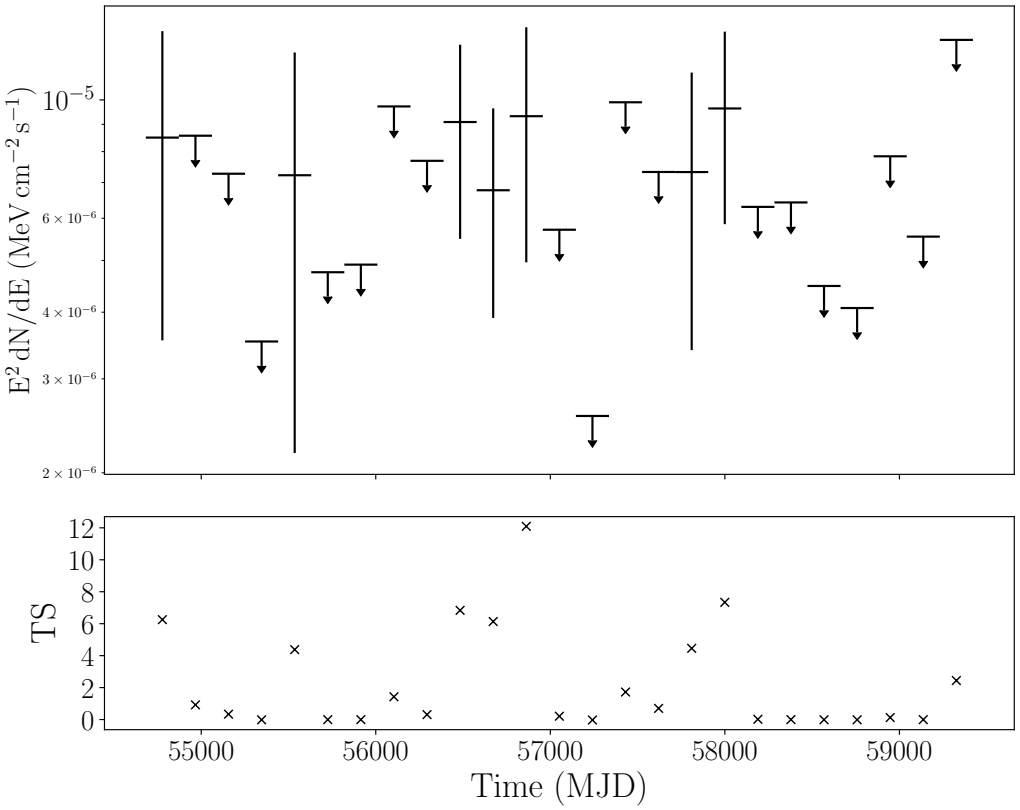

Figure 8.11: The light-curve at the position of 1E 1740.7-2942, with approximately 6 monthly bins. The top panel shows energy flux against time, and the bottom panel shows the TS of each bin. Upper limits are placed on any bins where the TS < 4.

I measure a γ-ray flux in 7 of the 25 bins of the 6 monthly binned light-curve generated from the position of 1E1740, but no significant persistent γ-ray excess (Figure 8.11). The most significant of these bins appears with $z = 3.5\sigma$ significance, and there is no significant variability in the flux levels of the γ-ray light-curve. An X-ray light-curve of 1E1740 is unavailable from either MAXI or *Swift*-BAT however, so it is not possible to establish a correlation with the γ-ray light-curve.

8.2.2 1A 1742-294

1A 1742-294 (Lewin et al., 1976) (aka GC X-1, henceforth referred to as 1A1742) is a low mass X-ray binary with an orbital period of 12.3 days. Given the detection of thermonuclear X-ray bursts from 1A1742, the compact object is known to be a

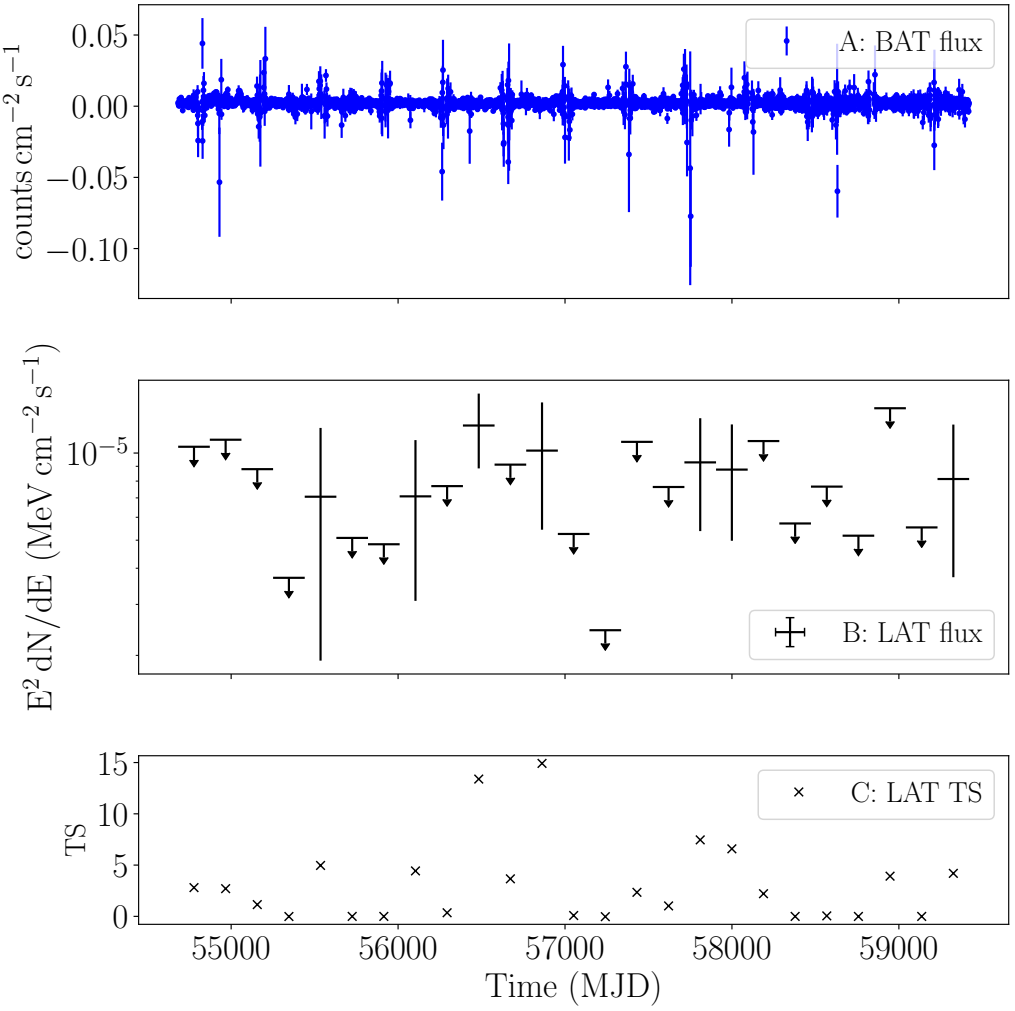

Figure 8.12: Panel A shows the X-ray light-curve of 1A 1742-294 with daily bins from *Swift*-BAT observations. Panels B and C show the energy flux and TS of the γ-ray excess light-curve with approximately 6 monthly bins. Upper limits on energy flux are placed on any bins where the TS < 4.

neutron star (Lutovinov et al. 2001 & Churazov et al. 1995). The nature of the companion star is unknown in this system. We observe a persistent, but weak, γ-ray excess coincident with the position of 1A1742 with TS = 12.3 ($z = 3.5\sigma$), and a number of flux measurements in the bins of the 6 month light-curve, where *Swift*-BAT X-ray data is also available for consideration.

There is no significant pattern in the γ-ray light-curve, with the flux values appearing to be broadly non-variable, and hence there is no correlation with the X-ray data. It is not possible to localise this excess, or analyse its spectrum due to poor statistics (TS = 12.3). The orbital period is short, and uncertainties are too large to perform a phase folded analysis. It is therefore not possible to associate this excess with 1A1742, and given that it is approximately 0.5° away from the luminous sources 4FGL J1747.2-2957 (the pulsar: PSR J1747-2958, TS = 6300) and also the Galactic centre source 4FGL J1745.6-2859 (TS = 18700, in this analysis), one cannot eliminate source confusion as the cause of this γ-ray excess.

8.2.3 GC X-2

GC X-2 is a suspected LMXB system observed only in the X-ray waveband, with an unclassified accretor and companion star, and no known orbital period (Cruddace et al., 1978). While no persistent γ-ray excess is observed to be coincident with GC X-2, the light-curve condition indicates that there is some evidence for transient emission (Figure 8.13). There is no observable variability, and with so few flux points it is impossible to discern any pattern. The lack of known binary parameters makes it impossible to associate these weak transient excesses with the binary. As the Galactic centre source 4FGL J1745.6-2859 (TS = 18700) lies with an angular offset of 0.456° from the position of GC X-2, it is entirely possible that these excesses are due to source confusion with this source.

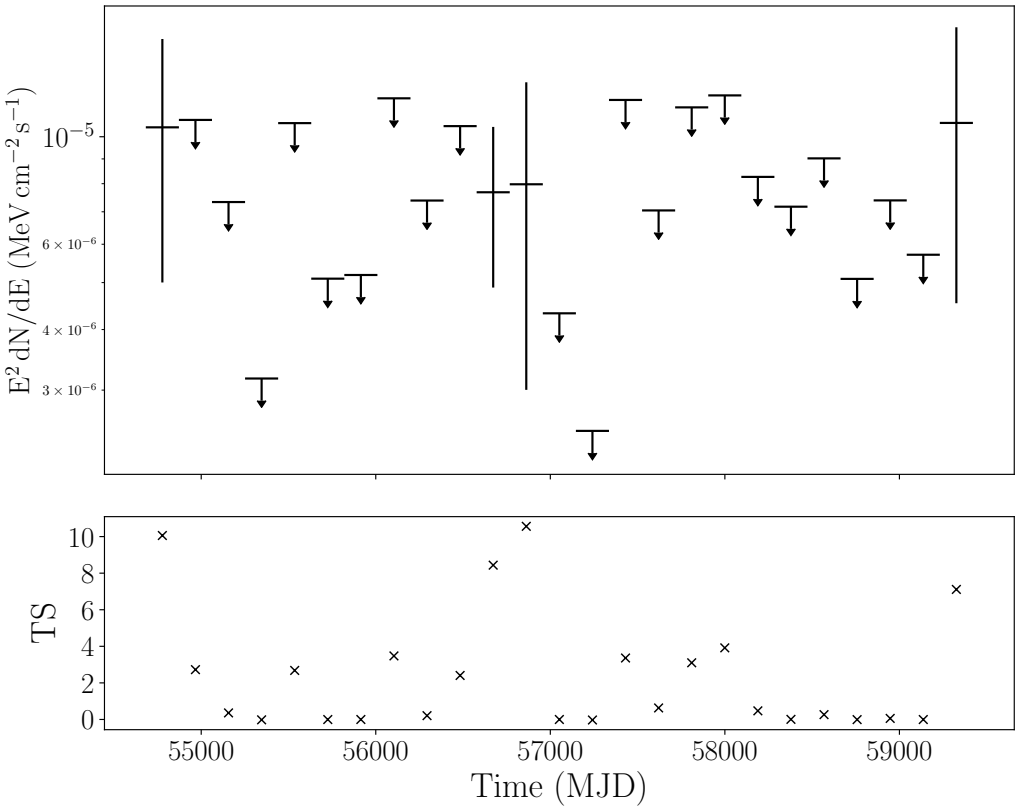

Figure 8.13: The light-curve at the position of GC X-2, with approximately 6 monthly bins. The top panel shows energy flux against time, and the bottom panel shows the TS of each bin. Upper limits are placed on any bins where the TS < 4.

8.2.4 GC X-4

GC X-4 is a suspected LMXB system observed only in the X-ray waveband with an unclassified accretor and companion star and no known orbital period (Cruddace et al., 1978). This system is similar to GC X-2; while no persistent γ-ray excess is observed coincident with GC X-4, the light-curve condition indicates that there is some evidence for transient emission (Figure 8.14). The light-curves of GC X-2 and GC X-4 are similar, with all but 2 of the significant flux bins being correlated. This indicates that there is likely source confusion between GC X-2 and X-4, and possibly a third source, making it impossible to associate these transient γ-ray excesses with either binary.

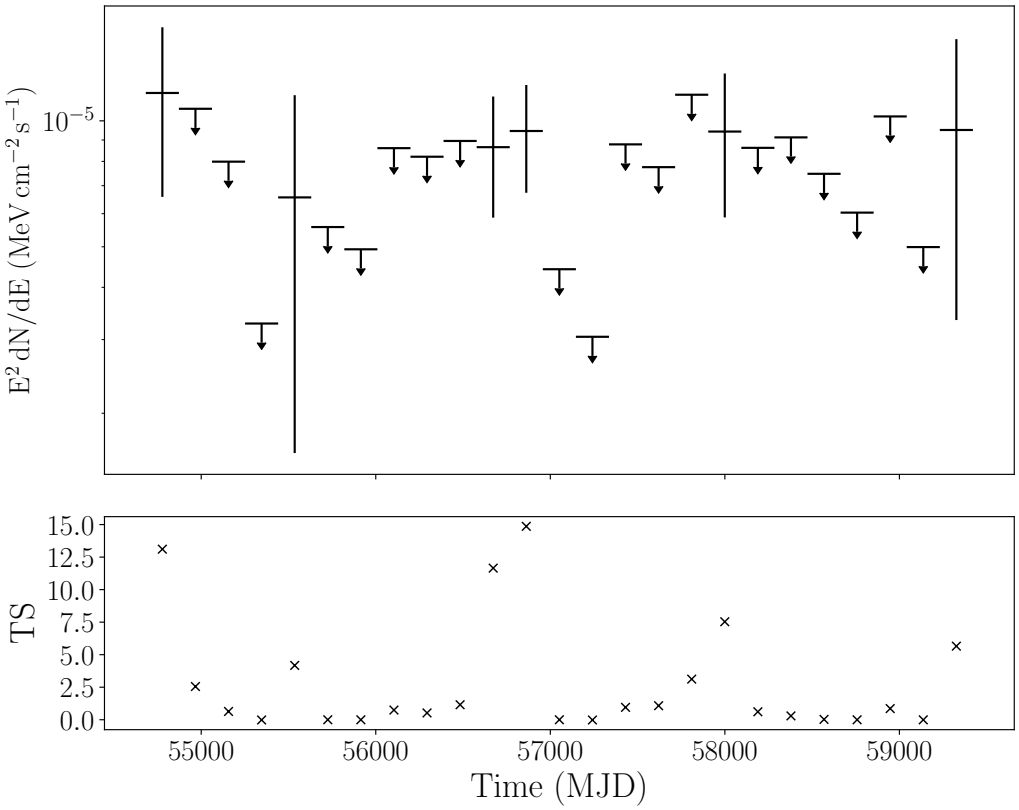

Figure 8.14: The light-curve at the position of GC X-4, with approximately 6 monthly bins. The top panel shows energy flux against time, and the bottom panel shows the TS of each bin. Upper limits are placed on any bins where the TS < 4.

8.2.5 GRS 1741.2-2859

GRS 1741.2-2859 (Sunyaev, 1990) is a low mass X-ray binary system, offset from the luminous Galactic centre γ-ray source 4FGL J1745.6-2859 (TS = 16900 in this analysis) by 0.159° and lies on the 0.25° circle which bounds the inner Galactic centre LMXBs. A persistent γ-ray excess is observed to be coincident with the position of GRS 1741.2-2859 with TS = 53.6 ($z = 7.3\sigma$) across the full mission lifetime of *Fermi*. The separation from 4FGL J1745.6-2859 together with the TS of the observed excess results in a similar situation to that of the excess apparently coincident with the nearby LMXB GRS 1741.9-2853.

The TS of 53.6 provides sufficient photon statistics to perform a localisation of the

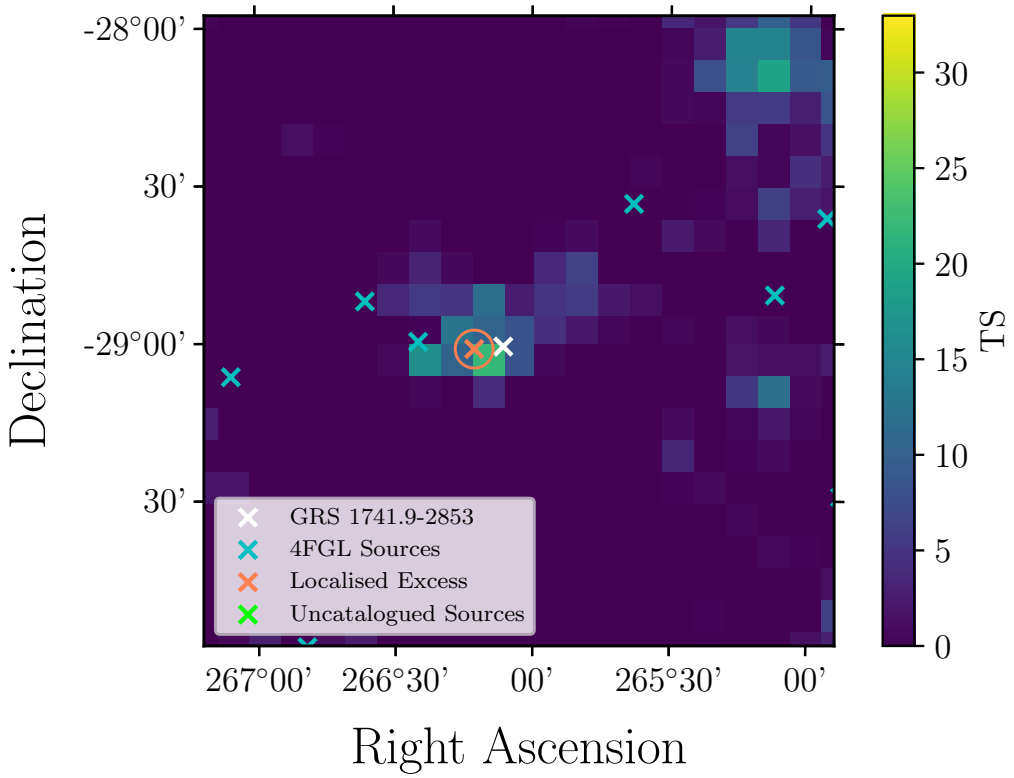

Figure 8.15: The TS map of the region around GRS 1741.2-2859 with a width of 2°. Here the X-ray position of GRS 1741.2-2859 is indicated by the white cross, and the localised position of the γ-ray excess is indicated by the orange cross. The orange circle indicates the 95% positional uncertainty of the localised excess, and the blue crosses indicate 4FGL γ-ray sources.

excess. The optimal position of the excess shifts to LII $= 359.8399° \pm 0.0233°$, BII $= 0.1007° \pm 0.0271°$, with a 95% positional uncertainty of 0.0602°, and the TS of the excess increases to 81.5. The new position of the γ-ray excess is no longer coincident with the position of the X-ray binary GRS 1741.2-2859, and therefore it is highly unlikely that this excess represents γ-ray emission from the LMXB.

8.2.6 XTE J1748-288

XTE J1748-288 (Smith et al. 1998, Hjellming et al. 1998 and Strohmayer et al. 1998) (henceforth XTE17) is a LMXB and Galactic microquasar with a suspected black hole accretor in orbit around an unclassified stellar companion. XTE17 is an X-ray transient, with the last microquasar outburst occurring in 1998, outside the

Fermi-LAT observation period, although recent observations in the radio waveband indicate the possibility of faint emission (Hyman et al., 2021).

I note a persistent weak γ-ray excess from the position of XTE17 with TS = 11.9 ($z = 3.4\sigma$) over the 13 years of *Fermi*-LAT data, however there is significant variable activity in the light-curve of the excess, with bins reaching a peak TS of 60. This light-curve is shown in Figure 8.16 together with the *Swift*-BAT hard X-ray daily light-curve, which shows the source in a quiescent state. The closest sources to this excess are 4FGL J1746.4-2852 (PWN G0.13-0.11, TS = 1374 and an angular offset from the excess of 0.536°), the unknown source 4FGL J1748.3-2906 (TS = 345, angular offset: 0.636°) and the Sgr A* associated 4FGL J1745.6-2859 (TS = 19000, angular offset: 0.746°). None of these three γ-ray sources are apparently variable given their variability indices in the 4FGL-DR2, indicating the excess coincident with XTE17 is likely independent of these sources.

It is not possible to perform a spectral analysis or source localisation on the weak excess in the 13-year dataset. Upon performing a full likelihood fit during the time bin where TS = 60, I find the excess only has a TS of 13.4, again insufficiently significant to perform spectral analysis or source localisation. Therefore whilst it is likely that this excess is independent of nearby sources, there is a lack of evidence to associate it with the microquasar XTE17.

8.3 The 1° to 2° LMXBs

In the region of 1° to 2° away from the Galactic centre, there are far more 4FGL sources (17) and fewer LMXBs with coincident γ-ray excesses than in the inner regions of the Galactic centre. The 4 LMXBs with coincident excesses are: SLX 1744-300, SAX J1750.8-2900, 4U 1735-28 and IGR J17497-2821 (Figure 8.17). As all four of these systems are reasonably well removed from one another I consider their coincident excesses separately.

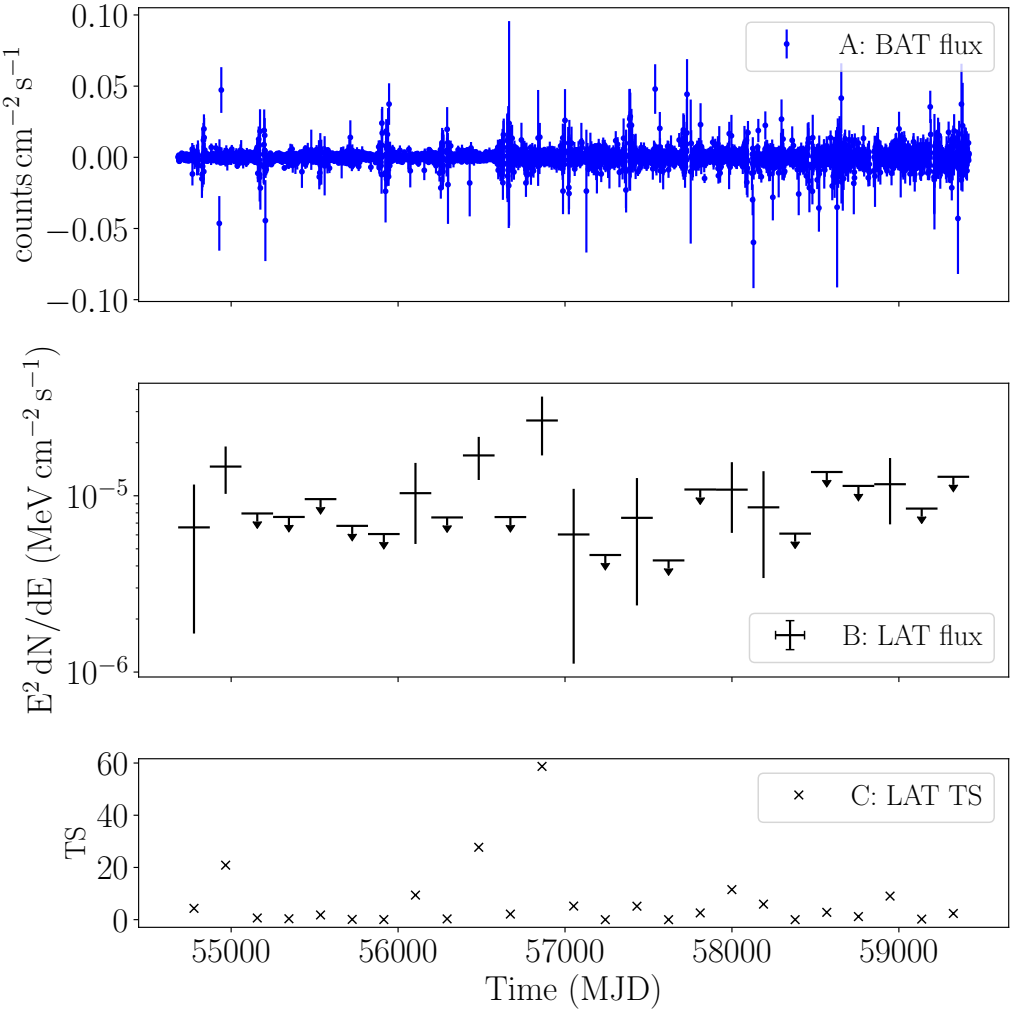

Figure 8.16: Panel A shows the X-ray light-curve of XTE J1748-288 with daily bins from *Swift*-BAT observations. Panels B and C show the energy flux and TS of the γ-ray excess light-curve with approximately 6 monthly bins. Upper limits on energy flux are placed on any bins where the TS < 4.

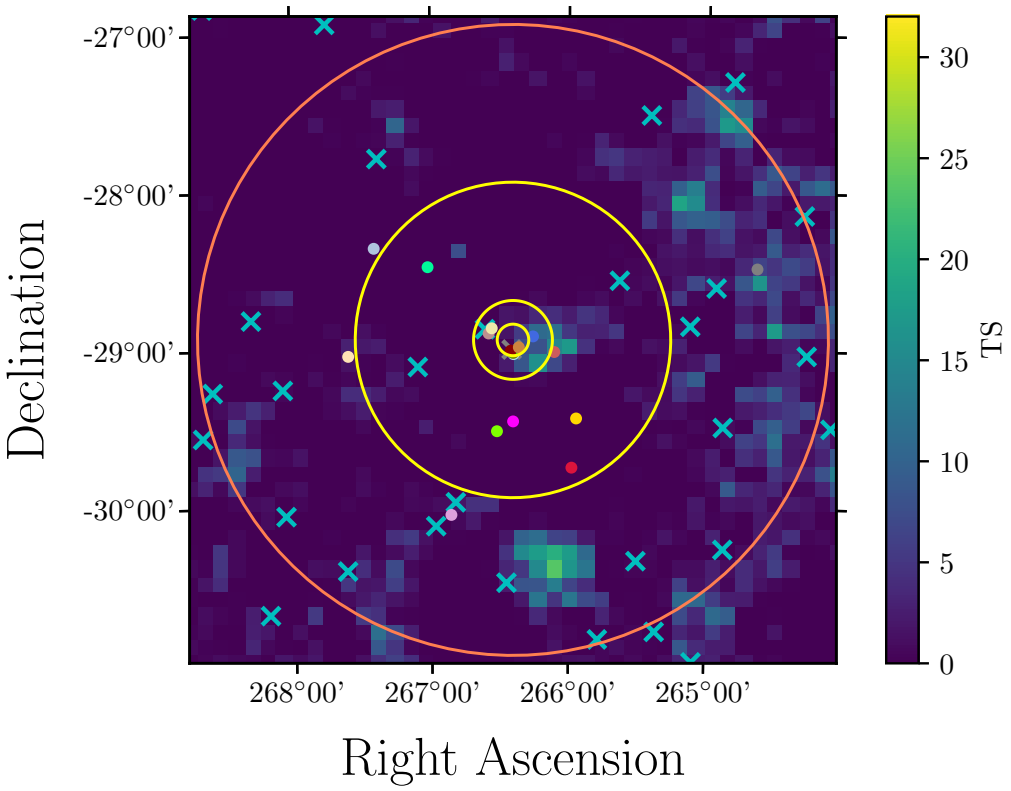

Figure 8.17: A TS map of the Galactic centre calculated from the independent Galactic centre analysis. This TS map has 4° width and a spatial binning size of 0.1°. The icons on this map correspond to the legend in Figure 8.1. The outer orange circle has a 2° radius whereas the inner yellow circles have radii of 1°, 0.25° and 0.1° and correspond to those displayed in Figure 8.10. All circles, and the map itself is centered on the geographic centre of the Galaxy (LII = 0°, BII = 0°). In this section, I consider the 4 LMXBs enclosed by the orange circle, however excluded by the yellow rings.

8.3.1 SLX 1744-300

SLX 1744-300 (Yamauchi and Koyama, 1990) (henceforth SLX17) is an LMXB with an unclassified companion star and neutron star accretor, and is an X-ray burster (Galloway et al., 2008). My analysis shows a γ-ray excess coincident with the position of SLX 1744-300 with TS = 15.7, and several flux measurements in the light-curve exceed the 2σ level. SLX 1744-300 is extremely close to another LMXB, SLX 1744-299 (Skinner et al., 1987) from which there is no coincident γ-ray excess.

Figure 8.18 shows a TS map of the region around SLX 1744-300; there are two

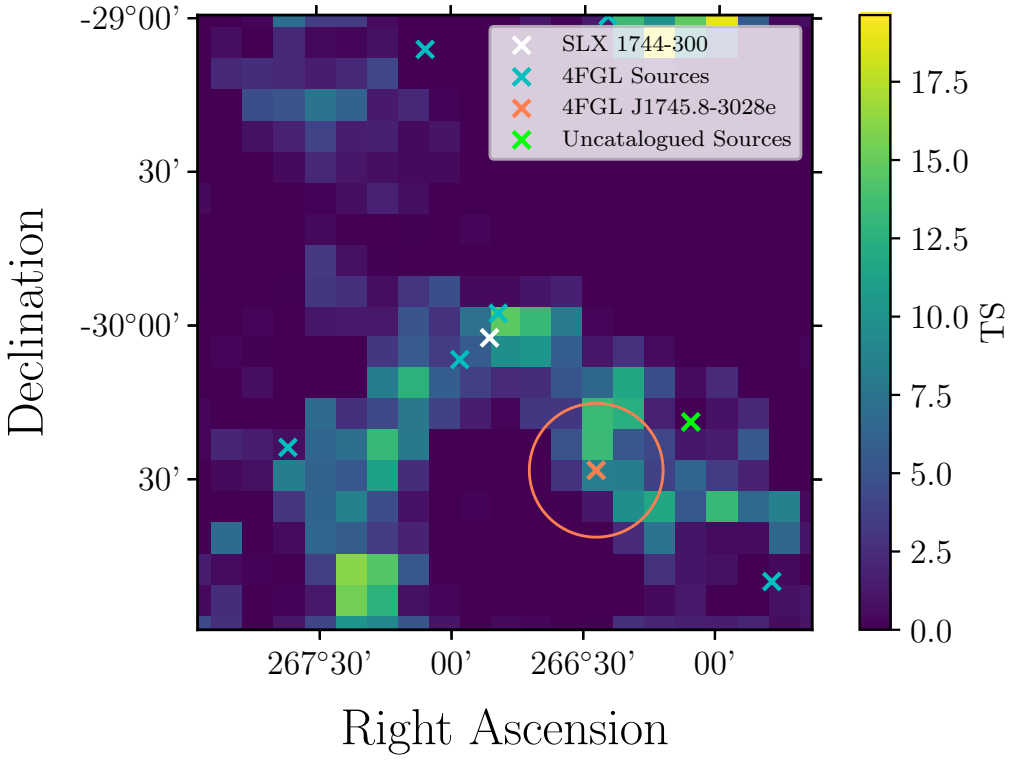

Figure 8.18: A TS map centered on the position of SLX 1744-300, with 2° width and spatial binning of 0.1°. Here the white cross represents the X-ray position of SLX J1744-300, the blue crosses represent 4FGL sources, the green crosses represent uncatalogued sources and the orange circle represents the extent of the extended source 4FGL J1745.8-3028e.

sources very close to the position of the excess. The first and more significant is the pulsar 4FGL J1747.2-2957 (a.k.a. PSR J1747-2958), which has a high TS of 5950 (77.1σ) and is offset 0.085° from the position of SLX17. The second, and far less significant, is the unassociated source 4FGL J1747.8-3006, TS = 21.1 and an offset of 0.120°.

The low significance of the SLX17 excess means that meaningful spectral analysis and positional localisation are not possible, nor is a search for orbital modulation given the orbital period of the system is unknown. It is likely that this γ-ray excess is the product of source confusion with either of the nearby sources, more likely the pulsar given its very significant γ-ray emission and closer proximity.

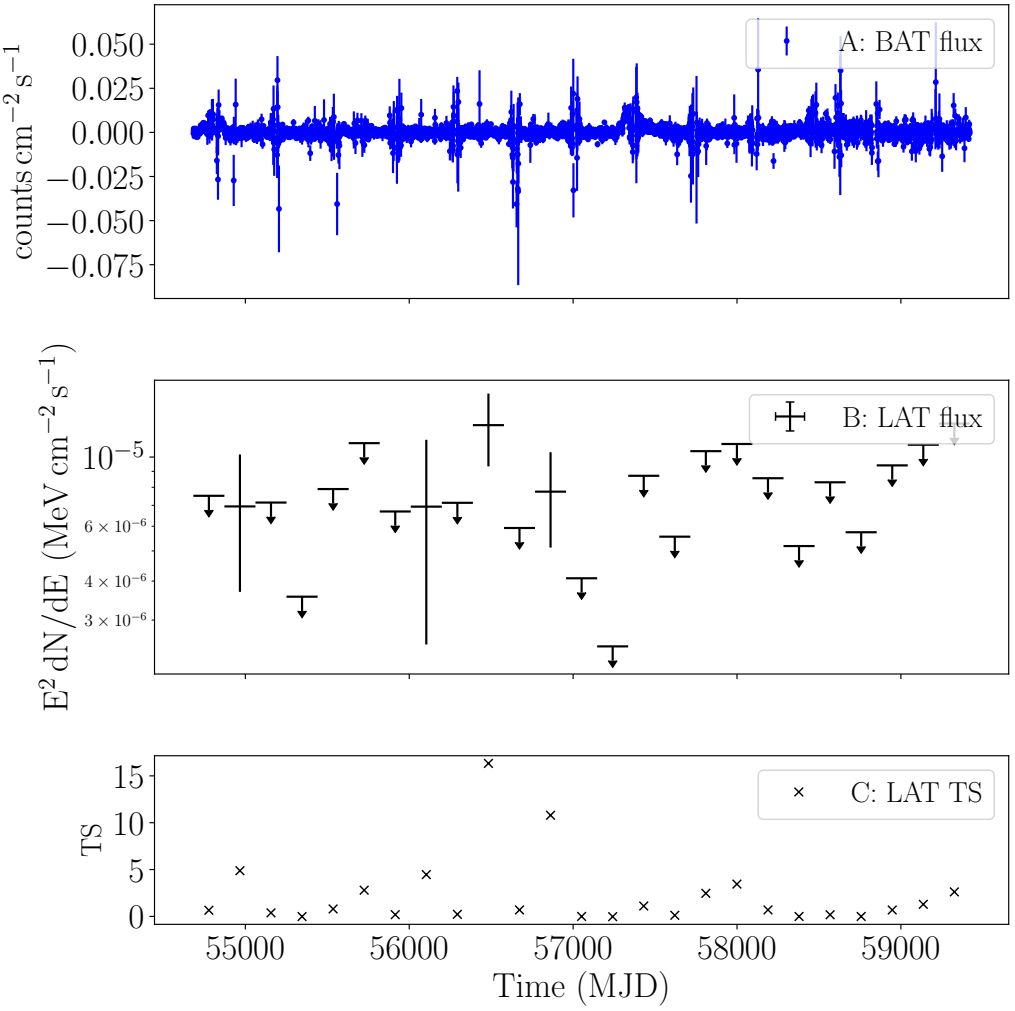

Figure 8.19: Panel A shows the X-ray light-curve of SAX J1750.8-2900 with daily bins from *Swift*-BAT observations. Panels B and C show the energy flux and TS of the γ-ray excess light-curve with approximately 6 monthly bins. Upper limits on energy flux are placed on any bins where the TS < 4.

8.3.2 SAX J1750.8-2900

SAX J1750.8-2900 (in't Zand et al. 1997 & Bazzano et al. 1997b) (henceforth SAX17) is a transient neutron star LMXB, known for its Type-I thermonuclear X-ray outbursts (e.g Natalucci et al. 1999 & Allen et al. 2015). No orbital period is known for the system, and although a variable infrared source has previously been associated with SAX17, no spectral type for the companion star is known due to the high rate of dust extinction hindering observations (Torres et al., 2008).

My analysis shows no significant, persistent γ-ray excess, however the light-curve condition is satisfied for this source, indicating that there is some significant γ-ray emission in the bins of the light-curve. Figure 8.19 shows the light-curve at the position of SAX17 together with *Swift*-BAT data. There is no correlation between the X-ray and γ-ray data. The source itself has largely been in quiescence since 2011, although its X-ray flux is known to be variable at softer energies than the BAT measures. MAXI data are not available for this system.

The two nearest 4FGL sources to SAX17 are 4FGL J1748.3-2906 (TS = 341, angular offset: 0.446°) and 4FGL J1752.3-2914 (TS = 105, angular offset: 0.467°). Neither of these sources have a known multi-wavelength counterpart, or a known source type in the 4FGL, and neither of them is variable on monthly timescales. My results show there *may* be some very tentative evidence for variability from the position of SAX17 that is unlikely to be associated with nearby catalogued sources. However, given that SAX17 lies close to the Galactic centre, and there is no multi-wavelength correlation between the γ-ray bins and any other waveband, there is also insufficient evidence to associate this weak transient excess with SAX17.

8.3.3 4U 1735-28

4U 1735-28 (Kellogg et al., 1971) is a transient LMXB system with a possible neutron star accretor, unclassified companion and no known orbital period (Campana et al., 1998). There is no persistent γ-ray excess coincident with the position of

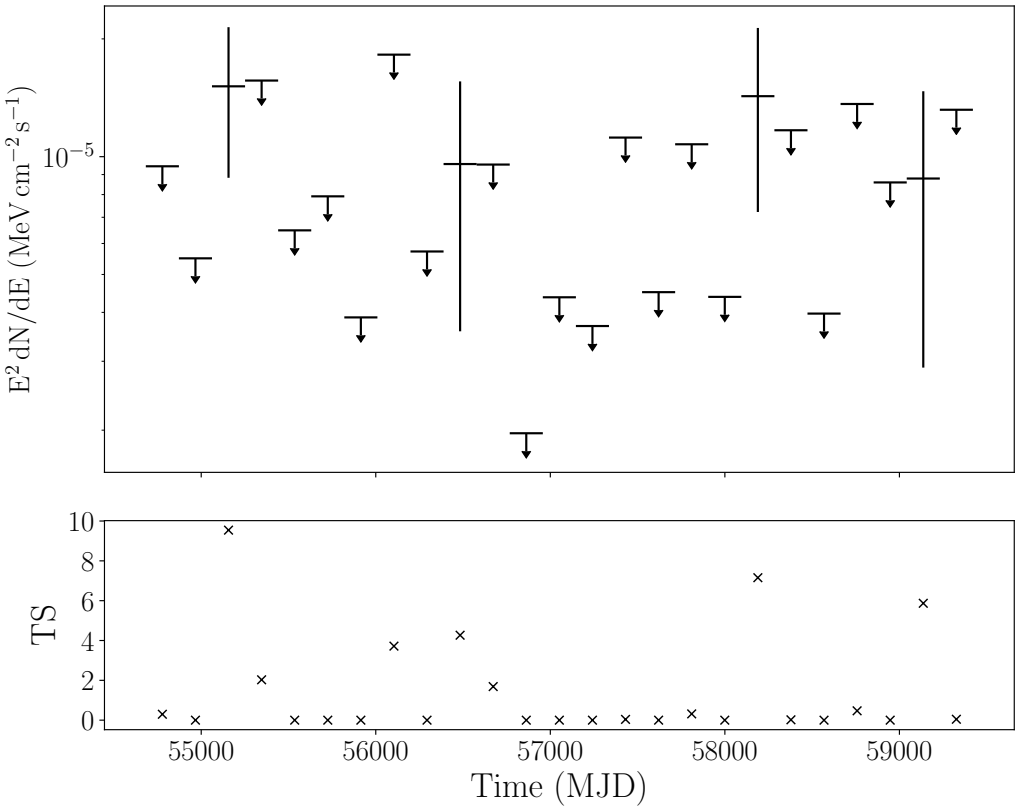

Figure 8.20: The *Fermi*-LAT light-curve of the position of 4U 1735-28. Panels A and B show the energy flux and TS of the γ-ray excess light-curve with approximately 6 monthly bins. Upper limits on energy flux are placed on any bins where the TS < 4.

4U 1735-28, however the light-curve condition is fulfilled at the position of the LMXB, indicating some level of γ-ray emission spread across the bins of the light-curve.

Figure 8.20 shows the *Fermi*-LAT light-curve of the position of 4U 1735-28, in which there are 4 bins with significances in the $2\sigma < z < 3\sigma$ range, and upper limits otherwise. No multi-wavelength data are available during this period*, and thus it is not possible to associate these (weak) flux points with 4U 1735-28.

The nearest 4FGL source to 4U 1735-28 by angular offset is the unidentified, and non-variable, source 4FGL J1739.7-2836 (TS = 105, angular offset: 0.286°). Given the close proximity of this source to the position of 4U 1735-28, and the inability

**Swift*-BAT very recently began observing this source, however there is no useful data available for my time period.

to localise any γ-ray excess, I conclude that the emission seen in the light-curve of 4U 1735-28 is likely a false positive caused by source confusion with 4FGL J1739.7-2836.

8.3.4 IGR J17497-2821

IGR 17497-2821 (henceforth referred to as IGR1749) (Soldi et al., 2006) is a hard X-ray transient LMXB, or possibly a HMXB according to the WATCHDOG database (Tetarenko et al., 2016). IGR1749 consists of a black hole accretor alongside an unclassified companion, so wind interactions are impossible for this system (Walter et al., 2007). There is no persistent γ-ray excess coincident with the position of IGR1749, however the light-curve condition indicates some level of γ-ray emission spread across the bins of the light-curve.

Figure 8.21 shows the *Fermi*-LAT and *Swift*-BAT light-curves of IGR1749, where two bins in the $3.5\sigma \leq z < 4\sigma$ range are seen in the LAT light-curve. It is unlikely that these arise by chance coincidence given there are only 25 bins in the light-curve. However, no significant X-ray emission has been seen from this LMXB since its initial discovery in 2006, and no significant enhancement is observed with *Swift*-BAT during the LAT observation time.

The three closest 4FGL-DR2 sources by angular offset to IGR1749 are the supernova remnant 4FGL J1749.5-2747 (SNR G001.4-00.1, TS = 81.6, angular offset: 0.569°), the unassociated 4FGL J1748.3-2906 (TS = 326, angular offset: 0.800°), and the pulsar wind nebula 4FGL J1746.4-2852 (PWN G0.13-0.11, TS = 1330, offset: 0.871°). None of these sources are variable according to their 4FGL variability indices, hence it is very unlikely that γ-ray flaring from one of these objects is causing source confusion at the position of IGR1749.

As a black hole, one would expect γ-ray emission to correlate with an X-ray outburst (i.e. as a microquasar outburst), however as this is not the case with regards to either of the γ-ray flux bins, it is unlikely that this emission originates from this

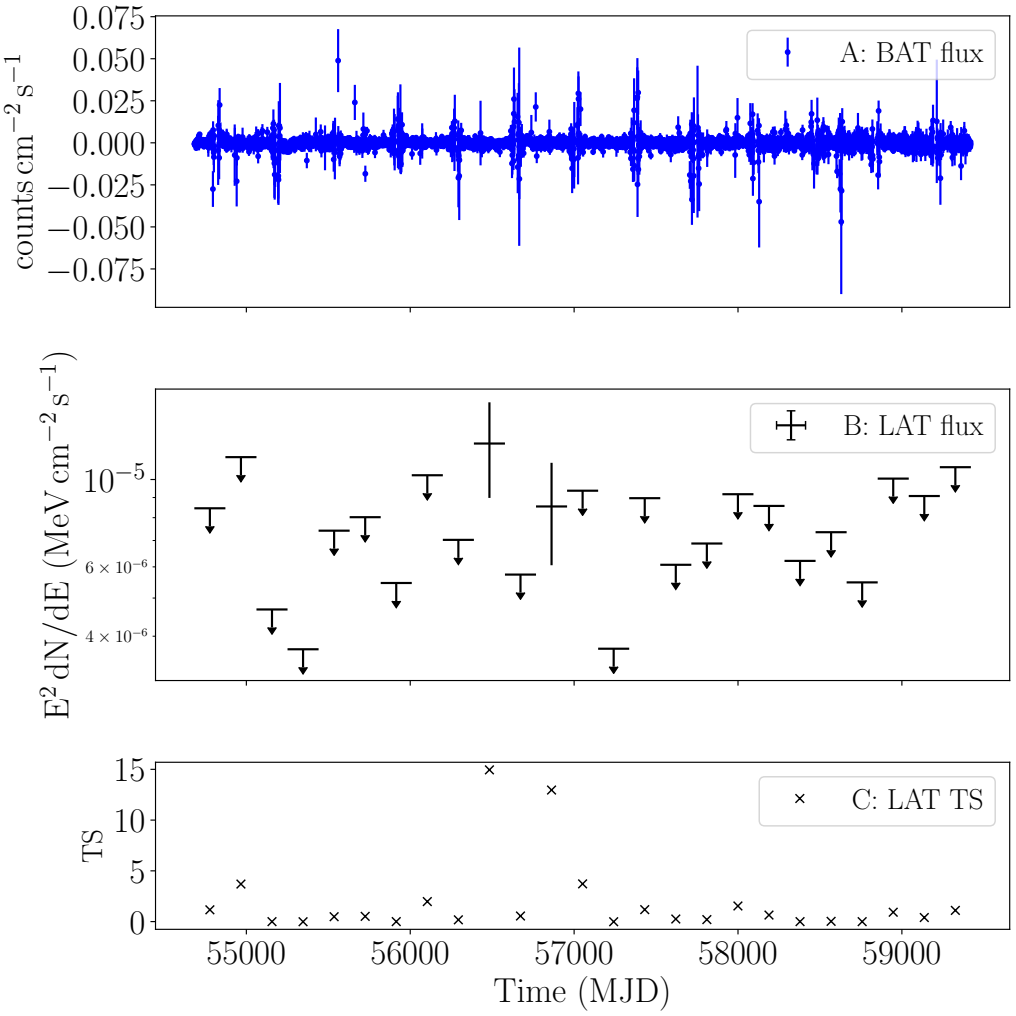

Figure 8.21: Panel A shows the X-ray light-curve of IGR J17497-2821 with daily bins from *Swift*-BAT observations. Panels B and C show the energy flux and TS of the γ-ray excess light-curve with approximately 6 monthly bins. Upper limits on energy flux are placed on any bins where the TS < 4.

system unless via a previously unseen mechanism, such as stellar-scale black hole wind emission (Ajello et al., 2021b), is responsible. There is therefore no evidence to associate the two excess bins in the light-curve with IGR1749, or with any known 4FGL source. It is possible that these excesses are caused either by a previously undetected γ-ray emitter in the Galactic centre.

8.4 Summarising the Galactic Centre LMXBs

We see γ-ray excesses coincident with 18 LMXBs in the Galactic centre, defined as a 3° circle centered on LII = 0°, BII = 0°. These excesses are a mix of those transient or variable γ-ray excesses as indicated by the fulfillment of the light-curve condition, or persistent excesses where TS > 9. Many of these LMXBs are transient, poorly understood systems, and it is likely one only sees such systems in X-rays because there are a great number of them present in the Galactic centre stellar population. This increases the difficulty in associating γ-ray emission with individual systems, as X-ray data is not available. Furthermore, source confusion is responsible for many false positives, particularly within the innermost regions of the Galactic centre where r $< 0.25°$, many associated with 4FGL J1745.6-2859/Sgr A* and the pulsar wind nebula 4FGL J1746.4-285/PWN G0.13-0.11/HESS J1746-285.

The only systems where there *may* be a possibility of γ-rays originating from an LMXB are SAX J1750.8-2900 and the black hole candidate IGR J17497-2821, where there appears to be no source confusion. It must be stressed that in these cases, no persistent γ-ray excess is identified and that the only evidence for emission is the spatial coincidence itself. Furthermore, given the column density (and thus the strong potential of $\gamma\gamma$ absorption) of the Galactic centre, there are likely many other unresolved γ-ray sources which could cause source confusion at the position of these LMXBs.

Figure 8.22: The eighth labour of Heracles, stealing the flesh-eating mares of Diomedes, King of Thrace. By Jean Baptiste Marie Pierre (1752).

Chapter 9

Synthesising the X-ray Binary Population

I have examined the X-ray binary population using *Fermi*-LAT, and whilst some promising indications of γ-ray emission are seen from a number of new systems, particularly amongst the HMXBs, the vast majority of the X-ray binary population is still not known to emit any detectable γ-rays. In this chapter, I examine the XRB population (both high and low mass) which are already known to emit γ-rays independently of the survey given in Chapters 5 - 8. All of these XRBs have associated 4FGL sources in the 4FGL-DR3, although to remain consistent with the analysis of chapters 5 - 8, the 4FGL-DR2 is used for analysis of the *Fermi*-LAT data, allowing the 4FGL-XRB population to be examined alongside the survey results. Any common features of the γ-ray emitting XRB population can be deduced as part of a population synthesis, the goal of which is to understand why only such a small number of XRBs are γ-ray emitters.

9.1 The 4FGL-XRB Population

There are 30 γ-ray emitting binary star systems included in the 4FGL-DR3, excluding binary pulsar systems where the companion star has little impact on the

Binary Name	4FGL Name	Mass	LII	BII
LMC P3	4FGL J0535.2-6736	High	277.7525°	−32.1602°
PSR B1259-63	4FGL J1302.9-6349	High	304.1965°	−0.9868°
4FGL J1405.1-6119	4FGL J1405.1-6119	High	311.6595°	0.2836°
1FGL J1018.6-5856	4FGL J1018.9-5856	High	284.3546°	−1.6849°
LS 5039	4FGL J1826.2-1450	High	16.8810°	−1.2906°
HESS J1832-093	4FGL J1832.9-0913	High	22.6177°	−0.1387°
HESS J0632+057	4FGL J0632.8+0550	High	205.6115°	−1.4479°
Cygnus X-1	4FGL J1958.5+3512	High	71.3544°	3.0366°
Cygnus X-3	4FGL J2032.6+4053	High	79.8143°	0.6347°
LSI +61 303	4FGL J0240.5+6113	High	135.6802°	1.0876°
4FGL J0540.0-7552	4FGL J0540.0-7552	Low	287.2820°	−30.5822°
1SXPS J042749.2-670434	4FGL J0427.8-6704	Low	279.1443°	−38.5517°
2S 0921-630	4FGL J0407.7-5702	Low	281.7689°	−9.4007°
4FGL J0407.7-5702	4FGL J0407.7-5702	Low	267.7967°	−44.4116°
1RXS J154439.4-112820	4FGL J1544.5-1126	Low	356.1769°	32.9939°
PSR J1023+0038	4FGL J1023.7+0038	Low	243.4800°	45.7825°
4FGL J0336.0+7502	4FGL J0336.0+7502	Low	133.0828°	15.5279°
2SXPS J094023.5-761001	4FGL J0940.3-7610	Low	292.2483°	−17.4495°

Table 9.1: The 4FGL X-ray binaries which are analysed in this chapter. The 'binary name' column refers to the most common name of each system, whilst the '4FGL Name' gives the name from the 4FGL-DR2. Where the '4FGL Name' and 'Binary Name' columns equal each other for a source, this indicates that a binary was first discovered by *Fermi*-LAT, rather than at another waveband and that the 4FGL name is the most commonly used designation for this system. The 'Mass' column refers to the mass of the companion star, and indicates whether a system is considered a high mass X-ray binary or a low mass X-ray binary in the 4FGL-DR3. LII and BII give the Galactic coordinates of each system.

production of γ-rays. Of these 30 systems, 11 are colliding wind binaries, classical novae or other systems, and the remaining 19 are XRBs; eleven of these are HMXBs and 8 are LMXBs. In this Chapter, we analyse 18 of these 19 XRBs (Table 9.1). The one 4FGL-XRB not analysed is the HMXB 1RXS J172006.1-311702/4FGL J1720.0-3117c; this system is excluded so that the 4FGL-DR2 can be used in the analysis to maintain consistency with the previous analyses from Chapters 5 - 8, as this system was only added in the 4FGL-DR3, and therefore it is not included in the catalogue I used for analysis. All of the XRBs listed in Table 9.1 are Galactic sources with the exception of LMC P3, which is located in the Large Magellanic Cloud. The majority of the 4FGL-XRB population is not included in the Liu et al. (2006) and Liu et al. (2007) catalogues, as these systems were first discovered by

4FGL-XRB Observation Period (Dates)	04/08/2008 - 26/07/2021
4FGL-XRB Observation Period (MET)	239557417 - 648950405
4FGL-XRB Observation Period (MJD)	54682 - 59421
Energy Range (GeV)	0.1 - 500
Data ROI width	10°
Model ROI Width	15°
Zenith Angle	$< 90°$
GTI Filter	`DATA_QUAL>0 && LAT_CONFIG==1`
Instrument Response	`P8R3_SOURCE_V2`
Isotropic Diffuse Model	`iso_P8R3_SOURCE_V2_v1`
Galactic Diffuse Model	`gll_iem_v07`
Point Source Catalogue	4FGL-DR2
Extended Source Templates	8 Year Templates

Table 9.2: The parameters used in the likelihood analysis of the regions of interest around the 4FGL X-ray binary systems.

Fermi-LAT, which first launched in 2008 after the publication of the catalogues.

9.2 *Fermi*-LAT Observations of the 4FGL-XRBs

I analyse the 4FGL-XRBs in a similar way to the survey analysis performed in Chapter 5. The parameters for this analysis are given in Table 9.2, and again I use `Fermipy 0.19.0` alongside `Fermitools 1.2.23` to analyse the data.

A model centered on the 4FGL source of each XRB in Table 9.1 is created and fitted with MLE using the method described in Chapter 5. The only difference is that no point source is fitted to the centre of the ROI, as the XRBs are already added to the models with prior parameters from the 4FGL-DR2. Having fitted the model to the data, I then generate a TS map and residual map to check the quality of the modelling. Finally, in the case of each XRB an SED is produced, and a light-curve is generated with 25 bins (approximately 6 months in length). The SED for each XRB is given in Appendix G, and the light-curve for each XRB is given in Appendix H.

9.3 The High Mass X-ray Binaries

Each of the high mass X-ray binaries is detected more significantly in my analysis than in the 4FGL-DR3*. The TS values and corresponding z-scores are given in Table 9.3 alongside the 4FGL-DR3 detection z-scores for reference. The factor by which the analysis z-scores increases over the 4FGL values varies considerably, with a marginal increase in the case of Cygnus X-1 (9.4σ to 9.5σ) to increases by a factor of 2 to 3 in cases such as PSR B1259-63 and Cygnus X-3. Several of these 4FGL-HMXBs (Cyg X-1, Cyg X-3, LS 5039 and LSI +61 303) are also analysed in Chapter 5 over a slightly shorter timescale, where we see a similar increase in TS value.

Spectra are generated for each of the 4FGL-HMXBs, with the number of bins based on available photon statistics (i.e. more significant sources have narrower bins). Each binary is fitted well by either a soft power law or a log-parabola. Unsurprisingly, the spectral shapes match those in the catalogue; I use 13.5 years of data for analysis whereas the 4FGL-DR3 uses 12, only a relatively modest increase in observation time. Additionally, the X-ray binary population is not generally known to have spectral variability, so such behaviour would have been unexpected.

Given that the majority of the HMXB population is expected to harbour a neutron star, some of which may be pulsars (themselves γ-ray emitters), one cannot discount the possibility that the pulsars within binary systems are emitting γ-rays independently of any wider interactions with the companion stars. It would be necessary to reclassify such systems as γ-ray pulsars (which are serendipitously part of a binary), rather than γ-ray emitting X-ray binaries. Pulsars however, have a unique spectral shape when compared to other γ-ray sources: a power law with a super-exponential cut-off†. As none of these binaries have such a spectrum, we can

*The catalogue z-scores are taken from the 4FGL-DR3, although the DR2 is used for analysis. This is because the DR3 provides a more up-to-date and accurate z-score than the DR2, which better reflects the values calculated in my analysis.

†There are several different spectral models called 'power law with a super-exponential cutoff' used in the analysis of *Fermi* data. I use the PLSu-

Binary Name	TS	z-Score	4FGL z-Score	Spectral Shape	Type	VHE?	Accretor
LMC P3	384	19.6σ	18.7σ	Log-Parabola	γ-Bin	Yes	NS(?)
PSR B1259-63	347	18.6σ	5.4σ	Power-Law	γ-Bin	Yes	NS
4FGL J1405.1-6119	2470	49.7σ	26.2σ	Log-Parabola	γ-Bin	No	NS(?)
1FGL J1018.6-5856	26800	163σ	86.9σ	Log-Parabola	γ-Bin	No	NS(?)
LS 5039	18300	135σ	61.6σ	Log-Parabola	γ-Bin/MQr(?)	Yes	NS(?)
HESS J1832-093	142	11.9σ	10.8σ	Power-Law	γ-Bin	Yes	NS(?)
HESS J0632+057	36.7	6.1σ	4.3σ	Power-Law	γ-Bin	Yes	NS(?)
Cygnus X-1	89.6	9.5σ	9.4σ	Power-Law	MQr	No	BH
Cygnus X-3	1200	34.7σ	16.1σ	Log-Parabola	MQr	No	BH(?)
LSI +61 303	175000	417σ	250σ	Log-Parabola	γ-Bin/MQr(?)	Yes	NS
SAX J1324.4-6200	12.8/28.7(Tr)	3.6σ/5.4σ(Tr)	N/A	Power Law (Tr)	γ-Bin(?)	No	NS
GRO J1008-57	7.9/15.6(Tr)	2.8σ/3.9σ(Tr)	N/A	Unknown	γ-Bin(?)	No	NS
1A 0535+262	12.4	3.5σ	N/A	Unknown	γ-Bin	No	NS
RX J2030.5+4751	30.8	5.5σ	N/A	Unknown	γ-Bin?	No	NS(?)

Table 9.3: The properties of the γ-ray emitting HMXB population. The top section of the table lists the 4FGL-XRBs, and the bottom section lists the most likely candidate binaries discussed in Chapters 5 and 6. The TS and z-Score columns informs of the statistical significance of each system from my analysis using parameters described in this Chapter for the upper section, and Chapter 5. The sole difference between the analysis parameters used in Chapters 5 and 9 is the observation timescale. The (Tr) tag indicates that a statistic was calculated for a transient event, and not the full observation period. The 4FGL z-Score informs of the statistical significance of each source in the 4FGL-DR3. The spectral shape informs of the best fit equation to the spectrum of each system. Type indicates whether a system is a known microquasar (MQr) or γ-ray binary (γ-Bin), or thought to be both. The (?) tag, indicates that a system is speculated to fit one of these categories but evidence is weak for this association. The VHE column indicates whether each system has been detected at Very High Energies, and hence has a corresponding entry into TeVCAT. The accretor column indicates whether the compact object of a system is a neutron star (NS) or a black hole (BH). The (?) tag indicates that there is some uncertainty as to the nature of the accretor.

be reasonably confident that their emission is not dominated by pulsar emission, at least in the cases where photon statistics are significant enough to calculate the spectral model and parameters of the binary accurately enough. Pulsations in the γ-ray data would also be a key indicator of pulsar dominated γ-ray emission; this is not seen in any of the binaries listed in Table 9.3.

9.3.1 The γ-ray Emitting Microquasars

In general, there are two broad populations of γ-ray emitting HMXBs shown in Table 9.3, the smaller of which is the microquasars. Two of the known eleven 4FGL-HMXBs are microquasars, Cygnus X-1 and Cygnus X-3. Neither of these sources is detected at VHE, and Cyg X-1 has a power law spectral shape, whereas Cyg X-3 has a log-parabola spectrum.

Cyg X-1 is one of two γ-ray emitting X-ray binaries where there is solid evidence for a black hole accretor (Fabian et al., 1989), the other being SS 433 (Section 9.3.1.1). The system is persistently observed in the γ-ray regime whenever a jet is known to be present, but there is no observed link between the γ-ray emission and the hardness-intensity cycle in this system (Zanin et al., 2016).

Cyg X-3 is expected to have a low mass black hole companion, although there is still debate over this (Shrader et al. 2010 & Zdziarski et al. 2013). Cyg X-3 is a unique system as it contains the only known Wolf-Rayet star in an X-ray binary system. Unlike in Cyg X-1 where γ-ray emission is persistent, in Cyg X-3 it is highly variable and is associated with the transition from the hard state into the soft state, typically where highly relativistic discrete ejecta ('blobs') are seen moving down the jet, which cause radio flares (Corbel et al. 2012 & Bodaghee et al. 2013). Cyg X-3 has an orbital period of 4.8 hours (Bhargava et al., 2017) and orbital modulation is seen in the γ-ray data which is consistent with this period (Abdo et al., 2009b). Whilst orbital modulation is typically seen in X-ray binaries

perExpCutoff2 model, the full description of which can be found here: https://fermi.gsfc.nasa.gov/ssc/data/analysis/scitools/source_models.html

as a result of wind-wind interactions (i.e. in γ-ray binaries), in this case the orbital modulation originates from the jets. This implies that the γ-ray emission zone in the jet must be reasonably close to the central compact object.

What ties these two systems together is that the γ-ray emission originates in the jet. Indeed, as Cyg X-1 and probably Cyg X-3 have black hole companions, a wind-wind interaction between a pulsar wind and stellar wind is impossible, at least in the case of Cyg X-1. The presence of orbitally modulated γ-ray emission in Cyg X-3 is typically an indicator of a companion star (in this case a WR star with powerful stellar winds) and a neutron star wind. Hence, one cannot rule out some wind-wind contribution to the γ-ray emission in this case, although correlated variability with the radio activity of the jet indicates that the γ-ray emission in Cyg X-3 is jet dominated.

There has been debate as to whether the γ-ray emission from microquasar jets originates from leptonic or hadronic mechanisms, although it is now established that the more likely cause of the γ-ray emission in Cyg X-1 and Cyg X-3 is leptonic (Bosch-Ramon and Khangulyan 2009 & Zanin et al. 2016). In the leptonic scenario, the electrons in the jet transfer their energy to the surrounding photon field through inverse-Compton scattering thus producing γ-rays (Chapter 3). The seed photon field could originate from a number of places; close to the compact object it is likely to be dominated by thermal emission from the accretion disc, whereas further away from the black hole it is likely to be dominated by emission from the companion star (Kafatos et al. 1981 & Romero et al. 2014). Additionally, if there is a synchrotron component to the jet emission, these synchrotron photons which originate from the jet electrons could re-interact with them and upscatter into γ-ray emission via synchrotron self Compton emission (Ghisellini, 2013). Given that γ-ray emission is seen to peak when discrete blobs (where the electron Lorentz factor, $\Gamma > 2$) move down the jet in Cyg X-3, it thus follows that the γ-ray emission in these microquasars is caused by inverse Compton scattering from the jet.

What is unclear is why only these two microquasars (again, excepting SS 433) are

seen to be γ-ray emitters when there are now a number of microquasars which we have seen to go through similar behaviours. In Chapter 4 we examined the case of V404 Cygni and its giant outburst in 2015. Like Cyg X-1 and Cyg X-3 this system contains a stellar mass black hole, although the companion star is low mass, so that accretion will occur through Roche lobe overflow rather than stellar wind accretion. The AGILE data show a weak γ-ray excess corresponding to the hard to soft state change, where jet blobs are expected to occur. However, there is no evidence for γ-ray emission with *Fermi*-LAT, following my analysis (Chapter 4), and the AGILE data remain the only hint of γ-ray emission from this system. Other famous high and low-mass microquasars are covered in the γ-ray survey and no evidence for emission is found from any of these sources*. Cyg X-3 is unique in that it has a massive hot WR companion star, however the Cyg X-1 system has an O-type companion with stellar mass of $20M_{\odot} \pm 5M_{\odot}$ (Ziółkowski, 2005), which isn't unusual amongst the HMXB population. It is also unlikely that distance plays a major part in the detection of these source, as whilst Cygnus X-1 is relatively close by (2.25 kpc), so are other microquasars such as V404 Cygni (2.39 kpc) where no γ-ray emission is detected. furthermore, the other two γ-ray emitting microquasars are considerably further away; SS 433 at 5.5 kpc and Cyg X-3 at 7.4 kpc. Without further data, and further microquasar detections at γ-ray wavelengths, it is not possible to determine why Cyg X-1 and Cyg X-3 in particular are γ-ray emitters.

9.3.1.1 The Exceptional SS 433

SS 433 is a HMXB which has a black hole accretor of approximately $19M_{\odot} \pm 7M_{\odot}$ (Gies et al., 2002), and a massive A3-7 I type donor star of mass $10.9M_{\odot} \pm 3.1M_{\odot}$ and an orbital period of 13.1 days (Hillwig et al., 2004). SS 433 is a unique system amongst the X-ray binaries for a number of reasons. It is located in the centre if the W50 nebula, a remnant of the compact object supernova.

*A false positive is observed from GRS 1915+105 but there is no evidence to associate this with the binary itself beyond spatial coincidence.

SS 433 is a supercritical Eddington accreting X-ray binary, the only such system to have been observed within our Galaxy (ULXs are strong candidates for extragalactic super-Eddington accretors). The relativistic jets typically associated with accretion above the Eddington limit have been seen consistently since the system's discovery (Okuda, 2002), and giant radio outbursts are seen of similar nature to those of Cyg X-3 (Jeffrey et al., 2016). The jet speeds are known to reach velocities as high as $0.32c$ during such outbursts, so particles must be accelerated to highly relativistic velocities in these jets. In addition to the 13 day orbital time period, the precession of the system is seen in the jet and as a result the jet and counterjet form a corkscrew pattern on the sky.

SS 433 is not a *catalogued* source in any iteration of the *Fermi*-LAT point source catalogues, but nonetheless is a known *Fermi*-LAT γ-ray source. SS 433 was first identified to be a γ-ray emitter with the LAT in 2015, and has subsequently been identified in a number of studies, where evidence for both the precession and orbital periods have been identified in the γ-ray data (Bordas et al. 2015, Xing et al. 2019, Rasul et al. 2019, & Li et al. 2020). This emission is very soft and terminates below 1 GeV. The γ-ray emission is also found to occur not from the central SS 433 binary itself, but offset towards the easternmost jet termination region. The consensus is that this is likely due to collisions between accelerated jet protons and the cold material in the regions surrounding SS 433 (e.g. Bordas et al. (2015)), although the presence of periodicity suggests that the emission region may lie closer to the central black hole (Rasul et al., 2019). SS 433 is also seen at TeV energies with the High Altitude Water Cherenkov Observatory (HAWC), where the emission is localised in both the east and the west termination shocks 40 pc away from the binary itself (Abeysekara et al., 2018b).

Given that the γ-ray emission in SS 433 is well localised to the termination shocks, the mechanisms for γ-ray production in this system are fundamentally different to those of Cyg X-1, Cyg X-3 and any possible emission in V404 Cygni. Furthermore, as SS 433 is a unique supercritical source, it is exceptional amongst X-ray binaries.

9.3.2 The γ-ray Binaries

The second, and much larger, group of γ-ray emitting XRBs is the γ-ray binaries. Whilst traditionally 'γ-ray binary' referred to any X-ray binary with the peak of its emission in the γ-ray waveband, I use it to refer to XRBs where γ-rays are produced by some means other than a jet (i.e. not a microquasar), regardless of where the peak of their emission lies on the EM spectrum. This group is made up of PSR B1259-63, 4FGL J1405.1-6119, 1FGL J1018.6-5856, LS 5039, HESS J1832-093, HESS J0632+057, LSI +61 303 and the extragalactic source LMC P3. Unlike the microquasars, which are not detected at VHE, all of the aforementioned systems are, with the exceptions of 4FGL J1405.1-6119 and 1FGL J1018.6-5856. The detection significances of the γ-ray binaries varies widely, from the weakly detected HESS J0632+057 at 6.1σ to the extremely luminous and significant LSI +61 303 at 417σ. In all of the cases discussed here, it is thought that interactions between a pulsar wind and a companion's stellar wind is causing the shocks which produce γ-rays.

Smaller stars are more common than larger stars, thus it is expected that more X-ray binaries have neutron star accretors (with masses below the $2.16M_{\odot}$ limit set by neutron degeneracy pressure) than black holes. Whilst the picture is slightly more complicated than the initial mass function describes (accretor mass is lost during the formation supernova and then regained through accretion from the companion), this prediction is generally true (Belczynski and Ziolkowski 2009 & Tetarenko et al. 2019), and is reflected in the nature of the accretors seen in Table 9.3. However, only a small number of NS-systems are known to emit γ-rays and it is unclear why.

Four candidate sources show evidence for γ-ray emission in my HMXB survey: SAX J1324.4-6200, GRO J1008-57, 1A 0535+262 and RX J2030.5+4751. All of these have confirmed or suspected neutron star accretors, like the rest of the γ-ray binary population, and the one source from which a spectrum can be obtained (SAX J1324.4-6200) yields a spectrum consistent with known 4FGL-HMXB spec-

tra, a soft power law. None of these systems are known microquasars. Including these four candidate sources with the 4FGL γ-ray binaries results in 13 systems with neutron star accretors, with a diverse set of characteristics between them.

9.3.2.1 Orbital modulation in γ-ray binaries

Orbital modulation is a universal feature amongst the 4FGL γ-ray binaries, and distinguishes these systems from the microquasars*. These are LS 5039 (Abdo et al., 2009c), PSR B1259-63, (Chang et al., 2018), LMC P3 (Corbet et al., 2016), 4FGL J1405.1-6119 (Corbet et al., 2019), 1FGL J1018.6-5856 (Ackermann et al., 2012) and LSI +61 303 (Abdo et al., 2009a) where the flux peaks just after periastron, HESS J0632+057 (Adams et al., 2021) which shows modulation but has an poorly understood ephemeris, and possibly HESS J1832-093 (Martí-Devesa and Reimer, 2020). Additionally, the γ-ray binaries also sometimes display a smaller peak preceding apastron. The spectra of the γ-ray binaries are not known to vary by orbital phase.

Orbital modulation is the strongest piece of evidence for association of an HMXB with a γ-ray excess. I search for orbital modulation in the candidate HMXBs from the survey where possible, and generate phased light-curves for 1A 0535+262 and GRO J1008-57, both of which show some evidence for orbital modulation in their emission. In the case of 1A 0535+252, a 3.5σ excess is seen in the bin immediately following periastron, and no emission is seen in any other bin. This corresponds to the orbital phase where the flux peaks in the majority of the 4FGL γ-ray binaries, and is strongly suggestive of orbital modulation in the excess. Additionally, there may be some correlation between γ-ray emission and the Type-II X-ray outbursts in this system, but this is tenuous. The case of GRO J1008-57 is more complex. We see evidence for γ-ray emission both preceding and following periastron, but with a lag in phase of approximately one bin. Whilst it is expected that there is

*As previously mentioned and indicated in Table 9.3, LS 5039 and LSI +61 303 may also be microquasars, although it is likely that their γ-ray emission is dominated by wind-wind interactions.

a small lag between periastron and the γ-ray peak, the size of the lag in this case is unusually long. Additionally, a small peak is seen at apastron, which is seen in other systems. Although the TS of the excesses associated with both are too low to claim a formal detection, the pattern of orbital modulation in both cases is indicative of these systems being γ-ray emitters, like the 4FGL γ-ray binaries.

As orbital modulation is *the* distinguishing feature of these systems, it is the optimal way of identifying new γ-ray binaries as is shown in Chapter 6, and also in studies such as Corbet et al. (2019). Unfortunately, many HMXBs have no identified orbital period, and blind searches for modulation in the LAT data can be difficult given that γ-ray sources tend to have low photon statistics and the LAT is not very sensitive to rapid variability. Furthermore, in many cases the orbital period in many systems is so short that producing a phase folded light-curve is not possible, as the uncertainties in the ephemeris are too large. Nonetheless, it is likely that at least some of the many unidentified sources in the 4FGL-DR3 are γ-ray binaries.

9.3.2.2 VHE emission from γ-ray binaries

Many of the γ-ray binaries are VHE emitters, a feature unique to these sources, as no microquasars are seen at TeV energies other than emission from the termination shocks of SS 433 seen with HAWC (Abeysekara et al., 2018b). Dubus (2013) and Dubus (2015) provide an in depth review of the γ-ray properties of these systems, where it is universally seen that the TeV component of the γ-ray binaries' spectra is part of the inverse Compton peak, whilst the *Fermi*-LAT observations form either part of the inverse Compton peak, the synchrotron peak, or both, depending on the binary in question. In many cases with *Fermi*-LAT, upper limits are seen at approximately $E > 10\,\mathrm{GeV}$ as the instrument is not sensitive enough to provide accurate flux measurements, particularly as this energy range tends to lie in the dip between the synchrotron and inverse Compton spectral components. TeV detectors such as H.E.S.S., MAGIC and VERITAS however all have a much better instantaneous sensitivity than *Fermi*-LAT, and are therefore better suited to prob-

ing both the dip and Inverse Compton components of these sources. Unlike the microquasars, it is not thought that the γ-ray binaries have a hadronic component to their spectra for a number of reasons, including that it is difficult to explain the characteristic orbital modulations with hadronic models (Aharonian et al. 2006b & Chernyakova et al. 2006).

In addition to the VHE emitting γ-ray binaries shown in Table 9.3, another system has been identified at VHE energies: PSR J2032+412, a pulsar-Be star system. VHE emission was observed with VERITAS and MAGIC, with observations taken over 19 months around periastron, on 17th November 2017 (Abeysekara et al., 2018a). PSR J2032+4127 has a much longer orbital period than the binaries detected with *Fermi*-LAT, at approximately 50 years (Ho et al., 2017). No modulation is seen with *Fermi*-LAT*, likely due to magnetospheric masking of the GeV γ-ray emission by the pulsar (Li et al., 2018).

The detection of a source with such a long period raises the possibility that many more of the γ-ray binary population may be transient. This is the most likely explanation for the observed transient excess in SAX J1324.4-6200, which exceeds the 5σ detection threshold over an 18 month period, which could lie at periastron if the system has a similarly long period. If this is the case, it would probably be decades before a window of opportunity for observations was once again open.

9.3.3 Conclusions on the γ-ray emitting HMXBs

The γ-ray emitting HMXBs are diverse, although all of them are observed with *Fermi*-LAT apart from PSR J2032+4127. It is difficult to identify a universal 'trigger' for γ-ray emission, as they are divided into two different subgroups with different emission mechanisms, the jet-powered microquasars and the wind-powered γ-ray binaries. In both sub-classes it is likely that inverse Compton scattering is the cause of γ-ray emission (although jet models may also have a hadronic compon-

*The pulsar in this system is a 4FGL source, however Li et al. (2018) reports that it does not vary in its emission at periastron.

ent). Orbital modulation is seen in both the microquasars and the γ-ray binaries, although it is an almost universal feature of the γ-ray binaries. Given the substantial differences between the microquasars and wind-driven systems it is necessary to treat them as separate populations, even though a neutron star microquasar may also have wind-driven interactions. There is no evidence for a HMXB with both wind driven and jet driven γ-ray emission.

The microquasar systems all vary significantly in their apparent properties. Cyg X-1 and Cyg X-3 appear as point sources which implies that γ-ray emission is taking place relatively closely to the compact object (thought to be a black hole in all three cases), but SS 433 appears extended, with emission localised to the termination shocks of the jets in both LAT data and at VHE. Rises in γ-ray flux rates are seen in all three systems corresponding with the giant radio flares associated with the transition between the hard state and the soft state. Persistent emission is seen in the supercritical SS 433 (where the jets are persistent) and Cygnus X-1, but not Cygnus X-3. In Cygnus X-3, no γ-ray emission is seen when the source is in the hard state, despite the fact that I find the γ-ray emission from Cyg X-3 (TS = 1200) is more significant than from Cyg X-1 (TS = 89.9). This implies fundamental differences between the individual γ-ray emitting microquasars, and it is clear that more detections of such sources need to be made at γ-ray wavelengths to expand the scientific understanding of these systems.

The γ-ray binaries are the larger of the two groups, with nine sources included in the *Fermi*-LAT catalogue, one with VHE emission only but no evidence for modulation in the LAT data, and four candidates identified in the survey presented in Chapters 5 and 6. Orbital modulation is an almost universal feature of these sources with at least some evidence for modulation in every 4FGL-DR3 system, and at least two of the four candidate sources from the survey. Additionally, variability is seen from both SAX J1324.4-6200 and RX J2030.5+4751 which may be suggestive of modulation on much longer timescales, similar to that seen in PSR J2032+412. Searching for orbital modulation at the positions of X-ray binaries may

help to reveal new systems, and similarly, orbital modulation found in any unidentified *Fermi*-LAT sources would likely indicate new γ-ray binaries. The emission mechanisms are well constrained to be wind driven inverse Compton mechanisms, unlike the microquasars where questions still remain to be answered.

9.4 The Low Mass X-ray Binaries

From the analysis of the 4FGL-XRBs, each of the low mass X-ray binaries is detected at approximately* the same significance as their 4FGL-DR3 values. The TS values and corresponding z-scores are given in Table 9.4. Like the HMXBs, the spectrum of each LMXB is fitted with either a power-law or a log-parabola, all of which match those in the 4FGL-DR3.

9.4.1 Galactic latitude and its impact on γ-ray emission

As mentioned previously, the LMXB population is spatially concentrated in globular clusters, the Galactic centre and otherwise across the Galactic plane. Consequently, LMXBs generally have low absolute† Galactic latitudes, as shown in Figure 9.1 which shows that the LMXBs included in the Liu et al. (2007) catalogue, have a mean absolute Galactic latitude of 5.85°, with 131 of the 187 LMXBs lying within 5° latitude of the plane. Using Kernel Density Estimation (KDE), a probability density function of the LMXBs' absolute Galactic latitudes is calculated, shown in Figure 9.2.

As expected, the shape of the probability density curve maps the distribution of the LMXBs in the histogram. As the absolute Galactic latitude represents a continuous probability distribution, using the mean absolute latitude, we are able to calculate a standard deviation from the mean of 9.39°, and therefore place 68% and 95% confidence limits on the sample. These limits are shown on Figure 9.2.

*'Approximately' means to within ±20% of the 4FGL-DR3 z-score

†For clarity, by 'absolute' I mean the modulus of the Galactic latitude coordinate, as measured in degrees on the sky.

Binary Name	TS	z-Score	4FGL z-Score	Spectral Shape	LII	BII	Accretor
4FGL J0540.0-7552	174	13.2σ	15.3σ	Log-Parabola	287.2820°	−30.5822°	NS (tMSP)
1SXPS J042749.2-670434	641	25.3σ	28.2σ	Power-Law	279.1443°	−38.5517	NS (tMSP)
2S 0921-630	67.3	8.2σ	9.0σ	Log-Parabola	281.7689°	−9.4007°	NS
4FGL J0407.7-5702	38.4	6.2σ	6.2σ	Power-Law	267.7967°	−44.4116°	NS (tMSP)
1RXS J154439.4-112820	674	26.0σ	23.3σ	Log-Parabola	356.1769°	32.9939°	NS (tMSP)
PSR J1023+0038	6560	81.0σ	72.3σ	Log-Parabola	243.4800°	45.7825°	NS (tMSP)
4FGL J0336.0+7502	1170	34.1σ	35.3σ	Log-Parabola	133.0828°	15.5279°	NS (tMSP)
2SXPS J094023.5-761001	557	23.6σ	23.6σ	Log-Parabola	292.2483°	−17.4495°	NS (tMSP)
GS 1826-238	27.6(Tr)	5.3σ(Tr)	N/A	Power-Law	9.350°	−6.0412°	NS

Table 9.4: The properties of the γ-ray emitting LMXB population. The top section of the table lists the 4FGL-XRBs, and the bottom section lists GS 1826-238 the most likely candidate LMXB discussed in Chapters 5 and 7. The TS and z-Score columns informs of the statistical significance of each system from my analysis using parameters described in this Chapter for the upper section, and Chapter 5. The sole difference between the analysis parameters used in Chapters 5 and 9 is the observation timescale. The (Tr) tag indicates that a statistic was calculated for a transient event, and not the full observation period. The 4FGL z-Score informs of the statistical significance of each source in the 4FGL-DR3. The spectral shape informs of the best fit equation to the spectrum of each system. The LII and BII columns give the Galactic coordinates of each system. The accretor column indicates whether the compact object of a system is a neutron star (NS) or a black hole (BH). The (tMSP) label indicates that the neutron star in this system is a transitioning millisecond pulsar (MSP).

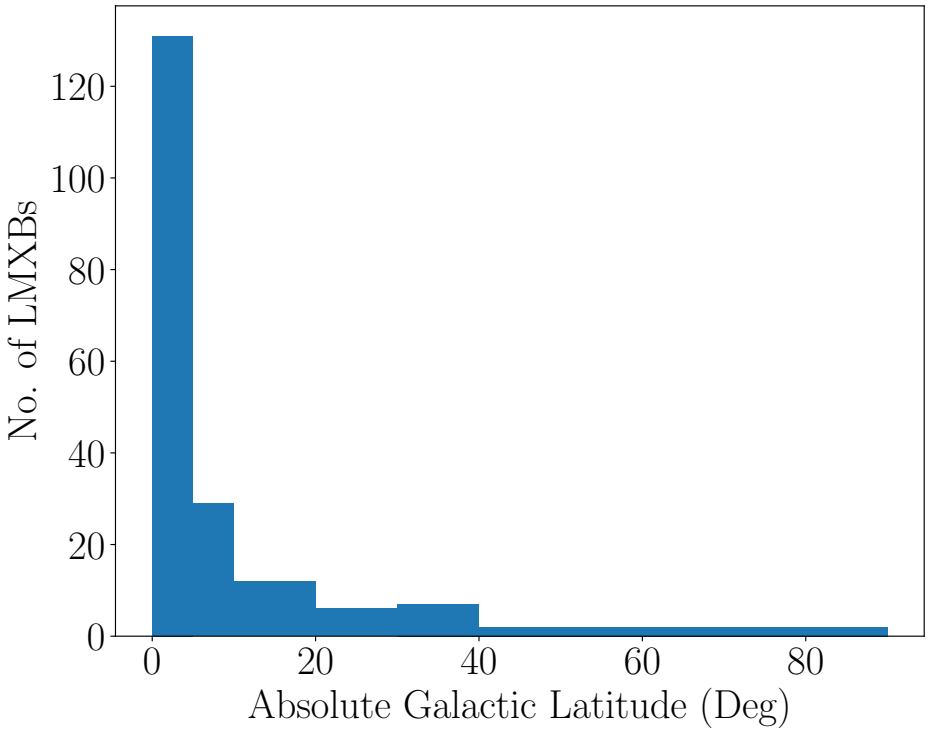

Figure 9.1: A histogram of the absolute Galactic latitudes of the LMXB population from the Liu et al. catalogue. The bin edges are 0°, 5°, 10°, 20°, 30°, 40° and 90°. None of the 4FGL LMXBs are included in this sample, as they are not included in the Liu et al. catalogue.

None of the 4FGL-DR3 LMXBs are included in Liu et al. (2007), as they were all discovered after the publication of this catalogue. Therefore, the 4FGL-DR3 LMXBs represent a separate population to those which were surveyed in Chapters 5 - 8. Table 9.4 gives the Galactic latitude of each of these LMXBs, and by taking the absolute value of these and calculating the mean, I obtain a mean absolute Galactic latitude of 29.33° off the Galactic plane for the 4FGL-DR3 LMXB population, which lies outside the 95% confidence figure (24.25°) for the LMXB population in Figure 9.2. This indicates that it is likely that the 4FGL-DR3 LMXB population is spatially distributed in a significantly different way to the bulk of the LMXB population from the Liu et al. (2007) catalogue.*

*As GS 1826-238 is not a confirmed γ-ray emitter, this LMXB is included in the Liu et al. (2007) population, and not the 4FGL-DR3 population for the purposes of this statistical analysis.

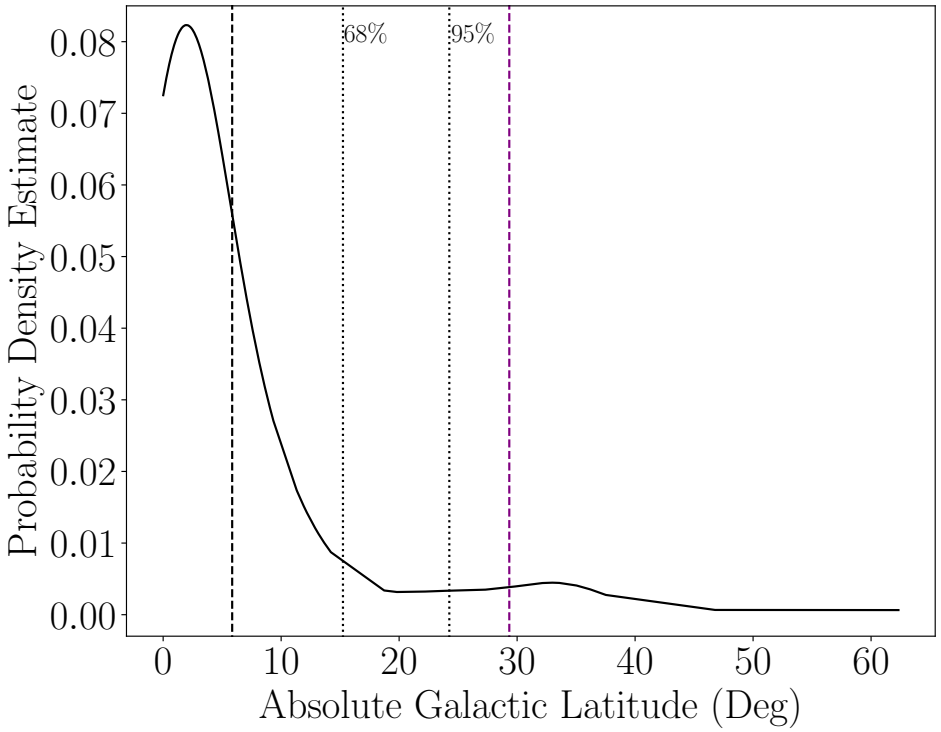

Figure 9.2: A probability density function of the absolute Galactic latitudes of the Liu et al. LMXB population obtained through Kernel Density Estimation of the population. The mean latitude of 5.85° is highlighted by the black dashed line, with the 68% and 95% confidence intervals indicated by the grey dotted lines. The purple dashed line indicates the mean value of the γ-ray emitting LMXB population included in the 4FGL-DR3. The 4FGL-DR3 LMXB population is not included in the Liu et al. population.

I perform a 2-sample KS test (Equation 4.1) on the two latitude populations in order to test whether they are drawn from the sample overall population (Kolmogorov 1933 & Smirnov 1948). From this test, I obtain a KS statistic of 0.856, which in turn gives a p-value of 6.98×10^{-6} that these two samples are drawn from the same population. This indicates a statistical difference in the Galactic latitudes of the 4FGL-DR3 and Liu et al. (2007) LMXB populations to a 4.5σ level.

As discussed in Appendix A, two populations of stars inhabit our galaxy. Population I stars are generally young and inhabit the spiral arms of the Milky Way, whereas Population II stars are generally older, and inhabit the central bulge, and

globular clusters of the galaxy. This distribution generally matches the two mass classes of XRB; the LMXBs are generally found towards the Galactic centre and in globular clusters which suggests that these systems are old and therefore further away. The HMXBs constitute much younger, and therefore closer, systems as their massive companion stars have much shorter timescales, on the order of Myr, rather than Gyr. If we act under the axiom that stars on the Galactic plane are *generally* further away than those off the plane, we can extend this to the LMXBs. Given that we have demonstrated that the majority of the LMXB population is concentrated on the Galactic plane (and particularly towards the Galactic centre), we can assume that the majority of these systems are a long way from the Earth. The γ-ray 4FGL-DR3 LMXBs however, are decidedly off-the-plane objects, therefore we can assume that, in general, these LMXBs are closer to the Earth than those on the plane. The primary reason we see 8 LMXBs with *Fermi*-LAT out of a population of several hundred is that we are seeing the systems that are nearby, and therefore have the most intense γ-ray flux.

9.4.2 The millisecond pulsar connection

The known population of γ-ray emitting LMXBs exclusively harbours neutron star accretors; all of the 4FGL-DR3 LMXBs are also transitioning millisecond pulsar candidates (tMSP)* with two exceptions. These are 2S 0921-630, where although it is established that the neutron star is accreting from the companion, it is currently unclear whether this neutron star is also a tMSP, and GS 1826-238, identified as a candidate γ-ray emitting LMXB in Chapter 7 which also hosts an accretion powered neutron star that does not appear to be a tMSP. GS 1826-238 is an X-ray burster, and would represent the first LMXB burster to be a confirmed γ-ray emitter.

It is highly unlikely to be a coincidence that the γ-ray emitting LMXBs are primarily tMSP systems. As Papitto and de Martino (2020) establish, tMSPs and tMSP

*As discussed in Chapter 3, a tMSP is a binary star system which appears to switch between an accreting X-ray binary stage, and a radio MSP stage.

candidates are rare; examining the known tMSP and candidate systems at the time, they found 4 out of 9 of these tMSPs are γ-ray emitters in the 4FGL* with CXOU J110926.4-650224 being spatially coincident with FL8Y J1109.8–6500†. Of the 4 or 5 tMSPs which are not γ-ray emitters, one is close to the Galactic centre (XMM J174457-2850.3) and two are located in globular clusters (Terzan 5 CX10 and IGR J18245-2452), further away from Earth than the other γ-ray LMXBs (Section 9.4.1). In addition to the 9 tMSPs discussed by Papitto and de Martino (2020), three more have been discovered since, all with γ-ray emission. These are 4FGL J0540.0-7552 (Strader et al., 2021), 4FGL J0336.0+7502 (Li et al., 2021), and 2SXPS J094023.5-761001 (Swihart et al., 2021). Including these 3 sources, the total tMSP population reaches 12 objects, 7 (8 if we include CXOU J110926.4-650224) of which are γ-ray emitting.

It is likely that there is a mechanism unique to the tMSP systems which is producing γ-ray emission in low mass X-ray binary systems. Given that γ-ray emitting MSPs are a well documented source class in the *Fermi*-LAT catalogues, and LMXBs are otherwise not, it is logical to assume that the γ-ray production in these tMSP systems occurs primarily during the pulsar-like rotation powered phase where radio emission is also seen, rather than the accretion powered X-ray phase. Given the presence of synchrotron radio emission, it follows that the γ-ray emission in these tMSP systems is likely due to inverse Compton mechanism as is seen in the rest of the γ-ray pulsar population (Lyutikov, 2013). Whilst many NS-LMXBs are observed in the radio waveband, tMSPs are the brightest, which suggests that the non-thermal emission in these systems may be stronger than the average NS-LMXB (Bogdanov et al., 2018). This supports the idea that tMSPs are a unique γ-ray emitting subclass of LMXB.

*These four LMXB/tMSPs are 1RXS J154439.4-112820, PSR J1023+0038, 1SXPS J042749.2-670434 and 4FGL J0407.7–5702

†The FL8Y was a preliminary source catalogue to the 4FGL with a very similar 8-year list of sources, but utilised the 4-year background models of the 3FGL.

9.4.3 Conclusions on the γ-ray emitting LMXBs

There are two features that the γ-ray emitting LMXBs share; almost all are tMSPs or tMSP candidates and they all have high absolute Galactic latitudes, indicating that they are likely close to us. Given that tMSPs are rare objects as it is, the fact that we see γ-ray emission only from those nearby indicates that this class of LMXB may generally emit γ-rays in their rotation powered state, but that many of these sources are too far away to obtain a measurable γ-ray flux from with current instrumentation.

Given that both MSPs and LMXBs are known to be concentrated in globular clusters, which are themselves γ-ray emitters, it is likely that some of the globular cluster LMXB population is part of the tMSP subclass, and that even though individual LMXBs cannot be identified, these sources contribute to the overall γ-ray emission from globular clusters (which is thought to be dominated by MSPs). Similarly, no evidence for γ-ray emission from individual LMXBs in the Galactic centre is found (Chapter 8), but as there is an apparent excess of GeV γ-rays in the Galactic centre as a whole (Hooper and Goodenough 2011 & Ackermann et al. 2017) it is thought this may be produced by a population of MSPs (Hooper and Mohlabeng, 2016). It is possible that the wider γ-ray Galactic diffuse emission is contributed to by the Galactic tMSP population that is too far away to be resolved as point sources.

The exception to the 'high-latitude, tMSP' rule appears to be 2S 0921-630 (4FGL J0921.7-6317), which is detected at 8.2σ. Whilst this source does have a neutron star accretor, it is not a known tMSP, and it is detected at a relatively low Galactic latitude of $-9.4007°$. There is no variability to associate 2S 0921-630 with the γ-ray emission, which is based on spatial coincidence alone. The fact that it doesn't fit with the pattern of being a higher latitude tMSP may suggest that 2S 0921-630 is erroneously associated with its γ-ray counterpart, 4FGL J0921.7-6317. If 4FGL J0921.7-6317 and 2S 0921-630 are, in fact, one and the same then it is likely that it

is a wind-driven γ-ray binary system, with shocks between the wind of the neutron star and the Roche lobe of the companion star. This would represent the first known 'classical' LMXB detected with *Fermi*-LAT; this would be a prime target for VHE observations with a southern hemisphere observatory.

Detected in the LMXB survey in Chapter 7, GS 1826-238 is also a neutron star LMXB with a low Galactic latitude, which is not a tMSP. GS 1826-238 is detected over a 30 month time period to 5.3σ in significance, presenting a similar case to the HMXB SAX J1324.4-6200. If this transient excess is, in fact, associated with GS 1826-238 then it is likely to be a wind-driven system, representing another low mass γ-ray binary.

Both V404 Cygni (Chapter 4) and GRS 1915+105 (Chapter 7.12) are well studied microquasars, where apparently significant excesses are observed to be coincident with these systems. In the case of V404 Cygni, there is evidence to prove that source confusion with a nearby blazar is responsible for the γ-ray excesses seen from the position of the binary. In the case of GRS 1915+105, evidence suggests that the γ-ray excess could be either part of a larger diffuse structure, or due to source confusion. There is therefore little evidence to indicate that γ-ray emission originates from LMXB microquasar systems.

There is a large number of unassociated *Fermi*-LAT sources, and studies such as Strader et al. (2021) and Li et al. (2021) have identified these as likely γ-ray counterparts to tMSP systems. In addition to the tMSPs, 2S 0921-630, and possibly GS 1826-238, are likely wind-driven systems and are low mass counterparts to the HMXB γ-ray binary population. It is likely that given the size of the companion star, there is simply not enough power to cause wind-driven shocks in the majority of NS-LMXBs which, coupled with the fact that LMXBs are generally further away from the Earth than HMXBs, means that very few more are likely to be seen with current instrumentation.

9.5 Comparisons between the mass classes

It is clear that the γ-ray emitting high mass and low mass X-ray binaries represent fundamentally different populations to one another. The high mass systems are mostly wind-driven γ-ray binary systems, with several γ-ray emitting microquasars included, whereas the low mass systems are almost all transitional millisecond pulsars. As a result, there are fundamental differences between the emission mechanisms of the high and low mass systems we observe, and also fundamental differences in the observed properties of these systems.

Microquasars are not exclusively high mass sources, however it is only the high mass systems which are seen at γ-ray wavelengths. There are numerous well known low mass microquasars, including V404 Cygni, Cir X-1 and GRS 1915+105 which have been explored in previous chapters but evidence for γ-ray emission from these systems is weak at best. It is difficult to understand why only the high mass systems are seen to emit γ-rays when the systems in question, Cyg X-1 (with persistent γ-ray emission), Cyg X-3 (with a WR star) and supercritical SS 433 are different from one another. Given that it is expected that microquasars primarily emit γ-rays through inverse Compton mechanisms, it may be the case that the photon seed field may be too low in the γ-ray producing region of the jet to produce a flux measurable with current instrumentation in the low mass systems due to the smaller, less luminous, companion stars.

In HMXBs, interaction between a stellar wind and a pulsar wind causes shocks and subsequent γ-ray emission. In the vast majority of pulsar-LMXBs, there are no powerful stellar winds from the companion, and accretion occurs through Roche lobe overflow. In this case, the pulsar wind is often powerful enough to begin companion ablation causing a spider binary system, and eventually, a millisecond pulsar. It would therefore appear that the analogue to the HMXB γ-ray binaries is the transitional millisecond pulsar class, which represents the vast majority of the γ-ray emitting LMXBs. Both γ-ray binaries and tMSPS are powered by neutron

star rotation and cannot be black hole systems.

With regards to the spatial distribution of the XRBs, both the high and low mass systems tend to be concentrated on the Galactic plane, however given that the HMXBs have more massive (Population I) companion stars, they generally lie in the spiral arms of the Milky Way. The LMXBs (Population II) however are known to be concentrated in the Galactic centre and the globular clusters, which are further away from the Earth. An examination of the spatial distribution of the LMXBs has revealed that the γ-ray emitting systems are statistically significantly concentrated off-the-plane, implying they are nearby sources. Distance measurements*, where available, imply that the HMXBs are largely nearby as expected, although some HMXBs can be seen from great distances, as shown by the extragalactic source LMC P3 in the Large Magellanic Cloud (Pietrzyński et al., 2013).

The vast majority of γ-ray emitting HMXBs produce γ-rays through shocks between the pulsar winds and the winds of the massive companion stars. As the intensity of shocks varies with the separation of the two binary stars, the γ-ray emission of these systems is orbitally modulated. The low mass systems switch between a rotation powered pulsar phase and an accretion powered X-ray binary phase. In the absence of a jet in the accretion powered phase (i.e. the system is not a microquasar), the γ-ray emission in these transitional millisecond pulsar systems is likely produced by the inverse Compton scattering of photons in the pulsar magnetosphere. These systems are closely related to the spider binaries in which the pulsar ablates the companion star, and several LMXBs are also considered to be spider binaries. The microquasars form a separate class of X-ray binary in which it is thought that the γ-rays are produced in the jet due via inverse Compton mechanisms, although some models account for hadronic mechanisms too. In the case of the microquasars in particular, further study of a larger population is required to establish the exact nature of these sources, for which it is likely that more sensitive instrumentation is required.

*See TeVCAT for a number of distance measurements, the literature otherwise.

Figure 9.3: The ninth labour of Heracles, retrieving the Belt of Hippolyta, Queen of the Amazons. By Antoon Claessens (Unknown Year).

Chapter 10

Concluding Remarks and Future Prospects

Having detailed my investigations, results and discussions in the previous chapters, I present a summary of my conclusions in this chapter before discussing future work. Finally, I discuss future γ-ray observatories, experiments and missions, and the impacts that these may have on our understanding of γ-ray emission from X-ray binaries.

10.1 Summary of Investigation

I have performed an investigation of the X-ray binary population using the *Fermi*-LAT data, supported by data from the X-ray telescopes *Swift*-BAT and MAXI, and optical data from AAVSO. This was done by performing a survey of the X-ray binary population using the Liu et al. (2006) and Liu et al. (2007) catalogues to provide coordinates for the majority of the X-ray binary population, as well as using entries from the 4FGL-DR2 and DR3 to analyse XRBs with known γ-ray emission, as not all of these are included in the Liu catalogues. To test for γ-ray emission at the position of X-ray binaries, I use a log-likelihood hypothesis test to generate a test statistic which gives the significance of any excess; light-curves are also

generated at the position of each binary, and a mathematical light-curve condition is defined to indicate whether any significant γ-ray excess can be found in the bins of the light-curve. In general, for most cases where there is a persistent excess, the light-curve condition is also fulfilled and vice versa, however there are some cases of a persistent excess only, or the light-curve condition being fulfilled without a persistent excess being present at the position of an X-ray binary. In Chapter 9, I have identified fundamental differences between the high and low mass X-ray binaries, and therefore conclude that these are fundamentally different populations of γ-ray emitter, with different emission mechanisms and spatial distributions. I therefore consider them separately below.

10.1.1 High Mass X-ray Binaries

I identify 20 HMXBs where there is a coincident γ-ray excess. I identify 8 of these to be false positives, caused by either source confusion with a catalogued γ-ray source, or poor positional localisation of a new source.

Of the remaining 12 excesses, I identify 4 which are likely new potential γ-ray emitting HMXBs. The remaining 8 non-false positive excesses lack any significant evidence for association with their respective X-ray binaries.

Two of the four X-ray binaries stand out because there is evidence for orbital modulation in their γ-ray excesses: 1A 0535+262 and GRO J1008-57. In both cases, there is some evidence for γ-ray emission at periastron, and in the case of 1A 0535+262 all of the γ-ray flux from the persistent excess appears in the bin proceeding periastron, strongly suggesting the likelihood of modulation. The light-curve of GRO J1008-57 appears to be slightly noisier than 1A 0535+262, and an excess is also seen at apastron in this case. The orbital modulation in both of these, together with the apparent lack of a relativistic jet, leads to the conclusion that these two HMXBs are likely γ-ray binaries, although a clear detection cannot be claimed as neither excess exceeds 5σ in significance.

The remaining two X-ray binaries do not have any evidence for orbital modulation, but there is evidence for variability in their light-curves and both exceed the 5σ level either as a persistent or transient excess. The first system is the neutron star HMXB SAX J1324.4-6200, where a 5.4σ γ-ray excess is seen over an 18 month period, no flux being measured in any other light-curve bins. This transient excess has a soft power law spectrum typical of HMXBs, and is well localised to the position of the binary. No multi-wavelength data are available for this source, hence it is impossible to claim a firm detection, however it is likely that this excess represents periastron in a long-period γ-ray binary. The second system is RX J2030.5+4751 where a persistent excess is observed at the position of the binary with a 5.4σ significance. This excess is apparently variable, with a flare seen in a 6 month light-curve bin, which may indicate an enhancement at periastron for this system, although the orbital period of this system is unknown, and no X-ray data are available. This system is potentially a γ-ray binary, as it has a neutron star accretor.

In Chapter 9, these excesses are considered alongside the rest of the γ-ray emitting X-ray binary population. The majority of the HMXB population are γ-ray binaries where VHE emission and orbital modulation are common features; the four excesses appear to fall into this category. In addition there are three HMXB microquasars with detectable γ-ray emission; these systems are jet-driven in nature and are all apparently unique within the microquasar population. These systems are not detected at VHE (with the exception of the jet termination region of SS 433).

There is no apparent pattern as to which HMXBs are γ-ray binaries, other than that they require a neutron star accretor rather than a black hole, however observation of weak phased γ-rays at periastron in both 1A 0535+262 and GRO J1008-57, and at VHE in PSR J2032+412, suggests that it may be the case that all neutron star HMXBs emit γ-rays on some level due to wind collision, and the limiting factor to our observation of them is instrument sensitivity.

With regards to the microquasars, theory predicts that γ-rays should be produced

due to internal shocks in the jets as the jet decouples from the central accretor. In reality, this is seen only in two systems, Cyg X-1, and Cyg X-3, as the emission from SS 433 is localised away from the central black hole, where the jet shocks against the interstellar medium. Again, that γ-rays are not seen from more microquasars may be due to a lack of instrument sensitivity, although given that microquasar emission has not been seen at VHE, it may be the case that the jet particle population is not energetic enough to produce γ-rays at such energies.

Future instruments (Section 10.3) with improved sensitivities will go some way to solving the problem of instrument sensitivity faced by current generation VHE observatories and *Fermi*-LAT. In particular, targeted observations of neutron star HMXBs at periastron is likely to reveal further γ-ray binaries, and observations of microquasars in the high intensity/soft X-ray state *may* yield further γ-ray emitting microquasars.

10.1.2 Low Mass X-ray Binaries

Of the low mass X-ray binary population, I identify 44 LMXBs where there is some evidence for spatially coincident γ-ray emission. Of these 44, 18 are located within the Galactic centre, 6 are located within globular clusters and the remaining 20 are located primarily on the Galactic plane. Of the Galactic centre LMXBs, almost all are caused by source confusion with other sources, notably 4FGL J1745.6-2859/Sgr A* and the pulsar wind nebula 4FGL J1746.4-285/PWN G0.13-0.11/HESS J1746-285. The only systems where there may be a possibility of γ-rays originating from an LMXB are SAX J1750.8-2900 and the black hole candidate IGR J17497-2821, where there appears to be no source confusion. In these cases the evidence for γ-ray emission from the LMXB is weak, consisting solely of spatial coincidence between an excess and the LMXB. Similarly, in the case of the 6 LMXBs within globular clusters it is not possible to separate any LMXB emission from that of the wider clusters, which host populations of MSPs. The globular cluster LMXBs are dealt

with in Appendix E, as due to the source confusion between the cluster itself and the LMXB within, they are not of relevance to this work.

Of the 20 LMXBs that are neither in the Galactic centre nor in a globular cluster, I find that 7 of these are definite false positives, and that in an additional 12 cases there insufficient evidence to associate the excess with the LMXB. Therefore of these 20 LMXBs, there is only one where there is sufficient evidence to suggest association between an excess and a LMXB. This system is the neutron star system GS 1826-238, where a transient γ-ray excess is localised to the position of the LMXB. It is unclear whether this is a wind-driven system, or otherwise.

This system is considered alongside the known γ-ray emitting LMXB population in Chapter 9, for a total of nine systems. Although there are a number of LMXB microquasars, and several are analysed in this thesis (e.g. GRS 1915+105, V404 Cygni and Circinus X-1), none of these nine systems are known to be microquasars, and there is no evidence for detectable γ-ray emission from LMXB microquasars, despite the fact that theory predicts γ-ray emission from internal shocks in the jets of such systems.

These nine systems are distributed significantly above the mean Galactic latitude of the overall LMXB population, and the γ-ray emitting LMXBs are distributed differently to the overall population with 4.5σ significance. As Galactic latitude can be used as a proxy for distance (for Galactic sources), this suggests that the γ-ray LMXBs are closer than the overall population, implying that we are simply seeing the nearby sources. Additionally, the vast majority (7 out of 9) of the LMXB population are transitional millisecond pulsars, which switch between a rotation powered pulsar phase and an accretion powered XRB phase. Furthermore, as the majority of the tMSP population is also γ-ray emitting, there is a strong correlation between γ-ray emission and the presence of a rotation powered pulsar phase in LMXBs. Therefore, unlike the HMXBs where it is difficult to pick out an overall trend to the systems which emit γ-rays, the LMXBs appear to generally be nearby tMSPs, and therefore it is likely that any such sources discovered in future will also

share these characteristics.

10.2 Future Work with *Fermi*-LAT

10.2.1 Further Galactic Detections of X-ray Binaries

I have explored the possibility of γ-ray emission from over 300 high and low mass X-ray binaries, using the Liu et al. (2006) and Liu et al. (2007) catalogues. Whilst these catalogues were exhaustive at the time of publication, new X-ray binaries have been detected since their publication. Therefore whilst the Liu et al. catalogues still represent the vast majority of the X-ray binary population, there are a number of more recently discovered systems which have not been analysed in Chapters 5 - Chapter 8. Such systems are therefore ideal targets for a smaller, follow-up survey. In addition, as *Fermi*-LAT came into operation in 2008, most of the systems which have been detected since the publication of the Liu et al. catalogues will have been observed in the lifespan of *Fermi*-LAT. Therefore, any newer systems detected during enhanced X-ray activity (the X-ray transients) are also likely to have contemporaneous *Fermi*-LAT data, increasing the probability of an association between the X-ray transient, and any observed γ-ray excess/source.

With regards to further detections of the X-ray binaries contained within the Liu et al. catalogues, prospects are mixed. As the observation time of a *Fermi*-LAT source doubles, the significance of a steady source increases by a factor of $\sqrt{2}$. Given that *Fermi*-LAT has now been operating for 14 years, for new significant steady sources to be detected, decades of observation time are now needed which is unlikely. It is therefore extremely unlikely that any new detectable steady sources of γ-ray emission are to be found coincident with the X-ray binaries included in the Liu et al. catalogues, as they would have (in principle) been detected in Chapters 5-8.

Where *Fermi*-LAT will continue to excel is as an all-sky monitor of transient γ-ray

emission. In two of the X-ray binaries from which γ-ray emission is likely observed (GS 1826-23 and SAX J1324.4-6200) the emission is transient, and in the other three cases some variability or orbital modulation is observed. Therefore whilst *Fermi*-LAT is unlikely to observe more steady sources, it is entirely possible that transient emission may be detected from the positions of the X-ray binary population. By generating light-curves of the X-ray binary population every few years, it may be possible to observe previously undetected sources by seeing transient emission. Furthermore, the likelihood of a detection dramatically increases if a source is undergoing a microquasar outburst where γ-rays are produced in a jet, or at periastron in the γ-ray binaries. Particular attention should be paid to systems at these times, although care must be taken to avoid false positives as seen in the case of V404 Cygni (Chapter 4).

10.2.2 Extragalactic Detections of X-ray Binaries

The observation of LMC P3 at γ-ray wavelengths has significant ramifications for the discovery of further HMXBs at γ-ray wavelengths, as it shows that such systems are detectable outside the Milky Way (Corbet et al., 2016). Liu et al. (2005) present a catalogue of the HMXBs within the Large and Small Magellanic Clouds, two of our nearest galaxies. In the LMC, spatially resolvable point sources of γ-rays are seen (e.g. LMC P3), and therefore it would be possible to search for γ-ray emission from the LMC binary population, using Liu et al. (2005) as a guide (Abdo et al., 2010b). Observations of the LMC with *Fermi*-LAT are likely to bring challenges, such as accounting for the background flux of the LMC (caused by star formation), however if these can be overcome, there may be previously undetected γ-ray emitting HMXBs in this galaxy, observable with *Fermi*-LAT.

In the case of the LMXBs, a catalogue of these systems within the LMC and SMC is included in Liu et al. (2007). Unlike the HMXBs however, which can be observed at 10s of kpc in distance, the analysis shown in Chapter 9 indicates that the LMXBs

are highly likely to be much closer systems to Earth. Therefore it is far less likely that LMXBs would be detected in the LMC than HMXBs.

10.2.3 The X-ray Burster Question

Classical novae (Section 3.2.2) occurring from Cataclysmic Variable binaries emit γ-rays during thermonuclear X-ray bursts, due to particle acceleration in internal shocks from the ejected material (Martin et al., 2018). Their detection with *Fermi* was unexpected, yet the nature of the thermonuclear bursts on the surface of white dwarf stars is similar in many ways to the Type I thermonuclear X-ray bursts seen on the surface of neutron stars in X-ray bursters, a subclass of X-ray binary.

To date, γ-rays have not been detected from an event which has been attributable to an X-ray burst in an XRB, however by surveying the X-ray burster population, γ-rays may be detectable from these sources during thermonuclear X-ray bursts. Such a survey would require a catalogue of X-ray bursting X-ray binaries, and these sources would need to be observed both during each burst, which differ in length between hours and days (Lewin et al., 1993), and also outside of any bursts to characterise the background. Nonetheless, given *Fermi*-LAT's all sky data, and the fact that the X-ray binary population has already been surveyed as a whole, an in-depth survey of X-ray bursts naturally follows on from the work done in this thesis.

10.3 Future Observatories and Missions

The 'current generation' of γ-ray instrumentation largely consists of detectors that have been taking data since the 2000s; this includes space telescopes such as INTEGRAL, AGILE and *Fermi*-LAT, IACTs like VERITAS, MAGIC and H.E.S.S. and WCDs like HAWC. Numerous successors to these observatories are currently in various stages of research, development and construction; in this section I highlight

three such projects which are likely to play a significant part in the future research of the high energy properties of X-ray binary systems.

10.3.1 The Cherenkov Telescope Array

The Cherenkov Telescope Array (CTA) is an upcoming array of IACTs, designed as the successor to VERITAS, MAGIC and H.E.S.S. CTA will use telescopes of three different sizes in order to encompass a wide energy range across the γ-ray waveband. These designs are the single mirror Large Sized Telescope (LST) and the Medium Sized Telescope (MST) and the dual mirror Schwarzschild-Couder Small Sized Telescope (SST); additionally, a second design of MST is in development which uses a Schwarzschild-Couder dual mirror design, similar to the SST (see Actis et al. (2011) and subsequent papers for details of the CTA telescope design). This medium sized telescope has been designated the Schwarzschild-Couder Telescope (SCT), and the prototype is pictured in Figure 10.1.

The LSTs are designed to observe the lowest energy γ-rays, which produce only a small amount of Cherenkov light, so require large reflecting areas to maximise the light observed, however are common so require only a few telescopes relatively close together. The SSTs observe the highest energy photons so require smaller mirrors as the Cherenkov light is more luminous, however these γ-rays are much rarer, hence many telescopes need to be spread across a much wider area than the LSTs. The MSTs have mirror sizes between the two, and telescopes distributed over an area between that of the LST and SSTs in order to observe γ-rays with energies between those observed by the LSTs and SSTs.

Previous IACT observatories have operated from a single location; currently VERITAS and MAGIC are located in the Northern Hemisphere, and H.E.S.S. is located in the southern hemisphere, thus each current generation observatory sees only a portion of the sky. By contrast, CTA will be built across two sites in order to maximise sky coverage. The northern site (CTA-North) will be built on the island

Figure 10.1: The prototype Schwarzschild-Couder dual mirror medium sized telescope, one of the two medium sized telescopes designed for CTA. The prototype SCT is located at the site of the VERITAS observatory, south of Tucson, Arizona.

	LST	MST/SCT	SST
Energy Range	20 GeV-3 TeV	80 GeV-50 TeV	1 TeV-300 TeV
F.S. Energy Range	20 GeV-150 GeV	150 GeV-5 TeV	5 TeV - 300 TeV
Number in North	4	15	0
Number in South	4	25	70
Primary Mirror Diameter	23m	11.5m/9.7m	4.3m
Second. Mirror Diameter	N.A.	N.A./5.4m	1.8m
Effective area	$370m^2$	$88m^2$ /$41m^2$	$8m^2$
Focal Length	28m	16m/5.6m	2.15m
Field of View	4.3°	7.7°/7.6°	10.5°
Photodetector Type	PMT	PMT/SiPM	SiPM
Slew Time	30s	90s	60s
Pointing Precision	< 14”	< 7”/< 10”	< 7”

Table 10.1: A table showing key design parameters of the different CTA designs. The energy range refers to the total energy range to which each design is sensitive to, and the F.S. energy range refers to the energy range where each telescope design operates with its full sensitivity. The planned number of telescopes to be built in CTA-North and CTA-South are given; note that the SSTs are exclusively planned to be built in the south. The diameter of each telescope's primary mirror is given, and well as the secondary mirror diameter in the case of the SCT and SST. The effective area of each telescope (accounting for shadowing) is given, as well as the telescope focal length and field of view. The different camera photodetectors are given; PMT refers to traditional photomultiplier tubes whereas SiPM refers to more modern Silicon Photomultipliers. The slew time refers to the maximum time for the telescopes to slew to any point in the sky above a 30° inclination above the horizon; all three designs are capable of observing any astrophysical source 24° above the horizon. The pointing precision gives the uncertainty on where a telescope is pointed, in arcseconds. This table is adapted from information here https://www.cta-observatory.org/wp-content/uploads/2019/12/CTA-Specifications_v08_formatted.pdf .

of La Palma, close to the MAGIC telescopes, whereas the southern site (CTA-South) will be built at the European Southern Observatory site in Paranal, Chile. CTA-South is intended to be home to more telescopes than CTA-North, due to the visibility of the Galactic centre in the south. Table 10.1 shows a summary of the properties of each telescope design, in addition to the number of each telescope design planned to be built in the final ('omega') configurations of the northern and southern arrays.

CTA as a whole will observe a wide range of targets divided up into Key Science Projects (KSPs) (Acharya et al., 2019). Under the Transients KSP, CTA will

observe the microquasars with known γ-ray emission observed with *Fermi*-LAT, but are not seen with current generation IACTs. These systems are Cyg X-1, Cyg X-3 and SS 433 (although the termination shock of SS 433 is seen with HAWC). In addition, CTA will observe microquasars where γ-ray emission has been predicted but not observed (such as GRS 1915+105) and is also likely to observe any X-ray binaries which evolve into microquasars once CTA is operational. It is expected that observations of microquasars with CTA will better test emission models to constrain the nature of the γ-ray producing particles in the microquasar jets, but will also shed light on jet formation processes, which are poorly understood.

CTA will also observe the γ-ray binary population, and given the much improved sensitivity of CTA over current generation instruments* (Abdalla et al., 2021). Through targeted observations of these systems, particularly at periastron, CTA is likely to discover γ-ray emission from a number of new systems, expanding our understanding of them. In addition to these, CTA will also observe the transitional millisecond pulsar population, both in rotation and accretion powered states. As tMSPs (and LMXBs in general) have not been detected at VHE, the discovery of such emission from these systems would allow for a better understanding of them, and the emission mechanisms in the wider neutron star population.

In addition to the Transients KSP the Galactic Plane Survey KSP will also provide serendipitous observations of a wide variety of HMXB targets, giving additional information on these sources in a variety of states. As the known γ-ray emitting tMSP LMXBs are generally at high Galactic latitudes, these will not be detected in this survey, however some are likely to be observed during observations for the Extragalactic Survey KSP.

CTA is entering the construction phase, and will likely begin taking useful scientific observations in the latter half of the 2020s. CTA will inevitably discover new γ-ray emitting X-ray binaries under its KSPs, and as the observatory will take observation

*CTA is approximately an order of magnitude more sensitive than VERITAS, MAGIC and H.E.S.S.

proposals there will likely be additional projects performed to supplement this work. Provided that *Fermi* is still operating when CTA begins full operations, the two will overlap in energy range providing a view from approximately 100 MeV to 300 TeV (although *Fermi* is much less sensitive than CTA will be), this will allow for a much broader view of the X-ray binary population as a whole.

10.3.2 Southern Wide-Field Gamma-ray Observatory and Large High Altitude Air Shower Observatory

The Southern Wide-Field Gamma-ray Observatory (SWGO) is a planned WCD system, designed as a successor to HAWC. SWGO is still in a relatively early stage of design, and will consist of photomultiplier tube based light detectors submerged either in either water tanks (like HAWC and LHAASO) or in a lake. Whilst HAWC and LHAASO are located in the northern hemisphere, SWGO will be located in the southern hemisphere, likely on a site in South America. The southern location and SWGO's planned wide field of view will allow a much wider view of the Galactic plane, and therefore a large fraction of the Galactic X-ray binary population will be visible to SWGO (Abreu et al. 2019 & Hinton 2021). As SWGO will have a much higher duty cycle than IACTs (close to 100% for a WCD compared to approximately 10% for an IACT), and improved sensitivity over current generation instruments, it has potential to observe transient phenomena at VHE from X-ray binaries at a high rate, which will be able to inform pointed instruments such as CTA to changes in the states of systems, allowing for follow-up observations.

SWGO will work alongside LHAASO (Large High Altitude Air Shower Observatory) a Northern Hemisphere WCD, which began observations in April 2021 (e.g. Cao et al. 2021a and Cao et al. 2021b), which similarly has a 100% duty cycle. LHAASO relies on a combination of technologies to observe. It contains 12 IACTs, in addition to over 5000 PMTs submerged across 3 ponds containing $10^5 m^3$ of water each to detect particles from air showers. LHAASO is able to observe transient

phenomena at the highest energies, and has the potential to probe the highest observable energies emitted by XRBs.

10.3.3 All-sky Medium Energy Gamma-ray Observatory

The All-sky Medium Energy Gamma-ray Observatory (AMEGO) is a planned space based telescope intended as both a successor to *Fermi*-LAT, and as a mission to explore the MeV gap. AMEGO will observe photons from 200 keV - 10 GeV, with an energy resolution of $< 1\%$ (at <2 MeV) up to 10% (at 10 GeV) and a wide field of view of 2.5 steradians, which is approximately 20% of the sky. AMEGO will provide new γ-ray observation techniques such as spectroscopy of nuclear lines, and will use both Compton scattering and pair production as detection methods in order to cover the wide energy gap (McEnery et al., 2019).

Given its effective energy range, AMEGO will provide a revolutionary view of X-ray binary systems at high energy, by providing a continuous spectrum of the known γ-ray emitting XRBs from the very hard X-ray/soft γ-rays up to the high energy GeV γ-rays, just below the bottom end of the energy range that the CTA LSTs will cover. The combination of these two instruments, together with observations from current generation instruments like *Fermi*-LAT, will strongly constrain the spectra of the X-ray binary population, and will allow for much more thorough testing of γ-ray emission models in X-ray binaries. AMEGO will be particularly useful in observing the microquasars and constraining models of jet formation and jet emission in these systems, as the broadband high energy spectra of microquasar jets are poorly understood at present; being able to continuously observe jets from the keV to GeV bands should heavily constrain models of jet γ-ray emission. As a wide field of view instrument, AMEGO, like SWGO, will be able to act as an all sky monitor of transient sources, and will observe phenomena such as γ-ray binary flares from orbital periastron, and state transitions in tMSPs.

10.3.4 Future Science and Closing Remarks

AMEGO, together with CTA, SWGO and other γ-ray detectors in the early stages of development show that the study of the high energy properties of X-ray binaries, and the wider compact binary population looks promising. Major scientific breakthroughs, both hypothesised and surprising will occur as these new generation detectors begin to come online over the next decade, with AMEGO currently slated for a 2030 launch, in the years following CTA coming online.

In Chapter 1, I set out two questions which my thesis attempted to answer:

1) Why is only a small fraction of the overall X-ray binary population seen to emit γ-rays?

2) Are there any other X-ray binaries with previously unidentified γ-ray emission?

I have answered both of these - but only to an extent. The five candidate γ-ray emitting XRBs identified in the survey all show evidence for some sort of variability. This is consistent with our view of the wider XRB population in the γ-ray waveband, where many systems are only detectable under certain conditions (such as during an outburst, or at orbital periastron). Therefore my work suggests that actually a much larger fraction of the X-ray binary population may emit γ-rays than we currently observe, however our current instruments, such as *Fermi*-LAT, are not sensitive enough to observe many of them. This is particularly the case for the microquasars, such as V404 Cygni, where recent work has shown that γ-ray emission from jets is likely not far below the sensitivity of current instruments Abe et al. (2022).

Due to the constraints of current instrument sensitivity it is therefore inevitable that there are X-ray binaries within our Galaxy with unidentified γ-ray emission. Additionally, the extragalactic γ-ray emitting X-ray binary LMC P3 represents a new population of which we have barely scratched the surface. Whilst the five candidates that I have identified in this survey each present an interesting new

discovery, they are all likely a drop in the ocean when compared to the potential future discoveries that will be uncovered by new instruments as they come online.

It is possible that SWGO and LHAASO will uncover transient XRBs at the highest energies as the approximately 100% duty cycle of these instruments lends itself well to transient studies. Whilst no transient XRBs have been observed by WCDs thus far, the detection of SS 433 by HAWC has shown that XRBs do emit at these energies, although SS 433 is undoubtedly a special case.

Greater potential lies with CTA, as current generation IACTs have already detected a number of γ-ray binaries. With the order of magnitude improvement in sensitivity that CTA provides, it is likely that more will be detected as part of CTA's observing program. In particular, CTA will be able to provide insight into how the emission of γ-ray binaries varies with period, as current generation instruments largely observe these objects at periastron, where emission is most luminous. With additional sensitivity, it is possible that detections at other points in the period could be made, shedding light on the impact of orbit on the γ-ray emission in these systems.

No microquasars other than SS 433 are currently detected at VHE, however given the results of Abe et al. (2022) it is possible that CTA will be able to make the first VHE observations of a microquasar in outburst. The detection of a microquasar at VHE would provide a huge insight into the processes at play in these systems, whether hadrons or leptons (or both) are responsible for the γ-ray emission detected, and at what point in the outburst γ-rays are produced. In particular, given that V404 Cygni goes into outburst every decade or two, it is likely that such an outburst from this system will occur during the operational lifetime of CTA, and whilst IACTs failed to detect emission during the 2015 outburst, CTA may detect emission during the next outburst.

AMEGO holds great potential for future XRB science. Like *Fermi*, AMEGO will observe the whole sky and will be able to catch transient events such as microquasar outbursts as they happen, and the nature of the instrument will lend itself well to

future surveys like the one presented in the preceding chapters. AMEGO's science payoff will occur from being a mission which targets the MeV energy range with greater sensitivity than any other instrument before it. The spectra of many XRBs dip between the synchrotron and inverse Compton radiation components in this range, and hence AMEGO will provide greater sensitivity in probing this gap, complementing CTA and WCDs at higher energies, and X-ray telescopes at lower energies. These observations will provide greater capability of examining the broad band spectra of XRBs of all types. AMEGO will also build on the science done with *Fermi*, which is itself a powerful tool for examining the variability and periodicity of XRBs, and will allow for greater investigation of how γ-ray variability is linked to the wider properties and state changes of XRBs.

Whilst I have managed to answer the two questions I set forth to an extent, the upcoming generation of instruments will allow scientists to go further in answering them. Improved instrument sensitivity will allow for the uncovering of new sources, both γ-ray binaries and, hopefully, the presently elusive microquasars. A better and broader view of the spectral and temporal properties of the different XRB populations will allow a better understanding of why only some XRBs are seen to emit, their links to other sources (such as ULXs, and X-ray bursters) and to uncover a range of new sources within our Galaxy, and beyond.

Figure 10.2: The tenth labour of Heracles, obtaining the cattle of the three headed giant, Geryon. By Lucas Cranach the Elder (After 1537).

Bibliography

B. P. Abbott et al. Observation of Gravitational Waves from a Binary Black Hole Merger. *Physical Review Letters*, 116(6):061102, Feb. 2016. ISSN 0031-9007, 1079-7114. doi: 10.1103/PhysRevLett.116.061102. URL http://arxiv.org/abs/1602.03837. arXiv: 1602.03837.

B. P. Abbott et al. GW170817: Observation of Gravitational Waves from a Binary Neutron Star Inspiral. *Physical Review Letters*, 119(16):161101, Oct. 2017. ISSN 0031-9007, 1079-7114. doi: 10.1103/PhysRevLett.119.161101. URL http://arxiv.org/abs/1710.05832. arXiv: 1710.05832.

R. Abbott et al. Observation of gravitational waves from two neutron star–black hole coalescences. *The Astrophysical Journal Letters*, 915(1):L5, Jun 2021. ISSN 2041-8213. doi: 10.3847/2041-8213/ac082e. URL http://dx.doi.org/10.3847/2041-8213/ac082e.

H. Abdalla et al. A search for very high-energy flares from the microquasars GRS 1915+105, Circinus X-1, and V4641 Sgr using contemporaneous H.E.S.S. and RXTE observations. *Astronomy and Astrophysics*, 612:A10, Apr. 2018. ISSN 0004-6361. doi: 10.1051/0004-6361/201527773. URL https://ui.adsabs.harvard.edu/abs/2018A&A...612A..10H/abstract.

H. Abdalla et al. A very-high-energy component deep in the gamma-ray

burst afterglow. *Nature*, 575(7783):464–467, Nov. 2019. ISSN 1476-4687. doi: 10.1038/s41586-019-1743-9. URL https://www.nature.com/articles/s41586-019-1743-9. Number: 7783 Publisher: Nature Publishing Group.

H. Abdalla et al. Detection of very-high-energy gamma-ray emission from the colliding wind binary eta-Car with H.E.S.S. *Astronomy & Astrophysics*, 635:A167, Mar. 2020. ISSN 0004-6361, 1432-0746. doi: 10.1051/0004-6361/201936761. URL https://www.aanda.org/articles/aa/abs/2020/03/aa36761-19/aa36761-19.html. Publisher: EDP Sciences.

H. Abdalla et al. Sensitivity of the Cherenkov Telescope Array for probing cosmology and fundamental physics with gamma-ray propagation. *Journal of Cosmology and Astroparticle Physics*, 2021(02):048–048, Feb. 2021. ISSN 1475-7516. doi: 10.1088/1475-7516/2021/02/048. URL https://doi.org/10.1088/1475-7516/2021/02/048. Publisher: IOP Publishing.

A. A. Abdo et al. Fermi LAT Observations of LS I +61°303: First Detection of an Orbital Modulation in GeV Gamma Rays. *The Astrophysical Journal*, 701:L123–L128, Aug. 2009a. ISSN 0004-637X. doi: 10.1088/0004-637X/701/2/L123. URL https://ui.adsabs.harvard.edu/abs/2009ApJ...701L.123A. ADS Bibcode: 2009ApJ...701L.123A.

A. A. Abdo et al. Fermi Large Area Telescope Gamma-Ray Detection of the Radio Galaxy M87. *The Astrophysical Journal*, 707:55–60, Dec. 2009b. ISSN 0004-637X. doi: 10.1088/0004-637X/707/1/55. URL http://adsabs.harvard.edu/abs/2009ApJ...707...55A.

A. A. Abdo et al. Fermi/LAT observations of LS 5039. *The Astrophysical Journal*, 706:L56–L61, Nov. 2009c. ISSN 0004-637X. doi: 10.1088/0004-637X/706/1/L56. URL https://ui.adsabs.harvard.edu/abs/2009ApJ...706L..56A. ADS Bibcode: 2009ApJ...706L..56A.

A. A. Abdo et al. Modulated High-Energy Gamma-Ray Emission from the Microquasar Cygnus X-3. *Science*, 326:1512, Dec. 2009d. ISSN 0036-8075. doi: 10.1126/science.1182174. URL http://adsabs.harvard.edu/abs/2009Sci...326.1512F.

A. A. Abdo et al. Fermi Large Area Telescope Observation of a Gamma-Ray Source at the Position of Eta-Carinae. *The Astrophysical Journal*, 723(1):649–657, Oct. 2010a. ISSN 0004-637X. doi: 10.1088/0004-637X/723/1/649. URL https://doi.org/10.1088/0004-637x/723/1/649. Publisher: American Astronomical Society.

A. A. Abdo et al. Observations of the Large Magellanic Cloud with Fermi. *Astronomy and Astrophysics*, 512:A7, Mar. 2010b. ISSN 0004-6361. doi: 10.1051/0004-6361/200913474. URL https://ui.adsabs.harvard.edu/abs/2010A&A...512A...7A/abstract.

A. A. Abdo et al. Spectrum of the Isotropic Diffuse Gamma-Ray Emission Derived from First-Year Fermi Large Area Telescope Data. *Physical Review Letters*, 104 (10):101101, Mar. 2010c. doi: 10.1103/PhysRevLett.104.101101. URL https://link.aps.org/doi/10.1103/PhysRevLett.104.101101. Publisher: American Physical Society.

S. Abdollahi et al. Fermi Large Area Telescope Fourth Source Catalog. *The Astrophysical Journal Supplement Series*, 247(1):33, Mar. 2020. ISSN 0067-0049. doi: 10.3847/1538-4365/ab6bcb. URL https://doi.org/10.3847%2F1538-4365%2Fab6bcb.

H. Abe et al. Gamma-ray observations of MAXI J1820+070 during the 2018 outburst. *Monthly Notices of the Royal Astronomical Society*, 517(4):4736–4751, Dec. 2022. ISSN 0035-8711. doi: 10.1093/mnras/stac2686. URL https://doi.org/10.1093/mnras/stac2686.

A. U. Abeysekara et al. Periastron Observations of TeV Gamma-Ray Emission from a Binary System with a 50-year Period. *The Astrophysical Journal*, 867: L19, Nov. 2018a. ISSN 0004-637X. doi: 10.3847/2041-8213/aae70e. URL `https://ui.adsabs.harvard.edu/abs/2018ApJ...867L..19A`. ADS Bibcode: 2018ApJ...867L..19A.

A. U. Abeysekara et al. Very high energy particle acceleration powered by the jets of the microquasar SS 433. *Nature*, 562(7725):82–85, Oct. 2018b. ISSN 0028-0836, 1476-4687. doi: 10.1038/s41586-018-0565-5. URL `http://arxiv.org/abs/1810.01892`. arXiv:1810.01892 [astro-ph].

P. Abreu et al. The Southern Wide-Field Gamma-Ray Observatory (SWGO): A Next-Generation Ground-Based Survey Instrument for VHE Gamma-Ray Astronomy, July 2019. URL `http://arxiv.org/abs/1907.07737`. arXiv:1907.07737 [astro-ph].

R. Abuter et al. Detection of orbital motions near the last stable circular orbit of the massive black hole SgrA*. *Astronomy & Astrophysics*, 618:L10, Oct. 2018. ISSN 0004-6361, 1432-0746. doi: 10.1051/0004-6361/201834294. URL `https://www.aanda.org/articles/aa/abs/2018/10/aa34294-18/aa34294-18.html`. Publisher: EDP Sciences.

V. A. Acciari et al. Gamma-ray observations of the Be/pulsar binary 1A 0535+262 during a giant X-ray outburst. *The Astrophysical Journal*, 733(2):96, June 2011. ISSN 0004-637X, 1538-4357. doi: 10.1088/0004-637X/733/2/96. URL `http://arxiv.org/abs/1103.3250`. arXiv: 1103.3250.

F. Acero et al. Development of the Model of Galactic Interstellar Emission for Standard Point Source Analysis of Fermi Large Area Telescope Data. *The Astrophysical Journal Supplement Series*, 223(2):26, Apr. 2016. ISSN 0067-0049. doi: 10.3847/0067-0049/223/2/26. URL `https://doi.org/10.3847/0067-0049/223/2/26`. Publisher: American Astronomical Society.

B. S. Acharya et al. *Science with the Cherenkov Telescope Array*. Mar. 2019. doi: 10.1142/10986. URL https://ui.adsabs.harvard.edu/abs/2019scta.book.....C. Publication Title: Science with the Cherenkov Telescope Array ADS Bibcode: 2019scta.book.....C.

M. Ackermann et al. Periodic Emission from the Gamma-Ray Binary 1FGL J1018.6-5856. *Science*, 335:189, Jan. 2012. ISSN 0036-8075. doi: 10.1126/science.1213974. URL https://ui.adsabs.harvard.edu/abs/2012Sci...335..189F. ADS Bibcode: 2012Sci...335..189F.

M. Ackermann et al. The Fermi All-sky Variability Analysis: A List of Flaring Gamma-Ray Sources and the Search for Transients in Our Galaxy. *The Astrophysical Journal*, 771:57, July 2013. ISSN 0004-637X. doi: 10.1088/0004-637X/771/1/57. URL http://adsabs.harvard.edu/abs/2013ApJ...771...57A.

M. Ackermann et al. The Fermi Galactic Center GeV Excess and Implications for Dark Matter. *The Astrophysical Journal*, 840:43, May 2017. ISSN 0004-637X. doi: 10.3847/1538-4357/aa6cab. URL https://ui.adsabs.harvard.edu/abs/2017ApJ...840...43A. ADS Bibcode: 2017ApJ...840...43A.

M. Actis et al. Design concepts for the Cherenkov Telescope Array CTA: an advanced facility for ground-based high-energy gamma-ray astronomy. *Experimental Astronomy*, 32:193–316, Dec. 2011. ISSN 0922-6435. doi: 10.1007/s10686-011-9247-0. URL https://ui.adsabs.harvard.edu/abs/2011ExA...32..193A. ADS Bibcode: 2011ExA....32..193A.

C. B. Adams et al. Observation of the Gamma-Ray Binary HESS J0632+057 with the H.E.S.S., MAGIC, and VERITAS Telescopes. *The Astrophysical Journal*, 923(2):241, Dec. 2021. ISSN 0004-637X. doi: 10.3847/1538-4357/ac29b7. URL https://iopscience.iop.org/article/10.3847/1538-4357/ac29b7/meta. Publisher: IOP Publishing.

W. S. Adams. An A-Type Star of Very Low Luminosity. *Publications of the Astronomical Society of the Pacific*, 26(155):198, Oct. 1914. ISSN 1538-3873. doi: 10.1086/122337. URL https://iopscience.iop.org/article/10.1086/122337/meta. Publisher: IOP Publishing.

F. Aharonian et al. The H.E.S.S. Survey of the Inner Galaxy in Very High Energy Gamma Rays. *The Astrophysical Journal*, 636:777–797, Jan. 2006a. ISSN 0004-637X. doi: 10.1086/498013. URL http://adsabs.harvard.edu/abs/2006ApJ...636..777A.

F. Aharonian et al. Microquasar LS 5039: a TeV gamma-ray emitter and a potential TeV neutrino source. *Journal of Physics: Conference Series*, 39:408–415, May 2006b. ISSN 1742-6596. doi: 10.1088/1742-6596/39/1/106. URL https://doi.org/10.1088/1742-6596/39/1/106. Publisher: IOP Publishing.

M. L. Ahnen et al. Super-orbital variability of LS I +61°303 at TeV energies. *Astronomy & Astrophysics*, 591:A76, July 2016. ISSN 0004-6361, 1432-0746. doi: 10.1051/0004-6361/201527964. URL https://www.aanda.org/articles/aa/abs/2016/07/aa27964-15/aa27964-15.html. Publisher: EDP Sciences.

M. L. Ahnen et al. MAGIC observations of the microquasar V404 Cygni during the 2015 outburst. *Monthly Notices of the Royal Astronomical Society*, 471(2): 1688–1693, Oct. 2017. ISSN 0035-8711, 1365-2966. doi: 10.1093/mnras/stx1690. URL http://arxiv.org/abs/1707.00887. arXiv: 1707.00887.

M. Ajello et al. A Decade of Gamma-Ray Bursts Observed by Fermi-LAT: The Second GRB Catalog. *The Astrophysical Journal*, 878:52, June 2019. ISSN 0004-637X. doi: 10.3847/1538-4357/ab1d4e. URL https://ui.adsabs.harvard.edu/abs/2019ApJ...878...52A. ADS Bibcode: 2019ApJ...878...52A.

M. Ajello et al. Fermi Large Area Telescope Performance after 10 Years of Operation. *The Astrophysical Journal Supplement Series*, 256(1):12, Sept. 2021a.

ISSN 0067-0049. doi: 10.3847/1538-4365/ac0ceb. URL https://doi.org/10.3847/1538-4365/ac0ceb. Publisher: American Astronomical Society.

M. Ajello et al. Gamma Rays from Fast Black-hole Winds. *The Astrophysical Journal*, 921(2):144, Nov. 2021b. ISSN 0004-637X. doi: 10.3847/1538-4357/ac1bb2. URL https://doi.org/10.3847/1538-4357/ac1bb2. Publisher: American Astronomical Society.

J. L. Allen et al. Spectral softening between outburst and quiesence in the neutron star low mass X-ray binary SAX J1750.8-2900. *The Astrophysical Journal*, 801 (1):10, Feb. 2015. ISSN 0004-637X. doi: 10.1088/0004-637X/801/1/10. URL https://doi.org/10.1088/0004-637x/801/1/10. Publisher: American Astronomical Society.

L. G. Althaus et al. Evolutionary and pulsational properties of white dwarf stars. *The Astronomy and Astrophysics Review*, 18(4):471–566, Oct. 2010. ISSN 0935-4956, 1432-0754. doi: 10.1007/s00159-010-0033-1. URL http://arxiv.org/abs/1007.2659. arXiv:1007.2659 [astro-ph].

F. Ambrosino et al. Optical pulsations from a transitional millisecond pulsar. *Nature Astronomy*, 1(12):854–858, Dec. 2017. ISSN 2397-3366. doi: 10.1038/s41550-017-0266-2. URL http://arxiv.org/abs/1709.01946. arXiv:1709.01946 [astro-ph].

P. R. Amnuel, O. K. Guseinov, and S. I. Rakhamimov. A catalog of X-ray sources. *The Astrophysical Journal Supplement Series*, 41:327–367, Oct. 1979. ISSN 0067-0049. doi: 10.1086/190621. URL https://ui.adsabs.harvard.edu/abs/1979ApJS...41..327A. ADS Bibcode: 1979ApJS...41..327A.

L. Angelini et al. Discovery of a new 170 S X-ray pulsar 1SAX J1324.4-6200. *Astronomy and Astrophysics*, 339:L41–L44, Nov. 1998. ISSN 0004-6361. URL http://adsabs.harvard.edu/abs/1998A%26A...339L..41A.

K. M. V. Apparao. X-ray emission from Be star/X-ray binaries. *Space Science Reviews*, 69(3):255–329, Aug. 1994. ISSN 1572-9672. doi: 10.1007/BF02101698. URL https://doi.org/10.1007/BF02101698.

A. Archer et al. Very-high-energy observations of the binaries V 404 Cyg and 4U 0115+634 during giant X-ray outbursts. *The Astrophysical Journal*, 831(1): 113, Oct. 2016. ISSN 1538-4357. doi: 10.3847/0004-637X/831/1/113. URL http://arxiv.org/abs/1608.06464. arXiv: 1608.06464.

M. Armas Padilla et al. Optical spectroscopy of 4U 1812-12. An ultra-compact X-ray binary seen through an H II region. *Astronomy & Astrophysics, Volume 644, id.A63, <NUMPAGES>6</NUMPAGES> pp.*, 644:A63, Dec. 2020. ISSN 0004-6361. doi: 10.1051/0004-6361/202038997. URL https://ui.adsabs.harvard.edu/abs/2020A%26A...644A..63A/abstract.

K. Atapin. *Ultraluminous X-ray Sources*. eprint: arXiv:1812.02516, Sept. 2018. URL https://ui.adsabs.harvard.edu/abs/2018acps.confE..38A. Conference Name: Accretion Processes in Cosmic Sources - II Pages: 38 ADS Bibcode: 2018acps.confE..38A.

W. Atwood et al. The Large Area Telescope on the Fermi Gamma-Ray Space Telescope Mission. *The Astrophysical Journal*, 697:1071–1102, 2009.

W. Atwood et al. Pass 8: Toward the Full Realization of the Fermi-LAT Scientific Potential, Mar. 2013. URL http://arxiv.org/abs/1303.3514. arXiv:1303.3514 [astro-ph].

W. B. Atwood et al. Gamma Large Area Silicon Telescope applying Si strip detector technology to the detection of gamma-rays in space. 356:227–232, Dec. 1992. URL https://ui.adsabs.harvard.edu/abs/1992ESASP.356..227A. Conference Name: Photon Detectors for Space Instrumentation ADS Bibcode: 1992ESASP.356..227A.

N. Añez-López et al. Modeling the Accretion Disk around the High-mass Protostar GGD 27-MM1. *The Astrophysical Journal*, 888(1):41, Jan. 2020. ISSN 1538-4357. doi: 10.3847/1538-4357/ab5dbc. URL https://iopscience.iop.org/article/10.3847/1538-4357/ab5dbc.

W. Baade. The Resolution of Messier 32, NGC 205, and the Central Region of the Andromeda Nebula. *The Astrophysical Journal*, 100:137, Sept. 1944. ISSN 0004-637X. doi: 10.1086/144650. URL https://ui.adsabs.harvard.edu/abs/1944ApJ...100..137B. ADS Bibcode: 1944ApJ...100..137B.

J. N. Bahcall and N. A. Bahcall. The Period and Light Curve of HZ Herculis. *The Astrophysical Journal*, 178:L1, Nov. 1972. ISSN 0004-637X. doi: 10.1086/181070. URL https://ui.adsabs.harvard.edu/abs/1972ApJ...178L...1B. ADS Bibcode: 1972ApJ...178L...1B.

C. D. Bailyn et al. Dynamical evidence for a black hole in the eclipsing X-ray nova GRO J1655 - 40. *Nature*, 378:157–159, Nov. 1995. ISSN 0028-0836. doi: 10.1038/378157a0. URL https://ui.adsabs.harvard.edu/abs/1995Natur.378..157B. ADS Bibcode: 1995Natur.378..157B.

B. Balick and R. L. Brown. Intense sub-arcsecond structure in the galactic center. *The Astrophysical Journal*, 194:265–270, Dec. 1974. ISSN 0004-637X. doi: 10.1086/153242. URL https://ui.adsabs.harvard.edu/abs/1974ApJ...194..265B. ADS Bibcode: 1974ApJ...194..265B.

J. Ballet et al. GRS 1716-249 = GRO J1719-24. *International Astronomical Union Circular*, 5874:1, Oct. 1993. ISSN 0081-0304. URL https://ui.adsabs.harvard.edu/abs/1993IAUC.5874....1B. ADS Bibcode: 1993IAUC.5874....1B.

J. Ballet et al. Fermi Large Area Telescope Fourth Source Catalog Data Release 2. *arXiv:2005.11208 [astro-ph]*, Oct. 2020. URL http://arxiv.org/abs/2005.11208. arXiv: 2005.11208.

R. M. Bandyopadhyay et al. Infrared spectroscopy of low-mass X-ray binaries - II. *Monthly Notices of the Royal Astronomical Society*, 306:417–426, June 1999. ISSN 0035-8711. doi: 10.1046/j.1365-8711.1999.02547.x. URL https://ui.adsabs.harvard.edu/abs/1999MNRAS.306..417B. ADS Bibcode: 1999MNRAS.306..417B.

G. Barbiellini et al. The AGILE silicon tracker: testbeam results of the prototype silicon detector. *Nuclear Instruments and Methods in Physics Research A*, 490: 146–158, Sept. 2002. ISSN 0168-9002. doi: 10.1016/S0168-9002(02)01062-8. URL https://ui.adsabs.harvard.edu/abs/2002NIMPA.490..146B. ADS Bibcode: 2002NIMPA.490..146B.

D. P. Barsukov, E. M. Kantor, and A. I. Tsygan. Gamma-ray curvature radiation from the polar regions of a radio pulsar with an axisymmetric magnetic field. *Astronomy Reports*, 50(2):159–166, Feb. 2006. ISSN 1562-6881. doi: 10.1134/S1063772906020090. URL https://doi.org/10.1134/S1063772906020090.

S. D. Barthelmy et al. The Burst Alert Telescope (BAT) on the SWIFT Midex Mission. *Space Science Reviews*, 120:143–164, Oct. 2005. ISSN 0038-6308. doi: 10.1007/s11214-005-5096-3. URL https://ui.adsabs.harvard.edu/abs/2005SSRv..120..143B. ADS Bibcode: 2005SSRv..120..143B.

S. D. Barthelmy et al. Swift trigger 643949 is V404 Cyg. *GRB Coordinates Network, Circular Service, No. 17929, #1 (2015)*, 7929:1, 2015. URL http://adsabs.harvard.edu/abs/2015GCN.17929....1B.

S. D. Barthelmy et al. Swift Trigger 894268: Detection of GRO J2058+42 in outburst. *GRB Coordinates Network*, 23985:1, Jan. 2019. URL https://ui.adsabs.harvard.edu/abs/2019GCN.23985....1B.

T. Bassi et al. On the nature of the soft gamma-ray emission in the hard state of the black hole transient GRS 1716-249. *Monthly Notices of the Royal Astronomical Society*, 494:571–583, May 2020. ISSN 0035-8711. doi: 10.1093/mnras/

staa739. URL https://ui.adsabs.harvard.edu/abs/2020MNRAS.494..571B. ADS Bibcode: 2020MNRAS.494..571B.

A. Baykal, M. J. Stark, and J. Swank. Discovery of the Orbit of the Transient X-Ray Pulsar SAX J2103.5+4545. *The Astrophysical Journal*, 544:L129–L132, Dec. 2000. ISSN 0004-637X. doi: 10.1086/317320. URL https://ui.adsabs.harvard.edu/abs/2000ApJ...544L.129B.

A. Bazzano et al. New X-ray bursters with the WFCs on board SAX: SAX J1750.8-2900, GS 1826-24 and SLX 1735-269. 410:729–733, May 1997a. doi: 10.1063/1.54003. URL https://ui.adsabs.harvard.edu/abs/1997AIPC..410..729B. Conference Name: Proceedings of the Fourth Compton Symposium ADS Bibcode: 1997AIPC..410..729B.

A. Bazzano et al. SAX J1750.8-2900. *International Astronomical Union Circular*, 6597:1, Mar. 1997b. ISSN 0081-0304. URL https://ui.adsabs.harvard.edu/abs/1997IAUC.6597....1B. ADS Bibcode: 1997IAUC.6597....1B.

E. R. Beasor et al. A critical re-evaluation of the Thorne–Żytkow object candidate HV 2112. *Monthly Notices of the Royal Astronomical Society*, 479(3):3101–3105, Sept. 2018. ISSN 0035-8711. doi: 10.1093/mnras/sty1744. URL https://doi.org/10.1093/mnras/sty1744.

W. Becker and B. Aschenbach. X-ray Observations of Neutron Stars and Pulsars: First Results from XMM-Newton. In *Proceedings of the 270. WE-Heraeus Seminar on Neutron Stars, Pulsars, and Supernova Remnants. MPE Report 278.*, volume 270, eprint: arXiv:astro-ph/0208466, Jan. 2002. URL https://ui.adsabs.harvard.edu/abs/2002nsps.conf...64B. Conference Name: Neutron Stars, Pulsars, and Supernova Remnants Pages: 64 ADS Bibcode: 2002nsps.conf...64B.

K. Belczynski and J. Ziolkowski. On The Apparent Lack of Be X-ray Binaries with Black Holes. *The Astrophysical Journal*, 707(2):870–877, Dec. 2009.

ISSN 0004-637X, 1538-4357. doi: 10.1088/0004-637X/707/2/870. URL https://iopscience.iop.org/article/10.1088/0004-637X/707/2/870.

T. Belloni et al. An Unstable Central Disk in the Superluminal Black Hole X-Ray Binary GRS 1915+105. *The Astrophysical Journal*, 479:L145–L148, Apr. 1997. ISSN 0004-637X. doi: 10.1086/310595. URL https://ui.adsabs.harvard.edu/abs/1997ApJ...479L.145B. ADS Bibcode: 1997ApJ...479L.145B.

K. Bennett. COS-B: The highlights. *Nuclear Physics B Proceedings Supplements*, 14:23–34, Apr. 1990. ISSN 0920-5632. doi: 10.1016/0920-5632(90)90362-X. URL https://ui.adsabs.harvard.edu/abs/1990NuPhS..14...23B. ADS Bibcode: 1990NuPhS..14...23B.

E. Berger. Short-Duration Gamma-Ray Bursts. *Annual Review of Astronomy and Astrophysics*, 52:43–105, Aug. 2014. ISSN 0066-4146. doi: 10.1146/annurev-astro-081913-035926. URL https://ui.adsabs.harvard.edu/abs/2014ARA&A..52...43B/abstract.

M. G. Bernardini et al. Trigger 1007266: Swift detection of 1A 0535+262. *GRB Coordinates Network*, 28919:1, Nov. 2020. URL https://ui.adsabs.harvard.edu/abs/2020GCN.28919....1B.

Y. Bhargava et al. A Precise Measurement of the Orbital Period Parameters of Cygnus X-3. *The Astrophysical Journal*, 849(2):141, Nov. 2017. ISSN 0004-637X. doi: 10.3847/1538-4357/aa8ea4. URL https://doi.org/10.3847/1538-4357/aa8ea4. Publisher: American Astronomical Society.

M. Bissinger et al. GRO J1008 57: a laboratory for accretion physics. page 017, July 2013. doi: 10.22323/1.176.0017.

R. Blandford, D. Meier, and A. Readhead. Relativistic Jets in Active Galactic Nuclei. *Annual Review of Astronomy and Astrophysics*, 57(1):467–509, Aug. 2019. ISSN 0066-4146, 1545-4282. doi: 10.1146/annurev-astro-081817-051948. URL http://arxiv.org/abs/1812.06025. arXiv:1812.06025 [astro-ph].

R. D. Blandford and R. L. Znajek. Electromagnetic extraction of energy from Kerr black holes. *Monthly Notices of the Royal Astronomical Society*, 179: 433–456, May 1977. ISSN 0035-8711. doi: 10.1093/mnras/179.3.433. URL https://ui.adsabs.harvard.edu/abs/1977MNRAS.179..433B. ADS Bibcode: 1977MNRAS.179..433B.

P. Blay et al. SAX J2103.5+4545, the Closest Be+Neutron Star Galactic System. *Conference Name: The X-ray Universe 2005*, 604:243, Jan. 2006. URL https://ui.adsabs.harvard.edu/abs/2006ESASP.604..243B. Conference Name: The X-ray Universe 2005.

A. Bodaghee et al. Chandra observations of five integral sources: New X-ray positions for IGR J16393-4643 and IGR J17091-3624. *Astrophysical Journal*, 751, Mar. 2012. doi: 10.1088/0004-637X/751/2/113.

A. Bodaghee et al. Gamma-Ray Observations of the Microquasars Cygnus X-1, Cygnus X-3, GRS 1915+105, and GX 339-4 with the Fermi Large Area Telescope. *The Astrophysical Journal*, 775:98, Oct. 2013. ISSN 0004-637X. doi: 10.1088/0004-637X/775/2/98. URL http://adsabs.harvard.edu/abs/2013ApJ...775...98B.

M. Boeer, J. Greiner, and C. Motch. The optical content of the error box of GRS 1915+105. *Astronomy and Astrophysics, v.305, p.835*, 305:835, Jan. 1996. ISSN 0004-6361. URL https://ui.adsabs.harvard.edu/abs/1996A%26A...305..835B/abstract.

S. Bogdanov et al. Simultaneous Chandra and VLA Observations of the Transitional Millisecond Pulsar PSR J1023+0038: Anti-correlated X-Ray and Radio Variability. *The Astrophysical Journal*, 856:54, Mar. 2018. ISSN 0004-637X. doi: 10.3847/1538-4357/aaaeb9. URL https://ui.adsabs.harvard.edu/abs/2018ApJ...856...54B. ADS Bibcode: 2018ApJ...856...54B.

P. Bordas et al. The Detection of Persistent Gamma-Ray Emission Toward SS433/W50. *The Astrophysical Journal*, 807(1):L8, June 2015. ISSN 2041-8205. doi: 10.1088/2041-8205/807/1/L8. URL https://doi.org/10.1088/2041-8205/807/1/l8. Publisher: American Astronomical Society.

V. Bosch-Ramon. Non-Thermal Emission from Galactic Jets. 8:84–95, Jan. 2012. doi: 10.1142/S201019451200445X. URL https://ui.adsabs.harvard.edu/abs/2012IJMPS...8...84B. Conference Name: International Journal of Modern Physics Conference Series Place: eprint: arXiv:1108.5260 ADS Bibcode: 2012IJMPS...8...84B.

V. Bosch-Ramon and D. Khangulyan. Understanding the Very High-Energy Emission from Microquasars. *International Journal of Modern Physics D*, 18(03):347–387, Mar. 2009. ISSN 0218-2718, 1793-6594. doi: 10.1142/S0218271809014601. URL http://arxiv.org/abs/0805.4123. arXiv:0805.4123 [astro-ph].

V. Bosch-Ramon, G. E. Romero, and J. M. Paredes. A broadband leptonic model for gamma-ray emitting microquasars. *Astronomy and Astrophysics*, 447:263–276, Feb. 2006. ISSN 0004-6361. doi: 10.1051/0004-6361:20053633. URL http://adsabs.harvard.edu/abs/2006A%26A...447..263B.

L. Bouchet et al. SIGMA Discovery of Variable E +- E - Annihilation Radiation from the Near Galactic Center Variable Compact Source 1E 1740.7-2942. *The Astrophysical Journal*, 383:L45, Dec. 1991. ISSN 0004-637X. doi: 10.1086/186237. URL https://ui.adsabs.harvard.edu/abs/1991ApJ...383L..45B. ADS Bibcode: 1991ApJ...383L..45B.

E. Bozzo et al. Multi-wavelength observations of IGR J17544-2619 from quiescence to outburst. *Astronomy & Astrophysics*, 596:A16, Dec. 2016. ISSN 0004-6361, 1432-0746. doi: 10.1051/0004-6361/201629311. URL http://www.aanda.org/10.1051/0004-6361/201629311.

W. N. Brandt, P. Podsiadlowski, and S. Sigurdsson. On the high space velocity of X-ray Nova Sco 1994: implications for the formation of its black hole. *Monthly Notices of the Royal Astronomical Society*, 277(1):L35–L40, Nov. 1995. ISSN 0035-8711. doi: 10.1093/mnras/277.1.L35. URL https://doi.org/10.1093/mnras/277.1.L35.

J. Bregeon. Design and performance of the silicon strip tracker of the Fermi Large Area Telescope. *Journal of Instrumentation*, 6(12):C12043–C12043, Dec. 2011. ISSN 1748-0221. doi: 10.1088/1748-0221/6/12/C12043. URL https://doi.org/10.1088/1748-0221/6/12/c12043. Publisher: IOP Publishing.

P. Bruel et al. Fermi-LAT improved Pass~8 event selection. *arXiv:1810.11394 [astro-ph]*, Oct. 2018. URL http://arxiv.org/abs/1810.11394. arXiv: 1810.11394.

A. Bulgarelli et al. The Second AGILE Catalog of Gamma-Ray Sources. *Astronomy & Astrophysics*, 627:A13, July 2019. ISSN 0004-6361, 1432-0746. doi: 10.1051/0004-6361/201834143. URL http://arxiv.org/abs/1903.06957. arXiv: 1903.06957.

L. Burderi et al. New ephemeris of the ADC source 2A 1822–371: a stable orbital-period derivative over 30 years. *Astronomy and Astrophysics*, 515:A44, June 2010. ISSN 0004-6361, 1432-0746. doi: 10.1051/0004-6361/200912881. URL http://www.aanda.org/10.1051/0004-6361/200912881.

M. Burgay et al. An increased estimate of the merger rate of double neutron stars from observations of a highly relativistic system. *Nature*, 426(6966):531–533, Dec. 2003. ISSN 1476-4687. doi: 10.1038/nature02124. URL https://www.nature.com/articles/nature02124. Bandiera_abtest: a Cg_type: Nature Research Journals Number: 6966 Primary_atype: Research Publisher: Nature Publishing Group.

D. N. Burrows et al. The Swift X-Ray Telescope. *Space Science Reviews*, 120(3): 165–195, Oct. 2005. ISSN 1572-9672. doi: 10.1007/s11214-005-5097-2. URL https://doi.org/10.1007/s11214-005-5097-2.

M. Buxton and S. Vennes. Atmospheric Modelling of the Companion Star in GRO J1655-40. *Publications of the Astronomical Society of Australia*, 18:91–97, Jan. 2001. ISSN 1323-3580. doi: 10.1071/AS01011. URL https://ui.adsabs.harvard.edu/abs/2001PASA...18...91B. ADS Bibcode: 2001PASA...18...91B.

E. M. Cackett, R. Wijnands, and R. Remillard. XMM-Newton discovery of the X-ray transient XMMU J181227.8-181234 in the Galactic plane. *Monthly Notices of the Royal Astronomical Society*, 369:1965–1971, July 2006. ISSN 0035-8711. doi: 10.1111/j.1365-2966.2006.10444.x. URL https://ui.adsabs.harvard.edu/abs/2006MNRAS.369.1965C. ADS Bibcode: 2006MNRAS.369.1965C.

F. Cafardo and R. Nemmen. Fermi-LAT Observations of Sagittarius A\ast: Imaging Analysis. *The Astrophysical Journal*, 918(1):30, Sept. 2021. ISSN 0004-637X. doi: 10.3847/1538-4357/ac0efe. URL https://doi.org/10.3847/1538-4357/ac0efe. Publisher: American Astronomical Society.

S. Campana et al. The neutron stars of Soft X–ray Transients. *The Astronomy and Astrophysics Review*, 8(4):279–316, Aug. 1998. ISSN 1432-0754. doi: 10.1007/s001590050012. URL https://doi.org/10.1007/s001590050012.

Z. Cao et al. Discovery of a New Gamma-Ray Source, LHAASO J0341+5258, with Emission up to 200 TeV. *The Astrophysical Journal*, 917:L4, Aug. 2021a. ISSN 0004-637X. doi: 10.3847/2041-8213/ac0fd5. URL https://ui.adsabs.harvard.edu/abs/2021ApJ...917L...4C. ADS Bibcode: 2021ApJ...917L...4C.

Z. Cao et al. Ultrahigh-energy photons up to 1.4 petaelectronvolts from 12 gamma-ray Galactic sources. *Nature*, 594(7861):33–36, June 2021b. ISSN 1476-4687. doi: 10.1038/s41586-021-03498-z. URL https://www.nature.com/articles/s41586-021-03498-z. Number: 7861 Publisher: Nature Publishing Group.

G. F. Carpenter et al. New cosmic X-ray sources observed by the RMC experiment on Ariel V. *Monthly Notices of the Royal Astronomical Society*, 179: 27P–34, Apr. 1977. ISSN 0035-8711. doi: 10.1093/mnras/179.1.27P. URL https://ui.adsabs.harvard.edu/abs/1977MNRAS.179P..27C. ADS Bibcode: 1977MNRAS.179P..27C.

J. Casares, P. G. Jonker, and G. Israelian. X-Ray Binaries. In A. W. Alsabti and P. Murdin, editors, *Handbook of Supernovae*, pages 1–28. Springer International Publishing, Cham, 2016. ISBN 978-3-319-20794-0. doi: 10.1007/978-3-319-20794-0_111-1. URL https://doi.org/10.1007/978-3-319-20794-0_111-1.

A. J. Castro-Tirado, S. Brandt, and N. Lund. GRS 1915+105. *International Astronomical Union Circular*, 5590:2, Aug. 1992. ISSN 0081-0304. URL https://ui.adsabs.harvard.edu/abs/1992IAUC.5590....2C. ADS Bibcode: 1992IAUC.5590....2C.

A. Cattaneo, M. G. Haehnelt, and M. J. Rees. The distribution of supermassive black holes in the nuclei of nearby galaxies. *Monthly Notices of the Royal Astronomical Society*, 308(1):77–81, Sept. 1999. ISSN 0035-8711. doi: 10.1046/j.1365-8711.1999.02693.x. URL https://doi.org/10.1046/j.1365-8711.1999.02693.x.

G. Chabrier. Galactic Stellar and Substellar Initial Mass Function. *Publications of the Astronomical Society of the Pacific*, 115:763–795, July 2003. ISSN 0004-6280. doi: 10.1086/376392. URL https://ui.adsabs.harvard.edu/abs/2003PASP..115..763C. ADS Bibcode: 2003PASP..115..763C.

S. Chandrasekhar. The Maximum Mass of Ideal White Dwarfs. *The Astrophysical Journal*, 74:81, July 1931. ISSN 0004-637X. doi: 10.1086/143324. URL https://ui.adsabs.harvard.edu/abs/1931ApJ....74...81C. ADS Bibcode: 1931ApJ....74...81C.

Z. Chang et al. The GeV emission of PSR B1259-63 during its last three periastron passages observed by Fermi-LAT. *Research in Astronomy and Astrophysics*, 18: 152, Dec. 2018. ISSN 1674-4527. doi: 10.1088/1674-4527/18/12/152. URL http://adsabs.harvard.edu/abs/2018RAA....18..152C.

S. Chaty et al. Multi-wavelength observations of Galactic hard X-ray sources discovered by INTEGRAL. I. The nature of the companion star. *Astronomy and Astrophysics*, 484:783–800, June 2008. ISSN 0004-6361. doi: 10.1051/0004-6361:20078768. URL http://adsabs.harvard.edu/abs/2008A%26A...484..783C.

J. Chenevez et al. A new outburst of XTE J1812-182 detected by INTEGRAL/JEM-X. *The Astronomer's Telegram*, 13581:1, Mar. 2020. URL https://ui.adsabs.harvard.edu/abs/2020ATel13581....1C. ADS Bibcode: 2020ATel13581....1C.

M. Chernyakova and D. Malyshev. Gamma-ray binaries. In *Proceedings of Science*, volume 362, Palemero, Italy, Dec. 2020. doi: https://doi.org/10.22323/1.362.0045. URL http://arxiv.org/abs/2006.03615. arXiv: 2006.03615.

M. Chernyakova, A. Neronov, and R. Walter. INTEGRAL and XMM-Newton observations of LSI +61 303. *Monthly Notices of the Royal Astronomical Society*, 372(4):1585–1592, Nov. 2006. ISSN 0035-8711, 1365-2966. doi: 10.1111/j.1365-2966.2006.10946.x. URL https://academic.oup.com/mnras/article-lookup/doi/10.1111/j.1365-2966.2006.10946.x.

P. Christillin. Nuclear Compton scattering. *Journal of Physics G: Nuclear Physics*, 12(9):837–851, Sept. 1986. ISSN 0305-4616. doi: 10.1088/0305-4616/12/9/008. URL https://doi.org/10.1088/0305-4616/12/9/008. Publisher: IOP Publishing.

T. Chronis et al. Characteristics of Thunderstorms That Produce Terrestrial Gamma Ray Flashes. *Bulletin of the American Meteorological Society*, 97(4):639–653, Apr. 2016. ISSN 0003-0007, 1520-0477. doi: 10.1175/

BAMS-D-14-00239.1. URL https://journals.ametsoc.org/view/journals/bams/97/4/bams-d-14-00239.1.xml. Publisher: American Meteorological Society Section: Bulletin of the American Meteorological Society.

E. Churazov et al. Detection of the A1742-294 X-Ray Burster above 35 keV. *The Astrophysical Journal*, 443:341, Apr. 1995. ISSN 0004-637X. doi: 10.1086/175529. URL https://ui.adsabs.harvard.edu/abs/1995ApJ...443..341C. ADS Bibcode: 1995ApJ...443..341C.

M. J. Church and M. Balucinska-Church. A review of the Z-track sources. In *Memorie della Societa Astronomica Italiana*, volume 83, page 170, Oct. 2011. URL http://arxiv.org/abs/1110.1281. arXiv: 1110.1281.

D. Ciampa, R. W. Clay, and P. G. Edwards. Evidence for Ultra-High-Energy Gamma-Ray Emission from the Low-Mass X-Ray Binary 2A 1822-371. *The Astrophysical Journal*, 346:151, Nov. 1989. ISSN 0004-637X. doi: 10.1086/167994. URL https://ui.adsabs.harvard.edu/abs/1989ApJ...346..151C. ADS Bibcode: 1989ApJ...346..151C.

D. H. Clark and P. Murdin. An unusual emission-line star/X-ray source/radio star, possibly associated with an SNR. *Nature*, 276(5683):44–45, Nov. 1978. ISSN 1476-4687. doi: 10.1038/276044a0. URL https://www.nature.com/articles/276044a0. Number: 5683 Publisher: Nature Publishing Group.

G. W. Clark, T. H. Markert, and F. K. Li. Observations of variable X-ray sources in globular clusters. *The Astrophysical Journal*, 199:L93–L96, July 1975. ISSN 0004-637X. doi: 10.1086/181856. URL https://ui.adsabs.harvard.edu/abs/1975ApJ...199L..93C. ADS Bibcode: 1975ApJ...199L..93C.

W. I. Clarkson, P. A. Charles, and N. Onyett. X-ray behaviour of Circinus X-1 — I. X-ray dips as a diagnostic of periodic behaviour. *Monthly Notices of the Royal Astronomical Society*, 348(2):458–468, Feb. 2004. ISSN 0035-8711.

doi: 10.1111/j.1365-2966.2004.07293.x. URL https://doi.org/10.1111/j.1365-2966.2004.07293.x.

L. Cominsky et al. Transient X-ray sources in the galactic plane. *The Astrophysical Journal*, 224:46–52, Aug. 1978. ISSN 0004-637X. doi: 10.1086/156348. URL https://ui.adsabs.harvard.edu/abs/1978ApJ...224...46C. ADS Bibcode: 1978ApJ...224...46C.

A. H. Compton. A Quantum Theory of the Scattering of X-rays by Light Elements. *Physical Review*, 21(5):483–502, May 1923. doi: 10.1103/PhysRev.21.483. URL https://link.aps.org/doi/10.1103/PhysRev.21.483. Publisher: American Physical Society.

S. Corbel et al. A giant radio flare from Cygnus X-3 with associated Gamma-ray emission. *Monthly Notices of the Royal Astronomical Society*, 421(4):2947–2955, Apr. 2012. ISSN 00358711. doi: 10.1111/j.1365-2966.2012.20517.x. URL http://arxiv.org/abs/1201.3356. arXiv: 1201.3356.

R. H. D. Corbet et al. A Luminous Gamma-Ray Binary In The Large Magellanic Cloud. *The Astrophysical Journal*, 829(2):105, Sept. 2016. ISSN 0004-637X. doi: 10.3847/0004-637X/829/2/105. URL https://doi.org/10.3847/0004-637x/829/2/105. Publisher: American Astronomical Society.

R. H. D. Corbet et al. Discovery of the Galactic High-mass Gamma-Ray Binary 4FGL J1405.1-6119. *The Astrophysical Journal*, 884:93, Oct. 2019. ISSN 0004-637X. doi: 10.3847/1538-4357/ab3e32. URL https://ui.adsabs.harvard.edu/abs/2019ApJ...884...93C. ADS Bibcode: 2019ApJ...884...93C.

M. F. Corcoran. X-ray emission from colliding wind binaries. In *Revista Mexicana de Astronomia y Astrofisica Conference Series*, volume 5, pages 54–60, Dec. 1996. URL https://ui.adsabs.harvard.edu/abs/1996RMxAC...5...54C. Conference Name: Revista Mexicana de Astronomia y Astrofisica Conference Series ADS Bibcode: 1996RMxAC...5...54C.

M. Coriat et al. The twisted jets of Circinus X-1. *Monthly Notices of the Royal Astronomical Society*, 484(2):1672–1686, Apr. 2019. ISSN 0035-8711. doi: 10.1093/mnras/stz099. URL https://doi.org/10.1093/mnras/stz099.

R. Cornelisse et al. BeppoSAX Wide Field Cameras observations of six type I X-ray bursters. *Astronomy and Astrophysics, v.392, p.885-893 (2002)*, 392:885, Sept. 2002. ISSN 0004-6361. doi: 10.1051/0004-6361:20020707. URL https://ui.adsabs.harvard.edu/abs/2002A%26A...392..885C/abstract.

A. P. Cowley, D. Crampton, and J. B. Hutchings. The low mass X-ray binary 2A 1822-371. *The Astrophysical Journal*, 255:596, Apr. 1982. ISSN 0004-637X, 1538-4357. doi: 10.1086/159861. URL http://adsabs.harvard.edu/doi/10.1086/159861.

P. A. Crowther. Stellar Winds from Massive Stars. In D. Vanbeveren, editor, *The Influence of Binaries on Stellar Population Studies*, Astrophysics and Space Science Library, pages 215–230. Springer Netherlands, Dordrecht, 2001. ISBN 978-94-015-9723-4. doi: 10.1007/978-94-015-9723-4_17. URL https://doi.org/10.1007/978-94-015-9723-4_17.

R. G. Cruddace et al. High-resolution observations of X-ray sources at the galactic center. *The Astrophysical Journal*, 222:L95–L98, June 1978. ISSN 0004-637X. doi: 10.1086/182700. URL https://ui.adsabs.harvard.edu/abs/1978ApJ...222L..95C. ADS Bibcode: 1978ApJ...222L..95C.

V. A. Cúneo et al. Discovery of optical outflows and inflows in the black hole candidate GRS 1716-249. *Monthly Notices of the Royal Astronomical Society*, 498:25–32, Oct. 2020. ISSN 0035-8711. doi: 10.1093/mnras/staa2241. URL https://ui.adsabs.harvard.edu/abs/2020MNRAS.498...25C. ADS Bibcode: 2020MNRAS.498...25C.

R. de Menezes. easyFermi: A graphical interface for performing Fermi-LAT data analyses. *Astronomy and Computing*, 40:100609, July 2022. ISSN 2213-1337.

doi: 10.1016/j.ascom.2022.100609. URL https://ui.adsabs.harvard.edu/abs/2022A&C....4000609D/abstract.

C. Deil et al. Gammapy - A prototype for the CTA science tools. 301:766, Jan. 2017. URL https://ui.adsabs.harvard.edu/abs/2017ICRC...35..766D. Conference Name: 35th International Cosmic Ray Conference (ICRC2017) Place: eprint: arXiv:1709.01751 ADS Bibcode: 2017ICRC...35..766D.

B.-O. Demory et al. Mass-radius relation of low and very low-mass stars revisited with the VLTI. *Astronomy and Astrophysics, Volume 505, Issue 1, 2009, pp.205-215*, 505(1):205, Oct. 2009. ISSN 0004-6361. doi: 10.1051/0004-6361/200911976. URL https://ui.adsabs.harvard.edu/abs/2009A%26A...505..205D/abstract.

P. R. den Hartog et al. IGR J00370+6122 - A new high-mass X-ray binary. *The Astronomer's Telegram*, 281:1, May 2004. URL https://ui.adsabs.harvard.edu/abs/2004ATel..281....1D.

S. M. Derdeyn et al. Sas-b digitized spark chamber gamma ray telescope. *Nucl. Instrum. Meth.*, 98:557–566, 1972. doi: 10.1016/0029-554X(72)90243-1.

L. Di Gesu et al. INTEGRAL detection of enhanced activity from the HMXB 4U 2206+543. *The Astronomer's Telegram*, 10519:1, June 2017. URL https://ui.adsabs.harvard.edu/abs/2017ATel10519....1D/abstract.

T. di Salvo et al. Orbital evolution of an accreting millisecond pulsar: witnessing the banquet of a hidden black widow? *Monthly Notices of the Royal Astronomical Society*, 389:1851–1857, Oct. 2008. ISSN 0035-8711. doi: 10.1111/j.1365-2966.2008.13709.x. URL https://ui.adsabs.harvard.edu/abs/2008MNRAS.389.1851D. ADS Bibcode: 2008MNRAS.389.1851D.

S. M. Dougherty et al. Radio emission models of colliding-wind binary systems. *Astronomy and Astrophysics, v.409, p.217-233 (2003)*, 409:217, Oct. 2003.

ISSN 0004-6361. doi: 10.1051/0004-6361:20031048. URL https://ui.adsabs.harvard.edu/abs/2003A%26A...409..217D/abstract.

G. Dubus. Gamma-ray binaries and related systems. *The Astronomy and Astrophysics Review*, 21(1):64, Nov. 2013. ISSN 0935-4956, 1432-0754. doi: 10.1007/s00159-013-0064-5. URL http://arxiv.org/abs/1307.7083. arXiv: 1307.7083.

G. Dubus. Gamma-ray emission from binaries in context. *arXiv:1507.00935 [astro-ph]*, July 2015. URL http://arxiv.org/abs/1507.00935. arXiv: 1507.00935.

G. Dubus, A. Lamberts, and S. Fromang. Modelling the high-energy emission from gamma-ray binaries using numerical relativistic hydrodynamics. *Astronomy & Astrophysics*, 581:A27, Sept. 2015. ISSN 0004-6361, 1432-0746. doi: 10.1051/0004-6361/201425394. URL https://www.aanda.org/articles/aa/abs/2015/09/aa25394-14/aa25394-14.html. Publisher: EDP Sciences.

L. Ducci et al. Renewed hard X-ray activity of SAX J2103.5+4545 detected by INTEGRAL. *The Astronomer's Telegram*, 12812:1, May 2019. URL https://ui.adsabs.harvard.edu/abs/2019ATel12812....1D.

G. Duchene and A. Kraus. Stellar Multiplicity. *Annual Review of Astronomy and Astrophysics*, 51(1):269–310, Aug. 2013. ISSN 0066-4146. doi: 10.1146/annurev-astro-081710-102602. URL https://www.annualreviews.org/doi/10.1146/annurev-astro-081710-102602. Publisher: Annual Reviews.

M. M. Dunham et al. *The Evolution of Protostars: Insights from Ten Years of Infrared Surveys with Spitzer and Herschel*. eprint: arXiv:1401.1809, Jan. 2014. doi: 10.2458/azu_uapress_9780816531240-ch009. URL https://ui.adsabs.harvard.edu/abs/2014prpl.conf..195D. Conference Name: Protostars and Planets VI Pages: 195 ADS Bibcode: 2014prpl.conf..195D.

P. P. Eggleton. Aproximations to the radii of Roche lobes. *The Astrophysical Journal*, 268:368–369, May 1983. ISSN 0004-637X. doi: 10.1086/160960. URL

https://ui.adsabs.harvard.edu/abs/1983ApJ...268..368E. ADS Bibcode: 1983ApJ...268..368E.

C. M. Espinoza et al. Six millisecond pulsars detected by the Fermi Large Area Telescope and the radio/gamma-ray connection of millisecond pulsars. *Monthly Notices of the Royal Astronomical Society*, 430(1):571–587, Mar. 2013. ISSN 0035-8711. doi: 10.1093/mnras/sts657. URL https://doi.org/10.1093/mnras/sts657.

A. C. Fabian and M. J. Rees. SS 433 - A double jet in action. *Monthly Notices of the Royal Astronomical Society*, 187:13P–16P, Apr. 1979. ISSN 0035-8711. doi: 10.1093/mnras/187.1.13P. URL http://adsabs.harvard.edu/abs/1979MNRAS.187P..13F.

A. C. Fabian et al. X-ray fluorescence from the inner disc in Cygnus X-1. *Monthly Notices of the Royal Astronomical Society*, 238:729–736, May 1989. ISSN 0035-8711. doi: 10.1093/mnras/238.3.729. URL https://ui.adsabs.harvard.edu/abs/1989MNRAS.238..729F. ADS Bibcode: 1989MNRAS.238..729F.

S. Fabrika. The jets and supercritical accretion disk in SS433. *Astrophysics and Space Physics Reviews*, 12:1–152, 2004. URL http://adsabs.harvard.edu/abs/2004ASPRv..12....1F.

W. M. Farr et al. The Mass Distribution of Stellar Mass Black Holes. *The Astrophysical Journal*, 741(2):103, Oct. 2011. ISSN 0004-637X. doi: 10.1088/0004-637X/741/2/103. URL https://doi.org/10.1088/0004-637x/741/2/103. Publisher: American Astronomical Society.

S. A. Farrell et al. An intermediate-mass black hole of over 500 solar masses in the galaxy ESO 243-49. *Nature*, 460(7251):73–75, July 2009. ISSN 1476-4687. doi: 10.1038/nature08083. URL https://www.nature.com/articles/nature08083. Number: 7251 Publisher: Nature Publishing Group.

R. Fender et al. An Asymmetric Arcsecond Radio Jet from Circinus X-1. *The Astrophysical Journal*, 506(2):L121, Sept. 1998. ISSN 0004-637X. doi: 10.1086/311660. URL https://iopscience.iop.org/article/10.1086/311660/meta. Publisher: IOP Publishing.

R. P. Fender, T. M. Belloni, and E. Gallo. Towards a unified model for black hole X-ray binary jets. *Monthly Notices of the Royal Astronomical Society*, 355: 1105–1118, Dec. 2004. ISSN 0035-8711. doi: 10.1111/j.1365-2966.2004.08384.x. URL http://adsabs.harvard.edu/abs/2004MNRAS.355.1105F.

M. Feroci et al. SuperAGILE: The hard X-ray imager for the AGILE space mission. *Nuclear Instruments and Methods in Physics Research Section A: Accelerators, Spectrometers, Detectors and Associated Equipment*, 581:728–754, Nov. 2007. doi: 10.1016/j.nima.2007.07.147.

C. E. Fichtel et al. High-energy gamma-ray results from the second Small Astronomy Satellite. *The Astrophysical Journal*, 198:163–182, May 1975. ISSN 0004-637X. doi: 10.1086/153590. URL https://ui.adsabs.harvard.edu/abs/1975ApJ...198..163F. ADS Bibcode: 1975ApJ...198..163F.

M. Finger et al. Spin-Down of the Long-Period Accreting Pulsar 4U 2206+54. *ApJ*, 709, Aug. 2009. doi: 10.1088/0004-637X/709/2/1249.

M. H. Finger, R. B. Wilson, and B. A. Harmon. Quasi-periodic Oscillations during a Giant Outburst of A0535+262. *The Astrophysical Journal*, 459:288, Mar. 1996. ISSN 0004-637X. doi: 10.1086/176892. URL https://ui.adsabs.harvard.edu/abs/1996ApJ...459..288F/abstract.

M. Fiori et al. Modelling the gamma-ray pulsar wind nebulae population in our galaxy. *Monthly Notices of the Royal Astronomical Society*, 511:1439–1453, Mar. 2022. ISSN 0035-8711. doi: 10.1093/mnras/stac019. URL https://ui.adsabs.harvard.edu/abs/2022MNRAS.511.1439F. ADS Bibcode: 2022MNRAS.511.1439F.

R. A. Fisher. On the mathematical foundations of theoretical statistics. *Philosophical Transactions of the Royal Society of London. Series A, Containing Papers of a Mathematical or Physical Character*, 222(594-604):309–368, Jan. 1922. doi: 10.1098/rsta.1922.0009. URL https://royalsocietypublishing.org/doi/10.1098/rsta.1922.0009. Publisher: Royal Society.

J. R. Fleischman. Detection of a new X-ray burst source. *Astronomy and Astrophysics, Vol. 153, p. 106-108 (1985)*, 153:106, Dec. 1985. ISSN 0004-6361. URL https://ui.adsabs.harvard.edu/abs/1985A%26A...153..106F/abstract.

W. Forman, C. Jones, and H. Tananbaum. Uhuru observations of the galactic plane in 1970, 1971, and 1972. *The Astrophysical Journal*, 206:L29–L35, May 1976. ISSN 0004-637X. doi: 10.1086/182126. URL https://ui.adsabs.harvard.edu/abs/1976ApJ...206L..29F. ADS Bibcode: 1976ApJ...206L..29F.

W. Forman et al. The fourth Uhuru catalog of X-ray sources. *The Astrophysical Journal Supplement Series*, 38:357–412, Dec. 1978. ISSN 0067-0049. doi: 10.1086/190561. URL https://ui.adsabs.harvard.edu/abs/1978ApJS...38..357F. ADS Bibcode: 1978ApJS...38..357F.

M. Fornasa and M. A. Sanchez-Conde. The nature of the Diffuse Gamma-Ray Background. *Physics Reports*, 598:1–58, Oct. 2015. ISSN 03701573. doi: 10.1016/j.physrep.2015.09.002. URL http://arxiv.org/abs/1502.02866. arXiv:1502.02866 [astro-ph].

R. S. Foster et al. Radio and X-Ray Variability of the Galactic Superluminal Source GRS 1915+105. *The Astrophysical Journal*, 467:L81, Aug. 1996. ISSN 0004-637X. doi: 10.1086/310199. URL https://ui.adsabs.harvard.edu/abs/1996ApJ...467L..81F. ADS Bibcode: 1996ApJ...467L..81F.

J. Frank, A. King, and D. J. Raine. *Accretion Power in Astrophysics: Third Edition*. Jan. 2002. URL https://ui.adsabs.harvard.edu/abs/2002apa.

.book.....F. Publication Title: Accretion Power in Astrophysics ADS Bibcode: 2002apa..book.....F.

A. S. Fruchter, D. R. Stinebring, and J. H. Taylor. A millisecond pulsar in an eclipsing binary. *Nature*, 333(6170):237–239, May 1988. ISSN 1476-4687. doi: 10.1038/333237a0. URL https://www.nature.com/articles/333237a0. Bandiera_abtest: a Cg_type: Nature Research Journals Number: 6170 Primary_atype: Research Publisher: Nature Publishing Group.

D. K. Galloway et al. Thermonuclear (Type I) X-Ray Bursts Observed by the Rossi X-Ray Timing Explorer. *The Astrophysical Journal Supplement Series*, 179:360–422, Dec. 2008. ISSN 0067-0049. doi: 10.1086/592044. URL https://ui.adsabs.harvard.edu/abs/2008ApJS..179..360G. ADS Bibcode: 2008ApJS..179..360G.

A. F. Gambino et al. New orbital ephemerides for the dipping source 4U 1323-619: constraining the distance to the source. *Astronomy & Astrophysics*, 589:A34, May 2016. ISSN 0004-6361, 1432-0746. doi: 10.1051/0004-6361/201527512. URL https://www.aanda.org/articles/aa/abs/2016/05/aa27512-15/aa27512-15.html. Publisher: EDP Sciences.

F. Garcia et al. Spectral evolution of the supergiant HMXB IGR J16320-4751 along its orbit using XMM-Newton. *Astronomy & Astrophysics*, 618:A61, Oct. 2018. ISSN 0004-6361, 1432-0746. doi: 10.1051/0004-6361/201833365. URL http://arxiv.org/abs/1810.01910. arXiv: 1810.01910.

N. Gehrels et al. GLAST: the next-generation high energy gamma-ray astronomy mission. *Astroparticle Physics*, 11:277–282, June 1999. ISSN 0927-6505. doi: 10.1016/S0927-6505(99)00066-3. URL https://ui.adsabs.harvard.edu/abs/1999APh....11..277G. ADS Bibcode: 1999APh....11..277G.

A. Generozov et al. An overabundance of black hole X-ray binaries in the Galactic Centre from tidal captures. *Monthly Notices of the Royal Astronomical Society*,

478(3):4030–4051, Aug. 2018. ISSN 0035-8711. doi: 10.1093/mnras/sty1262. URL https://doi.org/10.1093/mnras/sty1262.

R. Genzel, F. Eisenhauer, and S. Gillessen. The Galactic Center massive black hole and nuclear star cluster. *Reviews of Modern Physics*, 82(4):3121–3195, Dec. 2010. doi: 10.1103/RevModPhys.82.3121. URL https://link.aps.org/doi/10.1103/RevModPhys.82.3121. Publisher: American Physical Society.

R. Genzel et al. On the nature of the dark mass in the centre of the Milky Way. *Monthly Notices of the Royal Astronomical Society*, 291:219–234, Oct. 1997. ISSN 0035-8711. doi: 10.1093/mnras/291.1.219. URL https://ui.adsabs.harvard.edu/abs/1997MNRAS.291..219G. ADS Bibcode: 1997MNRAS.291..219G.

A. M. Ghez et al. High Proper-Motion Stars in the Vicinity of Sagittarius A*: Evidence for a Supermassive Black Hole at the Center of Our Galaxy. *The Astrophysical Journal*, 509(2):678, Dec. 1998. ISSN 0004-637X. doi: 10.1086/306528. URL https://iopscience.iop.org/article/10.1086/306528/meta. Publisher: IOP Publishing.

A. M. Ghez et al. Measuring Distance and Properties of the Milky Way's Central Supermassive Black Hole with Stellar Orbits. *The Astrophysical Journal*, 689:1044–1062, Dec. 2008. ISSN 0004-637X. doi: 10.1086/592738. URL https://ui.adsabs.harvard.edu/abs/2008ApJ...689.1044G. ADS Bibcode: 2008ApJ...689.1044G.

G. Ghisellini. Synchrotron Self-Compton. In G. Ghisellini, editor, *Radiative Processes in High Energy Astrophysics*, Lecture Notes in Physics, pages 89–93. Springer International Publishing, Heidelberg, 2013. ISBN 978-3-319-00612-3. doi: 10.1007/978-3-319-00612-3_6. URL https://doi.org/10.1007/978-3-319-00612-3_6.

R. Giacconi et al. An X-Ray Scan of the Galactic Plane from UHURU. *The Astrophysical Journal*, 165:L27, Apr. 1971. ISSN 0004-637X. doi: 10.1086/

180711. URL https://ui.adsabs.harvard.edu/abs/1971ApJ...165L..27G. ADS Bibcode: 1971ApJ...165L..27G.

R. Giacconi et al. The Uhuru catalog of X-ray sources. *The Astrophysical Journal*, 178:281–308, Dec. 1972. ISSN 0004-637X. doi: 10.1086/151790. URL https://ui.adsabs.harvard.edu/abs/1972ApJ...178..281G. ADS Bibcode: 1972ApJ...178..281G.

R. Giacconi et al. Further X-ray observations of Hercules X-1 from Uhuru. *The Astrophysical Journal*, 184:227, Aug. 1973. ISSN 0004-637X. doi: 10.1086/152321. URL https://ui.adsabs.harvard.edu/abs/1973ApJ...184..227G. ADS Bibcode: 1973ApJ...184..227G.

D. R. Gies, W. Huang, and M. V. McSwain. The Spectrum of the Mass Donor Star in SS 433. *The Astrophysical Journal*, 578(1):L67–L70, Oct. 2002. ISSN 0004637X, 15384357. doi: 10.1086/344436. URL https://iopscience.iop.org/article/10.1086/344436.

A. Giménez et al. Omc: AN Optical Monitoring Camera for Integral. *Astrophysical Letters and Communications, Vol. 39, p.347*, 39:347, 1999. ISSN 0888-6512. URL https://ui.adsabs.harvard.edu/abs/1999ApL%26C..39..347G/abstract.

A. J. Goodwin et al. XMMU J181227.8-181234: a new ultracompact X-ray binary candidate. *Monthly Notices of the Royal Astronomical Society*, 486:4149–4157, July 2019. ISSN 0035-8711. doi: 10.1093/mnras/stz1094. URL https://ui.adsabs.harvard.edu/abs/2019MNRAS.486.4149G. ADS Bibcode: 2019MNRAS.486.4149G.

E. V. Gotthelf and G. Vasisht. Kes 73: A Young Supernova Remnant with an X-ray Bright, Radio-quiet Central Source. *The Astrophysical Journal*, 486(2):L133–L136, Sept. 1997. ISSN 0004637X. doi: 10.1086/310846. URL http://arxiv.org/abs/astro-ph/9706057. arXiv: astro-ph/9706057.

A. W. Gregory and M. R. Veall. Formulating Wald Tests of Nonlinear Restrictions. *Econometrica*, 53(6):1465–1468, 1985. ISSN 0012-9682. doi: 10.2307/1913221. URL https://www.jstor.org/stable/1913221. Publisher: [Wiley, Econometric Society].

J. Greiner et al. Identification of the donor in the X-ray binary GRS 1915+105. *Astronomy and Astrophysics, v.373, p.L37-L40 (2001)*, 373:L37, July 2001. ISSN 0004-6361. doi: 10.1051/0004-6361:20010771. URL https://ui.adsabs.harvard.edu/abs/2001A%26A...373L..37G/abstract.

I. A. Grenier and A. K. Harding. Gamma-ray pulsars: A gold mine. *Comptes Rendus Physique*, 16(6):641–660, Aug. 2015. ISSN 1631-0705. doi: 10.1016/j.crhy.2015.08.013. URL https://www.sciencedirect.com/science/article/pii/S1631070515001486.

R. E. Griffiths et al. Positions and identifications for galactic X-ray sources 2A 1822-371 and 2S 1254-690. *Nature*, 276:247–249, Nov. 1978. ISSN 0028-0836. doi: 10.1038/276247a0. URL https://ui.adsabs.harvard.edu/abs/1978Natur.276..247G. ADS Bibcode: 1978Natur.276..247G.

E. Grimaldo et al. Proton Acceleration in Colliding Stellar Wind Binaries. *The Astrophysical Journal*, 871(1):55, Jan. 2019. ISSN 0004-637X. doi: 10.3847/1538-4357/aaf6ee. URL https://doi.org/10.3847/1538-4357/aaf6ee. Publisher: American Astronomical Society.

J. E. Grove. GRO J2058+42. *International Astronomical Union Circular*, 6239:2, Sept. 1995. ISSN 0081-0304. URL https://ui.adsabs.harvard.edu/abs/1995IAUC.6239....2G.

J. E. Grove and W. N. Johnson. The calorimeter of the Fermi Large Area Telescope. 7732:77320J, July 2010. doi: 10.1117/12.857839. URL https://ui.adsabs.harvard.edu/abs/2010SPIE.7732E..0JG. Conference Name: Space

Telescopes and Instrumentation 2010: Ultraviolet to Gamma Ray ADS Bibcode: 2010SPIE.7732E..0JG.

J. H. Grunhut, C. T. Bolton, and M. V. McSwain. Orbit and properties of the massive X-ray binary BD +60 73=IGR J00370+6122. *Astronomy & Astrophysics, Volume 563, id.A1, <NUMPAGES>8</NUMPAGES> pp.*, 563: A1, Mar. 2014. ISSN 0004-6361. doi: 10.1051/0004-6361/201322738. URL https://ui.adsabs.harvard.edu/abs/2014A%26A...563A...1G/abstract.

D. Haggard et al. Low Mass X-Ray Binaries in the Inner Galaxy: Implications for Millisecond Pulsars and the GeV Excess. *Journal of Cosmology and Astroparticle Physics*, 2017(05):056–056, May 2017. ISSN 1475-7516. doi: 10.1088/1475-7516/2017/05/056. URL http://arxiv.org/abs/1701.02726. arXiv: 1701.02726.

X. Han and R. M. Hjellming. Radio observations of the 1989 transient event in V404 Cygni (=GS 2023+338). *The Astrophysical Journal*, 400:304–314, Nov. 1992. ISSN 0004-637X. doi: 10.1086/171996. URL http://adsabs.harvard.edu/abs/1992ApJ...400..304H.

D. C. Hannikainen et al. Discovery of a new INTEGRAL source: IGR J19140+0951. *Astronomy & Astrophysics*, 423(2):L17–L20, Aug. 2004. ISSN 0004-6361, 1432-0746. doi: 10.1051/0004-6361:200400021. URL https://www.aanda.org/articles/aa/abs/2004/32/aage174/aage174.html. Number: 2 Publisher: EDP Sciences.

D. C. Hannikainen et al. The nature of the infrared counterpart of IGR J19140+0951. *Monthly Notices of the Royal Astronomical Society*, 380(2):665–668, Sept. 2007. ISSN 0035-8711. doi: 10.1111/j.1365-2966.2007.12092.x. URL https://doi.org/10.1111/j.1365-2966.2007.12092.x.

B. A. Harmon et al. X-Ray Nova in Ophiuchus. *International Astronomical Union Circular*, 5900:1, Dec. 1993. ISSN 0081-0304. URL

https://ui.adsabs.harvard.edu/abs/1993IAUC.5900....1H. ADS Bibcode: 1993IAUC.5900....1H.

W. E. Harris. A Catalog of Parameters for Globular Clusters in the Milky Way. *The Astronomical Journal*, 112:1487, Oct. 1996. ISSN 0004-6256. doi: 10.1086/118116. URL https://ui.adsabs.harvard.edu/abs/1996AJ....112.1487H. ADS Bibcode: 1996AJ....112.1487H.

W. E. Harris. A New Catalog of Globular Clusters in the Milky Way. *arXiv:1012.3224 [astro-ph]*, Dec. 2010. URL http://arxiv.org/abs/1012.3224. arXiv: 1012.3224.

S. W. Hawking. Black hole explosions? *Nature*, 248(5443):30–31, Mar. 1974. ISSN 1476-4687. doi: 10.1038/248030a0. URL https://www.nature.com/articles/248030a0. Number: 5443 Publisher: Nature Publishing Group.

M. Haywood et al. The age structure of stellar populations in the solar vicinity. Clues of a two-phase formation history of the Milky Way disk. *Astronomy & Astrophysics, Volume 560, id.A109, <NUMPAGES>18</NUMPAGES> pp.*, 560:A109, Dec. 2013. ISSN 0004-6361. doi: 10.1051/0004-6361/201321397. URL https://ui.adsabs.harvard.edu/abs/2013A%26A...560A.109H/abstract.

A. Heger and S. E. Woosley. The Nucleosynthetic Signature of Population III. *The Astrophysical Journal*, 567(1):532, Mar. 2002. ISSN 0004-637X. doi: 10.1086/338487. URL https://iopscience.iop.org/article/10.1086/338487/meta. Publisher: IOP Publishing.

S. Heinz et al. Evidence of a Parsec-Scale X-Ray Jet from the Accreting Neutron Star Circinus X-1. *The Astrophysical Journal*, 663(2):L93–L96, July 2007. ISSN 0004-637X, 1538-4357. doi: 10.1086/519950. URL https://iopscience.iop.org/article/10.1086/519950.

S. Heinz et al. The Youngest Known X-ray Binary: Circinus X-1 and its Natal Supernova Remnant. *The Astrophysical Journal*, 779(2):171, Dec. 2013. ISSN

0004-637X. doi: 10.1088/0004-637X/779/2/171. URL https://doi.org/10.1088/0004-637x/779/2/171. Publisher: American Astronomical Society.

D. Heinzeller and W. J. Duschl. On the Eddington limit in accretion discs. *Monthly Notices of the Royal Astronomical Society*, 374(3):1146–1154, Jan. 2007. ISSN 0035-8711. doi: 10.1111/j.1365-2966.2006.11233.x. URL https://doi.org/10.1111/j.1365-2966.2006.11233.x.

O. Helene. Upper limit of peak area. *Nuclear Instruments and Methods in Physics Research*, 212(1):319–322, July 1983. ISSN 0167-5087. doi: 10.1016/0167-5087(83)90709-3. URL https://www.sciencedirect.com/science/article/pii/0167508783907093.

W. Herschel. XVIII. Catalogue of 500 new neb nebulous stars, planetary nebula:, and clusters of stars; with remarks on the construction of the heavens. *Philosophical Transactions of the Royal Society of London*, 92:477–528, Jan. 1802. doi: 10.1098/rstl.1802.0021. URL https://royalsocietypublishing.org/doi/10.1098/rstl.1802.0021. Publisher: Royal Society.

W. Herschel and D. Watson. XII. Catalogue of double stars. *Philosophical Transactions of the Royal Society of London*, 72:112–162, Jan. 1782. doi: 10.1098/rstl.1782.0014. URL https://royalsocietypublishing.org/doi/10.1098/rstl.1782.0014. Publisher: Royal Society.

P. Hertz and J. E. Grindlay. The Einstein galactic plane survey : statistical analysis of the complete X-ray sample. *The Astrophysical Journal*, 278:137–149, Mar. 1984. ISSN 0004-637X. doi: 10.1086/161775. URL https://ui.adsabs.harvard.edu/abs/1984ApJ...278..137H. ADS Bibcode: 1984ApJ...278..137H.

V. Hess. On the Observations of the Penetrating Radiation during Seven Balloon Flights. Technical report, July 1912. URL https://ui.adsabs.harvard.edu/abs/2018arXiv180802927H. Publication Title: arXiv e-prints ADS Bibcode: 2018arXiv180802927H Type: article.

A. Hewish et al. Observation of a Rapidly Pulsating Radio Source. *Nature*, 217 (5130):709–713, Feb. 1968. ISSN 1476-4687. doi: 10.1038/217709a0. URL https://www.nature.com/articles/217709a0. Number: 5130 Publisher: Nature Publishing Group.

A. M. Hillas. Differences between gamma-ray and hadronic showers. *Space Science Reviews*, 75(1):17–30, Jan. 1996. ISSN 1572-9672. doi: 10.1007/BF00195021. URL https://doi.org/10.1007/BF00195021.

T. C. Hillwig et al. Identification of the Mass Donor Star's Spectrum in SS 433. *The Astrophysical Journal*, 615(1):422, Nov. 2004. ISSN 0004-637X. doi: 10.1086/423927. URL https://iopscience.iop.org/article/10.1086/423927/meta. Publisher: IOP Publishing.

J. Hinton. The Southern Wide-field Gamma-ray Observatory: Status and Prospects. In *Proceedings of 37th International Cosmic Ray Conference — PoS(ICRC2021)*, page 023, Berlin, Germany - Online, Nov. 2021. Sissa Medialab. doi: 10.22323/1.395.0023. URL https://pos.sissa.it/395/023. J. Hinton for the SWGO Collaboration.

S. Hirano et al. One Hundred First Stars: Protostellar Evolution and the Final Masses. *The Astrophysical Journal*, 781:60, Feb. 2014. ISSN 0004-637X. doi: 10.1088/0004-637X/781/2/60. URL https://ui.adsabs.harvard.edu/abs/2014ApJ...781...60H. ADS Bibcode: 2014ApJ...781...60H.

R. M. Hjellming and M. P. Rupen. Episodic ejection of relativistic jets by the X-ray transient GRO J1655 - 40. *Nature*, 375:464–468, June 1995. ISSN 0028-0836. doi: 10.1038/375464a0. URL https://ui.adsabs.harvard.edu/abs/1995Natur.375..464H. ADS Bibcode: 1995Natur.375..464H.

R. M. Hjellming et al. XTE J1748-288. *International Astronomical Union Circular*, 6937:1, June 1998. ISSN 0081-0304. URL https://ui.adsabs.harvard.edu/abs/1998IAUC.6937....1H. ADS Bibcode: 1998IAUC.6937....1H.

W. C. G. Ho et al. Multiwavelength monitoring and X-ray brightening of Be X-ray binary PSR J2032+4127/MT91 213 on its approach to periastron. *Monthly Notices of the Royal Astronomical Society*, 464:1211–1219, Jan. 2017. ISSN 0035-8711. doi: 10.1093/mnras/stw2420. URL `https://ui.adsabs.harvard.edu/abs/2017MNRAS.464.1211H`. ADS Bibcode: 2017MNRAS.464.1211H.

L. Homer, P. A. Charles, and D. O'Donoghue. Evidence for a 2-h optical modulation in GS 1826-24. *Monthly Notices of the Royal Astronomical Society*, 298:497–501, Aug. 1998. ISSN 0035-8711. doi: 10.1046/j.1365-8711.1998.01656.x. URL `https://ui.adsabs.harvard.edu/abs/1998MNRAS.298..497H`. ADS Bibcode: 1998MNRAS.298..497H.

D. Hooper and L. Goodenough. Dark Matter Annihilation in The Galactic Center As Seen by the Fermi Gamma Ray Space Telescope. *Physics Letters B*, 697(5): 412–428, Mar. 2011. ISSN 03702693. doi: 10.1016/j.physletb.2011.02.029. URL `http://arxiv.org/abs/1010.2752`. arXiv: 1010.2752.

D. Hooper and G. Mohlabeng. The Gamma-Ray Luminosity Function of Millisecond Pulsars and Implications for the GeV Excess. *Journal of Cosmology and Astroparticle Physics*, 2016(03):049–049, Mar. 2016. ISSN 1475-7516. doi: 10.1088/1475-7516/2016/03/049. URL `http://arxiv.org/abs/1512.04966`. arXiv:1512.04966 [astro-ph, physics:hep-ph].

R. H. H. Huang et al. X-Ray Studies of the Black Widow Pulsar PSR B1957+20. *The Astrophysical Journal*, 760:92, Nov. 2012. ISSN 0004-637X. doi: 10.1088/0004-637X/760/1/92. URL `https://ui.adsabs.harvard.edu/abs/2012ApJ...760...92H`. ADS Bibcode: 2012ApJ...760...92H.

H. E. Huckle et al. Discovery of two periodic X-ray pulsators. *Monthly Notices of the Royal Astronomical Society*, 180(1):21P–26P, Sept. 1977. ISSN 0035-8711. doi: 10.1093/mnras/180.1.21P. URL `https://doi.org/10.1093/mnras/180.1.21P`.

C. Y. Hui and K. L. Li. High Energy Radiation from Spider Pulsars. *Galaxies*, 7:93, Dec. 2019. doi: 10.3390/galaxies7040093. URL https://ui.adsabs.harvard.edu/abs/2019Galax...7...93H. ADS Bibcode: 2019Galax...7...93H.

F. Hulleman, J. J. M. in 't Zand, and J. Heise. Discovery of the transient X-ray pulsar SAX J2103.5+4545. *Astronomy and Astrophysics, v.337, p.L25-L28 (1998)*, 337:L25, Sept. 1998. ISSN 0004-6361. URL https://ui.adsabs.harvard.edu/abs/1998A%26A...337L..25H/abstract.

R. A. Hulse and J. H. Taylor. Discovery of a pulsar in a binary system. *The Astrophysical Journal*, 195:L51–L53, Jan. 1975. ISSN 0004-637X. doi: 10.1086/181708. URL https://ui.adsabs.harvard.edu/abs/1975ApJ...195L..51H. ADS Bibcode: 1975ApJ...195L..51H.

J. R. Hurley, C. A. Tout, and O. R. Pols. Evolution of binary stars and the effect of tides on binary populations. *Monthly Notices of the Royal Astronomical Society*, 329(4):897–928, Feb. 2002. ISSN 0035-8711. doi: 10.1046/j.1365-8711.2002.05038.x. URL https://doi.org/10.1046/j.1365-8711.2002.05038.x.

S. D. Hyman et al. Faint Radio Emission from the X-ray Transient, XTE J1748-288. *The Astronomer's Telegram*, 14369:1, Feb. 2021. URL https://ui.adsabs.harvard.edu/abs/2021ATel14369....1H. ADS Bibcode: 2021ATel14369....1H.

J. in't Zand et al. Galactic Center Region. *International Astronomical Union Circular*, 6618:1, Apr. 1997. ISSN 0081-0304. URL https://ui.adsabs.harvard.edu/abs/1997IAUC.6618....1I. ADS Bibcode: 1997IAUC.6618....1I.

J. J. M. in't Zand et al. Optical identification of IGR J19140+0951. *Astronomy & Astrophysics*, 448(3):1101–1106, Mar. 2006. ISSN 0004-6361, 1432-0746. doi: 10.1051/0004-6361:20053411. URL https://www.aanda.org/articles/aa/abs/2006/12/aa3411-05/aa3411-05.html. Number: 3 Publisher: EDP Sciences.

J. J. M. in't Zand et al. A probable accretion-powered X-ray pulsar in IGR J00370+6122. *Astronomy and Astrophysics, Volume 469, Issue 3, July III*

2007, pp.1063-1068, 469(3):1063, July 2007. ISSN 0004-6361. doi: 10.1051/0004-6361:20077189. URL https://ui.adsabs.harvard.edu/abs/2007A%26A...469.1063I/abstract.

J. J. M. in't Zand et al. Identification of XMMU J181227.8-181234 = XTE J1812-182 as a neutron star low-mass X-ray binary. *The Astronomer's Telegram*, 10567: 1, July 2017a. URL https://ui.adsabs.harvard.edu/abs/2017ATel10567....1I. ADS Bibcode: 2017ATel10567....1I.

J. J. M. in't Zand et al. Neutron star cooling and the rp process in thermonuclear X-ray bursts. *Astronomy & Astrophysics, Volume 606, id.A130, <NUMPAGES>17</NUMPAGES> pp.*, 606:A130, Oct. 2017b. ISSN 0004-6361. doi: 10.1051/0004-6361/201731281. URL https://ui.adsabs.harvard.edu/abs/2017A%26A...606A.130I/abstract.

G. Israel et al. The Discovery of 13 second X-Ray Pulsations from the Hydrogen-depleted Subdwarf O6 Star Binary HD 49798. *The Astrophysical Journal Letters*, 474:L53, Jan. 2009. doi: 10.1086/310418.

N. Ivanova. Low-mass X-ray binaries in globular clusters: puzzles and solutions. *Memorie della Societa Astronomica Italiana*, 84:123, Jan. 2013. ISSN 0037-8720. URL https://ui.adsabs.harvard.edu/abs/2013MmSAI..84..123I. ADS Bibcode: 2013MmSAI..84..123I.

N. Ivanova et al. Formation and evolution of compact binaries in globular clusters – I. Binaries with white dwarfs. *Monthly Notices of the Royal Astronomical Society*, 372(3):1043–1059, Nov. 2006. ISSN 0035-8711. doi: 10.1111/j.1365-2966.2006.10876.x. URL https://doi.org/10.1111/j.1365-2966.2006.10876.x.

G. K. Jaisawal et al. NICER and NuSTAR observations of the Be/X-ray binary pulsar 1A 0535+262 during the 2020 November giant outburst. *The Astronomer's Telegram*, 14179:1, Nov. 2020. URL https://ui.adsabs.harvard.edu/abs/2020ATel14179....1J/abstract.

J. H. Jeans. The Stability of a Spherical Nebula. *Philosophical Transactions of the Royal Society of London Series A*, 199:1–53, Jan. 1902. ISSN 1364-503X0080-46140962-8436. doi: 10.1098/rsta.1902.0012. URL https://ui.adsabs.harvard.edu/abs/1902RSPTA.199....1J. ADS Bibcode: 1902RSPTA.199....1J.

R. M. Jeffrey et al. Fast launch speeds in radio flares, from a new determination of the intrinsic motions of SS 433's jet bolides. *Monthly Notices of the Royal Astronomical Society*, 461(1):312–320, Sept. 2016. ISSN 0035-8711, 1365-2966. doi: 10.1093/mnras/stw1322. URL http://arxiv.org/abs/1606.01240. arXiv:1606.01240 [astro-ph].

J. Jiang et al. A NuSTAR view of GRS 1716-249 in the hard and intermediate states. *Monthly Notices of the Royal Astronomical Society*, 492: 1947–1956, Feb. 2020. ISSN 0035-8711. doi: 10.1093/mnras/staa017. URL https://ui.adsabs.harvard.edu/abs/2020MNRAS.492.1947J. ADS Bibcode: 2020MNRAS.492.1947J.

W. N. Johnson et al. Initial results from OSSE on the Compton Observatory. *Astronomy and Astrophysics, Suppl. Ser., Vol. 97, p. 21-25 (1993)*, 97:21, Jan. 1993a. ISSN 0365-0138. URL https://ui.adsabs.harvard.edu/abs/1993A%26AS...97...21J/abstract.

W. N. Johnson et al. The Oriented Scintillation Spectrometer Experiment: Instrument Description. *The Astrophysical Journal Supplement Series*, 86:693, June 1993b. ISSN 0067-0049. doi: 10.1086/191795. URL https://ui.adsabs.harvard.edu/abs/1993ApJS...86..693J. ADS Bibcode: 1993ApJS...86..693J.

H. M. Johnston, R. Soria, and J. Gibson. The nature of the companion star in Circinus X-1. *Monthly Notices of the Royal Astronomical Society*, 456(1):347–355, Feb. 2016. ISSN 0035-8711. doi: 10.1093/mnras/stv2669. URL https://doi.org/10.1093/mnras/stv2669.

F. C. Jones. Inverse Compton Scattering of Cosmic-Ray Electrons. *Physical Review*, 137(5B):B1306–B1311, Mar. 1965. doi: 10.1103/PhysRev.137.B1306. URL https://link.aps.org/doi/10.1103/PhysRev.137.B1306. Publisher: American Physical Society.

F. C. Jones. Calculated Spectrum of Inverse-Compton-Scattered Photons. *Physical Review*, 167(5):1159–1169, Mar. 1968. doi: 10.1103/PhysRev.167.1159. URL https://link.aps.org/doi/10.1103/PhysRev.167.1159. Publisher: American Physical Society.

P. G. Jonker and M. van der Klis. Discovery of an X-Ray Pulsar in the Low-Mass X-Ray Binary 2A 1822-371. *The Astrophysical Journal*, 553:L43–L46, May 2001. ISSN 0004-637X. doi: 10.1086/320510. URL https://ui.adsabs.harvard.edu/abs/2001ApJ...553L..43J. ADS Bibcode: 2001ApJ...553L..43J.

P. G. Jonker, G. Nelemans, and C. G. Bassa. Detection of the radial velocity curve of the B5-A0 supergiant companion star of Cir X-1? *Monthly Notices of the Royal Astronomical Society*, 374:999–1005, Jan. 2007. ISSN 0035-8711. doi: 10.1111/j.1365-2966.2006.11210.x. URL https://ui.adsabs.harvard.edu/abs/2007MNRAS.374..999J. ADS Bibcode: 2007MNRAS.374..999J.

A. M. Juett and D. Chakrabarty. X-Ray Spectroscopy of Candidate Ultracompact X-Ray Binaries. *The Astrophysical Journal*, 627:926–932, July 2005. ISSN 0004-637X. doi: 10.1086/430633. URL https://ui.adsabs.harvard.edu/abs/2005ApJ...627..926J. ADS Bibcode: 2005ApJ...627..926J.

P. Kaaret, H. Feng, and T. P. Roberts. Ultraluminous X-Ray Sources. *Annual Review of Astronomy and Astrophysics*, 55(1):303–341, Aug. 2017. ISSN 0066-4146. doi: 10.1146/annurev-astro-091916-055259. URL https://ui.adsabs.harvard.edu/abs/2017ARA&A..55..303K/abstract.

M. Kafatos, M. M. Shapiro, and R. Silberberg. Extragalactic Variable Sources and Cosmic-Ray Acceleration Near Massive Black Holes. *Comments on Astrophysics*,

9:179, Jan. 1981. ISSN 0146-2970. URL https://ui.adsabs.harvard.edu/abs/1981ComAp...9..179K. ADS Bibcode: 1981ComAp...9..179K.

L. J. Kaluzienski et al. Evidence for a 16.6 day period from Circinus X-1. *The Astrophysical Journal*, 208:L71–L75, Sept. 1976. ISSN 0004-637X. doi: 10.1086/182235. URL https://ui.adsabs.harvard.edu/abs/1976ApJ...208L..71K. ADS Bibcode: 1976ApJ...208L..71K.

Y. Kaneko et al. The Complete Spectral Catalog of Bright BATSE Gamma-Ray Bursts. *The Astrophysical Journal Supplement Series*, 166:298–340, Sept. 2006. ISSN 0067-0049. doi: 10.1086/505911. URL https://ui.adsabs.harvard.edu/abs/2006ApJS..166..298K. ADS Bibcode: 2006ApJS..166..298K.

D. L. Kaplan et al. Lost and Found: A New Position and Infrared Counterpart for the X-ray Binary Scutum X-1. *The Astrophysical Journal*, 661(1):437–446, May 2007. ISSN 0004-637X, 1538-4357. doi: 10.1086/513712. URL http://arxiv.org/abs/astro-ph/0701092. arXiv: astro-ph/0701092.

E. Kara et al. Gamma-Ray Emission from Two Blazars Behind the Galactic Plane: B2013+370 & B2023+336. *The Astrophysical Journal*, 746(2):159, Feb. 2012. ISSN 0004-637X, 1538-4357. doi: 10.1088/0004-637X/746/2/159. URL http://arxiv.org/abs/1112.3312. arXiv: 1112.3312.

V. M. Kaspi and A. M. Beloborodov. Magnetars. *Annual Review of Astronomy and Astrophysics*, 55(1):261–301, Aug. 2017. ISSN 0066-4146. doi: 10.1146/annurev-astro-081915-023329. URL https://ui.adsabs.harvard.edu/abs/2017ARA&A..55..261K/abstract.

R. Kaur et al. Chandra and XMM-Newton observations of the low-luminosity X-ray pulsators SAX J1324.4-6200 and SAX J1452.8-5949. *Monthly Notices of the Royal Astronomical Society*, 394:1597–1604, Apr. 2009. ISSN 0035-8711. doi: 10.1111/j.1365-2966.2009.14438.x. URL http://adsabs.harvard.edu/abs/2009MNRAS.394.1597K.

R. Kaur et al. Near-infrared/optical identification of five low-luminosity X-ray pulsators. *Monthly Notices of the Royal Astronomical Society*, 402(4):2388–2396, Mar. 2010. ISSN 00358711, 13652966. doi: 10.1111/j.1365-2966.2009.15919.x. URL https://academic.oup.com/mnras/article-lookup/doi/10.1111/j.1365-2966.2009.15919.x.

E. Kellogg et al. X-Ray Sources Near the Galactic Center Observed by UHURU. *The Astrophysical Journal*, 169:L99, Nov. 1971. ISSN 0004-637X. doi: 10.1086/180820. URL https://ui.adsabs.harvard.edu/abs/1971ApJ...169L..99K. ADS Bibcode: 1971ApJ...169L..99K.

R. P. Kerr. Gravitational Field of a Spinning Mass as an Example of Algebraically Special Metrics. *Physical Review Letters*, 11:237–238, Sept. 1963. ISSN 0031-9007. doi: 10.1103/PhysRevLett.11.237. URL https://ui.adsabs.harvard.edu/abs/1963PhRvL..11..237K. ADS Bibcode: 1963PhRvL..11..237K.

P. Kervella, F. Thévenin, and C. Lovis. Proxima's orbit around alpha Centauri. *Astronomy & Astrophysics*, 598:L7, Feb. 2017. ISSN 0004-6361, 1432-0746. doi: 10.1051/0004-6361/201629930. URL https://www.aanda.org/articles/aa/abs/2017/02/aa29930-16/aa29930-16.html. Publisher: EDP Sciences.

U. Keshet et al. Gamma-Rays from Intergalactic Shocks. *The Astrophysical Journal*, 585(1):128–150, Mar. 2003. ISSN 0004-637X, 1538-4357. doi: 10.1086/345946. URL http://arxiv.org/abs/astro-ph/0202318. arXiv:astro-ph/0202318.

D. Khangulyan, F. A. Aharonian, and S. R. Kelner. Simple Analytical Approximations for Treatment of Inverse Compton Scattering of Relativistic Electrons in the Blackbody Radiation Field. *The Astrophysical Journal*, 783:100, Mar. 2014. ISSN 0004-637X. doi: 10.1088/0004-637X/783/2/100. URL https://ui.adsabs.harvard.edu/abs/2014ApJ...783..100K. ADS Bibcode: 2014ApJ...783..100K.

J. Khargharia, C. S. Froning, and E. L. Robinson. Near-infrared spectroscopy of low-mass x-ray binaries: Accretion disk contamination and compact object mass determination in V404 Cyg and Cen X-4. *The Astrophysical Journal*, 716(2): 1105–1117, May 2010. ISSN 0004-637X. doi: 10.1088/0004-637X/716/2/1105. URL https://doi.org/10.1088%2F0004-637x%2F716%2F2%2F1105.

J. Kildea et al. The Whipple Observatory 10m gamma-ray telescope, 1997–2006. *Astroparticle Physics*, 28(2):182–195, Oct. 2007. ISSN 0927-6505. doi: 10.1016/j.astropartphys.2007.05.004. URL https://www.sciencedirect.com/science/article/pii/S0927650507000746.

A. R. King, M. B. Davies, and M. E. Beer. Black widow pulsars: the price of promiscuity. *Monthly Notices of the Royal Astronomical Society*, 345:678–682, Oct. 2003. ISSN 0035-8711. doi: 10.1046/j.1365-8711.2003.06990.x. URL https://ui.adsabs.harvard.edu/abs/2003MNRAS.345..678K. ADS Bibcode: 2003MNRAS.345..678K.

S. Kitamoto et al. GS2023 + 338 - A new class of X-ray transient source? *Nature*, 342:518–520, Nov. 1989. ISSN 0028-0836. doi: 10.1038/342518a0. URL http://adsabs.harvard.edu/abs/1989Natur.342..518K.

B. Kiziltan, H. Baumgardt, and A. Loeb. An intermediate-mass black hole in the centre of the globular cluster 47 Tucanae. *Nature*, 542(7640):203–205, Feb. 2017. ISSN 1476-4687. doi: 10.1038/nature21361. URL https://www.nature.com/articles/nature21361. Number: 7640 Publisher: Nature Publishing Group.

A. N. Kolmogorov. Sulla determinazione empirica di una legge di distribuzione. *Giornale dell'Istituto Italiano degli Attuari.*, 4:83–91, 1933.

A. K. H. Kong et al. Discovery of an Unidentified Fermi Object as a Black Widow-like Millisecond Pulsar. *The Astrophysical Journal*, 747:L3, Mar. 2012. ISSN 0004-637X. doi: 10.1088/2041-8205/747/1/L3. URL https://ui.adsabs.harvard.edu/abs/2012ApJ...747L...3K. ADS Bibcode: 2012ApJ...747L...3K.

C. Korntreff, T. Kaczmarek, and S. Pfalzner. Towards the field binary population: influence of orbital decay on close binaries. *Astronomy & Astrophysics*, 543:A126, July 2012. ISSN 0004-6361, 1432-0746. doi: 10.1051/0004-6361/201118019. URL http://www.aanda.org/10.1051/0004-6361/201118019.

W. Kraushaar, G. W. Clark, G. Garmire, H. Helmken, P. Higbie, and M. Agogino. Explorer XI Experiment on Cosmic Gamma Rays. *The Astrophysical Journal*, 141:845, Apr. 1965.

W. L. Kraushaar and G. W. Clark. Search for Primary Cosmic Gamma Rays with the Satellite Explorer XI. *Physical Review Letters*, 8(3):106–109, Feb. 1962. doi: 10.1103/PhysRevLett.8.106. URL https://link.aps.org/doi/10.1103/PhysRevLett.8.106. Publisher: American Physical Society.

W. L. Kraushaar, G. W. Clark, G. P. Garmire, R. Borken, P. Higbie, V. Leong, and T. Thorsos. High-Energy Cosmic Gamma-Ray Observations from the OSO-3 Satellite. *The Astrophysical Journal*, 177:341, Nov. 1972.

M. I. Krauss et al. XTE J1814-338. *International Astronomical Union Circular*, 8154:3, June 2003. ISSN 0081-0304. URL https://ui.adsabs.harvard.edu/abs/2003IAUC.8154....3K. ADS Bibcode: 2003IAUC.8154....3K.

K. Kremer et al. Fast Optical Transients from Stellar-mass Black Hole Tidal Disruption Events in Young Star Clusters. *The Astrophysical Journal*, 911 (2):104, Apr. 2021. ISSN 0004-637X. doi: 10.3847/1538-4357/abeb14. URL https://doi.org/10.3847/1538-4357/abeb14. Publisher: American Astronomical Society.

H. A. Krimm et al. Transient X-ray pulsar GRO J2058+42 is in outburst. *The Astronomer's Telegram*, 1516:1, May 2008. URL https://ui.adsabs.harvard.edu/abs/2008ATel.1516....1K.

P. Kroupa. On the variation of the initial mass function. *Monthly Notices of the Royal Astronomical Society*, 322:231–246, Apr. 2001. ISSN 0035-8711. doi: 10.

1046/j.1365-8711.2001.04022.x. URL https://ui.adsabs.harvard.edu/abs/2001MNRAS.322..231K. ADS Bibcode: 2001MNRAS.322..231K.

G. P. Kuiper. The Empirical Mass-Luminosity Relation. *The Astrophysical Journal*, 88:472, Nov. 1938. ISSN 0004-637X. doi: 10.1086/143999. URL https://ui.adsabs.harvard.edu/abs/1938ApJ....88..472K. ADS Bibcode: 1938ApJ....88..472K.

T. Kupfer et al. The First Ultracompact Roche Lobe–Filling Hot Subdwarf Binary. *The Astrophysical Journal*, 891(1):45, Mar. 2020. ISSN 0004-637X. doi: 10.3847/1538-4357/ab72ff. URL https://doi.org/10.3847/1538-4357/ab72ff. Publisher: American Astronomical Society.

J. D. Kurfess et al. Overview of the Compton Observatory instruments. In *AIP Conference Proceedings*, pages 509–523, Williamsburg, Virginia (USA), 1997. AIP. doi: 10.1063/1.54011. URL http://aip.scitation.org/doi/abs/10.1063/1.54011.

E. Kuulkers and M. van der Klis. The first radius-expansion X-ray burst from GX 3+1. *Astronomy and Astrophysics, v.356, p.L45-L48 (2000)*, 356:L45, Apr. 2000. ISSN 0004-6361. URL https://ui.adsabs.harvard.edu/abs/2000A%26A...356L..45K/abstract.

M. Kühnel et al. GRO J1008-57: an (almost) predictable transient X-ray binary. *Astronomy & Astrophysics*, 555:A95, July 2013. ISSN 0004-6361, 1432-0746. doi: 10.1051/0004-6361/201321203. URL http://arxiv.org/abs/1305.2936. arXiv: 1305.2936.

V. La Parola et al. Detection of an orbital period in the supergiant high-mass X-ray binary IGR J16465-4507 with Swift-BAT. *Monthly Notices of the Royal Astronomical Society*, 405:L66–L70, June 2010. ISSN 0035-8711. doi: 10.1111/j.1745-3933.2010.00860.x. URL http://adsabs.harvard.edu/abs/2010MNRAS.405L..66L.

E. M. Levesque et al. Discovery of a Thorne–Żytkow object candidate in the Small Magellanic Cloud. *Monthly Notices of the Royal Astronomical Society: Letters*, 443(1):L94–L98, Sept. 2014. ISSN 1745-3925. doi: 10.1093/mnrasl/slu080. URL https://doi.org/10.1093/mnrasl/slu080.

A. Levinson and J. R. Mattox. EGRET Upper Limits on the High-Energy Gamma-Ray Emission of X-Ray Novae. *The Astrophysical Journal*, 462:L67, May 1996. ISSN 0004-637X. doi: 10.1086/310040. URL https://ui.adsabs.harvard.edu/abs/1996ApJ...462L..67L. ADS Bibcode: 1996ApJ...462L..67L.

W. H. G. Lewin, J. Van Paradijs, and R. E. Taam. X-ray bursts. *Space Science Reviews*, 62(3):223–389, Sept. 1993. ISSN 1572-9672. doi: 10.1007/BF00196124. URL https://doi.org/10.1007/BF00196124.

W. H. G. Lewin et al. Discovery of X-ray bursts from several sources near the galactic centre. *Monthly Notices of the Royal Astronomical Society*, 177: 83P–92, Dec. 1976. ISSN 0035-8711. doi: 10.1093/mnras/177.1.83P. URL https://ui.adsabs.harvard.edu/abs/1976MNRAS.177P..83L. ADS Bibcode: 1976MNRAS.177P..83L.

J. Li et al. Gamma-ray heartbeat powered by the microquasar SS 433. *Nature Astronomy*, pages 1–8, Aug. 2020. ISSN 2397-3366. doi: 10.1038/s41550-020-1164-6. URL https://www.nature.com/articles/s41550-020-1164-6. Publisher: Nature Publishing Group.

K. L. Li et al. The X-Ray Modulation of PSR J2032+4127/MT91 213 during the Periastron Passage in 2017. *The Astrophysical Journal*, 857:123, Apr. 2018. ISSN 0004-637X. doi: 10.3847/1538-4357/aab848. URL https://ui.adsabs.harvard.edu/abs/2018ApJ...857..123L. ADS Bibcode: 2018ApJ...857..123L.

K.-L. Li et al. Revealing a New Black Widow Binary 4FGL J0336.0+7502. *The Astrophysical Journal*, 911:92, Apr. 2021. ISSN 0004-637X. doi: 10.3847/

1538-4357/abeb76. URL https://ui.adsabs.harvard.edu/abs/2021ApJ...911...92L. ADS Bibcode: 2021ApJ...911...92L.

X.-D. Li. The Nature of the Compact X-Ray Source in Supernova Remnant RCW 103. *The Astrophysical Journal*, 666(2):L81, Aug. 2007. ISSN 0004-637X. doi: 10.1086/521791. URL https://iopscience.iop.org/article/10.1086/521791/meta. Publisher: IOP Publishing.

X.-D. Li. The youngest X-ray binaries. *Research in Astronomy and Astrophysics*, 20(10):162, Oct. 2020. ISSN 1674-4527. doi: 10.1088/1674-4527/20/10/162. URL https://doi.org/10.1088/1674-4527/20/10/162. Publisher: IOP Publishing.

Q. Z. Liu, J. van Paradijs, and E. P. J. van den Heuvel. High-mass X-ray binaries in the Magellanic Clouds. *Astronomy & Astrophysics*, 442(3):1135–1138, Nov. 2005. ISSN 0004-6361, 1432-0746. doi: 10.1051/0004-6361:20053718. URL http://www.aanda.org/10.1051/0004-6361:20053718.

Q. Z. Liu, J. van Paradijs, and E. P. J. van den Heuvel. Catalogue of high-mass X-ray binaries in the Galaxy (4th edition). *Astronomy and Astrophysics*, 455:1165–1168, Sept. 2006. ISSN 0004-6361. doi: 10.1051/0004-6361:20064987. URL http://adsabs.harvard.edu/abs/2006A%26A...455.1165L.

Q. Z. Liu, J. van Paradijs, and E. P. J. van den Heuvel. A catalogue of low-mass X-ray binaries in the Galaxy, LMC, and SMC (Fourth edition). *Astronomy and Astrophysics*, 469:807–810, July 2007. ISSN 0004-6361. doi: 10.1051/0004-6361:20077303. URL http://adsabs.harvard.edu/abs/2007A%26A...469..807L.

S. J. Lloyd, P. M. Chadwick, and A. M. Brown. Gamma-ray emission from high Galactic latitude globular clusters. *Monthly Notices of the Royal Astronomical Society*, 480:4782–4796, Nov. 2018. ISSN 0035-8711. doi: 10.1093/mnras/sty2150. URL https://ui.adsabs.harvard.edu/abs/2018MNRAS.480.4782L. ADS Bibcode: 2018MNRAS.480.4782L.

A. Loh et al. High-energy gamma-ray observations of the accreting black hole V404 Cygni during its June 2015 outburst. *Monthly Notices of the Royal Astronomical Society: Letters*, 462(1):L111–L115, Oct. 2016. ISSN 1745-3925, 1745-3933. doi: 10.1093/mnrasl/slw142. URL http://arxiv.org/abs/1607.06239. arXiv: 1607.06239.

D. R. Lorimer. Binary and Millisecond Pulsars. *Living Reviews in Relativity*, 11(1):8, Nov. 2008. ISSN 1433-8351. doi: 10.12942/lrr-2008-8. URL https://doi.org/10.12942/lrr-2008-8.

N. Lund et al. Jem-X the X-Ray Monitor on Integral. *Astrophysical Letters and Communications*, 39:339, 1999. ISSN 0888-6512. URL https://ui.adsabs.harvard.edu/abs/1999ApL&C..39..339L/abstract.

M. Lundy. TeV and optical observations of the Be/pulsar binary 1A0535+262 during the 2020 giant outburst. *Proceedings of 37th International Cosmic Ray Conference — PoS(ICRC2021)*, page 856, July 2021. doi: 10.22323/1.395.0856. URL http://arxiv.org/abs/2108.09350. arXiv: 2108.09350.

A. Lutovinov et al. NTEGRAL discovered a new transient source IGRJ16465-4507. *The Astronomer's Telegram*, 329, Sept. 2004. URL http://adsabs.harvard.edu/abs/2004ATel..329....1L.

A. Lutovinov et al. Discovery of X-ray pulsations from IGR J16320-4751 = AX J1631.9-4752. *Astronomy and Astrophysics*, 433:L41–L44, Apr. 2005. ISSN 0004-6361. doi: 10.1051/0004-6361:200500092. URL http://adsabs.harvard.edu/abs/2005A%26A...433L..41L.

A. A. Lutovinov et al. X-ray bursts from the source A1742-294 in the Galactic-center region. *Astronomy Letters*, 27(8):501–506, Aug. 2001. ISSN 1562-6873. doi: 10.1134/1.1388917. URL https://doi.org/10.1134/1.1388917.

A. G. Lyne et al. Discovery of a binary millisecond pulsar in the globular cluster M4. *Nature*, 332(6159):45–47, Mar. 1988. ISSN 1476-4687. doi: 10.1038/332045a0.

URL https://www.nature.com/articles/332045a0. Bandiera_abtest: a Cg_type: Nature Research Journals Number: 6159 Primary_atype: Research Publisher: Nature Publishing Group.

M. Lyutikov. Inverse Compton model of pulsar high-energy emission. *Monthly Notices of the Royal Astronomical Society*, 431(3):2580–2589, May 2013. ISSN 0035-8711. doi: 10.1093/mnras/stt351. URL https://doi.org/10.1093/mnras/stt351.

F. Makino. GS 1826-24. *International Astronomical Union Circular*, 4653:2, Sept. 1988. ISSN 0081-0304. URL https://ui.adsabs.harvard.edu/abs/1988IAUC.4653....2M. ADS Bibcode: 1988IAUC.4653....2M.

F. Makino. GS 2023+338. *International Astronomical Union Circular*, 4782:1, May 1989. ISSN 0081-0304. URL http://adsabs.harvard.edu/abs/1989IAUC.4782....1M.

F. Makino et al. Scutum X-1. *International Astronomical Union Circular*, 4679:2, Nov. 1988. ISSN 0081-0304. URL http://adsabs.harvard.edu/abs/1988IAUC.4679....2M.

D. Malyshev et al. Leptonic origin of the 100 MeV gamma-ray emission from the Galactic centre. *Astronomy & Astrophysics*, 582:A11, Oct. 2015. ISSN 0004-6361, 1432-0746. doi: 10.1051/0004-6361/201526120. URL https://www.aanda.org/articles/aa/abs/2015/10/aa26120-15/aa26120-15.html. Publisher: EDP Sciences.

R. N. Manchester et al. The Australia Telescope National Facility Pulsar Catalogue. *The Astronomical Journal*, 129:1993–2006, Apr. 2005. ISSN 0004-6256. doi: 10.1086/428488. URL https://ui.adsabs.harvard.edu/abs/2005AJ....129.1993M. ADS Bibcode: 2005AJ....129.1993M.

H. B. Mann and D. R. Whitney. On a Test of Whether one of Two Random Variables is Stochastically Larger than the Other. *Annals of Mathem-*

atical Statistics, 18(1):50–60, Mar. 1947. ISSN 0003-4851, 2168-8990. doi: 10.1214/aoms/1177730491. URL https://projecteuclid.org/euclid.aoms/1177730491. Publisher: Institute of Mathematical Statistics.

D. Maoz, F. Mannucci, and G. Nelemans. Observational Clues to the Progenitors of Type Ia Supernovae. *Annual Review of Astronomy and Astrophysics*, 52(1):107–170, 2014. doi: 10.1146/annurev-astro-082812-141031. URL https://doi.org/10.1146/annurev-astro-082812-141031. _eprint: https://doi.org/10.1146/annurev-astro-082812-141031.

B. Margon et al. Evidence for a Highly Compact X-Ray Source. *The Astrophysical Journal*, 169:L45, Oct. 1971a. ISSN 0004-637X. doi: 10.1086/180811. URL https://ui.adsabs.harvard.edu/abs/1971ApJ...169L..45M. ADS Bibcode: 1971ApJ...169L..45M.

B. Margon et al. A Pulsing X-Ray Source in Circinus. *The Astrophysical Journal*, 169:L23, Oct. 1971b. ISSN 0004-637X. doi: 10.1086/180806. URL https://ui.adsabs.harvard.edu/abs/1971ApJ...169L..23M. ADS Bibcode: 1971ApJ...169L..23M.

C. B. Markwardt and J. H. Swank. XTE J1814-338. *International Astronomical Union Circular*, 8144:1, June 2003. ISSN 0081-0304. URL https://ui.adsabs.harvard.edu/abs/2003IAUC.8144....1M. ADS Bibcode: 2003IAUC.8144....1M.

C. B. Markwardt, T. E. Strohmayer, and J. H. Swank. Revised Orbit and Burst Oscillations from the Millisecond Pulsar XTE J1814-338. *The Astronomer's Telegram*, 164:1, June 2003. URL https://ui.adsabs.harvard.edu/abs/2003ATel..164....1M. ADS Bibcode: 2003ATel..164....1M.

C. B. Markwardt, D. Pereira, and J. H. Swank. RXTE Detects a Transient, XTE J1812-182 (= XMMU J181227.8-181234 ?). *The Astronomer's Telegram*, 1685:

1, Aug. 2008. URL https://ui.adsabs.harvard.edu/abs/2008ATel.1685...
.1M. ADS Bibcode: 2008ATel.1685....1M.

P. Martin et al. Gamma-ray emission from internal shocks in novae. *Astronomy & Astrophysics*, 612:A38, Apr. 2018. ISSN 0004-6361, 1432-0746. doi: 10.1051/0004-6361/201731692. URL https://www.aanda.org/articles/aa/abs/2018/04/aa31692-17/aa31692-17.html. Publisher: EDP Sciences.

G. Martí-Devesa and O. Reimer. X-ray and gamma-ray orbital variability from the gamma-ray binary HESS J1832-093. *Astronomy & Astrophysics*, 637:A23, May 2020. ISSN 0004-6361, 1432-0746. doi: 10.1051/0004-6361/202037442. URL https://www.aanda.org/articles/aa/abs/2020/05/aa37442-20/aa37442-20.html. Publisher: EDP Sciences.

G. Martí-Devesa et al. Hints of gamma-ray orbital variability from gamma-Velorum. *Astronomy & Astrophysics*, 635:A141, Mar. 2020. ISSN 0004-6361, 1432-0746. doi: 10.1051/0004-6361/202037462. URL http://arxiv.org/abs/2001.02708. arXiv: 2001.02708.

K. O. Mason and F. A. Cordova. Infrared photometry of the X-ray binary 2A 1822-371 - A model for the ultraviolet, optical, and infrared light curve. *The Astrophysical Journal*, 262:253, Nov. 1982. ISSN 0004-637X, 1538-4357. doi: 10.1086/160416. URL http://adsabs.harvard.edu/doi/10.1086/160416.

E. Matsuba et al. Discovery of X-Ray Bursts from GX 13+1 (4U 1811-17). *Publications of the Astronomical Society of Japan*, 47:575–580, Oct. 1995. ISSN 0004-6264. URL https://ui.adsabs.harvard.edu/abs/1995PASJ...47..575M. ADS Bibcode: 1995PASJ...47..575M.

J. R. Mattox et al. The Likelihood Analysis of EGRET Data. *The Astrophysical Journal*, 461:396, Apr. 1996. doi: 10.1086/177068. URL https://ui.adsabs.harvard.edu/abs/1996ApJ...461..396M/abstract.

J. E. McClintock et al. The Spin of the Near-Extreme Kerr Black Hole GRS 1915+105. *The Astrophysical Journal*, 652:518–539, Nov. 2006. ISSN 0004-637X. doi: 10.1086/508457. URL https://ui.adsabs.harvard.edu/abs/2006ApJ...652..518M. ADS Bibcode: 2006ApJ...652..518M.

J. McEnery et al. All-sky Medium Energy Gamma-ray Observatory: Exploring the Extreme Multimessenger Universe. *arXiv:1907.07558 [astro-ph]*, Nov. 2019. URL http://arxiv.org/abs/1907.07558. arXiv: 1907.07558.

C. Meegan et al. The Fermi Gamma-Ray Burst Monitor. *The Astrophysical Journal*, 702:791, 2009.

S. Mereghetti, P. Romano, and L. Sidoli. Swift observations of the X-ray pulsar SAX J1324–6200. *Astronomy & Astrophysics*, 483(1):249–251, May 2008. ISSN 0004-6361, 1432-0746. doi: 10.1051/0004-6361:200809397. URL https://www.aanda.org/articles/aa/abs/2008/19/aa09397-08/aa09397-08.html. Number: 1 Publisher: EDP Sciences.

M. Meyer, J. D. Scargle, and R. D. Blandford. Characterizing the Gamma-Ray Variability of the Brightest Flat Spectrum Radio Quasars Observed with the Fermi LAT. *The Astrophysical Journal*, 877(1):39, May 2019. ISSN 0004-637X. doi: 10.3847/1538-4357/ab1651. URL https://doi.org/10.3847%2F1538-4357%2Fab1651. Publisher: American Astronomical Society.

J. Middleditch and J. Nelson. Studies of optical pulsations from HZ Herculis/Hercules X-1: a determination of the mass of the neutron star. *The Astrophysical Journal*, 208:567–586, Sept. 1976. ISSN 0004-637X. doi: 10.1086/154638. URL https://ui.adsabs.harvard.edu/abs/1976ApJ...208..567M. ADS Bibcode: 1976ApJ...208..567M.

M. Middleton, J. Miller-Jones, and R. Fender. The low or retrograde spin of the first extragalactic microquasar: implications for Blandford-Znajek powering of jets. *Monthly Notices of the Royal Astronomical Society*, 439(2):1740–1748, Apr.

2014. ISSN 0035-8711, 1365-2966. doi: 10.1093/mnras/stu056. URL http://arxiv.org/abs/1401.1829. arXiv:1401.1829 [astro-ph].

M. Middleton et al. Black hole spin in GRS 1915+105. *Monthly Notices of the Royal Astronomical Society*, 373:1004–1012, Dec. 2006. ISSN 0035-8711. doi: 10.1111/j.1365-2966.2006.11077.x. URL https://ui.adsabs.harvard.edu/abs/2006MNRAS.373.1004M. ADS Bibcode: 2006MNRAS.373.1004M.

S. Migliari et al. Discovery of type I X-ray bursts from the low-mass X-ray binary 4U 1708 – 40. *Monthly Notices of the Royal Astronomical Society*, 342(3):909–914, July 2003. ISSN 0035-8711. doi: 10.1046/j.1365-8711.2003.06597.x. URL https://doi.org/10.1046/j.1365-8711.2003.06597.x.

I. F. Mirabel. Gamma-ray binaries. In J. M. Paredes, O. Reimer, and D. F. Torres, editors, *The Multi-Messenger Approach to High-Energy Gamma-Ray Sources*, pages 267–270, Dordrecht, 2007. Springer Netherlands. ISBN 978-1-4020-6118-9. doi: 10.1007/978-1-4020-6118-9_41.

I. F. Mirabel and L. F. Rodriguez. A superluminal source in the Galaxy. *Nature*, 371(6492):46–48, Sept. 1994. ISSN 1476-4687. doi: 10.1038/371046a0. URL https://www.nature.com/articles/371046a0. Number: 6492 Publisher: Nature Publishing Group.

A. F. J. Moffat. Colliding Winds in Binaries: Observations. *Astrophysics and Space Science, v. 260, Issue 1/2, p. 225-242 (1998).*, 260:225, Oct. 1998. ISSN 0004-640X. doi: 10.1023/A:1001853205215. URL https://ui.adsabs.harvard.edu/abs/1998Ap%26SS.260..225M/abstract.

P. J. Morris et al. Gamma-ray Novae: Rare or Nearby? *Monthly Notices of the Royal Astronomical Society*, 465(1):1218–1226, Feb. 2017. ISSN 0035-8711, 1365-2966. doi: 10.1093/mnras/stw2776. URL http://arxiv.org/abs/1610.09941. arXiv: 1610.09941.

P. Morrison. On gamma-ray astronomy. *Il Nuovo Cimento (1955-1965)*, 7(6): 858–865, Mar. 1958. ISSN 1827-6121. doi: 10.1007/BF02745590. URL https://doi.org/10.1007/BF02745590.

S. E. Motta et al. Swift observations of V404 Cyg during the 2015 outburst: X-ray outflows from super-Eddington accretion. *Monthly Notices of the Royal Astronomical Society*, 471(2):1797–1818, Oct. 2017. ISSN 0035-8711, 1365-2966. doi: 10.1093/mnras/stx1699. URL http://arxiv.org/abs/1707.01076. arXiv: 1707.01076.

K. Mukerjee, H. M. Antia, and T. Katoch. AstroSat observations of GRO J2058+42 during the 2019 outburst. *The Astrophysical Journal*, 897(1):73, July 2020. ISSN 1538-4357. doi: 10.3847/1538-4357/ab97b6. URL http://arxiv.org/abs/2005.14044. arXiv: 2005.14044.

J. M. Muller et al. 1SAX J1603.9-7753. *IAU Circulars*, 6842:2, Mar. 1998.

T. Murakami et al. Discovery of two new X-ray burst sources XB 1812-12 in Serpens and XB1940-04 in Aquila. *Publications of the Astronomical Society of Japan*, 35: 531–537, Jan. 1983. ISSN 0004-6264. URL https://ui.adsabs.harvard.edu/abs/1983PASJ...35..531M. ADS Bibcode: 1983PASJ...35..531M.

A. Mücke et al. Photohadronic Processes in Astrophysical Environments. *Publications of the Astronomical Society of Australia*, 16(2):160–166, 1999. ISSN 1323-3580, 1448-6083. doi: 10.1071/AS99160. URL https://www.cambridge.org/core/product/identifier/S1323358000005853/type/journal_article.

M. Nakajima et al. MAXI/GSC observation of the onset of a giant outburst from Be/X-ray binary pulsar GRO J1008-57. *The Astronomer's Telegram*, 3750, May 2020a. URL http://adsabs.harvard.edu/abs/2020ATel13750....1N.

M. Nakajima et al. MAXI/GSC observation of flaring activity from Be/X-ray binary pulsar GRO J1008-57. *The Astronomer's Telegram*, 3544, Mar. 2020b. URL http://adsabs.harvard.edu/abs/2020ATel13544....1N.

L. Natalucci et al. A New Bursting X-Ray Transient: SAX J1750.8-2900. *The Astrophysical Journal*, 523:L45–L49, Sept. 1999. ISSN 0004-637X. doi: 10.1086/312263. URL https://ui.adsabs.harvard.edu/abs/1999ApJ...523L..45N. ADS Bibcode: 1999ApJ...523L..45N.

H. Negoro et al. MAXI/GSC detection of a new outburst from GRS 1716-249/GRO J1719-24 or a new X-ray transient MAXI J1719-254. *The Astronomer's Telegram*, 9876:1, Dec. 2016. URL https://ui.adsabs.harvard.edu/abs/2016ATel.9876....1N. ADS Bibcode: 2016ATel.9876....1N.

I. Negueruela and P. Reig. Bd +60 73 = Igr J00370+6122. *The Astronomer's Telegram*, 285:1, May 2004. URL https://ui.adsabs.harvard.edu/abs/2004ATel..285....1N.

I. Negueruela and M. P. E. Schurch. A search for counterparts to massive X-ray binaries using photometric catalogues. *Astronomy and Astrophysics*, 461: 631–639, Jan. 2007. ISSN 0004-6361. doi: 10.1051/0004-6361:20066054. URL http://adsabs.harvard.edu/abs/2007A%26A...461..631N.

E. Nespoli, J. Fabregat, and R. E. Mennickent. K-band spectroscopy of IGR J16358-4726 and IGR J16393-4643: two new symbiotic X-ray binaries. *Astronomy & Astrophysics*, 516:A94, June 2010. ISSN 0004-6361, 1432-0746. doi: 10.1051/0004-6361/200913410. URL https://www.aanda.org/articles/aa/abs/2010/08/aa13410-09/aa13410-09.html. Publisher: EDP Sciences.

J. Neyman and E. S. Pearson. IX. On the problem of the most efficient tests of statistical hypotheses. *Philosophical Transactions of the Royal Society of London. Series A, Containing Papers of a Mathematical or Physical Character*, 231(694-706):289–337, Feb. 1933. doi: 10.1098/rsta.1933.0009. URL https://royalsocietypublishing.org/doi/10.1098/rsta.1933.0009. Publisher: Royal Society.

P. L. Nolan et al. EGRET Observations of High-Energy Gamma Rays from Geminga. 181:112.03, Dec. 1992a. URL https://ui.adsabs.harvard.edu/abs/1992AAS...18111203N. Conference Name: American Astronomical Society Meeting Abstracts ADS Bibcode: 1992AAS...18111203N.

P. L. Nolan et al. Performance of the EGRET astronomical gamma ray telescope. *IEEE Transactions on Nuclear Science*, 39:993–996, Aug. 1992b. ISSN 0018-9499. doi: 10.1109/23.159747. URL https://ui.adsabs.harvard.edu/abs/1992ITNS...39..993N. ADS Bibcode: 1992ITNS...39..993N.

S. R. Oates et al. Swift UVOT observations of the 2015 outburst of V404 Cygni. *Monthly Notices of the Royal Astronomical Society*, 488(4):4843–4857, Oct. 2019. ISSN 0035-8711, 1365-2966. doi: 10.1093/mnras/stz1998. URL http://arxiv.org/abs/1809.03237. arXiv: 1809.03237.

T. Okuda. Super-Eddington Black-Hole Models for SS 433. *Publications of the Astronomical Society of Japan*, 54(2):253–266, Apr. 2002. ISSN 0004-6264, 2053-051X. doi: 10.1093/pasj/54.2.253. URL https://academic.oup.com/pasj/article-lookup/doi/10.1093/pasj/54.2.253.

H. Olsen. Opening Angles of Electron-Positron Pairs. *Physical Review*, 131(1):406–415, July 1963. doi: 10.1103/PhysRev.131.406. URL https://link.aps.org/doi/10.1103/PhysRev.131.406. Publisher: American Physical Society.

M. Orellana et al. Leptonic secondary emission in a hadronic microquasar model. *Astronomy and Astrophysics*, 476:9–15, Dec. 2007. ISSN 0004-6361. doi: 10.1051/0004-6361:20078495. URL http://adsabs.harvard.edu/abs/2007A%26A...476....9O.

K. J. Orford. Analytical treatment of oversampling. *Experimental Astronomy*, 1(5):305–310, Sept. 1990. ISSN 1572-9508. doi: 10.1007/BF00454327. URL https://doi.org/10.1007/BF00454327.

D. Ostlie and B. Carroll. *An Introduction to Modern Stellar Astrophysics*. Pearson Addison-Wesley, 2007. ISBN 978-0-8053-0348-3. URL https://books.google.co.uk/books?id=BNpFAQAAIAAJ.

B. Paczyński. Evolutionary Processes in Close Binary Systems. *Annual Review of Astronomy and Astrophysics*, 9:183, 1971. ISSN 0066-4146. doi: 10.1146/annurev.aa.09.090171.001151. URL https://ui.adsabs.harvard.edu/abs/1971ARA&A...9..183P/abstract.

A. Papitto and D. de Martino. Transitional millisecond pulsars (preprint book chapter). Technical Report arXiv:2010.09060, arXiv, Oct. 2020. URL http://arxiv.org/abs/2010.09060. arXiv:2010.09060 [astro-ph] type: chapter.

A. N. Parmar et al. The Discovery of 2.93 Hour Periodic Intensity Dips from X1323-619. *The Astrophysical Journal*, 338:1024, Mar. 1989. ISSN 0004-637X. doi: 10.1086/167255. URL https://ui.adsabs.harvard.edu/abs/1989ApJ...338.1024P. ADS Bibcode: 1989ApJ...338.1024P.

R. Parsons et al. Sgr A* Observations with H.E.S.S. II. In *Proceedings of Science*, volume 34, page 830, The Hague, Netherlands, July 2015. URL https://ui.adsabs.harvard.edu/abs/2015ICRC...34..830P. Conference Name: 34th International Cosmic Ray Conference (ICRC2015) Place: eprint: arXiv:1509.03425 ADS Bibcode: 2015ICRC...34..830P.

A. Patruno et al. The ultraluminous X-ray source in M82: an intermediate-mass black hole with a giant companion. *Monthly Notices of the Royal Astronomical Society: Letters*, 370(1):L6–L9, July 2006. ISSN 1745-3925. doi: 10.1111/j.1745-3933.2006.00176.x. URL https://doi.org/10.1111/j.1745-3933.2006.00176.x.

A. W. A. Pauldrach, D. Vanbeveren, and T. L. Hoffmann. Radiation-driven winds of hot luminous stars XVI. Expanding atmospheres of massive and very massive stars and the evolution of dense stellar clusters. *Astronomy & As-*

trophysics, 538:A75, Feb. 2012. ISSN 0004-6361, 1432-0746. doi: 10.1051/0004-6361/201117621. URL https://www.aanda.org/articles/aa/abs/2012/02/aa17621-11/aa17621-11.html. Publisher: EDP Sciences.

M. N. Pavlinsky, S. A. Grebenev, and R. A. Sunyaev. X-Ray Images of the Galactic Center Obtained with Art-P/Granat: Discovery of New Sources, Variability of Persistent Sources, and Localization of X-Ray Bursters. *The Astrophysical Journal*, 425:110, Apr. 1994. ISSN 0004-637X. doi: 10.1086/173967. URL https://ui.adsabs.harvard.edu/abs/1994ApJ...425..110P. ADS Bibcode: 1994ApJ...425..110P.

Q.-h. Peng and H. Tong. The physics of strong magnetic fields in neutron stars. *Monthly Notices of the Royal Astronomical Society*, 378(1):159–162, June 2007. ISSN 0035-8711. doi: 10.1111/j.1365-2966.2007.11772.x. URL https://doi.org/10.1111/j.1365-2966.2007.11772.x.

W. Penninx et al. Quasi-periodic oscillations in the Z source GX 340+0. *Monthly Notices of the Royal Astronomical Society*, 249:113, Mar. 1991. ISSN 0035-8711. doi: 10.1093/mnras/249.1.113. URL https://ui.adsabs.harvard.edu/abs/1991MNRAS.249..113P. ADS Bibcode: 1991MNRAS.249..113P.

R. Penrose and R. M. Floyd. Extraction of Rotational Energy from a Black Hole. *Nature Physical Science*, 229(6):177–179, Feb. 1971. ISSN 2058-1106. doi: 10.1038/physci229177a0. URL https://www.nature.com/articles/physci229177a0. Number: 6 Publisher: Nature Publishing Group.

L. E. Peterson and A. S. Jacobson. The Spectrum of Scorpius XR-1 to 50 KEV. *The Astrophysical Journal*, 145:962, Sept. 1966. ISSN 0004-637X. doi: 10.1086/148848. URL https://ui.adsabs.harvard.edu/abs/1966ApJ...145..962P. ADS Bibcode: 1966ApJ...145..962P.

R. Petre and N. Gehrels. GRO J1008-57. *International Astronomical Union Cir-*

cular, 5877:3, Oct. 1993. ISSN 0081-0304. URL http://adsabs.harvard.edu/abs/1993IAUC.5877....3P.

G. Piano et al. High-energy Gamma-Ray Activity from V404 Cygni Detected by AGILE during the 2015 June Outburst. *The Astrophysical Journal*, 839: 84, Apr. 2017. ISSN 0004-637X. doi: 10.3847/1538-4357/aa6796. URL http://adsabs.harvard.edu/abs/2017ApJ...839...84P.

G. Pietrzyński et al. An eclipsing-binary distance to the Large Magellanic Cloud accurate to two per cent. *Nature*, 495(7439):76–79, Mar. 2013. ISSN 1476-4687. doi: 10.1038/nature11878. URL https://www.nature.com/articles/nature11878. Number: 7439 Publisher: Nature Publishing Group.

J. M. Pittard and I. R. Stevens. Theoretical X-ray properties of colliding stellar winds in O+O star binaries. *Monthly Notices of the Royal Astronomical Society*, 292:298–316, Dec. 1997. ISSN 0035-8711. doi: 10.1093/mnras/292.2.298. URL https://ui.adsabs.harvard.edu/abs/1997MNRAS.292..298P. ADS Bibcode: 1997MNRAS.292..298P.

C. Pittori et al. First AGILE catalog of high-confidence gamma-ray sources. *Astronomy and Astrophysics*, 506:1563–1574, Nov. 2009. ISSN 0004-6361. doi: 10.1051/0004-6361/200911783. URL http://adsabs.harvard.edu/abs/2009A%26A...506.1563P.

P. Podsiadlowski, S. Rappaport, and E. D. Pfahl. Evolutionary Sequences for Low- and Intermediate-Mass X-Ray Binaries. *The Astrophysical Journal*, 565(2):1107, Feb. 2002. ISSN 0004-637X. doi: 10.1086/324686. URL https://iopscience.iop.org/article/10.1086/324686/meta. Publisher: IOP Publishing.

S. Poolakkil et al. The Fermi GBM Gamma-Ray Burst Spectral Catalog: 10 Years of Data. *The Astrophysical Journal*, 913(1):60, May 2021. ISSN 0004-637X, 1538-4357. doi: 10.3847/1538-4357/abf24d. URL http://arxiv.org/abs/2103.13528. arXiv:2103.13528 [astro-ph].

K. A. Postnov and L. R. Yungelson. The Evolution of Compact Binary Star Systems. *Living Reviews in Relativity*, 17:3, May 2014. doi: 10.12942/lrr-2014-3. URL https://ui.adsabs.harvard.edu/abs/2014LRR....17...3P. ADS Bibcode: 2014LRR....17....3P.

M. Prest et al. The AGILE silicon tracker: an innovative /gamma-ray instrument for space. *Nuclear Instruments and Methods in Physics Research A*, 501:280–287, Mar. 2003. ISSN 0168-9002. doi: 10.1016/S0168-9002(02)02047-8. URL https://ui.adsabs.harvard.edu/abs/2003NIMPA.501..280P. ADS Bibcode: 2003NIMPA.501..280P.

M. S. Pshirkov. The Fermi-LAT view of the colliding wind binaries. *Monthly Notices of the Royal Astronomical Society: Letters*, 457(1):L99–L102, Mar. 2016. ISSN 1745-3925. doi: 10.1093/mnrasl/slv205. URL https://doi.org/10.1093/mnrasl/slv205.

D. Raghavan et al. A Survey of Stellar Families: Multiplicity of Solar-type Stars. *The Astrophysical Journal Supplement Series*, 190:1–42, Sept. 2010. ISSN 0067-0049. doi: 10.1088/0067-0049/190/1/1. URL https://ui.adsabs.harvard.edu/abs/2010ApJS..190....1R. ADS Bibcode: 2010ApJS..190....1R.

F. Rahoui and others. Multi-wavelength observations of Galactic hard X-ray sources discovered by INTEGRAL. II. The environment of the companion star. *Astronomy and Astrophysics*, 484:801–813, June 2008. ISSN 0004-6361. doi: 10.1051/0004-6361:20078774. URL http://adsabs.harvard.edu/abs/2008A%26A...484..801R.

M. V. S. Rao and B. V. Sreekantan. *Extensive Air Showers*. WORLD SCIENTIFIC, Oct. 1998. ISBN 978-981-02-2888-0 978-981-281-721-1. doi: 10.1142/3307. URL http://www.worldscientific.com/worldscibooks/10.1142/3307.

K. Rasul et al. Gamma-rays from SS433: evidence for periodicity. *Monthly Notices of the Royal Astronomical Society*, 485(2):2970–2975, May 2019. ISSN 0035-

8711, 1365-2966. doi: 10.1093/mnras/stz559. URL http://arxiv.org/abs/1903.00299. arXiv: 1903.00299.

M. J. Reid et al. A Parallax Distance to the Microquasar GRS 1915+105 and a Revised Estimate of its Black Hole Mass. *The Astrophysical Journal*, 796: 2, Nov. 2014. ISSN 0004-637X. doi: 10.1088/0004-637X/796/1/2. URL https://ui.adsabs.harvard.edu/abs/2014ApJ...796....2R. ADS Bibcode: 2014ApJ...796....2R.

P. Reig et al. Identification of the optical counterparts of high-mass X-ray binaries through optical photometry and spectroscopy. *Astronomy and Astrophysics, Volume 440, Issue 2, September III 2005, pp.637-646*, 440(2):637, Sept. 2005. ISSN 0004-6361. doi: 10.1051/0004-6361:20052684. URL https://ui.adsabs.harvard.edu/abs/2005A%26A...440..637R/abstract.

O. Reimer and A. Iyudin. EGRET Observations of Galactic Relativistic Jet Sources. In *Proceedings of the 28th International Cosmic Ray Conference*, volume 4, page 2341, Tsukuba, Japan, July 2003. IAU. URL https://ui.adsabs.harvard.edu/abs/2003ICRC....4.2341R. Conference Name: International Cosmic Ray Conference ADS Bibcode: 2003ICRC....4.2341R.

M. Revnivtsev, A. Lutovinov, and K. Ebisawa. IGR J16358-4726 in archival data of ASCA and BeppoSAX. *The Astronomer's Telegram*, 131, Mar. 2003. URL http://adsabs.harvard.edu/abs/2003ATel..131....1R.

M. Revnivtsev et al. Low-mass X-ray binaries in the bulge of the Milky Way. *Astronomy & Astrophysics*, 491(1):209–217, Nov. 2008. ISSN 0004-6361, 1432-0746. doi: 10.1051/0004-6361:200810115. URL http://www.aanda.org/10.1051/0004-6361:200810115.

J. Rho et al. Discovery of an X-ray pulsar with 36 sec period in the supernova remnant W63. *AAS/High Energy Astrophysics Division*, 8:17.30, Aug. 2004.

URL https://ui.adsabs.harvard.edu/abs/2004HEAD....8.1730R. Conference Name: AAS/High Energy Astrophysics Division #8.

G. A. Richter. V404 Cyg - a Further Outburst in 1956. *Information Bulletin on Variable Stars*, 3362:1, Aug. 1989. ISSN 0374-0676. URL http://adsabs.harvard.edu/abs/1989IBVS.3362....1R.

M. S. E. Roberts. Surrounded by spiders! New black widows and redbacks in the Galactic field. *Proceedings of the International Astronomical Union*, 8(S291):127–132, Aug. 2012. ISSN 1743-9213, 1743-9221. doi: 10.1017/S174392131202337X. URL https://www.cambridge.org/core/journals/proceedings-of-the-international-astronomical-union/article/surrounded-by-spiders-new-black-widows-and-redbacks-in-the-galactic-field/012003A07765852C1155E6DCADCA82B9. Publisher: Cambridge University Press.

C. Rodriguez et al. A Compact Supermassive Binary Black Hole System. *The Astrophysical Journal*, 646:49–60, July 2006. ISSN 0004-637X. doi: 10.1086/504825. URL https://ui.adsabs.harvard.edu/abs/2006ApJ...646...49R. ADS Bibcode: 2006ApJ...646...49R.

J. Rodriguez et al. An XMM-Newton observation of IGR J16320-4751 = AX J1631.9-4752. *Astronomy & Astrophysics*, 407(2):L41–L45, Aug. 2003. ISSN 0004-6361, 1432-0746. doi: 10.1051/0004-6361:20031093. URL http://www.aanda.org/10.1051/0004-6361:20031093.

J. Rodriguez et al. Correlated optical, X-ray, and gamma-ray flaring activity seen with INTEGRAL during the 2015 outburst of V404 Cygni. *Astronomy and Astrophysics*, 581:L9, Sept. 2015. ISSN 0004-6361. doi: 10.1051/0004-6361/201527043. URL http://adsabs.harvard.edu/abs/2015A%26A...581L...9R.

P. Romano et al. The 100-month Swift catalogue of supergiant fast X-ray transients - I. BAT on-board and transient monitor flares. *Astronomy & Astrophysics*, 562:A2, Feb. 2014. ISSN 0004-6361, 1432-0746. doi: 10.1051/

0004-6361/201322516. URL https://www.aanda.org/articles/aa/abs/2014/02/aa22516-13/aa22516-13.html. Publisher: EDP Sciences.

G. E. Romero, F. L. Vieyro, and S. Chaty. Coronal origin of the polarization of the high-energy emission of Cygnus X-1. *Astronomy & Astrophysics*, 562:L7, Feb. 2014. ISSN 0004-6361, 1432-0746. doi: 10.1051/0004-6361/201323316. URL https://www.aanda.org/articles/aa/abs/2014/02/aa23316-13/aa23316-13.html. Publisher: EDP Sciences.

J.-P. Roques et al. First INTEGRAL observations of V404 Cygni during the 2015 outburst : spectral behavior in the 20 - 650 keV energy range. *The Astrophysical Journal*, 813(1):L22, Oct. 2015. ISSN 2041-8213. doi: 10.1088/2041-8205/813/1/L22. URL http://arxiv.org/abs/1510.03677. arXiv: 1510.03677.

H. N. Russell. Relations between the Spectra and other Characteristics of the Stars. *Nature*, 93(2324):281–286, May 1914. ISSN 1476-4687. doi: 10.1038/093281a0. URL https://www.nature.com/articles/093281a0. Number: 2324 Publisher: Nature Publishing Group.

C.-E. Rydberg et al. Detection of isolated Population III stars with the James Webb Space Telescope. *Monthly Notices of the Royal Astronomical Society*, 429 (4):3658–3664, Mar. 2013. ISSN 0035-8711. doi: 10.1093/mnras/sts653. URL https://doi.org/10.1093/mnras/sts653.

B. Ryden and B. Peterson. *Foundations of Astrophysics*. Cambridge University Press, 2020. ISBN 978-1-108-83195-6. URL https://books.google.co.uk/books?id=pp3wDwAAQBAJ.

S. Sabatini et al. On The Angular Resolution of the AGILE Gamma-Ray Imagingy Detector. *The Astrophysical Journal*, 809(1):60, Aug. 2015. ISSN 0004-637X. doi: 10.1088/0004-637X/809/1/60. URL https://doi.org/10.1088/0004-637x/809/1/60. Publisher: American Astronomical Society.

F. Sabbadin. The elliptical supernova remnant W63 (G82.2+5.3). *Journal of the Royal Astronomical Society of Canada*, 89(4):175–176, Mar. 1976. ISSN 0035-872X. URL `https://ui.adsabs.harvard.edu/abs/1995JRASC..89..175L/abstract`.

M. Sakano et al. Discovery of a Slow X-Ray Pulsator, AX J1740.1-2847, in the Galactic Center Region. *Publications of the Astronomical Society of Japan*, 52, Sept. 2000. doi: 10.1093/pasj/52.6.1141.

M. Salaris, L. G. Althaus, and E. García-Berro. Comparison of theoretical white dwarf cooling timescales. *Astronomy & Astrophysics*, 555:A96, July 2013. ISSN 0004-6361, 1432-0746. doi: 10.1051/0004-6361/201220622. URL `https://www.aanda.org/articles/aa/abs/2013/07/aa20622-12/aa20622-12.html`. Publisher: EDP Sciences.

J. Salcido et al. Music from the heavens - Gravitational waves from supermassive black hole mergers in the EAGLE simulations. *Monthly Notices of the Royal Astronomical Society*, 463(1):870–885, Aug. 2016. ISSN 0035-8711, 1365-2966. doi: 10.1093/mnras/stw2048. URL `http://arxiv.org/abs/1601.06156`. arXiv: 1601.06156.

E. E. Salpeter. Accretion of Interstellar Matter by Massive Objects. *The Astrophysical Journal*, 140:796–800, Aug. 1964. ISSN 0004-637X. doi: 10.1086/147973. URL `http://adsabs.harvard.edu/abs/1964ApJ...140..796S`.

D. A. Sanchez and C. Deil. Enrico : A Python Package to Simplify Fermi-LAT Analysis. 33:2784, Jan. 2013. URL `https://ui.adsabs.harvard.edu/abs/2013ICRC...33.2784S`. Conference Name: International Cosmic Ray Conference Place: eprint: arXiv:1307.4534 ADS Bibcode: 2013ICRC...33.2784S.

D. Schaerer. On the properties of massive Population III stars and metal-free stellar populations. *Astronomy and Astrophysics, v.382, p.28-42 (2002)*, 382:28,

Jan. 2002. ISSN 0004-6361. doi: 10.1051/0004-6361:20011619. URL https://ui.adsabs.harvard.edu/abs/2002A%26A...382...28S/abstract.

E. J. Schneid et al. EGRET Measurements of Energetic Gamma Rays from the Gamma-Ray Bursts of 1992 June 22 and 1994 March 1. *The Astrophysical Journal*, 453:95, Nov. 1995. ISSN 0004-637X. doi: 10.1086/176373. URL https://ui.adsabs.harvard.edu/abs/1995ApJ...453...95S. ADS Bibcode: 1995ApJ...453...95S.

V. Schoenfelder et al. Instrument Description and Performance of the Imaging Gamma-Ray Telescope COMPTEL aboard the Compton Gamma-Ray Observatory. *The Astrophysical Journal Supplement Series*, 86:657, June 1993. ISSN 0067-0049. doi: 10.1086/191794. URL https://ui.adsabs.harvard.edu/abs/1993ApJS...86..657S. ADS Bibcode: 1993ApJS...86..657S.

R. A. Schwartz et al. Fermi GBM and LAT Solar Flare X Ray and gamma Ray Observations. 216:404.06, May 2010. URL https://ui.adsabs.harvard.edu/abs/2010AAS...21640406S. Conference Name: American Astronomical Society Meeting Abstracts #216 ADS Bibcode: 2010AAS...21640406S.

M. Servillat et al. DASCH 100-yr light curves of high-mass X-ray binaries. *Proceedings of Science*, Mar. 2013.

F. D. Seward et al. X-ray sources in the southern Milky Way. *Monthly Notices of the Royal Astronomical Society*, 177:13P–20, Oct. 1976. ISSN 0035-8711. doi: 10.1093/mnras/177.1.13P. URL https://ui.adsabs.harvard.edu/abs/1976MNRAS.177P..13S. ADS Bibcode: 1976MNRAS.177P..13S.

M. Shibata et al. Constraint on the maximum mass of neutron stars using GW170817 event. *Physical Review D*, 100(2):023015, July 2019. doi: 10.1103/PhysRevD.100.023015. URL https://link.aps.org/doi/10.1103/PhysRevD.100.023015. Publisher: American Physical Society.

C. R. Shrader, L. Titarchuk, and N. Shaposhnikov. New Evidence for a Black Hole in the Compact Binary Cygnus X-3. *The Astrophysical Journal*, 718:488–493, July 2010. ISSN 0004-637X. doi: 10.1088/0004-637X/718/1/488. URL https://ui.adsabs.harvard.edu/abs/2010ApJ...718..488S. ADS Bibcode: 2010ApJ...718..488S.

S. D. Silvey. The Lagrangian Multiplier Test. *The Annals of Mathematical Statistics*, 30(2):389–407, June 1959. ISSN 0003-4851, 2168-8990. doi: 10.1214/aoms/1177706259. URL https://projecteuclid.org/journals/annals-of-mathematical-statistics/volume-30/issue-2/The-Lagrangian-Multiplier-Test/10.1214/aoms/1177706259.full. Publisher: Institute of Mathematical Statistics.

G. Sinnis. Air shower detectors in gamma-ray astronomy. *New Journal of Physics*, 11(5):055007, May 2009. ISSN 1367-2630. doi: 10.1088/1367-2630/11/5/055007. URL https://iopscience.iop.org/article/10.1088/1367-2630/11/5/055007.

E. M. Sion et al. The White Dwarfs Within 20 Parsecs of the Sun: Kinematics and Statistics. *The Astronomical Journal*, 138:1681–1689, Dec. 2009. ISSN 0004-6256. doi: 10.1088/0004-6256/138/6/1681. URL https://ui.adsabs.harvard.edu/abs/2009AJ....138.1681S. ADS Bibcode: 2009AJ....138.1681S.

G. K. Skinner et al. Hard X-ray images of the galactic centre. *Nature*, 330:544–547, Dec. 1987. ISSN 0028-0836. doi: 10.1038/330544a0. URL https://ui.adsabs.harvard.edu/abs/1987Natur.330..544S. ADS Bibcode: 1987Natur.330..544S.

G. K. Skinner et al. Localization of one of the galactic centre X-ray burst sources. *Monthly Notices of the Royal Astronomical Society*, 243:72–77, Mar. 1990. ISSN 0035-8711. doi: 10.1093/mnras/243.1.72. URL https://ui.adsabs.harvard.edu/abs/1990MNRAS.243...72S. ADS Bibcode: 1990MNRAS.243...72S.

N. Smirnov. Table for Estimating the Goodness of Fit of Empirical Distributions. *The Annals of Mathematical Statistics*, 19(2):279–281, June 1948. ISSN 0003-4851, 2168-8990. doi: 10.1214/aoms/1177730256. URL https://projecteuclid.org/euclid.aoms/1177730256.

A. J. Smith. HAWC: Design, Operation, Reconstruction and Analysis. 34:966, July 2015. URL https://ui.adsabs.harvard.edu/abs/2015ICRC...34..966S. Conference Name: 34th International Cosmic Ray Conference (ICRC2015) Place: eprint: arXiv:1508.05826 ADS Bibcode: 2015ICRC...34..966S.

D. A. Smith, A. Levine, and A. Wood. XTE J1748-288. *International Astronomical Union Circular*, 6932:1, June 1998. ISSN 0081-0304. URL https://ui.adsabs.harvard.edu/abs/1998IAUC.6932....1S. ADS Bibcode: 1998IAUC.6932....1S.

R. C. Smith. Cataclysmic variables. *Contemporary Physics*, 47(6):363–386, Nov. 2006. ISSN 0010-7514. doi: 10.1080/00107510601181175. URL https://doi.org/10.1080/00107510601181175. Publisher: Taylor & Francis _eprint: https://doi.org/10.1080/00107510601181175.

S. Soldi et al. IGR J17497-2821: a new hard X-ray transient detected by INTEGRAL. *The Astronomer's Telegram*, 885:1, Sept. 2006. URL https://ui.adsabs.harvard.edu/abs/2006ATel..885....1S. ADS Bibcode: 2006ATel..885....1S.

S. W. Stahler. Deuterium and the Stellar Birthline. *The Astrophysical Journal*, 332:804, Sept. 1988. ISSN 0004-637X. doi: 10.1086/166694. URL https://ui.adsabs.harvard.edu/abs/1988ApJ...332..804S. ADS Bibcode: 1988ApJ...332..804S.

D. Steeghs. XTE J1814-338. *International Astronomical Union Circular*, 8155: 2, June 2003. ISSN 0081-0304. URL https://ui.adsabs.harvard.edu/abs/2003IAUC.8155....2S. ADS Bibcode: 2003IAUC.8155....2S.

D. Steeghs et al. The Not-so-massive Black Hole in the Microquasar GRS1915+105. *The Astrophysical Journal*, 768:185, May 2013. ISSN 0004-637X. doi: 10.1088/

0004-637X/768/2/185. URL https://ui.adsabs.harvard.edu/abs/2013ApJ...768..185S. ADS Bibcode: 2013ApJ...768..185S.

R. T. Stewart et al. Circinus X – 1: a runaway binary with curved radio jets. *Monthly Notices of the Royal Astronomical Society*, 261(3):593–598, Apr. 1993. ISSN 0035-8711. doi: 10.1093/mnras/261.3.593. URL https://doi.org/10.1093/mnras/261.3.593.

J. Strader et al. Multiwavelength Evidence for a New Flare-mode Transitional Millisecond Pulsar. *The Astrophysical Journal*, 917:69, Aug. 2021. ISSN 0004-637X. doi: 10.3847/1538-4357/ac0b47. URL https://ui.adsabs.harvard.edu/abs/2021ApJ...917...69S. ADS Bibcode: 2021ApJ...917...69S.

E. Striani et al. Variable Gamma-ray Emission from the Crab Nebula: Short Flares and Long "Waves". *The Astrophysical Journal*, 765(1):52, Feb. 2013. ISSN 0004-637X. doi: 10.1088/0004-637X/765/1/52. URL https://doi.org/10.1088/0004-637x/765/1/52. Publisher: American Astronomical Society.

T. Strohmayer et al. XTE J1748-288. *International Astronomical Union Circular*, 6934:2, June 1998. ISSN 0081-0304. URL https://ui.adsabs.harvard.edu/abs/1998IAUC.6934....2S. ADS Bibcode: 1998IAUC.6934....2S.

T. E. Strohmayer et al. X-Ray Bursts from the Accreting Millisecond Pulsar XTE J1814-338. *The Astrophysical Journal*, 596:L67–L70, Oct. 2003. ISSN 0004-637X. doi: 10.1086/379158. URL https://ui.adsabs.harvard.edu/abs/2003ApJ...596L..67S. ADS Bibcode: 2003ApJ...596L..67S.

M. Su, T. R. Slatyer, and D. P. Finkbeiner. Giant Gamma-ray Bubbles from Fermi-LAT: AGN Activity or Bipolar Galactic Wind? *The Astrophysical Journal*, 724 (2):1044–1082, Dec. 2010. ISSN 0004-637X, 1538-4357. doi: 10.1088/0004-637X/724/2/1044. URL http://arxiv.org/abs/1005.5480. arXiv: 1005.5480.

R. Sunyaev. GX 1+4, KS 1731-260, GRS 1741.9-2853, A1524-62. *International Astronomical Union Circular*, 5104:1, Sept. 1990. ISSN 0081-0304. URL

https://ui.adsabs.harvard.edu/abs/1990IAUC.5104....1S. ADS Bibcode: 1990IAUC.5104....1S.

R. Sunyaev et al. Three Spectral States of 1E 1740.7-2942: From Standard Cygnus X-1 Type Spectrum to the Evidence of Electron-Positron Annihilation Feature. *The Astrophysical Journal*, 383:L49, Dec. 1991. ISSN 0004-637X. doi: 10.1086/186238. URL https://ui.adsabs.harvard.edu/abs/1991ApJ...383L..49S. ADS Bibcode: 1991ApJ...383L..49S.

S. J. Swihart et al. Discovery of a New Redback Millisecond Pulsar Candidate: 4FGL J0940.3-7610. *The Astrophysical Journal*, 909:185, Mar. 2021. ISSN 0004-637X. doi: 10.3847/1538-4357/abe1be. URL https://ui.adsabs.harvard.edu/abs/2021ApJ...909..185S. ADS Bibcode: 2021ApJ...909..185S.

R. Takagi et al. MAXI/GSC detection of an intense hard X-ray flare from GRS 1915+105. *The Astronomer's Telegram*, 13478:1, Feb. 2020. URL https://ui.adsabs.harvard.edu/abs/2020ATel13478....1T. ADS Bibcode: 2020ATel13478....1T.

H. Tananbaum et al. Discovery of a Periodic Pulsating Binary X-Ray Source in Hercules from UHURU. *The Astrophysical Journal*, 174:L143, June 1972. ISSN 0004-637X. doi: 10.1086/180968. URL https://ui.adsabs.harvard.edu/abs/1972ApJ...174L.143T. ADS Bibcode: 1972ApJ...174L.143T.

Y. Tang and S. Liu. Radial Profiles of Non-thermal Emission from Supernova Remnant RX J1713.7-3946. *The Astrophysical Journal*, 909:46, Mar. 2021. ISSN 0004-637X. doi: 10.3847/1538-4357/abdd31. URL https://ui.adsabs.harvard.edu/abs/2021ApJ...909...46T. ADS Bibcode: 2021ApJ...909...46T.

M. Tavani et al. The AGILE Mission. *Astronomy & Astrophysics*, 502(3):995–1013, Aug. 2009a. ISSN 0004-6361, 1432-0746. doi: 10.1051/0004-6361/200810527. URL http://www.aanda.org/10.1051/0004-6361/200810527.

M. Tavani et al. Extreme particle acceleration in the microquasar CygnusX-3. *Nature*, 462:620–623, Dec. 2009b. ISSN 0028-0836. doi: 10.1038/nature08578. URL http://adsabs.harvard.edu/abs/2009Natur.462..620T.

A. F. Tennant, A. C. Fabian, and R. A. Shafer. Observations of type I X-ray bursts from CIR X-1. *Monthly Notices of the Royal Astronomical Society*, 221: 27P–31, July 1986. ISSN 0035-8711. doi: 10.1093/mnras/221.1.27P. URL https://ui.adsabs.harvard.edu/abs/1986MNRAS.221P..27T. ADS Bibcode: 1986MNRAS.221P..27T.

A. J. Tetarenko et al. Tracking the variable jets of V404 Cygni during its 2015 outburst. *Monthly Notices of the Royal Astronomical Society*, 482(3):2950–2972, Jan. 2019. ISSN 0035-8711, 1365-2966. doi: 10.1093/mnras/sty2853. URL http://arxiv.org/abs/1810.05709. arXiv: 1810.05709.

B. E. Tetarenko et al. WATCHDOG: A Comprehensive All-sky Database of Galactic Black Hole X-ray Binaries. *The Astrophysical Journal Supplement Series*, 222:15, Feb. 2016. ISSN 0067-0049. doi: 10.3847/0067-0049/222/2/15. URL https://ui.adsabs.harvard.edu/abs/2016ApJS..222...15T. ADS Bibcode: 2016ApJS..222...15T.

K. S. Thorne and A. N. Zytkow. Stars with degenerate neutron cores. I. Structure of equilibrium models. *The Astrophysical Journal*, 212:832–858, Mar. 1977. ISSN 0004-637X. doi: 10.1086/155109. URL https://ui.adsabs.harvard.edu/abs/1977ApJ...212..832T. ADS Bibcode: 1977ApJ...212..832T.

S. J. Tingay et al. Relativistic motion in a nearby bright X-ray source. *Nature*, 374:141–143, Mar. 1995. ISSN 0028-0836. doi: 10.1038/374141a0. URL https://ui.adsabs.harvard.edu/abs/1995Natur.374..141T. ADS Bibcode: 1995Natur.374..141T.

P. Tipler and G. Mosca. *Physics for Scientists and Engineers*. Number pt. 133 in

Physics for Scientists and Engineers. W. H. Freeman, 2007. ISBN 978-1-4292-0124-7. URL https://books.google.co.uk/books?id=AttDBYgLeZkC.

M. A. P. Torres et al. A candidate near-infrared counterpart to SAX J1750.8-2900. *The Astronomer's Telegram*, 1472:1, Apr. 2008. URL https://ui.adsabs.harvard.edu/abs/2008ATel.1472....1T. ADS Bibcode: 2008ATel.1472....1T.

E. Troja et al. A luminous blue kilonova and an off-axis jet from a compact binary merger at z = 0.1341. *Nature Communications*, 9(1), Oct 2018. ISSN 2041-1723. doi: 10.1038/s41467-018-06558-7. URL http://dx.doi.org/10.1038/s41467-018-06558-7.

S. A. Trushkin et al. Most bright radio flare of GRS 1915+105 for last decade. *The Astronomer's Telegram*, 13442:1, Feb. 2020. URL https://ui.adsabs.harvard.edu/abs/2020ATel13442....1T. ADS Bibcode: 2020ATel13442....1T.

I. Tuohy and G. Garmire. Discovery of a compact X-ray source at the center of the SNR RCW 103. *The Astrophysical Journal*, 239:L107–L110, Aug. 1980. ISSN 0004-637X. doi: 10.1086/183303. URL https://ui.adsabs.harvard.edu/abs/1980ApJ...239L.107T. ADS Bibcode: 1980ApJ...239L.107T.

J. Tyler. *Muon identification with VERITAS using the Hough Transform.* PhD thesis, Jan. 2012. URL https://ui.adsabs.harvard.edu/abs/2012MsT.....18T. Pages: 18 Publication Title: Masters Thesis ADS Bibcode: 2012MsT.....18T.

P. Ubertini et al. Bursts from GS 1826-238: A Clocked Thermonuclear Flashes Generator. *The Astrophysical Journal*, 514:L27–L30, Mar. 1999a. ISSN 0004-637X. doi: 10.1086/311933. URL https://ui.adsabs.harvard.edu/abs/1999ApJ...514L..27U. ADS Bibcode: 1999ApJ...514L..27U.

P. Ubertini et al. The Gamma-Ray Imager on Board Integral. *Astrophysical Letters and Communications*, 39:331, 1999b. ISSN 0888-6512. URL https://ui.adsabs.harvard.edu/abs/1999ApL&C..39..331U/abstract.

M. J. Valtonen et al. A massive binary black-hole system in OJ 287 and a test of general relativity. *Nature*, 452(7189):851–853, Apr. 2008. ISSN 1476-4687. doi: 10.1038/nature06896. URL https://www.nature.com/articles/nature06896. Bandiera_abtest: a Cg_type: Nature Research Journals Number: 7189 Primary_atype: Research Publisher: Nature Publishing Group.

J. van den Eijnden et al. VLA detection of the radio counterpart of the BeXRB 1A 0535+262. *The Astronomer's Telegram*, 14193:1, Nov. 2020. URL https://ui.adsabs.harvard.edu/abs/2020ATel14193....1V. ADS Bibcode: 2020ATel14193....1V.

M. H. van Kerkwijk, R. P. Breton, and S. R. Kulkarni. Evidence for a Massive Neutron Star from a Radial-velocity Study of the Companion to the Black-widow Pulsar PSR B1957+20. *The Astrophysical Journal*, 728:95, Feb. 2011. ISSN 0004-637X. doi: 10.1088/0004-637X/728/2/95. URL https://ui.adsabs.harvard.edu/abs/2011ApJ...728...95V. ADS Bibcode: 2011ApJ...728...95V.

J. Van Paradijs and M. Van der Klis. Low-mass X-ray binaries. In J. A. M. Bleeker, J. Geiss, and M. C. E. Huber, editors, *The Century of Space Science*, pages 811–822. Springer Netherlands, Dordrecht, 2001. ISBN 978-94-010-0320-9. doi: 10.1007/978-94-010-0320-9_34. URL https://doi.org/10.1007/978-94-010-0320-9_34.

J. van Paradijs et al. Quasi-periodic oscillations in the bright galactic bulge X-ray source GX 340+0. *Monthly Notices of the Royal Astronomical Society*, 231 (2):379–389, Mar. 1988. ISSN 0035-8711. doi: 10.1093/mnras/231.2.379. URL https://doi.org/10.1093/mnras/231.2.379.

F. Verbunt. Origin and evolution of X-ray binaries and binary radio pulsars. *Annual Review of Astronomy and Astrophysics*, 31:93–127, 1993. ISSN 0066-4146. doi: 10.1146/annurev.aa.31.090193.000521. URL http://adsabs.harvard.edu/abs/1993ARA%26A..31...93V.

N. V. Vidal and K. C. Freeman. The X-ray source MX-0513-40 and the globular cluster NGC 1851. *The Astrophysical Journal*, 200:L9–L11, Aug. 1975. ISSN 0004-637X. doi: 10.1086/181885. URL https://ui.adsabs.harvard.edu/abs/1975ApJ...200L...9V. ADS Bibcode: 1975ApJ...200L...9V.

G. Villa et al. The Ariel V Sky Survey Instrument and new observations of the Milky Way. *Monthly Notices of the Royal Astronomical Society*, 176:609–620, Sept. 1976. ISSN 0035-8711. doi: 10.1093/mnras/176.3.609. URL https://ui.adsabs.harvard.edu/abs/1976MNRAS.176..609V.

R. M. Wagner et al. V404 Cygni = GS 2023+338. *International Astronomical Union Circular*, 4783:1, May 1989. ISSN 0081-0304. URL http://adsabs.harvard.edu/abs/1989IAUC.4783....1W.

R. M. Wagner et al. Periodic photometric variability of the black hole binary V404 Cygni. *The Astrophysical Journal Letters*, 401:L97–L100, Dec. 1992. ISSN 0004-637X. doi: 10.1086/186680. URL http://adsabs.harvard.edu/abs/1992ApJ...401L..97W.

R. Walder. Colliding Winds in Binary Star Systems: Theory, Models. *Astrophysics and Space Science, v. 260, Issue 1/2, p. 243-252 (1998).*, 260:243, Oct. 1998. ISSN 0004-640X. doi: 10.1023/A:1001857322053. URL https://ui.adsabs.harvard.edu/abs/1998Ap%26SS.260..243W/abstract.

R. Walter et al. IGR J17497-2821: a new X-ray nova. *Astronomy and Astrophysics, Volume 461, Issue 2, 2007, pp.L17-L20*, 461(2):L17, Jan. 2007. ISSN 0004-6361. doi: 10.1051/0004-6361:20066520. URL https://ui.adsabs.harvard.edu/abs/2007A%26A...461L..17W/abstract.

W. Wang. Spin and spectral variations of a peculiar high-mass X-ray binary 4U 2206+54. *Monthly Notices of the Royal Astronomical Society*, 432(2):954–966, June 2013. ISSN 0035-8711. doi: 10.1093/mnras/stt516. URL https://doi.org/10.1093/mnras/stt516.

W. Wenzel, E. Splittgerber, and J. Greiner. Unsuccessful Search for an Optical Counterpart of GRS 1915+105. *Information Bulletin on Variable Stars*, 3882: 1, May 1993. ISSN 0374-0676. URL https://ui.adsabs.harvard.edu/abs/1993IBVS.3882....1W. ADS Bibcode: 1993IBVS.3882....1W.

N. E. White. X-ray binaries. *The Astronomy and Astrophysics Review*, 1(1):85–110, Mar. 1989. ISSN 1432-0754. doi: 10.1007/BF00872485. URL https://doi.org/10.1007/BF00872485.

N. E. White and J. van Paradijs. The Galactic Distribution of Black Hole Candidates in Low Mass X-ray Binary Systems. *The Astrophysical Journal*, 473:L25, Dec. 1996. ISSN 0004-637X. doi: 10.1086/310380. URL https://ui.adsabs.harvard.edu/abs/1996ApJ...473L..25W. ADS Bibcode: 1996ApJ...473L..25W.

S. S. Wilks. The Large-Sample Distribution of the Likelihood Ratio for Testing Composite Hypotheses. *The Annals of Mathematical Statistics*, 9(1):60–62, Mar. 1938. ISSN 0003-4851, 2168-8990. doi: 10.1214/aoms/1177732360. URL https://projecteuclid.org/euclid.aoms/1177732360.

C. A. Wilson, M. H. Finger, and D. M. Scott. GRO J2058+42 Observations with BATSE and RXTE. *AIP Conference Proceedings*, 510:208–212, Apr. 2000. doi: 10.1063/1.1303204. URL https://ui.adsabs.harvard.edu/abs/2000AIPC..510..208W. Conference Name: The Fifth Compton Symposium.

C. A. Wilson et al. GRO J2058+42. *International Astronomical Union Circular*, 6238:1, Sept. 1995. ISSN 0081-0304. URL https://ui.adsabs.harvard.edu/abs/1995IAUC.6238....1W.

C. A. Wilson et al. Discovery of a Be/X-ray Binary Consistent with the Position of GRO J2058+42. *The Astrophysical Journal*, 622(2):1024–1032, Apr. 2005. ISSN 0004-637X, 1538-4357. doi: 10.1086/428381. URL http://arxiv.org/abs/astro-ph/0412527. arXiv: astro-ph/0412527.

C. A. Wilson-Hodge et al. NICER and Fermi GBM Observations of the First Galactic Ultraluminous X-Ray Pulsar Swift J0243.6+6124. *The Astrophysical Journal*, 863(1):9, Aug. 2018. ISSN 0004-637X. doi: 10.3847/1538-4357/aace60. URL https://dx.doi.org/10.3847/1538-4357/aace60. Publisher: The American Astronomical Society.

M. Wood et al. Fermipy: An open-source Python package for analysis of Fermi-LAT Data. *arXiv:1707.09551 [astro-ph]*, July 2017. URL http://arxiv.org/abs/1707.09551. arXiv: 1707.09551.

E. M. H. Wu et al. Orbital-phase-dependent gamma-Ray Emissions from the Black Widow Pulsar. *The Astrophysical Journal*, 761:181, Dec. 2012. ISSN 0004-637X. doi: 10.1088/0004-637X/761/2/181. URL https://ui.adsabs.harvard.edu/abs/2012ApJ...761..181W. ADS Bibcode: 2012ApJ...761..181W.

Y. Xing and Z. Wang. The Likely Fermi Detection of the Be X-Ray Binary GRO J1008-57. *The Astrophysical Journal*, 882(2):112, Sept. 2019. ISSN 0004-637X. doi: 10.3847/1538-4357/ab340e. URL https://doi.org/10.3847/1538-4357/ab340e. Publisher: American Astronomical Society.

Y. Xing and Z. Wang. Detection of the microquasar V404 Cygni at gamma-rays revisited: only one flaring event in quiescence. *arXiv:2006.15790 [astro-ph]*, June 2020. URL http://arxiv.org/abs/2006.15790. arXiv: 2006.15790.

Y. Xing et al. Fermi Observation of the Jets of the Microquasar SS 433. *The Astrophysical Journal*, 2019. doi: 10.3847/1538-4357/aafc60.

S. Yamauchi and K. Koyama. New X-Ray Sources near the Galactic Bulge Region. *Publications of the Astronomical Society of Japan*, 42:L83–L91, Dec. 1990. ISSN 0004-6264. URL https://ui.adsabs.harvard.edu/abs/1990PASJ...42L..83Y. ADS Bibcode: 1990PASJ...42L..83Y.

M. Zamfir, A. Cumming, and D. K. Galloway. Constraints on Neutron Star Mass and Radius in GS 1826-24 from Sub-Eddington X-Ray Bursts. *The Astrophysical*

Journal, 749:69, Apr. 2012. ISSN 0004-637X. doi: 10.1088/0004-637X/749/1/69. URL https://ui.adsabs.harvard.edu/abs/2012ApJ...749...69Z. ADS Bibcode: 2012ApJ...749...69Z.

R. Zanin et al. Gamma rays detected from Cygnus X-1 with likely jet origin. *Astronomy and Astrophysics*, 596:A55, Nov. 2016. ISSN 0004-6361. doi: 10.1051/0004-6361/201628917. URL http://adsabs.harvard.edu/abs/2016A%26A...596A..55Z.

J. L. Zdunik, M. Fortin, and P. Haensel. Neutron star properties and the equation of state for its core, Nov. 2016. URL http://arxiv.org/abs/1611.01357. Number: arXiv:1611.01357 arXiv:1611.01357 [astro-ph, physics:nucl-th].

A. A. Zdziarski, J. Mikolajewska, and K. Belczynski. Cyg X-3: a low-mass black hole or a neutron star. *Monthly Notices of the Royal Astronomical Society: Letters*, 429(1):L104–L108, Feb. 2013. ISSN 1745-3933, 1745-3925. doi: 10.1093/mnrasl/sls035. URL http://arxiv.org/abs/1208.5455. arXiv:1208.5455 [astro-ph].

A. A. Zdziarski et al. High-energy gamma-rays from Cyg X-1. *Monthly Notices of the Royal Astronomical Society*, 471(3):3657–3667, Nov. 2017. ISSN 0035-8711, 1365-2966. doi: 10.1093/mnras/stx1846. URL http://arxiv.org/abs/1607.05059. arXiv: 1607.05059.

S. N. Zhang et al. X-Ray Nova in Scorpius. *International Astronomical Union Circular*, 6046:1, Aug. 1994. ISSN 0081-0304. URL https://ui.adsabs.harvard.edu/abs/1994IAUC.6046....1Z. ADS Bibcode: 1994IAUC.6046....1Z.

B. Zhao et al. Formation and Evolution of Disks Around Young Stellar Objects. *Space Science Reviews*, 216(3):43, Apr. 2020. ISSN 1572-9672. doi: 10.1007/s11214-020-00664-z. URL https://doi.org/10.1007/s11214-020-00664-z.

J. Ziółkowski. Evolutionary constraints on the masses of the components of the HDE 226868/Cyg X-1 binary system. *Monthly Notices of the Royal Astronomical*

Society, 358:851–859, Apr. 2005. ISSN 0035-8711. doi: 10.1111/j.1365-2966.2005.08796.x. URL https://ui.adsabs.harvard.edu/abs/2005MNRAS.358..851Z. ADS Bibcode: 2005MNRAS.358..851Z.

D. R. Zurek et al. An Ultracompact X-Ray Binary in the Globular Cluster NGC 1851. *The Astrophysical Journal*, 699:1113–1118, July 2009. ISSN 0004-637X. doi: 10.1088/0004-637X/699/2/1113. URL https://ui.adsabs.harvard.edu/abs/2009ApJ...699.1113Z. ADS Bibcode: 2009ApJ...699.1113Z.

Appendix A

Stellar Evolution

This appendix contains supplementary material to Chapter 3, and explains stellar populations and the fundamentals of stellar evolution, which is relevant to the subject of compact binaries, and particularly X-ray binaries, which are the main topic of this thesis.

A.1 Stellar Populations

All stars in the universe today can be grouped into one of three 'populations' (e.g. Baade 1944, Heger and Woosley 2002, & Haywood et al. 2013. Population I stars are those such as ours, metal[†] rich stars found lying in the spiral arms of the Milky way. Due to the presence of metals, they are relatively young as the formation of metals in these stars must have come from an earlier population of stars, as only hydrogen and helium were created from the Big Bang. Population II stars, are metal poor stars, and are typically found in the Galactic bulge, and the globular clusters of the Milky way. Due to the lack of metals, they are assumed to be older than Population I stars, having formed when the universal metallicity fraction was smaller. They are *generally* lower mass, and older, systems than Population I stars by necessity, as high mass stars tend to complete the cycle of stellar evolution more quickly, driving the metallicity of their local environment up.

[†]As is standard in astrophysics, a metal is any element that is not hydrogen or helium.

Population III stars are a heretofore unobserved group, which are predicted to consist of the first stars to form in the Universe, with a metallicity of approximately zero (Schaerer, 2002). No Population III stars exist in the Milky Way, and are predicted to be only observable at extremely high redshifts, roughly corresponding to the cosmological period of re-ionisation. Such stars may have been far more massive than either Population I or II stars, although this is debatable (Hirano et al., 2014). The direct detection of Population III stars is a key objective of the stellar astrophysics community, and is a major goal of the James Webb Space Telescope mission (Rydberg et al., 2013).

A.2 Protostar Formation

All stars form through the gravitational collapse of clouds of molecular gas, whether Population I, II or III. In order for this collapse to begin, the internal force of gravity within the cloud must be greater than the internal gas pressure of the cloud, i.e. the cloud is *not* in hydrostatic equilibrium. In general, for a cloud of density, ρ, sound speed, c, and radius, R, the critical mass of this cloud before gravitational collapse begins is given by the Jeans Mass, M_J, shown in Equation A.1 (Jeans, 1902).

$$M_J = \frac{4\pi}{3}\rho R^3 \tag{A.1}$$

When a molecular cloud collapses, a dense gaseous core forms where pressure balances the force of gravity. This dense core is known as the protostar; matter continues to fall onto the protostar, and due to the angular momentum of this matter, an accretion disc will form around the protostar (as opposed to Bondi accretion occurring) (Dunham et al. 2014 & Zhao et al. 2020). At this point, the protostar is not hot enough for hydrogen to produce helium through either the proton-proton (PP) chain or the carbon-nitrogen-oxygen (CNO) cycle, however it

is predicted that deuterium burning (Equation A.2) occurs, forming helium-3, and causing the protostar to expand (Stahler, 1988).

$$\mathrm{H}^1 + \mathrm{H}^2 \longrightarrow \mathrm{He}^3 \tag{A.2}$$

Despite the possibility of some limited nuclear fusion occurring within the protostar, the majority of the energy generated by these systems comes from shocks on the surface of the protostar and accretion disc. The energy is released in the form of IR radiation, which is not powerful enough to prevent the continued infalling of matter onto the surface of the protostar, and thus prevent its continued growth (Dunham et al., 2014).

A.3 Main Sequence Stars

A protostar may eventually accrete matter to the point where nuclear fusion through the PP chain (for cooler stars) and CNO cycle occurs (for hotter stars), and true stellar nucleosynthesis begins. For this to occur the mass of the protostar must exceed $\mathrm{M} = 0.08\mathrm{M}_\odot$ else the protostar will evolve to become a Brown dwarf, which is only able to carry out deuterium fusion. Both the PP chain and CNO cycle have the same overall reaction, but by different pathways given in Equation A.3.

$$4\,^1\mathrm{H}^+ + 2\mathrm{e}^- \longrightarrow {}^4\mathrm{He}^{2+} + 2\nu_\mathrm{e} + 26.7\,\mathrm{MeV} \tag{A.3}$$

At this point the $\mathrm{H} \longrightarrow \mathrm{He}$ fusion becomes the dominant form of energy production in the star, increasing the internal pressure of the star causing hydrostatic equilibrium to reestablish itself, halting accretion onto the surface of the star. The radiation pressure from the star blows the surrounding gas away from the stellar surface, destroying the accretion disc, and dispersing any remaining molecular gas back into the interstellar medium. At this point, a star has moved onto the

main-sequence of the Hertzsprung-Russell diagram as it will be producing optical emission, where stars spend the majority of their lifespans converting their hydrogen into helium (Russell, 1914).

Main sequence stars vary significantly in their nature from case to case, with the smallest having a mass of $0.01M_{\odot}$ to the largest having masses of over $100M_{\odot}$ (Demory et al. 2009). The distribution of masses across the stellar population is given by an empirical function called the Initial Mass Function (IMF), which has been revised multiple times based on refined observations. The first form of the IMF was devised by Edwin Salpeter and takes the form of a power law in Equation A.4 (Salpeter, 1964).

$$\xi(m)\delta m = \xi_0(\frac{m}{M_{\odot}})^{-\alpha}(\frac{\delta m}{M_{\odot}}) \tag{A.4}$$

In this equation $\xi(m)\delta m$ is the number of stars within a given volume of space with masses in the range $m \longrightarrow m + \delta m$, ξ_0 is a constant related to the overall stellar density of the given volume, and α is the power-law index. In the case of the Salpeter IMF, $\alpha = 2.35$ for $0 > m > \infty$. Whilst the Salpeter IMF provides an accurate representation of the mass distribution of stars at $m > 1M_{\odot}$, it overestimates the number of stars at masses $m < 1M_{\odot}$. Therefore, several reevaluations of the IMF have been published, notably including Kroupa (2001) which introduces a series of power law breaks below $1M_{\odot}$ to account for the overestimation and Chabrier (2003) which introduces a log-parabola below $1M_{\odot}$ to also account for this overestimation. The initial mass functions of both Chabrier (2003) and Kroupa (2001) both agree with the Salpeter (1964) IMF at $m > 1M_{\odot}$.

The initial mass of a star is important, as the larger the mass the more luminous the star becomes due to an increase in the number of fusion reactions taking place because of a larger hydrogen fuel reserve within the star. The mass-luminosity relation describes this relation, and is again an empirical relationship, with varying

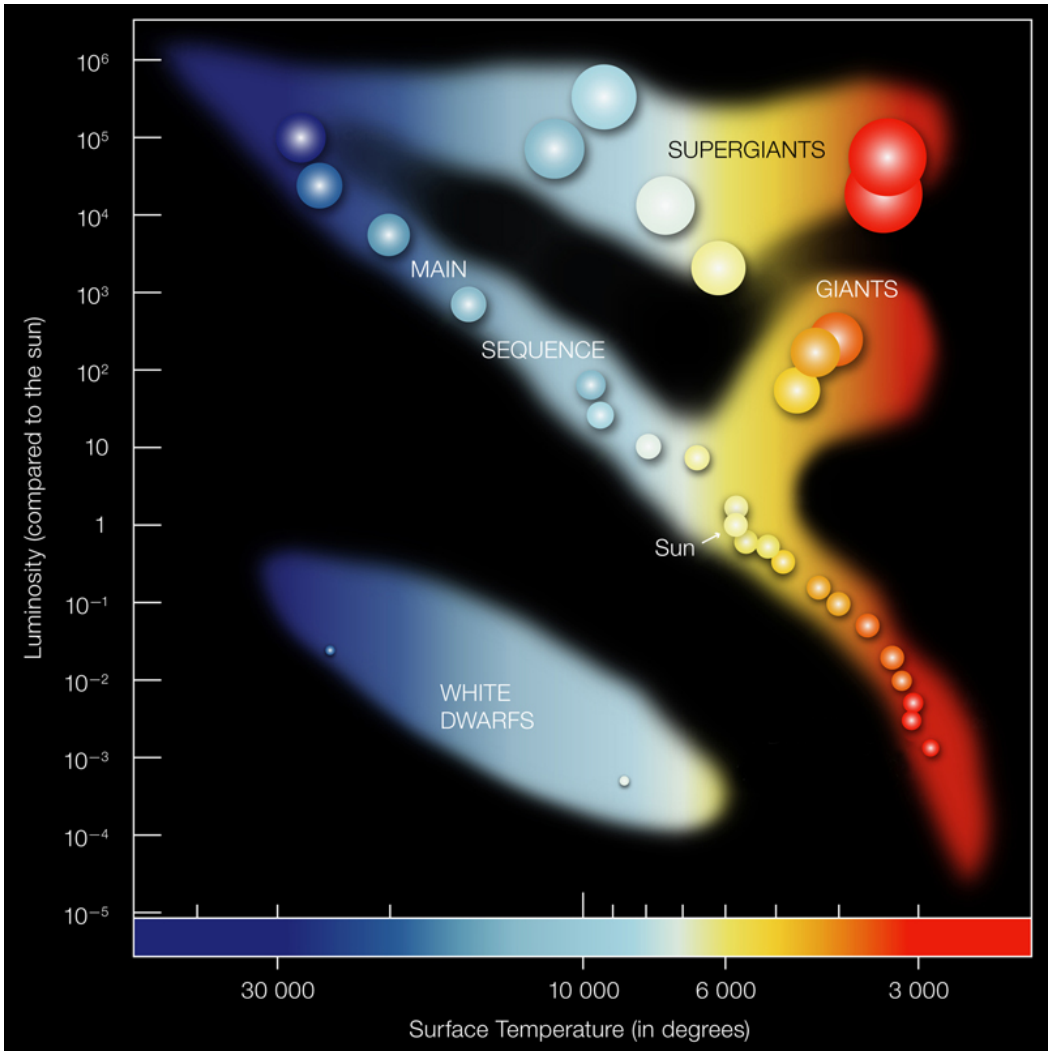

Figure A.1: A simplified Hertzsprung-Russell diagram. The vertical logarithmic axis plots stellar luminosity in units of solar luminosity ($L_\odot$). The horizontal logarithmic axis gives stellar surface temperature in units of degrees Kelvin. The colour scale along the temperature axis indicates the colour of the stellar surface. The dominant feature of this plot is the main sequence, which shows a strong positive correlation between surface temperature and solar luminosity. The white dwarfs lie below the main sequence, as these stars are comparatively smaller than a main sequence star of the same temperature, hence are far less luminous. Conversely, both the giants and supergiants lie above the main sequence, as these stars are comparatively larger, and hence more luminous, than main sequence stars of comparable temperatures. (Image credit: NASA/CXC/SAO)

values of α^* depending on the mass m of the star in question (Kuiper, 1938). The empirical mass relation is seen in Equation A.5.

$$\frac{L}{L_\odot} = (\frac{m}{M_\odot})^\alpha \tag{A.5}$$

Any given star will remain on the main sequence as long as it has enough hydrogen to burn in nuclear fusion, and this timescale is called the nuclear timescale. The nuclear timescale is given by Equation A.6.

$$t_{nuc} = \frac{-\eta \Delta m c^2}{L} \tag{A.6}$$

Here, η is the nuclear burning efficiency, Δm is the fraction of hydrogen already burned, c is the speed of light and L is the stellar luminosity. As the stellar luminosity is a function of stellar mass, the time that a star spends on the main sequence can be expressed in terms of stellar mass as:

$$t_{nuc} = \frac{-\eta \Delta m c^2}{L_\odot} (\frac{M_\odot}{m})^\alpha \tag{A.7}$$

Therefore, the time that a star spends on the main sequence is inversely proportional to its mass. from this, the sun is expected to have a nuclear timescale of about 100 Gyr, however in reality the nuclear timescale is a factor of 10 too large, as main sequence stars tend to evolve into red giant stars when 10% of their core hydrogen is fused into Helium, as the core temperature changes as Helium builds up, so the star expands to maintain hydrostatic equilibrium. A stellar mass star such as the sun is expected to have a nuclear timescale of approximately 10 Gyr, whereas a massive $m > 10 M_\odot$ star would only remain on the main sequence for a few million years, and a less massive star would remain on the main sequence for longer than the age of the universe.

*α is well constrained to be between $2.8 M_\odot$ and $4.0 M_\odot$ for all real values of m.

The relationships between stellar luminosity, mass and nuclear timescales have been established, however the temperature and colour of a star are also related to the stellar luminosity. As a star essentially radiates as a black body, the temperature and luminosity are linked by the Stefan-Boltzmann law which for a star of radius R is given by Equation A.8, and hence more luminous stars are intrinsically hotter.

$$L = 4\pi R^2 \sigma T^4 \tag{A.8}$$

As we treat the star as a blackbody, through applying Wien's Displacement Law (Equation A.9) we see that that the colour of a star changes with temperature, with the peak wavelength of the blackbody spectrum being inversely proportional to the stellar temperature.

$$\lambda_{peak} = \frac{b}{T} \tag{A.9}$$

From the relationships described above, we can deduce an important set of key characteristics about main sequence stars and the way that their properties are related to each other. The more massive a star is, the more luminous, hotter and bluer it is. As stellar mass increases, the time spent on the main sequence will decrease. Furthermore, more massive stars are significantly rarer than less massive ones. These relationships are important to clarify as the rest of this thesis deals with both high and low mass stars in a variety of contexts.

A.4 Post Main Sequence Evolution

The processes which occur after the main sequence vary based on stellar mass. For stars with a mass $m < 8M_{\odot}$, they expand into a red giant which begins fusing helium, and eventually the star sheds it's envelope leaving a white dwarf in the centre of as planetary nebula. For stars with a mass $m > 8M_{\odot}$ fusion of metals begins and continues up until the point where Iron fusion begins, which causes a

core collapse supernova, and leaves a compact object and the centre of a supernova remnant.

A.4.1 Less Massive stars

For a solar mass star, when the hydrogen in the stellar core becomes depleted pp-chain fusion ceases in the now purely Helium core, but continues in a shell around the core. At this point the Helium core is not hot enough to begin Helium fusion, and thus no heat is produced in the core, hence it begins to contract as hydrostatic equilibrium is no longer maintained in the core. The core begins to heat as it further contracts, and the Hydrogen shell continues fusion around the core which causes a force on the inert Hydrogen envelope around the shell. This causes the envelope of the star to expand as the core contracts causing the star to apparently cool and redden, hence earning the moniker of 'red giant'.

As the He core continues to contract and more Helium ash is added to the core from the hydrogen shell, the core density increases until it is balanced by electron degeneracy pressure. At this point, the core is hot enough for Helium fusion to begin through the triple-α process which converts Helium to Carbon shown in Equation A.10.

$$^4\mathrm{He} + {}^4\mathrm{He} \longrightarrow {}^8\mathrm{Be} \tag{A.10}$$

$$^4\mathrm{He} + {}^8\mathrm{Be} \longrightarrow {}^{12}\mathrm{C} + 7.275\,\mathrm{MeV}$$

The degenerate Helium in the core is unstable, hence when triple-α fusion begins, a large amount of Helium is fused at once in an explosive manner, this is known as the Helium flash. Following the Helium flash, Helium fusion continues and an inert carbon core forms, which once again contracts causing the star to expand further. Around this core is a layer of burning He and a layer of burning H, nested inside

one another. The Helium shell ignites only intermittently, and when it does so the force from the ignition causes the outer envelope of the star to be shed into the interstellar medium. This causes a gaseous cloud around the star to form called a planetary nebula. Eventually the Hydrogen and Helium layers are also ejected, and what is left is the extremely hot but inert Carbon core, which cannot collapse further due to electron degeneracy pressure (unless further mass is added to the star). This core is known as a white dwarf, and is the final remnant of the majority of stars.

A.4.2 More Massive Stars

For stars with mass $m > 8M_{\odot}$ a similar process is followed to the lower mass stars, but with the fusion of heavier elements. As with less massive stars, the envelope expands as the Helium core contracts, and the Helium core eventually begins triple-α fusion at the onset of the Helium flash. However, where less massive stars grow an inert carbon core, the core temperature and pressure in a more massive star allow carbon, and subsequent heavier elements to begin fusing. The result is Russian doll like star, successive layers of subsequently heavier and heavier elements are fusing as one move through the star to the core.

Eventually a core of Iron forms and as the fusion of Iron is an endothermic process rather than exothermic, fusion halts. Eventually, the iron core will build to a mass of $1.4M_{\odot}$ a limit known as the Chandrasekhar limit, where the electron degeneracy pressure can no longer counter the force of gravity. As a result, the core of the star begins to collapse causing an explosion of the outer layers of the star to be ejected into the interstellar medium. This process is called a or core collapse supernova, and supernovae are the only processes energetic enough in the universe to cause the fusion of elements heavier than Iron (which require endothermic fusion reactions). Supernovae are extraordinarily bright, often outshining their host galaxies. What remains of the original star is a dense compact object, either a neutron star or a black hole, depending on the initial pre-supernova mass of the star. This compact

object will only have a fraction of the original star's mass, as the majority of the stellar material will be ejected from the star during the core collapse supernova.

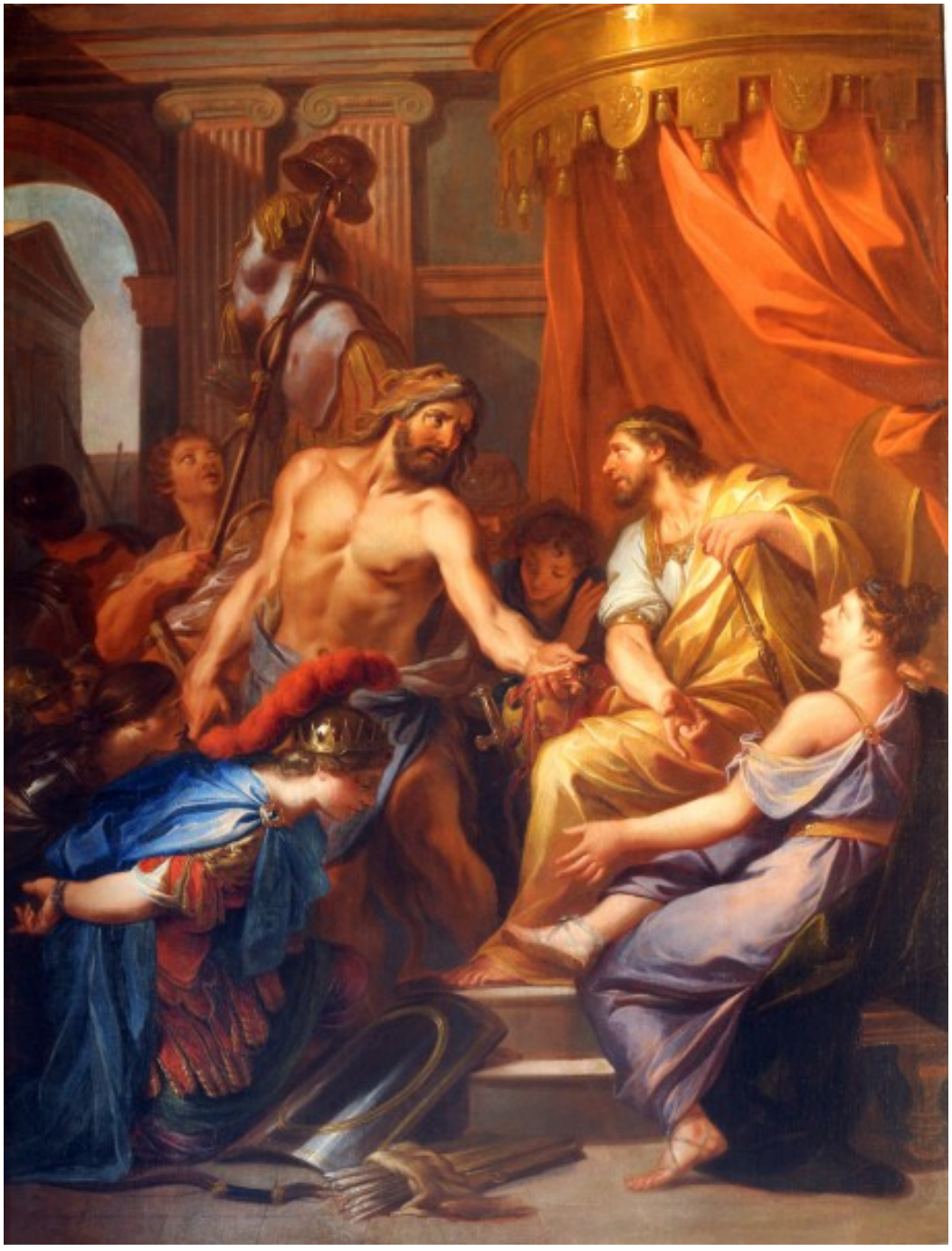

Figure A.2: Heracles and Eurystheus; having completed the 10 labours for Eurytheus as penance for murdering his family, Eurystheus decreed that two did not count as Heracles had help. Thus Heracles embarked upon an additional two labours. Daniel Sarrabat (Year Unknown)

Appendix **B**

High Mass X-ray Binary Survey Sample

The following section provides a table of each HMXB included in the survey; the binary name column gives the X-ray name of each X-ray binary included in the survey from the Liu et al. catalogue, and the alternate name column gives either the optical name of the system from Liu et al. or the most commonly used name for the system (i.e. Cyg X-1). LII and BII are the Galactic coordinates of the system used in our data analysis; the position type gives the waveband from which the coordinates were taken (for example, O corresponds to the coordinates of the optical counterpart, X to the X-ray, etc.). The period refers to the orbital period of the binary system measured in days; where no binary period is known a value of 0 is shown. The Flux U.L value refers to the 95% upper confidence limit on energy flux (with units of MeV $\mathrm{cm}^{-2}\,\mathrm{s}^{-}1$) obtained from the position of each HMXB where no measurement of a γ-ray flux is made. Where a measurement of energy flux is made, these are shown in Table 5.2.

Binary Name	Alt. Name	LII	BII	Position Type	Period	Flux U.L. (MeV cm^{-2} s^{-}1)
1H 1253-761	HD 109857	302.14353	-12.51748	O	0.0	4.19×10^{-8}
IGR J12349-6434	RT Cru	301.15792	-1.75063	X	0.0	9.60×10^{-8}
2RXP J130159.6-635806		304.08824	-1.12109	IR	0.0	8.66×10^{-8}
1H 1249-637	BZ Cru	301.95802	-0.20313	O	0.0	1.36×10^{-7}
4U 1223-624	BP CRU ?	300.09815	-0.03512	O	41.59	2.68×10^{-7}
2S 1417-624		313.02125	-1.59848	O	42.12	2.59×10^{-8}
2S 1145-619	V801 CEN	295.61107	-0.24028	O	187.5	1.52×10^{-7}
SAX J1324.4-6200		306.79301	0.60938	X	0.0	N.A.
1E 1145.1-6141	V830 CEN	295.48987	-0.00984	O	14.4	7.37×10^{-8}
1A 1118-615	HEN 3-640	292.49858	-0.89174	O	0.0	2.42×10^{-7}
4U 1258-61	V850 CEN	304.10272	1.24742	IR	133.0	1.32×10^{-7}
IGR J11435-6109		294.8992	0.70118	O	52.46	6.57×10^{-8}
1H 0749-600	HD 65663	273.69327	-16.85817	IR	0.0	N.A
1A 1244-604		302.45915	2.22543	X	0.0	9.76×10^{-8}
4U 1119-603	V779 CEN	292.09035	0.33556	X	2.09	4.74×10^{-8}
1H 1238-599		301.76038	2.65032	X	0.0	N.A.
IGR J11215-5952	HD 306414	291.89319	1.07292	O	0.0	7.96×10^{-8}
1A 1246-588		302.6956	3.74924	X	0.0	2.28×10^{-7}
GRO J1008-57		282.99992	-1.82173	O	135.0	N.A
1H 1255-567	MU.02 CRU	303.36468	5.70047	O	0.0	1.03×10^{-7}
RX J1037.5-5647	LS 1698	285.35291	1.4326	X	0.0	2.32×10^{-8}
XTE J1543-568		324.95121	-1.46121	X	75.56	6.93×10^{-8}
1H 1555-552	HD 141926	326.97618	-1.23892	O	0.0	2.45×10^{-7}
2S 1553-542		327.94412	-0.85703	X	30.6	2.83×10^{-8}
1H 0739-529	HD 63666	266.31268	-13.72584	O	0.0	3.66×10^{-8}
4U 1538-52	QV NOR	327.41949	2.1637	O	3.73	4.37×10^{-8}
IGR J16195-4945	HD 146628?	333.53932	0.33326	X	0.0	3.56×10^{-7}

Binary Name	Alt. Name	LII	BII	Position Type	Period	Flux U.L. ($MeV\,cm^{-2}\,s^{-1}$)
IGR J16318-4848		335.61599	-0.44776	O	0.0	2.46×10^{-8}
IGR J16283-4838		335.32671	0.10203	X	0.0	2.03×10^{-7}
IGR J16320-4751		336.32997	0.16892	X	8.96	N.A.
IGR J16358-4726		337.12311	-0.00089	X	0.0	N.A.
AX J1639.0-4642		338.00124	0.07508	IR	0.0	4.89×10^{-7}
IGR J16418-4532		339.19309	0.51511	X	0.0	4.72×10^{-8}
IGR J16479-4514		340.16406	-0.12466	X	0.0	6.75×10^{-7}
IGR J16465-4507		340.05357	0.13505	IR	0.0	N.A.
1WGA J0648.0-4419	HD 49798	253.70642	-19.1412	O	1.55	N.A.
IGR J16493-4348		341.37079	0.60251	X	0.0	1.67×10^{-7}
GS 0834-430		262.02096	-1.51074	O	105.8	4.05×10^{-8}
AX J1700-419		344.04452	0.23717	X	0.0	1.70×10^{-7}
OAO 1657-415		344.36915	0.31918	X	10.4	1.01×10^{-7}
4U 0900-40	HD 77581	263.05839	3.92993	O	8.96	3.22×10^{-8}
4U 1700-37	HD 153919	347.75446	2.1734	O	3.41	1.10×10^{-7}
IGR J17091-3624		349.52595	2.23569	R	0.0	1.50×10^{-7}
EXO 1722-363		351.49727	-0.35395	IR	9.74	8.00×10^{-8}
RX J0812.4-3114	LS 992	249.57107	1.5477	IR	81.3	1.81×10^{-8}
XTE J1739-302		358.06784	0.44517	X	0.0	6.75×10^{-7}
RX J1739.4-2942		358.64668	0.73046	X	0.0	2.37×10^{-7}
AX J1740.1-2847		359.49377	1.08387	X	0.0	1.08×10^{-7}
AX J1749.1-2733		1.5827	0.06234	X	0.0	6.49×10^{-7}
AX J1749.2-2725		1.701	0.1157	X	0.0	4.06×10^{-7}
RX J1744.7-2713	V3892 SGR	1.35781	1.05224	O	0.0	2.09×10^{-7}
GRO J1750-27		2.37283	0.50774	X	29.8	1.24×10^{-7}
IGR J17544-2619		3.23599	-0.33559	IR	0.0	N.A.
3A 0726-260	V441 PUP	240.28165	-4.05037	O	34.5	2.91×10^{-8}

Binary Name	Alt. Name	LII	BII	Position Type	Period	Flux U.L. ($MeV\,cm^{-2}\,s^{-}1$)
SAX J1819.3-2525	V4641 SGR	6.75638	-4.79765	O	2.8	9.69×10^{-8}
SAX J1802.7-2017		9.41747	1.04356	X	4.6	1.05×10^{-7}
SAX J1818.6-1703	HD 168078?	14.07813	-0.71028	X	0.0	1.04×10^{-7}
RX J1826.2-1450	LS 5039	16.88157	-1.28923	R	3.9	N.A.
AX J1820.5-1434		16.47185	0.06991	X	0.0	2.61×10^{-7}
4U 1807-10		18.60547	3.85183	X	0.0	2.91×10^{-7}
XTE J1829-098		21.69699	0.2786	X	0.0	3.42×10^{-7}
H 1833-076		24.46252	-0.16075	X	0.0	N.A
XTE J0658-073	[M81] I-33	220.12859	-1.76725	O	0.0	6.26×10^{-8}
AX J1838.0-0655		25.23678	-0.19035	X	0.0	1.47×10^{-7}
GS 1839-06		26.61754	-0.50815	X	0.0	1.05×10^{-7}
AX J1841.0-0536		26.76429	-0.23879	O	0.0	1.52×10^{-7}
AX 1845.0-0433		28.14552	-0.65617	X	0.0	2.62×10^{-8}
GS 1839-04		27.87383	0.11023	X	0.0	N.A.
IGR J18483-0311		29.74117	-0.75374	X	0.0	8.30×10^{-8}
GS 1855-02		31.24518	-2.70507	X	0.0	1.25×10^{-7}
XTE J1855-026		31.07627	-2.09629	X	6.067	5.84×10^{-8}
2S 1845-024		30.42054	-0.40562	X	241.0	7.22×10^{-7}
GS 1843+009		33.03653	1.6896	O	0.0	5.24×10^{-8}
XTE J1901+014		35.38393	-1.61576	O	0.0	2.16×10^{-7}
4U 1901+03		37.1618	-1.25	X	22.58	4.05×10^{-8}
XTE J1858+034		36.80574	-0.02467	O	0.0	4.31×10^{-7}
3A 1909+048	SS 433	39.69421	-2.2447	O,R	13.1	2.13×10^{-7}
SAX J0635.2+0533		206.15276	-1.04229	O	11.2	1.48×10^{-7}
4U 1909+07		41.89715	-0.81151	IR	4.4	1.04×10^{-7}
XTE J1859+083		41.14664	2.06249	X	0.0	8.31×10^{-8}
XTE J1906+09		42.49725	1.17483	O	0.0	1.21×10^{-7}

Binary Name	Alt. Name	LII	BII	Position Type	Period	Flux U.L. ($MeV\,cm^{-2}\,s^{-}1$)
4U 1907+09		43.74539	0.47045	O	8.38	1.04×10^{-7}
IGR J19140+0951		44.29629	-0.46868	X	13.558	3.68×10^{-7}
IGR J06074+2205		188.38516	0.81378	O	0.0	1.43×10^{-7}
1A 0535+262	V725 TAU	181.44505	-2.64342	O	111.0	N.A.
XTE J1946+274		63.20703	1.39573	O	169.2	1.57×10^{-7}
1H 0556+286	HD 249179	181.28416	1.85966	O	0.0	6.33×10^{-8}
KS 1947+300		66.08802	2.09797	O	40.4	7.62×10^{-8}
4U 0352+309	X PER	163.07842	-17.1335	O	250.3	6.67×10^{-8}
4U 1956+35	Cyg X-1	71.33508	3.0668	O,R	5.0	N.A.
EXO 2030+375		77.15175	-1.24157	O	46.02	6.64×10^{-8}
EXO 051910+3737.7	V420 AUR	170.05323	0.71029	O	0.0	2.16×10^{-7}
4U 2030+40	Cyg X-3	79.8426	0.69512	R	0.2	N.A.
GRO J2058+42		83.56978	-2.65543	O	55.03	N.A.
RX J0440.9+4431	LS V +44 17	159.84708	-1.27013	O	0.0	4.30×10^{-8}
W63 X-1		82.31659	5.42815	X	0.0	N.A.
SAX J2103.5+4545		87.12993	-0.68507	O	12.68	6.76×10^{-8}
RX J2030.5+4751	SAO 49725	85.2307	5.04764	O	0.0	N.A.
1H 2202+501	BD +49 3718	97.24782	-4.04112	O	0.0	2.81×10^{-8}
V 0332+53	BQ CAM	146.05195	-2.19388	O	34.25	7.04×10^{-8}
1H 1936+541	DM +53 2262	85.84987	15.9024	O	0.0	3.60×10^{-8}
4U 2206+543	BD +53 2790	100.60312	-1.10596	O	9.57	N.A.
XTE J0421+560	CI CAM	149.17637	4.13342	O	19.41	5.95×10^{-8}
1H 2138+579	V490 CEP	99.01253	3.31318	O	0.0	9.50×10^{-8}
2S 0053+604	GAMMA CAS	123.57681	-2.14848	O	203.59	1.01×10^{-7}
1E 0236.6+6100	LS I +61 303	135.67529	1.08626	O,R	26.496	N.A.
SAX J2239.3+6116		107.73456	2.36233	O	262.0	8.39×10^{-8}
RX J0146.9+6121	LS I +61 235	129.54108	-0.8001	O	0.0	1.19×10^{-7}

Binary Name	Alt. Name	LII	BII	Position Type	Period	Flux U.L. ($MeV\,cm^{-2}\,s^{-}1$)
IGR J00370+6122	BD +60 73	121.22213	-1.46464	O	15.665	1.48×10^{-7}
4U 0115+634	V635 CAS	125.92366	1.02574	O	24.3	6.47×10^{-8}
2S 0114+650	V662 CAS	125.70998	2.56353	O	11.6	5.65×10^{-8}
IGR J01363+6610	EM* GGR 212	127.39482	3.7248	O	0.0	4.44×10^{-8}
IGR J01583+6713		129.35216	5.18871	O	0.0	1.08×10^{-7}

Appendix C

High Mass X-ray Binary False Positive Results

C.1 IGR J16320-4751

IGR J16320-4751 (henceforth IGR1632) is a system thought to be a pulsar in orbit with either a giant K-type, or O/B, star (Rodriguez et al., 2003). It is notable for its variable nature in the X-ray waveband and particularly short orbital period of approximately 9 days (Garcia et al., 2018). Over the 12.5 year observation time, I obtain a TS of 31.1 in support of the hypothesis that there is a γ-ray source at this position, with numerous bins in the 6-month binned light-curve (Figure C.1) with $2\sigma \leq z < 3\sigma$, but no clear evidence for variability.

Whilst it is possible that this coincident γ-ray point source is associated with IGR1632, I strongly suspect source confusion has caused a false detection, as IGR1632 lies 0.087° away from 4FGL J1631.6-4756e (TS = 47.3) and 0.198° away from 4FGL J1633.0-4746e (TS = 4240). Both sources are associated in the 4FGL with the TeV PWN HESS J1632-478 (Aharonian et al., 2006a). Such proximity between any two sources can see one source (usually the more significant) contaminating the second with photons. IGR1632 is extremely close to *two* significant and extended sources rather than a single point source, and lies within the cal-

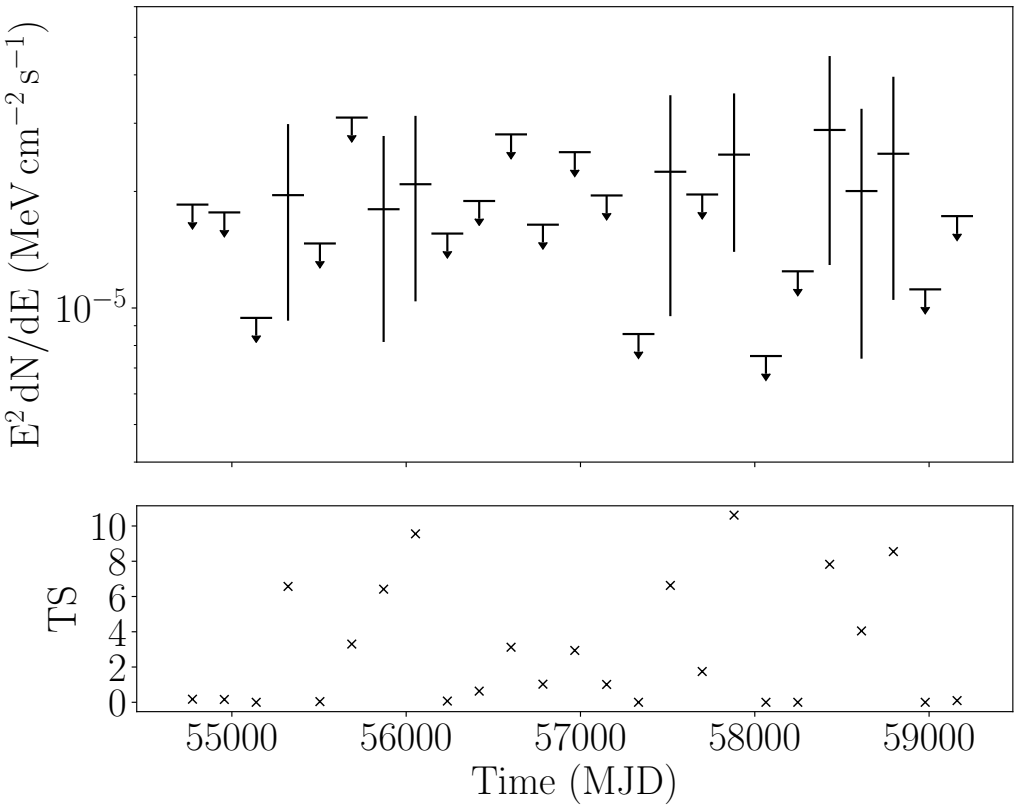

Figure C.1: The *Fermi*-LAT light-curve of the γ-ray excess coincident with IGR J16320-4751 with time bins of 6 month width. Upper limits are placed on any time bin where the TS of that bin is less than 4.

culated radius of the larger and more significant of the two, 4FGL J1633.0-4746e. Figure C.2 shows the extent of the coincident γ-ray excess with the position of IGR1632 overlaid, and the extent of the two extended sources shown to highlight the positional coincidence between these and the IGR1632 source.

We generate light-curves of both extended sources to compare against the IGR1632 light-curve to identify any correlated variability (a signature of source confusion), or differences in variability (a signature of source independence); however, neither of the extended sources is significantly variable (4FGL J1633.0-4746e is variable at the 2.00σ level, 4FGL J1631.6-4756e at the 0.20σ level), and no correlations are observed between these light-curves and the IGR1632 coincident source light-curve. Therefore, the light-curve calculation does neither supports nor rejects the hypothesis that the IGR1632 excess is the product of source confusion.

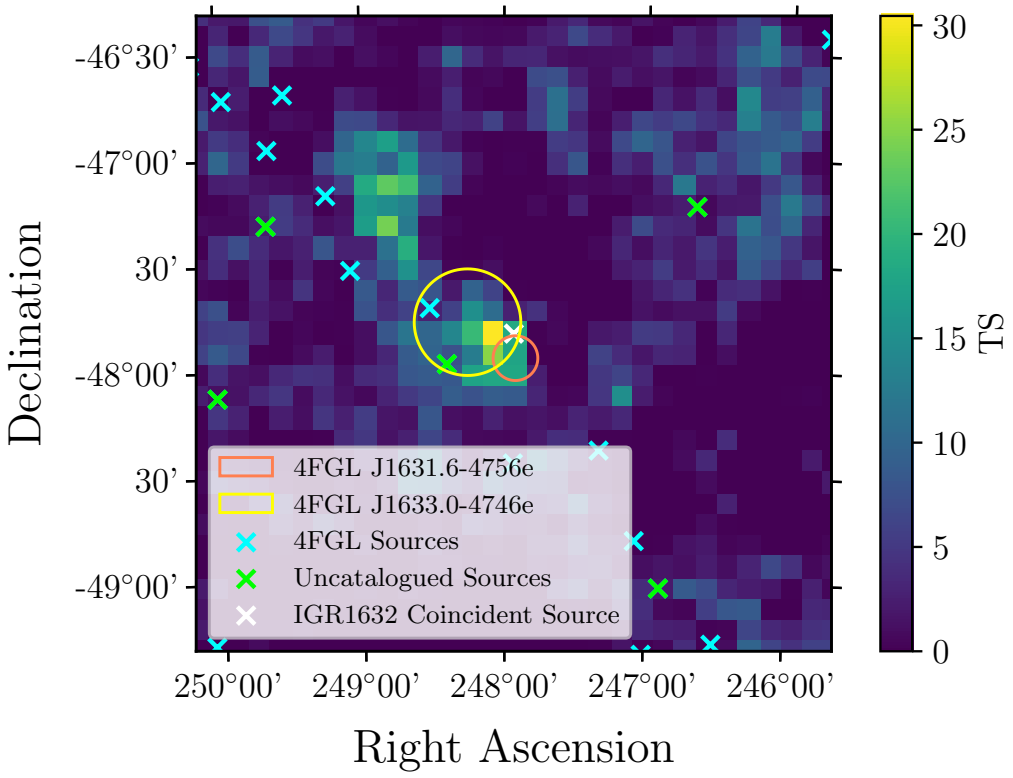

Figure C.2: A TS map showing the excess coincident with IGR J16320-4751 (white cross) and the position of the binary, the two extended sources, and other 4FGL sources (blue crosses), and additional sources identified by the `gta.find_sources` algorithm (green crosses).

We generate an SED of the IGR1632 coincident source across the entire energy range I employ, and find that the best fit to the data is a power law with spectral index $\Gamma = -2.04 \pm 0.09$, which indicates an almost flat spectrum source, although I note that this fit to the data appears to be poor. This SED is illustrated in Figure C.3. We also generate SEDs of 4FGL J1633.0-4746e, which has a log-parabola spectral shape, and 4FGL J1631.6-4756e which is best modelled by a hard power law. The 4FGL indicates a power law spectral index of $\Gamma = 2.17$ for the more significant of the two sources, 4FGL J1633.0-4746e, marginally softer than that of the IGR1632 coincident source. It is highly likely that the spectrum for this coincident source is essentially that of 4FGL J1633.0-4746e with a smaller normalisation and a contaminating component from 4FGL J1631.6-4756e which slightly hardens the spectral index. Given this, and the fact that the predicted counts of both extended

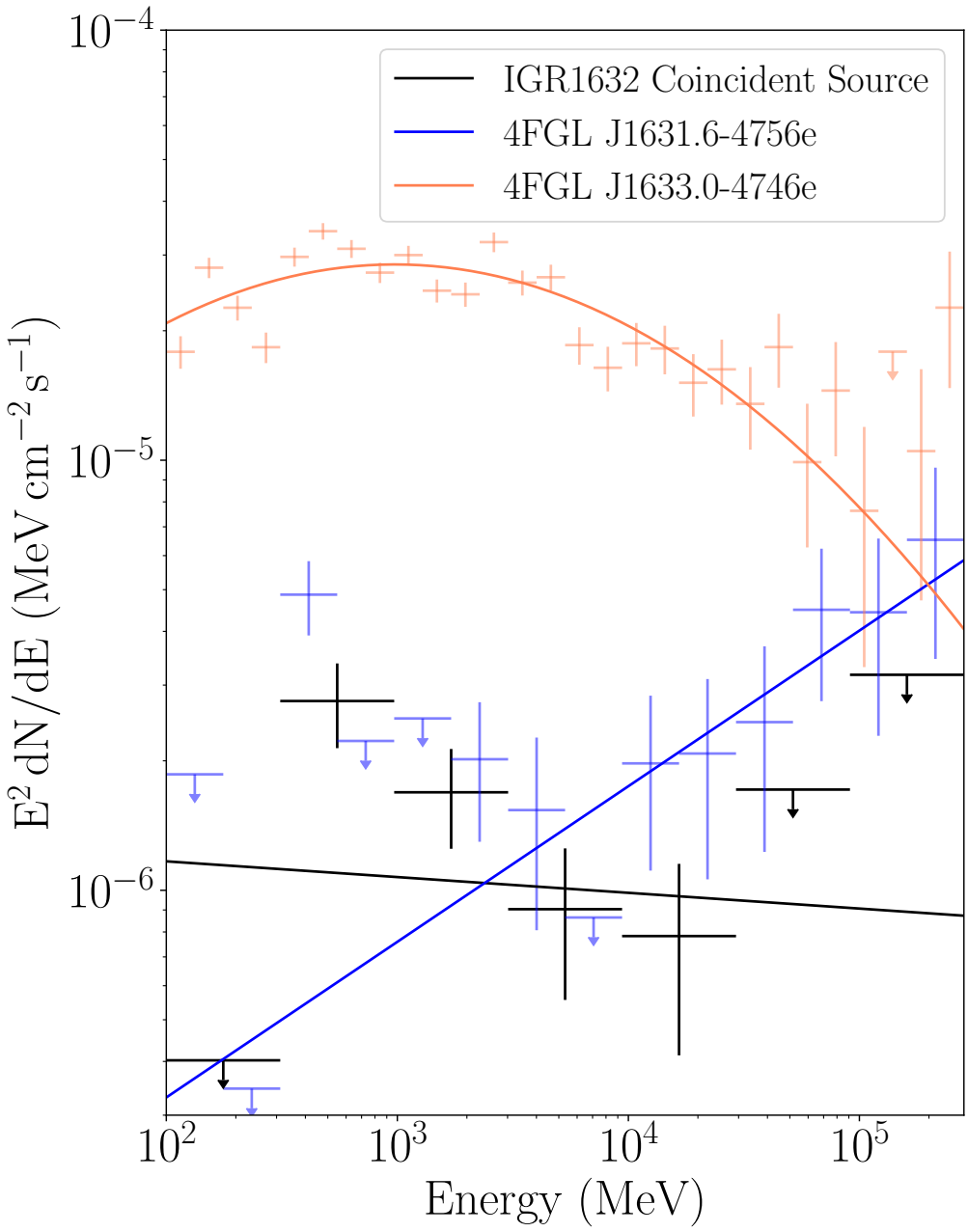

Figure C.3: The SEDs of the added source coincident with IGR J16320-4751 (black), and the two extended sources within which it lies: 4FGL J1631-4756e (blue) and 4FGL J1633.0-4746e (orange). The IGR J16320-4751 coincident source and 4FGL J1631-4756e are both fitted with power-law spectral models, and 4FGL J1633.0-4746e is fitted with a log-parabola. The number of bins per decade is chosen based on the available photon statistics for each source and upper limits are fitted to any bin with TS < 4.

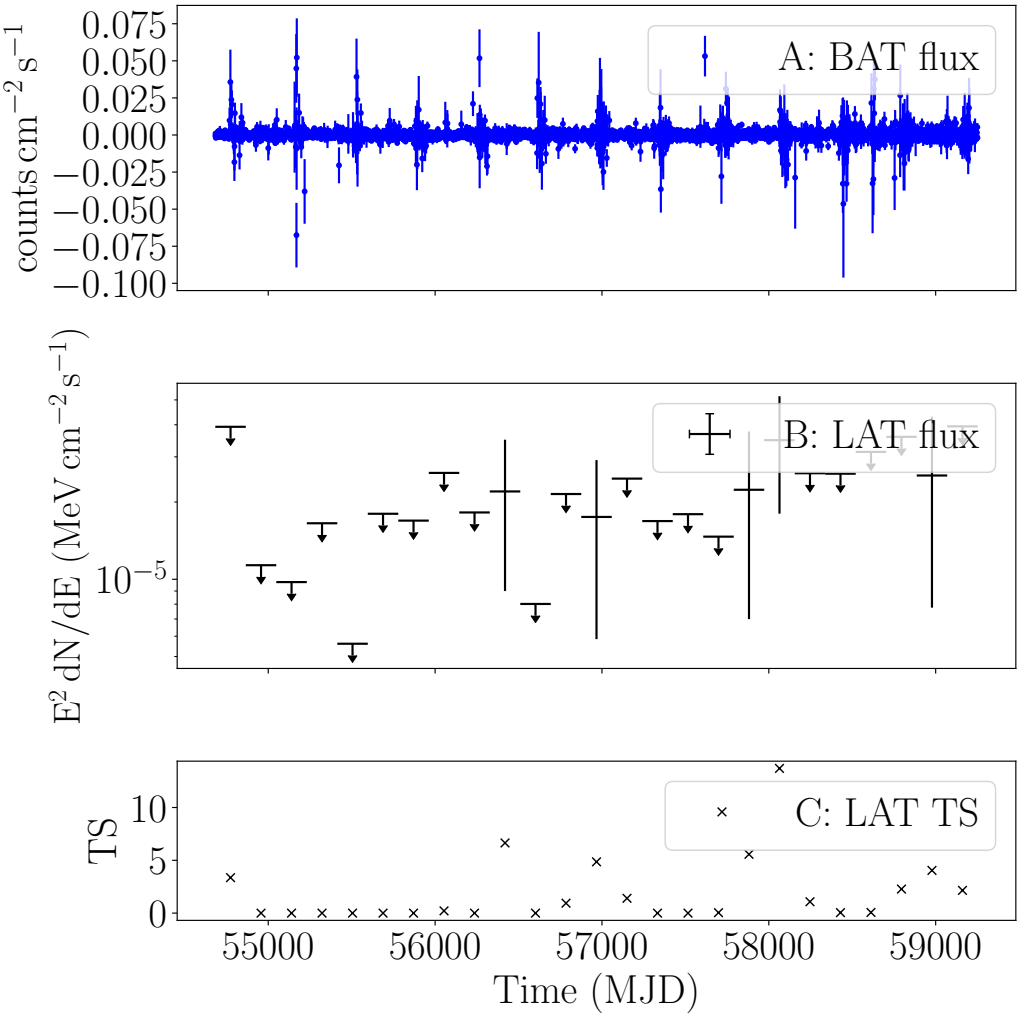

Figure C.4: The daily binned light-curve of IGR J16358-4726 taken with *Swift*-BAT shown in Panel A, with the calculated monthly-binned *Fermi*-LAT light-curve for a source fitted to the position of IGR J16358-4726 shown below in Panel B, and the corresponding TS values of these bins shown in Panel C. We place 95% confidence limits on any *Fermi*-LAT energy flux bins with TS < 4. Whilst some weak periodic activity is seen in the *Swift*-BAT light-curve, this does not correspond to any known timescales for the system, nor does it correlate with the γ-ray light-curve.

sources (in a reference model) decrease by roughly the same number of counts as is predicted for the IGR1632 coincident source, I conclude that this apparent source is a false positive, and the emission originates from the extended 4FGL sources.

C.2 IGR J16358-4726

IGR J16358-4728 (Revnivtsev et al. 2003 and Bodaghee et al. 2012) (henceforth IGR1635) is either a HMXB in which a pulsar orbits a super-giant Be star (Chaty et al. 2008 and Rahoui and others. 2008), or, based on the presence of CO lines in the K-band spectrum making the companion star a KM giant, a symbiotic LMXB (Nespoli et al., 2010). Under this former hypothesis, one might expect γ-ray emission at periastron. We detect a γ-ray excess coincident with this source with TS = 9.5 over the LAT observation period, and also measure a flux value where TS > 4 in 5 light-curve bins. This light-curve is shown together with the daily *Swift*-BAT light-curve in Figure C.4. Of the 5 bins which exceed the TS > 4 threshold in this light-curve, only one exceeds the 3σ level. This bin, and the preceding bin are the only adjacent bins, making it difficult to perform any subsequent analysis of this source.

It seems likely that the origin of this weak γ-ray excess is source confusion with the nearby, significantly extended source 4FGL J1636.3-4731e (SNR G337.0-00.1, TS = 1500) as they are separated by an angular offset of 0.087° and 4FGL J1636.3-4731e is extended by a radius of 0.11°, so the apparent excess is within the γ-ray extension of this SNR. We generate a light-curve for this source and find that it is not variable, with the exception of one particularly low flux point. Both the IGR1635 coincident source and the extended source are well-fitted by a steady source model.

We do not have sufficient photon statistics in the IGR1635 coincident excess for a comparative spectral analysis with 4FGL J1636.3-4731e. As one cannot effectively distinguish one source from the other with variability one cannot prove the independence of the IGR1635 excess from 4FGL J1636.3-4731e, nor associate this excess with the binary in question, hence I conclude it is likely a false positive caused by source confusion.

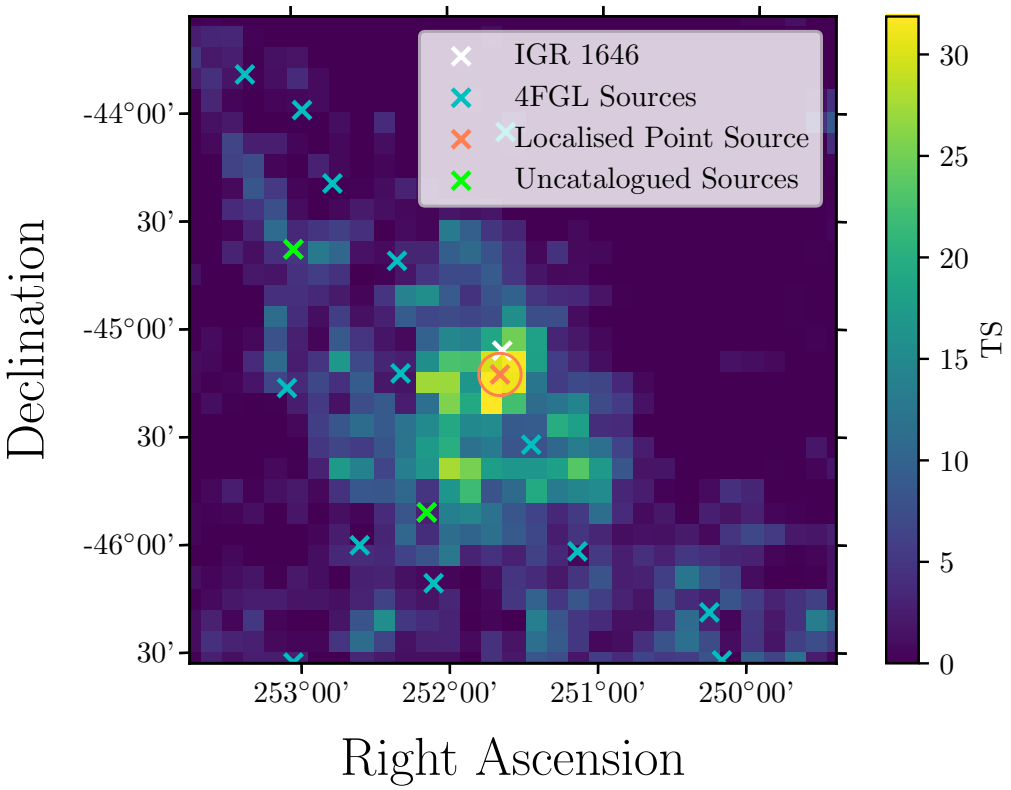

Figure C.5: A TS map with 0.1° bins, over the full 12.5 year observation time, showing the γ-ray excess and with the localised point source shown by the orange cross. The orange circle shows the 95% positional uncertainty on the point source, after localisation. The white cross indicates the infrared position of IGR J16465-4507. The blue crosses show the position of sources from the 4FGL-DR2, and the green crosses show the position of uncatalogued sources identified by the `gta.find_sources` algorithm. Note the presence of a 4FGL source (a blue cross) behind the legend of this figure.

C.3 IGR J16465-4507

IGR J16465-4507 (henceforth IGR1646) (Lutovinov et al. 2004 and Romano et al. 2014) is a supergiant HMXB system consisting of a Be star (Negueruela and Schurch, 2007) and a pulsar (Lutovinov et al., 2005) orbiting each other with a period of 30.2 days (La Parola et al., 2010). We detect a point source coincident with the position of IGR1646 to TS = 50.8, equivalent to $z = 7.1\sigma$, the most significant of all the coincident sources and excesses in my survey. The nearest sources to the IGR1646 coincident source are 4FGL J1645.8-4533c (angular offset = 0.456°,

TS = 417.93) which is tentatively associated with the LMXB 4U 1642-45. Further sources near the IGR1646 coincident source include 4FGL J1649.2-4513c (angular offset = 0.456°, TS = 417.93) and 4FGL J1649.3-4441 (angular offset = 0.642°, TS = 205.14). Neither source has a multi-wavelength counterpart.

Figure C.5 shows the TS map of the central part of the IGR1646 ROI, centered on the position of IGR1646. Given the significance of the recorded point source, I am able to localise the emission with the `gta.localize` algorithm and refit the point source to the peak of the γ-ray emission. We find the best positional fit for the point source is LII = 339.9764° ± 0.0324°, BII = 0.0557° ± 0.0498°. There is thus an angular offset from the position of IGR1646 of 0.1107°, compared to a 95% positional uncertainty of 0.0981°. The TS of the source also increases from 50.8 to 59.7 in its new position. Thus, following localisation I no longer consider this point source to be spatially coincident with the binary system and find it more likely that this new point source is either a product of source confusion with one of the nearby 4FGL sources, or an unknown new source which is unlikely to be associated with IGR1646.

C.4 1WGA J0648.0-4419

1WGA J0648.0-4419 (also known as HD 49798, and henceforth referred to as 1WGA06) is a binary system consisting of a pulsar (Israel et al., 2009) and an O-type subdwarf star (Kupfer et al., 2020). We find a γ-ray excess coincident with the position of 1WGA06 with a TS of 18.5, giving a z-score of 4.3σ. The nearest 4FGL source to 1WGA06 is 4FGL J0647.7-4418 (associated with the blazar SUMSS J064744-441946), with an angular offset of 0.068°, less than one spatial bin width from the position of the binary. With a point source fitted to the position of 1WGA06, the blazar is only marginally detected, with a TS of 8.18 (slightly below 3σ). This is far less than the detection significance given in the 4FGL-DR2, which is 8.3σ. It is possible that the γ-ray excess observed at the position of 1WGA06 is due to source

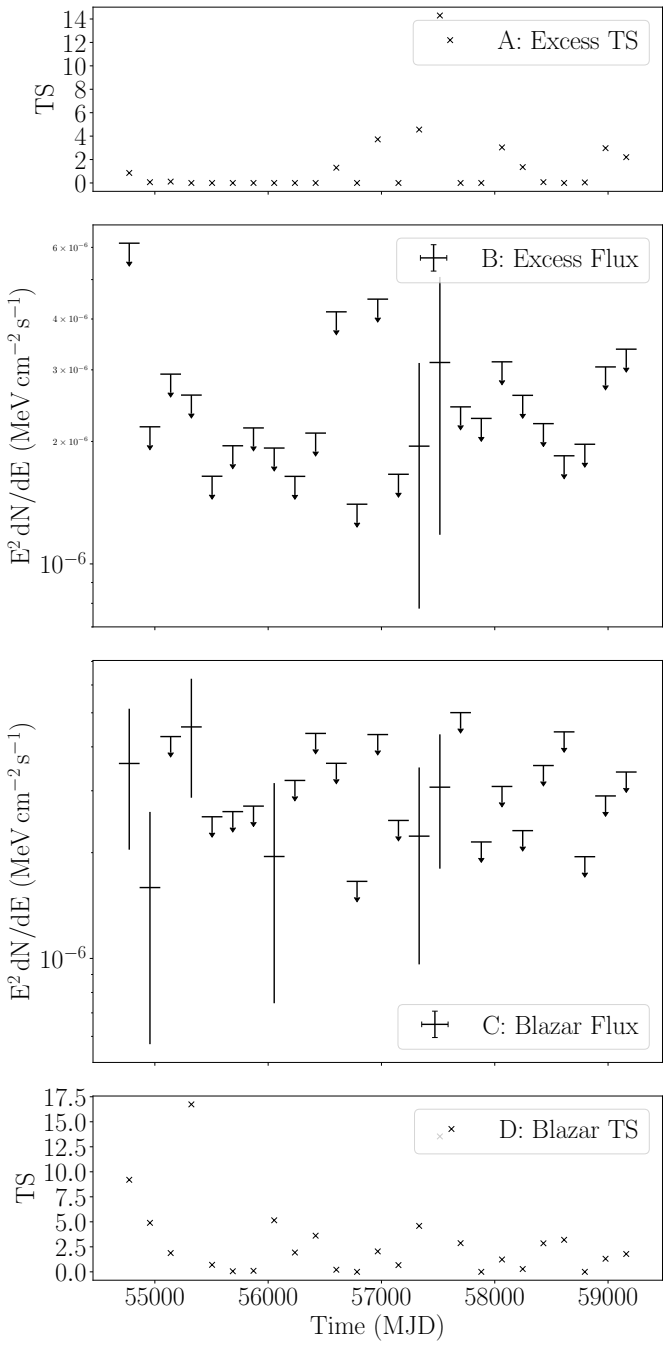

Figure C.6: Panels B and A show the γ-ray flux and associated TS values of these flux points for the excess coincident with the optical position of 1WGA J0648.0-4419. Panels C and D show the γ-ray flux and associated TS values of these flux values for the nearby blazar 4FGL J0647.7-4418, without the excess in the model. We use approximately 6 month bins in each of these light-curves, and 95% confidence upper limits on flux are used for any bin where the corresponding TS value is less than 4.

confusion with this blazar; temporal variability is used to test whether this is the case.

A similar occurrence of source confusion between a γ-ray excess at the position of an X-ray binary (in this case V404 Cygni), and a blazar is dealt with in Chapter 4, where the apparent γ-ray excess was actually originating from a nearby flaring blazar. Given that I measure only two γ-ray flux points in the 6-month binned light-curve of the 1WGA06 excess, I remove this excess from the model and generate a light-curve of the blazar to see whether these γ-ray flux points would otherwise be attributed to the blazar. If this is the case, then the excess at the position of 1WGA06 is not independent of the blazar, and source confusion is occurring. Figure C.6 shows both the light-curve of the 1WGA06 excess and the light-curve of the blazar. Given that there are only two γ-ray flux measurements amongst an otherwise complete set of upper limits for the excess, and there are corresponding flux points in the light-curve of the blazar, the γ-ray excess coincident with 1WGA06 is likely due to source confusion with the blazar.

C.5 AX J1740.1-2847

AX J1740.1-2847 (henceforth AX17) is a HMXB system with a long-period pulsar (Sakano et al., 2000) in orbit around an unknown companion star (Kaur et al., 2010). Over the entire observation window, I find a γ-ray excess coincident with the position of AX17 with a TS of 7.17, giving a z-score of 2.7σ. Across the 6 month binned light-curve I identify 5 bins with TS > 4, with the peak TS being 12.8 (3.6 σ). This γ-ray excess is very likely due to source confusion given that the nearest sources are 4FGL J1740.4-2850 (TS = 100 and an angular offset from AX17 of 0.082°) and 4FGL J1739.7-2836 (TS = 93.9, offset 0.218°). Neither of these sources has any association with sources at other wavelengths. The primary source confusion counterpart for the γ-ray excess is likely to be 4FGL J1740.4-2850, with an angular offset that is less than one bin width. This presents a similar case

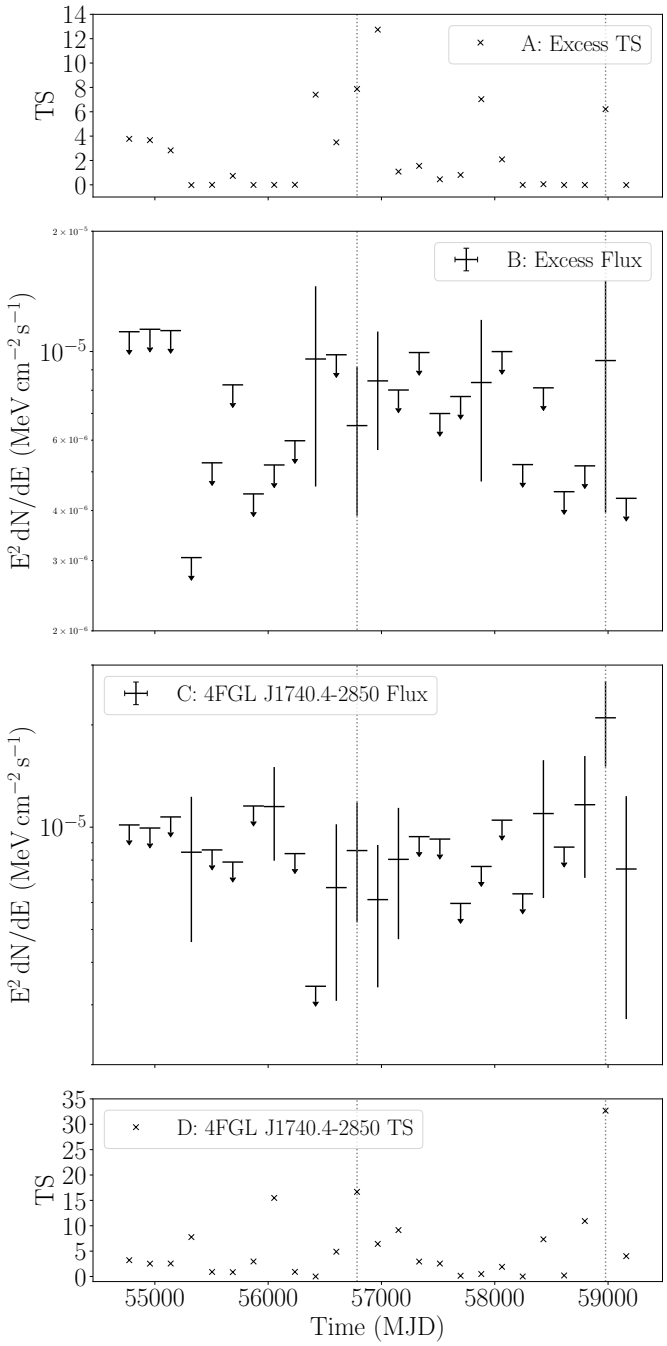

Figure C.7: Panels B and A show the γ-ray flux and associated TS values of these flux points for the excess coincident with the optical position of AX J1740.1-2847. Panels C and D show the γ-ray flux and associated TS values of these flux values for the nearby γ-ray source 4FGL J1740.4-2850, without the excess in the model. We use approximately 6 month bins in each of these light-curves, and 95% confidence upper limits on flux are used for any bin where the corresponding TS value is less than 4. The grey dotted lines indicate bins where source confusion between the 4FGL source and γ-ray excess are likely.

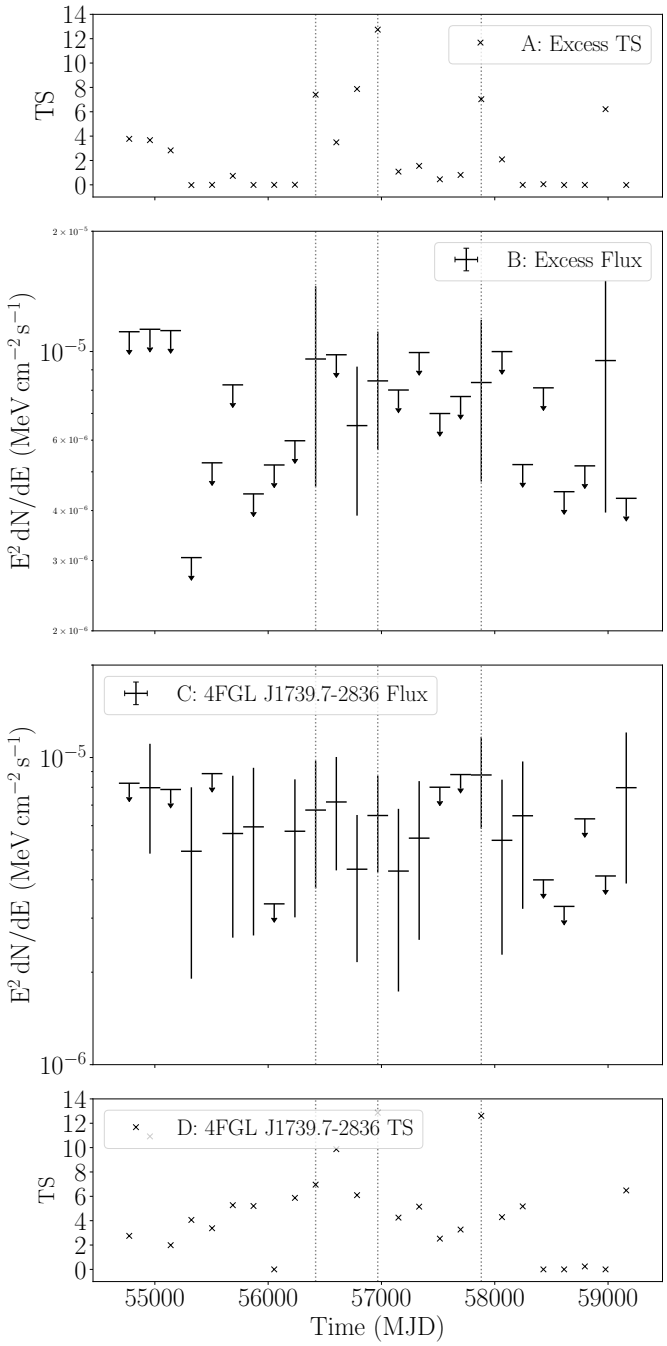

Figure C.8: Panels B and A show the γ-ray flux and associated TS values of these flux points for the excess coincident with the optical position of AX J1740.1-2847. Panels C and D show the γ-ray flux and associated TS values of these flux values for the nearby γ-ray source 4FGL J1739.7-2836, without the excess in the model. We use approximately 6 month bins in each of these light-curves, and 95% confidence upper limits on flux are used for any bin where the corresponding TS value is less than 4. The grey dotted lines indicate bins where source confusion between the 4FGL source and γ-ray excess are likely.

to 1WGA06, dealt with in Section C.4, where I establish that the γ-ray excess is not independent of its nearest 4FGL neighbour. We calculate the 6 monthly binned light-curves of the AX17 excess and 4FGL J1740.4-2850, shown in Figure C.7, and also 4FGL J1739.7-2836 (shown with the AX17 excess) in Figure C.8. Unlike 1WGA06, source confusion in this case cannot be attributed to a single source, but rather to contamination from both nearby sources.

Figures C.7 and C.8, show that the bins from the γ-ray excess where a flux is measured (as opposed to an upper limit) typically correlate with an enhancement in the TS values of one of the two nearby 4FGL sources. In particular, four of the five bins with measured γ-ray flux in the excess light-curve correlate in time with the two most significant bins from the 4FGL sources. These are indicated by the dotted grey lines. The evidence suggests that the γ-ray excess is not independent of either of its neighbouring sources, and therefore does not represent a legitimate detection of γ-rays from AX17.

C.6 H 1833-076

H 1833-076 (also known as Sct X-1 (Makino et al., 1988) and henceforth referred to as H18) is a high mass X-ray binary system, thought to consist of an accreting pulsar and red supergiant donor star (Kaplan et al., 2007). We identify a γ-ray excess coincident with the position of H18 with an angular offset from the X-ray position of H18 of 0.169°. This excess has a TS of 29.2 and a 95% positional uncertainty of 0.175°. Given that the position of this excess lies right at the edge of the positional uncertainty bound, I localise its position to improve the uncertainty. Using the `localize` algorithm, I find a best fit position for the excess of $\mathrm{LII} = 24.5019° \pm 0.0266°$, $\mathrm{BII} = -0.0371° \pm 0.0325°$ with an overall 95% positional uncertainty of 0.0717°. Given the shift in excess position and smaller, improved uncertainty, the γ-ray excess is no longer coincident with the position of H18 and I therefore believe it is unlikely to represent γ-ray emission from this X-ray binary.

C.7 GS 1839-04

GS 1839-04 (henceforth referred to as GS18) is an X-ray binary system with an unknown accretor and unknown companion star. We observe a γ-ray excess identified by the `gta.find_sources` algorithm coincident with the position of GS18 which is designated PS J1842.0-0418. This has a TS value of 17.8 and an angular offset from the position of GS18 of 0.147°, although the 95% positional uncertainty around PS J1842.0-0418 is unusually large at 1.01°. Contained within this uncertainty region are 7 4FGL sources, with the nearest neighbours to PS J1842.0-0418 being the unidentified source 4FGL J1842.5-0359c (TS = 318 and an angular offset from the position of GS18 of 0.498°) and 4FGL J1840.8-0453e, the young supernova remnant Kes 73 (Gotthelf and Vasisht, 1997) (TS = 1050, offset 0.501°). Given that the positional uncertainty of PS J1842.0-0418 is so large, encompasses numerous, luminous γ-ray sources and that PS J1842.0-0418 is extended, I localise its position, even though the TS of PS J1842.0-0418 is below 25*.

Figure C.9 shows a TS map centered on GS18, highlighting the extent of the PS J1842.0-0418 uncertainty and the sources within it. After localising the γ-ray emission from PS J1842.0-0418 I find that the 95% positional uncertainty shrinks by approximately an order of magnitude to 0.1234°. As shown by Figure C.9, this means that the X-ray position of GS18 is no longer within the 95% positional uncertainty of PS J1842.0-0418 and therefore PS J1842.0-0418 is very unlikely to represent γ-ray emission from GS18.

C.8 SAX J2103.5+4545

SAX J2103.5+4545 (henceforth SAX21) is a pulsar (Hulleman et al., 1998) accretor in orbit with a Be star companion (Reig et al., 2005) with an orbit of 12.7 days

*Usually we lack photon statistics for more advanced analysis methods at such low source significance.

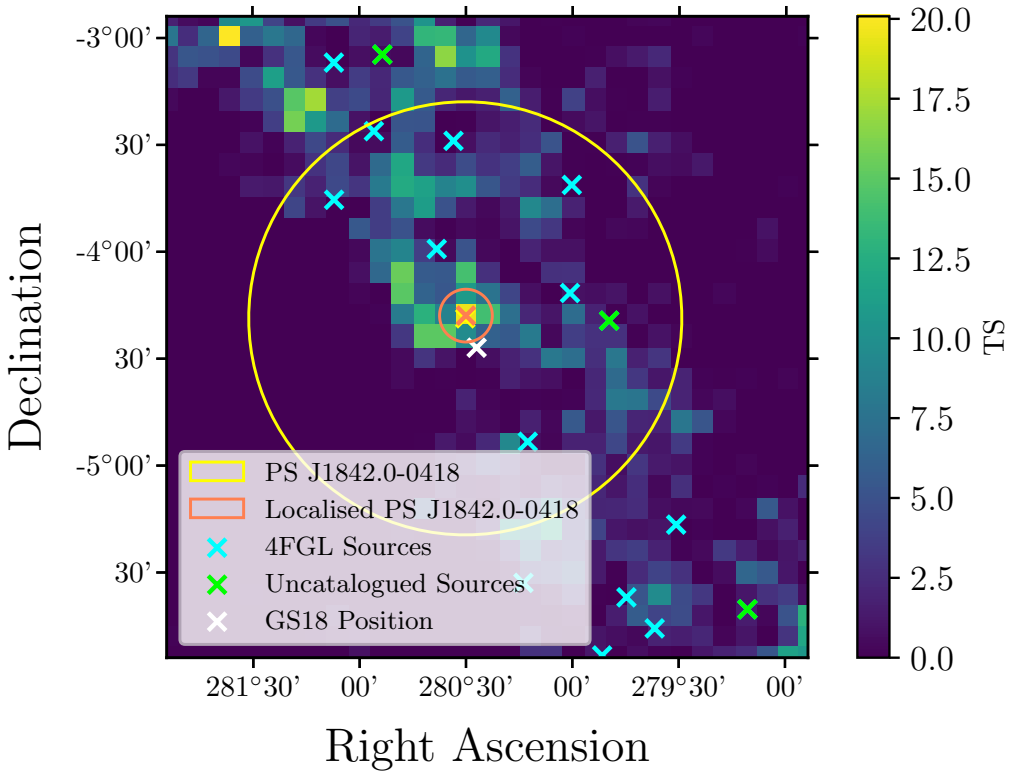

Figure C.9: The TS map of the central 3° of the GS 1839-04 ROI across the full 12.5 year observation time. Here, the positions of the closest 4FGL sources are indicated by blue crosses, whilst the positions of sources identified with the `gta.find_sources` algorithm are indicated by green crosses. The centroid (shown with a cross) and 95% positional uncertainty (shown with a circle) of PS J1842.0-0418 are given in yellow (before source localisation) and orange (after source localisation). The position of PS J1842.0-0418 barely shifts with localisation hence the orange and yellow markers overlap. The position of GS 1839-04 itself is indicated by the white cross, and is no longer spatially coincident with PS J1842.0-0418 following localisation. This TS map is generated after ROI optimization and fit, but before a point source for GS 1839-04 is fitted to the model, to highlight the spatial coincidence between the excess and the position of GS 1839-04. Bin widths are 0.1° across.

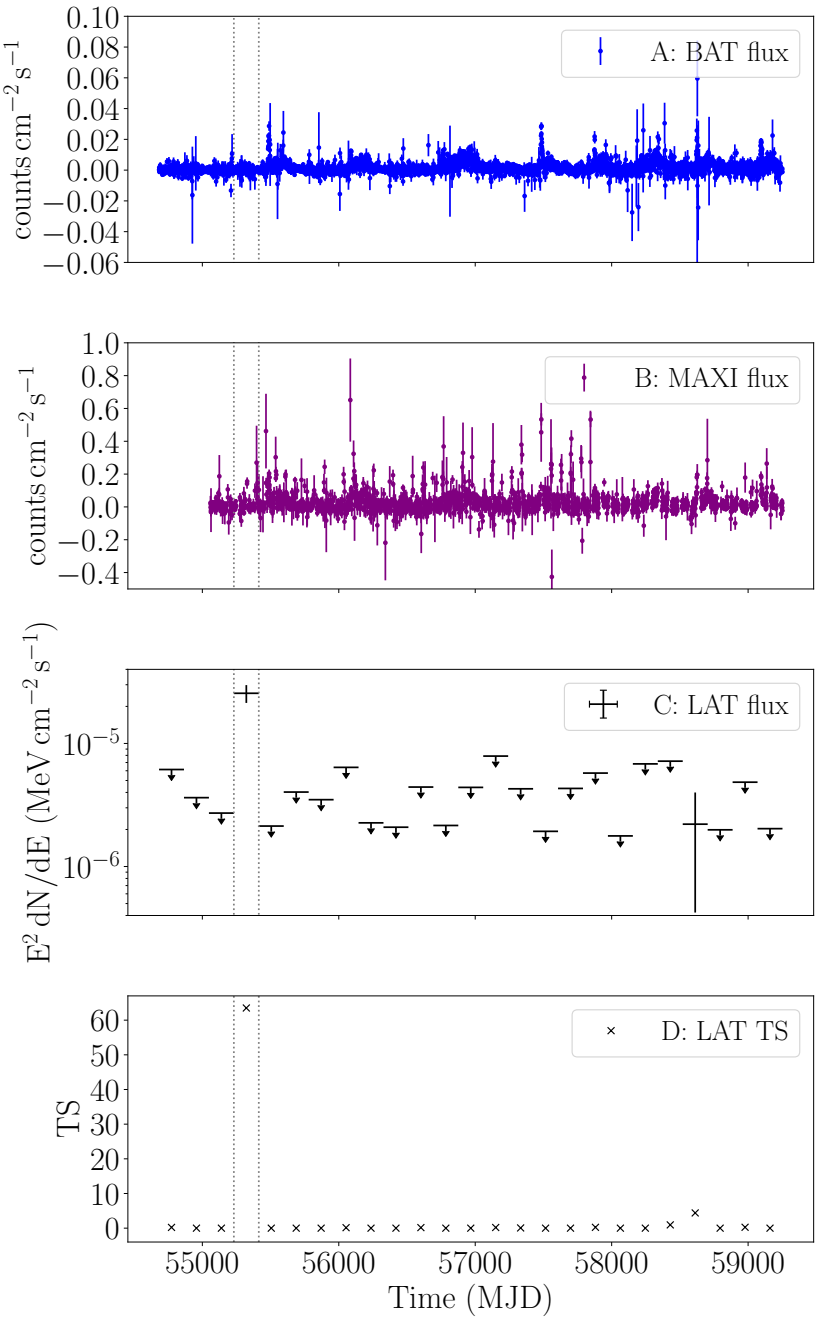

Figure C.10: The *Swift*-BAT and MAXI daily binned light-curves of SAX J2103.5+4545 are shown in Panels A and B respectively, with the 6-month energy flux measurements and TS values of the coincident γ-ray excess shown in Panels C and D respectively. We place 95% confidence limits on any *Fermi*-LAT energy flux bins with TS < 4. The vertical dashed lines indicate the beginning and end of the 6-month period when there is a significant enhancement in the γ-ray flux.

(Baykal et al., 2000). SAX21 is the closest known neutron star-Be star system to Earth (Blay et al., 2006). SAX21 is a well-studied system, with outbursts well documented since its discovery, the most recent of which was in 2019 (Ducci et al., 2019), and persistent monitoring with *Swift*-BAT meaning a wealth of multi-wavelength data is available for the source. Unlike the majority of X-ray binaries I report on here, I identify no persistent γ-ray excess coincident with the position of SAX21. However, I do identify significant transient emission in the 6-monthly binned light-curve.

Figure C.10 shows the X-ray light-curve of SAX21 together with the γ-ray light-curve generated at the position of SAX21. We measure 2 flux points, one with TS = 63.5 ($z = 8.0\sigma$) and the other with TS = 4.39 ($z = 2.1\sigma$). Given that there are 25 bins, one would expect one of these to be of 2σ in a simply noise dominated distribution, however given the significance of the 8σ bin, there is no statistical doubt that this represents a flaring γ-ray point source of some morphology.

To test whether this transient point source represents γ-ray emission from SAX21, or another undiscovered source, I perform a full analysis using the same parameters as detailed in Table 5.1, with the exception that the time range now exclusively encompasses the bin containing the 8.0σ γ-ray flare (MJD 55231 - MJD 55414). We then fit a γ-ray source to the position of SAX21 and localise its position. We then generate a TS map of the ROI, and plot the positions of all known sources, together with the position of SAX21 and the now localised position of the γ-ray excess, and its associated 95% positional uncertainty.

Figure C.11 shows the TS map of the SAX21 ROI during the 6 month period of the γ-ray flare, which is the dominant feature of the plot. Whilst the white cross indicates the position of the binary itself, the orange cross indicates the localised position of the γ-ray flare, with the orange circle representing the bound of the 95% positional uncertainty of the flare. As can be seen, SAX21 lies outside the positional uncertainty bound following localisation, so it is unlikely that SAX21 is the cause of this flare.

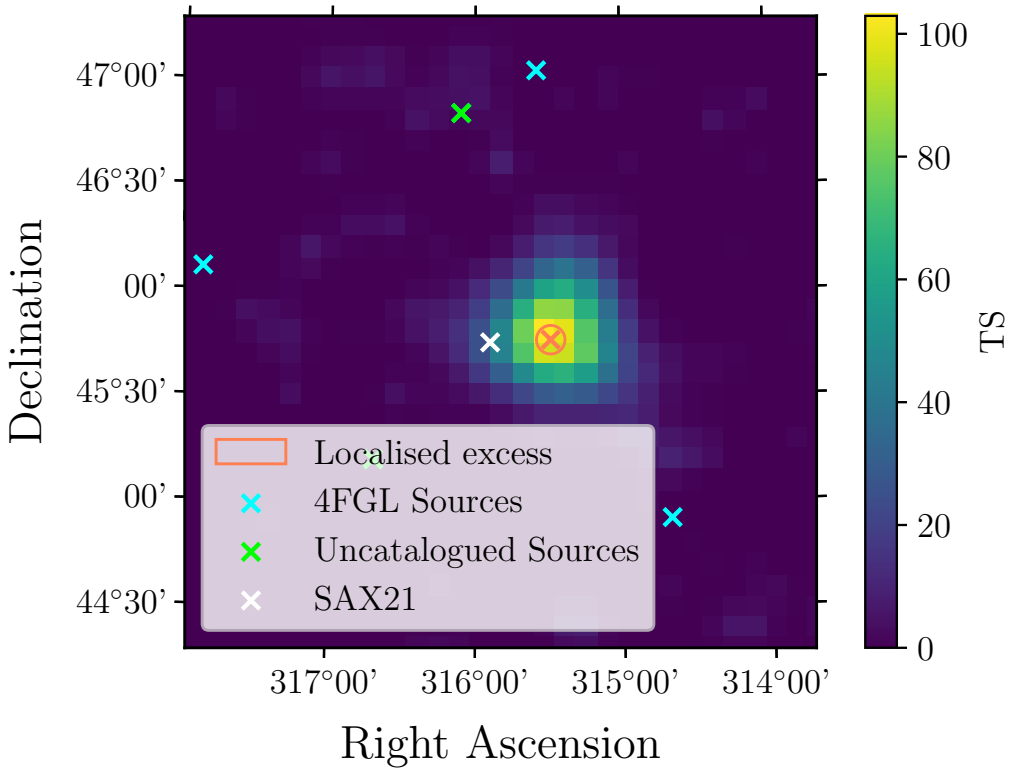

Figure C.11: The TS map of the central 3° of the SAX J2103.5+4545 ROI, after my likelihood fit and the `gta.find_sources` algorithm, over the MJD 55231 - MJD 55414 period. The blue crosses refer to the positions of 4FGL sources and the green crosses refer to the positions of uncatalogued sources. The white cross indicates the catalogued location of SAX21, whereas the orange cross and circle refer to the central position of the excess, and 95% uncertainty after localisation. Our spatial bins have an angular width of 0.1°.

Figure C.12: The eleventh labour of Heracles, stealing three of the golden apples of the Hesperides. By Lucas Cranach the Elder (After 1537).

Appendix D

Low Mass X-ray Binary Survey Sample

The following section provides a table of each LMXB included in the survey; the binary name column gives the X-ray name of each X-ray binary included in the survey from the Liu et al. catalogue, and the alternate name column gives either the optical name of the system from Liu et al. or the most commonly used name for the system (i.e. Cir X-1). The (GC) tag appended to an alternate name indicates that this system is located with LII and BII are the Galactic coordinates of the system used in our data analysis; the position type gives the waveband from which the coordinates were taken (for example, O corresponds to the coordinates of the optical counterpart, X to the X-ray, etc.). The period refers to the orbital period of the binary system measured in days; where no binary period is known a value of 0 is shown. The Flux U.L value refers to the 95% upper confidence limit on energy flux (with units of MeV cm^{-2} $s^{-}1$) obtained from the position of each HMXB where no measurement of a γ-ray flux is made. Where a measurement of energy flux is made, these are shown in Tables 5.4 and 5.5.

Binary Name	Alt. Name	LII	BII	Position Type	Period	Flux U.L. ($MeV\,cm^{-2}\,s^{-}1$)
SAX J1603.9-7753		312.42847	-18.73093	X	0.0	9.64×10^{-9}
2A 0521-720		283.09949	-32.69058	O	0.34	4.09×10^{-8}
RX J0532.7-6926		279.93933	-32.15468	X	0.0	7.78×10^{-8}
4U 1254-69	GR MUS	303.48189	-6.42396	O	0.1638	1.62×10^{-8}
GS 1124-684	GU MUS	295.30054	-7.07259	O	0.4325	7.79×10^{-8}
EXO 0748-676	UY VOL	279.97535	-19.81065	O	0.1592	1.94×10^{-8}
4U 1626-67	KZ TRA	321.78757	-13.0924	O	0.0288	2.88×10^{-8}
GS 1354-64	BW CIR	309.97775	-2.77969	O	2.5446	7.51×10^{-8}
2S 0921-630	V395 CAR	281.83558	-9.3385	O	9.0083	1.03×10^{-7}
SAX J1324.5-6313		306.63996	-0.5895	X	0.0	1.53×10^{-7}
4U 1543-624		321.75535	-6.33711	O	0.0126	3.59×10^{-8}
4U 1323-62		307.02849	0.45562	IR	0.1221	N.A.
1A 1524-61	KY TRA	320.31927	-4.42716	O	0.0	2.53×10^{-8}
4U 1556-60	LU TRA	324.13906	-5.9316	O	0.3792	4.27×10^{-8}
1A 1246-588		302.70257	3.78354	O	0.0	1.05×10^{-7}
3A 1516-569	Cir X-1	322.11848	0.03747	R	16.6	N.A.
XTE J1550-564	V381 NOR	325.88255	-1.82696	O	1.5521	4.17×10^{-8}
AX J1538.3-5541		324.81509	-0.32476	X	0.0	1.29×10^{-7}
4U 0919-54		275.85294	-3.84452	X	0.0	1.67×10^{-8}
4U 1636-536	V801 ARA	332.91489	-4.81797	O	0.1583	1.42×10^{-7}
IGR J11321-5311		291.08745	7.85411	X	0.0	5.11×10^{-8}
4U 1608-52	QX NOR	330.92634	-0.85047	O	0.5371	9.20×10^{-8}
1E 161348-5055.1		332.42893	-0.3739	X	0.2779	N.A.
XTE J1650-500		336.71827	-3.42707	X	0.3179	5.83×10^{-8}
4U 1624-49		334.91501	-0.26313	X	0.8704	1.78×10^{-7}
4U 1659-487	V821 ARA	338.93936	-4.3267	O	1.7558	1.67×10^{-7}
GRS 1632-477		336.86977	-0.34693	X	0.0	1.96×10^{-7}
4U 1543-47	IL LUP	330.91866	5.42579	O	1.1167	6.17×10^{-8}

Binary Name	Alt. Name	LII	BII	Position Type	Period	Flux U.L. (MeV $cm^{-2} s^{-1}$)
IGR J17269-4737		342.2033	-6.92301	O	0.0	8.84×10^{-8}
4U 1630-47		336.91127	0.25023	R	0.0	3.08×10^{-7}
XTE J1701-462		340.81331	-2.48835	O	0.0	1.95×10^{-7}
4U 1642-45	GX 340	339.58824	-0.07932	R	0.0	5.55×10^{-7}
GRS 1009-45	MM VEL	275.87846	9.3458	O	0.285	2.23×10^{-8}
4U 1735-444	V926 SCO	346.0543	-6.99387	O	0.1938	1.35×10^{-7}
4U 1705-44		343.32081	-2.34191	X	0.0	3.82×10^{-7}
4U 1702-429		343.88684	-1.31831	X	0.0	2.68×10^{-7}
1M 0836-425		261.95449	-1.12401	X	0.0	1.97×10^{-7}
SAX J1719.6-4254		345.43736	-3.2187	X	0.0	1.82×10^{-7}
4U 1708-40		346.32902	-0.92949	X	0.0	N.A.
1RXS J171824.2-402934		347.27684	-1.65162	X	0.0	2.62×10^{-7}
4U 0513-40	NGC 1851 (GC)	244.50988	-35.03673	O	0.0	N.A.
GRO J1655-40	V1033 SCO	344.98189	2.45597	O	2.62	N.A.
SAX J1711.6-3808		348.44071	0.79872	X	0.0	8.99×10^{-8}
XTE J1723-376		350.18357	-0.87487	X	0.0	3.09×10^{-7}
SAX J1712.6-3739		348.94117	0.91959	X	0.0	1.91×10^{-7}
2A 1822-371	V691 CRA	356.85012	-11.2908	O	0.2321	N.A.
4U 1746-37		353.53134	-5.00503	O	0.215	1.14×10^{-7}
SAX J1808.4-3658	V4580 SGR	355.38519	-8.14838	R	0.0839	5.86×10^{-8}
IGR J17098-3628		349.55377	2.07429	O	0.0	1.74×10^{-7}
3A 1702-363	V1101 SCO	349.10363	2.74841	R	0.9375	1.10×10^{-7}
XTE J1743-363		353.38012	-3.40891	X	0.0	2.47×10^{-7}
1A 1744-361		354.11997	-4.19207	R	0.0675	8.49×10^{-8}
X1724-356		352.23043	-0.46125	X	0.0	4.33×10^{-7}
2S 1711-339		352.06037	2.74577	X	0.0	N.A.
4U 1728-34		354.3034	-0.15072	R	0.0	1.84×10^{-7}
4U 1755-33	V4134 SGR	357.21545	-4.87234	O	0.1833	1.35×10^{-7}

Binary Name	Alt. Name	LII	BII	Position Type	Period	Flux U.L. ($MeV\,cm^{-2}\,s^{-}1$)
XTE J1814-338		358.74609	-7.58849	O	0.1781	N.A.
MXB 1730-335	LIL 1 (GC)	354.84099	-0.16039	R	0.0	N.A.
SLX 1746-331		356.80469	-2.97378	X	0.0	N.A.
XTE J1817-330		359.81722	-7.99557	R	0.0	6.25×10^{-8}
XB 1832-330	NGC 6652 (GC)	1.53086	-11.37056	X	0.0	N.A.
IGR J17254-3257		354.27986	1.47225	X	0.0	1.31×10^{-7}
GPS 1742-326		356.7769	-1.93202	X	0.0	3.12×10^{-7}
XTE J1755-324		358.03926	-3.63143	X	0.0	1.91×10^{-7}
1E 1746.7-3224		357.50066	-2.62334	X	0.0	3.00×10^{-7}
4U 1705-32		352.78003	4.6719	X	0.0	6.10×10^{-8}
H1743-322		357.25497	-1.83292	IR	0.0	3.34×10^{-7}
1H 1715-321		354.12765	3.06438	X	0.0	1.63×10^{-7}
XTE J1720-318		354.62374	3.1012	R	0.0	2.44×10^{-7}
4U 1456-32	V822 CEN	332.2426	23.88114	O	0.6292	2.70×10^{-8}
SAX J1752.3-3138		358.44419	-2.64018	X	0.0	4.22×10^{-7}
XTE J0929-314		260.1051	14.21456	O	0.0304	5.35×10^{-8}
GRS 1747-312	TER 6 (GC)	358.57278	-2.16292	X	0.515	3.04×10^{-7}
GRS 1730-312		356.7252	0.94421	X	0.0	3.58×10^{-8}
GRS 1737-31		357.58779	-0.09945	X	0.0	4.07×10^{-7}
4U 1724-307	TER 2 (GC)	356.3201	2.29776	X	0.0	1.76×10^{-7}
XTE J1751-305		359.18191	-1.91201	X	0.0296	1.38×10^{-7}
KS 1739-304		358.32749	-0.29242	X	0.0	2.63×10^{-7}
SLX 1732-304	TER 1 (GC)	357.55807	0.99114	R	0.0	7.66×10^{-8}
4U 1820-30	NGC 6624 (GC)	2.78816	-7.91341	R	0.0079	9.82×10^{-8}
SLX 1744-300		359.25653	-0.91103	X	0.0	N.A.
SLX 1744-299		359.29618	-0.88915	X	0.0	4.22×10^{-7}
MXB 1659-298	V2134 OPH	353.82704	7.26563	O	0.2963	4.19×10^{-8}
1E 1740.7-2942		359.11595	-0.10575	R	12.73	3.66×10^{-8}

Binary Name	Alt. Name	LII	BII	Position Type	Period	Flux U.L. (MeV $cm^{-2} s^{-1}$)
1A 1742-294		359.55897	-0.38817	X	0.0	N.A.
GC X-2		359.55868	-0.26855	X	0.0	3.32×10^{-8}
GC X-4		359.36663	0.08189	X	0.0	4.38×10^{-8}
XTE J1807-294		1.9353	-4.27258	X	0.0278	3.50×10^{-8}
IGR J17285-2922		357.62965	2.92262	X	0.0	1.09×10^{-7}
KS 1741-293		359.55538	-0.0751	X	0.0	7.84×10^{-8}
1E 1742.7-2902		359.92741	-0.11131	X	0.0	4.75×10^{-7}
SAX J1750.8-2900		0.45269	-0.94772	X	0.0	4.17×10^{-7}
AX J1745.6-2901		359.92134	-0.04375	X	0.35	N.A.
1A 1742-289		359.92926	-0.04233	R	0.3482	8.61×10^{-7}
GRS 1741.2-2859		359.79826	0.18336	X	0.0	N.A.
CXOGC J174540.0-290031		359.94354	-0.04655	X	0.3292	N.A.
2E 1742.5-2858		359.94929	-0.04701	X	0.0	N.A.
1E 1742.2-2857		359.94037	0.00715	X	0.0	N.A.
1E 1742.8-2853		0.05876	-0.05942	X	0.0	8.46×10^{-7}
GRS 1741.9-2853		359.95276	0.12016	X	0.0	N.A.
1E 1743.1-2852		0.11521	-0.11046	X	0.0	8.13×10^{-7}
1E 1742.9-2852		0.09444	-0.06032	X	0.0	7.34×10^{-7}
SAX J1747.0-2853		0.2073	-0.23849	X	0.0	2.28×10^{-7}
1E 1742.9-2849		0.13299	-0.07658	X	0.0	7.35×10^{-7}
1E 1742.5-2845		0.14296	0.06288	X	0.0	8.79×10^{-7}
GRO J1744-28		0.04447	0.30155	X	11.8342	2.42×10^{-7}
1E 1743.1-2843		0.26079	-0.02871	X	0.0	4.53×10^{-7}
1RXS J175229.0-282951		1.11929	-1.0275	X	0.0	1.59×10^{-7}
XTE J1739-285		359.71403	1.29805	X	0.0	3.90×10^{-7}
4U 1735-28		359.57332	1.55547	X	0.0	2.89×10^{-7}
XTE J1748-288		0.6756	-0.22208	R	0.0	N.A.
IGR J17497-2821		0.95317	-0.45278	X	0.0	2.21×10^{-8}

Binary Name	Alt. Name	LII	BII	Position Type	Period	Flux U.L. ($MeV\,cm^{-2}\,s^{-}1$)
SLX 1737-282		359.9731	1.24806	X	0.0	3.04×10^{-7}
XMMU J174716.0-281045		0.83424	0.08336	X	0.0	1.56×10^{-7}
XTE J1710-281		356.3571	6.922	X	0.1367	6.47×10^{-8}
GRS 1739-278		0.67213	1.17568	R	0.0	3.10×10^{-7}
GRO J1735-27		0.16084	2.59051	X	0.0	2.40×10^{-7}
IGR J17473-2721		1.55296	0.5104	IR	0.0	1.55×10^{-7}
SLX 1735-269		0.79612	2.40017	X	0.0	2.60×10^{-7}
XTE J1709-267		357.47254	7.91173	X	0.0	1.83×10^{-7}
GX 3+1		2.29377	0.79367	X	0.0	3.12×10^{-7}
SAX J1810.8-2609		5.19724	-3.43108	X	0.0	1.03×10^{-7}
KS 1731-260		1.07296	3.6525	X	0.0	1.64×10^{-7}
GRS 1758-258		4.50779	-1.36106	R	18.45	2.32×10^{-8}
4U 1705-250	V2107 OPH	358.58749	9.05683	O	0.5225	2.33×10^{-8}
4U 1758-25		5.07783	-1.01822	O	0.0	2.56×10^{-7}
GRO J1719-24	V2293 OPH	0.14233	6.99082	R	0.6125	N.A.
HETE J1900.1-2455		11.3049	-12.87278	O	0.0579	1.00×10^{-7}
AX J1824.5-2451	M28 (GC)	7.81085	-5.56185	X	0.0	1.36×10^{-7}
EXO 1745-248		3.83948	1.68529	X	0.0	2.74×10^{-7}
3A 1728-247	V2116 OPH	1.93708	4.79496	O	1160.8	1.65×10^{-7}
2S 1803-245		6.13831	-1.90747	X	0.0	1.26×10^{-7}
XTE J1818-245		7.44267	-4.19143	O	0.0	3.34×10^{-8}
SAX J1753.5-2349		5.30047	1.10162	X	0.0	3.51×10^{-7}
GS 1826-238	V4634 SGR	9.27238	-6.08779	O	0.087	1.79×10^{-7}
SAX J1806.5-2215		8.15099	-0.71197	X	0.0	5.89×10^{-8}
4U 1730-220		4.46713	5.88718	X	0.0	1.31×10^{-7}
IGR J17597-2201		7.56999	0.76988	X	0.0	3.28×10^{-7}
EXO 1747-214		6.99756	2.95099	X	0.0	1.69×10^{-7}
4U 1758-20		9.07679	1.15374	X	0.0	4.35×10^{-8}

Binary Name	Alt. Name	LII	BII	Position Type	Period	Flux U.L. ($MeV\,cm^{-2}\,s^{-}1$)
SAX J1805.5-2031		9.55424	0.34016	X	0.0	4.32×10^{-8}
SAX J1748.9-2021		7.7286	3.80368	X	0.0	1.56×10^{-7}
XMMU J181227.8-181234		12.35773	0.03367	X	0.0	N.A.
4U 1811-17	GX 13+1	13.51653	0.10636	R	24.0667	2.73×10^{-7}
4U 1728-16	V2216 OPH	8.51285	9.03773	O	0.175	4.54×10^{-8}
H 1617-155	V818 SCO	359.09423	23.78443	O	0.7875	2.30×10^{-8}
4U 1813-14		16.43218	1.27764	R	0.0	2.31×10^{-7}
4U 1812-12		18.03273	2.39779	O	0.0	3.82×10^{-7}
SAX J1828.5-1037		20.862	0.20352	X	0.0	5.85×10^{-7}
4U 1850-087		25.35538	-4.31984	X	0.0143	2.65×10^{-7}
XTE J2123-058	LZ AQR	46.48289	-36.19943	X	0.2483	5.44×10^{-8}
4U 1916-05	V1405 AQL	31.35776	-8.46359	X	0.0346	3.23×10^{-8}
XB 1940-04		35.30079	-13.16261	X	0.0	1.72×10^{-8}
EXO 1846-031		29.60894	-0.36243	X	0.0	4.29×10^{-7}
SWIFT J1753.5-0127		24.89768	12.18596	R	0.0	7.93×10^{-8}
1A 0620-00	V616 MON	209.95629	-6.53988	R	0.3229	4.22×10^{-8}
4U 1823-00		29.93908	5.79262	X	0.1333	2.24×10^{-7}
4U 1905+000		35.02446	-3.70715	O	0.0	9.71×10^{-8}
4U 1908+005	V1333 AQL	35.71839	-4.14297	O	0.7896	1.02×10^{-7}
3A 1837+049	MM SER	36.11822	4.84218	R	0.0	8.51×10^{-8}
XTE J1856+053		38.26928	1.27244	X	0.0	3.92×10^{-7}
IGR J18539+0727		39.84724	2.84551	X	0.0	2.28×10^{-7}
4U 0614+091	V1055 ORI	200.87741	-3.36308	O	2.0833	3.67×10^{-8}
XTE J1908+094		43.26342	0.43398	R	0.0	1.60×10^{-7}
GRS 1915+105	V1487 AQL	45.36573	-0.21909	R	33.5	N.A.
4U 1957+11	V1408 AQL	51.30869	-9.33049	O	0.3887	2.12×10^{-8}
CXO J212958.1+121002	M15 (GC)	65.01218	-27.31153	X	0.0157	N.A.
4U 2129+12	M 15 (GC)	65.01298	-27.31226	R	0.7125	N.A.

Binary Name	Alt. Name	LII	BII	Position Type	Period	Flux U.L. ($MeV\,cm^{-2}\,s^{-}1$)
SAX J1818.7+1424		42.32349	13.6516	X	0.0	2.37×10^{-8}
4U 1918+15		49.26911	0.44045	X	0.0	N.A.
XTE J1859+226	V406 VUL	54.04612	8.6075	O	0.3817	3.43×10^{-8}
SAX J0840.7+2248		202.411	33.58083	X	0.0	3.78×10^{-8}
4U 1700+24	HD 154791	45.15173	32.99065	O	404.0	3.42×10^{-8}
GS 2000+25	QZ VUL	63.36658	-2.99892	O	0.3442	8.45×10^{-8}
1E 1603.6+2600	UW CRB	42.75031	46.77855	O	0.0771	3.81×10^{-8}
3A 1954+319		68.39196	1.92693	O	0.0	1.19×10^{-7}
GRO J0422+32	V518 PER	165.88079	-11.91252	O	0.2122	8.17×10^{-8}
4U 0042+32		121.33767	-29.82994	X	0.0	6.97×10^{-8}
GS 2023+338	V404 CYG	73.119	-2.09119	O	6.475	1.20×10^{-7}
2A 1655+353	Her X-1	58.14908	37.52298	O	1.7	N.A.
XTE J2012+381		75.38838	2.24694	O	0.0	3.52×10^{-8}
4U 2142+38	V1341 CYG	87.32848	-11.31627	O	9.8417	3.74×10^{-8}
4U 2129+47	V1727 CYG	91.57742	-3.03653	O	0.2183	2.04×10^{-8}
XTE J1118+480	KV UMA	157.6605	62.32051	O	0.17	2.00×10^{-8}
SAX J2224.9+5421		102.56191	-2.60504	X	0.0	3.90×10^{-8}
IGR J00291+5934		120.09641	-3.1765	O	0.1025	2.07×10^{-8}
SWIFT J061223.0+701243.9		144.05455	22.20707	O	0.0125	2.04×10^{-8}

Appendix E

Low Mass X-ray Binaries in Globular Clusters

Numerous low mass X-ray binaries in the sample are within globular clusters, some of which are γ-ray emitting (for example M 15), and some of which are not known to be. Globular clusters are generally non-variable sources as their γ-ray emission primarily originates from pulsars within the cluster, and hence any variability could be indicative of emission from an LMXB within the cluster, rather than the wider cluster pulsar population.

The LMXBs within γ-ray emitting globular clusters are MXB 1730-335 in Liller 1, XB 1832-330 in NGC 6652, EXO 1745-248 in Terzan 5 and M 15 X-1 & X-2. None of these sources are known to be variable (given their variability indices in the 4FGL-DR3), which suggests that if the LMXBs contribute to the emission in these systems, they are not the dominant component. Additionally, a number of LMXBs are seen from globular clusters where there is no measured flux from the LMXB position (regardless of whether or not the globular cluster emits γ-rays) indicating no measurable γ-ray emission from the LMXB within. These are GRS 1747-312 in Terzan 6, 4U 1724-307 in Terzan 2, SLX 1732-304 in Terzan 1, 4U 1820-30 in NGC 6624 and AX J1824.5-2451 in M 28; upper limits for all of these LMXBs can be found in Appendix D.

Coordinates	RA(°)	Dec(°)
4U05 Optical Position	78.5267	-40.0439
PS J0514.1-4003	78.5400	-40.0625
Localised PS J0514.1-4003	78.5178 ± 0.0399	-40.0370 ± 0.03997

Table E.1: The optical positional coordinates of 4U 0513-40, the coordinates of PS J0514.1-4003 from the `find sources` algorithm, and the results of the localisation of this source (plus uncertainties) given in equatorial coordinates.

One LMXB within a globular cluster, 4U 0513-40 in NGC 1851, is found to have significant spatially coincident γ-ray emission, detailed below in Section E.1, although with the recent release of the 4FGL-DR3, the γ-ray source identified has been firmly associated with NGC 1851. Nonetheless, the analysis is still included for completeness.

E.1 4U 0513-40 in NGC 1851

4U 0513-40 (henceforth 4U05) (Clark et al. 1975 & Vidal and Freeman 1975) is an ultracompact X-ray binary consisting of a white dwarf donor, a neutron star accretor and an orbital period of 17 minutes (Zurek et al. 2009 & Juett and Chakrabarty 2005). 4U05 is located within the globular cluster NGC 1851, which itself is located off the Galactic plane. An uncatalogued γ-ray point source is observed with a very slight offset from the position of 4U05/NGC 1851 of 0.021° which is designated PS J0514.1-4003. PS J0514.1-4003 is a significant source of γ-rays with TS = 51.1 ($z = 7.1\sigma$), and the nearest catalogued γ-ray source is 4FGL J0521.8-3848 (the blazar PKS 0520-388), which has an angular offset from the position of 4U05/NGC 1851 of 1.946°, and a TS of 208 ($z = 14.4\sigma$). Given the separation from PS J0514.1-4003, source confusion with 4FGL J0521.8-3848 is not responsible for this γ-ray point source.

Given the significance of PS J0514.1-4003, localisation of the γ-ray emission is possible to further improve our knowledge of the sources position. We therefore use `localize` in order to find an improved positional fit for PS J0514.1-4003.

Table E.1 shows the results of this localisation; a very small adjustment is made to the position of PS J0514.1-4003, and the TS of the source increases slightly to 55.6 (7.5σ). The optical position of 4U05/NGC 1851 lies within the 67% (1σ) error radius of PS J0514.1-4003, indicating strong spatial coincidence between the γ-ray source and the binary and cluster. Neither low mass X-ray binaries nor globular clusters are extended sources when viewed with *Fermi*-LAT, however as PS J0514.1-4003 potentially represents a new system, it is important to test for spatial extension. We run `gta.extension` in order to test a radial disc model against the point source null hypothesis and find that the test statistic for this hypothesis test is 0, therefore firmly favouring the point source hypothesis over the extended source. We calculate a 95% upper confidence limit on radial extension of 0.110°. As a point source the spatial morphology of PS J0514.1-4003 resembles both the known globular cluster and X-ray binary populations when viewed with *Fermi*-LAT. Figure E.1 shows the spatial coincidence between the localised PS J0514.1-4003, and also it's point source nature.

In order to determine whether PS J0514.1-4003 is the counterpart to 4U05 or NGC 1851 (both of which can, in principle emit γ-rays), one may look at variability as an indicator. Globular clusters are non variable sources, with it being expected that the majority of their γ-ray emission comes from their pulsar populations (which themselves are non-variable).

Figure E.2 shows the γ-ray light-curve of PS J0514.1-4003 together with the X-ray light-curves of 4U05 with MAXI (soft X-ray, 2 - 20 keV) and with *Swift*-BAT (hard X-ray, 15 - 50 keV). There are no giant outbursts in the X-ray light-curves of 4U05, however there does appear to be variability on daily timescales in both X-ray light-curves. The γ-ray light-curve shows very little variability and is likely to be best fitted by a constant flux model, although the majority of bins are upper limits so it is not possible to reliably fit a model in this case. Given that the orbital period of 4U05 is 17 minutes, this is far too short a period to attempt to resolve phased γ-ray emission from PS J0514.1-4003.

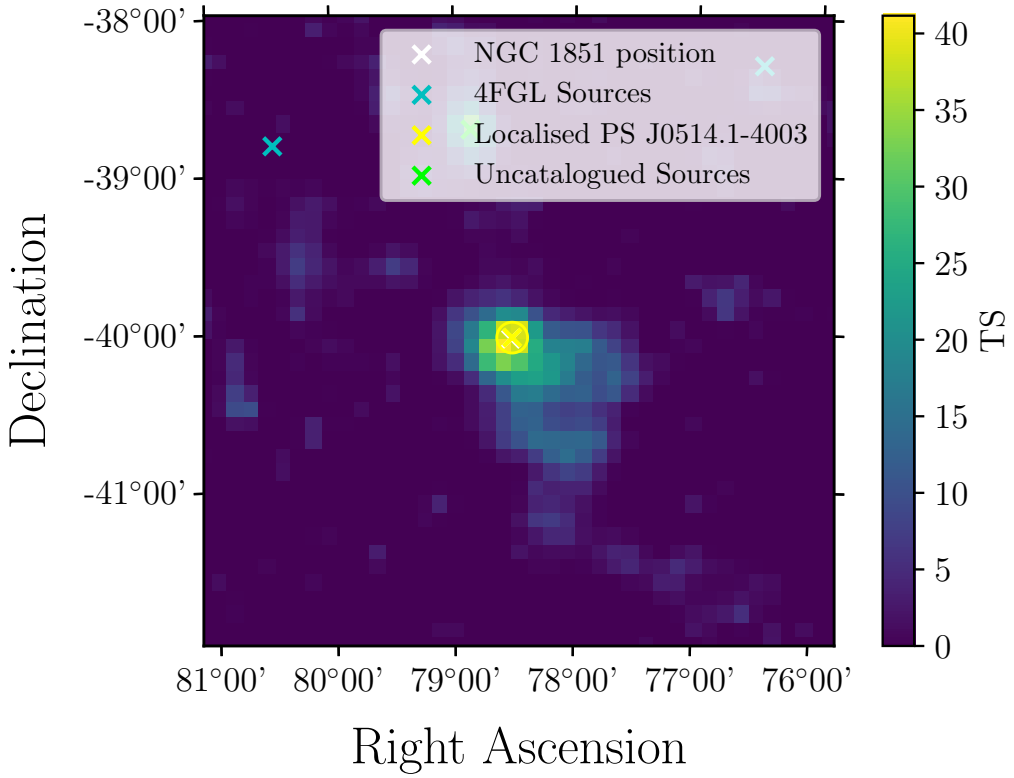

Figure E.1: The TS map of the central 4° of the 4U 0513-40 ROI over the full mission time. Here, the positions of the closest 4FGL sources are indicated in blue, whilst the position of 4U 0513-40/NGC 1851 is indicated in white. The positions of uncatalogued sources are indicated in green. Bin widths are 0.1°. The yellow cross indicates the localised position of PS J0514.1-4003, with the yellow circle showing the 95% positional uncertainty of PS J0514.1-4003.

Figure E.3 shows the SED of PS J0514.1-4003, where I find that the best fitting spectral shape is a soft power law. This is typical of both X-ray binaries and globular clusters, as both populations have a mixture of log-parabola and power-law spectral shapes. In both populations it is typical that the more significantly detected sources (with better photon statistics) have log-parabola spectral shapes, whereas less significant sources have power-law spectral shapes. However, a notable exception to this rule is 4FGL J0427.8-6704 (1SXPS J042749.2-670434), an eclipsing LMXB significantly detected at 25σ in the 4FGL-DR2, which has a power-law spectrum, rather than a log-parabola. Therefore I find that the spectrum of PS J0514.1-4003 is compatible with both a globular cluster and LMXB source model.

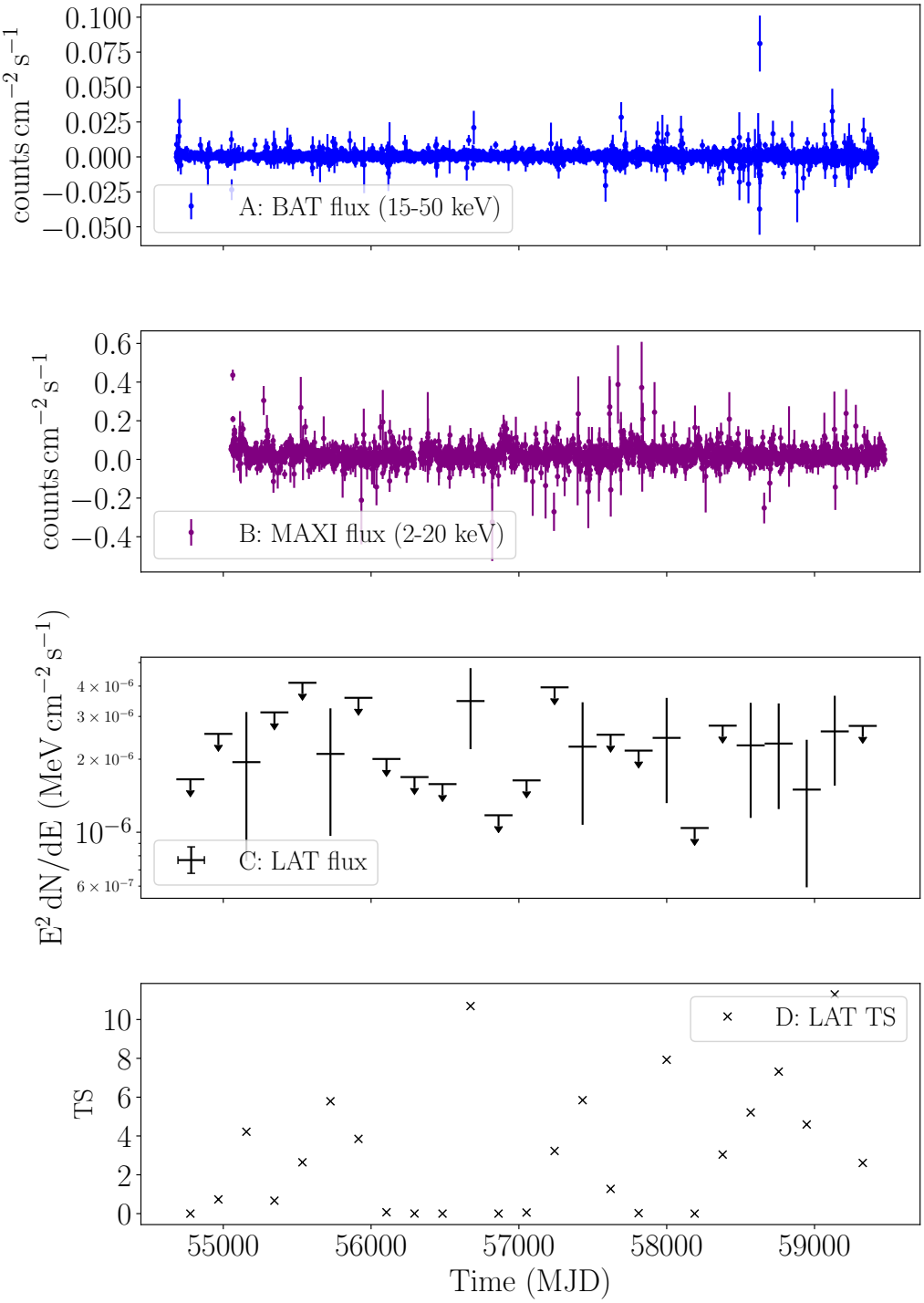

Figure E.2: Panels A and B show the daily hard and soft X-ray fluxes from *Swift*-BAT and MAXI respectively for 4U 0513-40. Panels C and D show the energy flux and respective TS of PS J0514.1-4003 where 95% confidence upper limits are placed on flux for any bin where TS < 4.

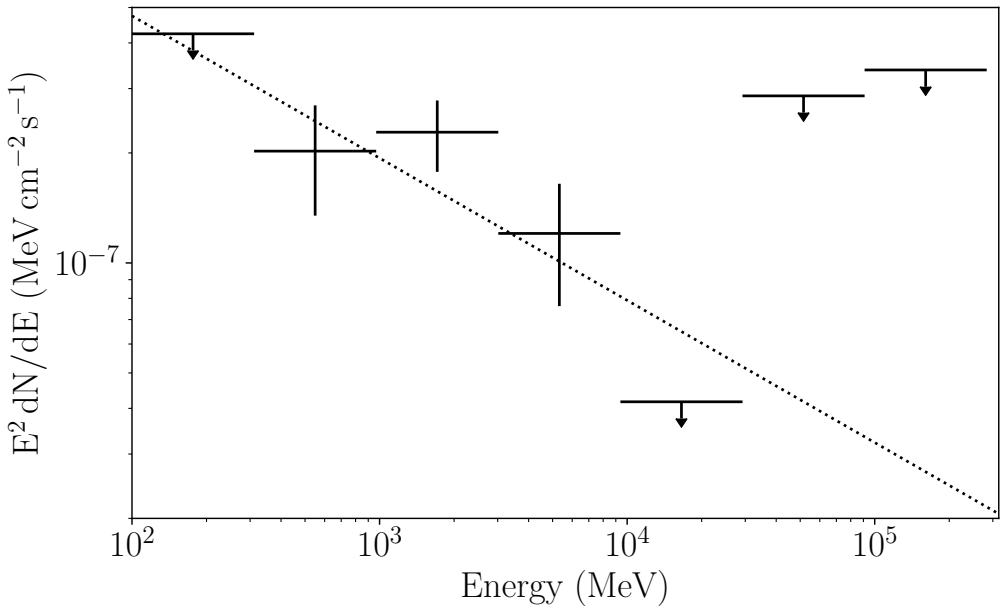

Figure E.3: The spectral energy distribution of PS J0514.1-4003 with 2 bins per decade in energy. A power-law spectral shape is fitted to this SED with the best-fit parameters of $N_0 = (1.936 \pm 0.319) \times 10^{-13}$, $\Gamma = 2.389 \pm 0.122$ and $E_0 = 1.0$ GeV. Upper limits are placed on energy bins where TS < 4.

Given the almost perfect positional coincidence between PS J0514.1-4003 and the NGC 1851 (and 4U05 within it), it is extremely likely that the γ-ray emission from PS J0514.1-4003 originates in either the binary or the wider globular cluster itself. The non variability in the light-curve of PS J0514.1-4003 (Figure E.2) is consistent with the non-variable behaviour of a globular cluster, although it is entirely possible that PS J0514.1-4003 is variable on timescales too short to detect from γ-ray emission, as this source is seen to have X-ray variability on daily timescales and a periodicity of just 17 minutes. The spectrum of PS J0514.1-4003 is consistent with both a globular cluster and an X-ray binary and spatially PS J0514.1-4003 is best modelled as a point source, again as all globular clusters and X-ray binaries are in the γ-ray regime. Hence the properties of PS J0514.1-4003 means the system outwardly resemble either a globular cluster or an X-ray binary, with no detectable variability tipping the scales slightly towards the Globular cluster hypothesis.

Considering the wider population of globular clusters, NGC 1851 is one of 157

such systems in the Milky Way (Harris 1996 & Harris 2010). Of these 157 systems, 30 are γ-ray emitters and are catalogued in the 4FGL-DR2, making 19% of the Galactic globular cluster population detected γ-ray emitting sources. There are slightly more LMXB systems known, at 187 (Liu et al., 2007), however of these systems only 4 are known γ-ray emitters, or 2% of the population. None of these systems are ultracompact X-ray binaries like 4U05. On balance, it is much more likely that PS J0514.1-4003 represents significant emission from a globular cluster than an LMXB, and hence I conclude that PS J0514.1-4003 represents novel γ-ray emission from NGC 1851, making this system the 31st globular cluster detected with *Fermi*-LAT at a significance of 7.5σ.

Appendix F

Low Mass X-ray Binary False Positive Results

F.1 1E 161348-5055.1

1E 161348-5055.1 (Tuohy and Garmire, 1980) (henceforth referred to as 1E16) is the central X-ray source in the supernova remnant RCW 103 and is either a low mass X-ray binary with an unclassified companion star and orbital period of 0.2779 days (Becker and Aschenbach, 2002), or an isolated neutron star (possibly a magnetar) accreting from a supernova fallback disc from RCW 103 (Li, 2007). A γ-ray source is identified coincident with the position of 1E16 with a TS value of 56.0 (7.5σ) (Figure F.1). 1E16 lies in a crowded field of γ-ray sources, with the closest catalogued source being 4FGL J1616.2-5054e, the extended pulsar wind nebula HESS J1616-508. Given the significance of the newly-detected source, positional localisation can be performed showing that the position of the excess shifts, so that it is no longer spatially coincident with 1E16. As 1E16 does not lie within the 99% positional uncertainty, there is $< 1\%$ chance that this excess represents γ-ray emission from 1E16.

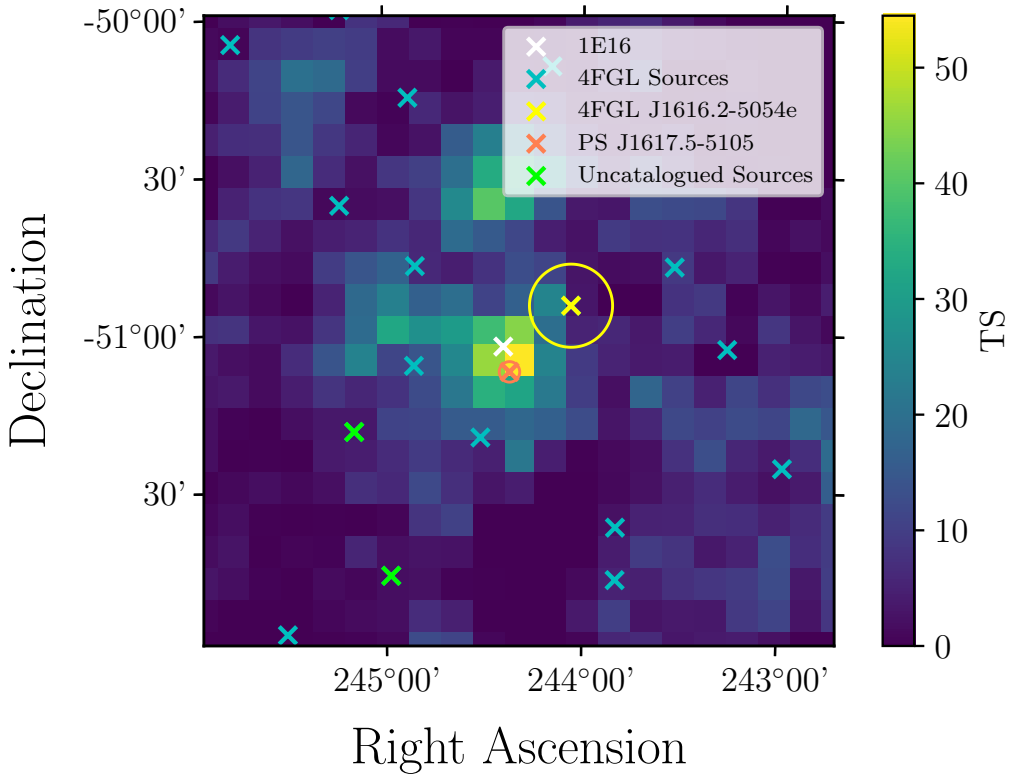

Figure F.1: The TS map of the central 2° of the 1E 161348-5055.1 ROI over the full mission time. Here, the positions of the closest 4FGL sources are indicated in blue, whilst the position of 1E 161348-5055.1 is indicated in white. The positions of uncatalogued sources are indicated in green. Bin widths are 0.1°. The orange cross and circle represent the localised position of PS J1617.5-5105, and the 95% positional uncertainty of this source. The yellow cross and circle represent the centroid, and extent of the nearby pulsar wind nebula 4FGL J1616.2-5054e.

F.2 GX 340+0 (4U 1642-45)

4U 1642-45 (also known, and henceforth referred, to as GX 340+0) is a Z-track* LMXB, with a neutron star accretor and an unclassified companion star (Margon et al. 1971a & Penninx et al. 1991). No orbital period is known for GX 340+0. The catalogued γ-ray source, 4FGL J1645.8-4533c, is spatially coincident† with

*The Z-track LMXBs are so named because of they make a 'Z' shape in their colour-colour and hardness-intensity diagrams. They are the brightest subgroup of LMXB, and display characteristic flaring, transient super-Eddington luminosity, and have neutron star compact objects (Church and Balucinska-Church, 2011).

†There is a small angular offset of 0.058° from the radio position of GX 340+0 used in Liu et al. (2007).

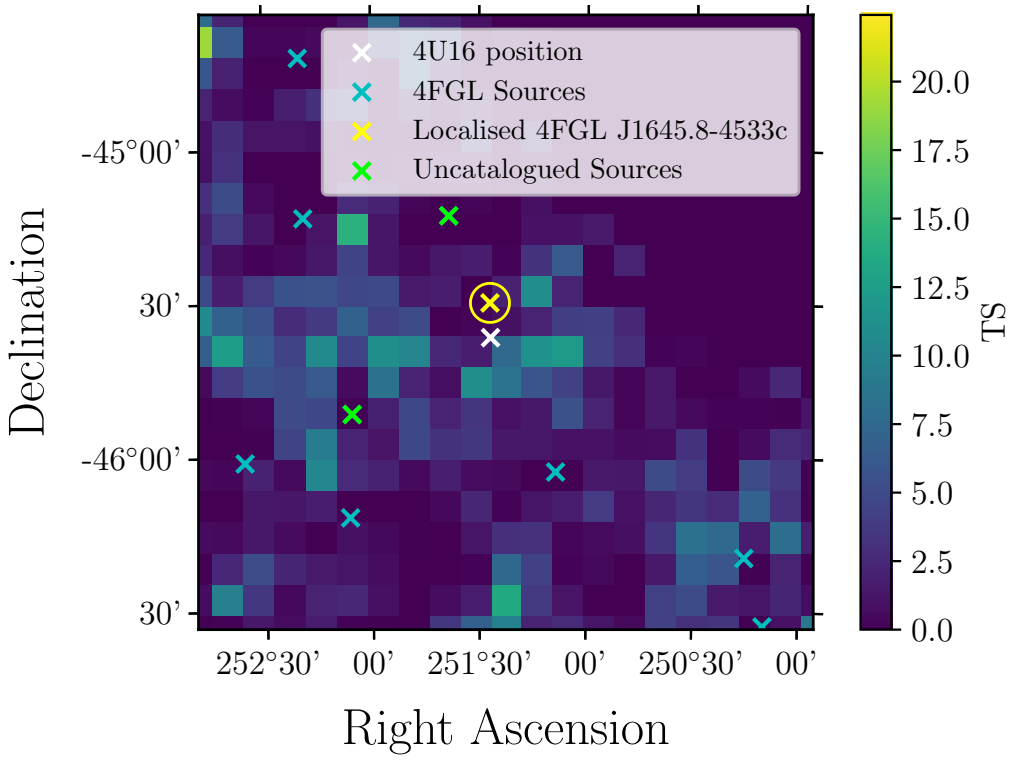

Figure F.2: The TS map of the central 2° of the GX 340+0 ROI over the full mission time. Here, the positions of the closest 4FGL sources are indicated in blue, whilst the position of GX 340+0 is indicated in white. The positions of uncatalogued sources are indicated in green. Bin widths are 0.1°. The yellow cross indicates the localised position of 4FGL J1645.8-4533c, with the yellow circle showing the 99% (i.e. most generous) positional uncertainty for 4FGL J1645.8-4533c.

the radio position of GX 340+0. 4FGL J1645.8-4533c is associated with GX 340+0 in the 4FGL-DR2, although the catalogue source type is 'unknown' rather than an 'lmb' (Low Mass X-ray Binary), indicating that whilst the source of the γ-rays may be GX 340+0, the mechanism for their production is unknown. When producing the 4FGL-DR2, two measures of association between catalogue sources and their multi-wavelength counterparts is used: a likelihood association probability and a Bayesian association probability. The probability of association for GX 340+0 and 4FGL J1645.8-4533c via the likelihood method is 0.961, however for the Bayesian method the probability fails to reach the probability threshold of 0.8. A lack of agreement between the two association probability calculations means that the association of GX 340+0 with 4FGL J1645.8-4533c is tentative.

Coordinates	RA(°)	Dec(°)
GX 340+0 Radio Position	251.4487	-45.6109
4FGL J1645.8-4533c	251.4550	45.5536
Localised 4FGL J1645.8-4533c	251.4578 ±0.0204	-45.4979 ± 0.0227

Table F.1: The positional information of GX 340+0, its associated 4FGL source, and the results of the localisation of this source (plus uncertainties).

Given the additional 3 years of observations available, compared to that of the 4FGL-DR2, a more detailed analysis of the connection between GX 340+0 and 4FGL J1645.8-4533c is now possible. Following the standard analysis chain described in Chapter 6, 4FGL J1645.8-4533c is detected with TS = 479 (22.9σ) and approximately 22000 predicted γ-ray counts from 13 years of data. This is a marked increase over the detection significance reported in the 4FGL-DR2: 12.7σ. Given the improved photon statistics for this source, I am able to present a refined positional fit for 4FGL J1645.8-4533c, by using the `Fermipy Localize` routine. Figure F.2 shows the TS map of the centre of the GX 340+0 ROI with the localised position of 4FGL J1645.8-4533c, with the 99% positional uncertainty, the largest uncertainty typically calculated in localisation*. As the radio position of GX 340+0 does not lie within the bounds of the positional uncertainty of 4FGL J1645.8-4533c, it is unlikely that this point source is coincident with the radio position of GX 340+0. Table F.1 gives the positional information of the GX 340+0 radio position from Liu et al. (2006), together with the catalogued 4FGL J1645.8-4533c positional information together with the refined fit with 13 years of data and its associated uncertainties.

As a Z-source, GX 340+0 is one of the most luminous, with clear variability seen when the system is on the flaring branch of the hardness-intensity diagram. GX 340+0 is additionally a source with known quasi-periodic oscillations (van Paradijs et al., 1988), although given the integration time required to make a γ-ray detection compared to other wavelengths, one would not expect to see QPOs in γ-ray emis-

*A reminder that my typical criterion for spatial coincidence is the stricter 95% positional uncertainty (i.e. 2σ confidence), I display the 99% uncertainty here to highlight the lack of apparent spatial coincidence between 4FGL J1645.8-4533c and GX 340+0.

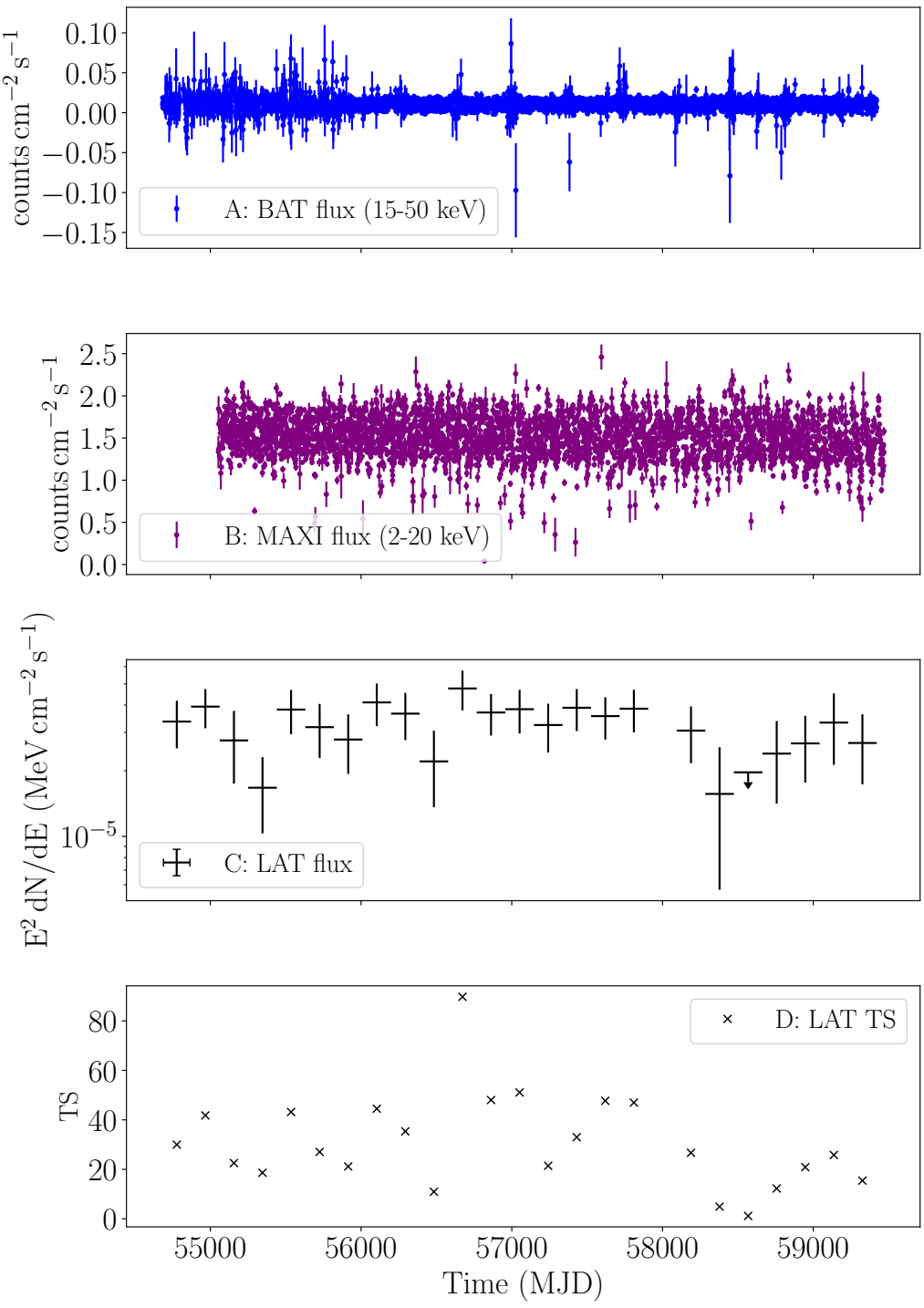

Figure F.3: Panels A and B show the daily hard and soft X-ray fluxes from *Swift*-BAT and MAXI respectively for GX 340+0. Panels C and D show the energy flux and respective TS of 4FGL J1645.8-4533c where 95% confidence upper limits are placed on flux for any bin where TS < 4.

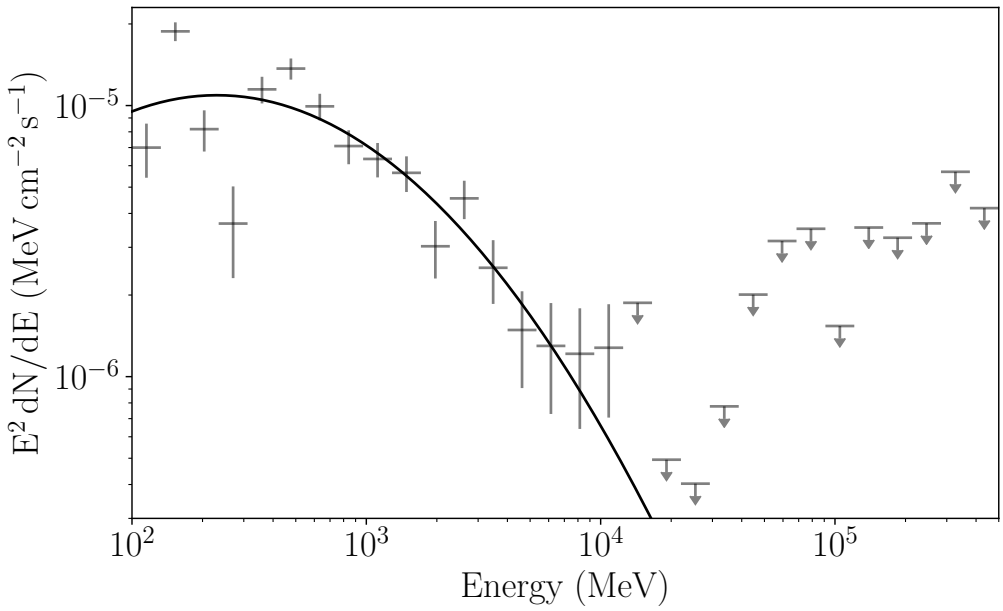

Figure F.4: The spectral energy distribution of GX 340+0 with 8 bins per decade. A log-parabola spectral shape is fitted to this SED with the best-fit parameters of $\alpha = 2.805 \pm 0.125$, $\beta = 0.1975 \pm 0.0259$, $N_0 = (1.531 \pm 0.193) \times 10^{-12}$ and $E_B = 1.77$ GeV

sion. Figure F.3 shows the X-ray light-curves of GX 340+0 from both *Swift*-BAT and MAXI, together with the 6 month binned light-curve of 4FGL J1645.8-4533c. 4FGL J1645.8-4533c appears to be a largely steady source, with reasonably consistent flux measurements being made in each bin (with the exception of one 6 month period where no significant emission was detected). The *Swift*-BAT light-curve shows no significant flaring, and the MAXI light-curve shows an average flux of $1.5\,\mathrm{counts\,cm^{-2}\,s^{-1}}$, there is significant variability above and below this flux, but no obvious long term trends. There is therefore no obvious link between the γ-ray light-curve of 4FGL J1645.8-4533c and the X-ray light-curve of GX 340+0, and as there are no known orbital or spin periods known for GX 340+0, a phased search is not possible.

Finally, the 4FGL-DR2 states that 4FGL J1645.8-4533c has a log-parabola spectral shape, as do 3 of the 4 catalogued 4FGL-DR2 LMXBs. My calculated spectrum is consistent with this although note that several points appear to significantly deviate

from expected spectrum in the 100 MeV - 1 GeV range, and that there appears to be a slight spectral hardening immediately before the high energy cutoff at approximately 10 GeV.

Based on the localisation of 4FGL J1645.8-4533c, it is unlikely ($< 1\%$ chance) that this γ-ray source is spatially coincident with the radio position of GX 340+0. Whilst in the case of other binaries (e.g. SS 433) offset emission is seen due to the presence of a relativistic jet, GX 340+0 is not a known microquasar, nor is is there any evidence for a jet. Furthermore, a lack of information regarding the period of the binary or spin of the neutron star* makes it difficult to search the 4FGL J1645.8-4533c data for signatures of binary emission and any detection of the rapid variability seen in the X-ray is unlikely with the LAT. Without longer term trends in the X-ray data or orbital periodicity data, it is not possible to associate 4FGL J1645.8-4533c firmly with GX 340+0. Whilst the log-parabola spectral shape is consistent with the understanding of LMXB γ-ray spectra, log-parabola spectra are also common in blazars. Therefore it is possible that 4FGL J1645.8-4533c is, in fact, a blazar with a hitherto unknown multi-wavelength counterpart, rather than representing γ-ray emission from GX 340+0.

F.3 2A 1822-371

2A 1822-371 (also known as 4U 1822-371 and V691 CrA; henceforth referred to as 2A18) is a LMXB system with a pulsar accretor in orbit with an unclassified companion star with an orbital period of 5.57 hours, it is notable for being viewed almost edge on at an 85° inclination angle, and its rapidly changing orbit implies a larger than average mass transfer rate between companion and accretor (e.g. Griffiths et al. 1978, Cowley et al. 1982, Mason and Cordova 1982, Jonker and van der Klis 2001, Burderi et al. 2010). A previous study, Ciampa et al. (1989), claimed detection of phase-modulated γ-ray emission from 2A18, however given

*Despite containing neutron stars, Z-binaries do not typically display pulsations.

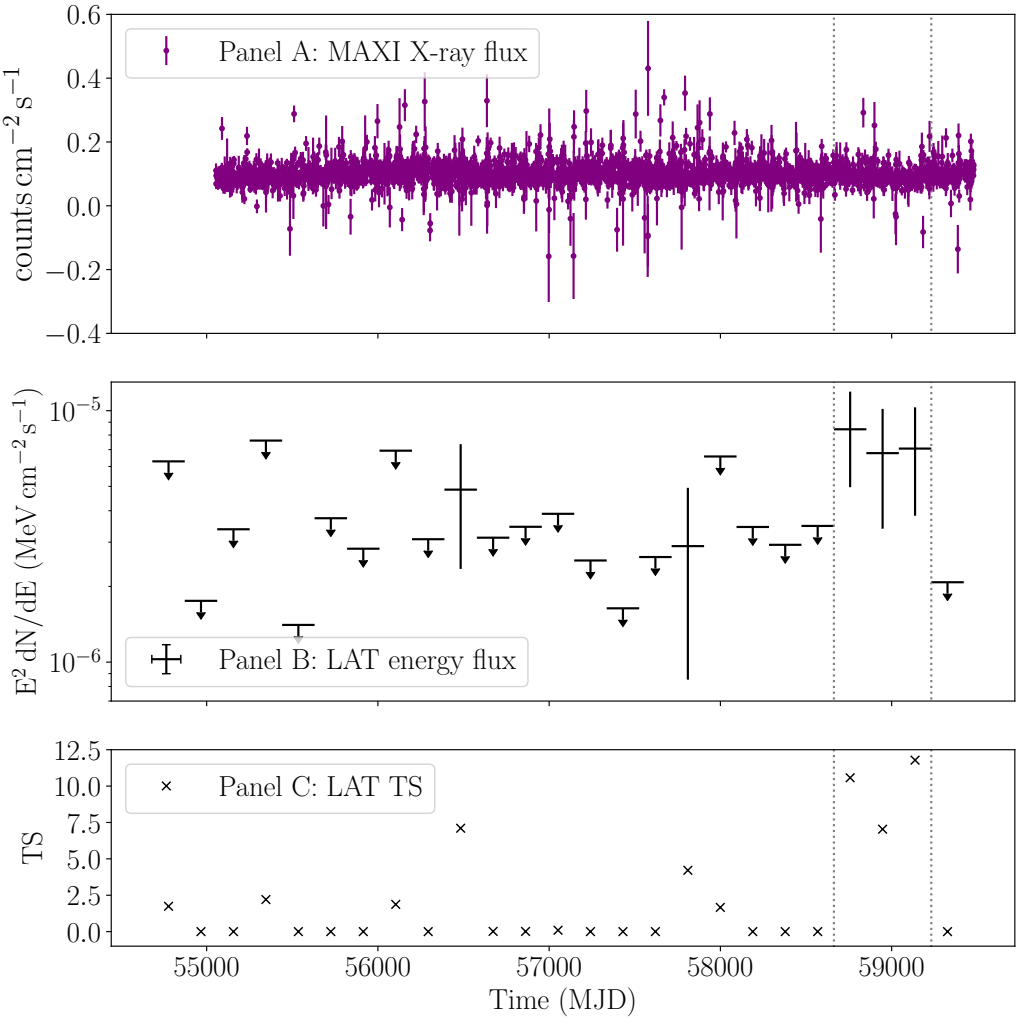

Figure F.5: Panel A shows the daily X-ray flux from MAXI for 2A 1822-371. Panels B and C show the energy flux and respective TS of PS J1825.5-3655 where 95% confidence upper limits are placed on flux for any bin where TS < 4. The grey dotted lines indicate the start and end of the 18 month period where the significant excess appears.

that this emission only reaches 2.4σ and this emission has not been observed by any subsequent γ-ray observatories, this emission was either transient and the binary simply hasn't emitted γ-rays since this time (there is no clear mechanism for this behaviour) or, more likely given the low significance, this result was due to either a background fluctuation or an nearby unresolved point source.

The 13-year dataset reveals a γ-ray excess dubbed PS J1825.5-3655 coincident with the position of 2A18 with TS = 12.6 (angular offset: 0.184°). Figure F.5 shows the

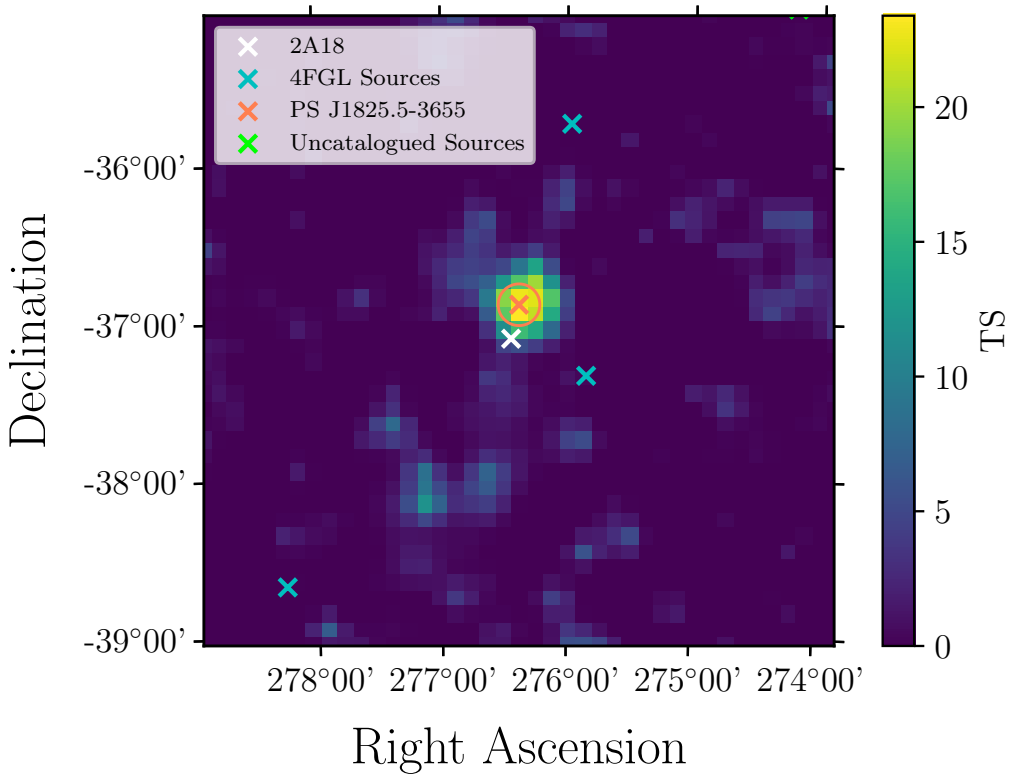

Figure F.6: The TS map of the central 4° of the 2A 1822-371 ROI over the 18 month excess period. Here, the positions of the closest 4FGL sources are indicated in blue, whilst the position of 2A 1822-371 is indicated in white. The positions of uncatalogued sources are indicated in green. Bin widths are 0.1°. The orange cross denotes the position of PS J1825.5-3655, whilst the orange circle shows the 95% positional uncertainty around PS J1825.5-3655.

MAXI light-curve of 2A18, together with the γ-ray light-curve of PS J1825.5-3655. An approximately 18 month period* towards the end of the observation period shows a consistent γ-ray flux, whereas the rest of the light-curve shows two less significant measurements and upper limits.

I reanalyse the ROI over this 18 month period, and find that the TS of PS J1825.5-3655 roughly doubles to 27.7 (5.3σ). During this period, PS J1825.5-3655 is the most significant γ-ray source within a 2° radius, meaning source confusion with a catalogued source is unlikely. We localise the position of PS J1825.5-3655, and find that it shifts slightly to LII = 357.0262° ± 0.0521, BII = −11.1525° ± 0.0562° with

*MJD 58662.9 - 59231.5

a 95% positional uncertainty radius of 0.1321°. Figure F.6 shows the TS map of the 2A18 ROI, with the γ-ray emission from 2A18 as the most luminous source present, and 2A18 lying outside of the uncertainty bound of PS J1825.5-3655. Therefore, PS J1825.5-3655 is no longer spatially coincident with the position of 2A18, and it is therefore unlikely to represent γ-ray emission from this LMXB. Given that it is more than 10° off the Galactic plane, it is likely that PS J1825.5-3655 represents a very faint flaring blazar which was undetectable prior to this 18 month period.

F.4 SLX 1746-331

SLX 1746-331 (Skinner et al., 1990) (henceforth SLX17) is an LMXB transient source and black hole candidate (White and van Paradijs 1996 & Tetarenko et al. 2016). The system has an unclassified companion star, the orbital period is unknown. An excess is observed at the position of SLX17 with TS = 19.29 (4.4σ), and the light-curve condition is also fulfilled in this case.

Swift-BAT and MAXI X-ray data are available for this system, and therefore I plot the daily X-ray light-curves alongside the γ-ray data in Figure F.7. In the γ-ray light-curve, I observe 4 bins in the $2\sigma \leq z < 3\sigma$ TS range, with upper limits otherwise. The flux measurements of each bin appear broadly consistent with one another, indicating that there is no detectable variability exhibited by this γ-ray excess. The γ-ray bins do not correlate with any known enhancements in the X-ray data. Given poor photon statistics, localisation and spectral analysis are not possible for this γ-ray excess.

Figure F.8 shows the TS map of the SLX17 ROI, where one clearly sees that SLX17 is coincident with the peak of a γ-ray excess. We also see a close catalogued source, 4FGL J1750.9-3301 (TS = 13.67, angular offset: 0.299°); this TS is low for a 4FGL source and the catalogue gives it's detection significance as 5.5σ, which should correspond to a TS of at least 30. Given the close proximity between 4FGL J1750.9-3301 and SLX17 it is inevitable that there is some source confusion

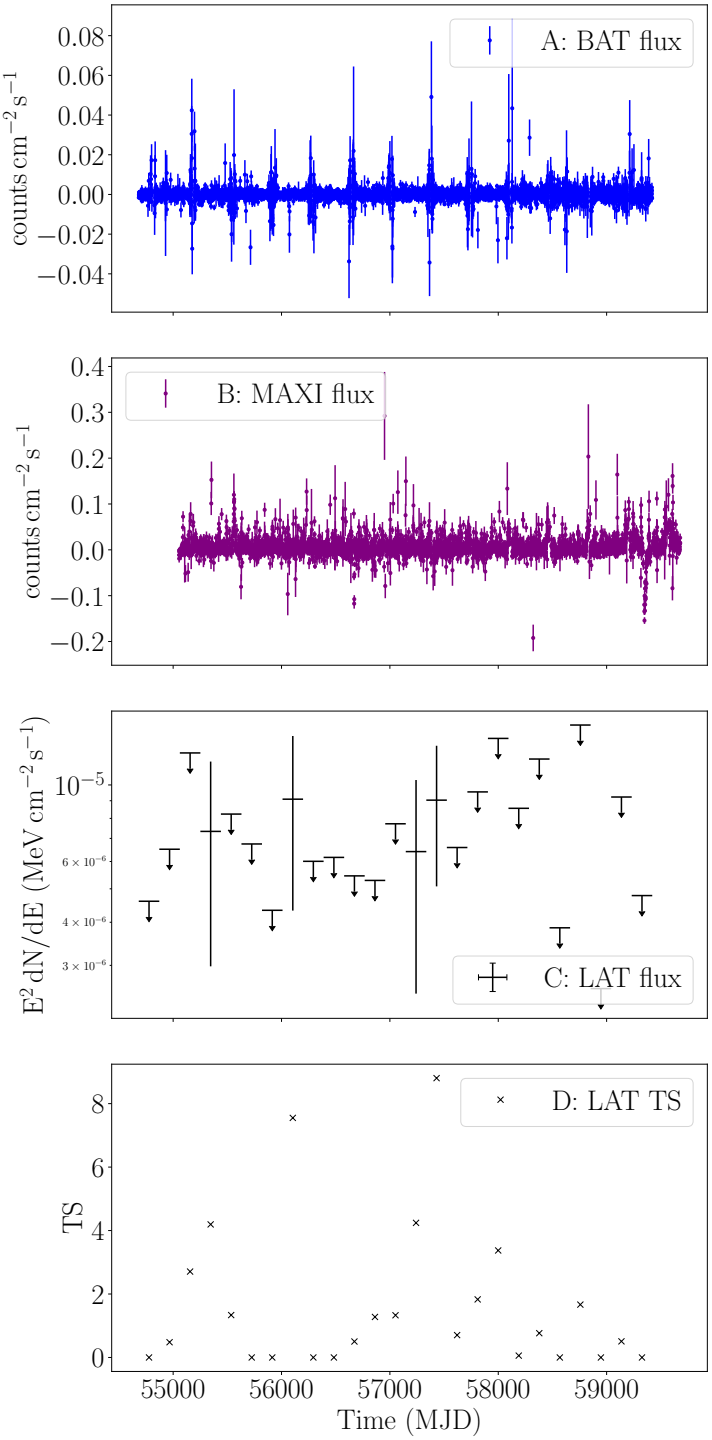

Figure F.7: Panels A and B show the daily hard and soft X-ray fluxes from *Swift*-BAT and MAXI respectively for SLX 1746-331. Panels C and D show the energy flux and respective TS of the coincident γ-ray excess where 95% confidence upper limits are placed on any bin where TS < 4.

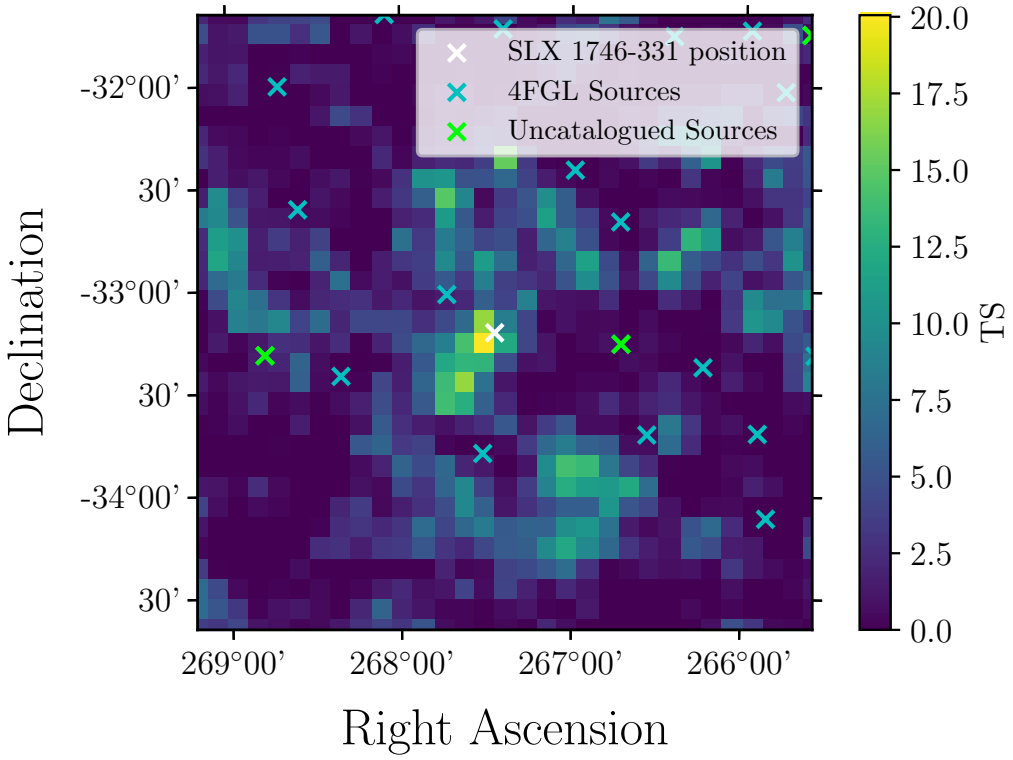

Figure F.8: The TS map of the central 3° of the SLX 1746-331 ROI over the full observation time. Here, the positions of the closest 4FGL sources are indicated by blue crosses, whilst the position of SLX 1746-331 is indicated with a white cross. The positions of uncatalogued sources are indicated by green crosses. Bin widths are 0.1°.

occurring here, and that this is responsible for the excess one sees at the position of the binary, and responsible for the apparent lack of observed significance from 4FGL J1750.9-3301.

F.5 4U 1811-17 (GX 13+1)

4U 1811-17 (Giacconi et al. 1971 & Giacconi et al. 1972), also known as GX 13+1 and Sgr X-2 is a low mass X-ray burster (e.g. Fleischman 1985, Matsuba et al. 1995 & Kuulkers and van der Klis 2000) with a neutron star accretor and a companion of spectral type K5III (Bandyopadhyay et al., 1999). Whilst I do not identify any persistent γ-ray excess coincident with the position of GX 13+1, the light-curve condition for this binary is fulfilled, indicating that there is some significant γ-ray

emission within the light-curve at the position of the binary.

Figure F.9 shows the X-ray light-curves of GX 13+1 as seen by MAXI and *Swift*-BAT along with the *Fermi*-LAT light-curve at this position. In the γ-ray light-curve all but two of the bins are upper limits, and these two bins are not consecutive. The first and less significant of the two bins occurs from MJD 55630 - 55819, and a TS of 7.18 (2.7σ) is calculated for this bin. The second and more significant bin occurs from MJD 56577 - 56767, with a TS of 19.7 (4.4σ). There are a number of above average points in the X-ray data corresponding to Type I thermonuclear X-ray bursts, however there appears to be no correlation between these and the γ-ray flux points, although the γ-ray flux bins are approximately 100 times longer than the X-ray bins, so direct comparisons can be difficult when short term (i.e. daily) variability occurs in the X-ray data. The flux measurements of both γ-ray bins appear to be broadly comparable with one another.

Considering only the time period of the more significant of the two bins (MJD 56577 - 56767), I generate a TS map of the ROI surrounding GX 13+1, shown in Figure F.10. Whilst GX 13+1 is spatially coincident with a γ-ray excess during this period, there is a 4FGL source less than one bin width away from the position of the binary. This source is 4FGL J1814.1-1710, a source with no previous association*.

The very small separation between the excesses seen in the GX 13+1 light-curve and 4FGL J1814.1-1710 makes it impossible to resolve emission between the two. There is therefore no significant evidence for any γ-ray emission from the GX 13+1 system.

*This source has been removed from the most recent iteration of the LAT point source catalogue, the 12-year 4FGL-DR3. This is likely due to it being insignificant. However, given that this source exceeds the 5σ level over the full lifetime of *Fermi*-LAT I choose to include it in my model, and not delete it.

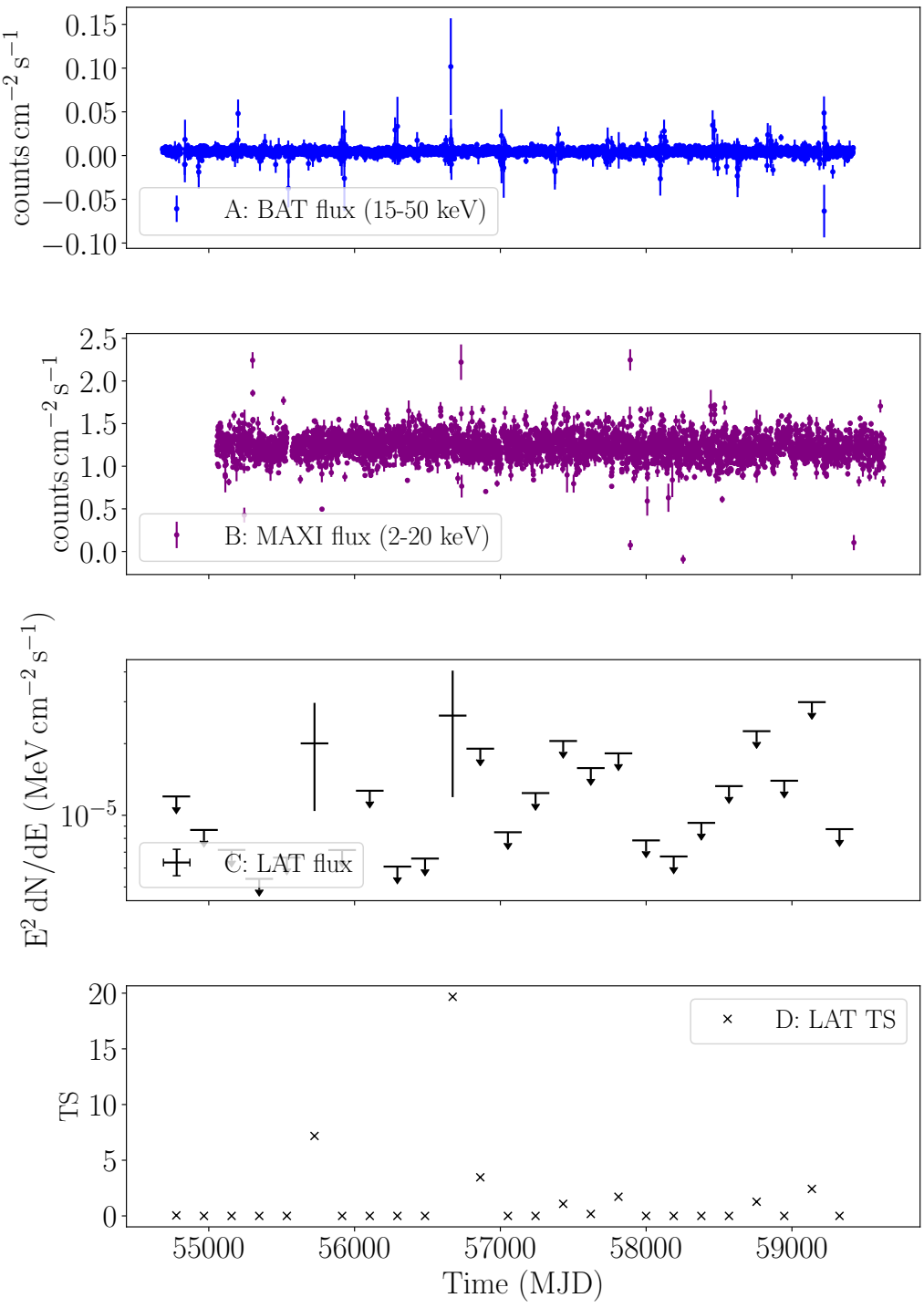

Figure F.9: Panel A shows the daily X-ray flux of GX 13+1 measured by MAXI; Panel B shows the daily X-ray flux of GX 13+1 measured by *Swift*-BAT. Panels C and D show the energy flux and respective TS of the position of GX 13+1 where 95% confidence upper limits are placed on flux for any bin where TS < 4.

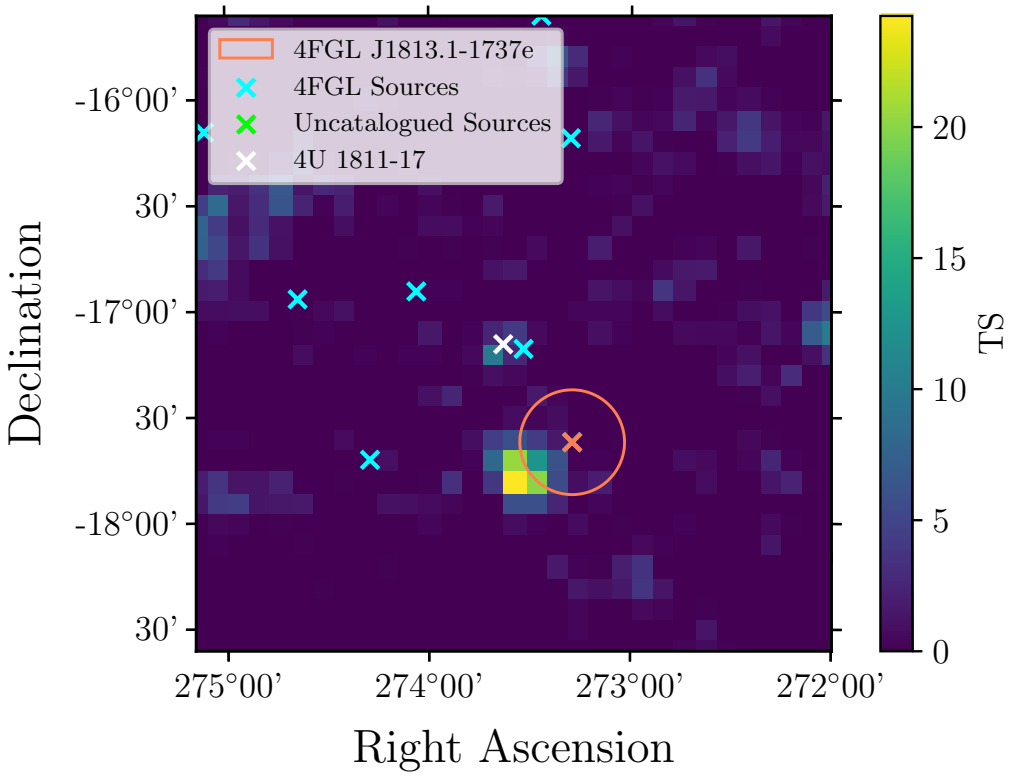

Figure F.10: The TS map of the central 3° of the GX 13+1 ROI during the period MJD 56577 - 56767, where the more significant excess is seen.. Here, the positions of the closest 4FGL sources are indicated by the blue crosses, whilst the position of GX 13+1 is indicated by the white cross. The positions of uncatalogued sources (including PS J1814.0-1750) are indicated by green crosses. The orange circle indicates the extent of the spatially extended pulsar wind nebula: 4FGL J1813.1-1737e, with the orange cross indicating the centroid of this source. Bin widths are 0.1°.

F.6 4U 1812-12

4U 1812-12 (henceforth 4U1812) (Forman et al. 1976 & Amnuel et al. 1979) is a low mass X-ray burster (Murakami et al., 1983), with a neutron star accretor, a companion star of unknown spectral class, although it is thought to be an evolved Helium-rich system (Armas Padilla et al., 2020). This system is an ultra-compact X-ray binary but has no known orbital period. Whilst no persistent γ-ray excess is identified at the position of 4U1812, the light-curve condition is fulfilled for the position of 4U1812, indicating the presence of significant γ-ray emission in the light-curve.

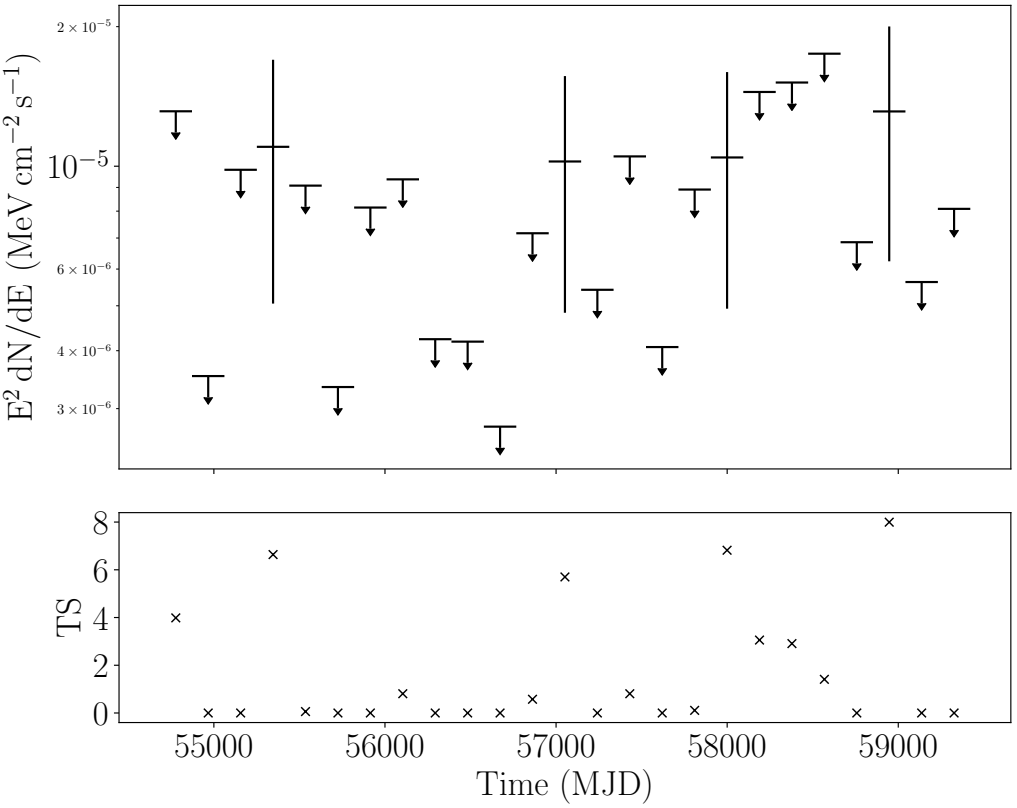

Figure F.11: The light-curve of the position of 4U 1812-12, with approximately 6 month bins. The top panel displays energy flux as a function of time, and the bottom panel displays the respective TS of each energy flux bin. Upper limits on flux are calculated for each bin where the respective TS < 4.

Figure F.11 shows this light-curve in which 21 of the 25 bins have upper limits, and 4 bins have evidence for emission in the $2.5\sigma < z < 3\sigma$ significance range. The flux points appear to be consistent with one another, although the uncertainty on each flux point is large. Whilst 4U1812 is a well established variable source in the X-ray waveband (due to its Type I bursts), no useful light-curve data are available for this source from either *Swift*-BAT or MAXI. It is therefore not possible to make a connection between these light-curve excesses and any multi-wavelength features.

Several sources are close to the position of 4U1812 in the sky: 4FGL J1816.5-1208c (TS = 68.6, angular offset from 4U1812: 0.353°) and 4FGL J1813.7-1152 (TS = 102, offset: 0.391°). Neither of these sources is known to be variable on monthly timescales. Additionally, the highly significant pulsar 4FGL J1813.4-1246/PSR

J1813-1246 (TS = 30400) also lies nearby (offset: 0.789°), and like the general pulsar population, is non-variable.

It is not possible to perform any advanced analysis due to a lack of a significant persistent emission, and no multi-wavelength data are available making it impossible to associate the excesses in this light-curve with 4U1812 itself. Given the proximity of 4U1812 to a number of steady γ-ray sources, it is likely that these excesses are the product of source confusion, rather than a genuine signature of γ-ray emission.

F.7 4U 1918+15

4U 1918+15 (Villa et al. 1976 & Forman et al. 1978) (henceforth 4U19) is a low mass X-ray binary system, and a soft X-ray transient thought to consist of a neutron star accretor and an unclassified companion star with an unknown orbital period (Cominsky et al. 1978 & Campana et al. 1998). We observe a significant γ-ray excess coincident with the position of 4U19 with a TS value of 38.6 (6.2σ), and also see that the light-curve condition for this X-ray binary is fulfilled indicating significant γ-ray emission in the light-curve of this source.

Given the large number of photons and the significance of the persistent γ-ray excess, I am able to perform a positional localisation on this excess. Figure F.12 shows the result of this localisation overlaid on the TS map of the ROI around 4U19. After localisation I find that the source moves so that it now has an angular offset of 0.2533° from 4U19, with the 99% positional uncertainty radius of this localisation being equal to 0.2164°. Consequentially there is a less than 1% chance that this excess is truly coincident with the binary, and therefore it is highly unlikely to represent γ-ray emission from 4U19.

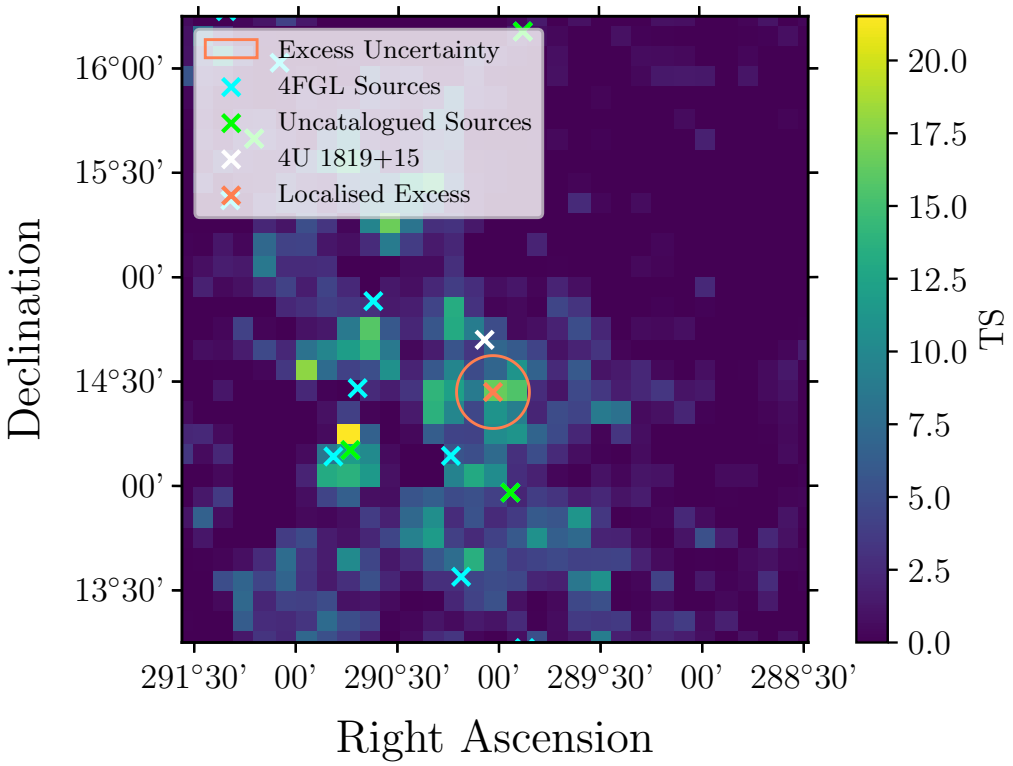

Figure F.12: The TS map of the central 3° around 4U 1918+15. The position of 4U 1918+15 is indicated by the white cross, with the positions of 4FGL sources indicated by blue crosses. Uncatalogued sources are indicated by green crosses. The orange cross indicates the position of the localised excess, with the orange circle indicating the 95% positional uncertainty of the localisation. Bin widths are 0.1° across.

Figure F.13: The twelfth labour of Heracles, the capture of Cerberus, the guardian of the underworld. By Peter Paul Rubens (1636-1637).

Appendix G

X-ray Binary γ-ray Spectra

This Appendix contains the spectral energy distributions of the known γ-ray emitting X-ray binaries which are analysed in Chapter 9 with a 13 year dataset. In most cases, 10 energy bins per decade are used to produce the SED, however in certain cases where the source significance is lower, 5 bins per decade were used to increase the photon statistics per bin, reducing the number of upper limit bins. Each SED is modelled with either a log-parabola, or power-law depending on which is the better fit to the data, and the parameters used are those calculated from these SEDs, as opposed to those given in the 4FGL. The parameters themselves for each SED are extremely similar to those provided in the 4FGL, so can be found in that catalogue.

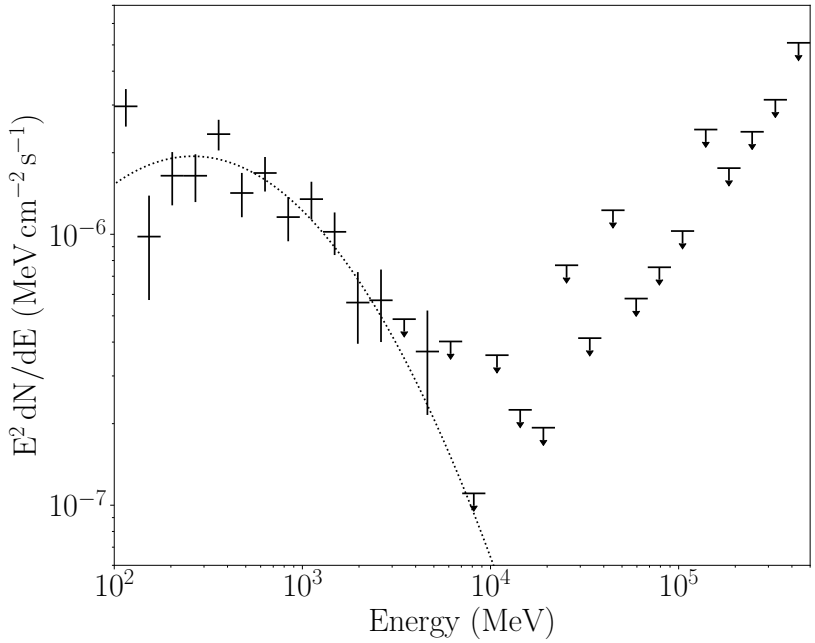

Figure G.1: The spectral energy distribution of the extragalactic high mass X-ray binary LMC P3, with 10 energy bins per decade. Upper limits are placed on any bin where TS < 4. The data is fitted with a log-parabola spectral model, using best fit parameters.

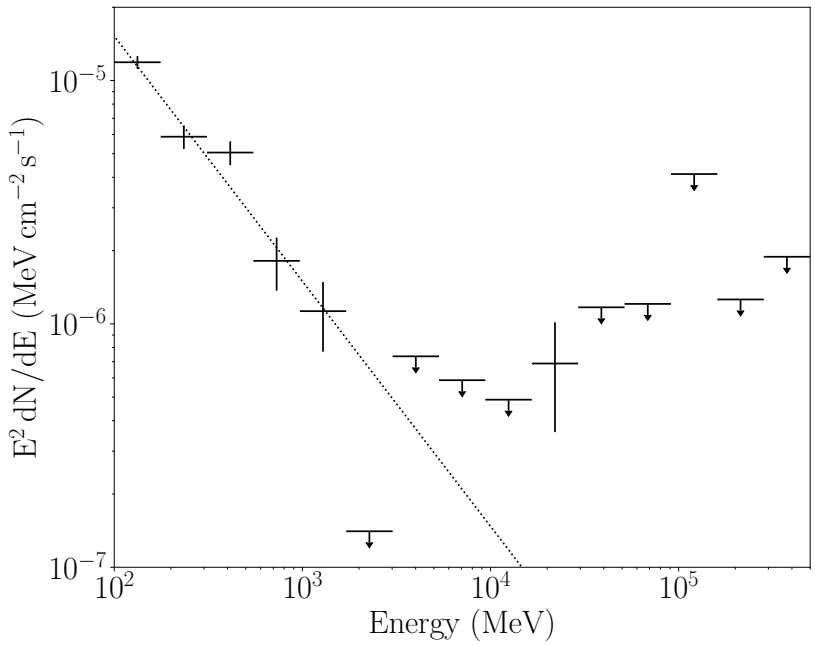

Figure G.2: The spectral energy distribution of the high mass X-ray binary PSR B1259-63, with 5 energy bins per decade. Upper limits are placed on any bin where TS < 4. The data is fitted with a power-law spectral model, using best fit parameters.

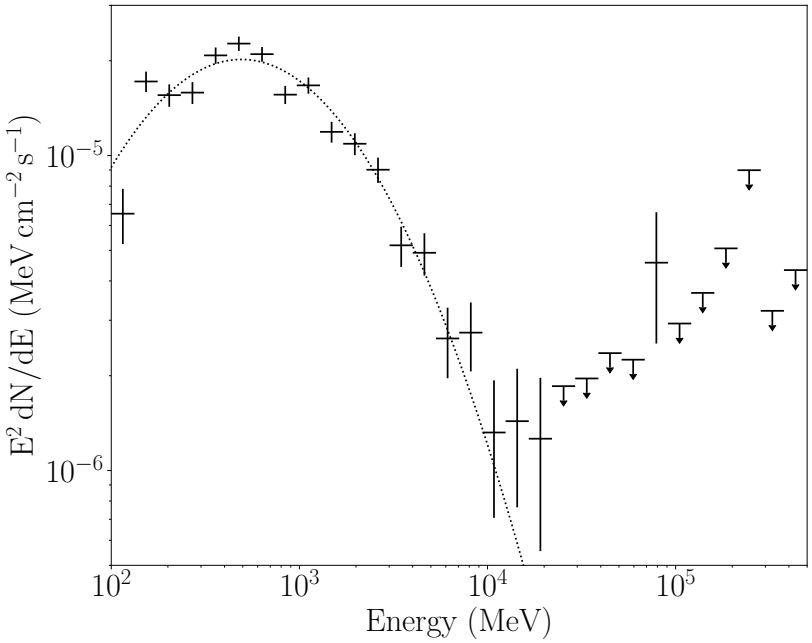

Figure G.3: The spectral energy distribution of the high mass X-ray binary 4FGL J1405.1-6119, with 10 energy bins per decade. Upper limits are placed on any bin where TS < 4. The data is fitted with a log-parabola spectral model, using best fit parameters.

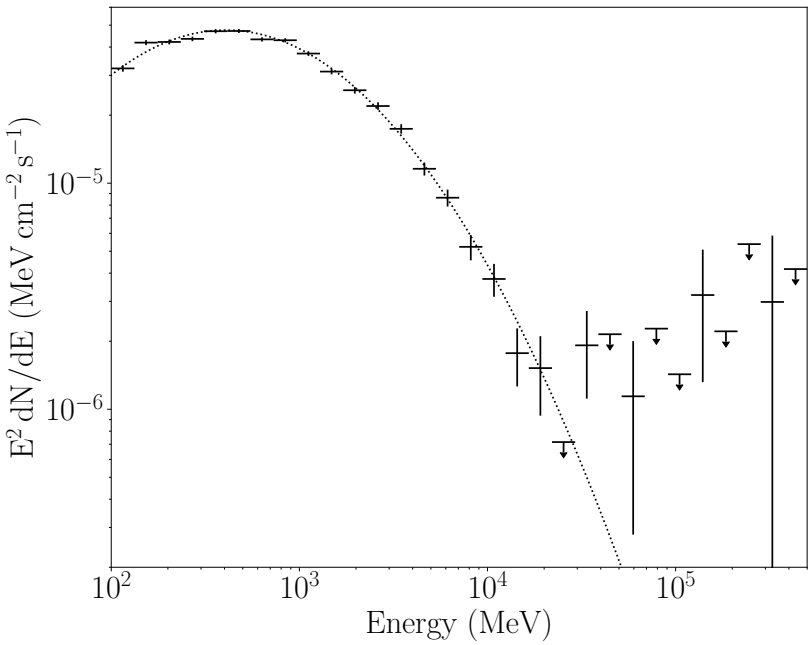

Figure G.4: The spectral energy distribution of the high mass X-ray binary 1FGL J1018.6-5856, with 10 energy bins per decade. Upper limits are placed on any bin where TS < 4. The data is fitted with a log-parabola spectral model, using best fit parameters.

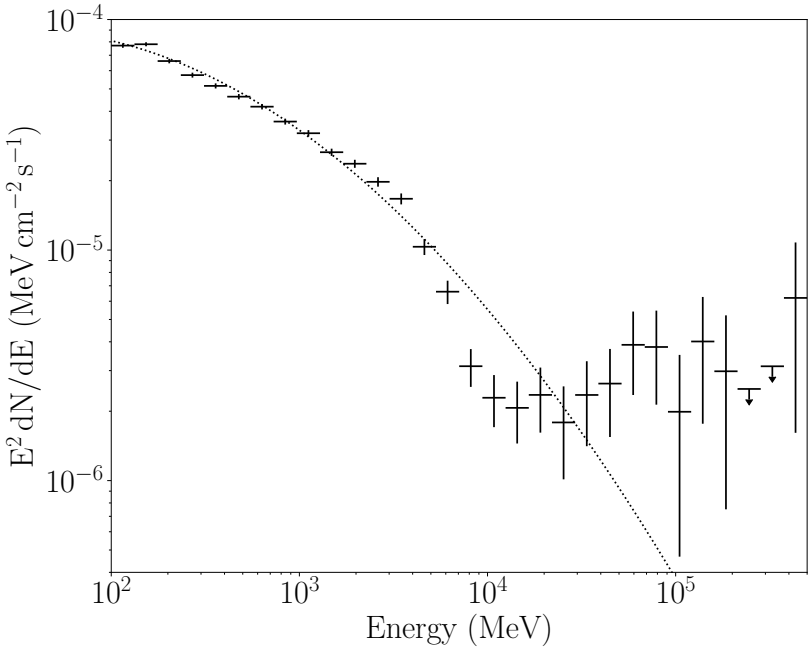

Figure G.5: The spectral energy distribution of the high mass X-ray binary LS 5039, with 10 energy bins per decade. Upper limits are placed on any bin where TS < 4. The data is fitted with a log-parabola spectral model, using best fit parameters.

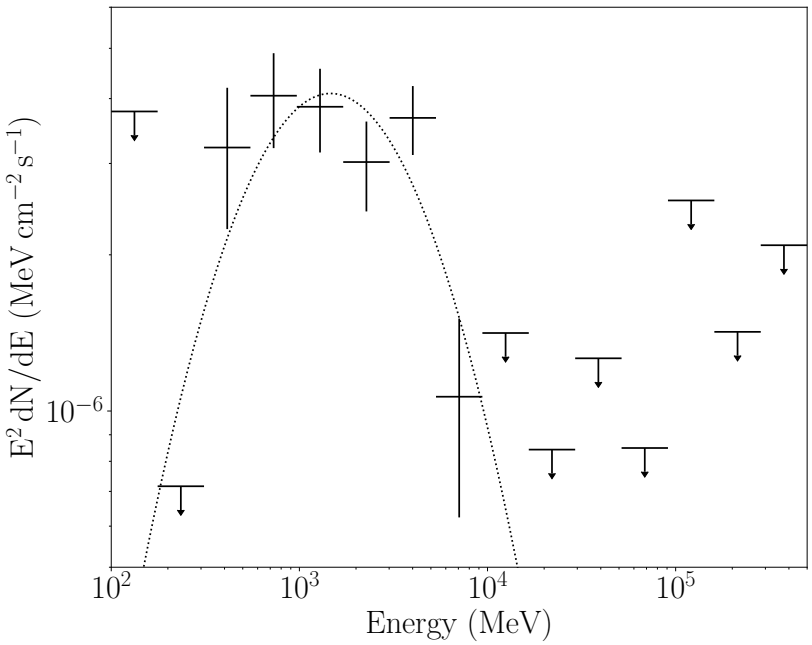

Figure G.6: The spectral energy distribution of the high mass X-ray binary HESS J1832-093, with 5 energy bins per decade. Upper limits are placed on any bin where TS < 4. The data is fitted with a log-parabola spectral model, using best fit parameters.

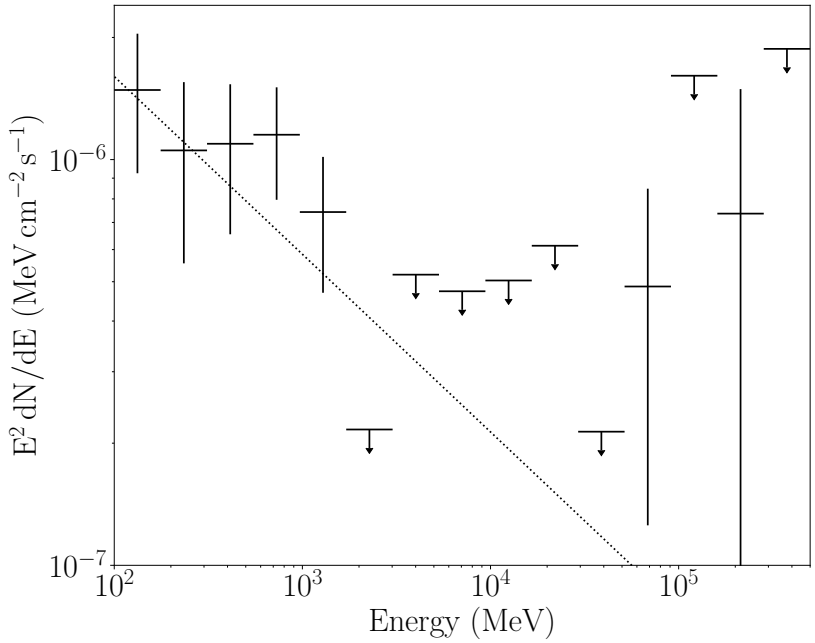

Figure G.7: The spectral energy distribution of the high mass X-ray binary HESS J0632+057, with 5 energy bins per decade. Upper limits are placed on any bin where TS < 4. The data is fitted with a power-law spectral model, using best fit parameters.

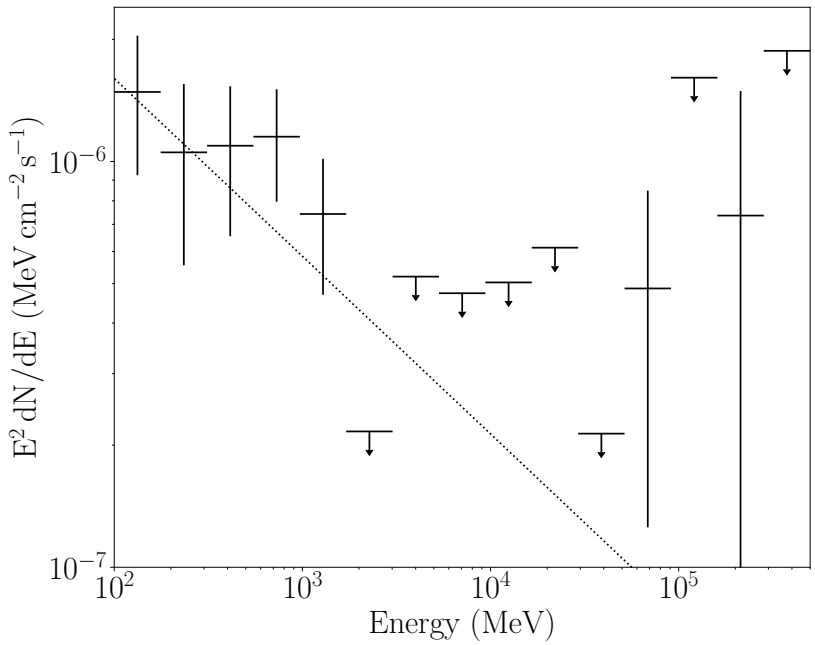

Figure G.8: The spectral energy distribution of the high mass X-ray binary HESS J0632+057, with 5 energy bins per decade. Upper limits are placed on any bin where TS < 4. The data is fitted with a power-law spectral model, using best fit parameters.

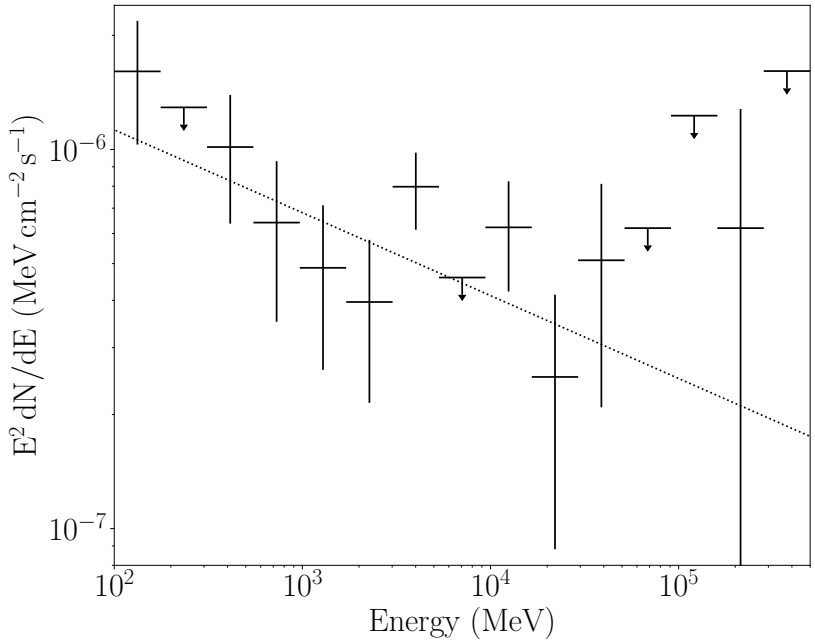

Figure G.9: The spectral energy distribution of the high mass X-ray binary Cygnus X-1, with 5 energy bins per decade. Upper limits are placed on any bin where TS < 4. The data is fitted with a power-law spectral model, using best fit parameters.

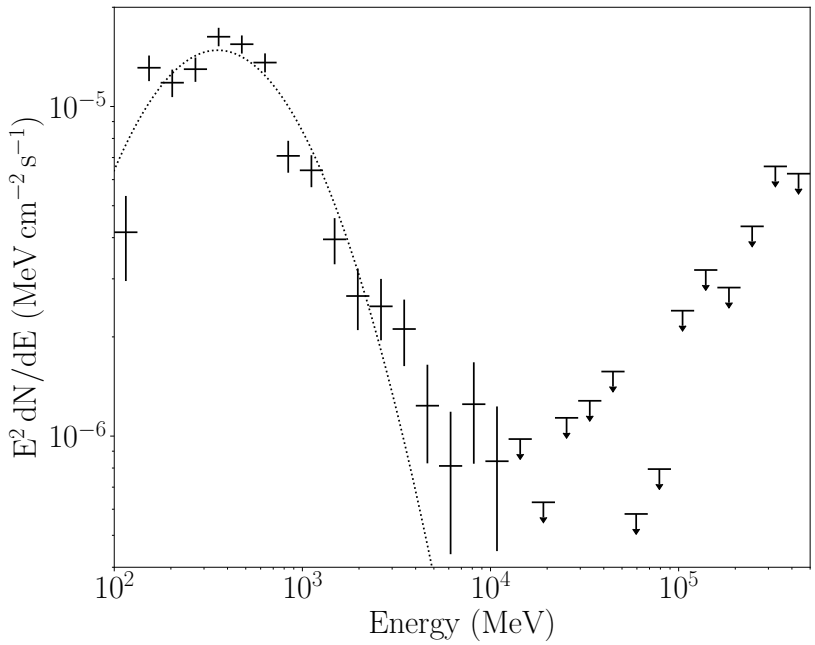

Figure G.10: The spectral energy distribution of the high mass X-ray binary Cygnus X-3, with 10 energy bins per decade. Upper limits are placed on any bin where TS < 4. The data is fitted with a log-parabola spectral model, using best fit parameters.

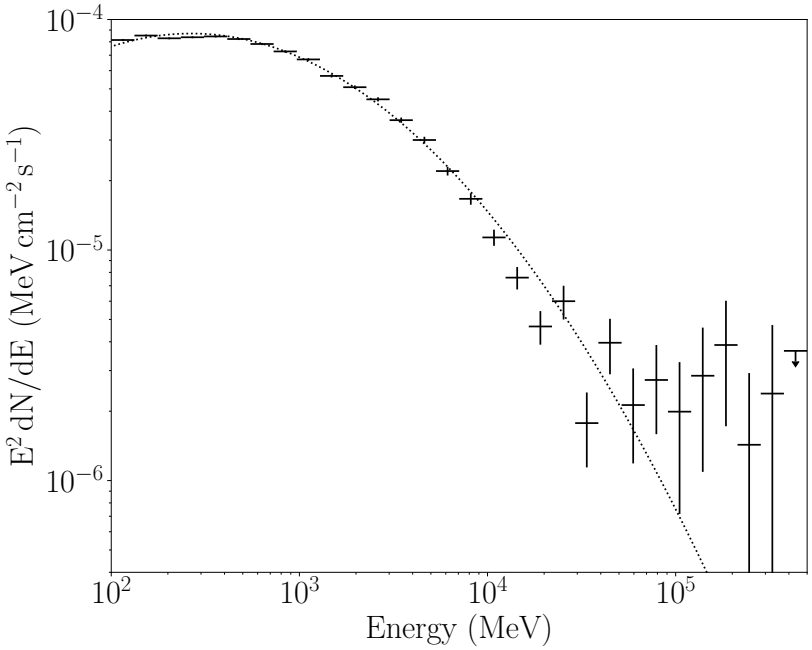

Figure G.11: The spectral energy distribution of the high mass X-ray binary LSI +61 303, with 10 energy bins per decade. Upper limits are placed on any bin where TS < 4. The data is fitted with a log-parabola spectral model, using best fit parameters.

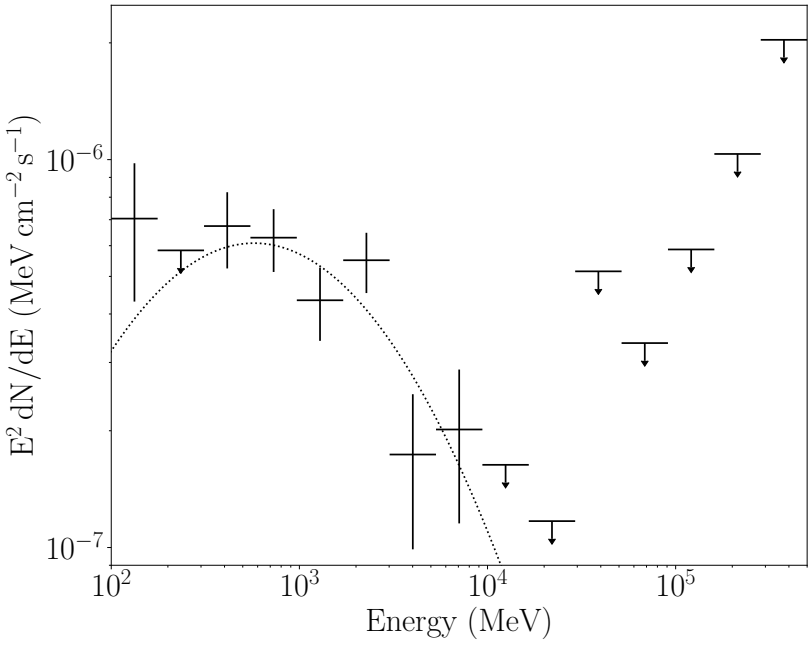

Figure G.12: The spectral energy distribution of the low mass X-ray binary 4FGL J0540.0-7552, with 5 energy bins per decade. Upper limits are placed on any bin where TS < 4. The data is fitted with a log-parabola spectral model, using best fit parameters.

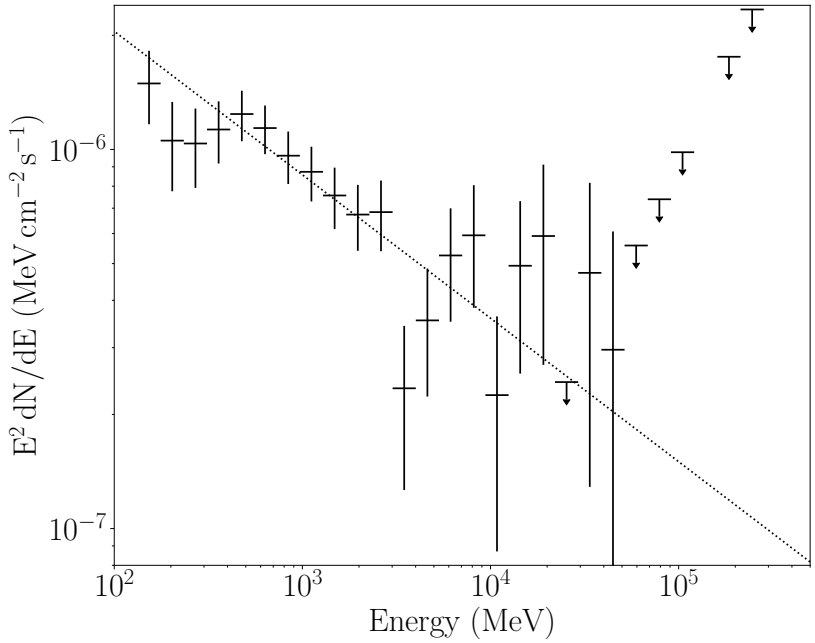

Figure G.13: The spectral energy distribution of the low mass X-ray binary 1SXPS J042749.2-670434, with 10 energy bins per decade. Upper limits are placed on any bin where TS < 4. The data is fitted with a power-law spectral model, using best fit parameters.

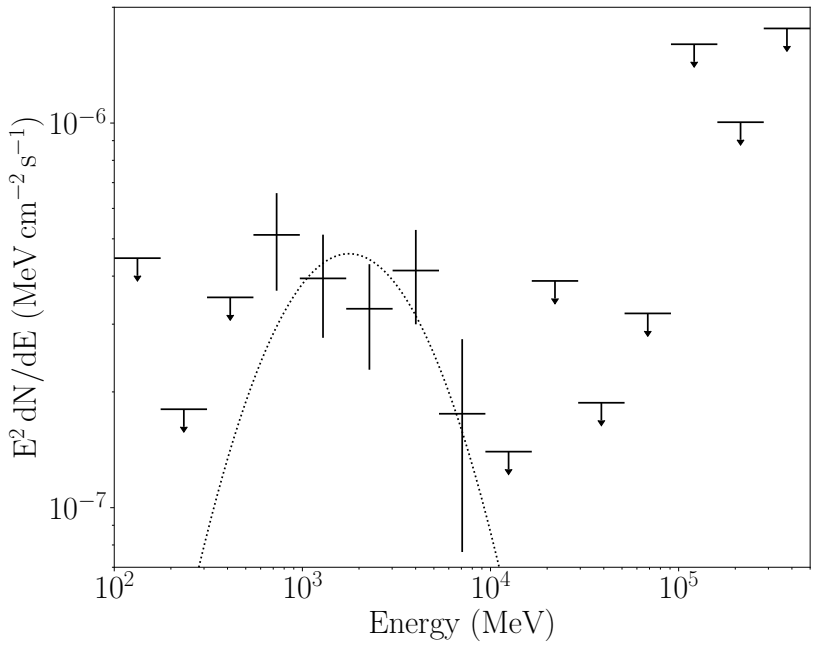

Figure G.14: The spectral energy distribution of the low mass X-ray binary 2S 0921-63, with 5 energy bins per decade. Upper limits are placed on any bin where TS < 4. The data is fitted with a log-parabola spectral model, using best fit parameters.

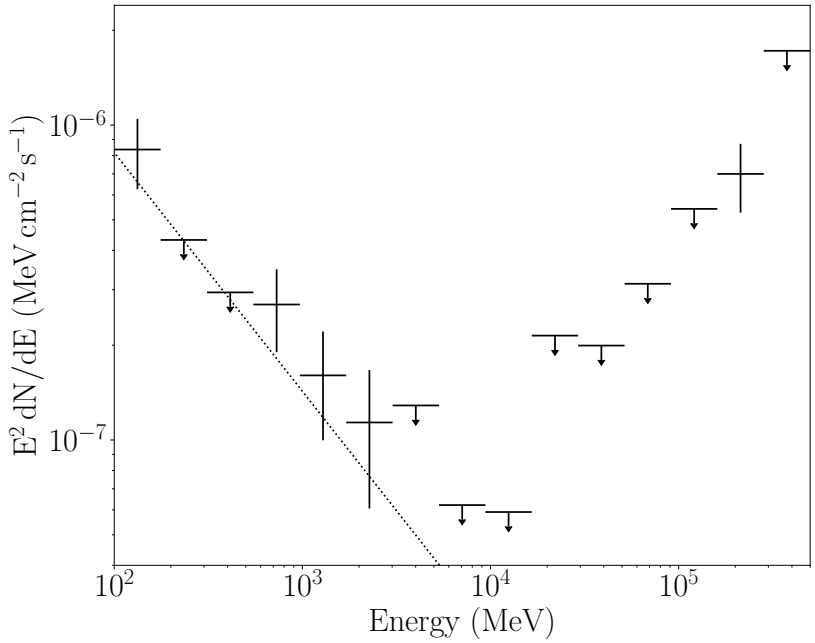

Figure G.15: The spectral energy distribution of the low mass X-ray binary 4FGL J0407.7-5702, with 5 energy bins per decade. Upper limits are placed on any bin where TS < 4. The data is fitted with a power-law spectral model, using best fit parameters.

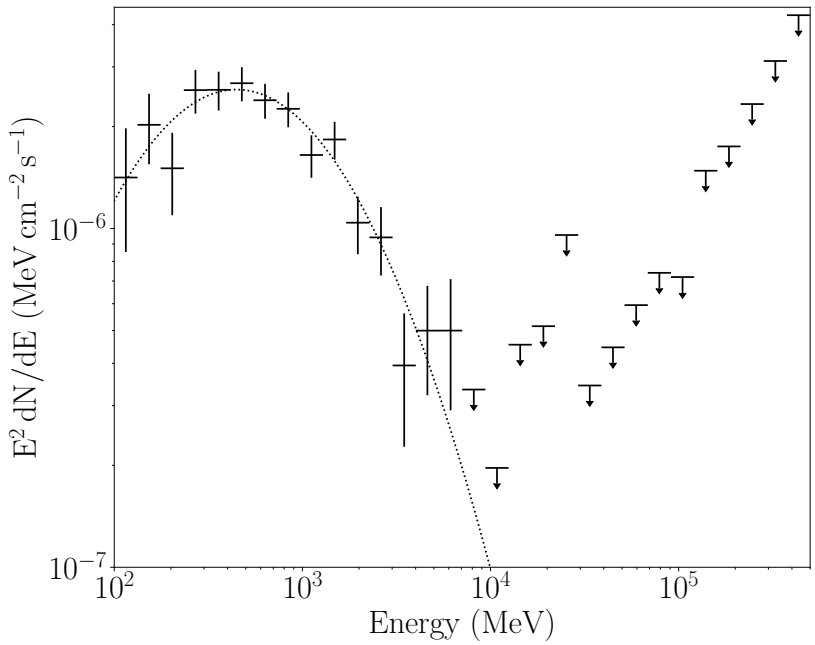

Figure G.16: The spectral energy distribution of the low mass X-ray binary 1RXS J154439.4-112820, with 10 energy bins per decade. Upper limits are placed on any bin where TS < 4. The data is fitted with a log-parabola spectral model, using best fit parameters.

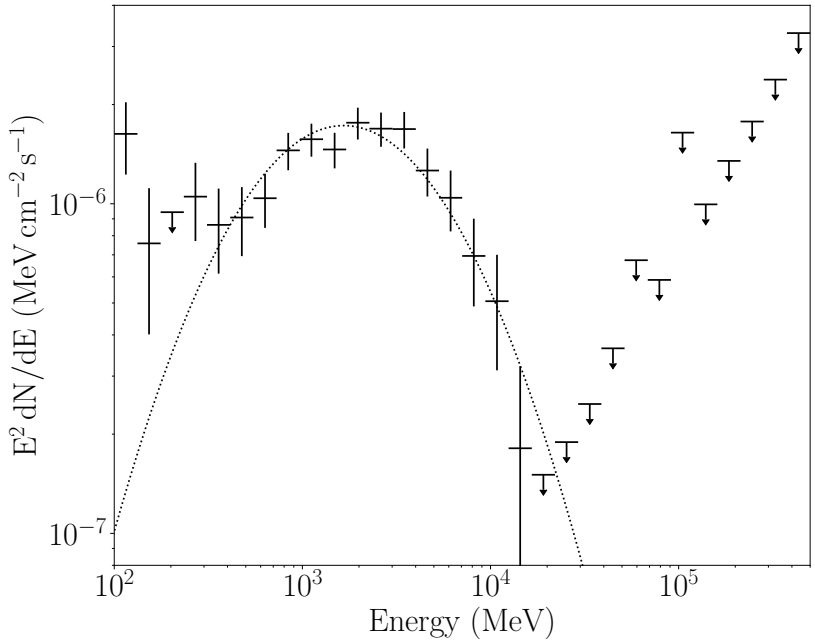

Figure G.17: The spectral energy distribution of the low mass X-ray binary 4FGL J0336.0+7502, with 10 energy bins per decade. Upper limits are placed on any bin where TS < 4. The data is fitted with a log-parabola spectral model, using best fit parameters.

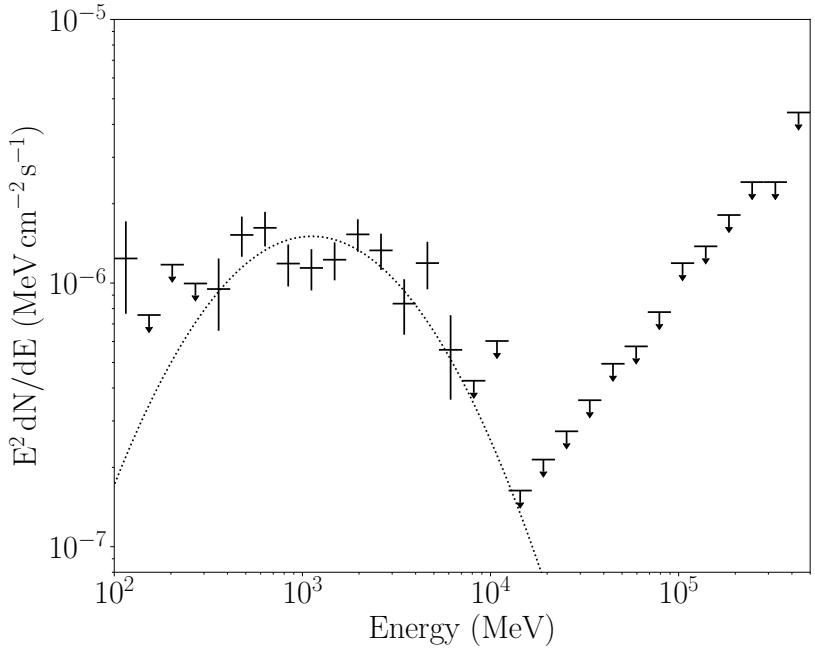

Figure G.18: The spectral energy distribution of the low mass X-ray binary 2SXPS J094023.5-7610, with 10 energy bins per decade. Upper limits are placed on any bin where TS < 4. The data is fitted with a log-parabola spectral model, using best fit parameters.

Appendix H

X-ray Binary Light-Curves

This Appendix contains the energy flux light-curves of the known γ-ray emitting X-ray binaries which are analysed in Chapter 9 with a 13 year dataset. In each light-curve, 25 bins are used of equal size, and the bins do not overlap. In addition to the energy flux values of each bin, the respective TS value of each bin is also shown. The variability of index for each light-curve can be found in the 4FGL, and gives a statistical measure of how variable each XRB is.

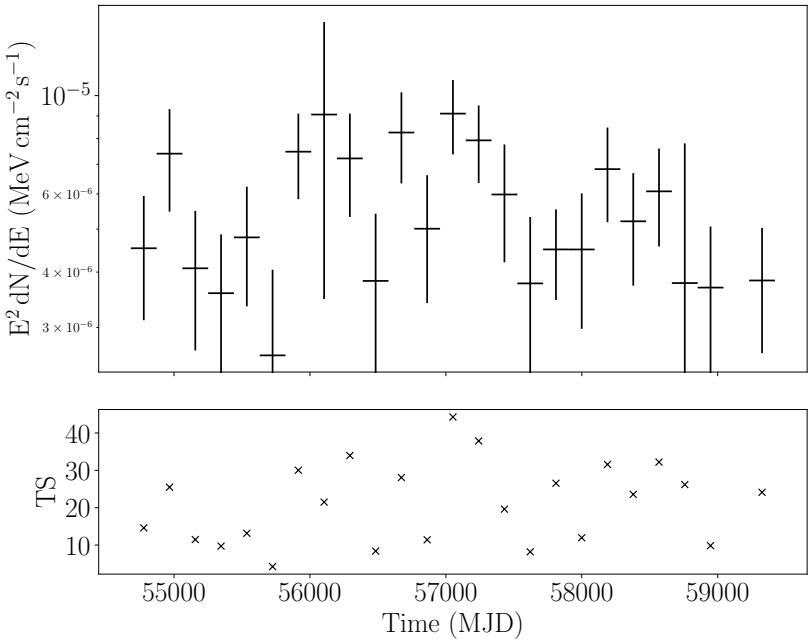

Figure H.1: The light-curve of the extragalactic high mass X-ray binary LMC P3. The upper panel shows energy flux, the lower panel shows TS. Upper limits are placed on any bin where TS < 4.

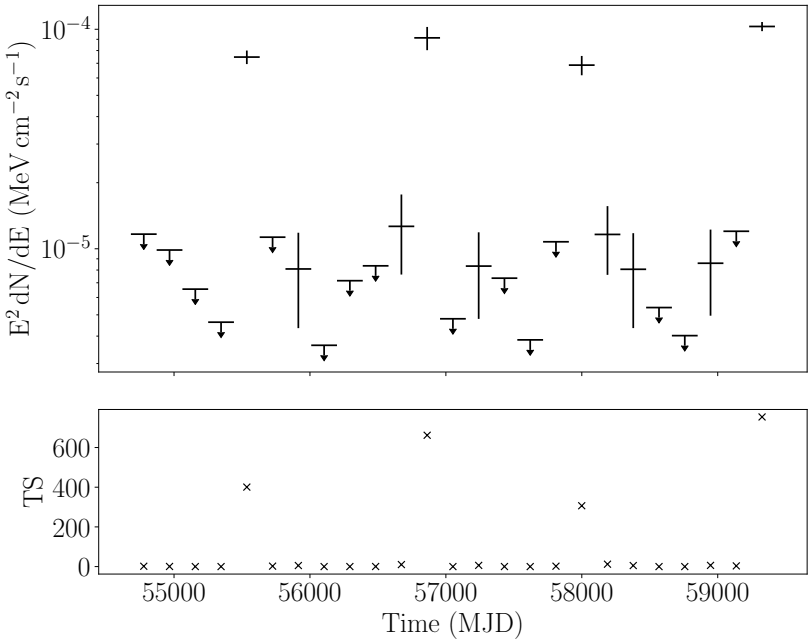

Figure H.2: The light-curve of the high mass X-ray binary PSR B1259-63. The upper panel shows energy flux, the lower panel shows TS. Upper limits are placed on any bin where TS < 4.

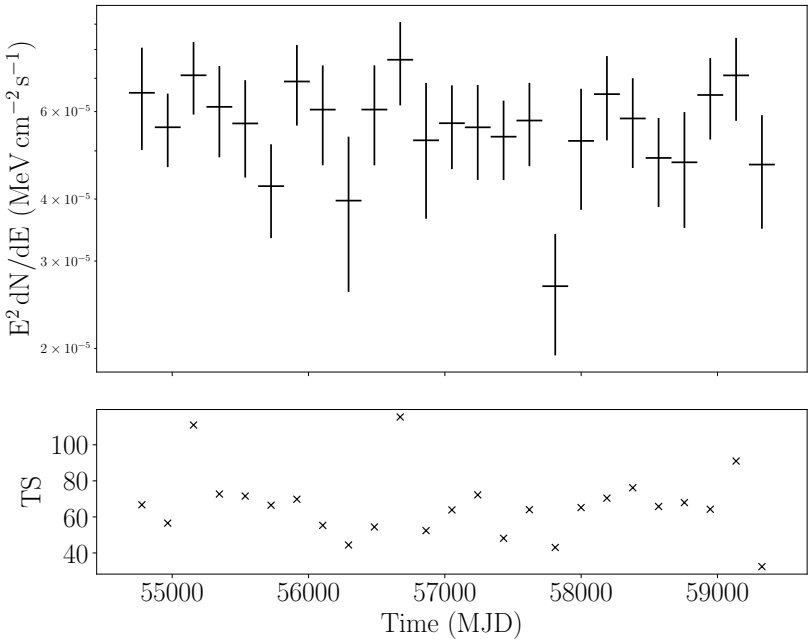

Figure H.3: The light-curve of the high mass X-ray binary 4FGL J1405.1-6119. The upper panel shows energy flux, the lower panel shows TS. Upper limits are placed on any bin where TS < 4.

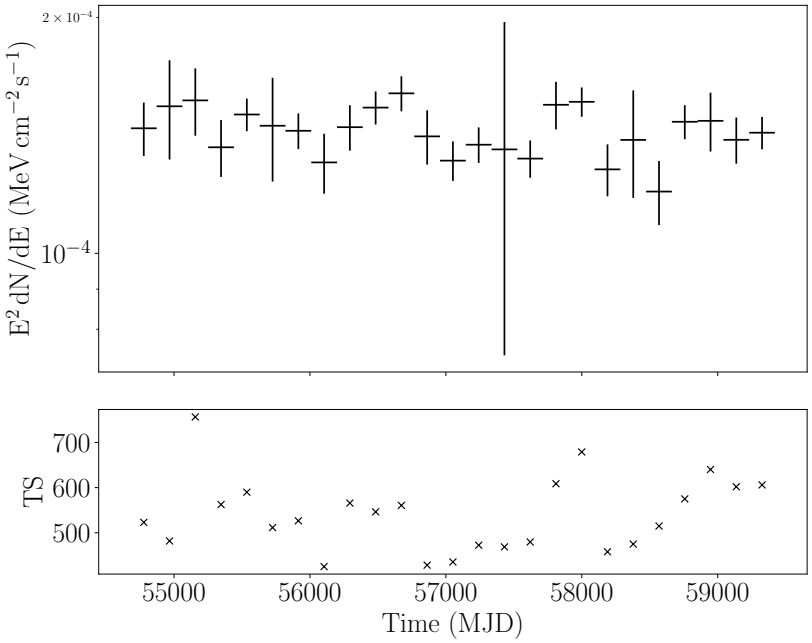

Figure H.4: The light-curve of the high mass X-ray binary 4FGL J1405.1-6119. The upper panel shows energy flux, the lower panel shows TS. Upper limits are placed on any bin where TS < 4.

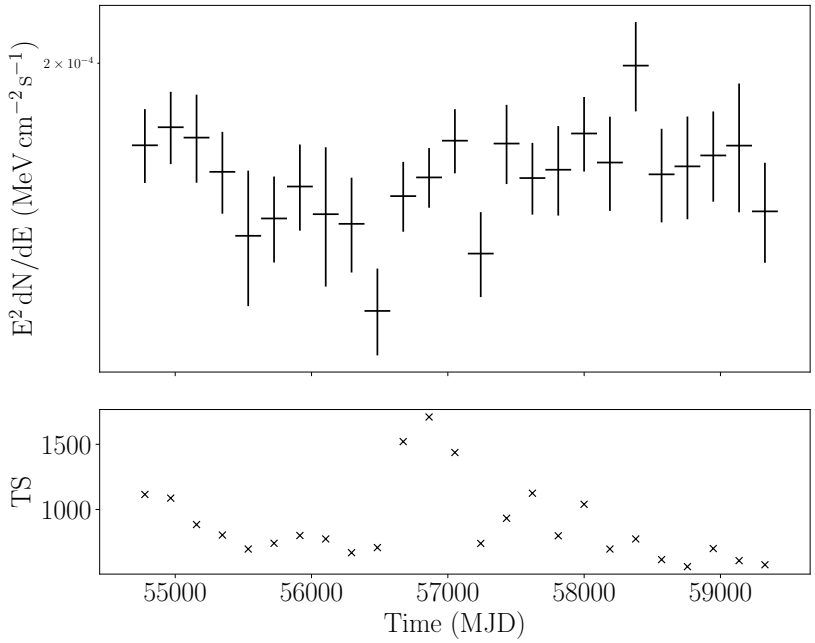

Figure H.5: The light-curve of the high mass X-ray binary LS 5039. The upper panel shows energy flux, the lower panel shows TS. Upper limits are placed on any bin where TS < 4.

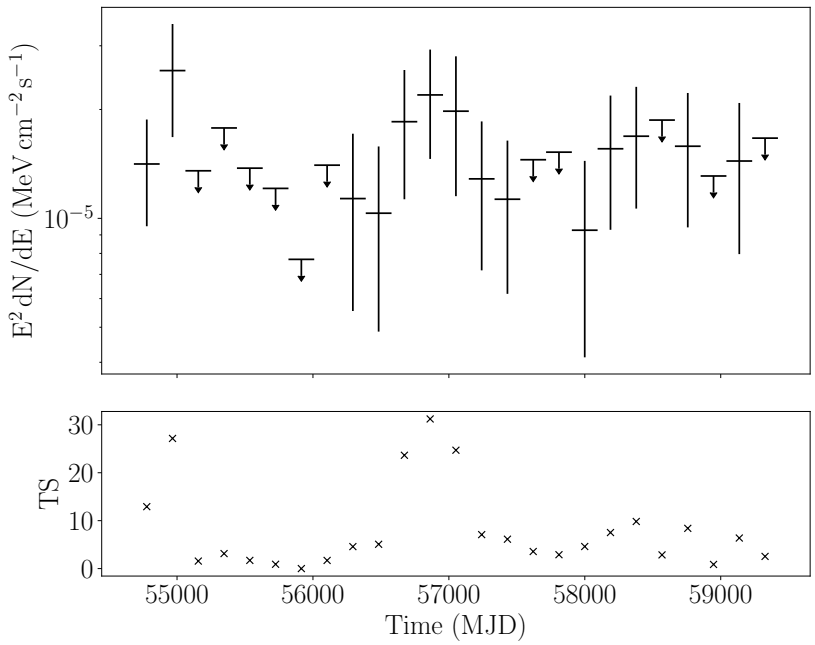

Figure H.6: The light-curve of the high mass X-ray binary HESS J1832-093. The upper panel shows energy flux, the lower panel shows TS. Upper limits are placed on any bin where TS < 4.

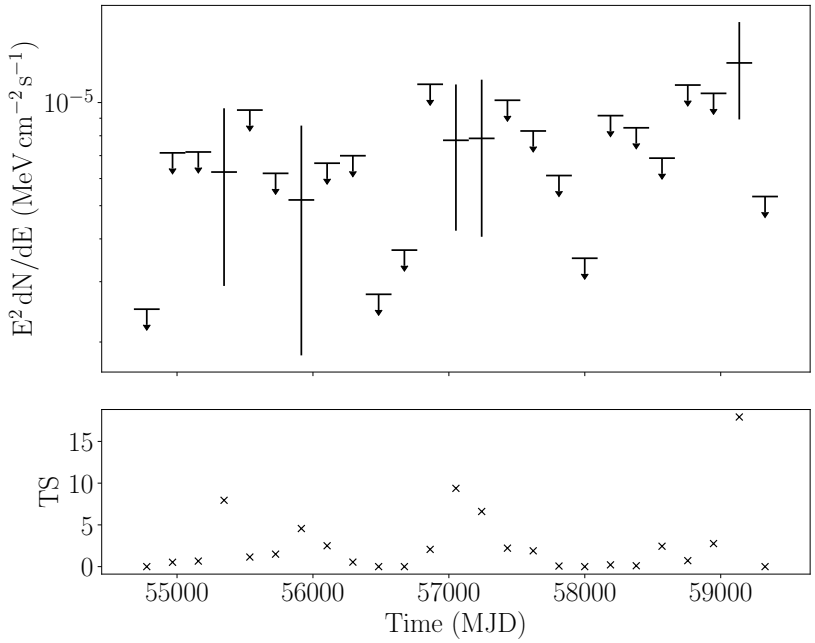

Figure H.7: The light-curve of the high mass X-ray binary HESS J0632+057. The upper panel shows energy flux, the lower panel shows TS. Upper limits are placed on any bin where TS < 4.

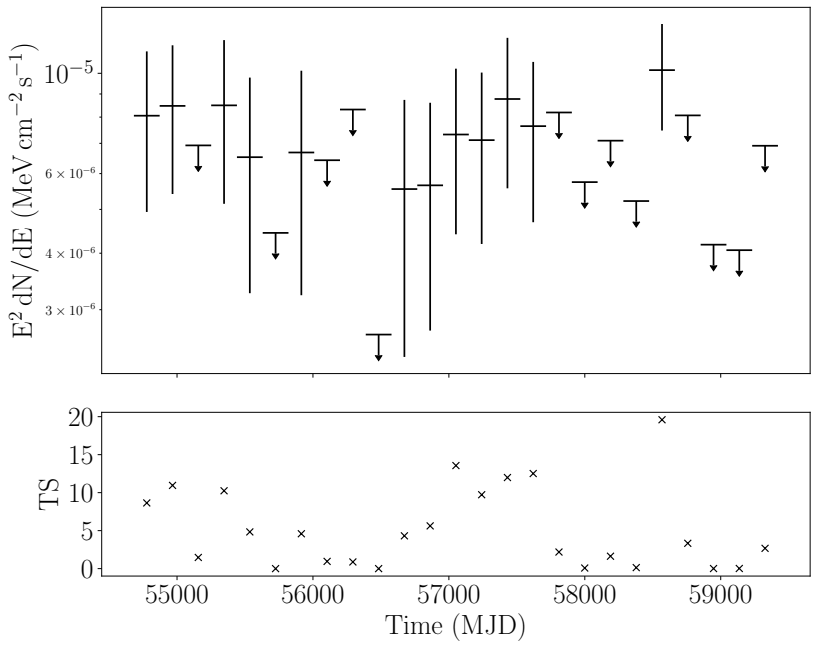

Figure H.8: The light-curve of the high mass X-ray binary Cyg X-1. The upper panel shows energy flux, the lower panel shows TS. Upper limits are placed on any bin where TS < 4.

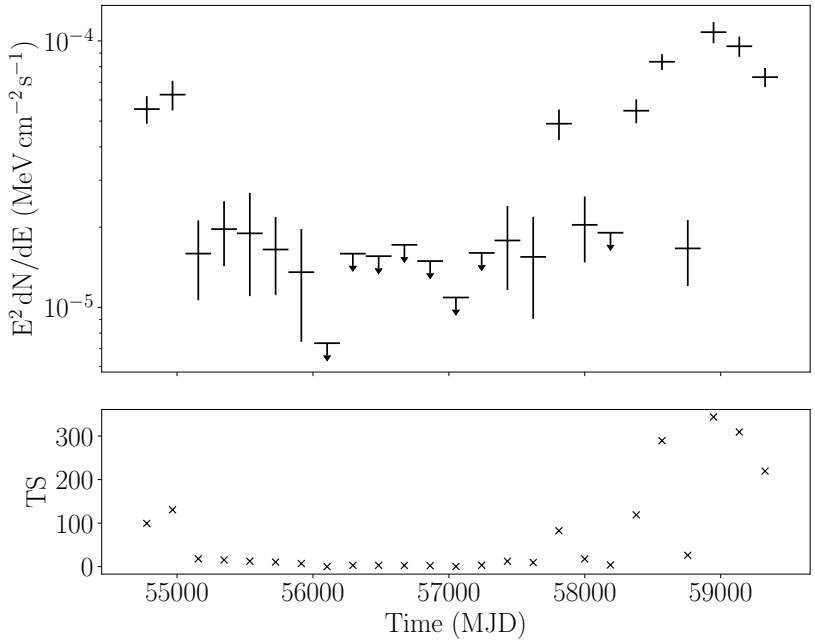

Figure H.9: The light-curve of the high mass X-ray binary Cyg X-3. The upper panel shows energy flux, the lower panel shows TS. Upper limits are placed on any bin where TS < 4.

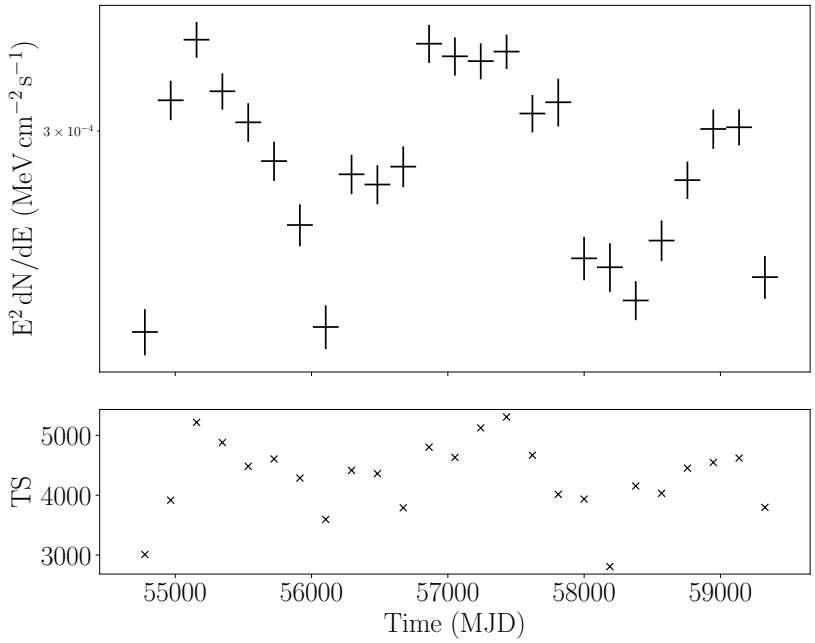

Figure H.10: The light-curve of the high mass X-ray binary LSI +61 303. The upper panel shows energy flux, the lower panel shows TS. Upper limits are placed on any bin where TS < 4.

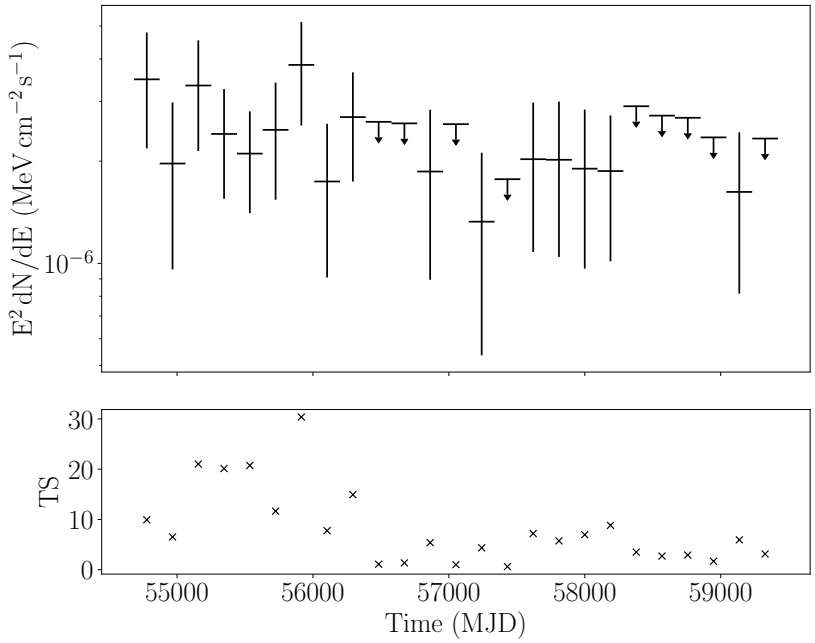

Figure H.11: The light-curve of the low mass X-ray binary 4FGL J0540.0-7552. The upper panel shows energy flux, the lower panel shows TS. Upper limits are placed on any bin where TS < 4.

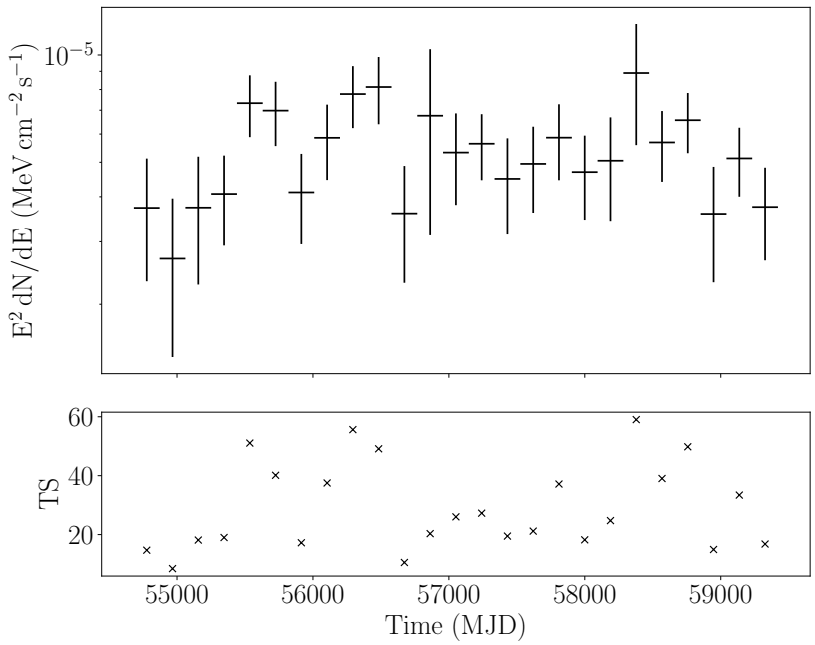

Figure H.12: The light-curve of the low mass X-ray binary 1SXPS J042749.2-670434. The upper panel shows energy flux, the lower panel shows TS. Upper limits are placed on any bin where TS < 4.

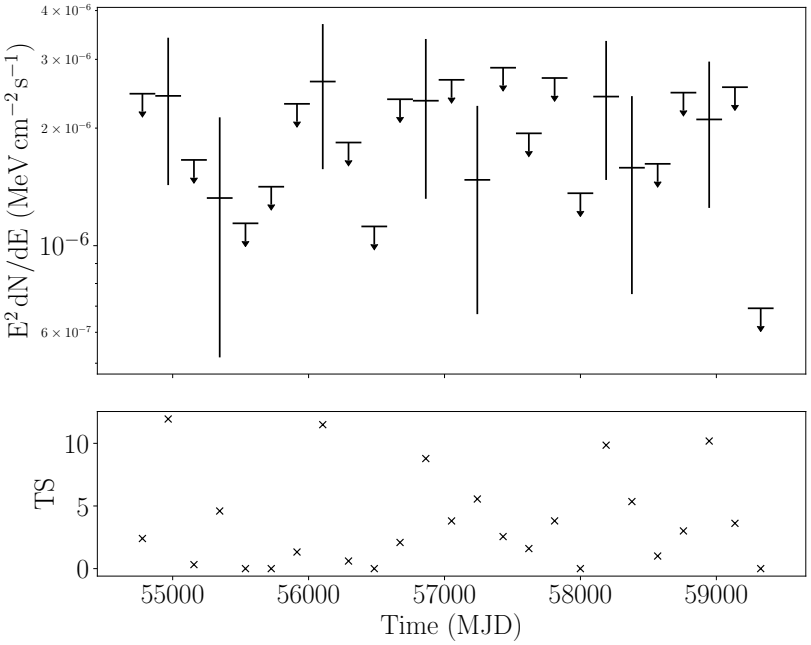

Figure H.13: The light-curve of the low mass X-ray binary 2S 0921-630. The upper panel shows energy flux, the lower panel shows TS. Upper limits are placed on any bin where TS < 4.

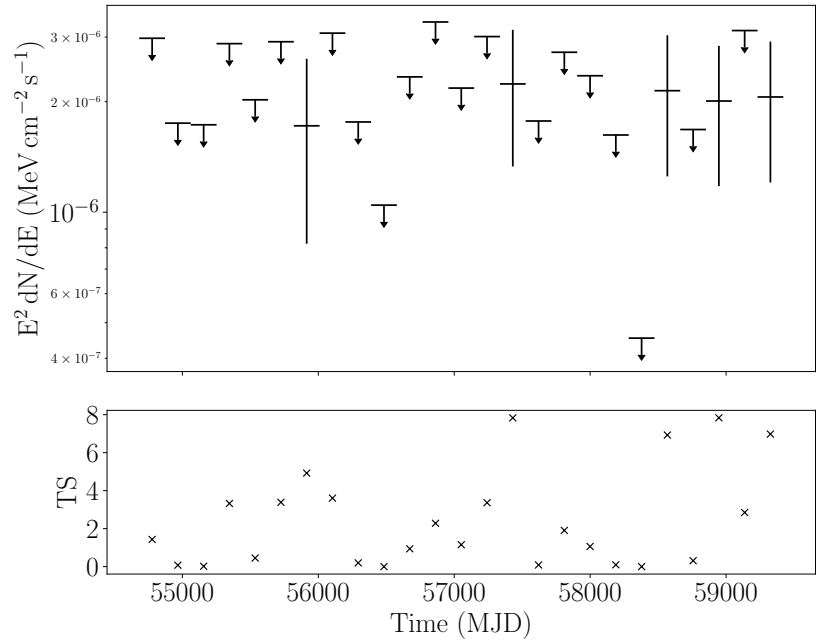

Figure H.14: The light-curve of the low mass X-ray binary 4FGL J0407.7-5702. The upper panel shows energy flux, the lower panel shows TS. Upper limits are placed on any bin where TS < 4.

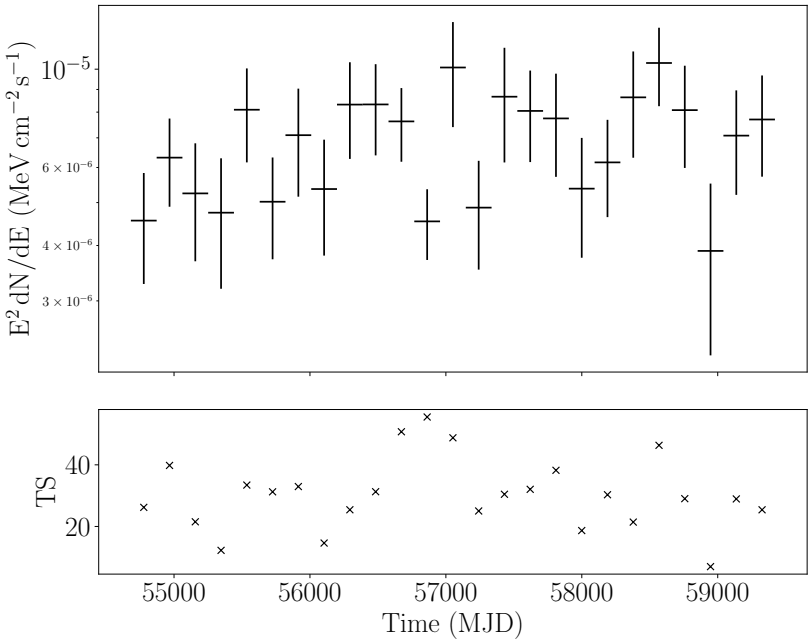

Figure H.15: The light-curve of the low mass X-ray binary 1RXS J154439.4-112820. The upper panel shows energy flux, the lower panel shows TS. Upper limits are placed on any bin where TS < 4.

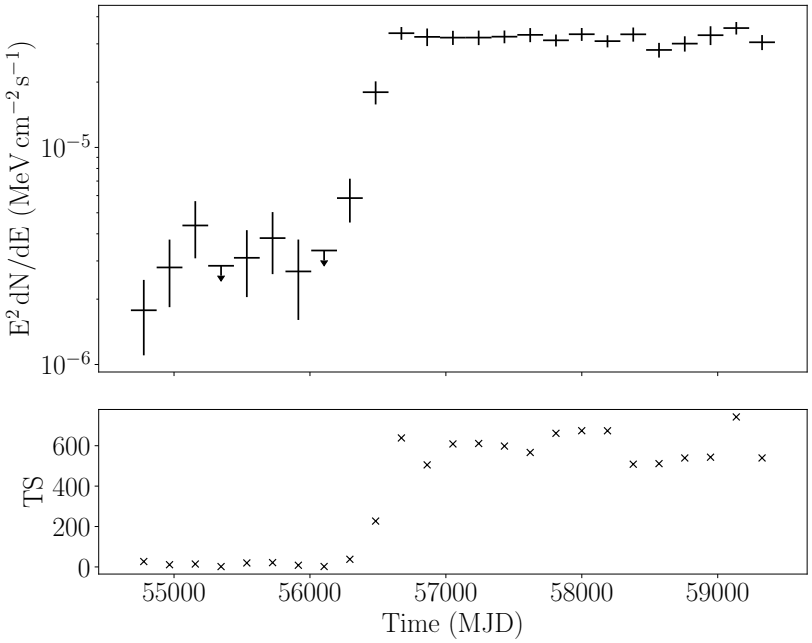

Figure H.16: The light-curve of the low mass X-ray binary PSR+J1023+0038. The upper panel shows energy flux, the lower panel shows TS. Upper limits are placed on any bin where TS < 4.

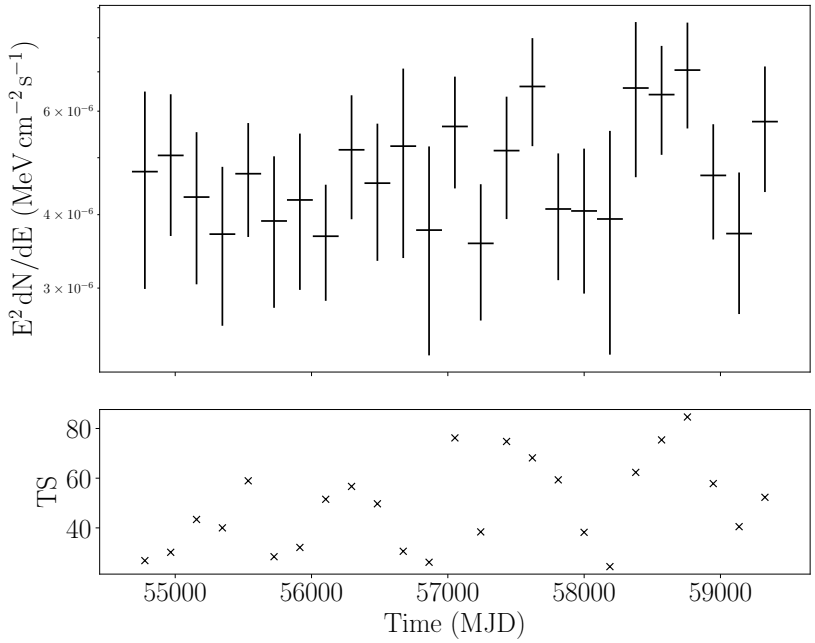

Figure H.17: The light-curve of the low mass X-ray binary 4FGL J0336.0+7502. The upper panel shows energy flux, the lower panel shows TS. Upper limits are placed on any bin where TS < 4.

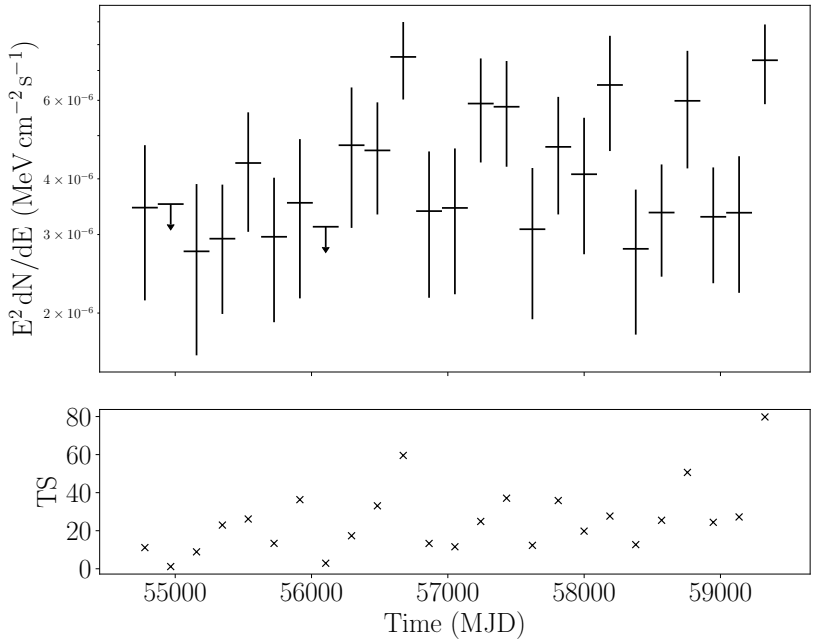

Figure H.18: The light-curve of the low mass X-ray binary 2SXPS J094023.5-761001. The upper panel shows energy flux, the lower panel shows TS. Upper limits are placed on any bin where TS < 4.

Appendix I

Data and Software Accessibility

The production of this thesis has made use of data from a variety of sources, all of which are fully accessible to the public. In addition to this, I have made use of a number of software packages, both written within the `Python 2` language, and otherwise. All of these are listed below with the relevant links to the documentation for each source.

- The *Fermi*-LAT P8R3 photon and spacecraft files, the LAT 8 year extended source templates and the 4FGL-DR2 fits catalogue, available from the LAT data server here: https://fermi.gsfc.nasa.gov/ssc/data/access/
- The *Swift*-BAT precomputed daily X-ray light-curves available from: https://swift.gsfc.nasa.gov/results/transients/
- The MAXI precomputed daily X-ray light-curves available from: http://maxi.riken.jp/top/lc.html
- Optical photometry measurements from the American Association of Variable Star Astronomers (AAVSO), available from the AAVSO data server here: https://www.aavso.org/databases
- The X-ray binary catalogues described in the Liu et al. (2006) and Liu et al. (2007), available in flexible image transfer system (fits) format here:

https://heasarc.gsfc.nasa.gov/W3Browse/all/lmxbcat.html

and here: https://heasarc.gsfc.nasa.gov/w3browse/all/hmxbcat.html

- Data and coordinates have been taken from the SIMBAD online database here:

  https://simbad.unistra.fr/simbad/

I.1 Software

- The `Fermitools` software, version 1.2.23, available here:

  https://github.com/fermi-lat/Fermitools-conda

- The `Fermipy` module, available here:

  https://github.com/fermiPy/fermipy/blob/master/docs/index.rst

- All code has been written in `Python` using the `Anaconda` distribution, and the `Jupyter Notebook` interface. All plots were made with `Matplotlib`. Anaconda and relevant packages can be found here:

  https://www.anaconda.com/

Figure I.1: Having completed the twelve labours in penance; Heracles is speculated to have joined Jason and the Argonauts in their search for the Golden Fleece (pictured). By Jean-Francois Detroy (Year Unknown).

Colophon

This thesis is based on a template developed by Matthew Townson and Andrew Reeves. It was typeset with LaTeX 2_ε. It was created using the *memoir* package, maintained by Lars Madsen, with the *madsen* chapter style. The font used is Latin Modern, derived from fonts designed by Donald E. Kunith.